

ADA035345

TECHNICAL REPORT

12

6

Final Technical Report, 1 11/70-
RESEARCH IN MATERIALS SCIENCE.

Sponsored By

Advanced Research Projects Agency

15

Contract No. N00014-75-C-1084

Order-2994

ADDITION

Best available copy
17 Jul 85

**CENTER FOR
MATERIALS SCIENCE AND ENGINEERING**

**Massachusetts Institute of Technology
Cambridge, Massachusetts 02139**

DISTRIBUTION STATEMENT A
Approved for public release
Distribution Unlimited

DDC
RECEIVED
FEB 7 1977
B

For Period June 1, 1975 - September 30, 1976

Final Technical Report. 1 Jun 75-30 Sep 76

RESEARCH IN MATERIALS SCIENCE.

Sponsored By

Advanced Research Projects Agency

Contract No. N00014-75-C-1084

ARPA Order-2994

ARPA Order No.: 2994
Program Code No.: 5D10

Contractor:

Massachusetts Institute of Technology
Cambridge, Massachusetts 02139

Principal Investigator:

N. J. Grant (617) 253-5638

Approved for public release;
Distribution Unlimited

ACCESSION FOR	
NTIS	White Section <input checked="" type="checkbox"/>
DDC	Bull Section <input type="checkbox"/>
UNANNOUNCED	<input type="checkbox"/>
JUSTIFICATION	
BY	
DISTRIBUTION/AVAILABILITY CODES	
Dist.	AVAIL. and/or SPECIAL
A	

Project Scientists or Engineers:

- I Optoelectronic Materials and Components: Miniaturized Thin Film Laser Sources and Modulators. D. J. Epstein (617) 253-4676
- ii Superconducting Transition Metal Alloys. R. M. Rose (617) 253-3230
M. MacVicar (617) 253-6261
- III Chemical Synthesis Using High Temperature Lithium Vapor Species.
R. Lagow (617) 253-5617

Effective Date of Contract: June 1, 1975
Contract Expiration Date: September 30, 1976
Amount of Contract: \$325,000

The views and conclusions contained in this document are those of the authors and should not be interpreted as necessarily representing the official policies, either expressed or implied of the Advanced Research Projects Agency or the U.S. Government.

Form Approved Budget Bureau No. 22R0293

077400

FINAL TECHNICAL REPORT

Period: June 1, 1975 - September 30, 1976

Title: Research in Materials Science

Project Title: Optoelectronic Materials and Components:
Miniaturized Laser Sources and Thin Film
Modulators

Contract Number: N00014-75-C-1084

ARPA Order No.: 2994

Program Code No.: 5D10

Name of Contractor: Massachusetts Institute of Technology
Cambridge, Massachusetts 02139

Principal Investigator: N.J. Grant - (617) 253-5638

Project Scientists
or Engineers: D.J. Epstein - (617) 253-4676
C.G. Fonstad - (617) 253-4634
H.P. Jenssen - (617) 253-6878
A. Linz - (617) 253-3208

Effective Date of
Contract: June 1, 1975

Contract Expiration
Date: September 30, 1976

Amount of Contract: \$325,000

Amount of Project: \$140,000

Sponsored by:

Advanced Research Projects Agency

ARPA Order No. 2994

The views and conclusions contained in this document are those of the authors and should not be interpreted as necessarily representing the official policies, either expressed or implied, of the Advanced Research Projects Agency or the U.S. Government.

OPTOELECTRONIC MATERIALS AND COMPONENTS:
MINIATURIZED LASERS AND THIN FILM MODULATORS

TABLE OF CONTENTS

	PAGE
I. INTRODUCTION	1
II. MINILASER DEVELOPMENT.	6
III. DIODE PUMPS.	9
IV. KTN THIN FILMS	16
V. PREPARATION OF FEED MATERIALS.	18
VI. PUBLICATIONS AND TALKS	19

ATTACHMENT I: Ph.D. Thesis by D.E. Castleberry,
"Energy Transfer in Sensitized Rare Earth Lasers".

ATTACHMENT II: Ph.D. Thesis by R.E. Fontana, Jr.,
"Potassium Tantalate Niobate Thin Films for
Integrated Optics Applications".

OPTOELECTRONIC MATERIAL AND COMPONENTS: MINIATURIZED LASERS AND THIN FILM MODULATORS

I. INTRODUCTION

In an official sense this report covers a contract that was initiated June 1, 1975, and concluded September 30, 1976. However, in substance, the research was begun under a contract that started on June 1, 1973, under ARPA support. As of May 31, 1975 responsibility for monitoring the program was transferred from ARPA to ONR and at that time a "new" contract was formally initiated. The research itself, however, continued through the transition without interruption.

On May 31, 1975, a "Final Technical Report" was issued that described accomplishments during the first two years of the research program. This present report has been prepared as an update of the earlier one. Certain necessary connections with the earlier report are made here, but it was not felt necessary to repeat many of the details presented previously. Consequently, to get a fully detailed view of the overall program it is necessary to read this report along with the earlier one. There are, however, two major sectors of the overall research that are fully documented in the form of Ph.D. theses that were begun and completed during the course of the total program. These are included as attachments to the present report, their titles and authors are: (1) "Energy Transfer in Sensitized Rare-Earth Lasers", D.E. Castleberry; (2) "Potassium-Tantalate-Niobate Thin Films for Integrated Optics Applications", R.E. Fontana, Jr.

The objectives of the overall program, as stated in our original proposal, were the following: (1) development of rare earth doped fluorides and oxide materials suitable for optically pumped miniaturized lasers; (2) the development of LED pumps for these lasers; (3) growth and evaluation of electrooptical thin films for optical modulators.

With regard to item (1) we decided at an early stage in the program to confine our principal effort to fluorides; where we anticipated that prospects for developing a successful minilaser were somewhat better than for oxide hosts. Our fluoride program did indeed prove successful as the reader will verify by referring to D.E. Castleberry's Ph.D. thesis, in particular to his Ch. 4. The development of oxide minilasers would have required a study of energy transfer in oxide hosts comparable to Castleberry's work on fluorides, but there was simply no time for an effort of such magnitude within this program. It remains, however, a challenging task for future study.

On item (3) we met the targets set forth in our proposal. We demonstrated that KTN films of reasonably good optical quality could be grown and that they were characterized by good electrooptical performance. Our work has opened up a number of interesting questions that must ultimately be faced. The dielectric properties of the films differ from bulk material of the same composition. Presumably the difference is caused by clamping of the film by the substrate. A systematic study of film versus bulk dielectric behavior for KTN, in particular, and for ferroelectrics in general would contribute not only to an understanding of the physics of thin film ferroelectrics but would provide a better basis for designing such films for dielectric and optical use. Our work has also pointed up a recurring problem encountered with waveguide films. Examination of the published literature shows that as the difference in index between film and substrate increases the optical losses begin to rise, and it is not atypical to find losses that run 5-20 db/cm. (Compare this with losses of 2 db/km obtained in glass fibers!). A possible source of the loss is again the lattice mismatch between film and substrate. The KTN system provides an excellent vehicle for testing this hypothesis because within this system it is possible to fabricate film and substrate combinations with well controlled lattice mismatch.

Our LED program, cited as item (2) above, had only partial success. We were able to fabricate a number of diodes having a emission spectrum matched to the pump bands of a sensitized Ho:YLF laser crystal.

We were not able, however, to develop diodes with sufficient output to provide the required pump power for laser operation at room temperature. It would have been a much easier task to design an LED pumped minilaser for operation at liquid nitrogen temperature (because of the reduced laser threshold at low temperature), but this option was ruled out based on our view that it was more important technologically to achieve operation at room temperature, and that to build a low temperature laser as an intermediate step would have been more an academic exercise than a sound engineering goal. Our diode problems have been fabrication difficulties associated with obtaining lower resistance contacts and better heat transfer from the diodes. We still believe that our original design goals can be met and, in fact, are continuing the LED development program under different sponsorship.

In our LED program we investigated a number of different material systems as likely candidates for pump diodes: GaAs:Si, GaAs_{1-x}Sb_x and the quaternary system Al-Ga-As-Sb. What may turn out to be a very important spinoff from our program is the recognition that diodes based on this quaternary system appear to be excellent candidates for LED's and lasers operating at 1.2 μ m, a wavelength that is of particular importance because fibers for optical communication have both low loss and low index dispersion at this wavelength.

Our experiences during this program have served to reaffirm what most of us already know about the synergistic benefits of carrying on materials research in an application context. The history of our work with the YLF:Ho laser is a good case in point. We began this program with a background of prior success in developing YLF as a successful host for flash-pumped lasers, and we believed that we had enough knowledge of material parameters to allow a reasonable stretch of previous calculations to the design of a minilaser. But the stretch was in fact beyond our prior knowledge. The role of upconversion losses in the energy transfer process (see Castleberry's thesis), which had not previously been taken into account, became crucial in the development of a cw minilaser. The net result has been a far better

understanding of energy-transfer lasers, an understanding essential for minilaser development but one that will also lead to the design of more efficient conventional lasers. Our experiences in the LED and thin film phases of the program afford comparable examples.

A summary of the principal achievements of the program is given in Table I.

Table I
Principal Accomplishments

I. Miniaturized Laser Sources

1. CW operation at 77°K of a 2.06 μm $\alpha\text{BYLF:Ho}$ minilaser operating in a 0.1mm³ internal reflection mode dielectric cavity.
2. Successful CW operation of LiYbF_4 : Tm, Ho minilaser using incoherent pump.
3. Demonstration of importance of upconversion losses in determining laser threshold.
4. Experimental and theoretical studies of threshold vs. temperature for various minilaser compositions.

II. Light Emitting Diodes

1. Fabrication of GaAs:Si LED's matched to the 0.96 μm pump band of Yb^{3+} .
2. Study of growth parameters for Ga(As,Sb):Si system; fabrication of LED's with emission bandwidth 25% narrower than for comparable GaAs:Si diodes.
3. Exploratory investigation of quaternary system Al-Ga-As-Sb as basis for LED's and lasers in near IR.

III. Electrooptic Thin Films

1. Growth by liquid phase epitaxy of KTN thin film waveguides.
2. Development of thin film modulator providing full modulation at 8 volts drive.
3. Demonstration of feasibility of growing multilayer electrooptic films.

II. MINILASER DEVELOPMENT

2.1 Sensitized Lasers

Miniaturized rare earth lasers are of potential importance as optical sources for communication and for integrated optics. In order to make an efficient minilaser it is necessary to have a large absorption coefficient at the pump wavelength. Typically, the largest peak absorption coefficient for useful pumping within the 4f levels in "100% doped" rare earth crystals is $\alpha^{-1} = 100 \mu\text{m}$. Thus, a miniaturized laser might have a dimension of this order in the pumping direction. However, "100% doped" rare earth crystal do not always work. For example, in laser hosts containing Nd^{3+} as the active ion, as the Nd^{3+} concentration is increased and the Nd^{3+} - Nd^{3+} separation decreases, ion-pair energy transfer occurs which quenches the upper laser level. In most hosts for Nd^{3+} , e.g. $\text{Y}_3\text{Al}_5\text{O}_{12}$ or LiYF_4 , significant quenching occurs at a Nd^{3+} doping of about 2%. Only in special hosts, where the rare earth sites are well separated, as in $\text{NdP}_5\text{O}_{14}$, does 100% doping work, and, indeed, in this material cw lasing in a crystalline fiber of $\text{Nd}_{0.5}\text{La}_{0.5}\text{P}_5\text{O}_{14}$, 0.68mm long and $12 \times 12 \mu\text{m}$ in cross section, has been reported (with a laser used as a pump source). However, Nd laser materials have the disadvantage of pump absorption bands that are relatively narrow, consequently, pumping with incoherent sources can be relatively inefficient. Sensitized lasers overcome these difficulties by incorporating into the host appropriate sensitizers that are specifically tailored to absorb the pump light and to effect efficient energy transfer to the active lasing ions. Sensitized laser materials have the advantage that "100% doping" of sensitizer ions can be achieved in many hosts and greater flexibility exists in picking ions to match a pump source. In Table II we show the richness of choice that exists in designing sensitized rare earth lasers.

2.2 Upconversion Processes

A major part of our research program was concerned with acquiring a

Table II
Activator-Sensitizer Combinations for
LED Pumped Lasers

Activator Ions	Sensitizer Ions	Laser Wavelengths	Pump Band
$\text{Ho}^{3+} \quad 5I_7 - 5I_8$	Er^{3+}	$2 \mu\text{m}$	$1.50 \mu\text{m}$
$\text{Ho}^{3+} \quad 5I_7 - 5I_8$	Ni^{2+}	$2 \mu\text{m}$	$1.20 \mu\text{m}$
$\text{Ho}^{3+} \quad 5I_7 - 5I_8$	Yb^{3+}	$2 \mu\text{m}$	$0.96 \mu\text{m}$
$\text{Tm}^{3+} \quad 3H_4 - 3H_6$	Er^{3+}	$1.8 - 1.9 \mu\text{m}$	$1.50 \mu\text{m}$
$\text{Tm}^{3+} \quad 3H_4 - 3H_6$	Yb^{3+}	$1.8 - 1.9 \mu\text{m}$	$0.96 \mu\text{m}$
$\text{Tm}^{3+} \quad 3F_4 - 3H_6$	Yb^{3+}	$\sim 1.5 \mu\text{m}$	$0.96 \mu\text{m}$
$\text{Tm}^{3+} \quad 3F_4 - 3H_5$	Cr^{3+}	$2.3 \mu\text{m}$	$0.65 \mu\text{m}$
$\text{Tm}^{3+} \quad 3F_4 - 3H_5$	Yb^{3+}	$2.3 \mu\text{m}$	$0.96 \mu\text{m}$
$\text{Nd}^{3+} \quad 4F_{3/2} - 4I_{11/2}$	Cr^{3+}	$1.06 \mu\text{m}$	$0.65 \mu\text{m}$

thorough understanding of energy transfer in sensitized rare earth lasers. It became evident at an early stage in our work that upconversion processes played a very important role in those laser systems of special interest to us: Ho^{3+} lasers containing Er^{3+} , Yb^{3+} and Tm^{3+} . The effect of upconversion in decreasing the efficiency of energy transfer and, thereby, degrading overall laser efficiency had not previously been recognized. This oversight is no doubt owing to the fact that the upconversion process is a nonlinear function of pumping rate and its effect on transfer efficiency is not seen at the low pumping rates used to carry out the usual spectroscopic measurements employed in evaluating laser materials. It is only at the high pump rates needed for laser operation that upconversion enters significantly enough to reduce energy-transfer efficiency, often to such an adverse extent that laser operation is never attained.

The reader interested in a more complete story of the issues noted above is referred to the Ph.D. thesis by D.E. Castleberry which is included as an Attachment to this final report. In his thesis, titled "Energy Transfer in Sensitized Rare Earth Lasers", Castleberry presents experimental and theoretical studies of energy transfer in LiYF_4 and related hosts containing Ho^{3+} as the lasing ion and containing various sensitizers including Er^{3+} , Yb^{3+} , Tm^{3+} . The relation of these studies to the design of miniaturized lasers is treated in some detail.

III. DIODE PUMPS

3.1 Overview of Program

Our pump diode program, structured as a combined research effort on materials and devices, evolved along the following lines. First, the development of materials tailored to produce a diode emission spectrum matched to the Yb^{3+} pump band at $0.96\mu\text{m}$; next, the design of suitable device geometries and the development of fabrication procedures to realize them; and finally, the testing and evaluation of diode prototypes.

The LED's that were built during the program were based on the system GaAs:Si in which silicon enters as an amphoteric dopant. Above $\sim 900^\circ\text{C}$ silicon is an n-type donor while below this temperature it is a p-type acceptor. Because of this feature it is possible to grow p-n junctions in a single step LPE process. Various alternatives to GaAs:Si were also considered, among them $\text{GaAs}_{1-x}\text{Sb}_x\text{:Si}$. The n-p transition for Si in this system was not previously known and our measurements, shown in Fig. 1, represent brand new data. Diodes fabricated from this material system were found to have a narrower emission spectrum than comparable diodes based on GaAs:Si , but unfortunately, had a lower overall efficiency. The system $\text{GaAs}_{1-x}\text{Sb}_x\text{:Si}$ has many attractive features for LED's in the $1\mu\text{m}$ region and it clearly deserves further investigation, primarily to improve the luminous efficiency.

In surveying other likely materials, we concluded that the quaternary system Al-Ga-As-Sb is one of great potential. In this system there exist compositions of different energy gap which have the same lattice constant. As a result it should be possible to grow heterostructure layers which avoid the deleterious effect of dislocations produced by lattice mismatch.

3.2 GaAs:Si Diodes

Our objective was the development of an LED capable of delivering enough power to the $0.96\mu\text{m}$ pump bands of Yb^{3+} to obtain cw room temperature laser operation

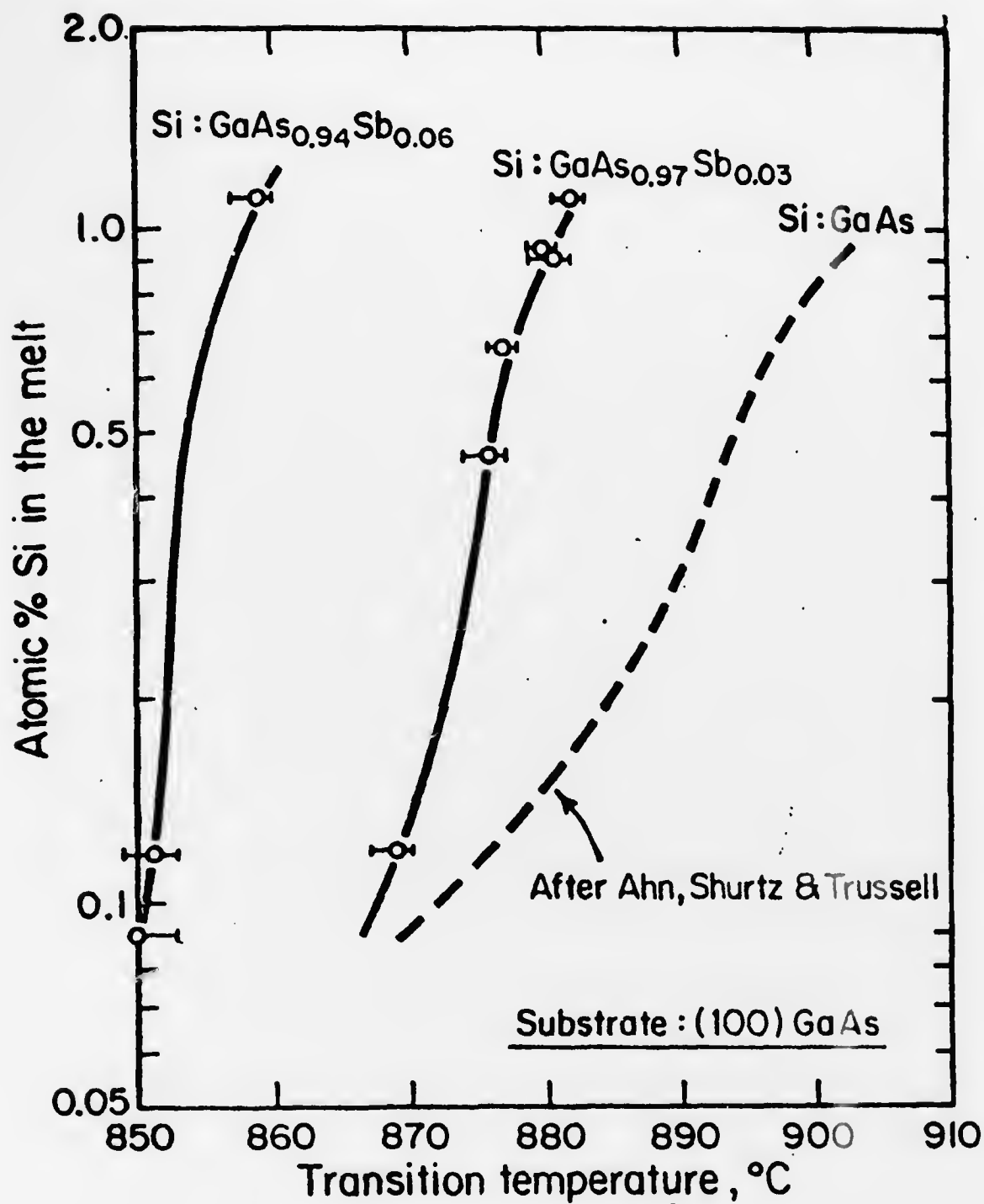


Fig. 1 The n- to p-type transition for amphoteric Si in GaAs_{1-x}Sb_x as a function of Si concentration in the melt.

in a small amount of LIVE TEXT

Page Not available

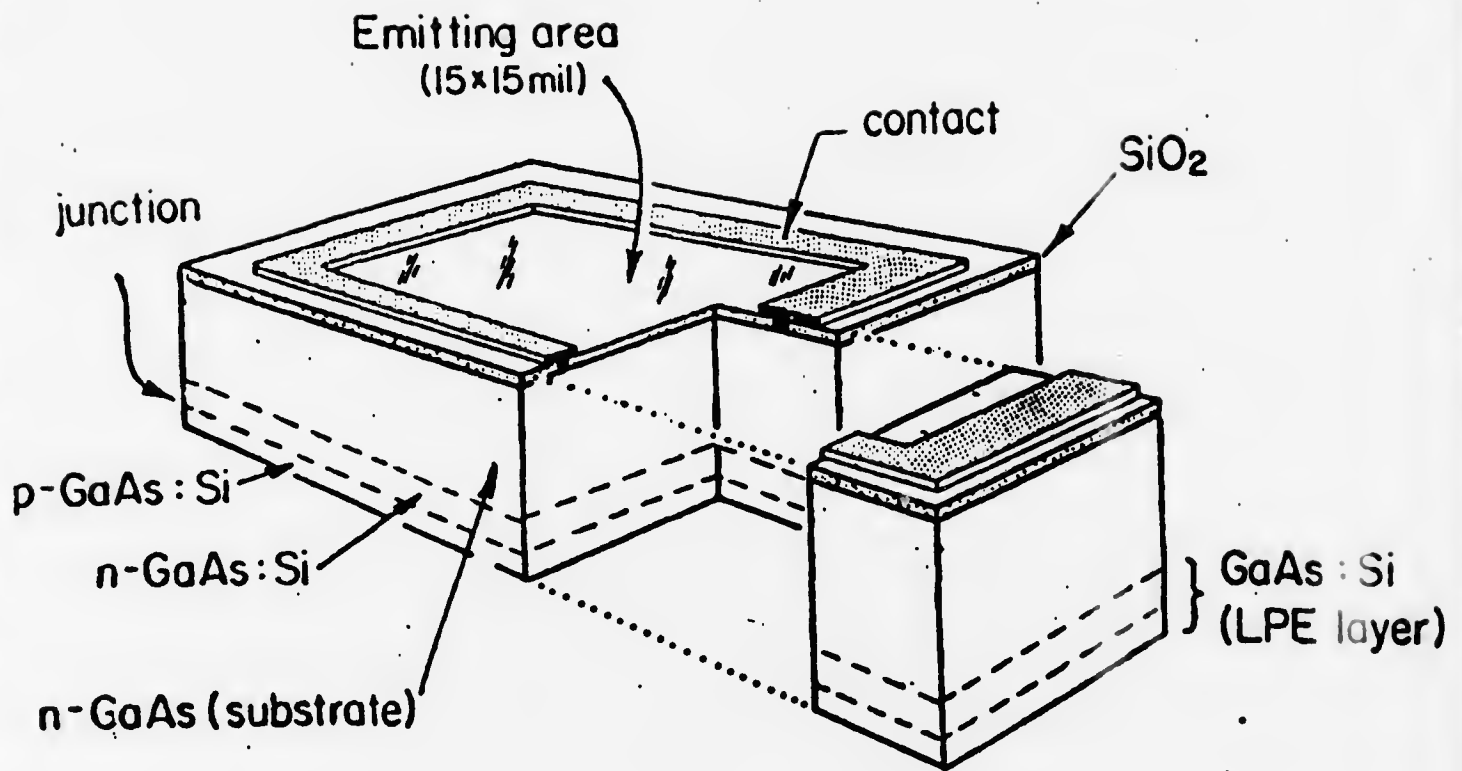


Fig. 2 Cutaway view of pump diode.

sphere, are shown in Fig. 3. The excitation current, in all cases, consisted of a train of 1 msec pulses with 1% duty cycle. The set of points labelled (b) shows the output for the "naked" diode emitting into air. This power includes not only the radiation which leaves the diode through the top emitting surface but also the radiation passing through the side surfaces. In (d) the side emission has been eliminated by coating the edges of the diode with an opaque black paint. The data show that slightly more than half the emission passes through the sides and is, therefore, lost as available pump power.

Diode emission into air is not efficient because only those rays that strike the surface at less than the critical angle can leave the diode. For GaAs the critical angle at the semiconductor - air interface is 16.6° . However, the laser material we intend to pump has an index $n=1.47$; when coupled to this interface the critical angle in GaAs opens up to 24.8° thereby increasing the light-extraction efficiency. This effect is shown by the data points (a) which have been obtained by coating the naked diode with an index oil to simulate contact with the laser crystal. When we correct these results to exclude the radiation lost through the diode edges, we obtain the curve (c), which shows that the desired threshold power of 8 watts/cm^2 can be obtained with a current density of 250 amp/cm^2 , or a total current of 0.5 amp. Because the energy of the transition is 1.2 volts the minimum power into the diode is 0.6 watt. In our diodes because of somewhat excessive contact resistance the dissipation at 0.5 amp input has been about 1 watt.

The external quantum efficiency of the diode in Fig. 3 was 2.2% for the naked diode emitting into air and 4.1% when coated with the index oil. When we exclude edge emission the external efficiency drops to about 2.2%.

Although we have not put together an operating minilaser, all the evidence we have confirms that our basic design approach has been sound and that our design goals are entirely feasible. We have previously noted that we will be continuing the LED program under different sponsorship and we have every expectation that the

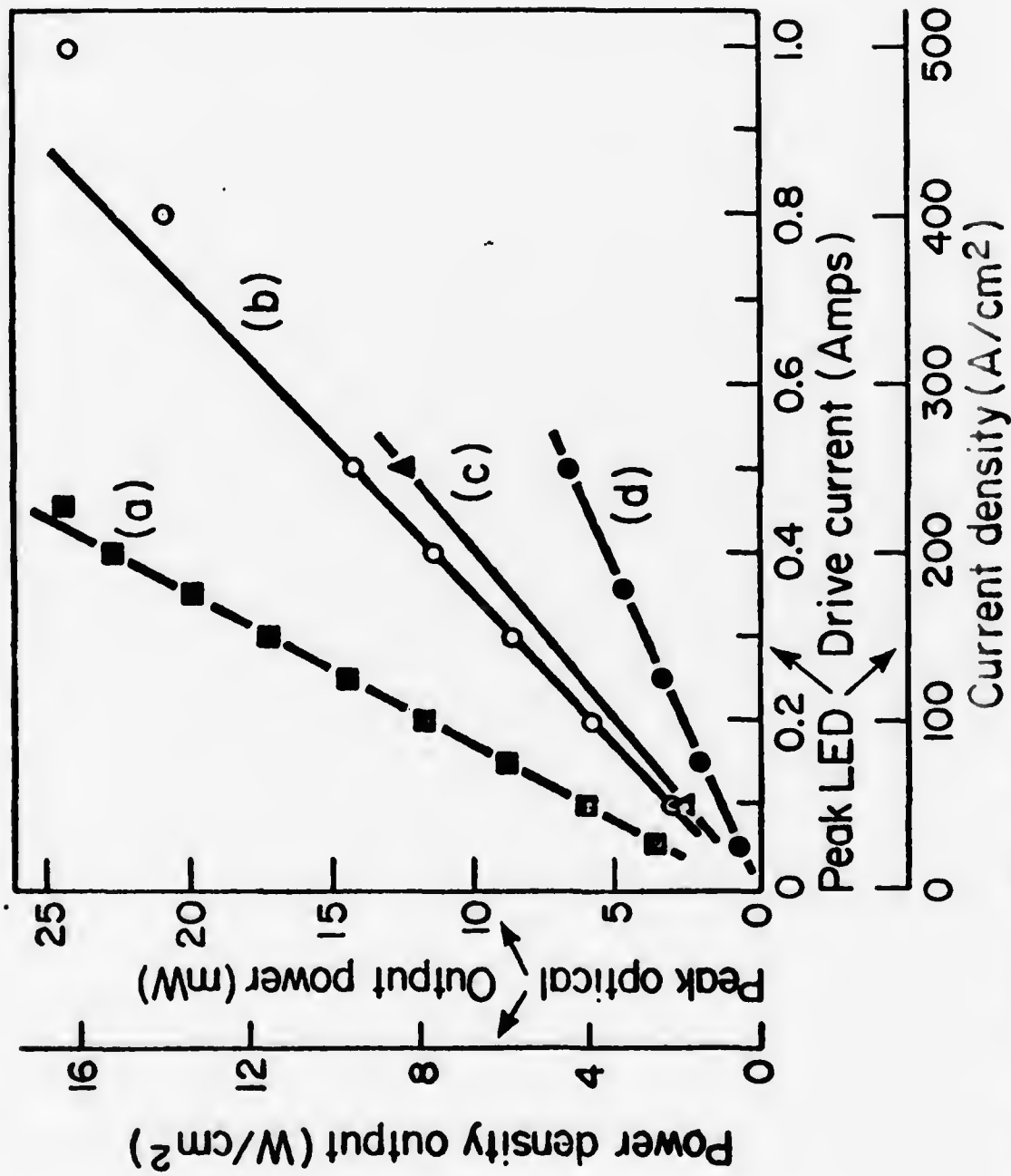


Fig. 3 Output power of GaAs:Si LED obtained with 1 msec current pulse train having 1% duty factor; (b) naked diode; (d) naked diode with edges masked; (a) measurements of (b) repeated with diode coated with index oil; (c) estimated power into laser crystal.

LED and laser host will be successfully "married" to produce a working minilaser that fulfills our original design expectations.

IV. KTN THIN FILMS

The goal of this phase of the program was to demonstrate the feasibility of growing KTN ($\text{KTa}_{1-x}\text{Nb}_x\text{O}_3$) films of good optical quality suitable for electrooptic thin film devices. For certain compositions KTN has an extremely large electrooptic coefficient and, consequently, has an excellent figure-of-merit for electrooptical modulation and switching. Moreover, the refractive index monotonically increases with increasing mole fraction of Nb and, therefore, it is possible to produce an optical waveguide by growing a Nb rich film on a substrate of lesser Nb concentration.

During the course of the program we were able to grow a number of KTN films capable of guiding light and, with these, succeeded in fabricating several thin film light modulators. The details of film growth, plus a discussion of film and modulator evaluation are contained in the attached thesis by R.E. Fontana, Jr., titled, "Potassium Tantalate Niobate Thin Films for Integrated Optics Applications".

A number of problems arose during our work which call for further study. The films, grown by LPE, did not grow with smooth surfaces. The "as-grown" films had to be carefully polished in order to obtain good optical guides. A more systematic study of the growth process than we were able to carry out in the available time should be undertaken.

We found that the dielectric parameters of our thin films differed from values reported for bulk crystals of the same composition. For example, the temperatures of the para-to-ferroelectric phase transition were higher for the thin films than for the comparable bulk material, and the dielectric permittivities, near the transition, were lower for the films. Most likely these disparities are a consequence of the strain clamping of the film by the substrate. A systematic investigation of the effect of clamping would not only provide better design information for electrooptical films but would no doubt lead to a far better understanding of the way in which quasi-two dimensional strain influences the ferroelectric phase transition

and the properties of the ferroelectric state.

The optical attenuations of electrooptical films is no doubt also seriously influenced by the state of strain. In our films the lowest attenuation we found was 8db/cm. This value is not much different from values reported for other ferroelectric films. It is worth noting that low attenuation, less than 1-2db/cm, has been reported in the literature only for situations in which the film and substrate are almost identical in index. When the difference is increased, the attenuation begins to rise rapidly. It has been suggested that edge dislocations produced by lattice mismatch may well be the source of the problem, but no systematic studies have yet been done. The KTN system is an ideal one in which to test this hypothesis, for in this system it is possible to build a systematic series of waveguide films on substrates which can be closely matched to the film in lattice constant and index, and then deliberately mismatched in a controlled way. The full range of device possibilities for electrooptical films and guides will not be achieved until there is a substantial reduction in optical attenuation below the best values now reported.

V. PREPARATION OF FEED MATERIALS

Because, in our sensitized rare earth minilaser, it was important to eliminate energy sinks that might interfere with efficient energy transfer, we went to great pains to prepare feed materials of extremely high purity. A variety of wet chemical synthesis techniques were developed as was a new low temperature hydrofluorination process for the synthesis of anhydrous rare earth fluorides. When required, feed materials were zoned refined in a controlled atmosphere furnace specially designed for fluoride systems. To avoid environmental recontamination during chemical processing, all open operations were carried out in a Class 100 cleanroom, built with funds provided by this program.

A description of the techniques and facilities used for the preparation of feed materials is contained in the Final Technical Report on contract DAHC-15-73-C-0317 submitted to ARPA in June 1975. The description is quite complete and will not be repeated here.

VI. PUBLICATIONS AND TALKS

1. "Single Mode 2.06 μm Miniature Laser", D. Castleberry, H.P. Jenssen and A. Linz; presented at the Integrated Optics Conference, New Orleans, January 1974.
2. "Growth and Characterization of Silicon Doped $\text{GaAs}_x\text{Sb}_{1-x}$ Luminescent Diodes", S.K. Brierly and C.G. Fonstad, Jr.; presented at the 1974 IEEE Specialist Conference on the Technology of Electroluminescent Diodes, November 20-21, 1974, Atlanta, Georgia.
3. "Analysis of the Optical Spectrum of Tm^{3+} in LiYF_4 ", H.P. Jenssen, A. Linz, R.P. Leavitt, C.A. Morrison and D.E. Wortman; Phys. Rev. B. 11, 92 (1975).
4. "Silicon Doped Gallium Arsenide Antimonide Electroluminescent Diodes Emitting to 1.06 μm ," S.K. Brierly and C.G. Fonstad, Jr.; J. Appl. Phys. 46, 3678 (1975).
5. "Epitaxially Grown Single Crystal KTN for Thin Film Optical Modulators", R.E. Fontana, D.J. Epstein, A. Linz; presented at the 1975 CLEA Conference, Washington, D.C.
6. D.E. Castleberry and A. Linz; "Measurement of the Refractive Index of LiYF_4 "; Applied Optics, 14, 2056 (1975).

Massachusetts Institute of Technology, Cambridge, Massachusetts
Department of Electrical Engineering and Computer Science and
Center for Materials Science and Engineering
Crystal Physics Laboratory

POTASSIUM TANTALATE NIOBATE THIN FILMS
FOR INTEGRATED OPTICS APPLICATIONS

by

Robert Edward Fontana, Jr.

TECHNICAL REPORT NO. 20

October, 1975

* The research covered by this Report was sponsored by the Advanced Research Projects Agency under Contract No. DAHC.15-73-C-0316, and by the Advanced Research Projects Agency and the Office of Naval Research under Contract No. N00014-75-C-1084. The views and conclusions contained in this document are those of the authors and should not be interpreted as necessarily representing the official policies, either expressed or implied, of the Advanced Research Projects Agency or the U.S. Government.

POTASSIUM TANTALATE NIOBATE THIN FILMS FOR INTEGRATED OPTICS APPLICATIONS

by

Robert Edward Fontana, Jr.

Submitted to the Department of Electrical Engineering and
Computer Science on October 7, 1975, in partial fulfillment
of the requirements for the Degree of Doctor of Philosophy.

ABSTRACT

The desirable properties of potassium tantalate niobate (KTN) for electrooptic applications have been known for some time, but the material has been used only as a bulk crystal. We report here the growth of KTN crystalline films on potassium tantalate (KTaO_3) substrates and, by using the large room temperature electrooptic effect in KTN, the efficient modulation of optical guided modes confined in these films. The optical and dielectric properties of the KTN films have been studied and their electrooptic performance has been evaluated by fabricating and testing several thin film diffraction modulators. The low drive voltage characteristics and planar geometry of these modulators make KTN thin film devices very attractive for integrated optics applications.

KTN thin films were grown using a liquid phase epitaxy (LPE) dipping method. Thin films were crystallized from nonstoichiometric melts onto KTaO_3 substrates by slowly lowering the furnace temperature at rates of $\sim 0.5^\circ\text{C}/\text{hour}$. After a growth time of 1-2 hours at temperatures between 1100 - 1150°C , films 15-20 microns thick with rippled surface features were obtained. By varying the growth temperature and melt compositions, $\text{KTa}_{1-x}\text{Nb}_x\text{O}_3$ films with Nb mole fractions from $x = 0.1$ to $x = 0.34$ were grown. Electron microprobe analysis showed Nb concentrations to be uniform throughout our films and that an abrupt film-substrate interface existed.

The films were polished to remove surface features and to reduce thicknesses to about 5 microns. The dielectric properties of the KTN films were found to differ substantially from the dielectric properties of bulk KTN with the same composition. Dielectric constants were measured from $2000 \epsilon_0$ to $4600 \epsilon_0$, depending on film composition. Loss tangents were large, $\tan \delta \approx 0.2$, and resulted in ac conductivities at 100 KHz of $10^{-4} (\Omega\text{-cm})^{-1}$. The optical loss for guided modes in the KTN films was in the 8-10 db/cm range. Our thin film modulators were operated at frequencies up to 500 KHz with pulse response times of $0.2 \mu\text{s}$. In a modulator using a $\text{KTa}_{0.66}\text{Nb}_{0.34}\text{O}_3$ film, 90% amplitude modulation was obtained with a drive voltage of 8 volts which for the electrode structure being used corresponded to a peak electric field in the

film of 3200 V/cm. The bandwidths of our fabricated modulators were limited by the power dissipation in the devices caused by the large frequency-dependent ac conductivity of the films. For frequencies near 100 KHz, temperature rises in the KTN films as great as 20°C were calculated.

Our work has demonstrated the feasibility of using KTN in thin film optics. The fact that KTN can now be grown in single crystal thin film form adds significantly to the versatility of the KTN material system because now planar and integrated circuit technologies can be used to fabricate more efficient and compact dielectric and optical devices.

Thesis Supervisor: David J. Epstein

Title: Professor of Electrical Engineering

ACKNOWLEDGEMENTS

The author wishes to thank Professor David J. Epstein for supervising this research; his suggestions and advice during the course of this work were greatly appreciated. I would like to thank Dr. Arthur Linz for his advice on the crystal growth issues of this thesis and Professor Clifton Fonstad for his suggestions on the device fabrication aspects of this research.

A special note of thanks goes to Dr. Hans Jenssen for first making the author aware of the research opportunities available in the Crystal Physics Laboratory at M.I.T. I wish to gratefully acknowledge the assistance I received from my fellow graduate students, in particular Dr. James Carlo and Dr. Donald Castleberry.

The technical assistance I received from the staff of the Crystal Physics Laboratory is also appreciated. I am particularly indebted to Mr. Vladimir Belruss for the growth of the excellent quality, large KTaO_3 single crystals which were used for substrates in my research. I would like to thank Mrs. Delphine Radcliffe for her patience and diligence in typing this manuscript.

Finally, the author thanks the National Science Foundation, the Sloan Research Foundation, and the Advanced Research Projects Agency for their financial support during his graduate years at M.I.T.

TABLE OF CONTENTS

	Page
ABSTRACT	2
ACKNOWLEDGEMENTS	4
TABLE OF CONTENTS	5
LIST OF FIGURES	9
LIST OF TABLES	13
 CHAPTER 1	
INTRODUCTION	14
1.1 Potassium Tantalate Niobate	15
1.1.1 Dielectric Properties	15
1.1.2 Optical Properties	19
1.2 Integrated Optics and KTN	22
1.2.1 Integrated Optics	22
1.2.2 Device Geometry	23
1.2.3 Advantages of a KTN Thin Film Device	25
1.3 Thesis Problem	26
 CHAPTER 2	
THIN FILM DIELECTRIC WAVEGUIDES: PROPAGATION THEORY AND CHARACTER- IZATION THEORY	28
2.1 Thin Film Waveguides	28
2.2 Waveguide Theory	30
2.2.1 Propagation	30
2.2.2 Loss	40
2.2.3 Coupling	42

TABLE OF CONTENTS (continued)

	Page
2.3 Methods for Thin Film Characterization	15
2.3.1 Composition	45
2.3.2 Optical Properties	48
2.3.3 Dielectric Properties and Conductivity	51
CHAPTER 3 THEORY FOR THIN FILM ELECTRO-OPTIC MODULATION	62
3.1 Review of Thin Film Electro-optic Devices	62
3.2 Electro-optic Effect in KTN Thin Films	65
3.2.1 KTN Electro-optic Effect	65
3.2.2 Plane Wave Propagation in Anisotropic Media	66
3.2.3 Electro-optically Induced Changes in the Guided Mode Index	69
3.3 Modulator Design Issues	73
3.3.1 Performance Figure	73
3.3.2 Design Equations	75
3.3.3 KTN and LiNbO_3 Device Comparison	76
3.4 Deflection-Diffraction Modulation Theory	77
CHAPTER 4 KTN SINGLE CRYSTAL FILMS: GROWTH AND CHARACTERIZATION	85
4.1 Bulk KTN Growth	85
4.2 Thin Film Single Crystal Growth	89
4.2.1 LPE Dipping Approach	89
4.2.2 Substrate Growth	94

TABLE OF CONTENTS (continued)

	Page
4.2.3 Substrate Preparation	95
4.2.4 Melt Preparation	99
4.2.5 Dipping Steps	103
4.2.6 Evolution of Growth Process	107
4.2.7 Film Appearance	108
4.2.8 Thin Film Growth by CVD	109
4.3 Thin Film Characterization	112
4.3.1 Composition	112
4.3.2 Optical Characterization	119
4.3.2.1 Optical Coupling	119
4.3.2.2 Synchronous Angle Measurements	119
4.3.2.3 Optical Loss	122
4.3.3 Dielectric Measurements	123
4.3.3.1 Dielectric Constant Measurements	127
4.3.3.2 Dielectric Loss	129
 CHAPTER 5 DEVICE FABRICATION AND EVALUATION	 133
5.1 Fabrication	133
5.1.1 Electrode Design	133
5.1.2 Electrode Metallization	134
5.1.3 Photolithography	134
5.1.4 Sample Mounting	136
5.2 Modulator Performance	137
5.2.1 Performance of a KTN ($x = 0.26$) Modulator	137

TABLE OF CONTENTS (continued)

	Page
5.2.2 Performance of a KTN ($x = 0.34$) Modulator	144
5.3 Interpretation of Device Performance	151
5.3.1 Thermal Effects on Bandwidth	151
5.3.2 dc Characteristics	154
5.4 KTN Device Applications	163
CHAPTER 6 CONCLUSIONS	167
6.1 Summary	167
6.2 Future Work	169
REFERENCES	172
BIOGRAPHICAL NOTE	179

LIST OF FIGURES

Figure No.		Page
1.1	KTN transition temperature vs Nb mole fraction, x , for the range $0 < x < 0.33$.	16
1.2	KTN transition temperature vs Nb mole fraction, x , for the range $0 < x < 1$.	17
1.3	Waveguide devices.	24
2.1	Waveguide geometry.	31
2.2	Ray theory geometry.	34
2.3	Effective index vs film thickness for TE modes in a 26 mole % Nb film at 633 nm.	36
2.4	Electric field profile of a TE_0 mode in a 26 mole % Nb film at 633 nm.	38
2.5	Electric field profile of a TE_3 mode in a 26 mole % Nb film at 633 nm.	39
2.6	Coupling schemes.	43
2.7	Lattice constant vs Nb mole fraction, x , for KTN.	47
2.8	Prism angles for synchronous angle measurements.	49
2.9	Interdigital electrode geometry.	52
2.10	Electric field calculations: (a) electrode cross section, (b) surface potential, (c) film-substrate geometry.	53
2.11	$E_x(o, z)$ vs z for $L = 25$ microns, $d = 5$ microns: (a) $\epsilon_2/\epsilon_1 = 0.025$, (b) $\epsilon_2/\epsilon_1 = 0.125$, (c) $\epsilon_2/\epsilon_1 = 1$.	56
2.12	$E_x(0, z)$ vs z for $L = 10$ microns, $d = 5$ microns: (a) $\epsilon_2/\epsilon_1 = 0.025$, (b) $\epsilon_2/\epsilon_1 = 0.125$, (c) $\epsilon_2/\epsilon_1 = 1$.	57
2.13	$E_x(x, -d/2)$ vs x for $L = 25$ microns, $d = 5$ microns: (a) $\epsilon_2/\epsilon_1 = 0.025$, (b) $\epsilon_2/\epsilon_1 = 0.125$, $\epsilon_2/\epsilon_1 = 1$.	59
2.14	Geometry factors G_1 , G_2 vs length ratio d/l_n .	61

LIST OF FIGURES (continued)

Figure No.		Page
3.1	Index change vs electric field for KTN ($x = 0.35$), KTN ($x = 0.26$), LiNbO_3 .	63
3.2	Optical indicatrix.	68
3.3	Thin film phase modulator geometry.	70
3.4	Equivalent circuit for drive and modulator.	74
3.5	Comparison of V_π , C_m , P_D/γ for KTN and LiNbO_3 as a function of Nb mole fraction, x .	78
3.6	Diffraction geometry.	80
4.1	KTN phase diagram.	87
4.2	Equilibrium state of the KTN melt at the growth temperature, T_g .	91
4.3	Temperature cycle for KTN dipping process.	93
4.4	Bulk KTaO_3 single crystals and seeds.	96
4.5	Polishing jig.	98
4.6	KTaO_3 substrates.	100
4.7	KTaO_3 substrate attached to platinum seed rod.	101
4.8	Dipping furnace.	104
4.9	KTN thin films: (a) rippled surface features, (b) film substrate interface.	110
4.10	System for growth of KTN by chemical vapor deposition.	111
4.11	X-ray diffraction peaks for KTN ($x = 0.26$) film on a KTaO_3 substrate.	114
4.12	X-ray diffraction peaks for KTN ($x = 0.34$) film on a KTaO_3 substrate.	115
4.13	Lapped film substrate.	117
4.14	Nb mole fraction, x , vs film thickness for a 1° lapped KTN film.	118
4.15	Prism coupler arrangement.	120

LIST OF FIGURES (continued)

<u>Figure No.</u>		<u>Page</u>
4.16	Experimental arrangement for synchronous angle measurements.	121
4.17	Loss for 5 TE modes in an $x = 0.34$ KTN film at 633 nm.	124
4.18	"M"-lines for TE modes in an $x = 0.34$ KTN film at 633 nm.	125
4.19	Loss vs wavelength for TE modes in an $x = 0.34$ KTN film.	126
4.20	Capacitance vs temperature for an $x = 0.26$ KTN film.	128
4.21	ac conductivity vs frequency for an $x = 0.26$ KTN film and an $x = 0.34$ KTN film.	131
5.1	Interdigital electrode.	135
5.2	Experimental configuration of KTN modulator.	138
5.3	Central beam intensity vs applied dc voltage for KTN ($x = 0.26$) modulator.	140
5.4	Profile of output light beam in the KTN ($x = 0.26$) modulator: (a) zero modulation voltage, (b) modulator voltage adjusted for maximum reduction of central beam.	141
5.5	Frequency behavior of KTN ($x = 0.26$) modulator: (a) no applied voltage, (b) 5-volt p-p modulating voltage superimposed on a 7-volt dc bias.	142
5.6	Frequency behavior of KTN ($x = 0.26$) modulator: (a) 16 volt p-p modulating voltage (b) 32-volt p-p modulating voltage.	143
5.7	Modulator efficiency vs applied voltage for three frequencies.	145
5.8	Central beam intensity vs applied dc voltage for a KTN ($x = 0.34$) modulator.	147
5.9	Frequency behavior of KTN ($x = 0.34$) modulator: (a) 500 Hz, (b) 500 KHz.	148
5.10	Pulse response time of KTN ($x = 0.34$) modulator.	149

LIST OF FIGURES (continued)

<u>Figure No.</u>		<u>Page</u>
5.11	Theoretical Klein-Cook fit to the experimental dc data of the KTN ($x = 0.26$) modulator.	159
5.12	Theoretical Klein-Cook fit to the experimental dc data of the KTN ($x = 0.34$) modulator.	160
5.13	dc modulation characteristics of the KTN ($x = 0.26$) and KTN ($x = 0.34$) modulators plotted as a function of phase shift induced in the devices.	162

LIST OF TABLES

Table No.		Page
1.1	KTN Dielectric Data.	20
1.2	KTN Optical Data.	20
4.1	Melt Compositions.	102
4.2	Growth Parameters for Runs 33, 48.	105
4.3	Lattice Mismatch Data for Samples 30, 47.	116
4.4	Synchronous Angle Measurements for TE Modes in a 34 mole % Nb Film at 633 nm.	116
5.1	Modulator Performance.	150

CHAPTER 1

INTRODUCTION

Potassium tantalate niobate (KTN) with chemical formula $\text{KTa}_{1-x}\text{Nb}_x\text{O}_3$ is an insulating ferroelectric material which, for certain compositions, exhibits a large room temperature electrooptic effect. During the mid sixties, KTN was the subject of extensive materials research for its potential applications to low drive-voltage bulk optical modulators, deflectors, and switches.^{1,2} Today, the advent of integrated optics has stimulated renewed interest in electrooptic materials, this time for thin film devices. The research reported here describes the materials and device problems relating to the use of KTN thin films for integrated optics.

The research was motivated by several factors. The possibility of using the large electrooptic effect in KTN together with the favorable geometry afforded by thin films provides modulating or switching voltages compatible with transistor circuitry. Because the optical and dielectric properties of KTN change with the Nb mole fraction, x , of the KTN composition, multi-layered thin film devices are possible. Finally, one of the limiting factors in bulk KTN device performance had been the presence of composition variations in the bulk KTN single crystals. It was expected that the different growth techniques required for thin film work plus the small film thicknesses required for device applications would greatly reduce the problem of composition variation in KTN single crystals.

In this introductory chapter, the dielectric and optical properties of KTN are presented together with a description of some integrated optics device issues relevant to the KTN material system. The thesis

organization and the research problem are detailed.

1.1 Potassium Tantalate Niobate

$\text{KTa}_{1-x}\text{Nb}_x\text{O}_3$ is a ferroelectric material which can be grown as a single crystal over the entire solid solution range $0 < x < 1$. One end member of this system is KTaO_3 . It is cubic at room temperature and exhibits no ferroelectric behavior down to 4°K . The other end member, KNbO_3 , is ferroelectric at room temperature (Curie temperature $T_c = 708^\circ\text{K}$) having orthorhombic symmetry. The mole fraction of Nb in KTN, x , directly influences the optical and dielectric properties of the material. Only compositions with $x < 0.38$, that is KTN compositions with cubic symmetry at room temperature, were used in this research. An excellent review of the compositional, dielectric, optical, and electro-optic properties of KTN has been compiled by Milek and Neuberger.³

1.1.1 Dielectric Properties

KTN has the perovskite structure and, depending on the mole fraction of Nb and the temperature, will be in a paraelectric state with cubic symmetry or in a ferroelectric state with either tetragonal, orthorhombic, or rhombohedral symmetry. The particular phases of the KTN system are illustrated in Fig. 1.1 for compositions $x < 0.33$. From the work by Todd⁴ no ferroelectric-paraelectric transition appears to exist for $x < 0.05$. Triebwasser⁵ did similar studies on KTN in the range $0.2 < x < 1.0$. His data is shown in Fig. 1.2 and compared with Todd's work.

The dielectric properties of KTN have been extensively studied by Triebwasser,⁵ Todd,⁴ and Reisman.^{6,7} For compositions with Nb mole fraction less than 0.38, KTN is cubic and in a paraelectric state. The

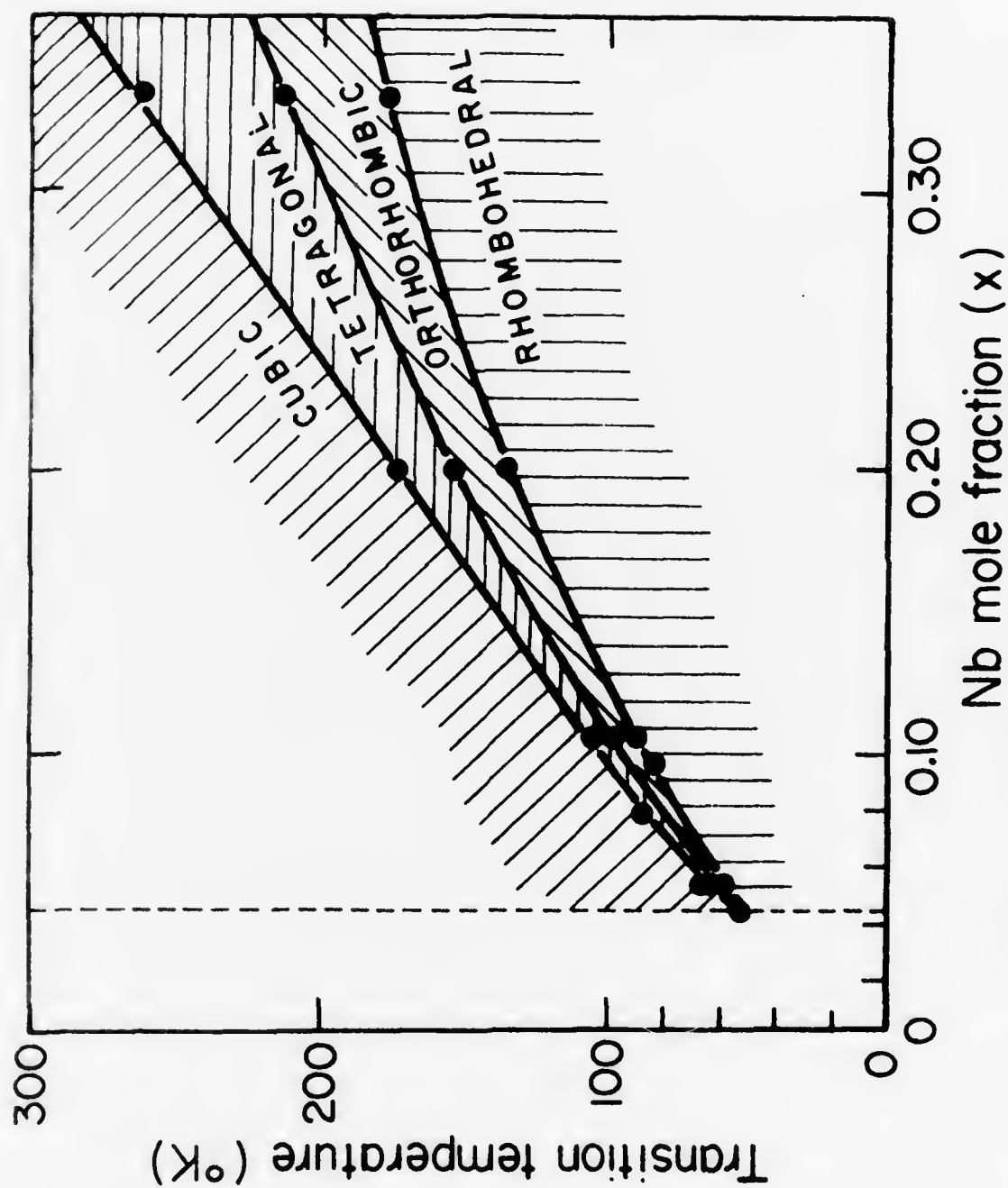
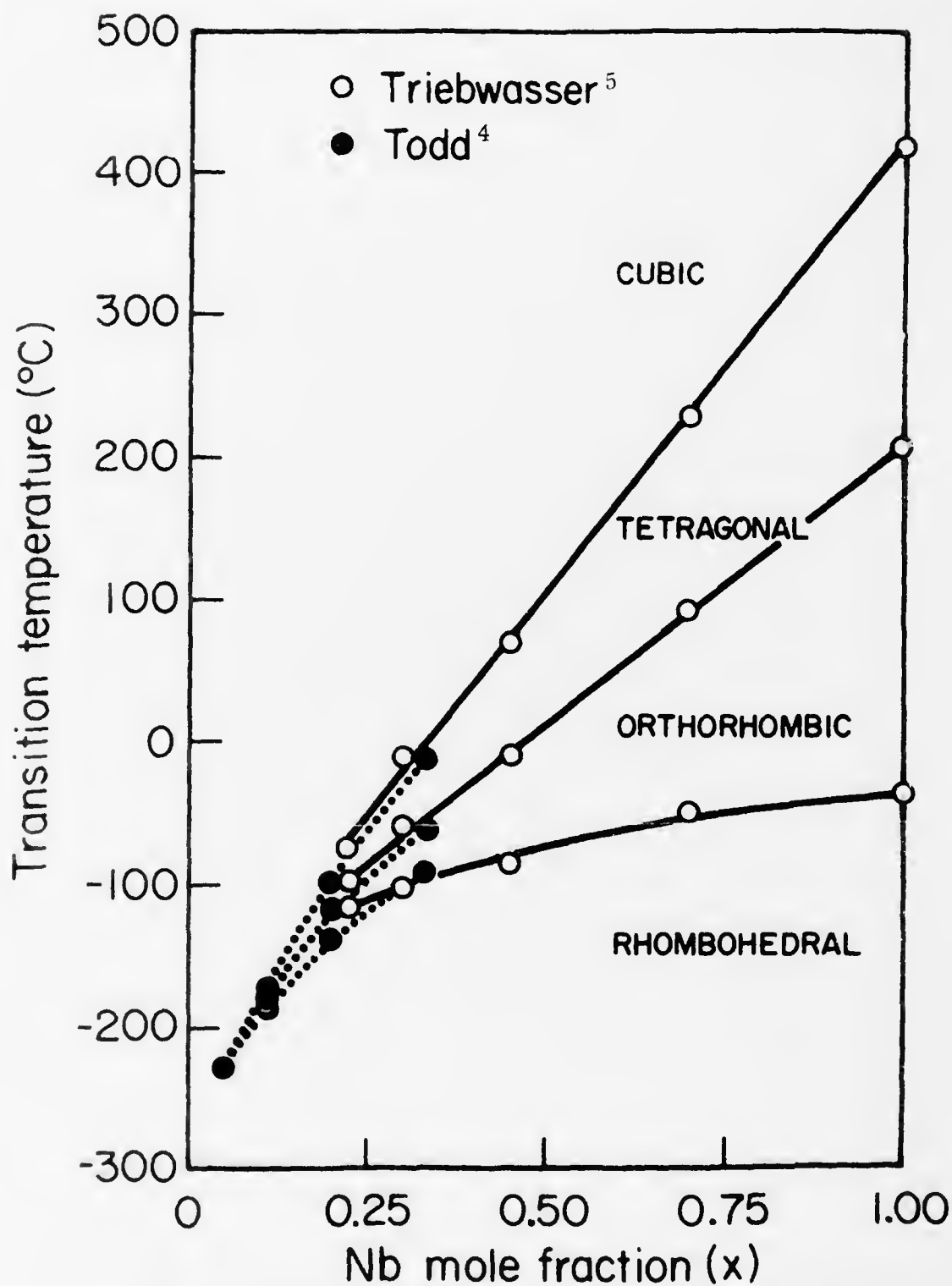


Fig. 1.1 KTN transition temperature vs Nb mole fraction, x , for the range $0 < x < 0.33$.



dielectric properties of paraelectric KTN can be described by the Devonshire relation,^{1,5}

$$E = \frac{T - T_0}{\epsilon_0 A} P + BP^3 + CP^5 \quad (1.1)$$

where E is the electric field, P the polarization, T the temperature, and T_0 the Curie-Weiss temperature. T_0 should be distinguished from the Curie temperature T_c which is associated with the first order paraelectric-ferroelectric phase transition of the KTN crystal. T_c is higher than T_0 ; for KTN ($x = 0.3$) $T_c - T_0 \approx 2^\circ\text{K}$. For a given composition, A , B , and C are coefficients which can be regarded as constant, although in more refined calculations their weak temperature dependence must be considered. Their variation with composition has been studied by Todd.⁴ In the composition range $0.20 < x < 0.60$ T_c has been observed to increase nearly linearly with composition;⁸ for $x = 0.38$, $T_0 = 25^\circ\text{C}$.

When the first term in Eq. (1.1) dominates, corresponding to operating temperatures well above the Curie temperature and to moderate electric field values, the dielectric constant for KTN can be written as

$$\epsilon = \frac{\epsilon_0 A}{T - T_0} \quad (1.2)$$

Todd's⁴ results showed only minor variation of less than 10% in the value of A as KTN composition changed, implying that any variation in dielectric constant resulting from composition changes is due mainly to the change in Curie temperature. Dielectric constants from $10,000 \epsilon_0$ to $30,000 \epsilon_0$ are not uncommon for KTN.^{1,4} Reported room temperature loss tangents for KTN vary from 0.001 to 0.006^{1,2} depending on the

Curie temperature of the KTN composition. Such values imply a dielectric conductivity at 1 MHz in the range $5 \times 10^{-6} (\Omega\text{-cm})^{-1}$ to $8.3 \times 10^{-7} (\Omega\text{-cm})^{-1}$. The dc conductivity can be as low as $10^{-12} (\Omega\text{-cm})^{-1}$,^{66, 67} but values considerably higher than this have been reported for crystals containing uncompensated impurity centers.^{66, 67} Dielectric data for three KTN compositions, $x = 0, 0.25, 0.35$, are given in Table 1.1. Dielectric and optical studies on KTN compositions other than these three compositions have not been reported in the literature. Consequently, in this research a linear interpolation of the existing data was used to determine the dielectric and optical properties of intermediate KTN compositions.

1.1.2 Optical Properties

KTN is transparent from 0.4 to 5 microns and thus is useful not only for applications in the visible but also for a number of other important wavelengths in the near infrared, e. g., at the GaAs LED and laser wavelengths (0.85 - 0.95 microns), the Nd:YAG wavelength (1.06 microns), and the eye-safe Ho:YLF wavelength (2.06 microns). The presence of impurities shifts the ultraviolet absorption edge into the visible region.

For cubic KTN, the room temperature optical index increases with Nb content. At 633 nm the optical index of an $x = 0.35$ composition is 2.29. Values of the order 2, as noted by Wemple and DiDomenico¹⁰ are characteristic of oxygen-octahedra ferroelectrics.

Paraelectric KTN belongs to the symmetry class P_{m3m} . Three quadratic electro-optic coefficients g_{11}, g_{12}, g_{44} determine optical index changes in the material. Formally, this change in index can be written as a function of the polarization P as

Table 1.1

KTN Dielectric Data

	KTaO_3 ⁹	$\text{KTa}_{0.75}\text{Nb}_{0.25}\text{O}_3$ ²	$\text{KTa}_{0.65}\text{Nb}_{0.35}\text{O}_3$ ^{1,2}
T_o (°K)	< 2°K	223°K	283°K
λ (°K)	6.32×10^4	1.45×10^5	1.45×10^5
ϵ (298°K)	242	2000	10,000

Table 1.2

KTN Optical Data

	KTaO_3 ^{10,11}	$\text{KTa}_{0.75}\text{Nb}_{0.25}\text{O}_3$	$\text{KTa}_{0.65}\text{Nb}_{0.35}\text{O}_3$ ^{1,10,11,12,13}
η	2.24	2.28	2.29
g_{11}	$0.14 \text{ m}^4/\text{c}^2$	$0.136 \text{ m}^4/\text{c}^2$	$0.136 \text{ m}^4/\text{c}^2$
g_{12}	$-0.02 \text{ m}^4/\text{c}^2$	$-0.038 \text{ m}^4/\text{c}^2$	$-0.038 \text{ m}^4/\text{c}^2$
g_{44}	$0.12 \text{ m}^4/\text{c}^2$	$0.147 \text{ m}^4/\text{c}^2$	$0.147 \text{ m}^4/\text{c}^2$
$\Delta\eta$ ($E = 5000 \text{ V/cm}$)	6.7×10^{-7}	6×10^{-5}	1.5×10^{-3}

$$\left(\frac{1}{\eta}\right)_{ij} = \left(\frac{1}{\eta_0}\right)_{ij} + g_{ijkl} P_k P_l \quad (1.3)$$

where η_0 is the unperturbed optical index. From an experimental point of view it is more convenient to work with electric fields than with polarization. Recalling that

$$P_k = \epsilon_{km} E_m \quad (1.4)$$

where ϵ_{km} is the dielectric tensor, Eq. (1.3) can be rewritten as

$$\left(\frac{1}{\eta}\right)_{ij} = \left(\frac{1}{\eta_0}\right)_{ij} + g_{ijkl} \epsilon_{km} \epsilon_{ln} E_n E_m \quad (1.5)$$

For a cubic material such as paraelectric KTN, ϵ_{km} is diagonal and equal to $\epsilon \delta_{km}$. Using this result and the expression for ϵ in Eq. 1.2, the change in optical index for a quadratic electro-optic material as a function of electric field strength can be written as

$$\left(\frac{1}{\eta}\right)_{ij} = \left(\frac{1}{\eta_0}\right)_{ij} + \epsilon^2 g_{ijkl} E_k E_l \quad (1.6)$$

$$= \left(\frac{1}{\eta_0}\right)_{ij} + \left(\frac{\epsilon_0 A}{T - T_0}\right)^2 g_{ijkl} E_k E_l$$

The values for g in KTN are very nearly constant as a function of Nb concentration.^{1, 10, 11} For wavelengths greater than 600 nm, variations of less than 7% have been reported for these coefficients.¹² These coefficients are in addition temperature independent.¹⁰

In view of Eq. (1.6) it is evident that KTN compositions with Curie

temperatures near room temperature have potentially large electro-optic effects. Electro-optically induced index changes as large as 0.001, i.e., 1 part in 2,000, can be obtained in the KTN system. Values for η , g , and optical index changes for three KTN compositions are given in Table 1.2.

1.2 Integrated Optics and KTN

1.2.1 Integrated Optics

Integrated optics is an emerging technology which employs thin film and integrated circuit techniques for the fabrication of optical devices and ultimately optical circuits. The operation of discrete laser sources, waveguides, modulators and detectors has been demonstrated in thin film geometry. The goal of integrated optics is to interconnect these devices to form efficient, compact optical circuits. Today such circuits are hybrid combinations of various thin film devices interconnected by optical fibers or waveguides. Only now is the problem of totally integrating these optical components on a single monolithic chip to form an integrated optical circuit being considered.

In this thesis, the term integrated optics is used to describe both the hybrid and integrated approaches which are being developed for the fabrication of optical circuits. The KTN waveguides and modulators studied in our research are integrated optics components because they are compact, thin film optical devices which can be used as modulation elements in hybrid optical circuits.

An early discussion of integrated optics was given by Miller¹⁴ in 1968. The issues of optical confinement and waveguiding in integrated optics thin film devices were discussed by Tien¹⁵ in 1971. The materials and device advances which have been achieved in integrated

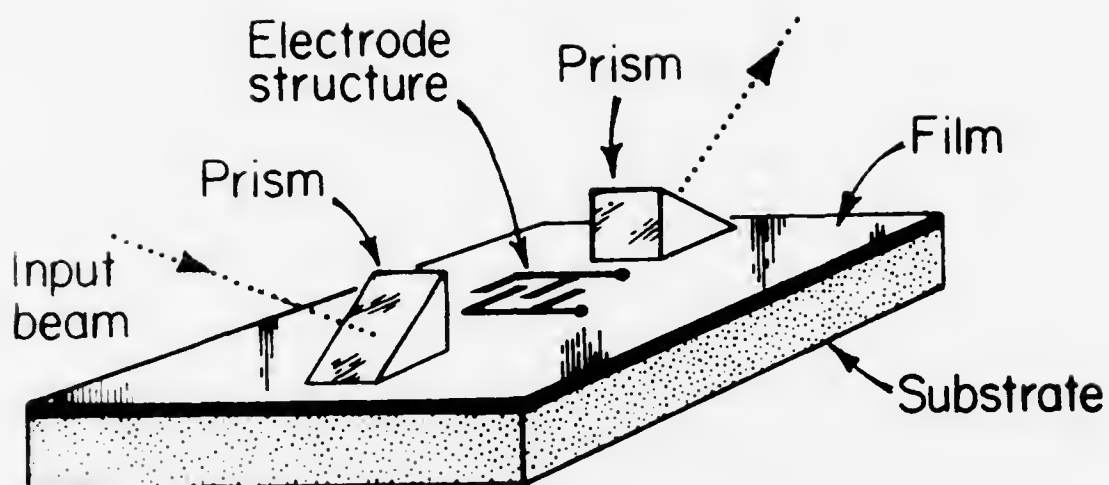
optics over the last five years are documented by the recent review articles of Chang et al,¹⁶ Kogelnik,¹⁷ Kaminow,¹⁸ Chang,¹⁹ and Evtuhov and Yariv.²⁰

1.2.2 Device Geometry

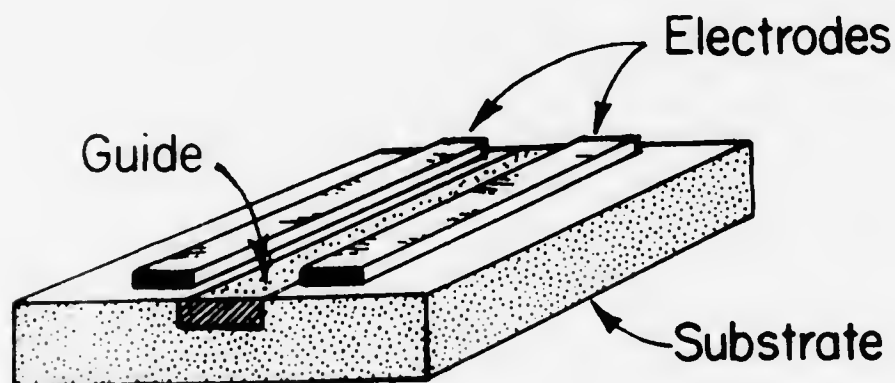
Device applications for KTN are to be found in the areas of modulation, beam deflection, and switching. In integrated optics such devices can have a planar structure shown in Fig. 1.3a, where the light is confined in one transverse direction or an embedded or ribbed structure shown in Fig. 1.3b, where the light is confined in both transverse directions.

In each of these cases the optical index of the guiding medium must be greater than that of the substrate or surrounding medium. Prisms, gratings, or edge illumination techniques have been used to couple light into and out of these devices. Electric fields, which can penetrate into the guiding medium when voltage is applied across appropriate electrode structures, create index changes in the guiding medium. The resulting perturbation in the propagation characteristics of the guided mode in the medium can be used to alter the phase and amplitude of the output light, to change its angular direction, or to cause mode conversion of the guided light.

For planar devices, film thicknesses can vary from 1-5 microns, and device lengths are of the order of 1-2 cm. In the embedded structures, guide widths of the order of 10-20 microns are common. The lower limit for this dimension is the wavelength of the light being used in the structure. In practice, fabrication constraints determine this dimension. Such device geometries have two advantages. The planar geometry allows the use of integrated circuit photolithography techniques.



a) Planar waveguide device



b) Embedded waveguide device

Fig. 1.3 Waveguide devices.

More important, since the electro-optic effect is field dependent and since the optical energy is confined only in the film or guiding region, surface electrodes with spacings on the order of film thickness or guide width can be used. As a result, low applied voltages can generate large electric fields in the guiding medium. For the surface electrode geometry of Fig. 1.3b with an electrode separation of 25 microns, 25 volts can generate an electric field of 10,000 V/cm in the guiding medium.

These device advantages are somewhat offset by stringent material requirements. One of the greatest difficulties is developing growth techniques for the guide and substrate material combinations. Material homogeneity must be maintained to achieve low optical scattering loss. Thickness and width variations must be controlled to insure uniform guiding properties.

To summarize, integrated optics devices have the overriding advantages of compactness and low power potential over their bulk counterparts.

1.2.3 Advantages of a KTN Thin Film Device

The KTN thin film devices in this research have the planar structure of Fig. 1.3a. Both film and substrate can be KTN compositions. This is possible because the optical index can be adjusted by controlling the Nb content. The choice of appropriate KTN film and substrate compositions can be determined from the following equations describing index and Curie temperature variations with Nb mole fraction content x :

$$\eta(x) = 2.24 + 0.14x \quad (\lambda = 633 \text{ nm}) \quad 0 < x < 0.38 \quad (1.7)$$

$$T - T_c(x) = 225 - 600x \quad (^{\circ}\text{C}) \quad 0.2 < x < 0.38 \quad (1.8)$$

The variation in Curie temperature has been verified by Whipps⁸ and Kurtz.² The optical index variation is a linear extrapolation based on the available data for KTaO_3 and $\text{KTa}_{0.65}\text{Nb}_{0.35}\text{O}_3$.

For this research, KTaO_3 , i. e., $x = 0$, was the substrate material. This choice was motivated by the existence of a well established single crystal growth process yielding large, high optical quality KTaO_3 plus the fact that this composition has the lowest optical index and weakest room temperature electro-optic effect in the KTN system. This substrate selection resulted in an active film-passive substrate combination. The KTN devices which were fabricated in this thesis research had film compositions from $x = 0.25$ to $x = 0.35$ in order to achieve large electro-optic effects. For KTaO_3 substrates this gave optical index discontinuities of 0.02 to 0.04 at 633 nm.

1.3 Thesis Problem

This thesis research was directed at demonstrating the potential of KTN thin film devices in integrated optics. The materials effort involved the development of a liquid phase epitaxy technique for growing single crystal KTN thin films and the experimental evaluation and interpretation of the optical, dielectric, and compositional quality of these films. The films were then examined in the context of a particular device problem, i. e., the fabrication and evaluation of a thin film diffraction modulator.

In Chapter 2 the waveguide properties of dielectric thin films are viewed as they apply to the KTN system. Chapter 3 addresses the device issues for KTN, emphasizing device performance compared to devices using different material systems. Chapters 4 and 5 present the experimental results of this thesis. The growth of KTN thin films by a

liquid phase epitaxy dipping technique is described. Experimental characterization results of the KTN thin films are presented and the fabrication and evaluation of two KTN thin film devices are detailed. Based on the experimental results, an appraisal of the potential of the KTN system in integrated optics is given in the concluding chapter.

CHAPTER 2

THIN FILM DIELECTRIC WAVEGUIDES: PROPAGATION THEORY AND CHARACTERIZATION TECHNIQUES

The guided mode propagation of light waves in dielectric thin films will be reviewed in this chapter. In particular the guiding characteristics of optical modes in KTN thin films will be discussed. The experimental techniques which were used in this research to evaluate the optical and dielectric quality of our KTN films will also be described.

2.1 Thin Film Waveguides

Many materials previously used for bulk optical devices are now finding applications in thin film waveguide devices. Thin film materials are deposited on substrates to provide mechanical support for the waveguiding films. Such films have been formed by sputtering, diffusion, ion implantation, and a variety of single crystal growth techniques. The thermal, mechanical, and lattice properties of the film and substrate, particularly in the case of single crystal growth, must be similar to insure high optical quality guiding layers. Because both the optical and modulating electric fields penetrate into the substrate, substrate quality plays an important role in influencing waveguiding performance.

A variety of organic compounds and sputtered materials have been used for waveguiding films. Photoresist guides²³ have been formed by coating glass slides with the resist and then spinning the slides at high speeds to obtain uniform films. PMMA (polymethylmethacrylate) guides²⁴ have been fabricated using a solution deposition technique. ZnO,¹⁵ Ta₂O₅,²⁵ and ZnS²⁶ were the earliest reported sputtered guides. Sputtered materials cover a broad index range from about 1.5 to 3.0.

Though most sputtered guides have been passive structures, electro-optic modulators have recently been fabricated using sputtered LiNbO_3 on a Corning glass substrate,²⁷ sputtered ZnO on glass slides,⁷⁸ and sputtered Nb_2O_5 ²⁸ and Ta_2O_5 ²⁹ on LiTaO_3 substrates.

Low loss electro-optic waveguides have been fabricated by diffusion of a dopant into a bulk crystal under conditions of controlled temperature, atmosphere, and time. Because the distribution of the diffused dopant has an error function profile, an index variation of the form

$$\Delta\eta = A \operatorname{ierfc}(x/c)^{31} \quad (2.1)$$

is created where A is the index change on the surface after the diffusion is completed and c is a parameter that may be considered a characteristic guide depth. The first reported diffusion work was with $\text{CdS}_x\text{Se}_{1-x}$ on CdS .³⁰ An outdiffusion process was reported by Kaminow and Carruthers³¹ in which, by heating, Li_2O was driven from highly polished LiNbO_3 and LiTaO_3 substrates. Although these were initially multimode guides, 100 microns thick with $A \approx 0.001$, control of the diffusion parameters, A and c , eventually resulted in single mode propagation. Recently, a variety of elements have been successfully indiffused into LiT_2O_3 (Nb)^{22, 32} and LiNbO_3 (Ti , V , Ni , Cu)^{33, 38} giving excellent guiding layers.

The last important category of guiding structures comprises the single crystal epitaxial films. The first such guide was a KDP-ADP mixture grown from solution on a KDP substrate.³⁸ ZnO single crystal films were grown on Al_2O_3 substrates by Hammer et al.³⁵ using a vapor deposition process. Guiding in magnetic garnet single crystal films, $(\text{Bi}, \text{Y}, \text{R.E.})_3(\text{Fe}, \text{Ga}, \text{Sc}, \text{Al})_5\text{O}_{12}$, on $\text{Gd}_3\text{Ga}_5\text{O}_{12}$ ^{36, 21}

substrates, has been demonstrated. Waveguide structures have also been fabricated in the GaAs - $\text{Ga}_{1-x}\text{Al}_x\text{As}$ ³⁷ system. Single crystal films have been grown by liquid phase⁷⁹ and molecular beam epitaxy⁸⁰ techniques. Current interest in the system is directed toward the integration of source, guide, and modulator on a single GaAs chip.

2.2 Waveguide Theory

2.2.1 Propagation

When light is confined in a dielectric film with a thickness of several wavelengths and when this film has a greater optical index than both the substrate and superstrate, waveguiding in distinct modes can be achieved. The geometry relevant to a discussion of optical waveguiding is shown in Fig. 2.1. Light propagates in the +y direction. Film index, η_1 , is greater than the substrate index, η_0 , which is assumed greater than the superstrate index (usually air), η_2 , and film thickness is W. For TE modes the electric field is polarized in the x direction and for TM modes the magnetic field is polarized in this direction.

For the TE case, the field solution for propagation confined to the guiding layer can be written as

$$E_0 = i_{\vec{x}} E_0 e^{+p_0 z} e^{i\beta y} \quad z < 0 \quad (2.2)$$

$$E_1 = i_{\vec{x}} \{E_1^+ e^{+iby} + E_1^- e^{-iby}\} e^{i\beta y} \quad 0 < z < W \quad (2.3)$$

$$E_2 = i_{\vec{x}} E_2 e^{-p_2(z-W)} e^{i\beta y} \quad z > W \quad (2.4)$$

where for guiding p_0 , p_2 , β , and b are real and positive. p_0 and p_2 are the decay constants associated with evanescent fields in the air and sub-

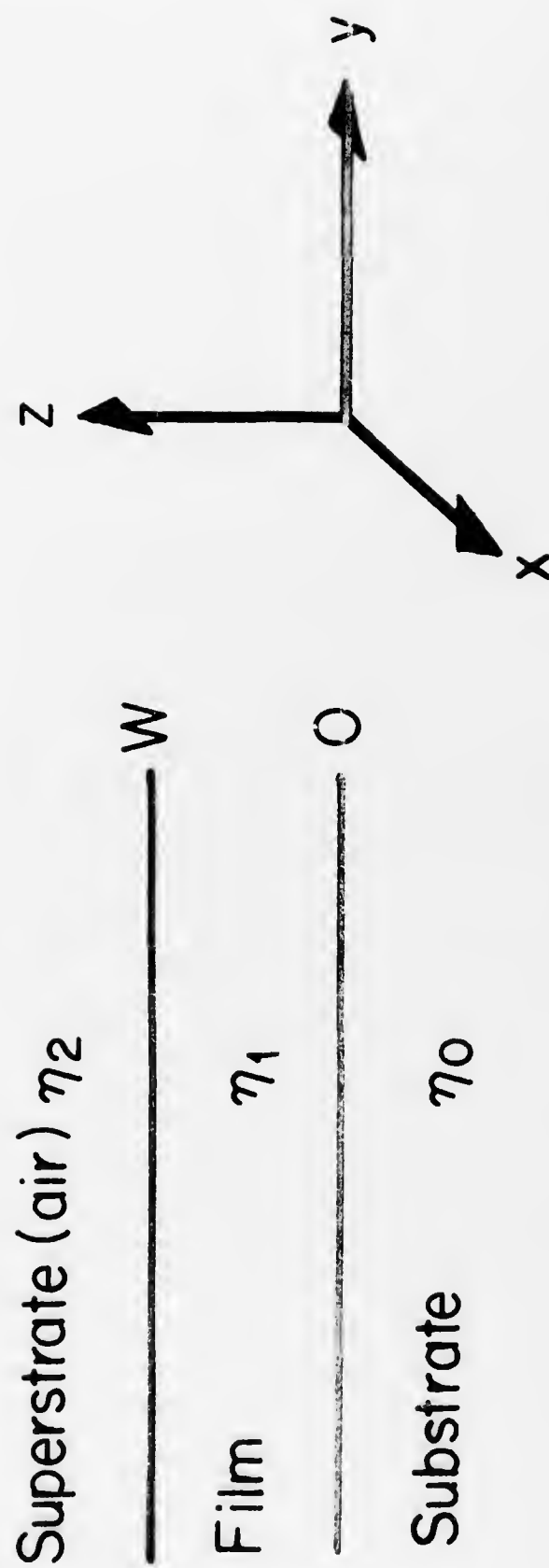


Fig. 2.1 Waveguide geometry.

strate regions. b determines the number of nodes the guided field pattern has in the film. β is the propagation constant associated with a particular guided mode. These four constants are related by the dispersion relations for each region.

$$-p_0^2 + \beta^2 = k_0^2 \eta_0^2 \quad (2.5)$$

$$b^2 + \beta^2 = k_0^2 \eta_1^2 \quad (2.6)$$

$$-p_2^2 + \beta^2 = k_0^2 \eta_2^2 \quad (2.7)$$

k_0 is equal to $2\pi/\lambda_0$ and λ_0 is the free space wavelength of the incident radiation. It is customary to define an effective guide index, or more simply a guide index, by

$$\beta \equiv k_0 \eta_g \quad (2.8)$$

Expressed in terms of η_g the following relations for p_0 , p_2 , and b result:

$$p_0 = k_0 (\eta_g^2 - \eta_0^2)^{\frac{1}{2}} \quad (2.9)$$

$$p_2 = k_0 (\eta_g^2 - \eta_2^2)^{\frac{1}{2}} \quad (2.10)$$

$$b = k_0 (\eta_1^2 - \eta_g^2)^{\frac{1}{2}} \quad (2.11)$$

From the requirement that b , p_0 , p_2 be real it is clear that guiding implies $\eta_1 > \eta_0, \eta_2$ and $\eta_1 > \eta_g > \eta_0$. By matching boundary conditions on the tangential components of E and H at $z = 0, W$, we obtain the following characteristic equation defining the TE modes,

$$2Wb - 2 \tan^{-1} \left(\frac{p_0}{b} \right) - 2 \tan^{-1} \left(\frac{p_2}{b} \right) = 2m\pi \quad (2.12)$$

or using Eqs. (2.9), (2.10), (2.11)

$$2Wk_o(\eta_1^2 - \eta_g^2)^{\frac{1}{2}} - 2 \tan^{-1} \left\{ \left(\frac{\eta_g^2 - \eta_o^2}{\eta_1^2 - \eta_g^2} \right)^{\frac{1}{2}} \right\} - 2 \tan^{-1} \left\{ \left(\frac{\eta_g^2 - \eta_2^2}{\eta_1^2 - \eta_g^2} \right)^{\frac{1}{2}} \right\} = 2m\pi \quad (2.13)$$

where m is an integer denoting mode number.

Some physical insight into this expression can be gained by using Tien's¹⁵ ray optics approach to derive this expression. The geometry for this approach is shown in Fig. 2.2. A guided mode follows a zig-zag path ($A \rightarrow B \rightarrow C$) in the film, making an incident angle θ with the film-air interface and film-substrate interface. Optical confinement occurs when the ray is totally internally reflected at both boundaries, i.e., when $\theta > \sin^{-1} \eta_o/\eta_1$. When $\sin^{-1} \eta_2/\eta_1 < \theta < \sin^{-1} \eta_o/\eta_1$, light will only be confined beneath the film-air interface. This is a substrate mode. If $\theta < \sin^{-1} \eta_2/\eta_1$, no confinement occurs and an air mode exists.

Using the incident angle approach, the following expressions for β , η_g , b , p_o , p_2 result:

$$\eta_g = \eta_1 \sin \theta \quad (2.14)$$

$$\beta = \eta_1 k_o \sin \theta \quad (2.15)$$

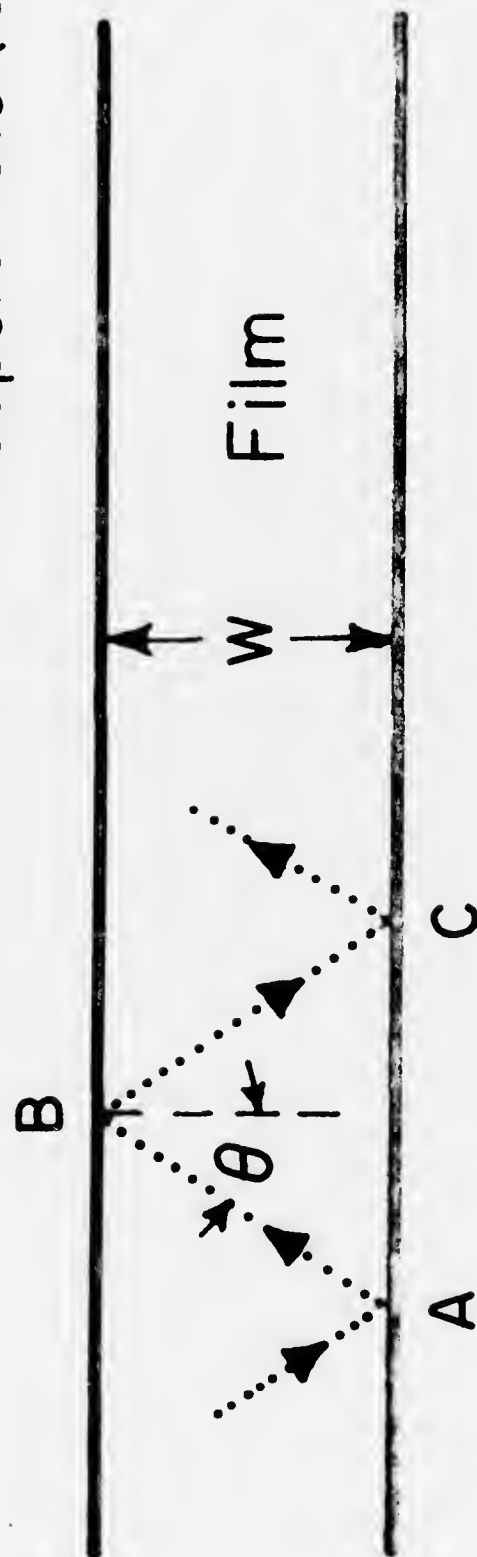
$$b = \eta_1 k_o \sin \theta \quad (2.16)$$

$$p_o = k_o (\eta_1^2 \sin^2 \theta - \eta_o^2)^{\frac{1}{2}} \quad (2.17)$$

$$p_2 = k_o (\eta_1^2 \sin^2 \theta - \eta_2^2)^{\frac{1}{2}} \quad (2.18)$$

Only a discrete set of incident angles θ will give both confinement and guiding. For waveguiding, the total phase shift in the transverse z

Superstrate (air)



Substrate

Fig. 2.2 Ray theory geometry.

direction that a ray experiences in one traverse from substrate to air to substrate ($A \rightarrow B \rightarrow C$) must be a multiple of 2π , i.e., constructive interference must occur. The beam travels a distance of $2W$ in the z direction. This contributes $2bW$ to the phase shift. At each interface the Goos-Haeschel phase shift resulting from total internal reflection at greater than critical angle incidence adds to the phase shift. By using Eqs. (2.2), (2.3) and evaluating the ratio of E_1^+/E_1^- at $z = 0$, the film substrate interface, this phase shift can be determined. Continuity of the tangential components of E and H gives

$$E_1^+ + E_1^- = E_0 \quad (2.19)$$

$$ib(E_1^+ - E_1^-) = p_0 E_0 \quad (2.20)$$

from which

$$\frac{E_1^+}{E_1^-} = \frac{1 - i \frac{p_0}{b}}{1 + i \frac{p_0}{b}} = \exp(-2i \tan^{-1} \frac{p_0}{b}) \quad (2.21)$$

The Goos-Haeschel phase shift is therefore $-2 \tan^{-1} \frac{p_0}{b}$.

From this discussion, the interpretation of Eq. (2.12) is straightforward. The first term is the phase shift from traveling a distance $2W$. The next two terms are phase shifts due to total internal reflections and the final term is the requirement for constructive interference.

Using Eq. (2.12), a plot of waveguide index, η_g , vs thickness for various modes can be constructed. Such a plot is shown in Fig. 2.3 for a KTN guide with film index 2.28 corresponding to a 26 mole % KTN composition and a substrate index of 2.24, i.e., a KTaO_3 substrate, for $\lambda_0 = 633 \text{ nm}$. As expected, the guide index falls between the film and substrate indices. As the guide thickness increases, more modes are

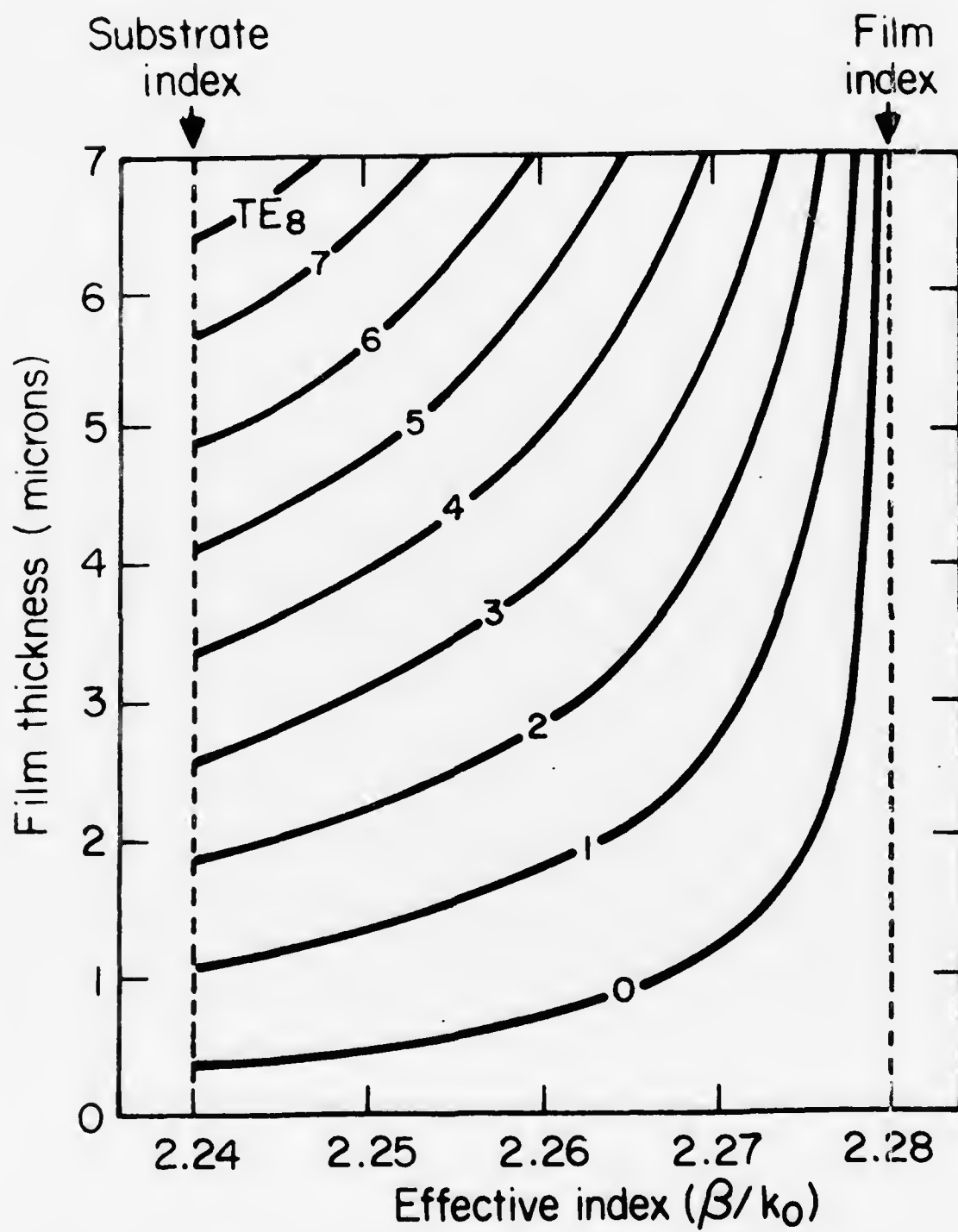


Fig. 2.3 Effective index vs film thickness for TE modes in a 26 mole % film at 633 nm.

excited and the lower order modes have an effective index approaching the film index value. This indicates that the guide is departing from its "thin film" nature since the phase velocity of the modes approaches the value in the bulk material.

Using the above data, a guide thickness of 3 microns results in 4 TE modes. The effective index and incident angle are listed below for each mode.

	η_g	θ
TE ₀	2.2777	87.42°
TE ₁	2.2719	85.17°
TE ₂	2.2619	82.78°
TE ₃	2.2483	80.43°

The incident angles are shallow because of the small (2%) variation between film and substrate index. Figures 2.4 and 2.5 are plots of the electric field pattern for the TE₀ and TE₃ modes. For the TE₃ mode a substantial electric field penetrates into the substrate. p_0 is 1.9 (microns)⁻¹.

An important guide parameter is the guide thickness below which a particular mode will no longer propagate. This critical thickness is attained when the effective mode index equals the substrate index.

Using Eq. (2.12), the cutoff thickness is

$$W_c = \frac{1}{k_0 (\eta_1^2 - \eta_0^2)^{\frac{1}{2}}} \left\{ m\pi + \tan^{-1} \left(\frac{\eta_0^2 - \eta_2^2}{\eta_1^2 - \eta_0^2} \right)^{\frac{1}{2}} \right\} \quad (2.22)$$

For the KTN film discussed above, the cutoff thickness below which no guided modes will exist is 0.325 microns.

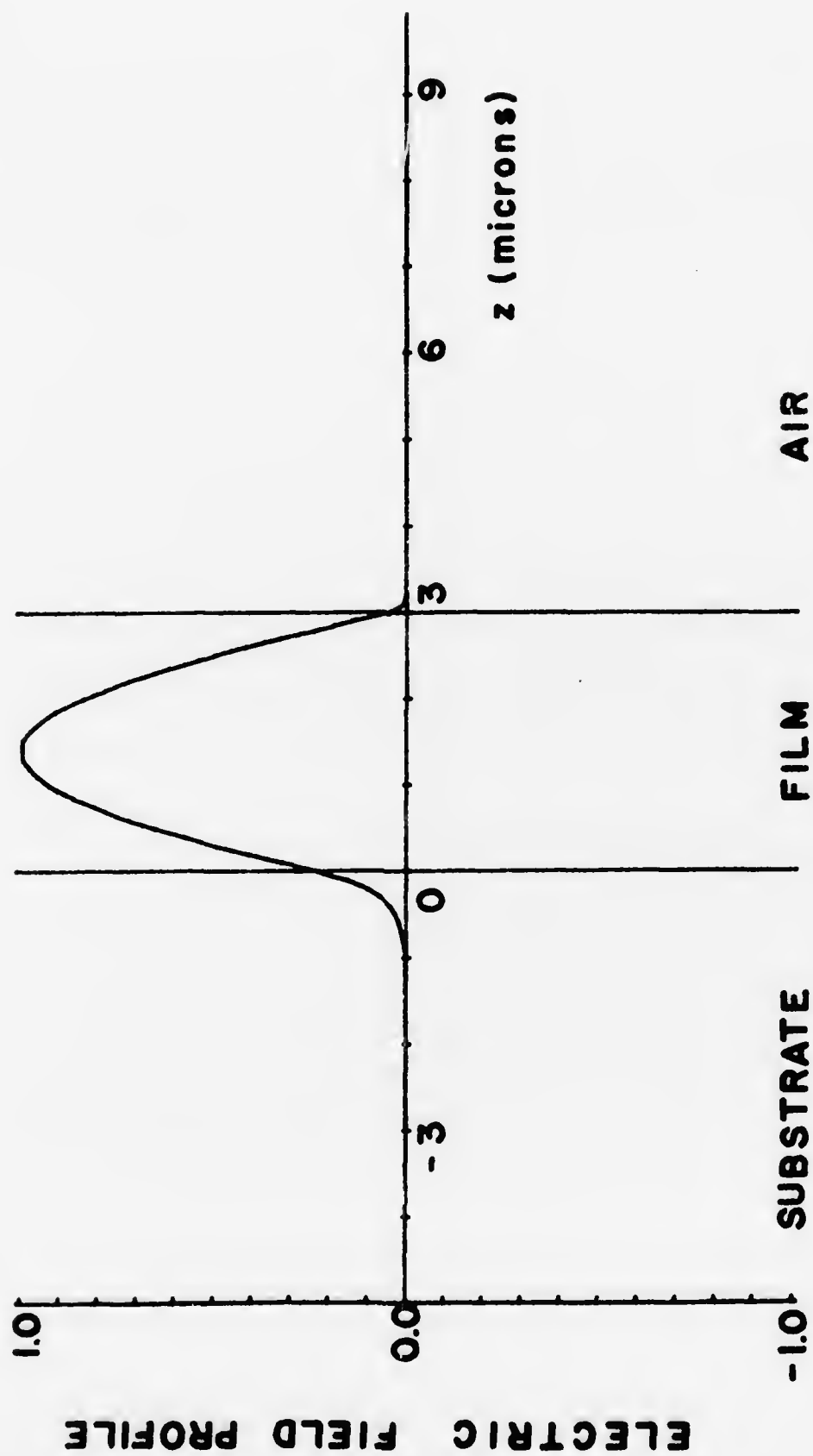


Fig. 2.4 Electric field profile of a TE_0 mode in a 26 mole % Nb film at 633 nm.

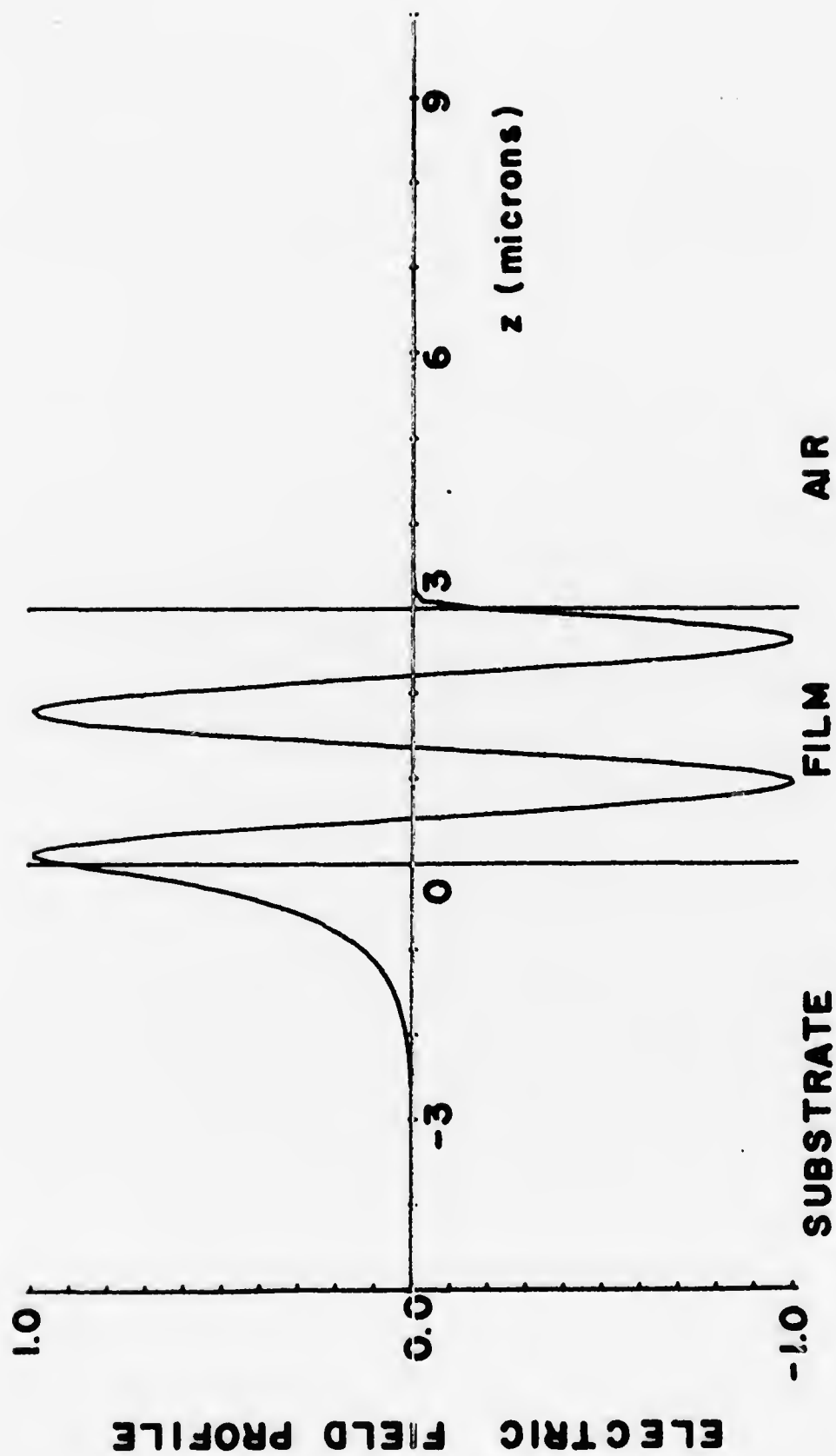


Fig. 2.5 Electric field profile of a TE_3 mode in a 26 mole % Nb film at 633 nm.

The KTN guides in this research were nominally 4-5 microns thick. Based on the foregoing discussion, the following general statements can be made about the KTN guides we studied. The waveguides are multimode; the critical angle reflections are shallow; the effective guide index varies by no more than 2% from either film or substrate values; modulation applications, which make use of the electro-optic performance of the KTN films, are better for lower order modes since a greater percentage of the optical field is confined in the film for these modes.

2.2.2 Loss

Optical loss in thin film dielectric guides has been studied by Tien¹⁵ and Chanin et al.³⁹ A qualitative review has been given by Chang et al.¹⁶ There are three major contributions to optical loss in guiding structures; volume loss due to intrinsic absorption, α_I , volume loss due to scattering, α_B , and surface scattering loss α_{SC} . The total attenuation can be written as

$$\alpha = \alpha_I + \alpha_B + \alpha_{SC} \quad (2.23)$$

assuming no interaction among the various loss mechanisms.

Loss due to intrinsic absorption is caused by atomic scale phenomena. Since device applications for most material systems use wavelengths well above the optical absorption edge, 4000 Å for KTN, volume absorption makes a small contribution to the overall optical loss of any guided mode.

Of major significance is optical loss due to either volume or surface scattering caused by index of refraction inhomogeneities in the dielectric film. Surface inhomogeneities can result from scratches or

pits on the film surface or from problems associated with substrate preparation, i. e., polishing, cleaning, which affect the film-substrate interface. In single crystal films, volume index variations can be caused by composition variations in the film and by large lattice mismatch between the film and substrate which can give rise to dislocations.⁸¹ In sputtered guides, the size of the crystallites which make up the film create index variations distributed through the bulk of the film.

A quantitative analysis of optical loss in thin films proceeds by decomposing the distribution of bulk and surface inhomogeneities into their spatial Fourier components and then examining the conversion, caused by these index variations, of a given guided mode into other modes, primarily substrate or air modes. When Rayleigh scattering theory^{15, 39} is used to describe the strength of this scattering process, a λ^{-4} dependence for optical attenuation results.

Tien's ray approach¹⁵ can be used to obtain a qualitative estimate of the dependence of loss on mode index, η_g . Surface loss depends on the number of bounces per unit propagation length the mode makes between the two guide interfaces. Volume loss depends on the total distance the guided mode ray travels in the guide for each bounce.

Using Eq. (2.14) one obtains

$$\alpha_B \propto \frac{\eta_f}{\eta_g} \quad (2.24a)$$

$$\alpha_{SC} \propto \frac{1}{\eta_g} (\eta_f^2 - \eta_g^2)^{\frac{1}{2}} \quad (2.24b)$$

where η_f is the film index.

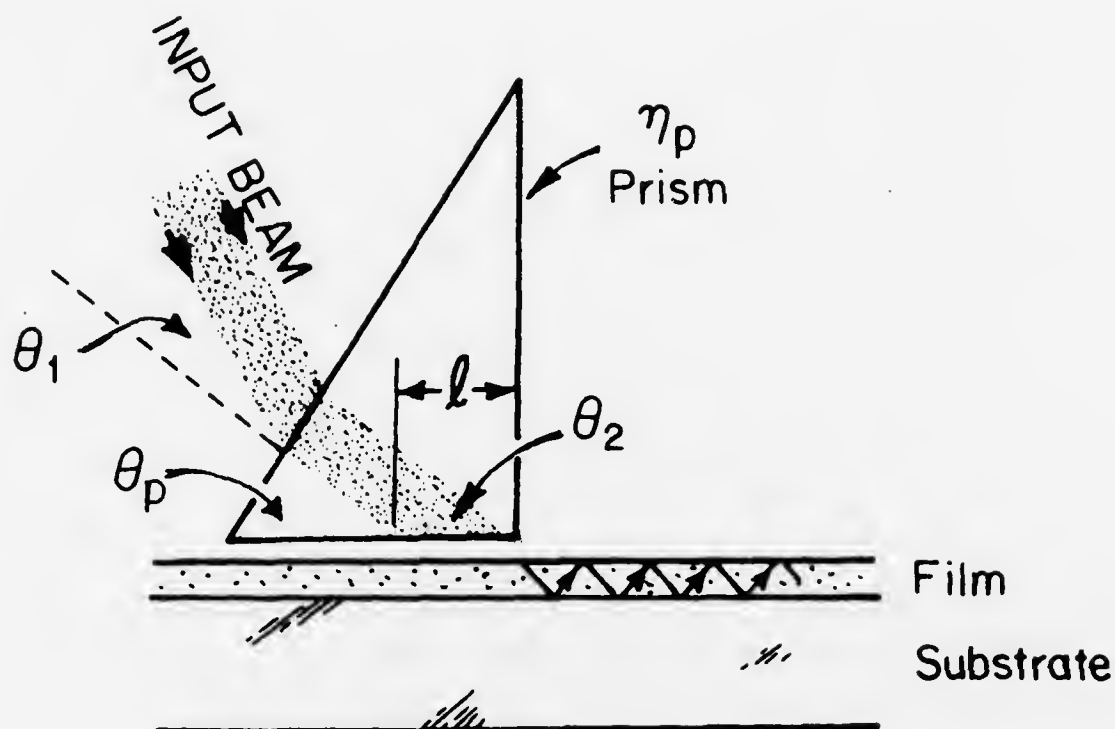
In both cases, loss increases with increasing mode number or decreasing index. This is to be expected since the lower order modes have shallower reflecting angles. For epitaxial ZnO films,³⁹ volume losses were found to dominate over surface scattering. For Ta₂O₅ sputtered films, surface scattering was observed to be the major cause of loss.

Optical loss in films varies from less than 1db/cm to as high as 70db/cm. Sputtered films have loss on the order of 20db/cm.¹⁵ Indiffused materials with $\Delta\eta \sim 0.002$ have losses less than 1db/cm.⁸¹ Single crystal films have reported loss in the 1-10db/cm³⁹ range. For single crystal films, the general trend is for higher loss for higher $\Delta\eta$.⁸¹

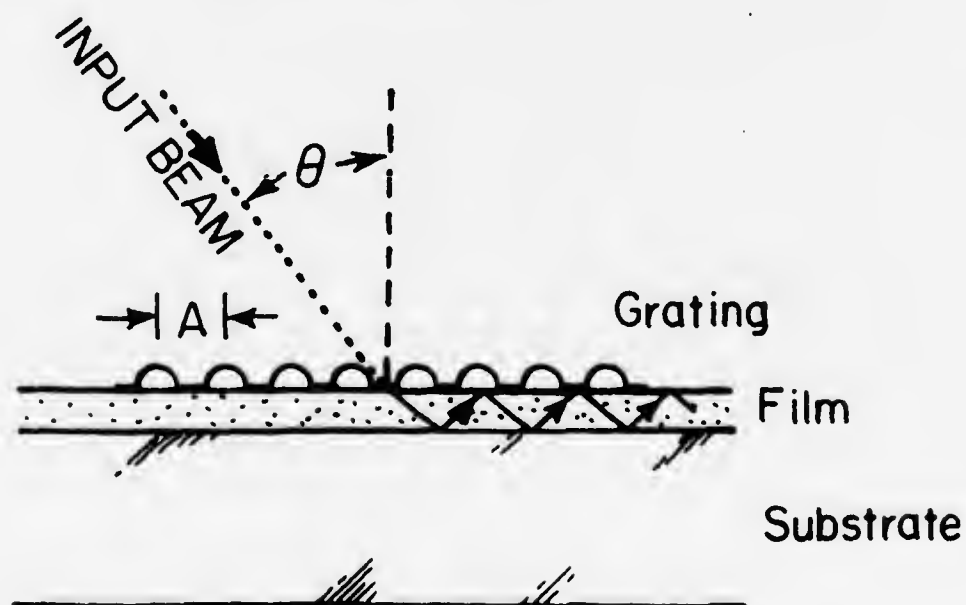
2.2.3 Coupling

Several efficient schemes for coupling light into and out of dielectric waveguides have been reported. Prism⁴⁰ and grating⁴¹ coupling are the standard techniques in use. Both approaches are illustrated in Fig. 2.6.

In this research, prism coupling was used exclusively. Light is incident on the face of a right-angle prism at an angle θ_1 , and is refracted within the prism. The refracted beam strikes the bottom prism surface over an interaction length, l , making an angle θ_2 with the film surface. Optical energy is coupled from the prism to the film by the evanescent field in the air gap separating the prism and substrate. This separation distance and the interaction length determine the coupling efficiency. Efficient coupling can be achieved with gap distances of several wavelengths. This requires both flat prism surfaces and film surfaces and the application of substantial mechanical



(a) Prism coupler



(b) Grating coupler

Fig. 2.6 Coupling schemes.

force to clamp the prism and film. For efficient coupling to occur, the y directed k vector in the prism must match one of the guided mode wave vectors, i. e.,

$$\eta_p k_o \cos \theta_2 = \eta_g k_o \quad (2.25)$$

and since

$$\eta_s < \eta_g < \eta_f \quad (2.26)$$

we have

$$\eta_s < \eta_p \cos \theta_2 < \eta_f \quad (2.27)$$

as the condition to be satisfied by θ_2 . The requirement on prism index is that it be greater than η_f . Theoretical coupling efficiencies have been calculated to be 81%.⁴⁰ Efficiencies as great as 60%¹⁵ have been reported.

For grating coupling an incident beam strikes a periodic structure, period A , on the surface of the film. Due to this periodic variation, the net y directed k vector at the film surface is

$$k_y = k_o \sin \theta + \frac{2\pi N}{A} \quad (2.28)$$

where N is an integer. When θ or A is selected so that k_y matches one of the guided mode indices, coupling occurs. Consider as an example a KTN film which supports a guided mode with $\eta_g = 2.25$. Let $\lambda_o = 633$ nm, $\theta = 45^\circ$, and couple into a forward going mode, i. e.,

$$k_o \cos 45^\circ + \frac{2\pi}{A} = k_o \eta_g \quad (2.29)$$

This requires a minimum spacing of 4300 Å for A if we use first order, $N = 1$, coupling. Holographic techniques⁴¹ are required to produce

gratings with this dimension. If one works with higher order coupling ($N > 1$)

$$A = N \cdot 4300 \text{ \AA} \quad (2.30)$$

the dimensional tolerances will be reduced, but at the expense of decreased efficiency. Theoretical maximum efficiency for grating couplers is about 80%.⁸² Experimental results indicate efficiencies in the 70% region.⁴¹

The grating coupler has the advantage of a planar geometry but the disadvantage of requiring sophisticated fabrication techniques. The prism coupler, though bulkier and requiring external pressure for clamping, has the overriding advantage, from a laboratory viewpoint, of greater convenience and ease of fabrication.

2.3 Methods for Thin Film Characterization

The composition of the KTN thin films and their dielectric and optical properties were determined using electron microprobe and X-ray analysis, resistance and capacitance measurements, and measurements of synchronous coupling angles. These experimental techniques are described below.

2.3.1 Composition

Composition was determined using an electron beam microprobe. When the microprobe beam is focused on the film surface, characteristic X-rays of each element, present in the irradiated region, are emitted and detected by an X-ray spectrometer. The standard beam voltage of 15 kV results in a spot size of 5 microns and a penetration depth of 5 microns. Since our KTN films were only 5-10 microns thick, and since composition variation as a function of film depth was of interest,

the beam voltage was reduced to 5 kV in order to decrease the penetration depth of the electrons. The 5 kV electron beam voltage gives a spot size of 25 microns and a penetration depth of 1 μm . Films were lapped at 1° . For this angle microprobe measurements along the lapped surface every 50 microns gave the thin film composition at 1 micron depth intervals. For low beam voltages, average Ta background counts were 10% and Nb background counts averaged 3%. If N is the mole % of Nb and T the mole % of Ta detected, the Nb mole fraction, x , is simply

$$x = \frac{N}{T + N} \quad (2.31)$$

and the root mean squared error in $\Delta x/x$ is

$$\frac{\Delta x}{x} = (1 - x) \left(\left(\frac{\Delta N}{N} \right)^2 + \left(\frac{\Delta T}{T} \right)^2 \right)^{\frac{1}{2}} \quad (2.32)$$

For $x = 0.25$ and $dN/N = 0.03$, $dT/T = 0.10$, an uncertainty in x of 7% results, i. e., $x = 0.25 \pm 0.02$.

X-ray analysis also gave an indication of the KTN composition. The variation in KTN cubic lattice constant, d , with Nb concentration follows Vegard's law.^{83, 7} This linear increase with mole fraction of Nb is shown in Fig. 2.7. At room temperature, $d(x=0) = 3.9885 \text{ \AA}$, $d(x=1) = 4.0033 \text{ \AA}$, implying a maximum lattice mismatch of 0.37% over the entire solid solution range. For an arbitrary lattice constant $d(x)$, the Nb concentration is

$$x = \frac{d(x) - d(0)}{d(1) - d(0)} \quad (2.33)$$

$d(x)$ is determined from X-ray diffractometer measurements of the

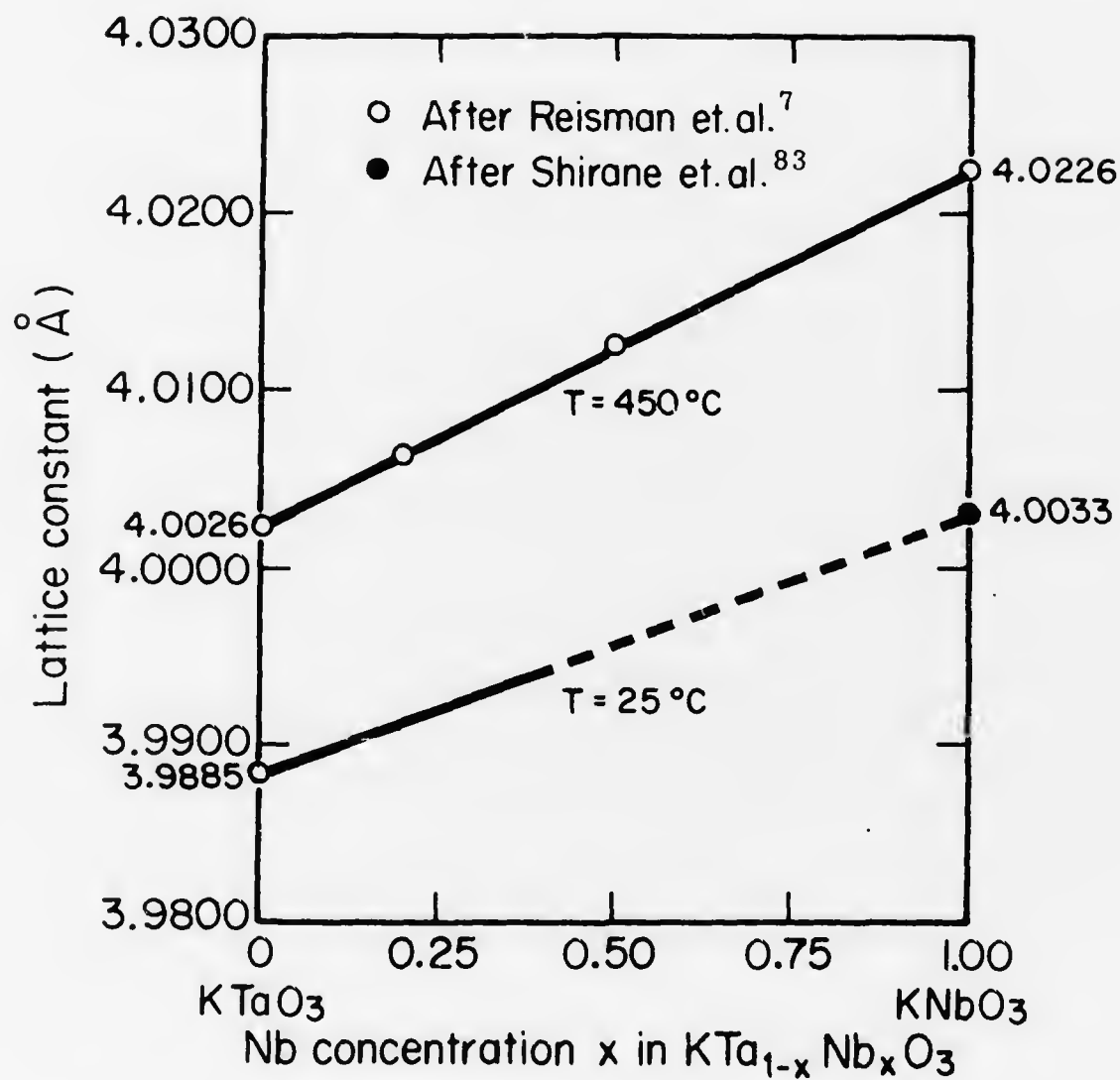


Fig. 2.7 Lattice constant vs Nb mole fraction, x , for KTN.

(h 0 0) lattice planes since the substrates are cut parallel to 100 directions.

In this work CuK_α radiation was used, and the (500) lattice peak was measured. From the Bragg equation

$$d = \frac{5}{2} \lambda \frac{1}{\sin \theta} \quad (2.34)$$

Typical angular accuracies are 0.025° or 4.4×10^{-4} radians. For $d \sim 4 \text{ \AA}$, $2\theta \approx 150^\circ$. The error in such measurements is

$$\Delta d / \Delta \theta = d \cot \theta \quad (2.35)$$

So $\Delta d = 0.0004 \text{ \AA}$, which implies a sensitivity in determining Δx of 0.03. The calculated penetration depth of CuK_α radiation in KTN is 10 microns.⁴² Clearly, reflections from both film and substrate will occur in these X-ray measurements.

This error analysis assumes that the films are not clamped. Clamping can change the lattice constant of the film and, if a clamped lattice constant were measured, a lower composition would be determined. This follows since the substrate has a smaller lattice constant than the film and because the clamping action of the substrate would tend to decrease the film lattice constant.

2.3.2 Optical Properties

The waveguide parameters η_g , η_s , η_f , and W were determined by measurement of the synchronous coupling angle, i. e., the angle θ_1 (see Fig. 2.6), at which coupling into a guided mode occurs. A more detailed geometry is shown in Fig. 2.8. θ_p and θ_1 are measured for each guided mode. η_g from Eq. (2.25) is

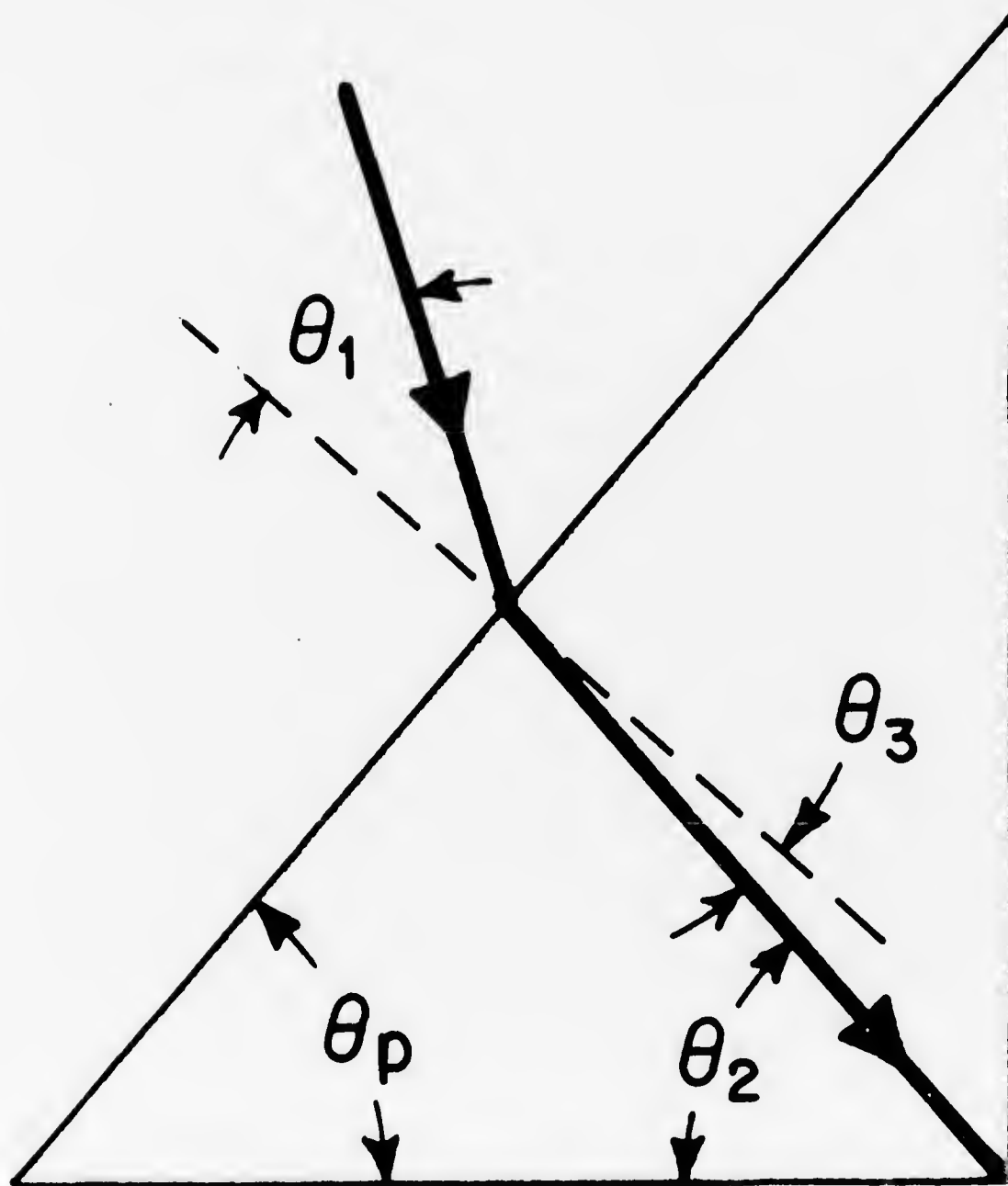


Fig. 2.8 Prism angles for synchronous angle measurements.

$$\eta_g = \eta_p \cos(90 - \theta_p + \sin^{-1}(\frac{1}{\eta_p} \sin \theta_1)) \quad (2.36)$$

Provided the guide is multimode, a set of values for η_g can be determined. Then, using Eq. (2.13), a best fit to this set can be made giving values for η_s , η_f , and W .⁴³ The difficult aspect of the experiment is accurately measuring θ_1 . The error in η_g is

$$\begin{aligned} \Delta\eta_g / \Delta\theta_1 &= \sin(90 - \theta_p + \sin^{-1}(\frac{1}{\eta_p} \sin \theta_1)) \cdot \cos \theta_1 \cdot \\ &\quad (1 - \frac{1}{\eta_p^2} \sin^2 \theta_1)^{-1} \end{aligned} \quad (2.37)$$

For a KTN film, $\theta_1 = 13^\circ$, $\eta_p = 2.872$, and $\eta_g = 2.2603$. This gives $\Delta\eta_g = 0.615 \times \Delta\theta$. For our system, accuracies of $\Delta\theta = 2$ minutes were possible. Thus, $\Delta\eta_g = \pm 0.0005$.

Optical loss was determined by measuring the scattered light in the guided mode streak on the surface of the film as a function of distance from the input prism. This detection is done with an optical fiber with diameter equal to the width of the guided streak. The assumption is that the scattered intensity at a position x , $I(x)$, is proportional to the power contained in the guide $I_g(x)$. Measurement at two points x_1 , x_2 gives the loss α

$$\alpha = \frac{1}{x_2 - x_1} \ln \left\{ \frac{I(x_1)}{I(x_2)} \right\} \quad (2.38)$$

By taking a series of measurements uniformly spaced along the guided path, a least means square fit of $\log I(x)$, x will give a more accurate value for α . The advantage of this measurement technique is that no absolute measurement of the loss is required; rather a ratio or relative

comparison is made.

Such measurements cannot distinguish between surface and volume losses. Also, in these experiments, it was observed that modes other than the synchronous mode were usually observed at the output prism, though at lower intensities than the synchronous mode. As a result, the loss determined from the measurements on any guided light streak should be interpreted as a weighted average of the loss associated with all the excited modes.

2.3.3 Dielectric Properties and Conductivity

The dielectric permittivity and ac and dc conductivity of the KTN thin films were determined by depositing an inter-digital electrode on the film surface and measuring the capacitance and resistance of the resulting thin film device. The electrode structure is shown in Fig. 2.9. Provided the electric field distribution within the film and substrate resulting from this electrode is known, capacitance and resistance can be related to σ and ϵ . Knowledge of this electric field distribution is necessary as well for any electro-optic device applications.

A side view of the electrode geometry is shown in Fig. 2.10a, b. There are N fingers of length, W , and spacing and width, L . Film thickness is d and parameters associated with film and substrate are subscripted 1, 2, respectively. For the field solution two assumptions are made. The electrode fingers are assumed to be infinite in extent, i.e., N is large, allowing a Fourier series expansion of the potential. The potential at the surface is assumed to be trapezoidal⁴⁴ as shown in Fig. 2.10c.

Now $\phi(x, 0)$ can be expressed in Fourier components as

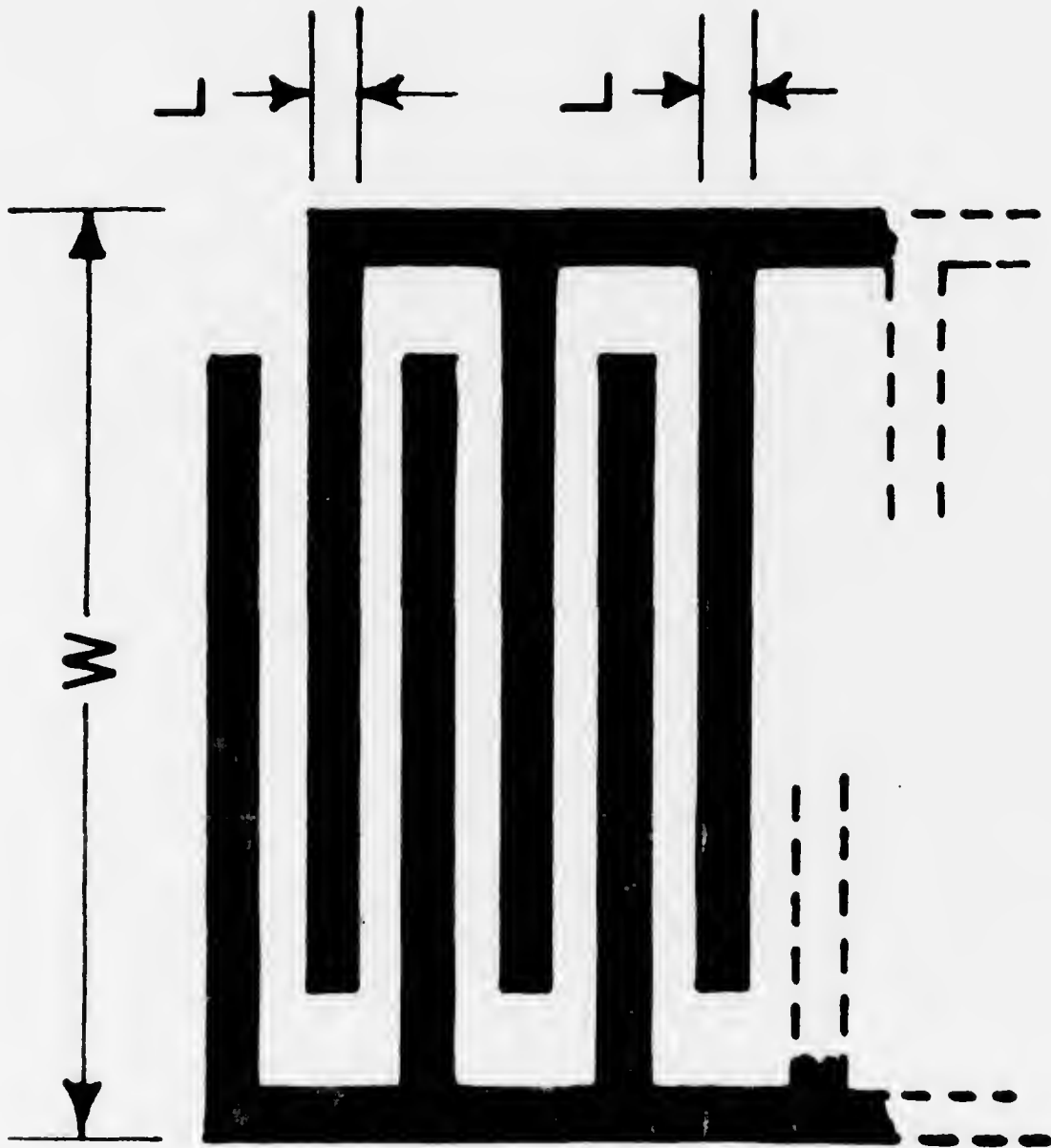


Fig. 2.9 Interdigital electrode geometry.

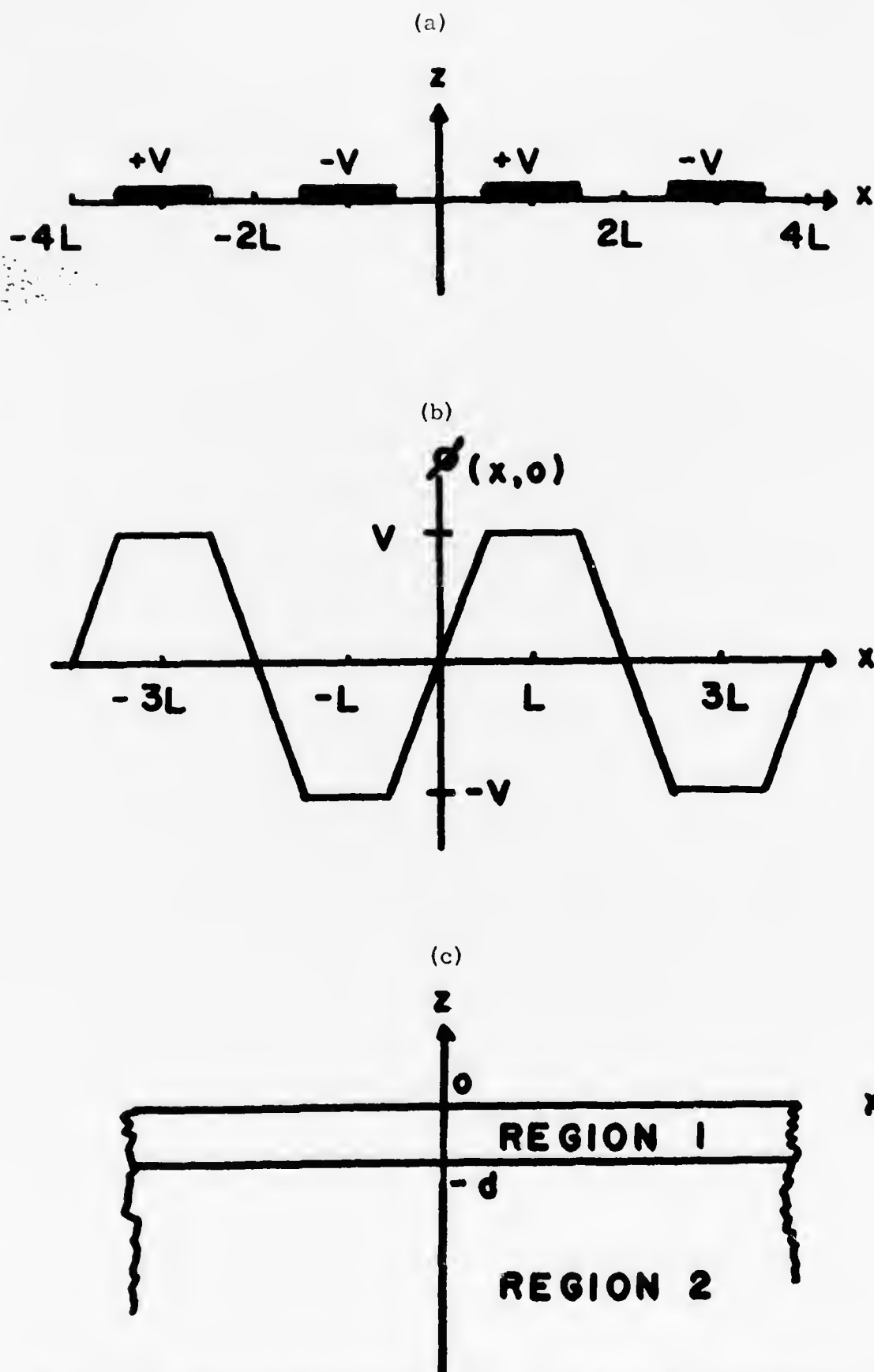


Fig. 2.10 Electric field calculations: (a) electrode cross section, (b) surface potential, (c) film substrate geometry.

$$\varphi(x, 0) = \sum A_n \sin \frac{x}{l_n} \quad (2.39)$$

$$A_n = 4V_0 \left(\frac{l_n}{L}\right)^2 \sin \frac{L}{2l_n} \quad (2.40)$$

$$l_n = \frac{2L}{(2n+1)\pi} \quad (2.41)$$

where l_n is the penetration depth of each Fourier component. The potential in the film and substrate may be written as

$$\varphi_1 = \sum \left\{ C_n \sin \frac{x}{l_n} \sinh \frac{z}{l_n} + B_n \sin \frac{x}{l_n} \cosh \frac{z}{l_n} \right\} \quad (2.42)$$

$$\varphi_2 = \sum D_n \sin \frac{x}{l_n} e^{(z+d)/l_n} \quad (2.43)$$

Continuity of φ at $x = 0$, $-d$ and continuity of normal displacement vector at $z = -d$ gives

$$B_n = A_n \quad (2.44)$$

$$C_n = A_n \left\{ \frac{\frac{\epsilon_2}{\epsilon_1} \cosh \frac{d}{l_n} + \sinh \frac{d}{l_n}}{\frac{\epsilon_2}{\epsilon_1} \sinh \frac{d}{l_n} + \cosh \frac{d}{l_n}} \right\} \equiv A_n \gamma_n \quad (2.45)$$

$$D_n = A_n \left\{ \frac{\epsilon_2}{\epsilon_1} \sinh \frac{d}{l_n} + \cosh \frac{d}{l_n} \right\}^{-1} \equiv A_n \xi_n \quad (2.46)$$

from which the field solutions are determined

$$E_{1x} = -\frac{2V_o}{L} \sum \frac{2}{L} \sin \frac{1}{2} \frac{L}{l_n} \left\{ \gamma_n \sinh \frac{z}{l_n} + \cosh \frac{z}{l_n} \right\} \cos \frac{x}{l_n} \quad (2.47)$$

$$E_{1z} = -\frac{2V_o}{L} \sum \frac{2}{L} \sin \frac{L}{2 l_n} \left\{ \gamma_n \cosh \frac{z}{l_n} + \sinh \frac{z}{l_n} \right\} \sin \frac{x}{l_n} \quad (2.48)$$

$$E_{2x} = -\frac{2V_o}{L} \sum \frac{2}{L} \sin \frac{L}{2 l_n} \left\{ \xi_n e^{(z+d)/l_n} \right\} \cos \frac{x}{l_n} \quad (2.49)$$

$$E_{2z} = -\frac{2V_o}{L} \sum \frac{2}{L} \sin \frac{L}{2 l_n} \left\{ \xi_n e^{(z+d)/l_n} \right\} \sin \frac{x}{l_n} \quad (2.50)$$

$\frac{2V_o}{L}$ is the magnitude of the electric field at the surface. Since $\epsilon_2 < \epsilon_1$ for our films and substrates, γ_n increases from $\frac{\epsilon_2}{\epsilon_1}$ to 1 as d/l_n increases. ξ_n , on the other hand, has a maximum value of 1 for $d/l_n = 0$ and decreases exponentially to 0. The amplitude of each electric field Fourier component decreases as $\frac{1}{2n+1}$ and its penetration depth is reduced by $\frac{1}{2n+1}$. Consequently only the first few terms contribute appreciably to the field solution.

In this work $L = 25$ microns, and film thicknesses were about 5 microns. The electric field behavior is shown in the following series of figures. Figure 2.11 is a plot of $E_x(o, z)$ vs z or depth into the film for $\epsilon_2/\epsilon_1 = 0.125, 0.025$, and 1. The case $\epsilon_2/\epsilon_1 = 1$ approximates an indiffused guiding structure as in LiNbO_3 . $\frac{\epsilon_2}{\epsilon_1} = 0.125$ are values for $\text{KTa}_{0.75}\text{Nb}_{0.25}\text{O}_3/\text{KTaO}_3$ and $\frac{\epsilon_2}{\epsilon_1} = 0.025$ are values for $\text{KTa}_{0.65}\text{Nb}_{0.35}\text{O}_3$. Note that the change in E_x for the KTN values is only 5% within the film, while for the LiNbO_3 values this change is 30%. The field is confined in the KTN film because the ratio of film to substrate dielectric constant is large. l_o for this data is 16 microns. Figure 2.12 shows the field

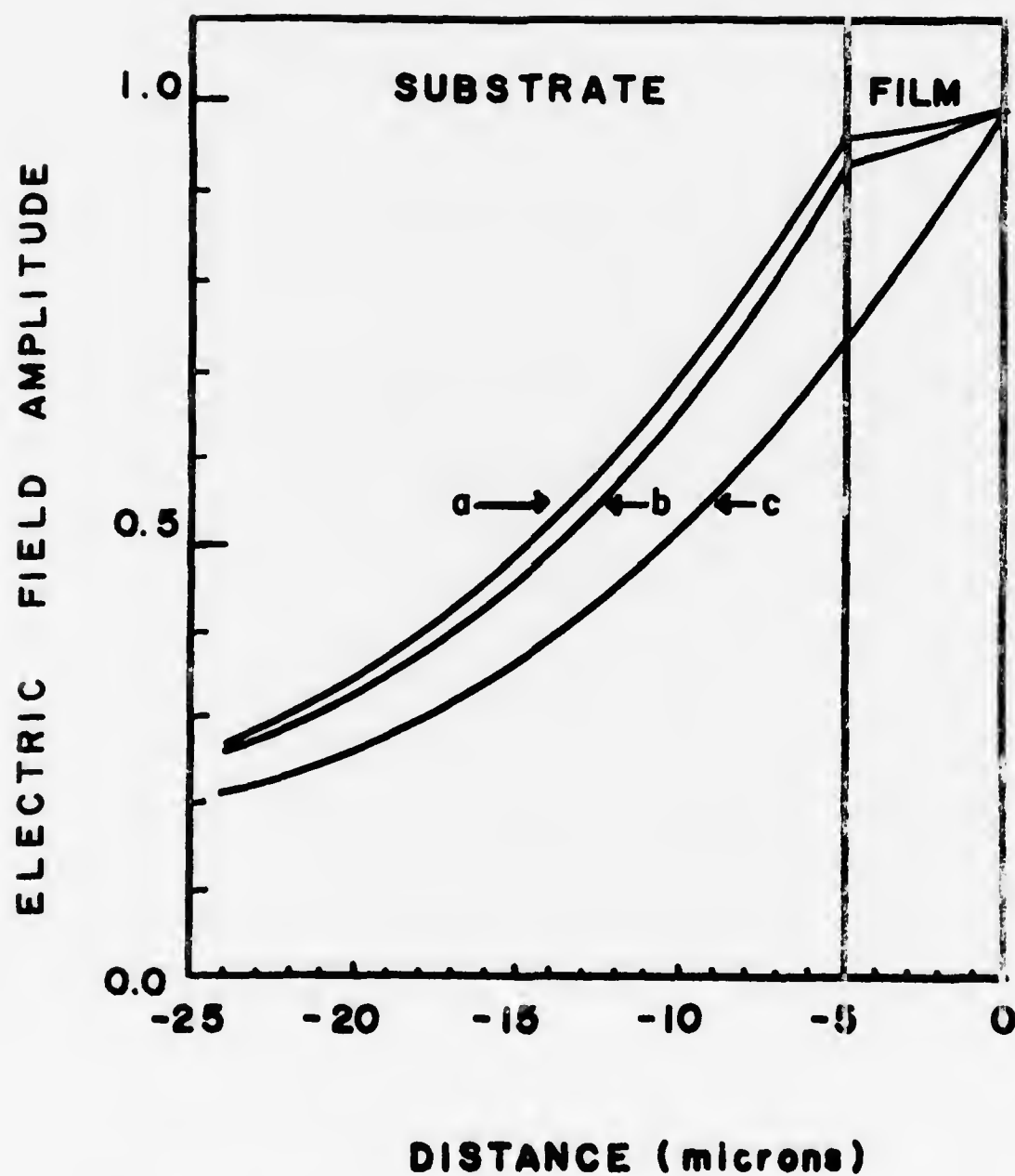


Fig. 2.11 $E_x(o, z)$ vs z for $L = 25$ microns, $d = 5$ microns:
 (a) $\epsilon_2/\epsilon_1 = 0.025$, (b) $\epsilon_2/\epsilon_1 = 0.125$, (c) $\epsilon_2/\epsilon_1 = 1$.

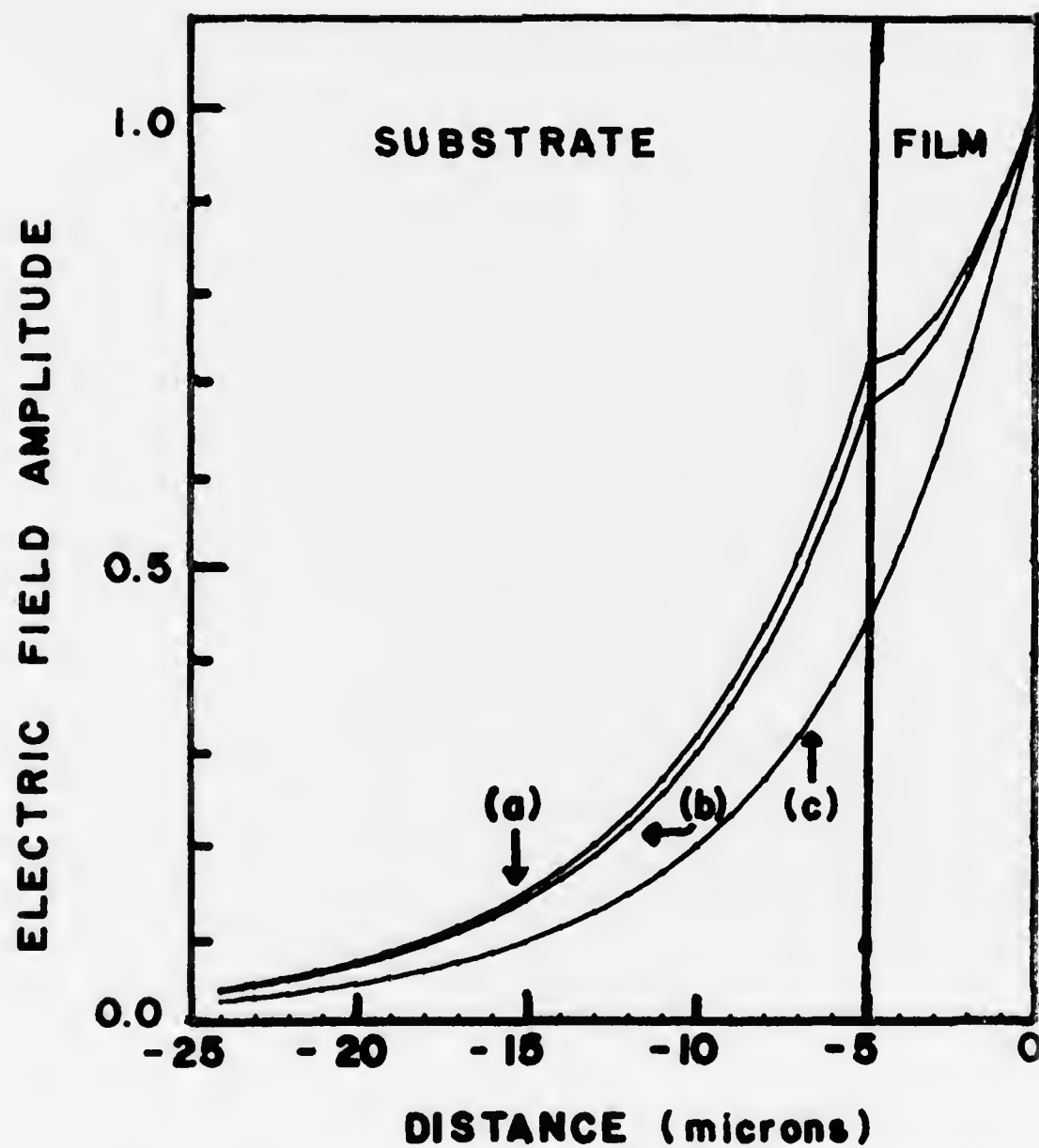


Fig. 2.12 $E_x(0, z)$ vs z for $L = 10$ microns, $d = 5$ microns:
 (a) $\epsilon_2/\epsilon_1 = 0.025$, (b) $\epsilon_2/\epsilon_1 = 0.125$, (c) $\epsilon_2/\epsilon_1 = 1$.

variation for $L = 10$ microns, $d = 5$ microns. In this case, the field decays more rapidly into the film. This results because the decay length is now only 6 microns, almost the width of the film. Figure 2.13 is a plot of $E_x(x, -\frac{d}{2})$. The field intensity variation in the horizontal dimension shows that the field is within 50% of its peak value for the gap between the electrodes and drops quickly to zero for the region beneath the electrode fingers. Note that for $L = 25$ microns and $V = 25$ volts a field of 10,000 V/cm is generated at the surface and for the KTN case the field will have a magnitude of about 9000 V/cm at the film-substrate interface.

Using these field solutions, and measured capacitance C , and conductance G of the sample, σ and ϵ may be determined. Recall the definition for C and G

$$\frac{1}{2} CV^2 = \frac{1}{2} \iiint \epsilon E \cdot E d^3r \quad (2.51)$$

$$\frac{1}{2} GV^2 = \frac{1}{2} \iiint \sigma E \cdot E d^3r \quad (2.52)$$

When the integration is performed over x , the orthogonality of the Fourier components simplifies the results. Defining two geometry factors, G_1 and G_2

$$G_1 = (1 + \gamma_n^2) \sinh \frac{2d}{l_n} + 2\gamma_n - 2\gamma_n \cosh \frac{2d}{l_n} \quad (2.53)$$

$$G_2 = 2 \xi_n^2 \quad (2.54)$$

C and G have the relation

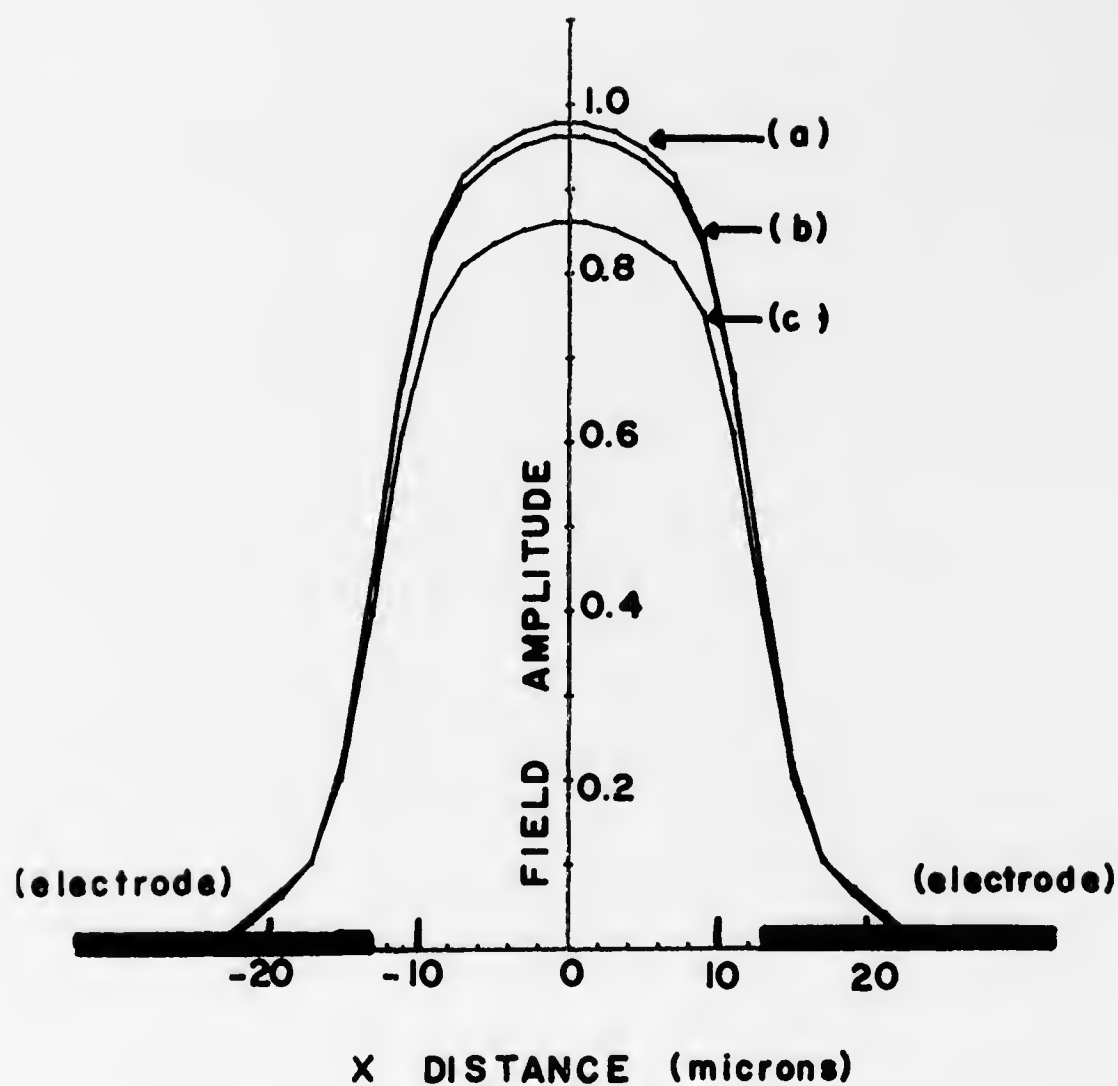


Fig. 2.13 $E_x(x, -d/2)$ vs x for $L = 25$ microns, $d = 5$ microns:
 (a) $\epsilon_2/\epsilon_1 = 0.025$, (b) $\epsilon_2/\epsilon_1 = 0.125$, (c) $\epsilon_2/\epsilon_1 = 1$.

$$C = \frac{8NW}{\pi^3} \sum \left(\frac{1}{2n+1}\right)^3 (\epsilon_1 G_1 \left(\frac{d}{l_n}\right) + \epsilon_2 G_2 \left(\frac{d}{l_n}\right)) \quad (2.55)$$

$$G = \frac{8NW}{\pi^3} \sum \left(\frac{1}{2n+1}\right)^3 (\sigma_1 G_1 \left(\frac{d}{l_n}\right) + \sigma_2 G_2 \left(\frac{d}{l_n}\right)) \quad (2.56)$$

A plot of $G_1 \left(\frac{d}{l_n}\right)$ and $G_2 \left(\frac{d}{l_n}\right)$ is shown in Fig. 2.14. Note both expressions are bounded by a value 2. Using Eqs. (2.55) and (2.56), dielectric constant and conductivity are easily determined from measured capacitance values.

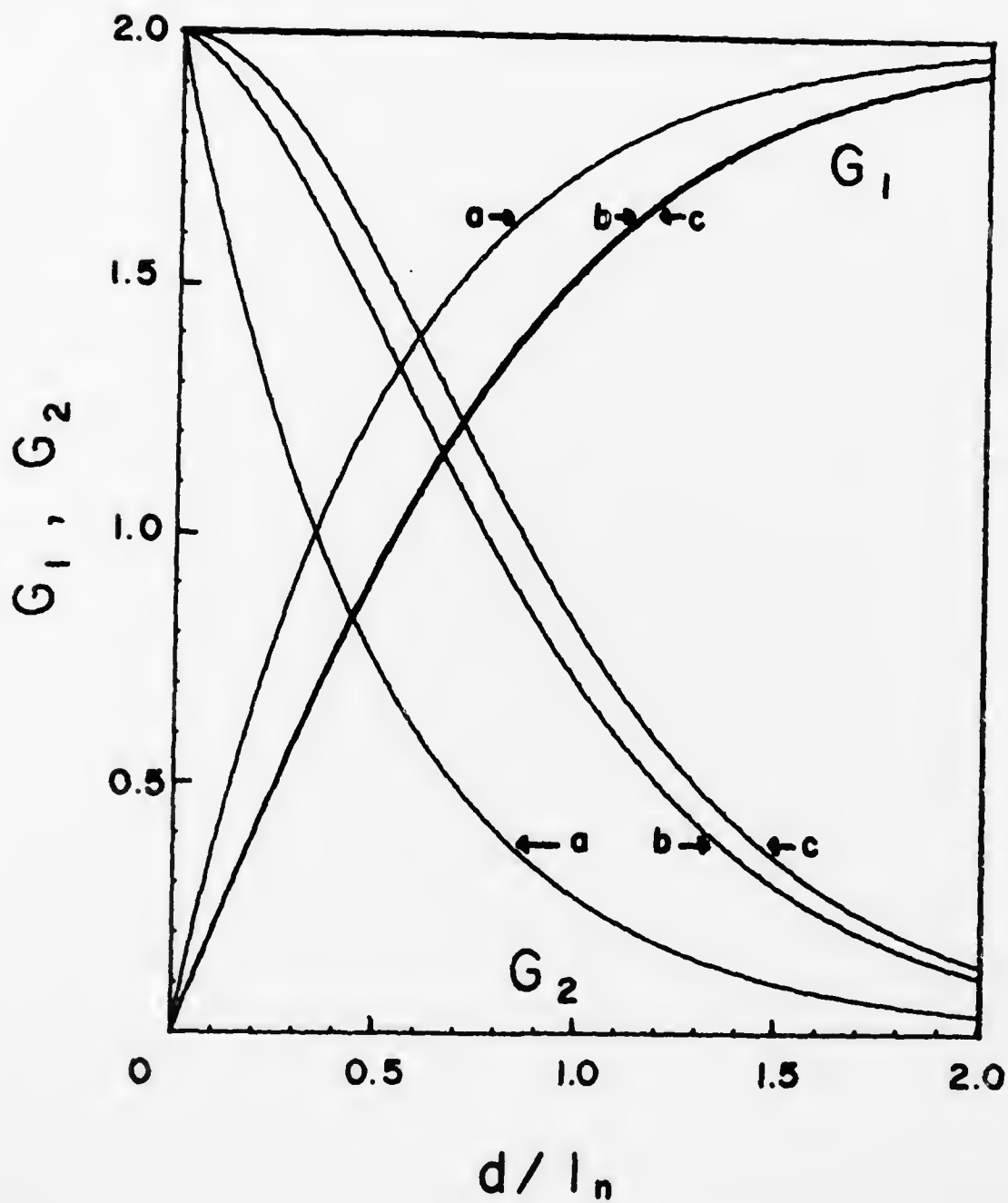


Fig. 2.14 Geometry factors G_1, G_2 vs length ratio d/l_n .

CHAPTER 3

THEORY FOR THIN FILM ELECTRO-OPTIC MODULATION

The primary reason for considering KTN as an integrated optics material is its large room temperature electro-optic effect for selected compositions. Figure 3.1 shows the optical index change as a function of electric field that occurs for two KTN compositions. Comparison of this change with corresponding index changes in LiTaO_3 makes it apparent that substantial reduction in drive voltage and power requirements can be achieved in KTN devices.

In this chapter we review the existing thin film electro-optic modulators. The electro-optic effect in KTN and its influence on guided modes in thin films will be described. Issues concerning device performance will be illustrated by examining the operation of a thin film phase modulator. Finally, the discussion will be directed toward the theory of beam diffraction and deflection in thin films, since this type of modulator was fabricated in our research.

3.1 Review of Thin Film Electro-optic Devices

In the past years, modulation and switching devices employing a thin film geometry have improved in performance because of the introduction of new film-substrate material combinations and the development of more sophisticated lithography techniques. As a result, drive voltages which were as high as 300 volts in early devices have been reduced to 1 to 4 volts.

The first reported electro-optic waveguide modulator using an insulating oxide material was fabricated by Channin.⁴⁵ Two parallel electrodes 1 cm long and separated by 75 microns were deposited on a

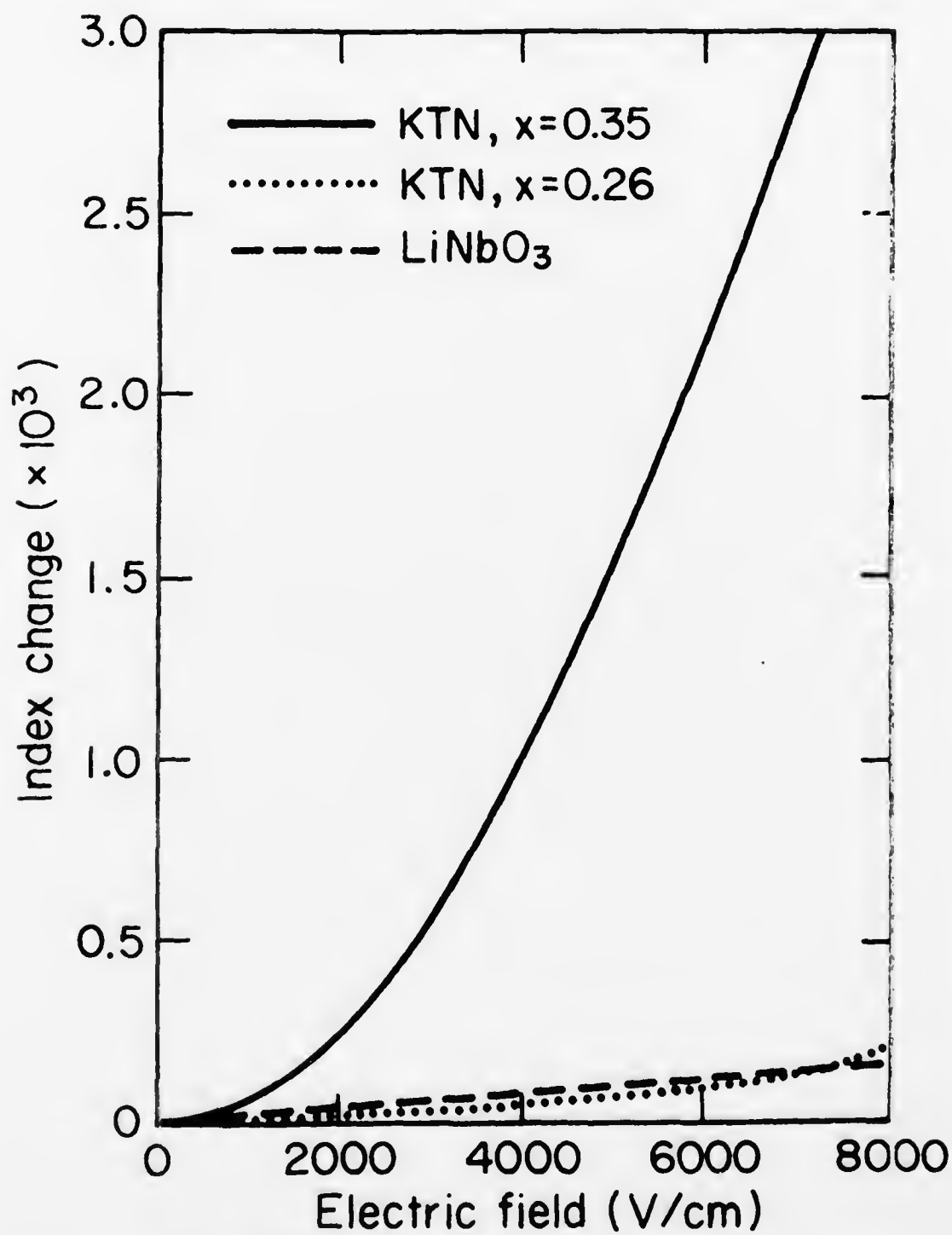


Fig. 3.1 Index change vs electric field for KTN ($x = 0.34$), KTN ($x = 0.26$), LiNbO_3 .

LiNbO_3 crystal. The application of a voltage increased the optical index in the region between the electrodes enough to allow optical guiding. This voltage induced waveguide behaved as a crude optical switch. Using a similar electrode structure, but on an out-diffused LiNbO_3 waveguide, Kaminow and Carruthers⁴⁶ built a phase modulator giving a phase shift of π radians for 8 volts. Tien et al.⁴⁷ designed a beam deflector using a LiNbO_3 epitaxial film that gave angular deflections of $\sim 4^\circ$ when an electric field was applied to large area electrodes, creating regions of high optical index that refracted the guided modes.

Amplitude modulation in thin film waveguides has been accomplished by using an interdigital electrode to create a periodic index variation along the path of the guided beam upon the application of an electric field. The beam is diffracted or deflected into one or more side order beams. This type of modulation has been demonstrated with liquid crystal films,⁴⁸ ZnO films,^{49, 50} and in in-diffused,²² out-diffused,⁵¹ and sputtered LiNbO_3 structures.²⁷

By using ion milling, etching, and selective diffusion techniques, strips or ridges of electro-optic material capable of supporting guided modes have been fabricated. The devices described previously were planar in nature. The ridge device confines the light beam in both transverse dimensions. Guide thicknesses are typically on the order of 1-3 microns and widths of 10-20 microns. These dimensions are presently limited by fabrication techniques.

The first electro-optic modulator using the ridge geometry, reported by Kaminow, was a phase modulator fabricated from an out-diffused LiNbO_3 guide⁵² in which the out-diffused surface was ion milled

away except for a 10-micron wide strip protected by a quartz rod during the milling process. A phase shift of π radians was obtained for a modulating voltage of 1.2 volts. Similar devices using indiffused guides have been reported by Noda^{53, 54} and Vehara.⁵⁵ Two closely spaced, parallel ridges on the same substrate have been demonstrated as optical couplers. The application of an electric field across these ridges can control the coupling efficiency. This procedure was employed by Zernike²⁹ in a "push-pull" modulator and Martin⁵⁶ in an optical switch.

3.2 Electro-optic Effect in KTN Thin Films

3.2.1 KTN Electro-optic Effect

The application of a modulating electric field to an electro-optic medium induces a change in the elements of the impermeability tensor $b_{ij} = (1/\eta^2)_{ij}$. For cubic KTN, which has a quadratic electro-optic effect, the change in the impermeability tensor is expressed as

$$\begin{aligned} b_{ij} &= \left(\frac{1}{\eta^2} \right)_{ij} = \frac{1}{\eta_o^2} \delta_{ij} + g_{ijkl} P_k P_l \\ &= \frac{1}{\eta_o^2} \delta_{ij} + g_{ijkl} \epsilon_{km} \epsilon_{ln} E_m E_n \end{aligned} \quad (3.1)$$

where P is the polarization, E is the modulating electric field, ϵ_{km} is the dielectric tensor relating P to E , g_{ijkl} is the quadratic electro-optic coefficient, and η_o is the unperturbed optical index of KTN. In Eq. (3.1) i, j, k take on values 1, 2, 3 which refer to the principal directions [100], [010], [001] of the KTN cubic lattice. These directions form a cartesian coordinate system, x, y, z .

For cubic KTN, there are three non-zero quadratic coefficients,

g_{11} , g_{12} , g_{44} , and the dielectric tensor is diagonal $\epsilon_{km} = \epsilon \delta_{km}$. The elements of the impermeability tensor are therefore

$$\left(\frac{1}{\eta^2}\right)_{11} = \frac{1}{\eta_0^2} + \epsilon^2 g_{11} E_1^2 + \epsilon^2 g_{12} (E_2^2 + E_3^2) \quad (3.2)$$

$$\left(\frac{1}{\eta^2}\right)_{22} = \frac{1}{\eta_0^2} + \epsilon^2 g_{11} E_2^2 + \epsilon^2 g_{12} (E_1^2 + E_3^2) \quad (3.3)$$

$$\left(\frac{1}{\eta^2}\right)_{33} = \frac{1}{\eta_0^2} + \epsilon^2 g_{11} E_3^2 + \epsilon^2 g_{12} (E_1^2 + E_2^2) \quad (3.4)$$

$$\left(\frac{1}{\eta^2}\right)_{13} = \left(\frac{1}{\eta^2}\right)_{31} = \epsilon^2 g_{44} E_1 E_3 \quad (3.5)$$

$$\left(\frac{1}{\eta^2}\right)_{12} = \left(\frac{1}{\eta^2}\right)_{21} = \epsilon^2 g_{44} E_1 E_2 \quad (3.6)$$

$$\left(\frac{1}{\eta^2}\right)_{23} = \left(\frac{1}{\eta^2}\right)_{32} = \epsilon^2 g_{44} E_2 E_3 \quad (3.7)$$

The application of a modulating electric field makes KTN optically anisotropic.

For modulator design it is necessary to relate these changes in the impermeability tensor to changes in the propagation characteristics of guided modes in KTN thin films.

3.2.2 Plane Wave Propagation in Anisotropic Media

The plane wave propagation of light in anisotropic media can be described by using the optical indicatrix or index ellipsoid which is defined as

$$\sum_{i,j} \left(\frac{1}{\eta^2} \right)_{ij} x_i x_j = 1 \quad (3.8)$$

The use of the indicatrix has been discussed in detail by Born and Wolf⁵⁷ and in the general modulation review articles by Chen,⁵⁸ Wemple and DiDomenico,¹⁰ and Kaminow and Turner.⁵⁹

In an anisotropic media, for any propagation direction two normal mode solutions for the displacement vector, D_a and D_b , with polarization directions i_a , i_b and optical indices η_a , η_b will exist. Any wave polarized with displacement vector along i_a or i_b will propagate in the anisotropic medium with phase velocity c/η_a or c/η_b and remain linearly polarized along its initial direction. Waves polarized along other directions will become elliptically polarized when propagating in the anisotropic medium.

The polarization directions i_a , i_b and indices η_a , η_b can be determined geometrically with the aid of the optical indicatrix. Equation (3.8) describes an ellipsoidal surface. The intersection of the plane which passes through the origin and is normal to the propagation direction of the plane wave with this surface defines an ellipse. The major and minor axes of this ellipse are the normal mode polarizations. The lengths of these axes are the optical indices. The geometrical approach is illustrated in Fig. 3.2.

This technique can be used for a common modulator configuration used for bulk optical device applications in KTN. The modulating electric field is applied transverse to the propagation direction of the light wave. In particular, let E be applied along the x direction and let the light travel along y . The impermeability tensor has the form

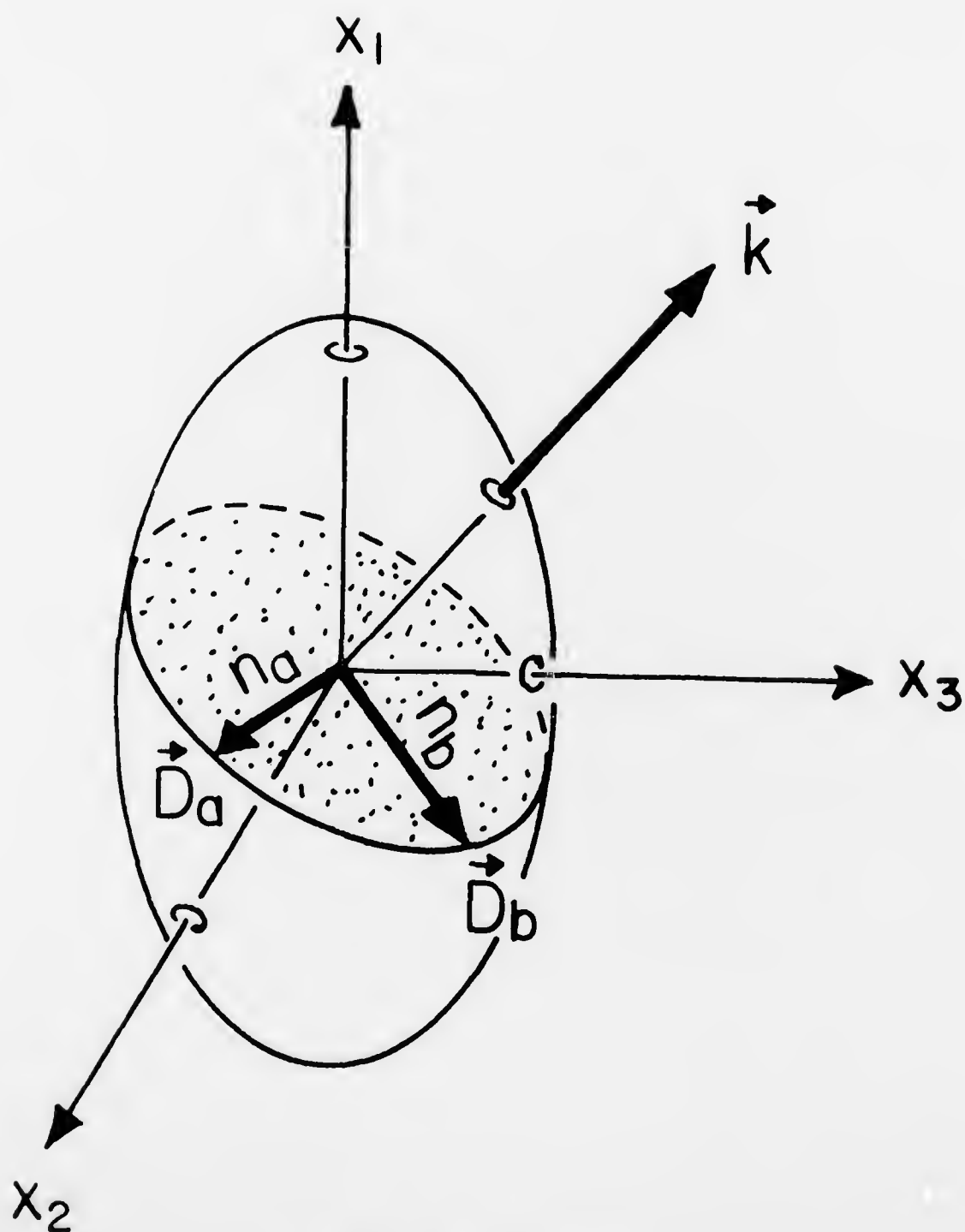


Fig. 3.2 Optical indicatrix.

$$\left(\frac{1}{\eta^2} \right) = \begin{bmatrix} \frac{1}{\eta_o^2} + g_{11} \epsilon^2 E^2 & 0 & 0 \\ 0 & \frac{1}{\eta_o^2} + g_{12} \epsilon^2 E^2 & 0 \\ 0 & 0 & \frac{1}{\eta_o^2} + g_{12} \epsilon^2 E^2 \end{bmatrix} \quad (3.9)$$

KTN is now uniaxial. For propagation in the y direction, the resulting ellipse intersecting the indicatrix has the equation

$$\left(\frac{1}{\eta_o^2} + g_{11} \epsilon^2 E^2 \right) x^2 + \left(\frac{1}{\eta_o^2} + g_{12} \epsilon^2 E^2 \right) z^2 = 1 \quad (3.10)$$

The normal mode polarization directions are i_x , i_z . Because the electro-optical index changes are small, the resulting indices are given, to a very good approximation, by

$$\eta = \eta_o - \frac{1}{2} \eta_o^3 g_{11} \epsilon^2 E^2 \quad (\text{x-polarization}) \quad (3.11)$$

$$\eta = \eta_o - \frac{1}{2} \eta_o^3 g_{12} \epsilon^2 E^2 \quad (\text{z-polarization}) \quad (3.12)$$

3.2.3 Electro-optically Induced Changes in the Guided Mode Index

In this section the index changes for plane waves propagating in bulk material will be used to determine changes in the guided mode index, η_g , of modes in electro-optic thin films. The geometry for this discussion is shown in Fig. 3.3. An optically guided mode is confined in a thin film between two surface electrodes of length W, separation L, and width L. The film thickness is d. The application of a voltage across the electrodes creates a principally x polarized modulating

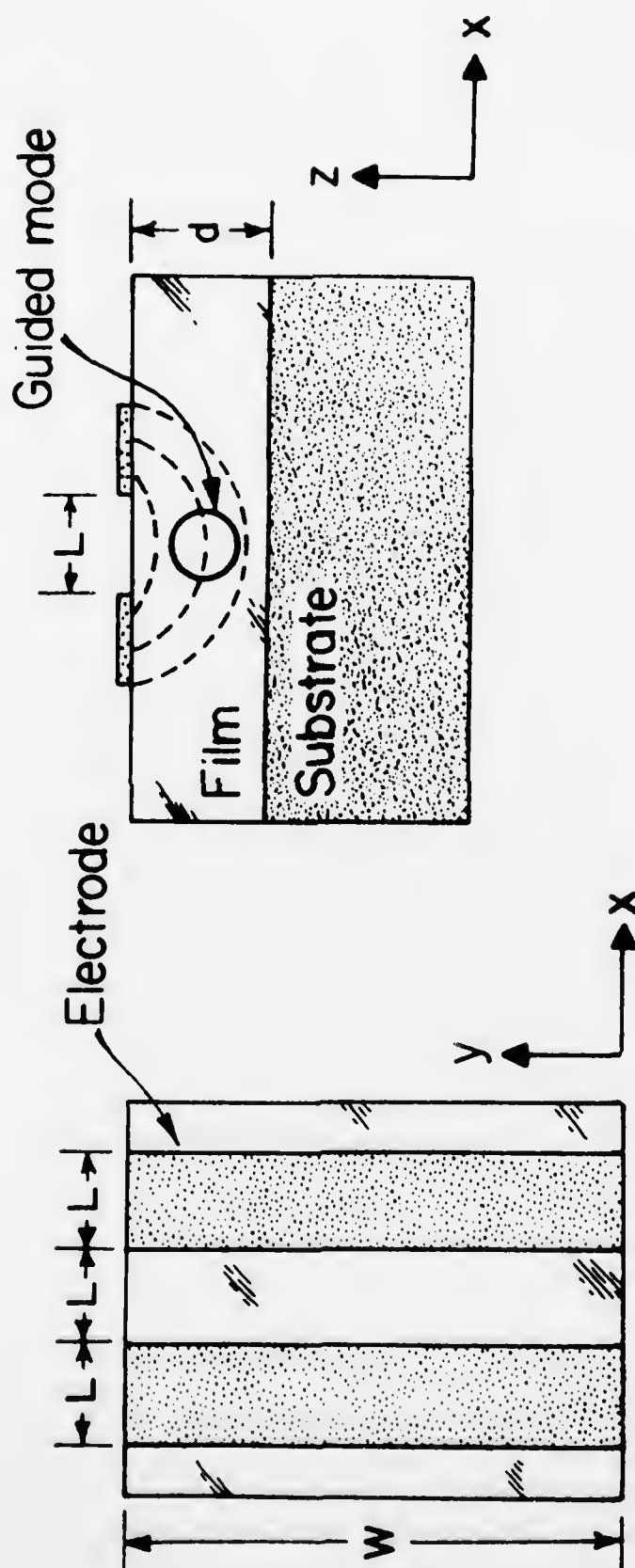


Fig. 3.3 Thin film phase modulator geometry.

electric field transverse to the mode propagation direction, y . In this geometry TE modes have their electric field polarized along x ; TM modes have their transverse electric fields polarized along z .

To calculate the change in guided mode index, the change in the KTN thin film index must first be determined. Several approximations are required to obtain this index change.

The z component of the modulating field is neglected. This eliminates off-diagonal terms, b_{13} and b_{31} , in the impermeability tensor and the normal mode polarization directions remain as i_x, i_z . Since E_z is small compared to E_x in the region where the field interacts with the guided mode (d is usually much less than L), this approximation is valid.

The problem is still complicated because the modulating field decays into the film. From Eqs. (3.11), (3.12), this will give rise to a graded index variation because the index change depends on the square of the modulating electric field. Since, as shown in Fig. (2.11), E_x changes by only 5% through the KTN film, the use of an average value of E_x^2 , defined as

$$\overline{E_x^2} = \frac{1}{L} \frac{1}{d} \int_{-d}^0 \int_{-L/2}^{L/2} E_x^2(x, z) dz dx \quad (3.13)$$

is justified for the calculation of the thin film index change.

Using these approximations, the film index will change by

$$\Delta\eta_f = -\frac{1}{2} g_{11} \epsilon^2 \overline{E_x^2} \eta_f^3 \quad \text{TE modes} \quad (3.14)$$

$$\Delta\eta_f = -\frac{1}{2} g_{12} \epsilon^2 \overline{E_x^2} \eta_f^3 \quad \text{TM modes} \quad (3.15)$$

The change in guided mode index can then be determined by resolving Eq. (2.13), the dispersion relation, for $\Delta\eta_f$ ($\Delta\eta_1$ in the notation of Eq. (2.13)). Since $\Delta\eta_f$ is small ($\Delta\eta_f/\eta_f \leq 0.0005$ for KTN) the change in guided mode index can be determined by expanding Eq. (2.13) in a Taylor series about the unperturbed guided mode index η_{g0} . If we designate the unperturbed film index by η_{f0} , we have

$$\Delta\eta_g = \left. \frac{\partial\eta_g}{\partial\eta_f} \right|_{\eta_{f0}} \Delta\eta_f \quad (3.16)$$

Tien has calculated $\partial\eta_g/\partial\eta_f$.¹⁵ The expression is

$$\frac{\partial\eta_g}{\partial\eta_f} = \frac{\eta_f}{\eta_g} \frac{W + \frac{p_0}{2 + b^2} + \frac{p_2}{2 + b^2}}{W + \frac{1}{p_0} + \frac{1}{p_2}} \quad (3.17)$$

For the TE_2 mode in a KTN ($x = 0.25$) film of thickness $W = 5$ microns, with $\lambda = 633$ nm, $\eta_f = 2.28$, $\eta_o = 2.24$, $\partial\eta_g/\partial\eta_f$ has the value 0.98. This occurs because the ratio η_f/η_g is at most 1.02 and because in thick guides W is greater than p_0^{-1} , p_2^{-1} , the decay lengths for lower order modes. Therefore, referring to Eq. (3.18), the change in guided mode index is equal to the change in film index within a few percent.

This approximation, $\partial\eta_g/\partial\eta_f \approx 1$, has been used successfully in explaining phase and amplitude modulation effects in ZnO films,^{49, 50} indiffused³² and outdiffused LiNbO₃ guides,⁴⁶ and in sputtered ZnO⁷⁸ and LiNbO₃²⁷ guides. It is valid provided η_g is associated with a low order mode and that the film-substrate index discontinuity is small. The net result is that the change in guided mode index is equal to the change in film index. Therefore, in KTN, we have

$$\Delta\eta_g = -\frac{1}{2} \eta_f^3 g_{11} \epsilon^2 \overline{E_x^2} \quad (\text{TE modes}) \quad (3.18)$$

$$\Delta\eta_g = -\frac{1}{2} \eta_f^3 g_{12} \epsilon^2 \overline{E_x^2} \quad (\text{TM modes}) \quad (3.19)$$

For comparison, for LiNbO_3 with c axis along x and either a axis along z , the index changes for guided modes will be

$$\Delta\eta_g = -\frac{1}{2} \eta_f^3 r_{13} \overline{E_x} \quad (\text{TE modes}) \quad (3.20)$$

$$\Delta\eta_g = -\frac{1}{2} \eta_f^3 r_{33} \overline{E_x} \quad (\text{TM modes}) \quad (3.21)$$

3.3 Modulator Design Issues

3.3.1 Performance Figure

Optical modulators are designed with the goals of minimizing drive-power requirements, P_D , and maximizing operating bandwidth, ν . The performance figure for an optical modulator is the power-bandwidth ratio, P_D/ν , which is quoted in units of mW/MHz. While P_D and ν will clearly depend on the external circuitry used to drive the modulator, the performance figure, which is a measure of the reactive energy stored in the device, depends only on the device geometry and the dielectric and electro-optic parameters of the modulator material.

The equivalent circuit for the drive and modulator is shown in Fig. 3.4. The modulator, a parallel R_m - C_m combination, is driven by a voltage source having source resistance R_s and is shunted by a resistance R_g in order to present the source with a matched load at dc. Because of the high resistivity of electro-optic oxide materials, R_m is usually in the megohm range. Power is therefore dissipated across the

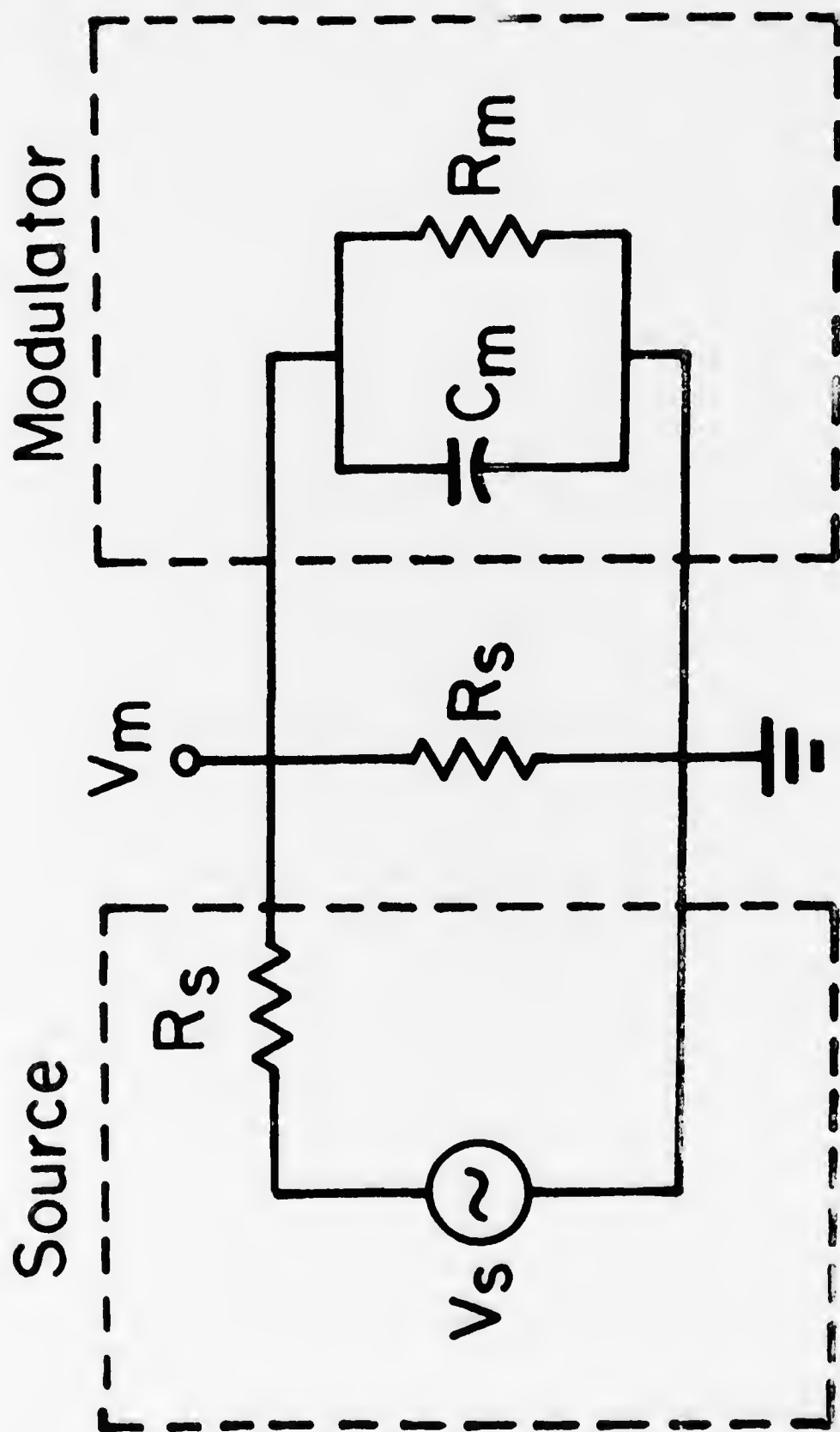


Fig. 3.4 Equivalent circuit for drive and modulator.

shunt resistor. Device bandwidth is defined as the frequency at which the transfer ratio $|V_m|/|V_s|$ is 0.707 of its dc value. One then obtains

$$P_D = \frac{1}{2} V_m^2 / R_s \quad (3.22)$$

$$\nu = (\pi R_s C_m)^{-1} \quad (3.23)$$

$$P_D/\nu = \frac{1}{2} \pi C_m V_m^2 \quad (3.24)$$

The performance figure P_D/ν can be enhanced, i. e., minimized, by either decreasing capacitance or decreasing drive voltage.

3.3.2 Design Equations for a KTN Phase Shifter

Most optical modulators, whether phase or amplitude in nature, require a modulating voltage which induces a phase shift or retardation of π radians in the optical path. This voltage, V_π , is determined by the device dimensions as well as by the properties of the electro-optic material. C_m clearly depends on the dielectric constant of the material.

The influence of material properties on device performance can be shown by considering the operation of a thin film phase shift device with the geometry of Fig. 3.2. A guided TE mode in this structure will experience a net phase retardation, $\Delta\phi$, in passing through the device of

$$\Delta\phi = k_o W \Delta\eta \quad (3.25)$$

where $k_o = 2\pi/\lambda$ is the free space wavenumber, and where $\Delta\eta$ is defined in Eq. (3.14). Assuming that $E_x^2 = V^2/L^2$ and that the electric field is essentially confined in the thin film with a thickness, d , we obtain

Page 76
Not available

Using Eq. (3.20), the following ratios can be determined

$$V_{\pi}(\text{KTN})/V_{\pi}(\text{LiNbO}_3) = \left(\frac{W}{\lambda}\right)^{\frac{1}{2}} \cdot \frac{\eta^{3/2} r_{13}}{g_{11} \epsilon_{\text{KTN}}} \quad (3.29)$$

$$C_m(\text{KTN})/C_m(\text{LiNbO}_3) = \epsilon_{\text{KTN}}/\epsilon_{\text{LiNbO}_3} \quad (3.30)$$

$$P_D/\nu(\text{KTN})/P_D/\nu(\text{LiNbO}_3) = \left(\frac{W}{\lambda}\right) \cdot \left(\frac{\eta_f^3 r_{13}^2}{\epsilon_{\text{KTN}} \epsilon_{\text{LiNbO}_3} g_{11}}\right) \quad (3.31)$$

By combining Eqs. (1.8) and (1.2), ϵ_{KTN} can be written in terms of the KTN Nb mole fraction, x , as

$$\epsilon_{\text{KTN}} = \epsilon_o \cdot \left(\frac{1.5 \times 10^5}{225 - 600x}\right) \quad (3.32)$$

Plots of Eqs. (3.29), (3.30), (3.31) as a function of x are shown in Fig. 3.5. By varying the KTN composition from $x = 0.25$ to 0.35 , power requirements can be reduced by a factor of 25 and overall performance (Fig. 3.5c) can be improved by a factor of 5. Figure 3.5b shows the penalty for changing composition, a decrease in bandwidth, as reflected in a larger device capacitance over this composition range.

Although LiNbO_3 devices have a greater bandwidth, KTN devices with identical geometries have lower drive voltages. The advantages offered by the use of KTN in optical devices are therefore in the areas of low drive-power and low speed switching and modulation applications.

3.4 Deflection-Diffraction Modulation Theory

The actual device fabricated in this work was a diffraction-deflection

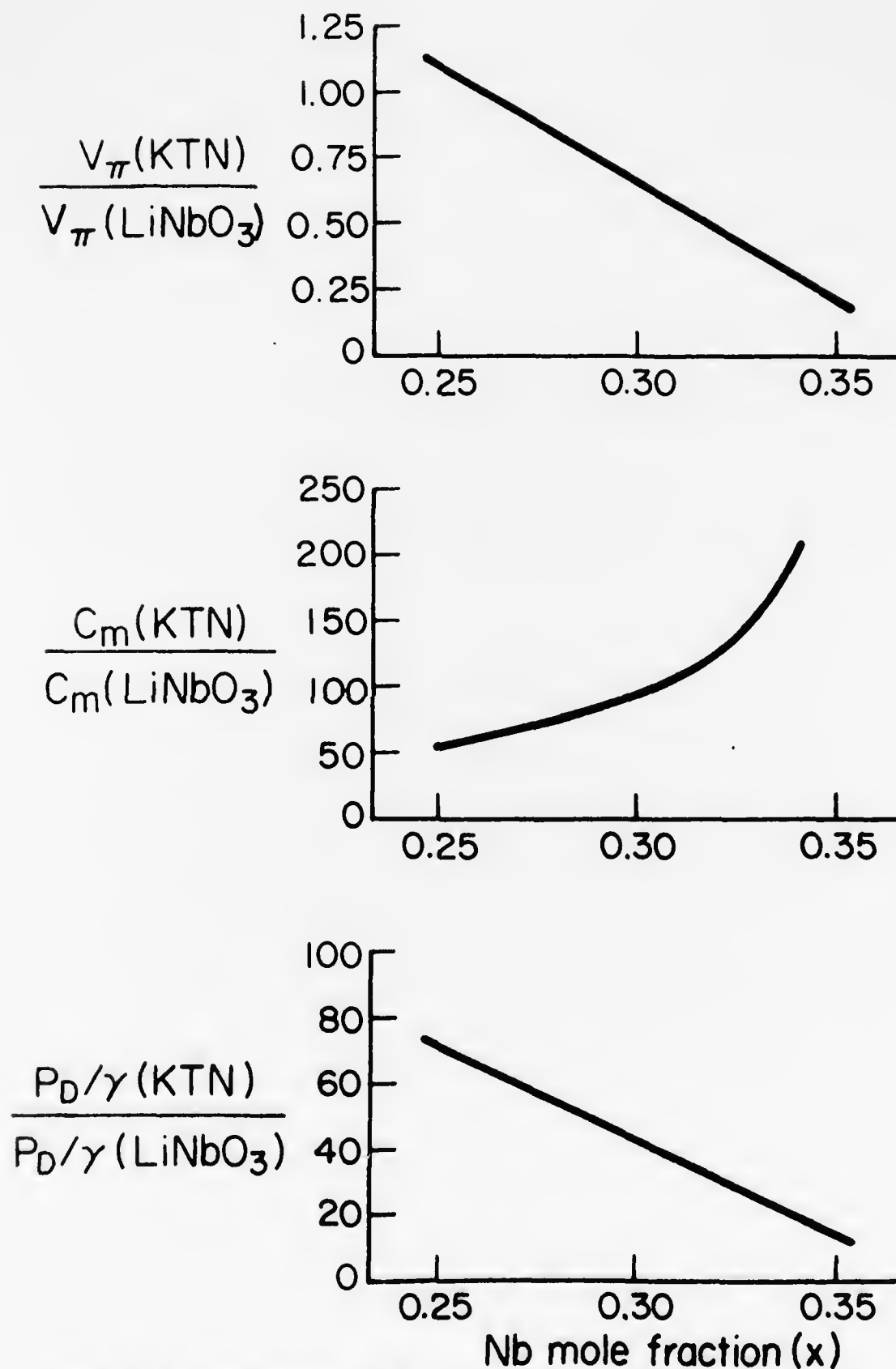


Fig. 3.5 Comparison of V_{π} , C_m , P_D/γ for KTN and LiNbO_3 as a function of Nb mole fraction, x .

modulator. It is fabricated by using an interdigital electrode pattern on the thin film surface of the optical waveguide. The electrode design is shown in Fig. 2.9. In a sense, this device is a series of N parallel phase shifting devices where N is the number of electrode fingers. With a voltage applied across the electrode, a guided mode will experience a periodic index variation transverse to its propagation direction. The beam can be scattered from the incident direction by the interaction of the k vector associated with the periodicity of the index perturbation with the guided mode k vector. The potential for amplitude modulation and beam steering make this an attractive integrated optics device.

The theory of intensity modulation induced by periodic index variations has been treated in detail for the plane wave case where both the optical beam and the index variation are considered infinite in extent. This diffraction theory, described by Klein and Cook,^{60, 61} has been applied with considerable success in the analysis of integrated optics thin film deflectors. In a thin film geometry, however, the beam is a guided mode having finite transverse dimensions which are only several electrode spacings in width. Similarly, the index variation is no longer uniform but decays exponentially into the film.

Figure 3.6 shows the geometry of the diffraction process in momentum space. A guided mode with propagation vector \vec{k} is incident at an angle θ on a periodic index variation of extent W and period L . The index variation may be written as

$$\eta = \eta_0 + \frac{1}{2i} \sum_l \eta_l (e^{i l k^* x} - e^{-i l k^* x}) \quad (3.33)$$

where $\eta_l \ll \eta_0$ and \vec{k}^* is the fundamental k vector associated with the index period, i.e.,

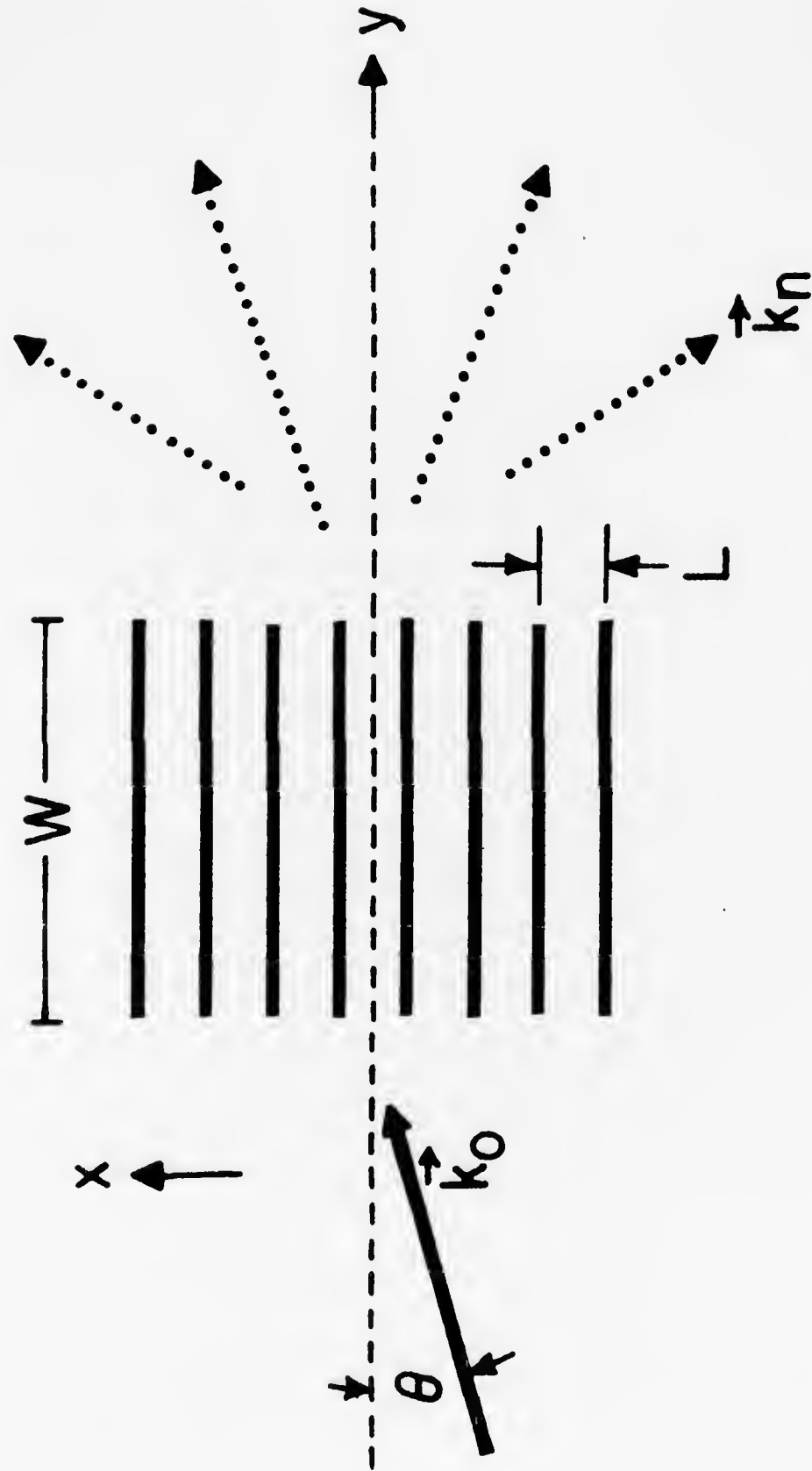


Fig. 3.6 Diffraction geometry.

$$\vec{k}^* = \frac{2\pi}{L} i_{\vec{x}} \quad (3.34)$$

The guided mode can be diffracted into a new direction represented by \vec{k}_n , i. e.,

$$\vec{k}_n = \vec{k} + n\vec{k}^* \quad (3.35)$$

where

$$\vec{k}_n \cdot \vec{r} = \eta_g k_o \cos \theta \cdot y i_{\vec{y}} + (\eta_g k_o \sin \theta + n k^*) \cdot x \cdot i_{\vec{x}} \quad (3.36)$$

The electric field distribution at $y = W$ is desired and can be determined assuming an expansion of the form

$$\mathcal{E} = \sum_n \varphi_n(y) e^{-i\vec{k}_n \cdot \vec{r}} \quad (3.37)$$

where

$$\varphi_n(0) = 0 \quad n \neq 0 \quad (3.38)$$

$$\varphi_0(0) = 1 \quad (3.39)$$

Using Eqs. (3.33), (3.36), (3.37) in the wave equation, a finite difference-differential equation is obtained for φ_n

$$\frac{d\varphi_n}{dy} + \frac{1}{2W} \sum_{j=1}^{\infty} v_j (\varphi_{n-j} - \varphi_{n+j}) = i \frac{nQ}{2W} (n - 2\alpha) \varphi_n \quad (3.40)$$

where

$$v_j = \eta_j k_o W \quad (3.41)$$

is the phase shift caused by the j^{th} harmonic index variation over a distance W and

$$\alpha = -\eta_o k \sin \theta / k^* \quad (3.42)$$

is the ratio of incident beam angle to the angle between diffraction orders and

$$Q = \frac{k^2 W}{\eta_0 k} = 2\pi \cdot \frac{W}{L} \cdot \frac{\lambda_g}{L} \quad (3.43)$$

is a coupling factor.

Three approximations were used in obtaining the set of equations. $\varphi_n(y)$ was assumed to be a slow varying function of y , so terms involving $d^2\varphi/dy^2$ were neglected. Since $\eta_j \ll \eta_0$, η^2 was expanded as

$$\eta^2 = \eta_0^2 + 2\Delta\eta \quad (3.44)$$

Finally, $\cos \theta$ was set to unity since in practical applications $\theta \approx 1^\circ$.

The expression for φ_n is simplified to a more tractable form by assuming only $\eta_j = \eta_1$ is significant in influencing Eq. (3.40), giving

$$\varphi'_n(y) + \frac{v_1}{2W} (\varphi_{n-1} - \varphi_{n+1}) = i \frac{nQ}{2W} (n - 2\alpha) \varphi_n \quad (3.45)$$

φ_n will only interact with adjacent terms in the electric field expansion and energy will be efficiently transferred to these terms only if $Q(n - 2\alpha)$ is small. Typical values for α are of the order unity. For $W = 3$ mm, $L = 50$ μ m, $\lambda_g = (0.6328/2.25)$ microns. $Q \approx 2.1$.

$Q \cdot (n - 2\alpha)$ will be small if either Q is very small, corresponding to electrode finger spacing L large compared to the guided mode wavelength or if Q is very large and $\alpha \approx n/2$. The latter case corresponds to the angle of incidence of the guided mode coinciding with the n^{th} output diffraction angle. When Q is small, Raman-Nath diffraction is said to occur. All φ_n 's will be excited so the output beam is diffracted into many side lobes over a large angular spread. When Q is large, the

diffraction is described as Bragg deflection. Only the single mode, n , where $n \approx 2\alpha$, will have energy coupled into it from the incident φ_0 . In particular, the most efficient coupling occurs when $\alpha = \frac{1}{2}$. Only φ_0 and φ_1 are excited at the $y = W$ plane.

For the Raman-Nath case, the intensity of the n^{th} mode I_n defined as $|\varphi_n|^2$ is

$$I_n = J_n^2 \left(v_1 \frac{\sin Q \alpha / 2}{Q \alpha / 2} \right) \quad (3.46)$$

which for normal incidence reduces to

$$I_n = J_n^2 (k_0 \eta_1 W) \quad (3.47)$$

For Bragg deflection, at incident angle $\theta = \frac{1}{2} k^* / \eta_g k_0$ the intensity at the $y = W$ plane is

$$I_0 = \cos^2 (k_0 \eta_1 W / 2) \quad (3.48)$$

$$I_1 = \sin^2 (k_0 \eta_1 W / 2) \quad (3.49)$$

In these expressions, η_1 , the first harmonic of the index variation can be approximated by the relation for $\Delta\eta_g$ given by Eqs. (3.14), (3.15) provided \bar{E}^2 is identified with the amplitude squared of the lowest order x harmonic of the electric field. $k_0 \eta_1 W$ can then be identified with the expression for $\Delta\varphi$, Eq. (3.25), from which voltage dependent intensity relations can be obtained for the Raman-Nath and Bragg cases.

Maximum intensity modulation for the central beam intensity, $n = 0$, occurs for $\Delta\varphi = 2.4$ for Raman-Nath diffraction and $\Delta\varphi = \pi/2$ for Bragg deflection. Using these constants, the device equations of

ection 3.3.2 apply to the diffraction modulator, as well, provided a factor of N in capacitance (or N^{-1} in bandwidth) is included to take into account the increased electrode area. The ability to modulate the amplitude of the central beam is achieved, however, by a reduction in P_D/ν by a factor of N^{-1} over comparable phase modulators. It should be noted that for an optimized device geometry, N would be reduced to the minimum number of fingers necessary to cover the guided mode beam width.

CHAPTER 4

KTN SINGLE CRYSTAL FILMS: GROWTH AND CHARACTERIZATION

A major goal in this research was the development of a satisfactory process for the growth of single crystal thin films of KTN. After an initial unsuccessful attempt to grow films by the process of chemical vapor deposition (CVD) we shifted to a liquid phase epitaxy (LPE) dipping process, an approach successfully used to produce single crystal magnetic garnet films,^{62, 63} electro-optic thin films of LiNbO_3 on LiTaO_3 ,⁶⁴ and acousto-optic thin films of the sellinite compounds grown on bismuth germanate.⁶⁵ In this chapter the growth by LPE of KTN thin films on KTaO_3 substrates will be described. The optical and dielectric properties of these films will be presented.

4.1 Bulk KTN Growth

Single crystal bulk KTN has been grown by Bonner et al.⁶⁶ using a modified Kyropoulos procedure and Wilcox and Fulmer⁶⁷ have reported success using a Czochralski technique. Both methods required temperature lowering to induce controlled crystallization on a seed crystal.

KTN single crystals have also been grown at a constant temperature, i. e., without temperature lowering, by utilizing a temperature gradient in the melt. Gentile and Andres,⁶⁸ and Whipps⁶⁹ used constant temperature methods for the growth of KTN with the top of the crucible maintained at a temperature 3 - 20°C cooler than the crucible bottom. The resulting thermal gradient created convection currents which circulated nutrient from the crucible bottom, where solid material was present, to the melt-crystal interface where crystallization was occurring

on the seed.

The starting materials in bulk KTN crystal growth were high purity chemical powders of K_2CO_3 , Ta_2O_5 , and Nb_2O_5 . A 5-15 mole % excess of K_2CO_3 served as a flux. The KTN phase diagram of Reisman et al.,⁷⁰ Fig. 4.1, has been routinely used in determining melt composition and seeding and growth temperatures for the growth of bulk KTN compositions. It should be recognized, however, that the phase diagram is truly applicable only to the binary $KTaO_3$ - $KNbO_3$ system and not to the actual three-component system in the melt. Examination of the phase diagram shows that KTN is a solid solution system that can be crystallized over the entire $KTaO_3$ - $KNbO_3$ range. For temperatures between $1039^\circ C$ and $1357^\circ C$, both a liquid and a solid solution of different compositions will exist in the melt at equilibrium. The difference in Nb mole fraction between the liquid and solid solution compositions can be as great as $x = 0.35$.

Bulk KTN single crystals have been characterized by variations in the Nb:Ta ratio along the crystals' growth directions. Such variations result in different optical indices and Curie temperatures throughout the material, both of which can severely degrade any optical device performance. Two types of composition variations have been observed in KTN: gross composition gradients caused by temperature lowering techniques and fine, periodic composition fluctuations referred to as lamellae.

Composition gradients resulted in crystals grown by the Czochralski and Kyropoulos methods because temperature was lowered on the order of $10^\circ C$ during the growth runs. An examination of the phase diagram shows that a difference of $x = 0.03$ in Nb mole fraction of the crystal near the seed and the Nb content of the crystal base could

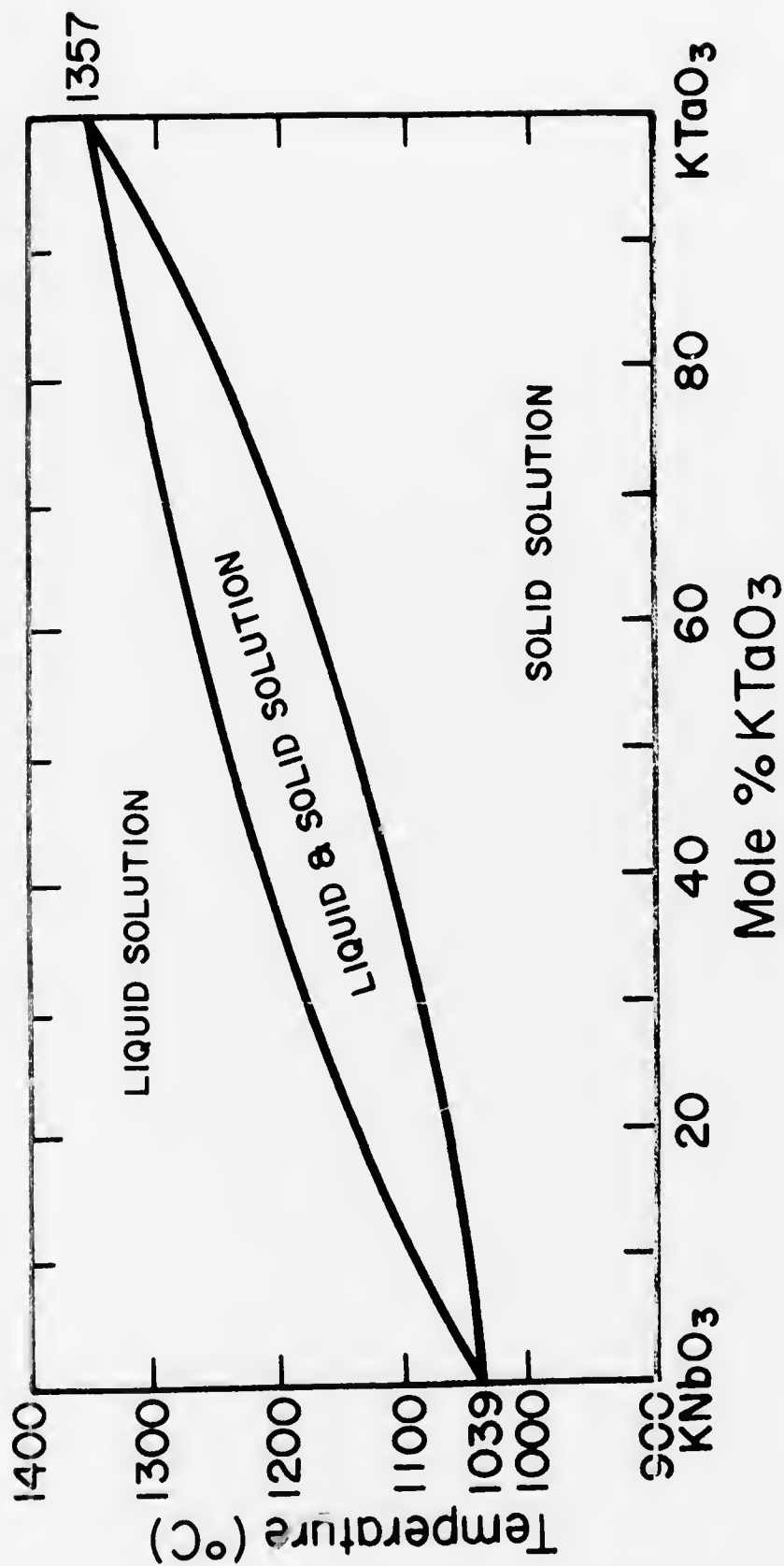


Fig. 4.1 KTN phase diagram.

exist. Since crystal lengths were about 10 mm, substantial composition gradients were possible. In the constant temperature approaches, uniform Nb:Ta ratios were maintained along the growth direction. However, in the radial direction normal to this growth direction, Nb mole fraction variations of 0.03 were observed due to the inability of maintaining a constant radial temperature profile along the melt-crystal interface.

Besides these gross composition variations, very fine, periodic variations in the Nb:Ta ratio were observed to occur in fine bands, 20-50 microns thick, in planes perpendicular to the growth direction of the KTN single crystal. These bands have been referred to as striae or lamellae^{71, 72} and their origin has been attributed to "melt surface" instabilities, in particular to Ta depletion at the substrate-melt interface caused by the crystallization of KTN compositions with a Ta:Nb ratio greater than the Ta:Nb ratio of the melt.

Though KTN is an insulator with normal conductivities less than $10^{-12} (\Omega\text{-cm})^{-1}$, KTN single crystals with conductivities as great as $10^{-8} (\Omega\text{-cm})^{-1}$ have been reported.^{66, 69} The addition of SnO_2 into the melt has resulted in producing low conductivity KTN near the $10^{-12} (\Omega\text{-cm})^{-1}$ range. Bonner⁶⁶ has suggested that oxygen vacancies in the crystal, which require the reduction of a Ta^{5+} or Nb^{5+} ion to a Ta^{4+} or Nb^{4+} valency to maintain charge neutrality, cause the high conductivity in KTN. Following his argument, the use of SnO_2 in the melt would result in Sn^{4+} ions entering the KTN lattice in place of Nb or Ta and would compensate for the oxygen vacancies. High conductivity has also been attributed to impurities present in the starting chemical powders used for the melt which enter the KTN lattice.⁶⁹

4.2 Thin Film Single Crystal Growth

The motivation for attempting the thin film growth of KTN by liquid phase epitaxy came from the experience the M.I.T. Crystal Physics Laboratory had developed in the bulk growth of KTaO_3 ⁷³ and KTN⁷⁴ and in the LPE growth of Ga:YIG films.⁷⁵ In addition, KTN thin film growth would have several advantages over bulk KTN growth. In thin film growth the substrate would be in contact with the melt for periods considerably shorter than the time required for bulk growth runs. Long-range temperature fluctuation and melt instabilities would have minimal effect on film quality. Since a very small amount of nutrient is removed from the melt during the crystallization of thin films, problems associated with Ta depletion would be reduced. Striae formation and composition variations occur in planes normal to the growth direction with periods of the order of 20-50 microns, but integrated optics thin films require thicknesses of the order of 10 microns or less. Clearly, then, problems associated with composition variations would affect the thin films to a lesser degree than the bulk material.

4.2.1 LPE Dipping Approach

In the LPE dipping process, a well polished substrate is lowered, i. e., dipped, into a molten melt for a period sufficient to crystallize a thin film on the substrate. For our case with the KTN system, the melt was maintained at a constant temperature for several hours prior to the dipping. The KTaO_3 substrates, with faces parallel to the melt surface, were axially rotated and lowered into a non-stoichiometric melt containing excess K_2CO_3 to a level 0.5 cm below the melt surface. A thin film would grow on both sides of the substrate. Crystallization was induced by the initiation of a small temperature lowering rate during the time the

substrate is in contact with the melt.

The melt temperature is maintained at a constant temperature prior to the dip to insure uniform film composition. From the KTN phase diagram, it is clear that changes in growth temperature are reflected by changes in the Nb:Ta ratio of the KTN crystal. The state of the melt prior to the actual substrate dipping can be described with the aid of Fig. 4.2. At the growth temperature T_g , there exists in the melt, for a starting melt composition C, a liquid solution of composition L_g and a solid solution with composition S_g . This equilibrium state of the melt is realized only after the melt has been maintained at the growth temperature for a soak period of several hours.

If crystallization were induced under these isothermal melt conditions, a film with uniform composition S_g would result. It was observed, however, that the introduction of a KTaO_3 substrate into a KTN melt after the soak period produced no thin film but only severe etching on the substrate surfaces. Small temperature lowering rates were necessary to induce crystallization. Temperature lowering immediately implies composition changes. The rates and duration of this cooling process were selected to limit the temperature change to less than 2°C during the growth run. A 2°C temperature change implies a maximum change in composition of $x = 0.005$. Best growth results were obtained when temperature lowering was initiated about 30 minutes prior to the actual dip. This presumably allowed the melt to respond to the changes in its isothermal equilibrium state.

As with bulk growth, melt compositions were nonstoichiometric mixtures of K_2CO_3 , Ta_2O_5 , and Nb_2O_5 . A slight excess of K_2CO_3 (5 - 15 mole %) served as a flux. Based on results for KTaO_3 growth,⁷

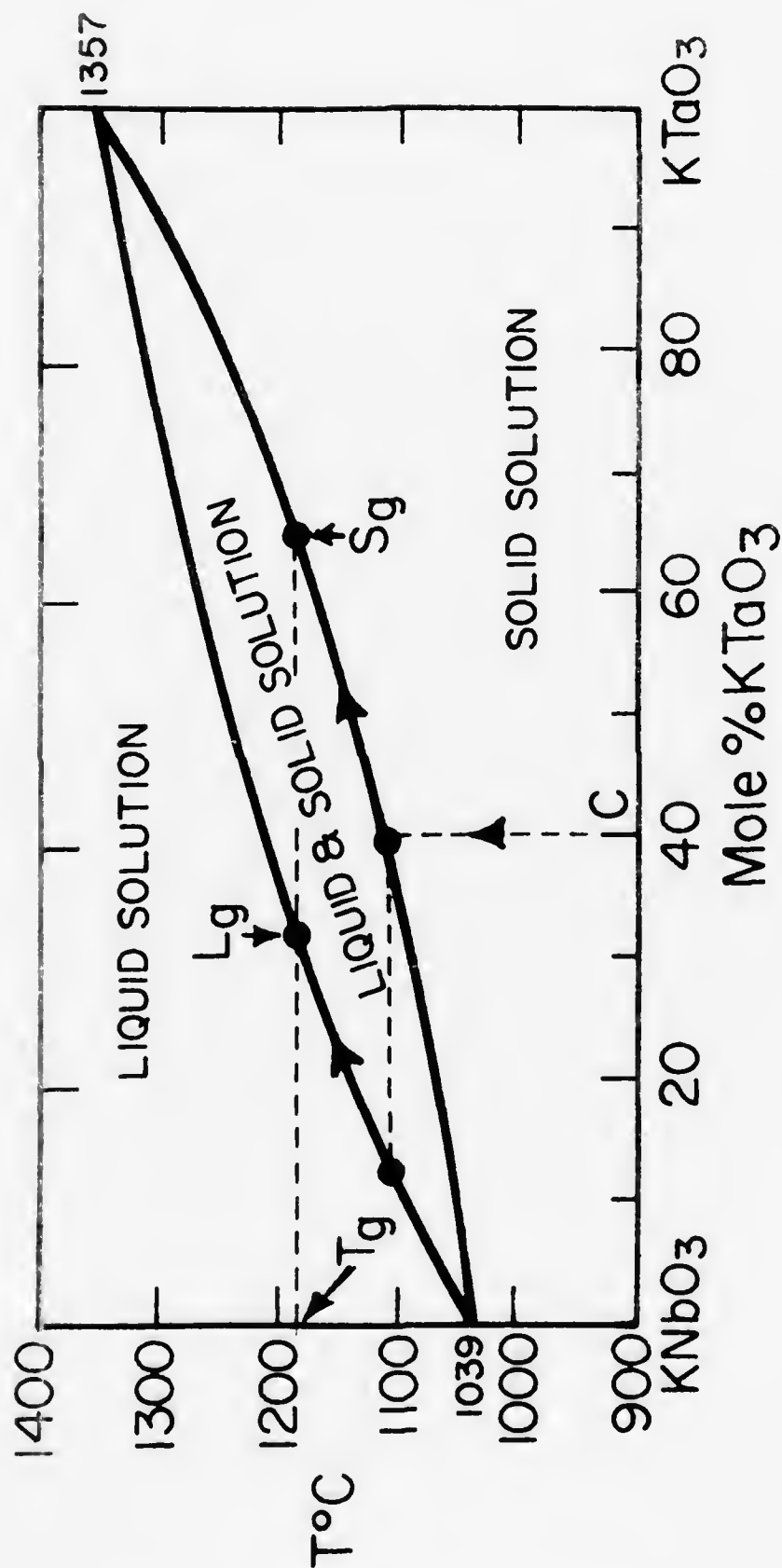


Fig. 4.2 Equilibrium state of the KTN melt at the growth temperature, T_g .

potassium excesses greater than 15 mole % would favor crystallization of different phases. The starting composition of the melt is selected to insure that the melt will be sufficiently liquid at the growth temperature. This prevents rapid crystallization and polycrystalline growth, which is a characteristic of melts having starting composition C very close to the solid solution composition S_g at the growth temperature.⁶⁸

The substrate is rotated while in contact with the melt. In our work substrate rotation resulted in more uniform film surfaces than when no rotation was used. In addition, as with the case of magnetic garnet film growth,^{62, 63} we speculated that substrate rotation would create a well-defined crystal liquid boundary layer and would allow for the controlled diffusion of crystal nutrient from the melt to the solid film.

A typical temperature cycle used in our growth runs is shown in Fig. 4.3. The starting melt composition is slowly heated to the growth temperature at a rate of 10-20°C/hr. The equilibrium state of the melt is established by a long soak period of 7-15 hours. Before the dip is made, temperature lowering at rates from 0.5 to 2°C/hr is initiated. After the growth period, the substrate is withdrawn from the melt and then the oven temperature is cycled down to a holding temperature of about 900°C.

This dipping process has two advantages which make KTN thin film growth attractive. The short growth times, ~ 2 hours, result in minimal evaporation loss during any single run. Consequently, the melt can be recycled several times without replenishing its contents. The thin film chemical composition is determined by the growth temperature. Different compositions can be grown by varying this temperature

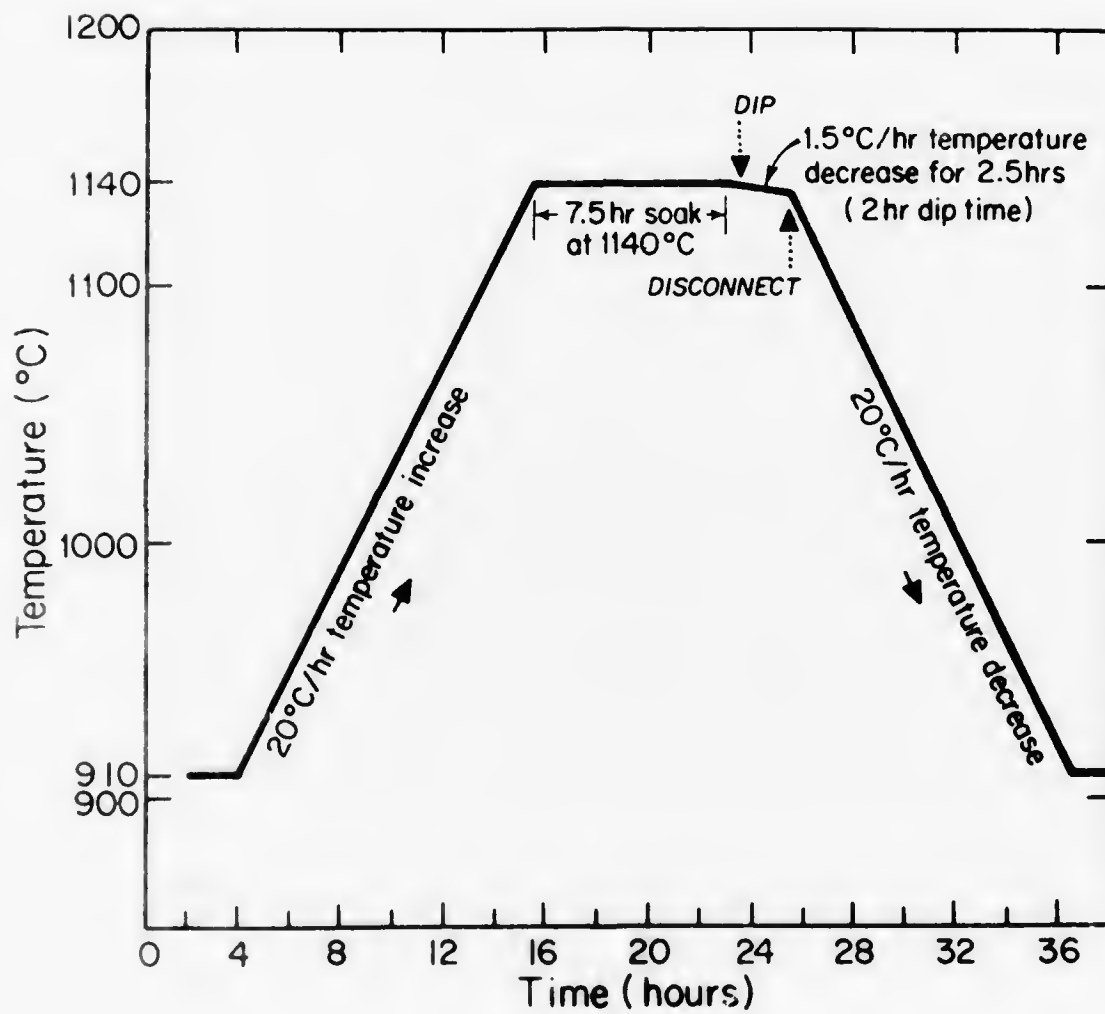


Fig. 4.3 Temperature cycle for KTN dipping process.

without changing the melt composition.

4.2.2 Substrate Growth

The substrate material was single crystal KTaO_3 grown by a top-seeded solution technique similar to the work of Wemple⁷³ and Beltruss et al.⁸⁵ A fire bricked furnace, having 12 SiC resistive heating elements, was used. Temperature was controlled by a Barber-Colman three-mode controller having proportioning band, rate, and reset capabilities. Temperature stability as great as 0.1°C can in principle be maintained. Temperature was monitored by Pt-Pt/10% Rh thermocouples. A KTaO_3 seed crystal (3 mm x 3 mm x 10 mm) oriented with a [100] direction parallel to the pulling direction was attached to a hollow platinum seed rod with 20-mil diameter platinum wire. The melt composition was 54 mole % K_2CO_3 and 46 mole % Ta_2O_5 .

The melt is soaked at 1400°C for 24 hours after which the seeding process is carried out. The seeding temperature for these melts was around 1360°C . Once seeding is verified, the seed is withdrawn from the melt. The effect is a temperature rise of $15\text{-}20^\circ\text{C}$, which destroys any spurious nucleation centers that might have developed during the seeding process. After 30 minutes, contact is again made with the melt at the previously determined seeding temperature. Furnace temperature is lowered at about 0.2°C/hr and the seed rod is cooled by forcing air through the hollow platinum rod. After 24 hours, the seeded crystal usually attains sufficient diameter to allow pulling at rates of $0.5 - 2 \text{ mm/hour}$ to begin. After 3 days the crystal is disconnected from the melt and temperature is lowered rapidly at 25°C/hour .

Resulting crystals have well defined (100) facets and are usually transparent. Some bulk KTaO_3 was grown having blue, yellow or milky

white regions in the crystal. Chemical analysis of the yellow crystals showed evidence of a vanadium contaminate most likely coming from the starting chemical powders used for the melt. It is suspected that these impurities are locally distributed throughout the chemical powders because from run to run, depending on the presence of the impurities, different color or transparent crystals would be produced from the same batch of starting chemicals. Bulk KTaO_3 material is shown in Fig. 4.4. The crystal in Fig. 4.4b is ≈ 22 mm in length. Such sizes are needed for integrated optics devices to accommodate input and output prisms and electrode structures.

4.2.3 Substrate Preparation

The substrate crystal is mounted on an x-ray goniometer, aligned along a $\langle 100 \rangle$ direction, and cut into 35-mil thick wafers normal to the direction using a 15-mil thick diamond saw blade. Typical accuracies of 1° are maintained in this cutting procedure. Sometimes the bulk material was ground to a cylindrical shape before cutting. Prior to sample polishing, two holes about 20 mils in diameter are drilled through the substrate using a small sandblasting tool. These are used for attaching the substrate to the seed rod. The edges of the substrate are rounded with 600 and 305 grit sandpaper to remove any chips or rough areas caused by the sawing and grinding steps.

Samples are polished on a GMI polishing machine using tin lapping plates impregnated with fine diamond grit paste. The lapping plate is rotated at one speed while a polishing jig which holds the sample and external weights is translated back and forth along the lapping plate at a different speed. When the periods of both motions are properly adjusted, the sample will make contact with the entire lapping plate

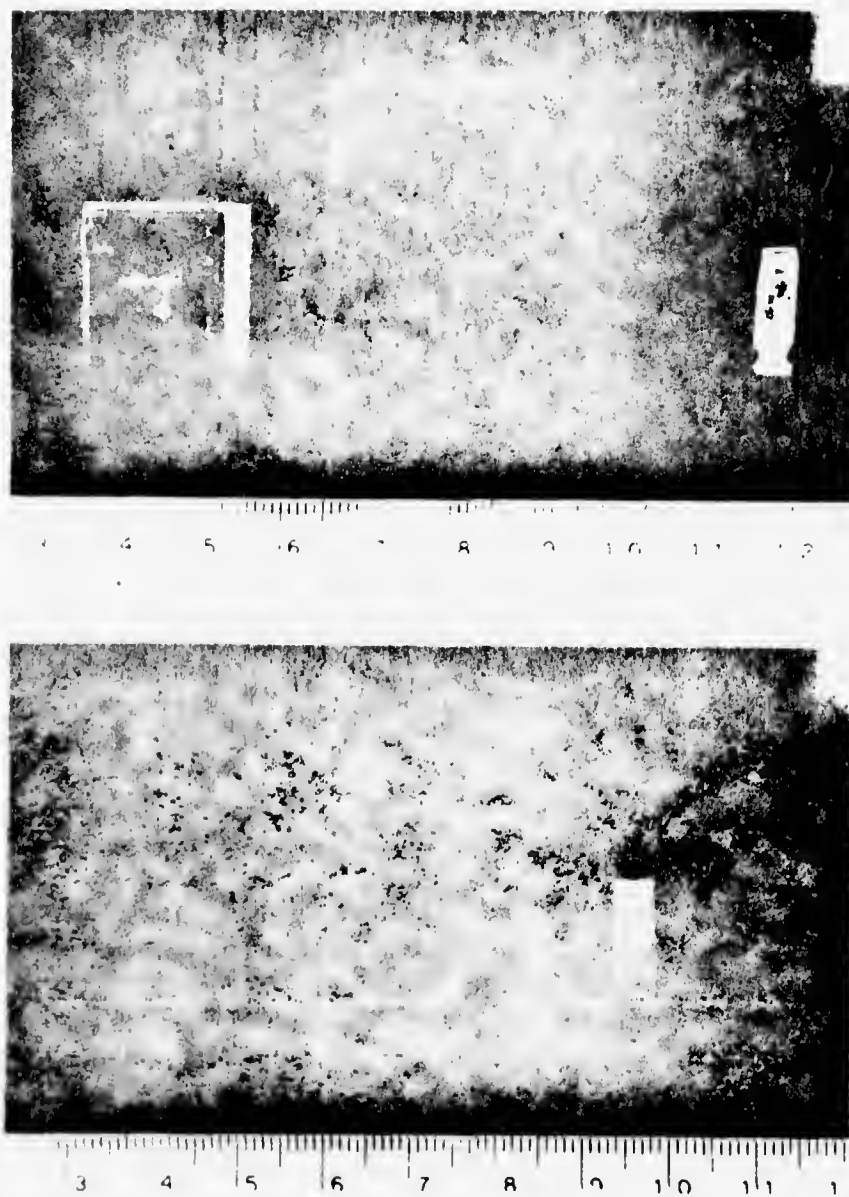


Fig. 4.4 Bulk KTaO_3 single crystals and seeds.

surface.

A cross section of the polishing jig is shown in Fig. 4.5. It consists of a stainless steel block $1\frac{1}{4}$ " square and 1" high with a $\frac{3}{4}$ " centered hole through which a brass rod $\frac{3}{4}$ " in diameter will slip fit. The sample is mounted on one end of the rod using a low melting temperature wax (CIBA). Four KTaO_3 "feet" are similarly mounted on the corner edges of the stainless steel block. These pads serve to distribute the weight of the polishing jig uniformly over the sample surface.

The polishing procedure begins with a manual lapping with 305 (American Optical Co.) grit on a glass plate to level the substrate and feet, followed by controlled lapping on the tin plates using 3, 1, and 0.25 micron diamond grits. The 3-micron grit removes the course surface features caused by the 305 polish. Scratches still remaining on the substrate surface are removed with the 1 micron grit. Substrate flatness is achieved with the 0.25 micron grit. A final polish with a Syton* solution, which is a chemical etch polish, is used to remove any damage or strain on the substrate surface caused by the previous abrasive polishes.

Average lapping time for each grit is about 30 minutes. The tin lapping plates are refaced to a depth of 5 mils after two polishing cycles to remove any contamination or used grit. Flatness of $\frac{1}{4}$ wavelength at 5000 Å over better than 80% of the substrate is routinely achieved with this polishing technique. Parallelism of the two substrate surfaces can be maintained by shifting the center point of the external weights on the

* Registered Trade Mark, Monsanto Corporation.

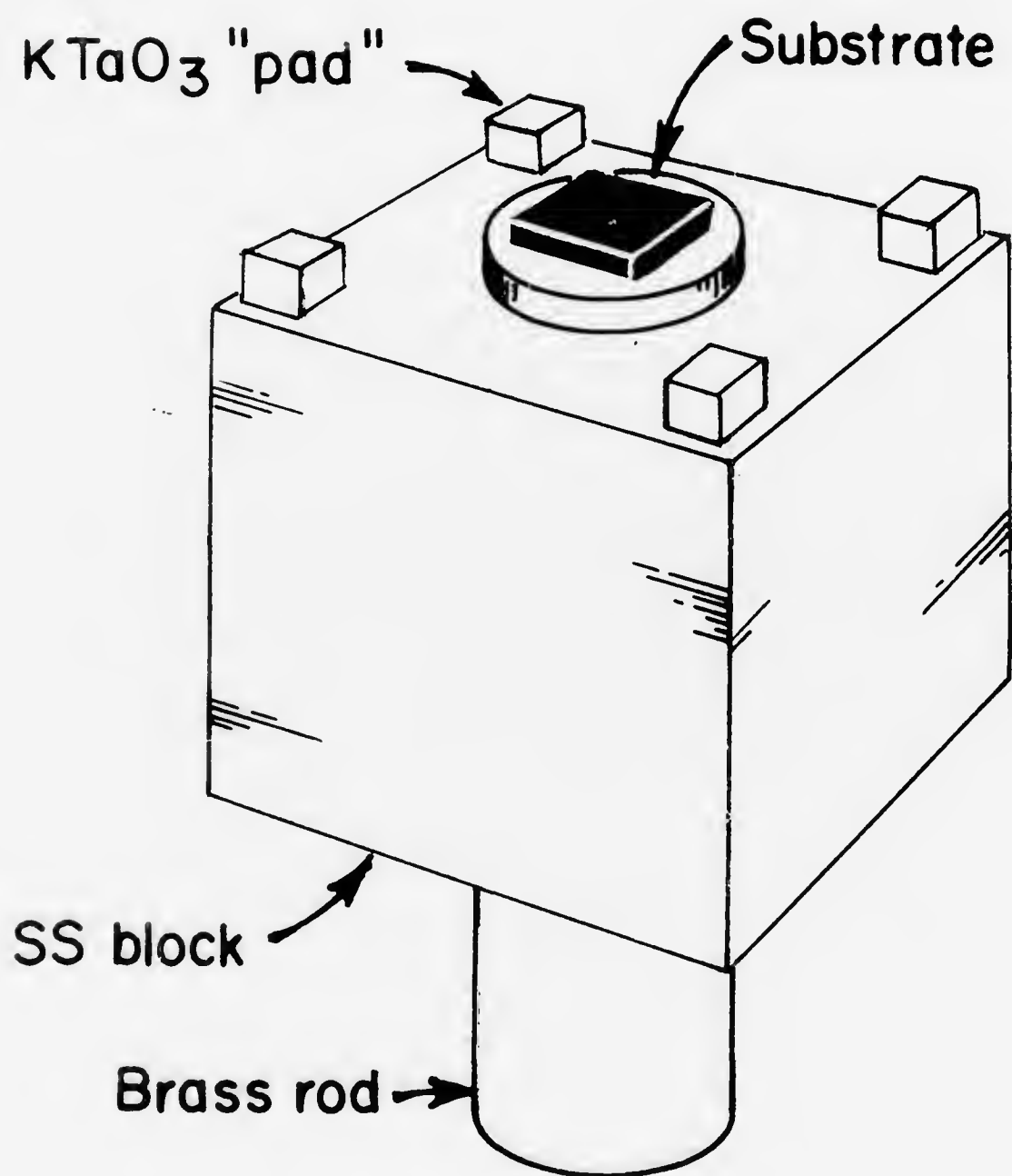


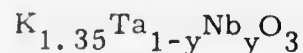
Fig. 4.5 Polishing jig.

polishing jig. Parallelism, determined by monitoring laser beam reflections from the two polished surfaces, can be better than 20 seconds of arc. Figure 4.6 shows some typical substrates.

The substrate is cleaned and degreased prior to the dipping process. The initial clean is a boil in a 10% by weight KOH and water solution which removes any Syton residue. The sample is then suspended 2-3 cm below a platinum seed rod by 20-mil diameter platinum wire threaded through the two holes in the substrate and then through the end of the seed rod. This is shown in Fig. 4.7. The sample and seed rod are then cleaned in acetone, methanol, and then, using an ultrasonic cleaner, in a warm solution of Alconox and water. This is followed by a rinse in distilled water and two 10-minute boils in distilled H₂O.

4.2.4 Melt Preparation

Table 4.1 lists the three melt compositions used in this research. The melts were non-stoichiometric with an excess of K₂CO₃ serving as a flux. At the growth temperatures of interest, 1100-1200°C, K₂CO₃ dissociates leaving K₂O in the melt. The melt composition can then be written as



where in our case $y = 0.4, 0.5, 0.6$. 0.1 mole % SnO₂ was used in melt 5.

Melts 1, 2, 3 were loaded into 100-ml platinum crucibles; melts 4, 5 were in 150-ml. crucibles. Two pre-meltings were needed before the chemical powders could be fully loaded into the crucibles. The Ta₂O₅ powder was optical grade quality supplied by Kawecki-Berylco, Inc. The Nb₂O₅ and K₂CO₃ were both Grade I purity supplied by United Mineral

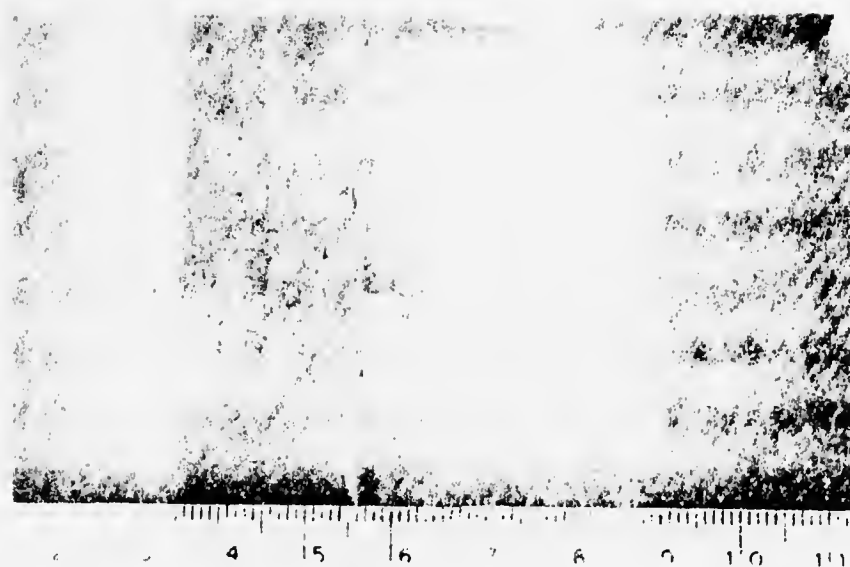


Fig. 4.6 KTaO₃ substrate.

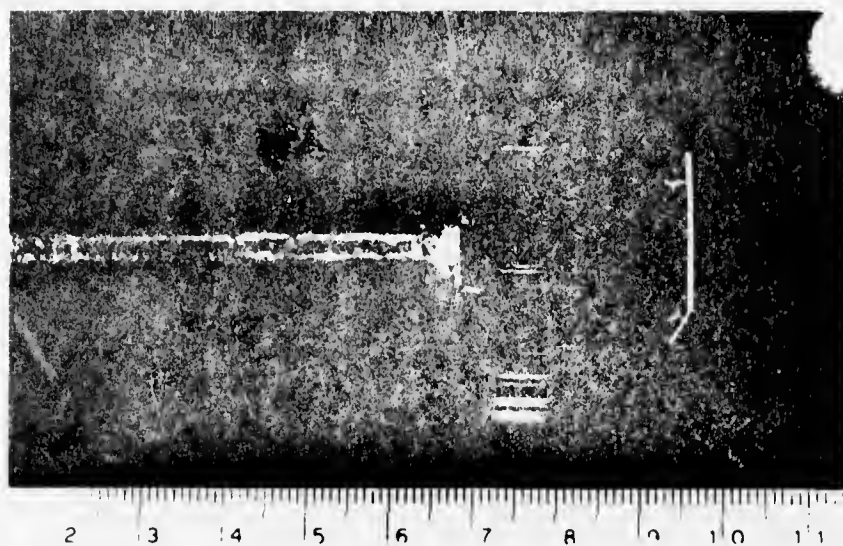


Fig. 4.7 KTaO₃ substrate attached to platinum seed rod.

Table 4.1
Melt Compositions

<u>Melt 1</u>			
<u>Chemical</u>	<u>Weight</u>	<u>Mole %</u>	<u>Mole Fractions</u>
Ta_2O_5	67.960	25.6	0.60
Nb_2O_5	26.980	16.9	0.40
K_2CO_3	47.725	57.5	1.35
<u>Melts 2, 3</u>			
Ta_2O_5	56.653	21.2	0.50
Nb_2O_5	34.078	21.2	0.50
K_2CO_3	48.207	57.6	1.35
<u>Melts 4, 5</u>			
Ta_2O_5	67.96	17.00	0.40
Nb_2O_5	61.34	25.40	0.60
K_2CO_3	72.31	57.6	1.35

and Chemical Corporation. Fresh melts were always soaked for 24 hours and then cycled to a holding temperature of 900°C before beginning a growth run.

4.2.5 Dipping Steps

A platinum/40% rhodium wire-wound furnace (Fig. 4.8) was used for the LPE dipping process. Three heating zones were incorporated into the furnace design, allowing for controlled temperature profiles. In this thin film growth work, a vertical temperature gradient of about $3^{\circ}\text{C}/\text{cm}$ was maintained through the crucible with the top cooler than the crucible bottom. The liquid melt was approximately 2 cm deep. To extend oven life, current through the platinum heating wires was always kept below 10 amperes.

As in the case of the KTaO_3 oven, temperature control was maintained by a Barber-Colman three-mode temperature controller with proportioning band, rate, and reset capabilities. The temperature stability of the oven could be as good as 0.1°C with proper placement of control thermocouples. The maximum temperature achieved in the oven was 1250°C for our work. Temperature could be lowered at rates from 0.5°C to $50^{\circ}\text{C}/\text{hr}$.

A pulling assembly allowed the substrate to be raised or lowered at rates from several mm/day to 20 mm/min. Substrate rotation rates from 15 rpm to 1000 rpm were available.

Table 4.2 lists the important growth parameters for Runs 33 and 48. In Run 33, made with an 18 mm diameter substrate, a KTN film with Nb mole fraction $x = 0.26$ was crystallized from a melt with composition $\text{K}_{1.35}\text{Ta}_{0.5}\text{Nb}_{0.5}\text{O}_3$. Run 48, also using an 18 mm diameter substrate, resulted in a KTN thin film with Nb mole fraction $x = 0.34$

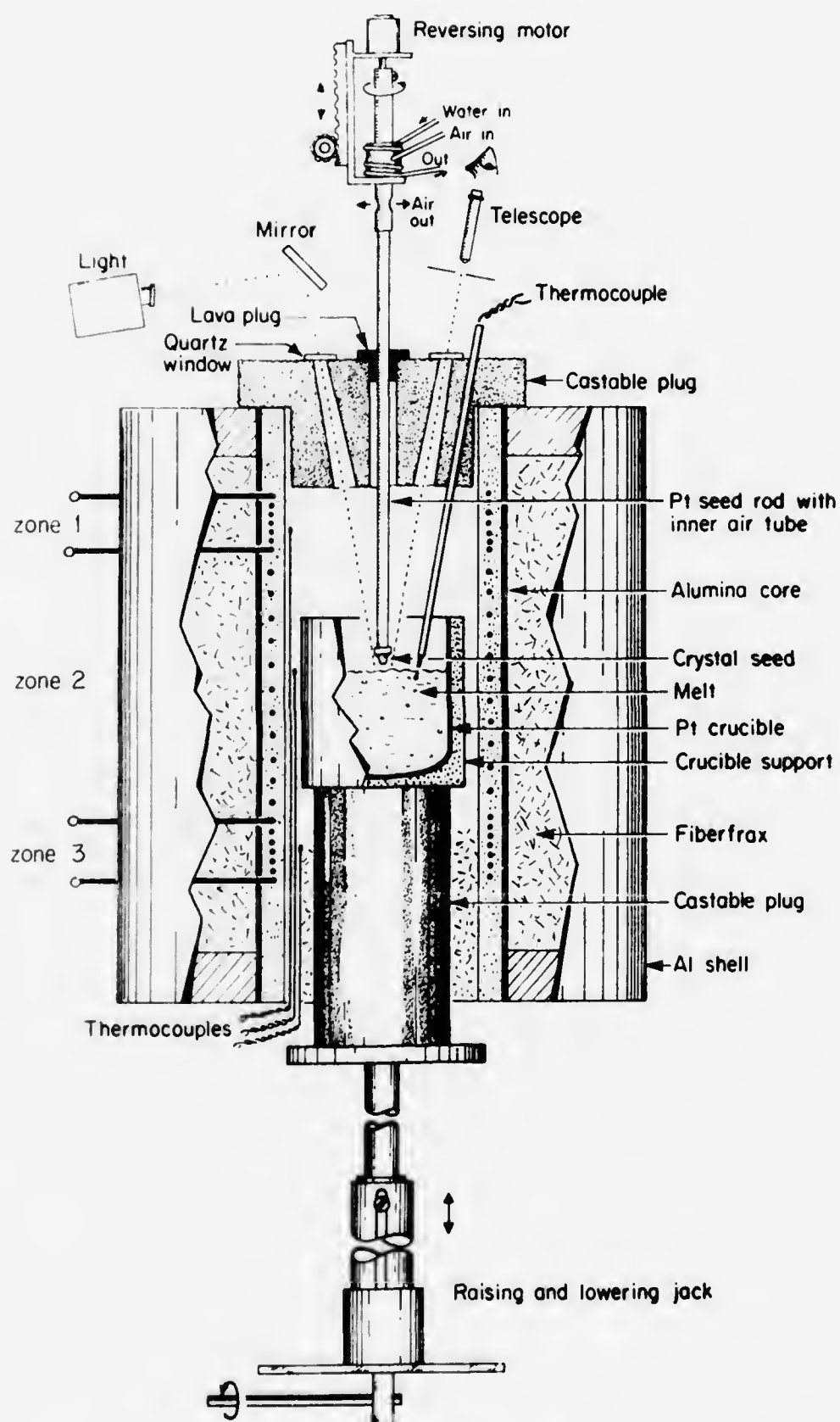


Fig. 4.8 Dipping furnace.

Table 4.2
Growth Parameters for Runs 33, 48

	<u>Run 33</u>	<u>Run 48</u>
Soak temperature	1141°C	1125°C
Soak period	7 hrs, 30 min.	13 hrs.
Rotation rate	60 rpm	80 rpm
Temperature lowering period before dip	20 min	30 min
Temperature lowering rate	1.25°C	0.75°/hr
Dipping time	2 hours	2 hrs, 15 min

from a $K_{1.35}Ta_{0.4}Nb_{0.6}O_3$ melt.

The steps used in the dipping process during these runs are summarized below.

1. The oven is brought to the growth temperature (1120° - 1140° C) at a rate never exceeding 20° C/hr.
2. The soaking period begins (7-15 hours).
3. After the soak period, the seed rod, with substrate attached, is lowered at an initial rate of 4 mm/min until well within the oven and then at a rate of 20 mm/min until the substrate is 2 cm above the melt surface. During this time the substrate is rotating (30 - 100 rpm).
4. The substrate is held at this position for 30 minutes while temperature cooling is initiated.
5. The sample, still rotating, is slowly lowered into the melt at a rate not exceeding 4 mm/min to a depth 5 mm below the melt surface.
6. The rotation rate is maintained during the desired growth time.
7. After the growth time has elapsed, rotation is stopped. The substrate is quickly withdrawn from the melt at a rate of 20 mm/min. Because of the viscosity of the melt, the substrate breaks contact with the melt about 2 mm higher than the level melt surface and small melt droplets remain on the film surface.
8. Immediately after disconnecting from the melt surface, the pulling is stopped and seed rod rotation is increased from 0 to 1000 rpm and back to 0, in a period of 10 seconds, to spin away any melt droplets on the film surface.
9. The sample is pulled to a level of 5 cm above the melt quickly

and then, with the substrate slowly rotating (20-30 rpm), is raised to the oven top at 4 mm/min.

10. When the substrate reaches the level of the castable plug (see Fig. 4.8), the pulling rate is decreased to 1 mm/min. This is the region of greatest temperature gradient, $> 100^{\circ}\text{C}/\text{cm}$.

11. A cover dish is placed on the top of the castable plug to prevent air currents from prematurely cooling the top film surface as it is drawn through the plug.

12. When the sample clears the top of the plug, the oven is capped and then cooled to 900°C at a rate of $20\text{-}40^{\circ}\text{C}/\text{hr}$. The sample cools above the oven in the protective cover dish.

4.2.6 Evolution of Growth Process

A series of 54 growth runs were performed in this research. In Runs 1-20, different soak periods were tried. Polishing techniques and substrate mounting procedures were gradually improved. Growth temperature was high, $\sim 1160^{\circ}\text{C}$, and temperature lowering rates were large, $\sim 10^{\circ}\text{C}/\text{hr}$. Rapid growth resulted with film compositions of $x = 0.10 - 0.19$ and thicknesses of 60 microns. Very inefficient guiding of optical modes could be achieved in these films.

In Runs 21-29, attempts were made to decrease growth rate by reducing the temperature cooling rate. Larger Nb content films were grown by reducing the growth temperature to 1140°C . Problems with the handling of large area substrate material were encountered. Finally, controlled slow growth of about 20 microns in 2 hours for cooling rates of $1^{\circ}\text{C}/\text{hour}$ were obtained.

Runs 30-35 produced good quality films on large 18-mm diameter substrates. Nb content was $x \sim 0.26$. Runs 36-48 were directed toward

the growth of higher Nb content films in the range $x \sim 0.35$. A $\text{K}_{1.35}\text{Ta}_{0.4}\text{Nb}_{0.6}$ melt was used and the growth temperatures were $\sim 1125^\circ\text{C}$. SnO_2 was added to the melt in hopes of decreasing the high conductivity observed in earlier films.

In Runs 49 and 50, multi-layered growths were tried, i.e., the growth of a film on a film. In Runs 51-54, initial efforts on determining growth rates were begun.

The growth research described above was obviously qualitative in approach. No quantitative measurements on the influences of temperature cooling rates, soak period, dipping duration, or rotation rates on growth rates or film thicknesses were made. It was observed that an increase in dipping period or cooling rate or rotation rate tended to increase the growth rate of the film. The thin film growth technique has evolved to the point that, with the parameters given in Table 4.2, KTN thin films, having reasonable optical quality sufficient for electro-optic device application, can be routinely grown. Optimization of the growth parameters still remains to be done.

4.2.7 Film Appearance

After a growth duration of 2 hours, KTN films about 20 microns thick, with rippled surface features resulted. Attempts at growing thinner films by reducing growth times resulted in either no growth or only local growth on the substrate. The "thick" nature of the films and the presence of surface features required the polishing of the film surface before any characterization or device work could be attempted. This inability to grow uniform thin films of any desired thickness is the most serious drawback in our LPE dipping procedure.

By carefully mounting the substrate on the polishing jig, a uniform

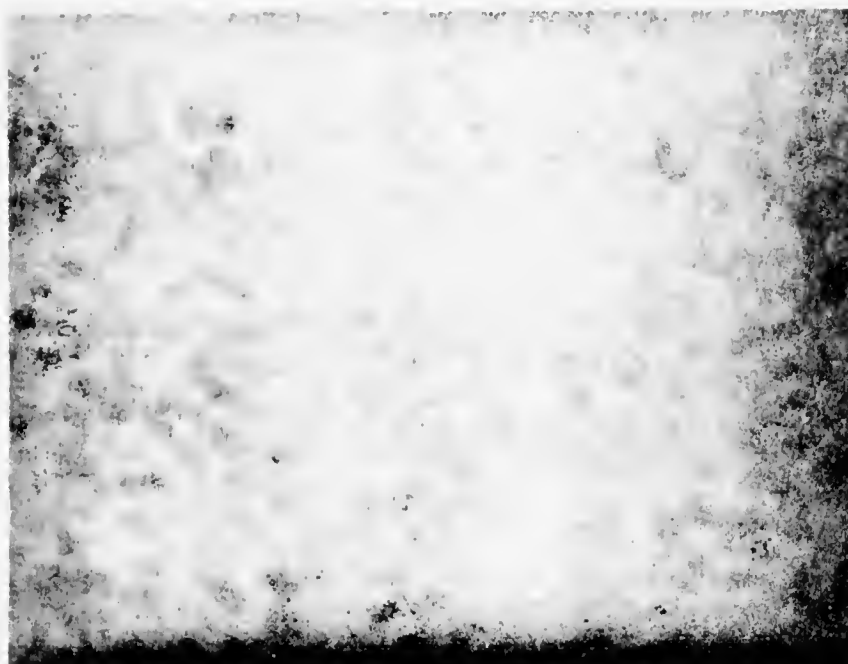
reduction of the film thickness was possible at rates of 2-3 microns in 15 minutes using 3-micron diamond grit and the GMI polishing unit. Film thicknesses of 5 microns with variations of less than 1 micron were achieved. Figure 4.9a shows the rippled surface features of a sample and Fig. 4.9b is an edge view of a film and substrate which was polished to a final thickness of 5 microns. Note the abrupt film-substrate interface.

In the early growth runs, the films had a distinct blue tint which was assumed to indicate oxygen deficiencies in the crystal.⁶⁶ The addition of SnO_2 to the melt resulted in clear films. After about 10 temperature cycles for any melt, the films appeared to have a yellow-white coloration. In bulk growth this was an indication of potassium depletion⁶⁷ from the melt caused by evaporation. A similar occurrence in our melts does not seem unreasonable.

4.2.8 Thin Film Growth by CVD

Initial efforts in the growth of single crystal KTN thin films concentrated on a chemical vapor deposition (CVD) approach. This was motivated by the success the Crystal Physics Laboratory had attained in the growth of high quality small (1-2 mms) bulk single crystal SnO_2 ⁷⁵ and in the growth of Ga:YIG films⁷⁶ by CVD processes. For KTN growth, a CVD technique offered the advantage of working in the vapor phase, thereby eliminating problems associated with melt instabilities. Constant Ta:Nb ratio in the system could be maintained by controlling the Cl_2 gas flow which reacts with the Ta and Nb metals to form TaCl_5 and NbCl_5 vapor.

The CVD system, shown in Fig. 4.10, had provisions for six independent gas flows. Two chlorine flows were used for the production



(a) Rippled surface features (1 cm \approx 150 microns).



(b) Film substrate interface.

Fig. 4.9 KTN thin films.

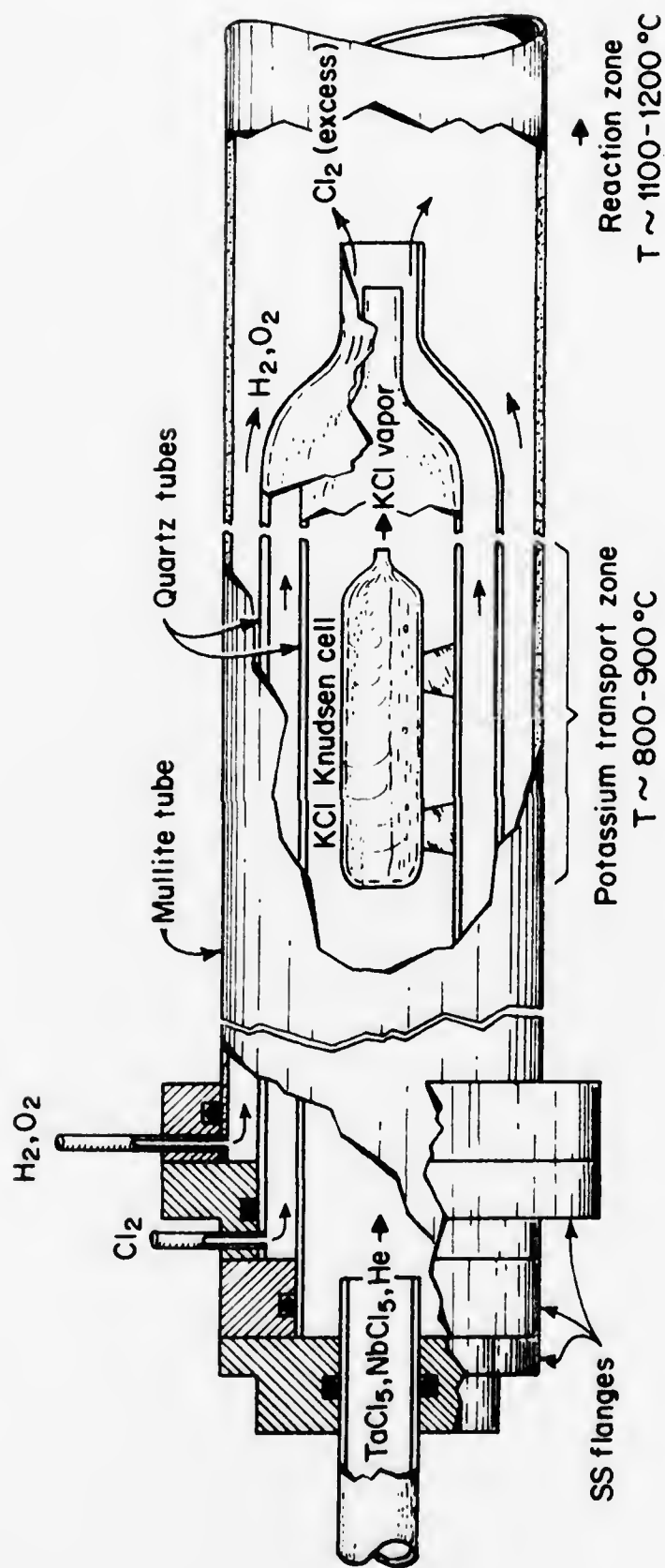


Fig. 4.10 System for growth of KTN by chemical vapor deposition.

of TaCl_5 and NbCl_5 vapor by the controlled chlorination of Ta and Nb metal. Monitored flows are provided for the oxygen and hydrogen necessary for the reaction.



To allow the reaction to occur downstream from the nozzle, a third chlorine flow was introduced to create a sheath between the metal chloride vapors and the H_2 and O_2 flows. Provision was made for the introduction of He as a carrier to establish the downstream flow of the gases and prevent any back diffusion.

The production of the TaCl_5 and NbCl_5 vapors was accomplished without difficulty. The Ta and Nb were chlorinated in external reactors heated to 240°C and the vapors were transported to the furnace in heated lines. The production of KCl vapor or more correctly the transport of potassium proved to be a problem that was not solved. The controlled transport of KCl gas was never achieved. Attempts to vaporize liquid KCl in a Knudsen cell using different temperature were unsuccessful. This, plus the problems faced in working with a three-component system for which there was insufficient thermodynamic data on the reaction, contributed to the realization that another growth approach, most notably LPE, merited consideration.

4.3 Thin Film Characterization

4.3.1 Composition

Since the KTN system follows Vegard's Law,⁷ thin film Nb content was determined through a measurement of thin film lattice constant. Lattice constant was determined from the 2θ x-ray intensity peaks associated with the (500) lattice planes. Since the substrate faces

were oriented normal to a $\langle 100 \rangle$ direction, very intense reflections would be observed for (h00) planes provided the substrate was properly aligned relative to the x-ray beam path. A beam voltage of 35 KeV and a current of 5 ma was required to observe the intensity peaks. The diffractometer was scanned through the (500) diffraction peaks at a rate of $0.125^\circ/\text{min}$. Figures 4.11 and 4.12 show the intensity pattern for samples from Runs 30, 47. Two pairs of lines are observed, one pair for the substrate and the other for the film. In each pair there is one component produced by $\text{CuK}_{\alpha 1}$ radiation and another by $\text{CuK}_{\alpha 2}$ radiation. The results for samples # 30, 47 are summarized in Table 4.3.

The ratio of Nb:Ta in the films was obtained using electron microprobe techniques. The translational accuracy of the probe is ± 12 microns. A 5 kV electron beam voltage was used. Samples were lapped at shallow angles, $1^\circ - 2^\circ$, using 3-micron diamond grit, mounted on 1" diameter quartz discs using Duco cement, and then coated with a thin evaporated layer of graphite. A photomicrograph of a lapped film substrate with a film slope of ~ 0.02 is shown in Fig. 4.13.

Microprobe results obtained by probing down a lapped surface of a 26 mole % Nb film are shown in Fig. 4.14. The scatter in the data is within the background errors discussed in Section 2.3.1. Within experimental accuracy, the film substrate interface is abrupt with a transition region of less than 0.5 microns and the film composition is uniform.

Both approaches, x-ray and microprobe, give compositions with an accuracy of $x \approx \pm 0.02$. Using these values, it is possible to determine Curie temperature (Fig. 1.1) and hence the electro-optic effect of the thin film. When these terms are known, the device performance of the KTN films can then be predicted.

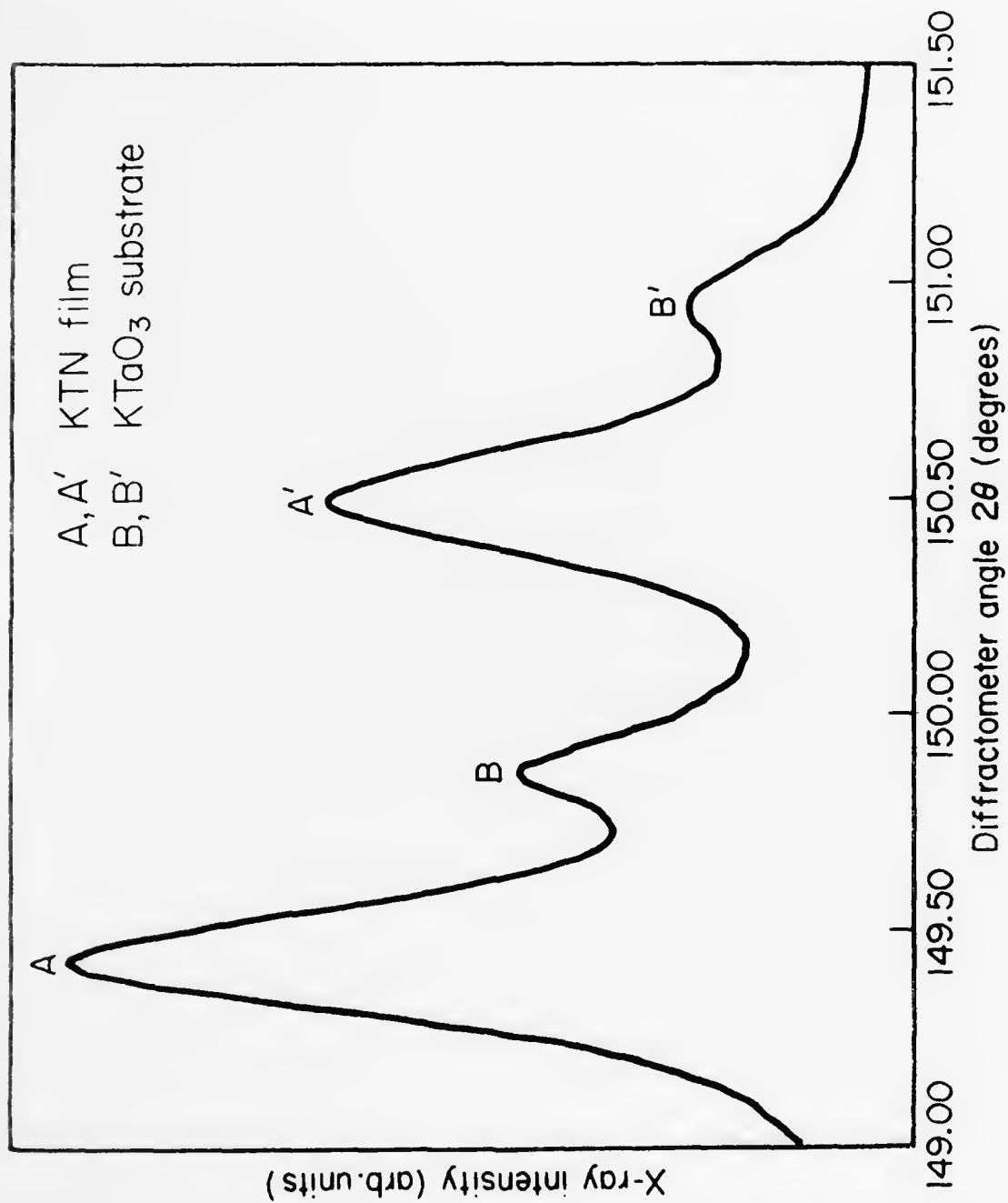


Fig. 4.11 X-ray diffraction peaks for a KTN ($x = 0.26$) film on a KTaO₃ substrate.

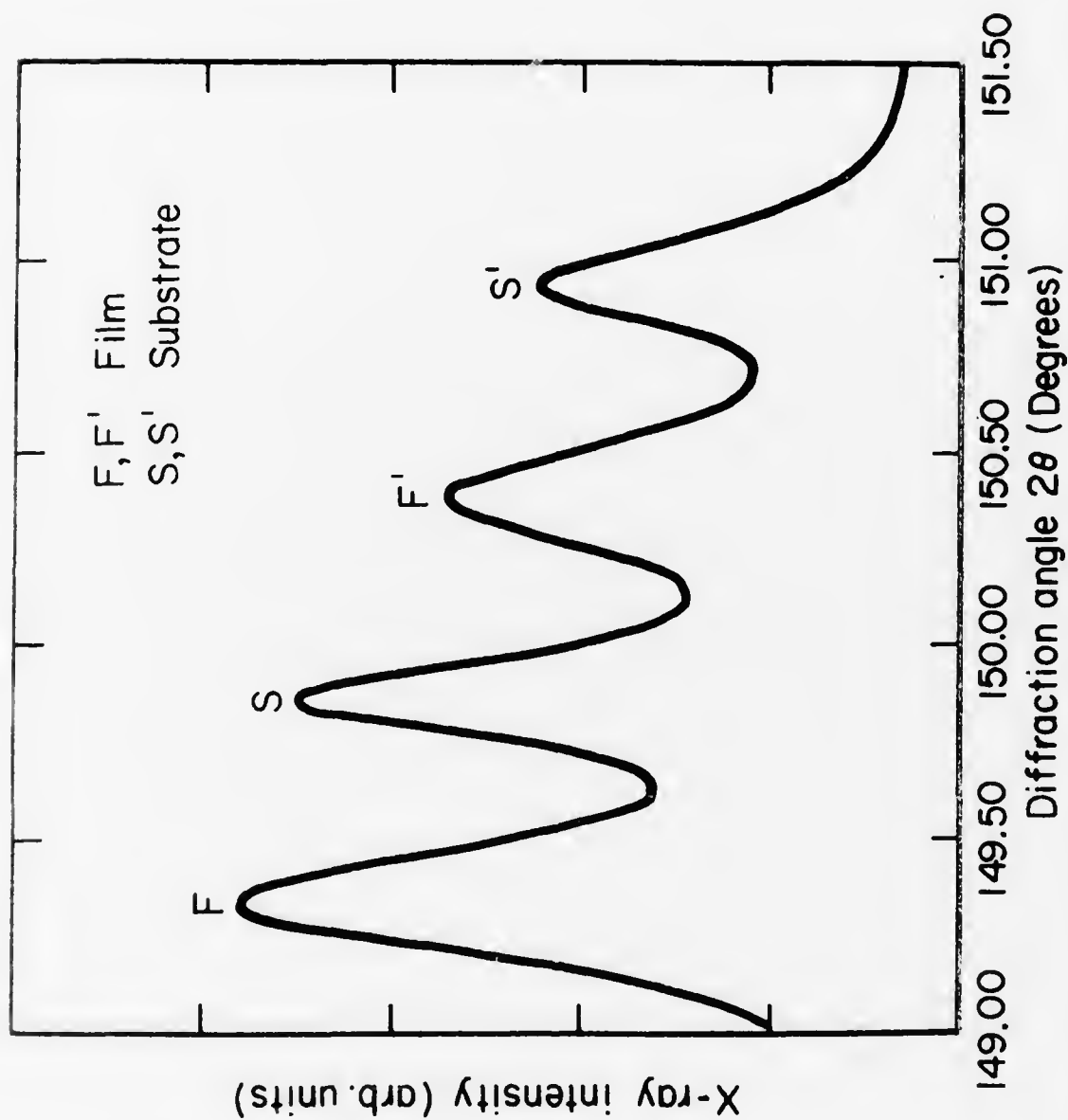


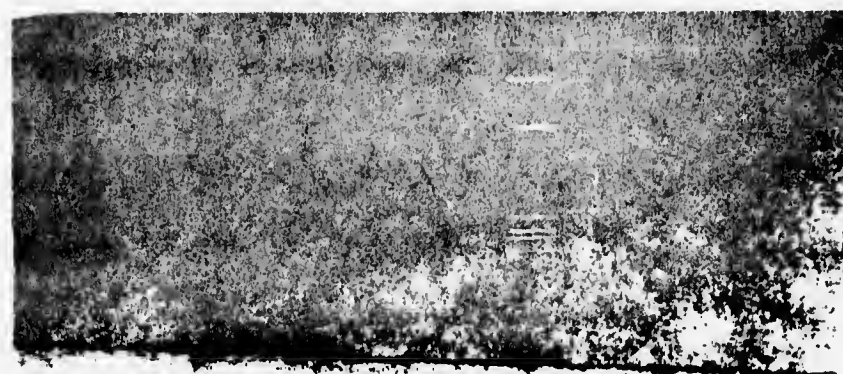
Fig. 4.12 X-ray diffraction peaks for KTN ($x = 0.34$) film on a KTaO_3 substrate.

Table 4.3Lattice Mismatch Data for Samples 30, 47

	<u>Sample 30</u>	<u>Sample 47</u>
Lattice Constant	3.9924	3.9934
Lattice Mismatch	0.1%	0.12%
Nb Mole Fraction	0.26	0.34

Table 4.4Synchronous Angle Measurements for TE Modes in a34 mole % Nb Film at 633 nm

<u>Mode</u>	θ_{sync}	η_g	η_g (best fit)
0	11.62 ^o	2.2748	2.2748
1	11.88 ^o	2.2721	2.2710
2	12.53 ^o	2.2653	2.2648
3	13.37 ^o	2.2564	2.2563
4	14.42 ^o	2.2453	2.2456

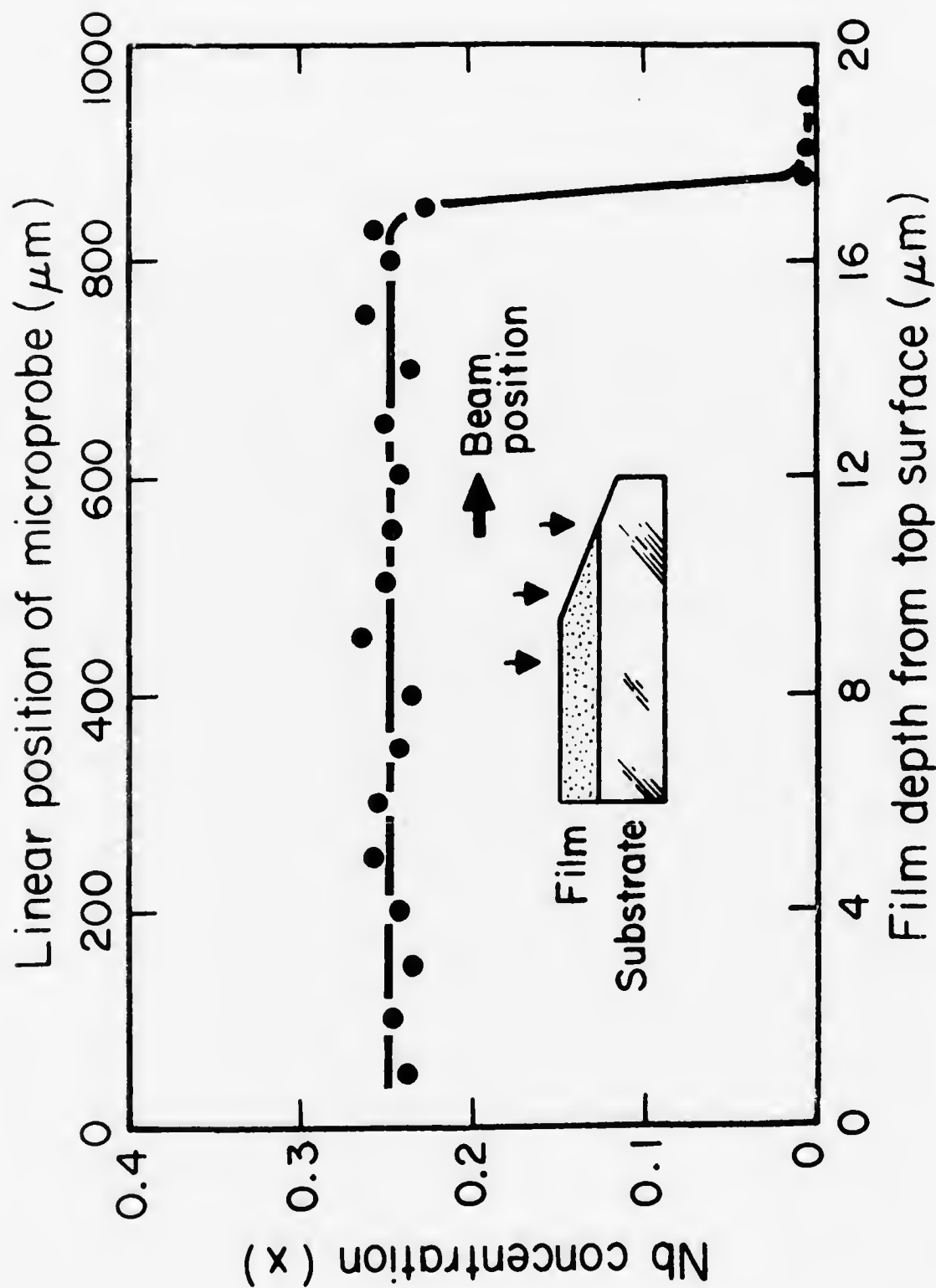


film ↑

substrate

┃ 50 microns

Fig. 4.13 Lapped film substrate.



4.3.2 Optical Characterization

Film thickness and the optical index of the film and substrate were determined by measurement of the properties of the optical guided modes in the films using synchronous angle techniques.

4.3.2.1 Optical Coupling

Rutile TiO_2 prisms were used for input and output coupling of optical guided modes. The rutile was grown in the Crystal Physics Laboratory by a flame fusion technique. Before cutting and polishing, the material was annealed at 800°C for 12 hours in a platinum crucible containing TiO_2 powder. The prisms were cut with a base angle of 55° with c axis parallel to right angle base edge. Prisms were about 4 mm wide and 5 mm high.

A prism-film holder was designed to clamp the film and prism by applying pressure only to the top of the prism. A bearing and pressure screw arrangement was used. The coupling jig is shown in Fig. 4.15. Substrates were mounted on glass slides using black wax in order to reduce reflection from the bottom film on the substrate. Coupling efficiencies were estimated from insertion losses to be 10-15% for each prism.

4.3.2.2 Synchronous Angle Measurements

The experimental set-up for the synchronous angle measurements is shown in Fig. 4.16. The prism coupler is mounted on a rotating platform (the z-y plane in which the synchronous angle is defined) which has x, y, and z translational freedom. In addition, the coupling angle in the x-y plane (the plane defined by the film) can be adjusted manually by $\pm 15^\circ$. The input laser beam passes through a polarizer,

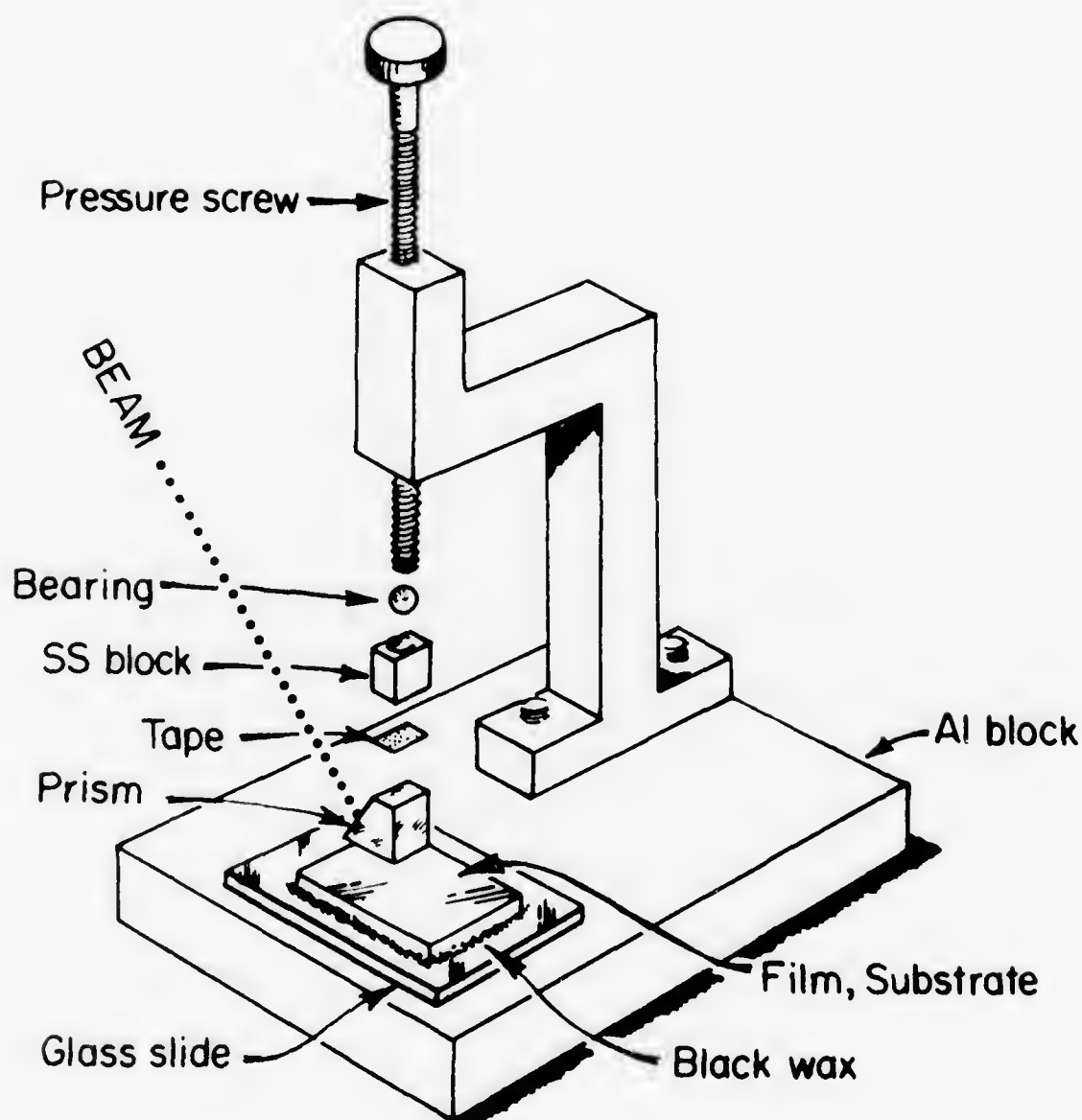


Fig. 4.15 Prism coupler arrangement.

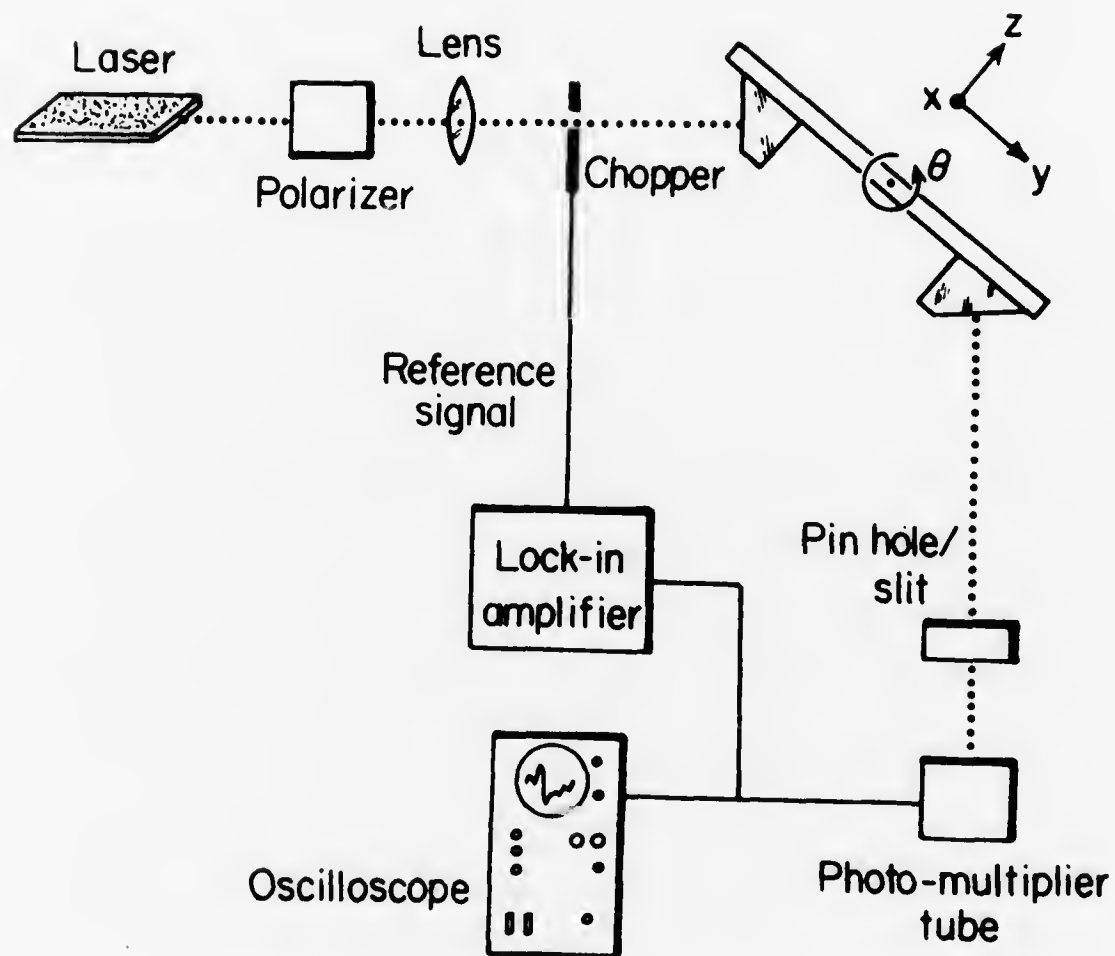


Fig. 4.16 Experimental arrangement for synchronous angle measurements.

for excitation of either TE or TM modes, and then is focussed through a 40 cm focal length lens onto the input prism face. The beam is chopped at 400 Hz and a reference signal fed into a lock-in amplifier. The output beam passes through either a slit or pinhole arrangement and onto a photomultiplier tube. The output can be displayed on an oscilloscope or synchronously detected with the lock-in amplifier.

By adjusting the incident angle in the y-z plane and noting a maximum in output intensity, the synchronous angles can be determined. For a 34 mole % Nb film from Run 48, 5 TE modes were detected for 633 nm light. In this experiment the prism base angle was 56.40° . From the synchronous angle measurements guide index, η_g , was determined for each mode. Using Eq. (2.13), a best fit for the data with $\eta_p = 2.872$ resulted in $w = 3.9$ microns, $\eta_f = 2.276$, $\eta_g = 2.240$. The results are shown in Table 4.4. With the exception of the TE_1 mode, the results fall within the accuracy of the measurement $\Delta\eta_g = \pm 0.0005$. A film index of 2.276 is lower than the expected index for a 34 mole % Nb film of 2.288 which would be predicted from previously reported bulk index values (see Eq. (1.8)).

4.3.2.3 Optical Loss

Optical loss was measured using essentially the same experimental configuration in Fig. 4.16, except that the output prism was removed and the pinhole or slit arrangement was replaced with an optical fiber mounted onto the front faceplate of the photomultiplier tube. The optical fiber was a single crystal Al_2O_3 sapphire rod, 20 mils in diameter, provided by the Arthur D. Little Company. Loss was measured by monitoring the amount of light that was scattered into the fiber from the guided mode streak in the film. Measurements were taken every 10 mils.

Early films, prior to run #40, had losses of 27-35 db/cm at 633 nm. With refinements in the growth procedures, improvements in polishing techniques, and possibly the addition of SnO_2 into the melt, the observed losses were reduced to 5-8 db/cm at 633 nm. Output intensity vs distance for 5 TE modes at 633 nm is shown in Fig. 4.17 for a film with 34 mole % Nb content. The loss in these modes increased from 5 db/cm to 15 db/cm with increasing mode number. The "m" lines associated with these modes are shown in Fig. 4.18. There is sufficient scattering in the films to result in the excitation of all the modes at any synchronous angle. As a result, the scattered light output measured with the optical fiber comes not only from the synchronous mode but also from every other mode in the film. The loss value that is assigned to any mode is really a weighted value reflecting the contributing effects of the other modes.

The guided mode beam was propagated along a $\langle 100 \rangle$ direction in these loss measurements. Coupling loss varied by 3-4 db/cm, depending on the location of the streak in the film. This is an indication of varying film quality. In Fig. 4.19, loss at three wavelengths, 457.9 nm, 514.5 nm, and 633 nm, was measured. The data points are insufficient to precisely attribute the loss to Rayleigh scattering with a λ^{-4} dependence but the loss trend does appear to follow this dependency.

4.3.3 Dielectric Measurements

Dielectric measurements were made using the interdigital electrode structure described in Section 2.3.2. The electrode parameters were $N = 18$, $L = 25$ microns, $w = 3$ mm. Dielectric constant and conductivity were obtained from ac impedance measurements by using Eqs. (2.55), (2.56).

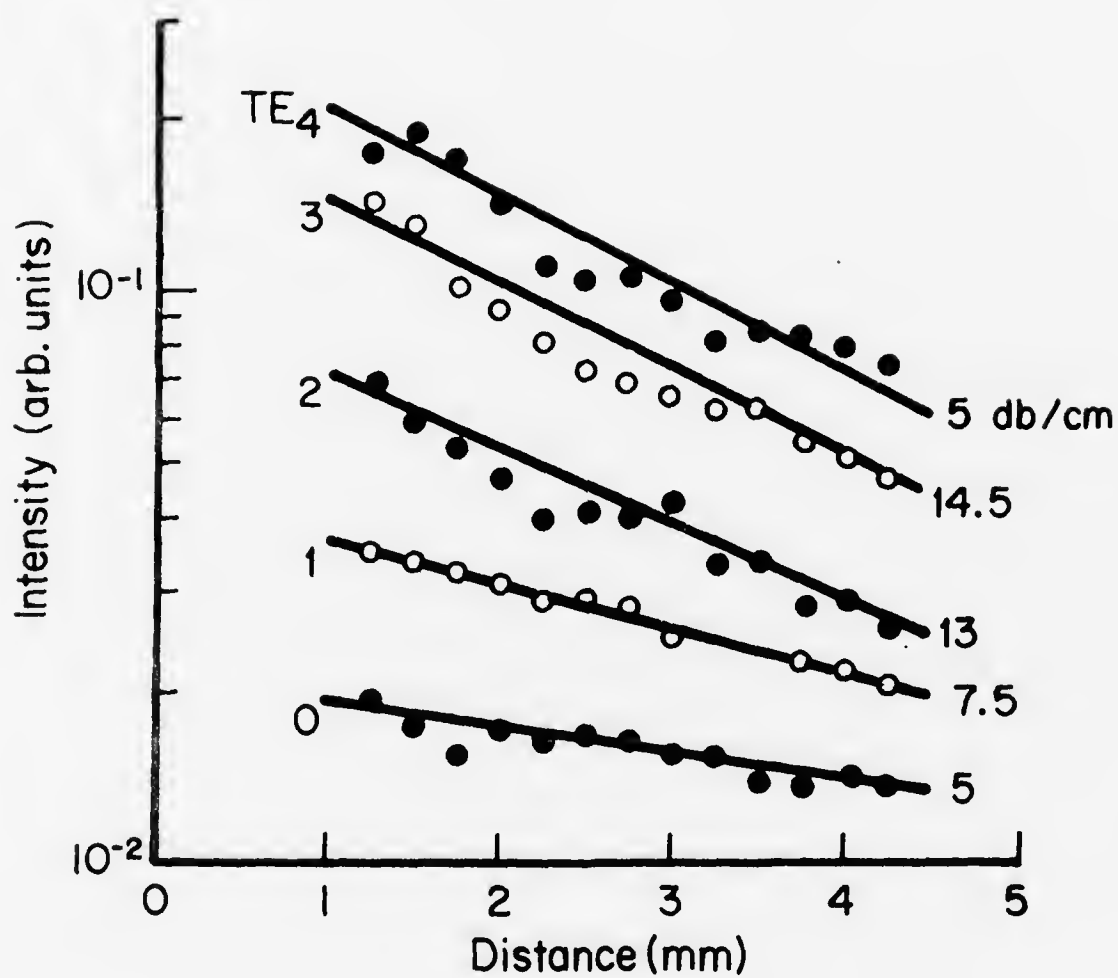


Fig. 4.17 Loss for 5 TE modes in an $x = 0.34$ KTN film at 633 nm.

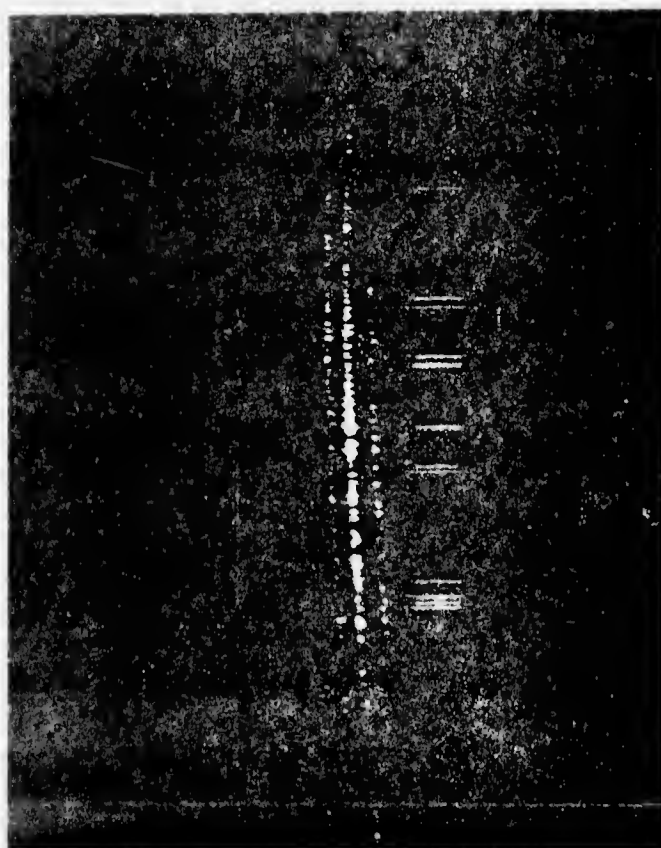


Fig. 4.18 "M" lines for TE modes in an $x = 0.34$ KTN film at 633 nm. (from left to right $TE_0 \cdots TE_4$)

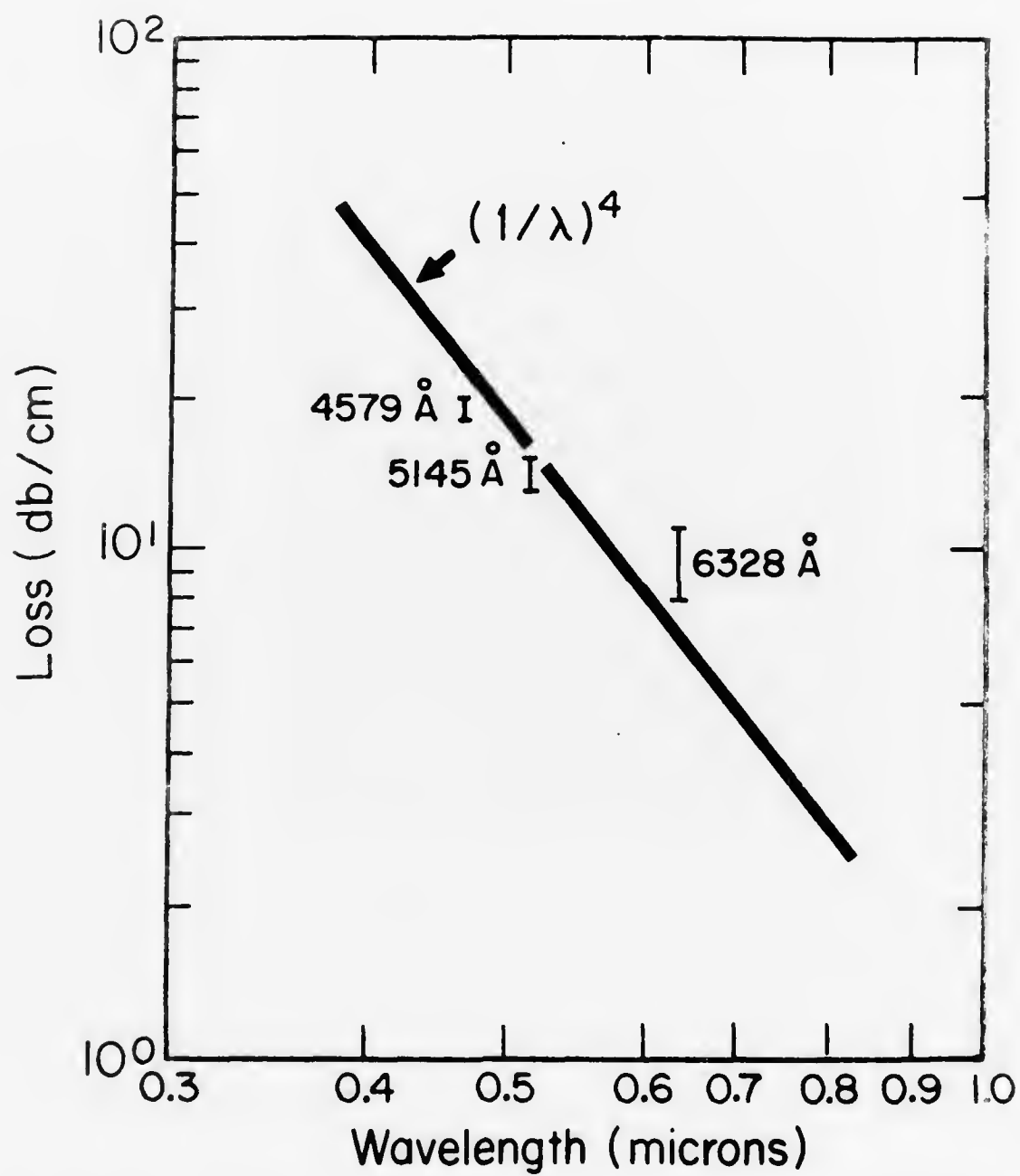


Fig. 4.19 Loss vs wavelength for TE modes in an $x = 0.34$ KTN film.

4.3.3.1 Dielectric Constant Measurement

Figure 4.20 is a plot of capacitance vs temperature for a 26 mole % Nb film. From the bulk data of Fig. 1.1 such a composition should undergo phase transition at -50°C , -103°C , -128°C . Associated with each transition should be a singularity in dielectric constant which should be reflected in capacitance measurements. The film-substrate was mounted on a polished copper block through which liquid nitrogen gas vapor was forced. By adjusting the gas vapor flow, a temperature decrease of $0.5^{\circ}\text{C}/\text{min}$ was maintained. The capacitance was measured with a Boonton capacitance meter at 1 MHz with a 15 mV peak voltage corresponding to a maximum electric field of 6 V/cm.

From the data of Fig. 4.20, the film undergoes transitions at 0, -52°C , -82°C . These transition temperatures do not match the bulk data for a 26 mole % Nb concentration, nor do they match very well to any other composition.

It is possible that the lattice mismatch at the film-substrate interface may contribute to strain on the film and cause the higher transition temperatures. To illustrate this point, recall that the substrate lattice constant is smaller than the film lattice constant. The film is therefore under compression in any plane parallel to the interface. For KTN at the cubic-tetragonal phase transition, the a and b lattice constants decrease,⁸³ i.e., compress, from their cubic values and the c lattice constant expands. The fact that the film is initially under compression should result in phase transitions occurring at temperatures greater than the bulk values, since presumably the bulk material is not under any compression forces.

The dielectric constant of this film was determined from the

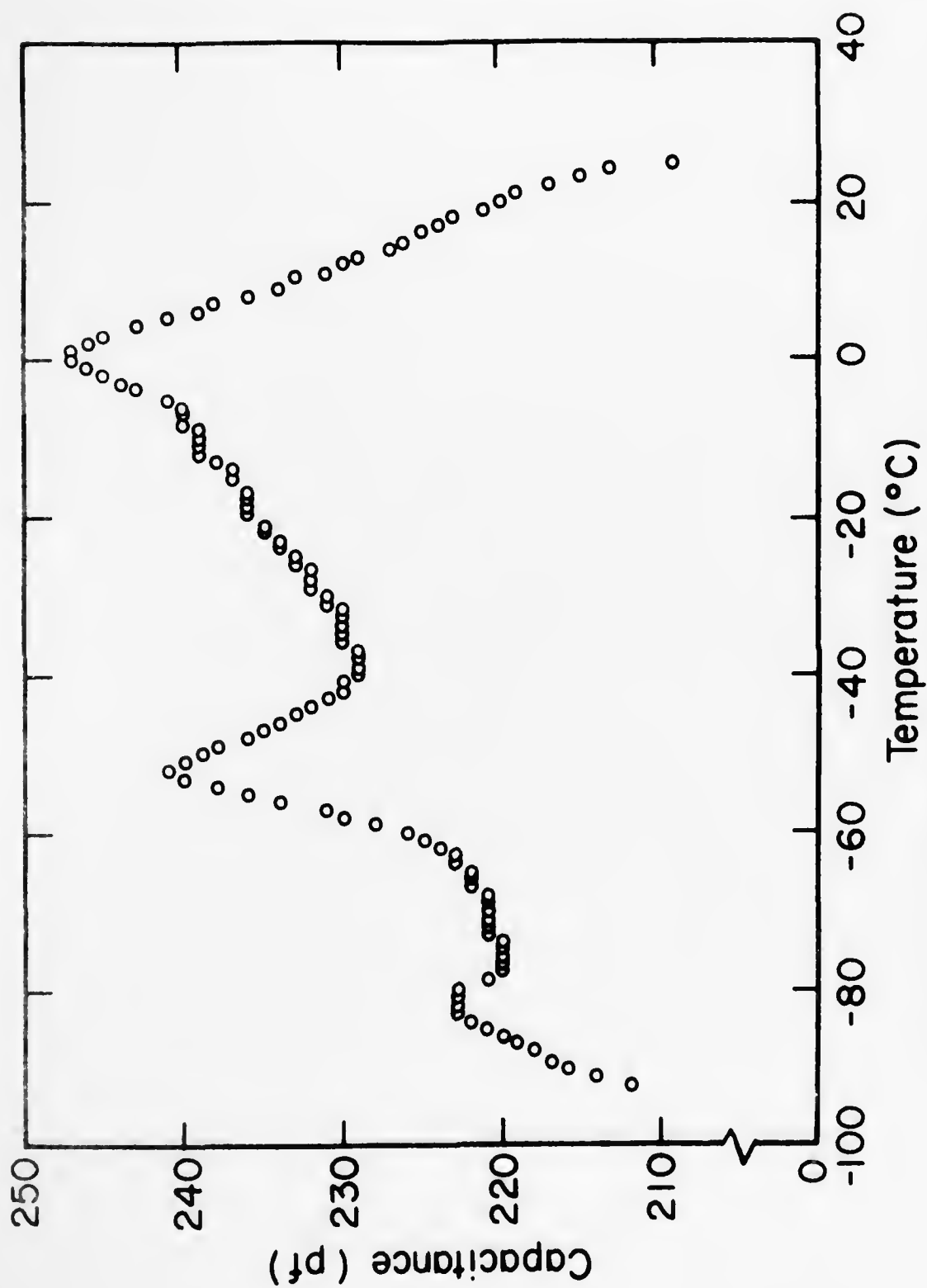


Fig. 4.20 Capacitance vs temperature for an $x = 0.26$ KTN film.

capacitance data using Eq. (2.55). The film was 5 microns thick. The geometry factors for $d/1_0 = 0.31$ were $G_1 = 0.62$, $G_2 = 1.72$, and for $d/1_1 = 0.94$ they were $G_1 = 1.46$ and $G_2 = 0.9$. Room temperature capacitance was 209 pf.

An attempt was made to fit the dielectric data above the transition temperature to a Curie-Weiss relation, Eq. (1.1), i.e.,

$$\epsilon = \epsilon_0 A / (T - T_0).$$

For this 26 mole % Nb film A was determined as 2.5×10^5 °K, while the bulk value would be 1.5×10^5 °K. Room temperature dielectric constant was $1920 \epsilon_0$, which compares favorably with a bulk value of $2000 \epsilon_0$. The peak dielectric constant occurring at 0°C was $2400 \epsilon_0$. A rough estimate for T_0 is -100°C . This value is suspect because the dielectric constant at the transition temperature is suppressed, being only 20% greater than the room temperature data, and because in bulk KTN transition temperature and T_0 vary by only a few degrees at most.

Similar capacitance vs temperature measurements were performed on a 34 mole % Nb film, 5 microns thick. From bulk data, a room temperature dielectric constant of $7200 \epsilon_0$ and a Curie temperature of 4°C would be expected. Experimental results gave a Curie temperature of 20°C and a room temperature dielectric constant of $4600 \epsilon_0$. Room temperature capacitance was 430 pf. The Curie-Weiss parameters were estimated to be 2×10^5 °K for A and -9°C for T_0 .

4.3.3.2 Dielectric Loss

In a dielectric material like KTN the imaginary part of the dielectric permittivity, ϵ'' , can contribute to a frequency-dependent dielectric conductivity, σ_{ac} , of the form

$$\sigma_{ac} = \omega \epsilon'' = \omega \epsilon' \tan \delta$$

where

$$\epsilon = \epsilon' - j\epsilon''$$

$$\tan \delta = \epsilon''/\epsilon'$$

At high frequencies, this conductivity can be of sufficient magnitude to severely limit device performance by increasing power dissipation in the device.

The dielectric conductivity of two KTN films was measured over a frequency range from 100 Hz to 100 KHz, using facilities available at the M.I.T. Laboratory for Insulation Research. The conductance resulting from the previously described interdigital electrode structure was related to the conductivity by using Eq. (2.56). One film had Nb mole fraction $x = 0.26$ and was 3 microns thick. The other had Nb mole fraction $x = 0.34$ and was 5 microns thick. This latter film was grown from a melt which had a small amount of SnO_2 (0.1 mole %) added to it. The inclusion of Sn into the KTN lattice may have contributed to the lower ac conductivity observed in the 34 mole % Nb film. However, with experimental evidence from just this one film, no real conclusions as to the influence of Sn in reducing dielectric loss in KTN films can be made.

As can be seen in the dielectric conductivity data of Fig. 4.21, the Sn compensated film has ac conductivity a factor of 8 lower than the undoped film. The slope of the conductivity data over a three-decade frequency range is 1.06. Such a linear behavior with frequency is expected for dielectric conductivity. The $\tan \delta$ for the uncompensated film ($x = 0.26$) was ~ 2.0 and for the doped film $\tan \delta \approx 0.20$. Device conductance, G , can be calculated from the film conductivity by

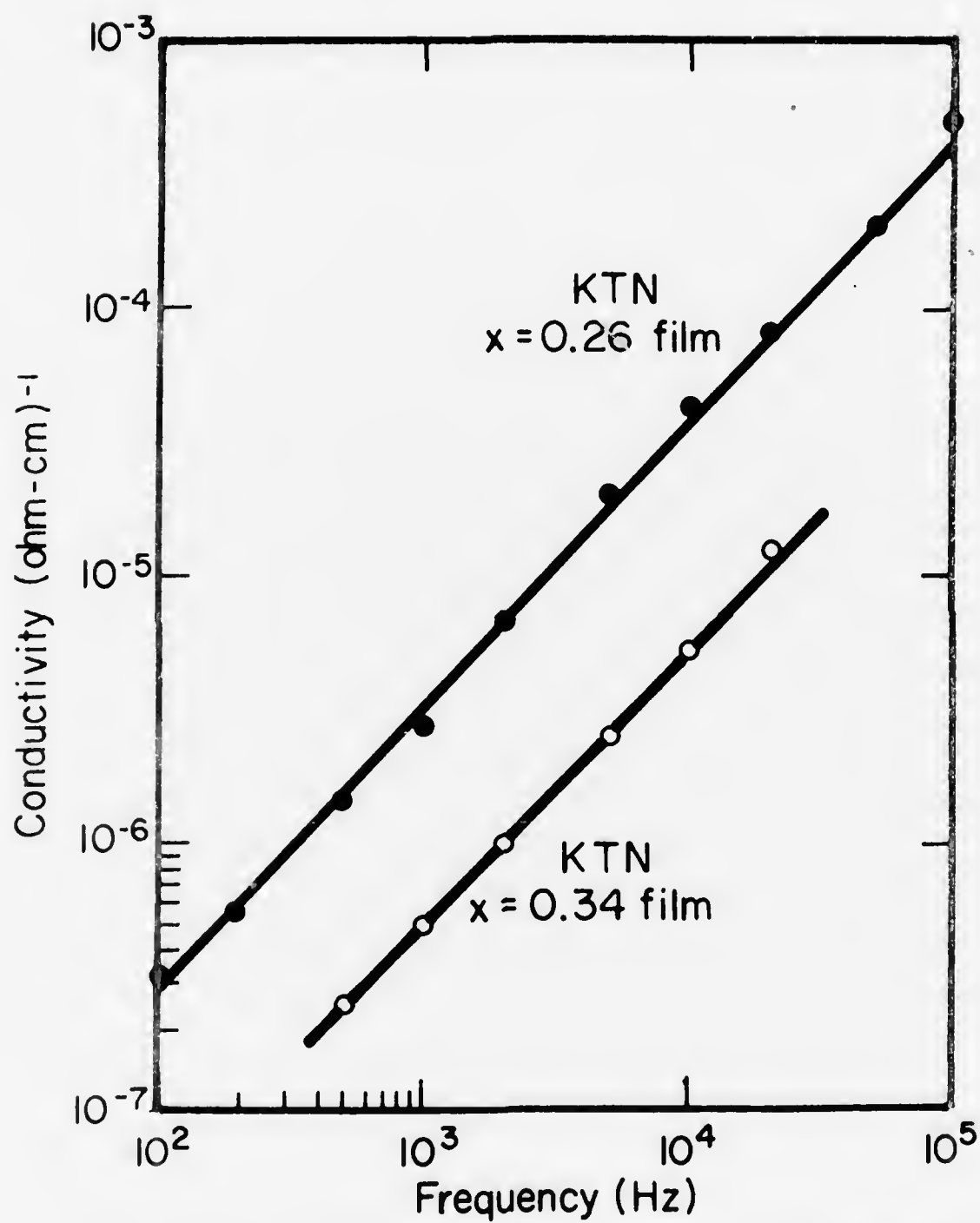


Fig. 4.21 ac conductivity vs frequency for an $x = 0.26$ KTN film and an $x = 0.34$ KTN film.

multiplying by 0.62 cm, for the 26 mole % Nb film, and by 0.98 cm for the thicker 34 mole % Nb film.

CHAPTER 5

DEVICE FABRICATION AND EVALUATION

To demonstrate the potential of KTN as an electro-optic material for thin film devices, two diffraction modulators were fabricated. In this chapter the fabrication and performance of these devices will be described.

5.1 Fabrication

5.1.1 Electrode Design

The diffraction modulators used a pair of interdigital metal electrodes (Fig. 2.9) deposited on the surface of the film. Electrode parameters were the number of fingers N , the finger length W , and the finger width and separation L . Adjacent fingers have a center-to-center spacing $2L$.

For a quadratic electro-optic material the period of the index variation which results when a voltage is applied across this electrode structure is $2L$. The Q for the electrode (see Eq. (3.43)) is therefore:

$$Q = \frac{\pi}{2\eta_0} \cdot \frac{W}{L} \cdot \frac{\lambda_0}{L} \quad (5.1)$$

Electrode dimensions were $w = 3$ mm, $L = 25$ microns and $N = 18$, giving $Q = 2.1$, and therefore the diffraction modulation for the KTN devices was in a regime midway between Raman-Nath and Bragg diffraction.

Our mask design used the minimum electrode spacing and maximum electrode length which could be fabricated in the M. I. T. Microcircuits Laboratory. It was not possible to etch fingers with widths less than 25 microns. Patterns with overall final dimensions greater than 3 mm could not be accommodated by the step and repeat

system when final mask patterns of the electrode were made. The actual electrode pattern is shown in Fig. 5.1.

Masks for this electrode pattern were fabricated by first reproducing a 100X magnification of the pattern on a Rubylith plastic sheet and then reducing this image by a factor of 10 using conventional photographic techniques. The 10X image was reduced by the final factor of 10 using a step and repeat system available in the M.I.T. Microcircuits Laboratory and then this final pattern was contact printed to a photographic glass plate.

5.1.2 Electrode Metallization

The electrodes were prepared by vacuum deposition of Ti on the KTN film followed by a subsequent deposition of Au to serve as a protective layer. Ti-Au electrodes were used because our experience with bulk KTN showed that this combination of metals adhered well to highly polished KTN surfaces. Two tungsten filament baskets, one containing 350 mg of 20-mil diameter Au wire (~ 7 cm in length) and the other containing 80 mg of 32-mil diameter Ti wire (~ 5 cm in length) were suspended 10 cm above the sample in a vacuum deposition bell jar. The sample as well as the tungsten filaments and metal wire were cleaned following the identical procedure outlined in Chapter 4 for substrate cleaning. The evaporation of the Ti first and then the Au takes place after a vacuum of 10^{-6} microns has been reached.

5.1.3 Photolithography

A positive resist, AZ 1350 manufactured by Shipley, was used to define the mask patterns on the sample. Immediately after the metal evaporation, the following steps are performed to obtain the desired

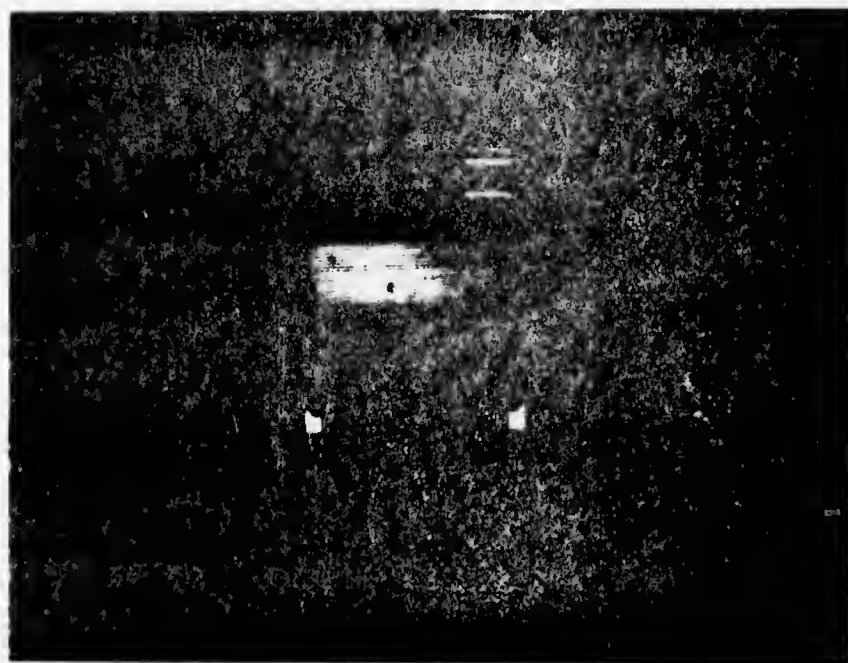


Fig. 5.1 Interdigital electrode.

electrode pattern:

1. Coat sample with 2 or 3 drops of AZ 1350 resist. Spin for 15 seconds at 3000 rpm.
2. Bake sample for 2.5 minutes at 85°C.
3. Repeat steps 1 and 2.
4. Transfer sample to mask aligner for pattern exposure.
5. Use maximum mask separation allowed. When mask pattern is properly positioned over the sample, expose sample to mercury arc lamp for 5 seconds.
6. Develop, i.e., remove, the exposed photoresist using the Shipley developing solution for one minute. Rinse in distilled water and then blow dry with N₂ gas. Repeat the process a second time.
7. Postbake the sample at 85°C for 30 minutes to harden the undeveloped, unexposed resist.
8. Etch the top Au layer using a 6:1 solution of HCl:HNO₃. The Au layer dissolves in about 30 seconds.
9. Etch the Ti layer using a 5:5:1 solution of H₂O:HNO₃:HF. The Ti layer dissolves in about 1-4 seconds.
10. Dip the sample again into the HCl:HNO₃ etch for a few seconds, rinse in distilled H₂O, and blow dry with N₂.
11. Remove the unexposed resist by soaking the sample in acetone for 5-10 minutes.

5.1.4 Sample Mounting

Au wires, 10 mils in diameter, were bonded to the electrode contact pads using a single component conducting epoxy, EPO-TEK H31. The epoxy is activated by heating the sample to 120°C for 1-2 hours. The sample is then mounted on a glass slide using black wax, and the

gold wires are soldered to miniature OSM coaxial connectors attached to the prism film holder described in Section 4.4. To minimize strain on the sample holder, semi-rigid coaxial cable was used to connect the device with the necessary test equipment.

5.2 Modulator Performance

Two thin film diffraction modulators were fabricated using the steps outlined in Section 5.1. All experiments were performed at 633 nm on TE modes. The device is shown schematically in Fig. 5.2.

The experimental setup for evaluation of the modulators was identical with the arrangement for synchronous angle measurements shown in Fig. 4.15. Rutile prisms were used for input and output coupling of light. The output coupled diffracted beam passed through a pinhole and onto a photomultiplier tube. The output signal can be displayed on an oscilloscope or synchronously detected using a lock-in amplifier. When dc modulating voltages were used, the input laser beam was mechanically chopped at 400 Hz in order to supply a reference frequency to the amplifier. For ac modulating voltages, the second harmonic of the modulating voltage frequency was used as the lock-in reference frequency.

5.2.1 Performance of a KTN ($x = 0.26$) Modulator

The film used for this modulator had Nb mole fraction $x = 0.26$ for which the dielectric constant from bulk data would be $2000 \epsilon_0$. Capacitance measurements on a film from the same substrate as the modulator film indicated a dielectric constant of $1920 \epsilon_0$. The modulator film thickness was 3 microns and the optical index was ~ 2.26 . Three TE and three TM modes could be propagated in this film. Optical loss

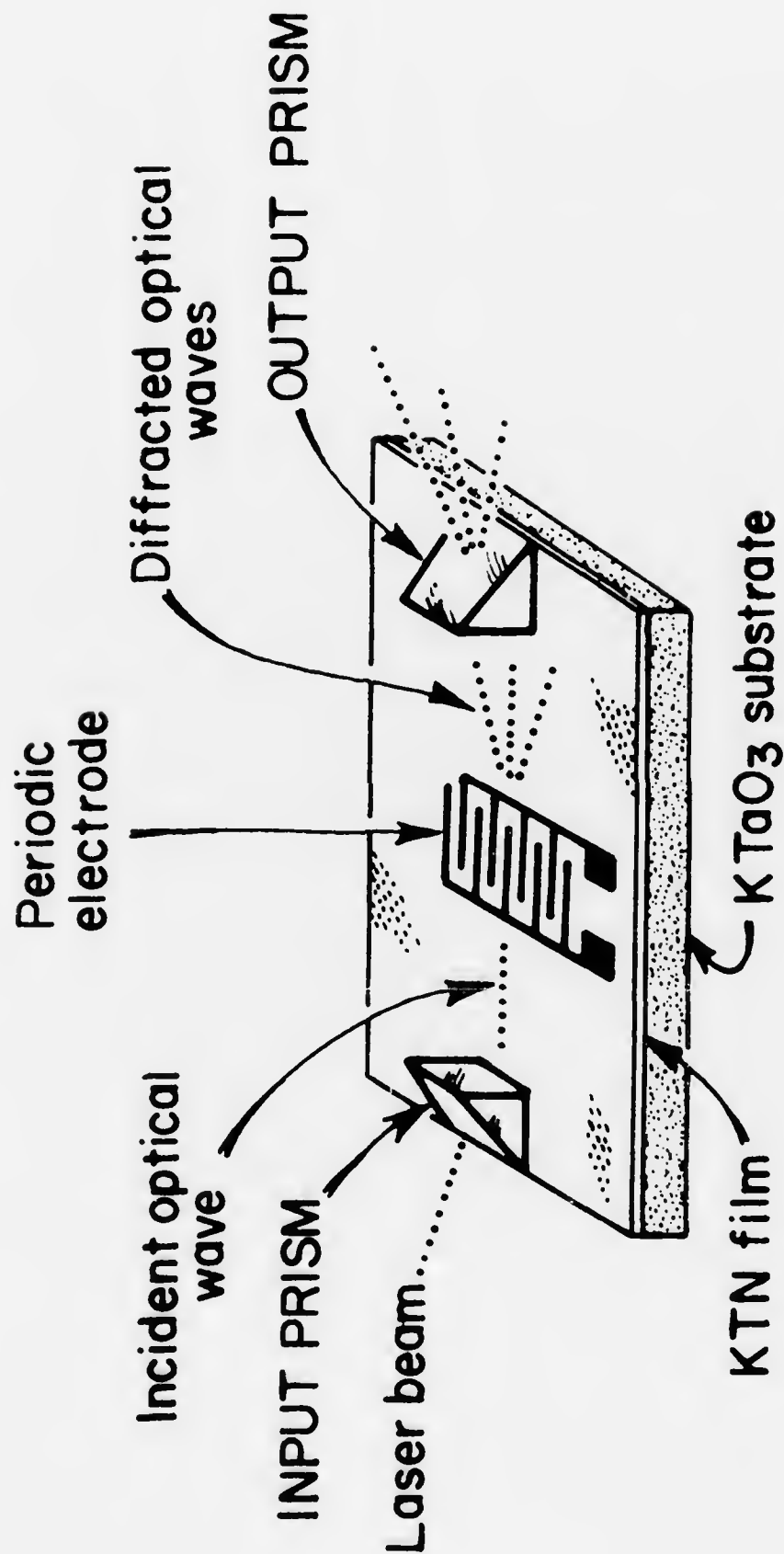


Fig. 5.2 Experimental configuration of KTN modulator.

for the modes was high, ~ 25 db/cm. $\tan \delta$ for the film was approximately 2.0. ac conductivity for the film is shown in Fig. 4.21.

The dc operating characteristics of this modulator are shown in Fig. 5.3. For a modulating voltage of 15 volts, 90% modulation of the central beam output was achieved. For $Q = 2.1$, maximum intensity modulation of the central beam should occur when a phase retardation of $\Delta\phi = 2.3^{61}$ is induced on the input guided mode in passing beneath the electrode. Using Eq. (3.25), $\Delta\phi = 2.3$ requires an index change $\Delta\eta = 7.7 \times 10^{-5}$. Using this value with $g = 0.134 \text{ m}^4/\text{c}^2$ and $E = 6000 \text{ V/cm}$, the dielectric constant of the film can be determined. A value of $1910 \epsilon_0$ in comparison with a value of 1920 from capacitance measurements results.

dc modulation of the central beam was further demonstrated by monitoring the diffracted light output of the central, first, and second order beams. To obtain these measurements, the photomultiplier tube was translated along the diffraction plane. In Fig. 5.4a the undiffracted light profile, with no applied voltage, is shown. In Fig. 5.4b, with about 15 volts applied, the central beam has been suppressed with the first and second side lobes becoming visible.

Low frequency, 100 Hz operation of the modulator is shown in Figs. 5.5, 5.6. The dc modulation characteristics show a region of linear intensity modulation from 4-10 volts. An ac voltage of 5 volts peak-to-peak was superimposed on a dc bias of 7 volts and applied to the modulator electrode. The linear intensity modulation in the form of a first harmonic frequency output is shown in Fig. 5.5b. The output intensity waveforms of Fig. 5.6 were obtained for large ac voltages corresponding to fields of 3000 V/cm and 6000 V/cm. The second

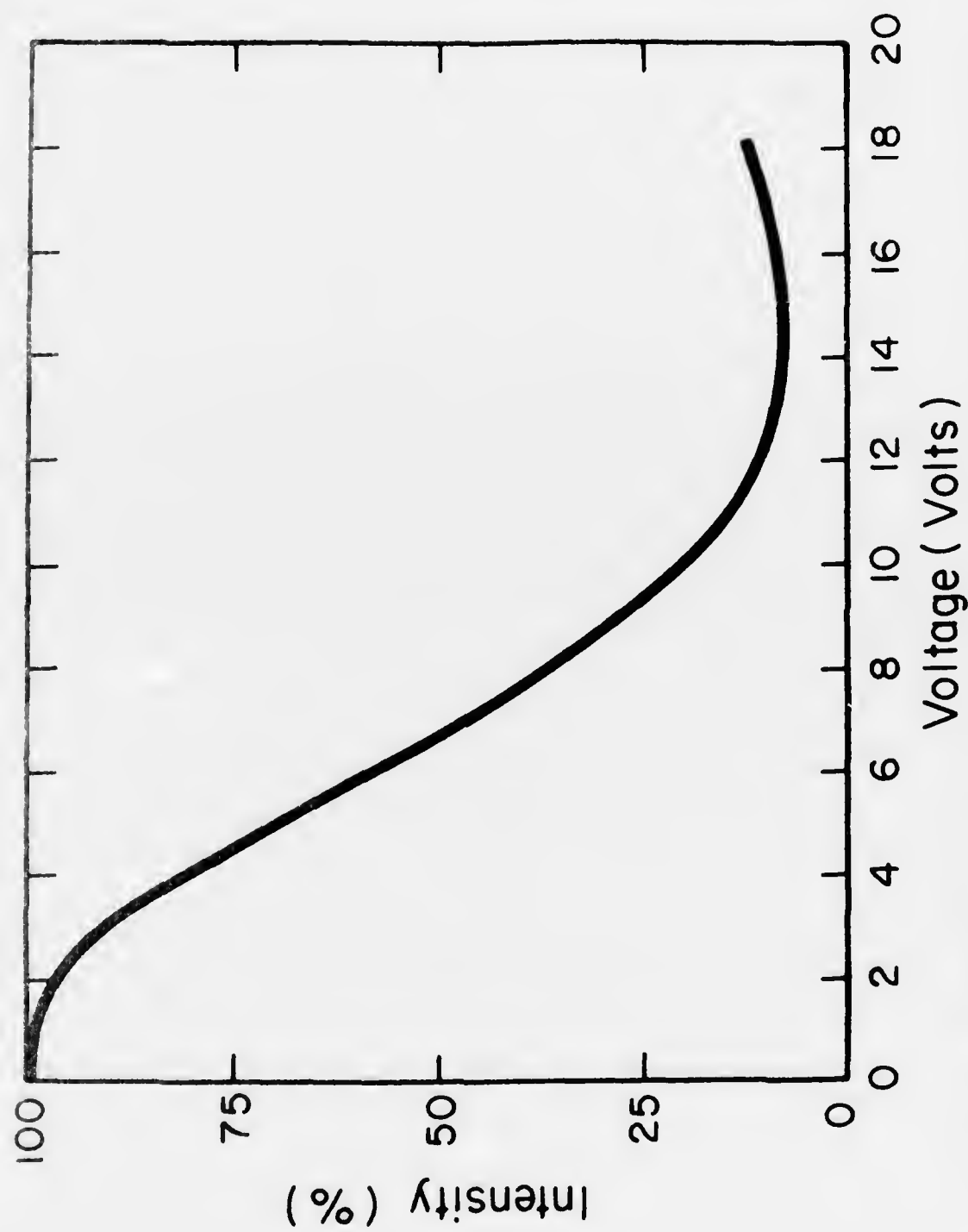


Fig. 5.3 Central beam intensity vs applied dc voltage for KTN ($x = 0.26$) modulator.

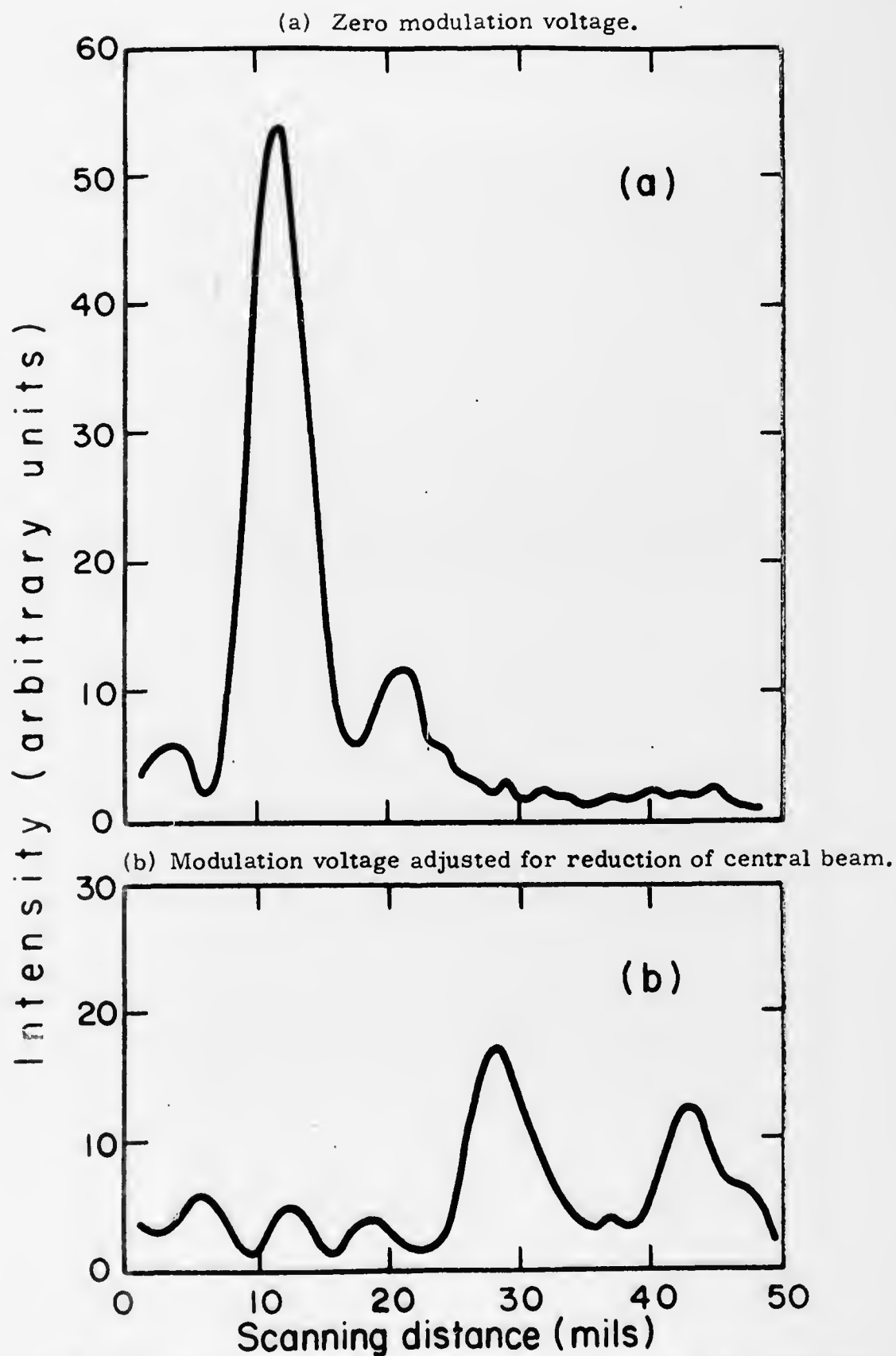
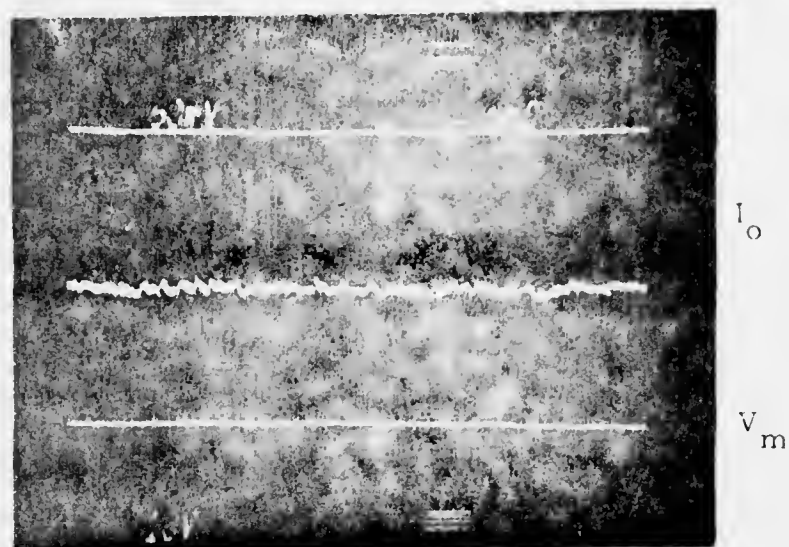


Fig. 5.4 Profile of output light beam in KTN ($x = 0.26$) modulator.

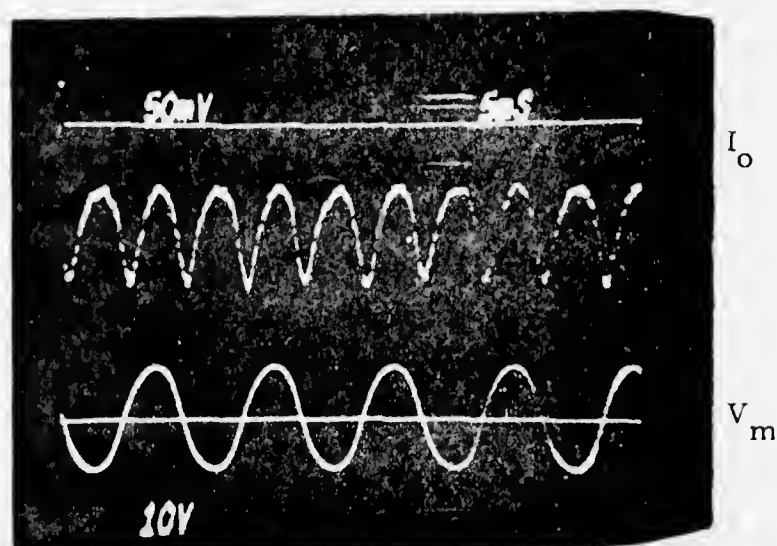


(a) Central beam intensity, I_o , with no applied voltage V_m .

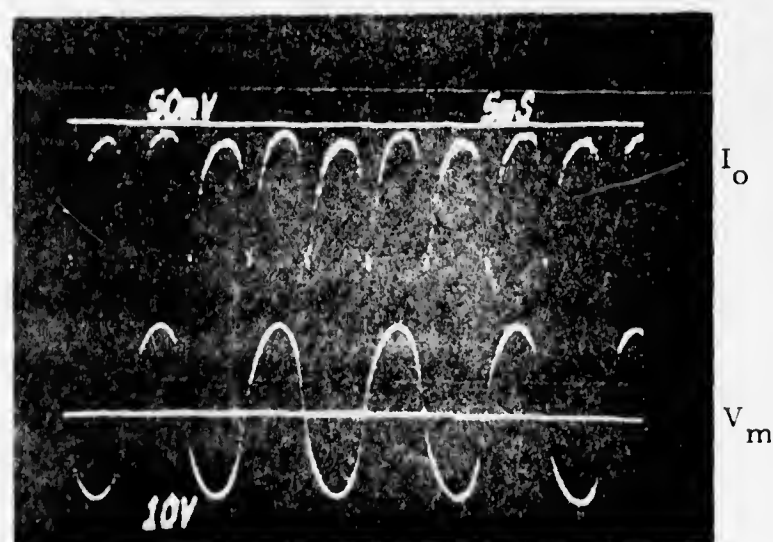


(b) Central beam intensity, I_o , with 5 volt p-p modulating voltage superimposed on 7 volt dc bias.

Fig. 5.5 Frequency behavior of KTN ($x = 0.26$) modulator.



(a) Central beam intensity, I_o , for a 16 volt p-p modulating voltage V_m .



(b) Central beam intensity, I_o , for a 32 volt p-p modulating voltage V_m .

Fig. 5.6 Frequency behavior of a KTN ($x = 0.26$) modulator.

harmonic nature of the modulated output intensity is consistent with the quadratic nature of the KTN electro-optic effect. With large applied fields of 6000 V/cm a first harmonic signal is observed. Such an effect may be due to strain in the film caused by lattice mismatches at the film-substrate boundary.

This modulator had a very restricted bandwidth. At 1 MHz the capacitance of the device, including connectors and coaxial cables, was measured at 600 picofarads. The cables and connectors contributed 400 pf of this value. This implies a bandwidth of 10 MHz if the device were shunted with a $50\ \Omega$ resistor. Modulation efficiency for sinusoidal excitation is shown in Fig. 5.7. At 10 KHz a severe reduction in modulator performance is observed. Response to a step function in input modulation voltage resulted in rise times of $3\ \mu\text{s}$. This implied that the maximum frequency for sinusoidal excitations would be 50-100 KHz. The difference between the circuit limited bandwidth of 10 MHz and the observed bandwidth of about 50 KHz can be attributed to temperature rises resulting from the high dielectric losses associated with the KTN film. Power dissipation in the film raises the temperature of the device and therefore reduces the electro-optic effect of the material. This issue will be discussed in Section 5.3.1.

5.2.2 Performance of a KTN ($x = 0.34$) Modulator

The KTN film used for this modulator had Nb mole fraction $x = 0.34$ and was grown from a melt containing 0.1 mole % SnO_2 . Bulk data would predict a value of $7200\ \epsilon_0$ for the dielectric constant for this KTN composition. Our measured dielectric constant from capacitance data was $4600\ \epsilon_0$. This film was 5-6 microns thick; it had an optical index of 2.276 at 633 nm. 6 TE and 6 TM modes can propagate in this

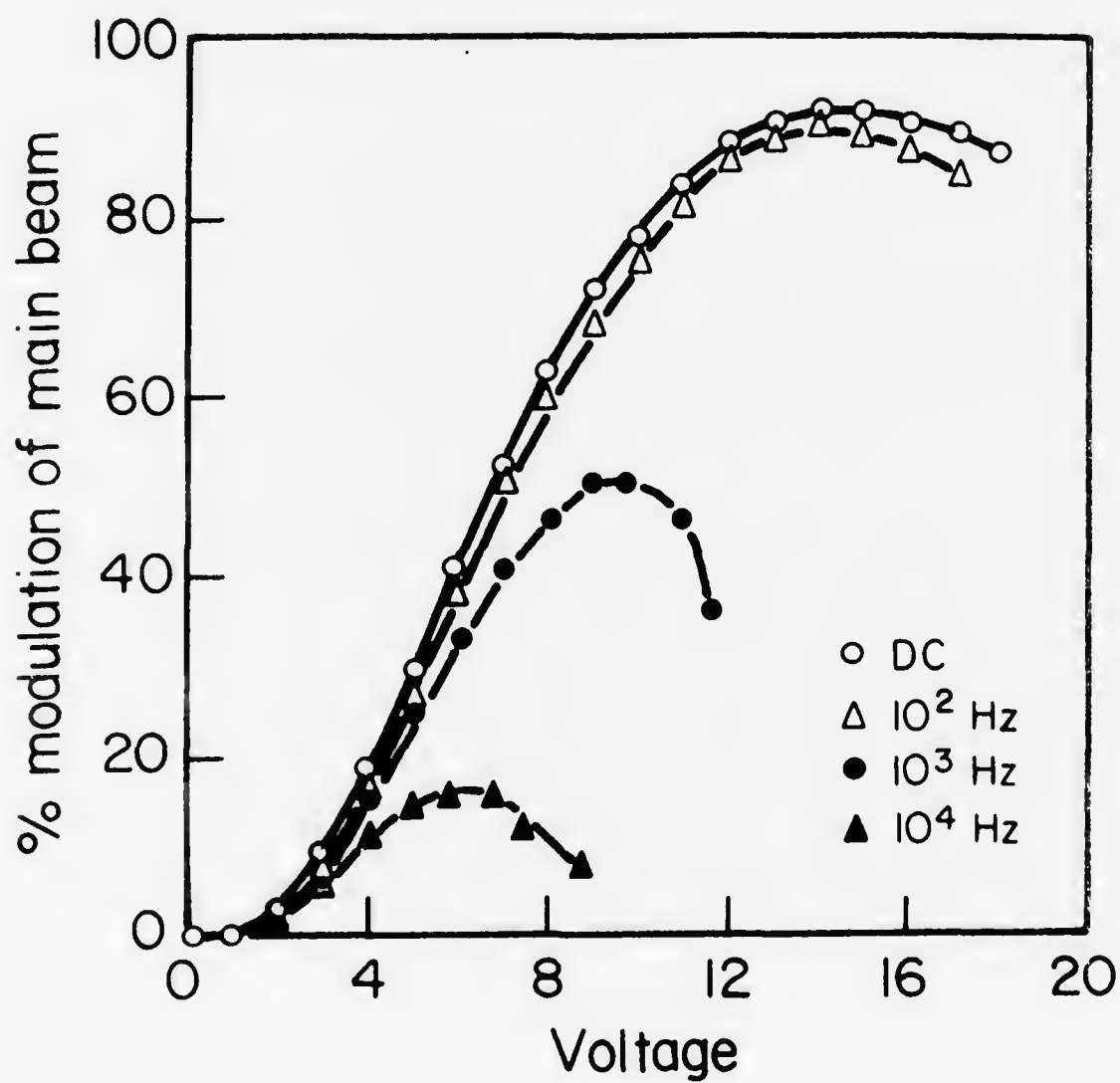


Fig. 5.7 Modulator efficiency vs applied voltage for three frequencies.

film and their losses ranged from 5-15 db/cm. $\tan \delta$ for the film was ~ 0.20 . The ac conductivity of the film is shown in Fig. 4.21.

Since the KTN ($x = 0.34$) film had a higher dielectric constant and had lower dielectric conductivity than the KTN ($x = 0.26$) film, it was expected that better performance with respect to drive voltage and bandwidth would result.

The dc modulation characteristics of the KTN ($x = 0.34$) modulator are shown in Fig. 5.8. A maximum intensity modulation of 90% was obtained for a voltage of 8 volts, corresponding to a maximum electric field strength of 3200 V/cm. Using Eq. (3.25) with $\Delta\phi = 2.3$ and Eq. (3.18), the calculated dielectric constant for the film is $3800 \epsilon_0$ and not the expected value of $4600 \epsilon_0$ measured for this 34 mole % Nb film from capacitance data. At 1 MHz the device capacitance, including connectors and coaxial cables, for this modulator was 1000 pf, 500 pf being contributed by the cables and connectors. This gives a bandwidth with a 50Ω shunt resistor across the device of 6 MHz. The operation of the device at 500 Hz and 500 KHz is shown in Fig. 5.9a, b. Modulation efficiency is down by about 15% at the higher frequency. As with the KTN ($x = 0.26$) device, a small first harmonic signal distortion is still present in these output waveforms.

The response of the modulator to a pulsed voltage excitation is shown in Fig. 5.10. Rise times of the order of 200 ns were observed. Sinusoidal frequency operation up to 0.8 MHz should therefore be possible. Again, there is the difference between circuit bandwidth and the observed device bandwidth which is caused by the power dissipation in the device.

The performance features of both KTN thin film modulators are listed in Table 5.1. The circuit limited bandwidth was calculated using

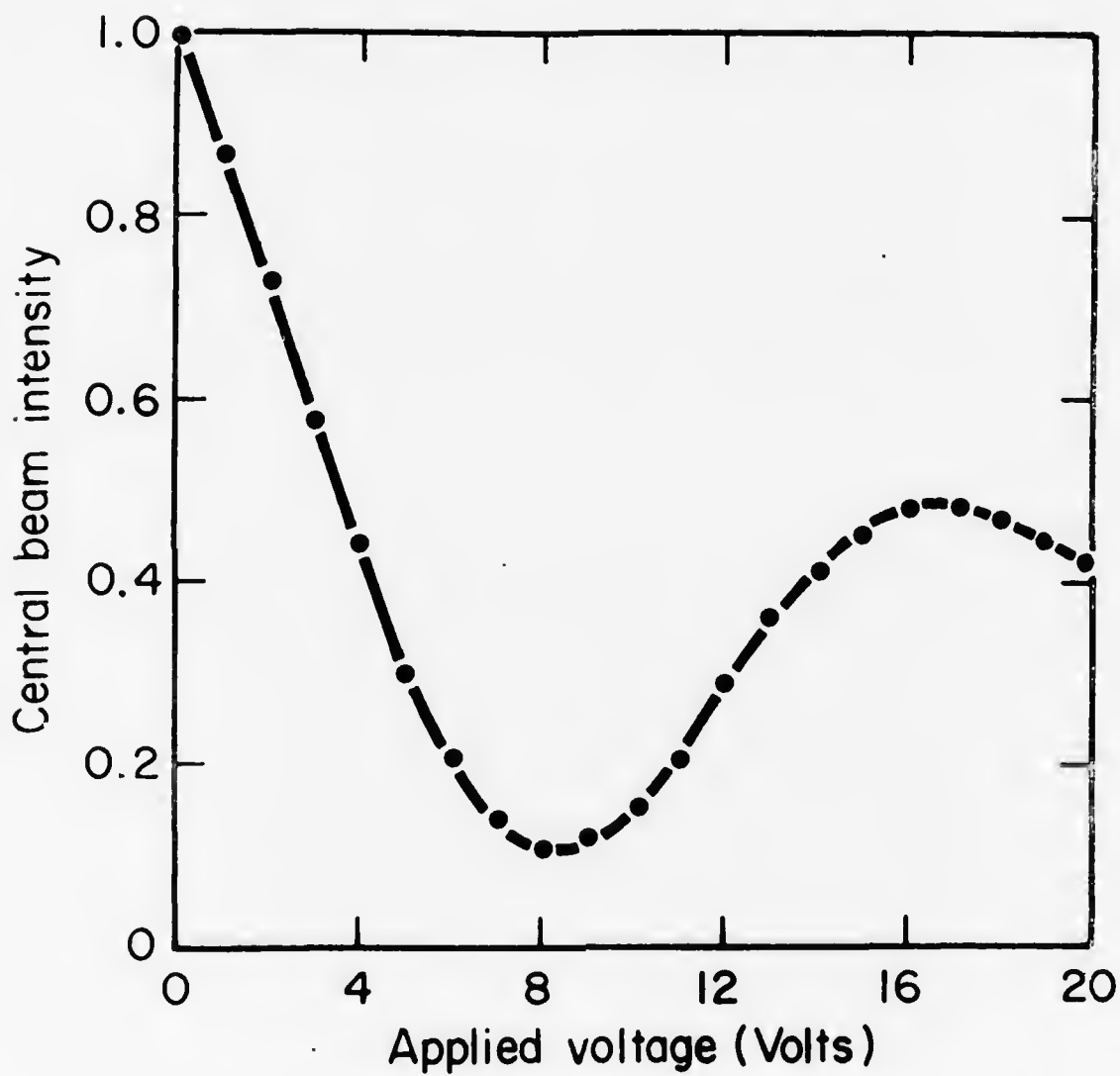
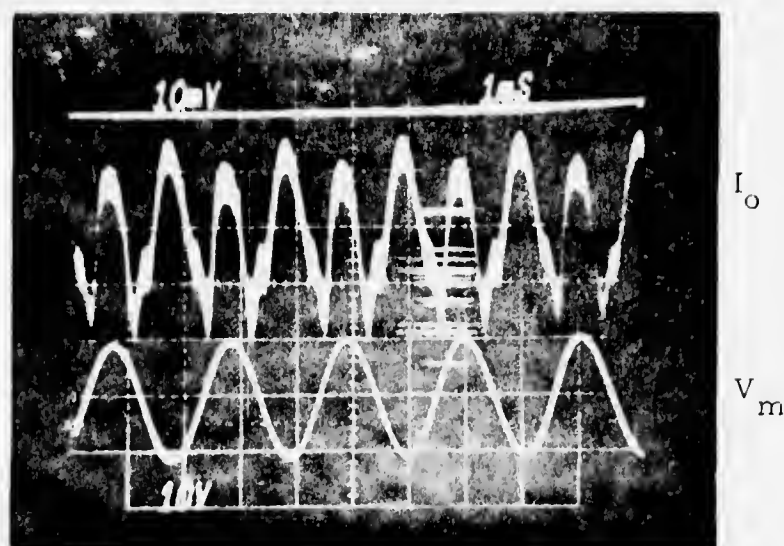
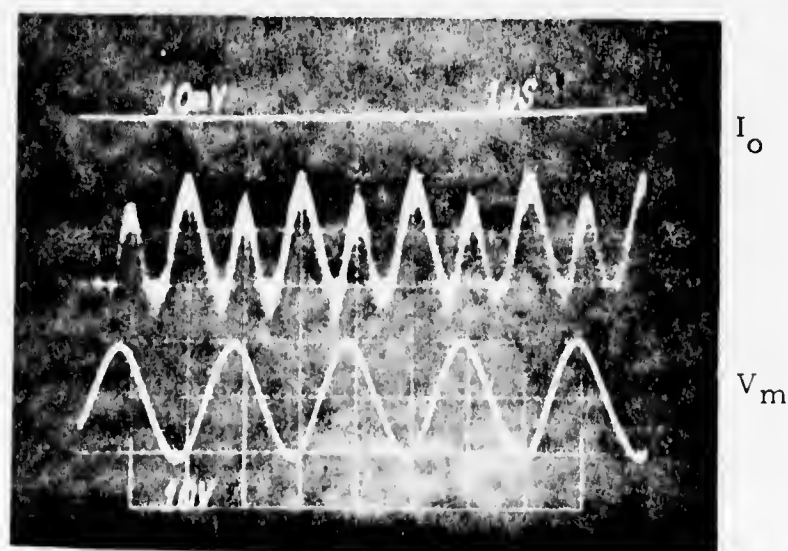


Fig. 5.8 Central beam intensity vs applied dc voltage for a KTN ($x = 0.34$) modulator.



(a) Central beam intensity, I_o , for 20 volt p-p modulating voltage, V_m , at 500 Hz.



(b) Central beam intensity, I_o , for 20 volt p-p modulating voltage, V_m , at 500 KHz.

Fig. 5.9 Frequency behavior of KTN ($x = 0.34$) modulator.

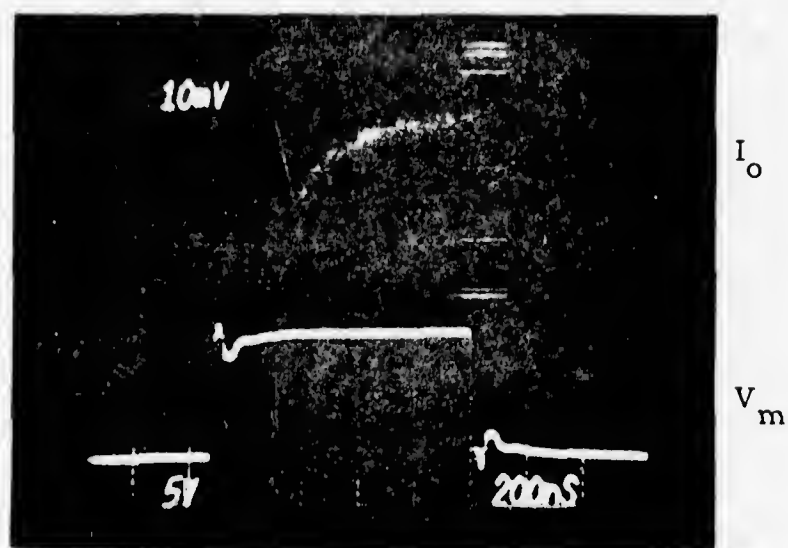


Fig. 5.10 Pulse response time of KTN
($x = 0.34$) modulator.

Table 5.1Modulator Performance

	<u>Modulator 1</u> KTN (x = 0.26)	<u>Modulator 2</u> KTN (x = 0.34)
Drive voltage (90% modulation)	15 volts	8 volts
ac resistance (50 KHz)	6.6 k Ω	33 k Ω
Power dissipation in device (90% modulation, 50 KHz)	34 mW	1.9 mW
Pulse response time	3 μ s	0.2 μ s
Circuit limited bandwidth	10 MHz	6 MHz
Actual bandwidth (Determined from rise times.)	~ 50 KHz	~ 800 KHz

the capacitance of the modulator, connectors, and cables. The actual bandwidth was determined from rise time measurements with the device being driven by an HP 214A Pulse Generator (internal source impedance 50Ω) and shunted with a 50Ω resistor.

5.3 Interpretation of Device Performance

5.3.1 Thermal Effects on Device Bandwidth

In both of our devices, the maximum frequency of operation was less than that which would be predicted by simple circuit considerations. This result can be attributed to the dielectric loss in the KTN thin films. Because of the large dielectric conductivity in the KTN films, substantial power is dissipated in the films at peak modulating voltages. Since the dielectric conductivity increases with frequency (Fig. 4.21), power dissipation and therefore temperature rises can be significant at high frequencies.

For diffraction modulation in thin films, the intensity of the central beam depends critically on the total phase shift, $\Delta\phi$, that is induced on the guided mode. For KTN devices $\Delta\phi$ is proportional to $(T - T_0)^{-2}$, where T_0 is the Curie-Weiss temperature and T is the temperature of the device, because index change depends on the square of the dielectric constant. Clearly, any temperature increase will reduce $\Delta\phi$ and consequently reduce modulator efficiency.

A rough estimate of the temperature rises that can occur in KTN films can be obtained by using the work of Mogelalde et al.⁷⁷ For a power density of $P_0 \text{ W/cm}^3$ in a thin film with thickness d , substrate thickness $a \gg d$, and thermal conductivity κ , the steady state temperature increase is given by

$$\Delta T = P_o d a / \kappa \quad (5.2)$$

This expression was obtained by assuming that heat flow occurs only through the substrate and that the substrate bottom is fixed at ambient temperature.

P_o for an interdigital electrode device with N parallel strips of material of width L , length W , and thickness d and with conductance G is

$$P_o = V^2 G / N W L a \quad (5.3)$$

so

$$\Delta T = V^2 G b / N W L \kappa \quad (5.4)$$

For our device geometry $N = 18$, $W = 0.3$ cm, $L = 25 \times 10^{-4}$ cm, $\kappa = 0.05$ W/cm $^{\circ}\text{C}$,¹ and $b = 0.3$ cm (glass supporting slide and substrate are considered as one unit), the change in temperature for KTN films is

$$\Delta T / P_d = 0.45^{\circ}\text{C/mW} \quad (5.5)$$

where

$$P_d \equiv V^2 G \quad (5.6)$$

To relate any temperature increase to changes in modulator efficiency, two approximations must be made. First, since the Q of our electrodes is 2.1, assume that the output intensity of the central beam can be approximated by the Raman-Nath expression $J_0^2(\Delta\phi)$. Second, since we lack experimental data for the behavior of the KTN dielectric constant in the thin films for temperatures greater than room temperature and because in our attempts to fit the low temperature dielectric data to a Curie-Weiss relation (sec 4.3.3.1) it became

apparent that the peak dielectric constant was suppressed, we shall use the bulk dielectric parameters, i. e., $T_0 = -50^\circ\text{C}$ for a 26 mole % film and $T_0 = 4^\circ\text{C}$ for a 34 mole % film, in our calculations.

The thermally limited bandwidth will be defined as the frequency at which the power dissipation in the device increases temperature so that modulating efficiency at the 100% modulating voltage is reduced to 50%. 50% modulating efficiency occurs when $J_0^2(\Delta\phi) = 0.5$, i. e., $\Delta\phi = 1.1$ radians.

For the KTN ($x = 0.26$) modulator, $\Delta\phi$ will be reduced to 1.1 radians when $\Delta T = 35^\circ\text{C}$. This change in temperature requires a power dissipation in the device of 70 mW. Using the power dissipation which occurs at 50 KHz for this device (from Table 5.1), and noting that power dissipation increases linearly with frequency, a thermally limited bandwidth of 100 KHz results. This is greater by a factor of 2 than the measured bandwidth.

For the KTN ($x = 0.34$) device, a temperature rise of 10°C will reduce modulator efficiency by 50%. A power dissipation of 22 mW is required to increase the temperature of the device by this amount. A thermally limited bandwidth of 600 KHz results, compared with a measured bandwidth of 800 KHz.

The thermally limited bandwidths calculated for these two KTN devices should be treated as giving only an estimate for the frequency limits of the devices. This is so because we do not have any dielectric data for the KTN thin films above room temperature. Furthermore, the heat flow problem in these films is very complicated. The use of Mogelalde's⁷⁷ boundary conditions for the KTN film is questionable, considering the low thermal conductivity of KTaO_3 . In all likelihood,

heat flow through both the substrate and through the top film surface is taking place in our KTN thin film devices.

The important point to be made in this section is that the operating frequency range of the KTN thin film modulators fabricated in this research was not limited by device capacitance but by the material problem of high dielectric loss in the thin films. Since dielectric loss or ac conductivity increase with frequency, power dissipation and temperature changes become significant as the frequency of the modulating voltage is increased.

5.3.2 dc Characteristics

Because the modulators were fabricated with an electrode pattern having $Q = 2.1$, neither the Raman-Nath nor Bragg diffraction theory discussed in Section 3.4 can be expected to give an accurate description of the dc characteristics of the modulators. An appropriate theory for this intermediate diffraction range can be developed by using the expression for index change in Eq. (3.18), the expression for E_{1x} in Eq. (2.47), and by following the Klein-Cook formalism described in Section 3.4 with the following assumptions. First, in the expression for the optical field of Eq. (3.37) retain only the five lowest order terms, i. e.,

$$\begin{aligned} \mathcal{E} \approx e^{ik_o \eta_o y} \{ & \varphi_o(y) + \varphi_1(y) e^{+ik^*y} + \varphi_{-1}(y) e^{-ik^*y} \\ & + \varphi_2(y) e^{+2ik^*y} + \varphi_{-2}(y) e^{-2ik^*y} \} \end{aligned} \quad (5.7)$$

where $k^* = 2\pi/2L$. Second, in the expression for the modulating x-directed electric field E_{1x} of Eq. (3.18), retain only the four lowest-

order terms and evaluate the field at the surface. Then

$$E_{1x} = B_0 \cos\left(\frac{\pi}{2L}\right)x + B_1 \cos\left(\frac{3\pi}{2L}\right)x + B_2 \cos\left(\frac{5\pi}{2L}\right)x + B_3 \cos\left(\frac{7\pi}{2L}\right)x \quad (5.8)$$

where

$$B_n = \frac{1}{2n+1} B_0 \quad n = 0, 1, 4, 5, \dots$$

$$B_n = -\frac{1}{2n+1} B_0 \quad n = 2, 3, 6, 7, \dots$$

$$B_0 = \frac{V}{L} \cdot \frac{2\sqrt{2}}{\pi}$$

The first assumption is justified provided that the optical field is incident parallel to the grating structure, i. e., $\theta = 0$, and that the change in optical index is sufficiently small to insure interaction only among the five terms in question. The second approximation is valid because of the decreasing amplitude of the Fourier components and the relatively constant dependence of the field distribution in the film as demonstrated in Fig. 2.11.

Now, the change in optical index experienced by a TE mode caused by an x-directed modulating field E_{1x} is

$$\Delta\eta = -\frac{1}{2}\eta_0^3 g_{11} \epsilon^2 E_{1x}^2 \equiv A E_{1x}^2 \quad (5.9)$$

Using Eq. (5.3), E_{1x}^2 can be written as

$$E_{1x}^2 = \frac{1}{4}(2B_0^2 + 2B_1^2 + 2B_2^2 + 2B_3^2 + \dots) \\ + \frac{1}{4}(e^{ik^*x} + e^{-ik^*x})(B_0^2 + 2B_0B_1 + 2B_1B_2 + 2B_2B_3 + \dots)$$

$$+ \frac{1}{4} (e^{2ik^*x} + e^{-2ik^*x}) (2B_0 B_1 + 2B_0 B_2 + 2B_1 B_2 + \dots) \quad (5.10)$$

which reduces to

$$\begin{aligned} E_{1x}^2 = & B_0^2 (0.59) + \frac{B_0^2}{2} (0.79) (e^{ik^*x} + e^{-ik^*x}) \\ & + \frac{B_0^2}{2} (0.03) (e^{2ik^*x} + e^{-2ik^*x}) \end{aligned} \quad (5.11)$$

As a result the change in index can be written as

$$\Delta\eta = a + \frac{b}{2} (e^{ik^*x} + e^{-ik^*x}) + \frac{c}{2} (e^{2ik^*x} + e^{-2ik^*x}) \quad (5.12)$$

where

$$a = AB_0^2 (0.59)$$

$$b = AB_0^2 (0.79)$$

$$c = AB_0^2 (0.03)$$

Since such an index change is small, η^2 has the form

$$\eta^2 = \eta_0^2 + 2\eta_0 a + b (e^{ik^*x} + e^{-ik^*x}) + c (e^{2ik^*x} + e^{-2ik^*x}) \quad (5.13)$$

Making the approximation that

$$\begin{aligned} \nabla^2 \mathcal{E} \approx & \frac{\partial^2 \mathcal{E}}{\partial x^2} - k_0^2 \eta_0^2 \mathcal{E} + 2ik_0 \eta_0 e^{ik_0 \eta_0 y} \left\{ \frac{d\varphi_0}{dy} + \frac{d\varphi_1}{dy} e^{ik^*x} \right. \\ & \left. + \frac{d\varphi_{-1}}{dy} e^{-ik^*x} + \frac{d\varphi_2}{dy} e^{2ik^*x} + \frac{d\varphi_{-2}}{dy} e^{-2ik^*x} \right\} \end{aligned} \quad (5.14)$$

and using the expressions for η^2 and ϵ in the wave equation yields the following set of equations

$$\varphi'_0 - ik_0 (a\varphi_0 + b\varphi_1 + c\varphi_2) = 0 \quad (5.15)$$

$$\varphi'_1 - ik_0 \left(\frac{b}{2}\varphi_0 + \left(a - D + \frac{c}{2}\right)\varphi_1 + \frac{b}{2}\varphi_2 \right) = 0 \quad (5.16)$$

$$\varphi'_2 - ik_0 \left(\frac{c}{2}\varphi_0 + \frac{b}{2}\varphi_1 + (a - 4D)\varphi_2 \right) = 0 \quad (5.17)$$

where φ_1 and φ_2 have been redefined as

$$\varphi_1 \equiv \frac{\varphi_1 + \varphi_{-1}}{2}$$

$$\varphi_2 \equiv \frac{\varphi_2 + \varphi_{-2}}{2}$$

and

$$D = \frac{1}{2} \cdot \frac{k^{*2}}{k_0^2 \eta_0}$$

This set of three differential equations can be solved using a variety of numerical techniques. It is useful, however, to obtain a closed form solution to obtain the functional dependence of voltage and dielectric constant on the optical field intensity. This can be accomplished by first noting that $c \ll a, b$. More important, since interest is centered in the voltage region where $|\varphi_0|^2$ reaches its first local minimum, one can assume that φ_1 will still dominate φ_2 , and hence eliminate Eq. (5.12) from the system of differential equations. Clearly this approximation is not valid for voltages at which $|\varphi_0|^2$ begins to increase in magnitude again.

Using these assumptions, and the initial conditions $\varphi_0(0) = 1$,

$\phi_1(0) = 0$, the intensity of the central beam at $y = W$ is

$$|\phi_0(W)|^2 = \cos^2 \frac{k_0 DW}{2} \cdot \left(1 + \frac{2b^2}{D^2}\right)^{\frac{1}{2}} + \frac{\sin^2 \frac{k_0 DW}{2} \left(1 + \frac{2b^2}{D^2}\right)^{\frac{1}{2}}}{\left(1 + \frac{2b^2}{D^2}\right)} \quad (5.18)$$

In this expression $k_0 DW/2$ depends only on the geometry of the electrode and the incident wavelength. For the modulators described in Section 5.2, $k_0 DW/2 = 0.532$. Similarly, D depends only on electrode dimensions and wavelength and has a value 3.56×10^{-5} . The voltage and dielectric constant dependence is contained in b . Recall that b has the functional dependence

$$\begin{aligned} b &= (0.79) (B_0)^2 \left(-\frac{1}{2} \eta_0^3 g \epsilon^2 \epsilon_0^2 V^2 / L^2\right) \\ &= 7 \times 10^{-14} \epsilon^2 V^2 \end{aligned} \quad (5.19)$$

Therefore

$$\frac{2b^2}{D^2} = 7.73 \times 10^{-18} \epsilon^4 V^4 \quad (5.20)$$

In Fig. 5.11, $|\phi_0(W)|^2$ is plotted as a function of modulating voltage for $\epsilon = 2200 \epsilon_0$ and compared with the actual dc modulating data from the KTN ($x = 0.26$) device. This value of dielectric constant, $2200 \epsilon_0$, was selected so that the theoretical and experimental curves would coincide at the intensity minimum. It is in good agreement with the measured dielectric constant of the film, $1920 \epsilon_0$.

Similarly, in Fig. 5.12, $|\phi_0(W)|^2$ is plotted as a function of modulating voltage for $\epsilon = 4000 \epsilon_0$ and compared with the experimental dc modulating data from the KTN ($x = 0.34$) device. Capacitance measure-

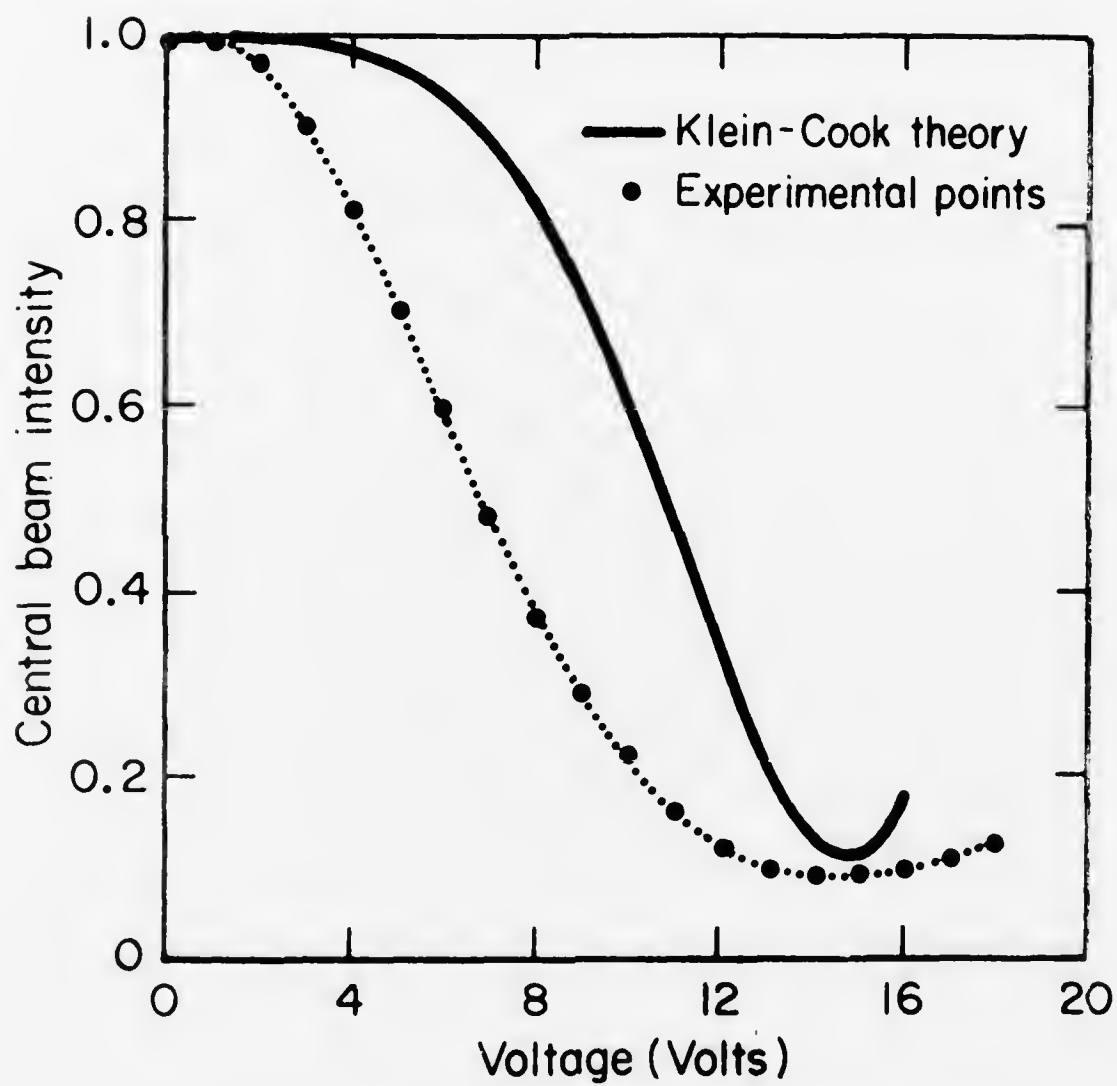


Fig. 5.11 Theoretical Klein-Cook fit to the experimental dc data of the KTN ($x = 0.26$) modulator.

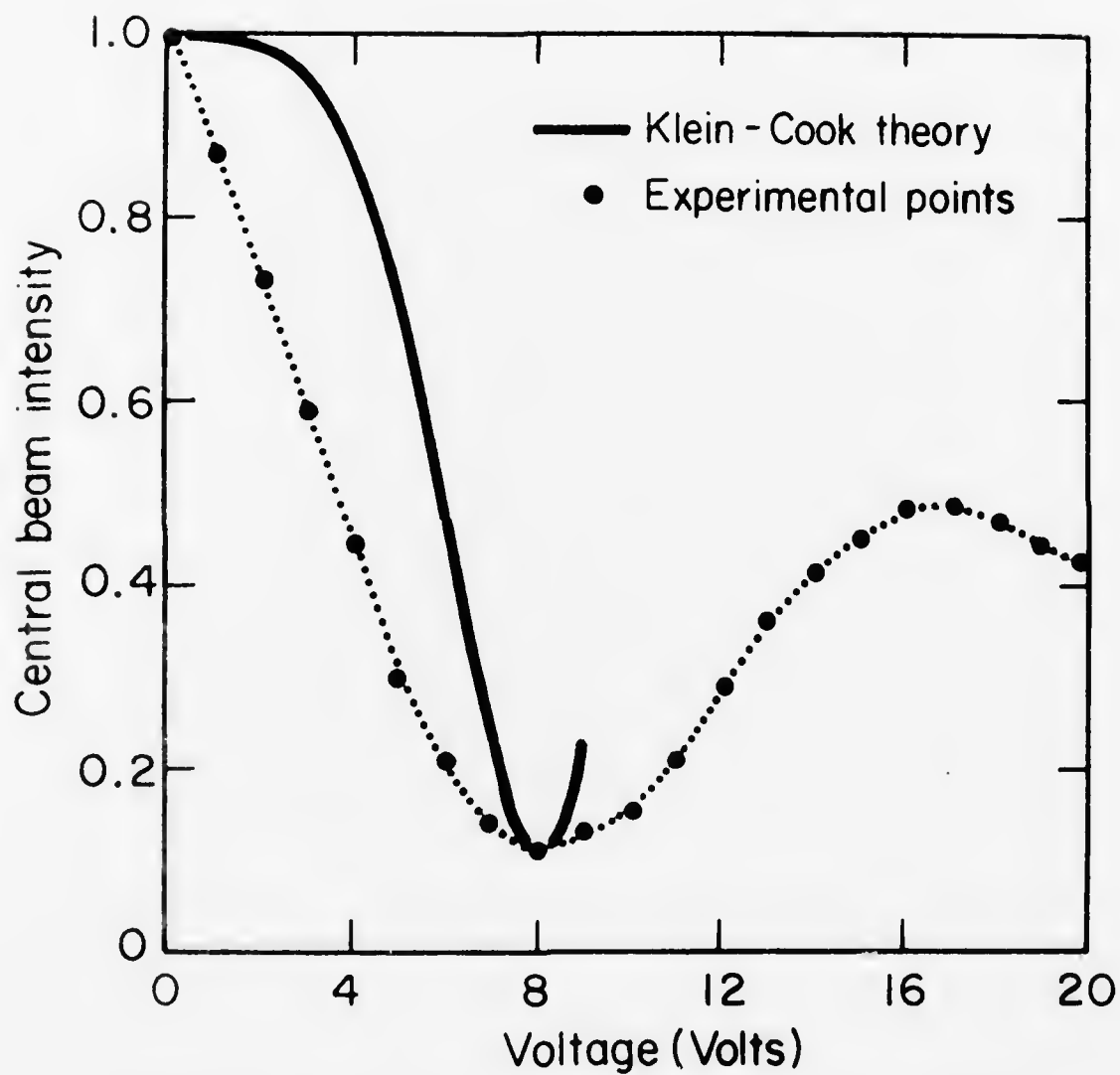


Fig. 5.12 Theoretical Klein-Cook fit to the experimental dc data of the KTN ($x = 0.34$) modulator.

ments predict a dielectric constant of $4600 \epsilon_0$ for this film, while a value of $4000 \epsilon_0$ is necessary for both curves to coincide at the intensity minimum. Agreement is within 15%.

In each figure, though the depth of modulation at the intensity minimum for both the experimental and theoretical curves are nearly identical, the experimental data for low modulating voltages indicates a much greater decrease in central beam intensity than that predicted by the theoretical curve. It is difficult to explain this discrepancy. Voltage induced scattering in the waveguide or mode conversion among the various modes might be possible mechanisms. Strain in the film could destroy the inversion symmetry of the KTN film and allow for linear electro-optic phenomena. Recall that the KTN films are under strain for at least two reasons. First, there is the lattice mismatch between the film and substrate. Second, considerable localized pressure is applied to the film surface in the areas where the coupling prisms are in contact with the film.

However, we do have evidence for a quadratic electro-optic phenomena occurring in these films. Klein and Cook⁶⁰ have noted that the normalized intensity expressions for diffraction modulators depend on $\Delta\phi$, the phase shift induced on the modulated beam passing through the device. Therefore, if the modulation characteristics of modulators having the same Q were plotted as a function of $\Delta\phi$, their curves would be identical. In Fig. 5.13, the dc characteristics of both of our modulators are plotted as a function of phase shift. The curves coincide very well. Since phase shift depends on the square of the modulating voltage for KTN (this is how we calculated phase shift from modulating voltage), the results of this normalization procedure give

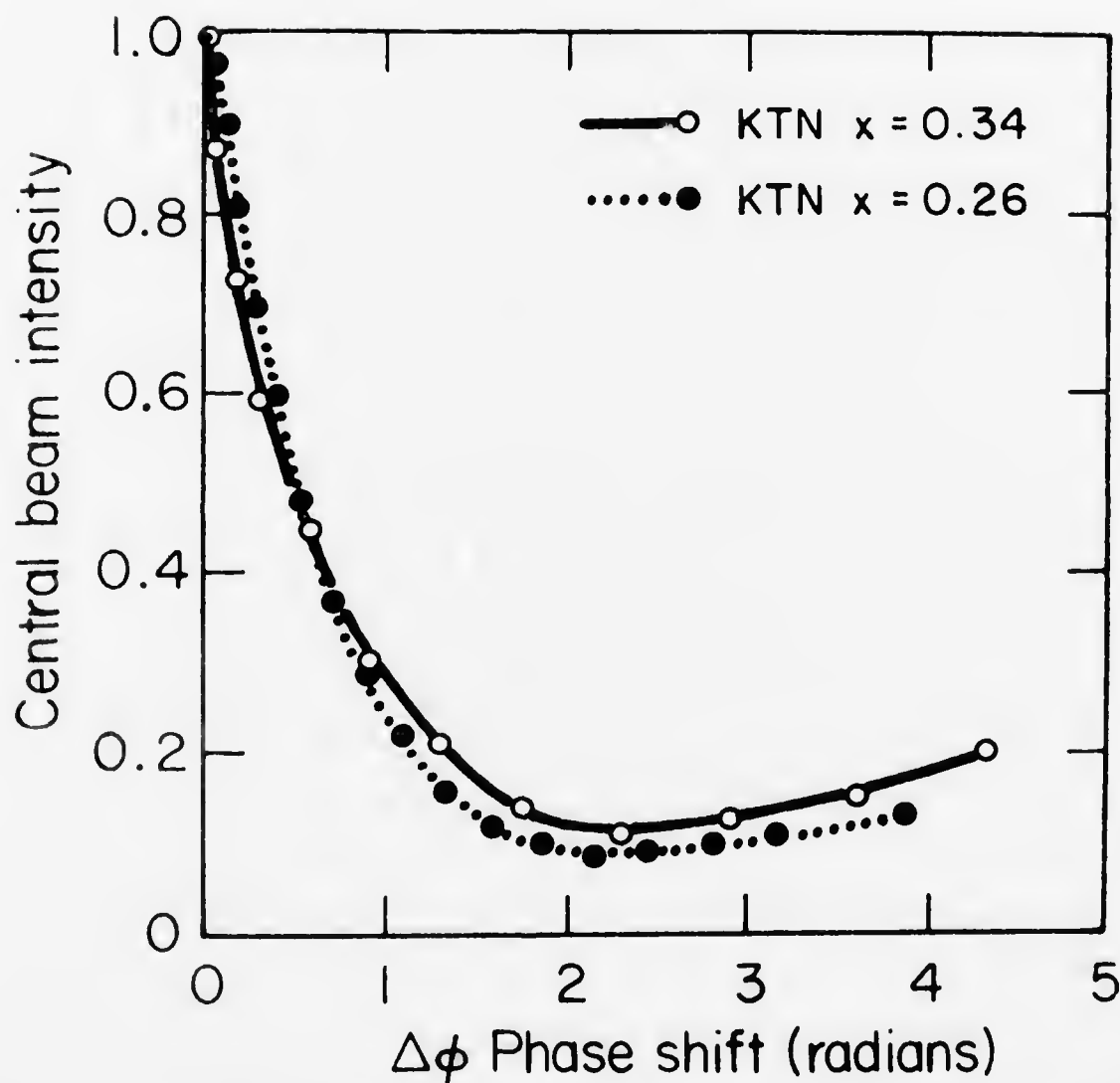


Fig. 5.13 dc modulation characteristics of the KTN ($x = 0.26$) and KTN ($x = 0.34$) modulators plotted as a function of phase shift induced in the devices.

strong support to the fact that the electro-optic effect in our KTN films is quadratic.

5.4 KTN Device Applications

Both of our KTN thin film modulators operated at low drive voltages but only over a limited frequency range. Even if thermal problems could have been eliminated in these devices by growing films with lower dielectric loss, the large dielectric constant of KTN would still impose a limit on bandwidth. As was illustrated in Fig. 3.5, KTN devices are best suited for low drive voltage applications which require neither high switching speeds nor a large frequency range of operation. It must be emphasized that KTN devices cannot be expected to operate at the information rates of 100-500 Mb/s currently envisioned for repeater stations using hybrid optical circuits.⁸⁴

Before one can seriously consider the use of KTN thin films for optical devices, two material problems must be solved. First, the growth process for KTN films must be improved so that films of appropriate thicknesses (about one micron) can be grown with smooth surfaces. This would eliminate the need for polishing our films and allow for single mode operation. From a device standpoint, thinner films, because device capacitance is proportional to film thickness, would result in higher operating bandwidths. Second, the dielectric loss of the thin films must be reduced so that power dissipation in the films will not degrade device performance.

If these two problems were solved, the operation of an improved thin film modulator using the same electrode dimensions as our fabricated devices can then be described. This device would be designed to have as low an operating voltage as possible since the nature of the KTN

electro-optic effect is to favor low drive voltage operation at the expense of bandwidth. Low dielectric loss films would be used to minimize the thermal problems which were encountered in our fabricated devices, i. e., to insure that device bandwidth was determined by circuit considerations and not power dissipation in the films. Most important, thin films limited in thickness only by the requirement of being able to support at least one guided mode would be used. Besides extending device bandwidth because of a reduced device capacitance, the use of thin films would also decrease the influence of thermal effects since power dissipation in the films depends on the conductance of the device and conductance, as well as capacitance, scales with film thickness.

Based on the above performance requirements, the improved device would use a $\text{KTa}_{0.65}\text{Nb}_{0.35}\text{O}_3$ film deposited on our usual substrate material KTaO_3 . This KTN composition has the highest reported room temperature dielectric constant, $10,000 \epsilon_0^1$ ($T_0 = 10^\circ\text{C}$). Single mode operation at 633 nm requires a film thickness between 0.3 and 0.95 microns; a thickness of 0.5 microns giving a tolerance of 0.2 microns will be used. From Eq. (2.55) device capacitance is 145 pf. Circuit limited bandwidth for a 50Ω shunt resistor is 44 MHz. From Fig. (3.25), 90% amplitude modulation will occur for a drive voltage of 2.9 volts. The thermally limited bandwidth will be greater than the circuit limited bandwidth if the temperature rise in the device is kept below 6°C at 44 MHz. (For this temperature rise, corresponding to 12 mW of power dissipation in the film, the depth of modulation will be reduced to 50% for a drive voltage of 2.9 volts.) Device conductance must therefore be less than 1.4×10^{-3} mhos at 44 MHz. Using Eq. (2.56),

$\tan \delta$ must be no greater than 0.05.

At first sight this seems to be a surprisingly large value for $\tan \delta$ compared to the best bulk values of 0.001.¹ It can be tolerated for two reasons. First, the film is a factor of 10 thinner than the films of our fabricated devices and device conductance is determined by film thickness. Second, the drive voltage of this optimum device is at the very least a factor of three less than the drive voltages of our fabricated devices. Since the dissipated power in the film goes as

$$P \propto V^2 G,$$

all other parameters being equal, power dissipation in the optimum device at any frequency would be about a factor 100 less than in our fabricated devices. This value should really be reduced to about 40, since the dielectric constant of the optimum device would be about 2.5 times greater than the films used in our device work. (Note $\sigma_{ac} \propto \epsilon$, assuming $\tan \delta$ constant.) Consequently, where for the devices fabricated in our research, $\tan \delta$ of about 0.05 would allow modulation operation up to 1 MHz, bandwidths up to about 40 MHz are now possible with the same value of $\tan \delta$.

To summarize, a modulator much improved over those we fabricated could be built using precisely the same electrode geometry. The modulator would use a $\text{KTa}_{0.65}\text{Nb}_{0.35}\text{O}_3$ film, 0.5 microns thick, deposited on a KTaO_3 substrate. The film would have a room temperature dielectric constant of 10,000 ϵ_0 and $\tan \delta$ should be no greater than 0.05. A voltage of 2.9 volts would give 90% modulation of the central beam and the device bandwidth limited only by device capacitance would be 44 MHz.

The above discussion must not be interpreted as implying that KTN thin film devices cannot be operated with drive voltages less than 3 volts or at frequencies greater than 44 MHz. It should be recognized that by changing our electrode geometry or by going to a phase modulator design, either higher bandwidth or lower drive voltage operation could be achieved.

CHAPTER 6

CONCLUSIONS

6.1 Summary

The goal of this research was to demonstrate the feasibility of potassium tantalate niobate for thin film optics. The program included the growth of single crystal KTN thin films on KTaO_3 substrates and the evaluation of their dielectric and electro-optic properties. We were able to successfully guide light in these films and to fabricate several KTN thin film modulators and evaluate their performance.

The KTN thin films were grown by an LPE dipping process. Thin films were crystallized from a melt, which had been stabilized at the growth temperature for a soak period of 12 hours, onto a substrate by lowering the furnace temperature at rates of $\sim 0.5^\circ\text{C}/\text{hour}$ for 1-2 hours. The composition of the KTN films was controlled by the growth temperature and by melt composition.

Within our experimental accuracy, the KTN films were found to be uniform in composition and the film-substrate interfaces were abrupt. The optical loss for guided modes propagating in these films, initially greater than 20 db/cm, was eventually reduced to values of 8-10 db/cm. The dielectric constants of the films ranged from 2000 ϵ_o to 4600 ϵ_o , depending on composition.

The thin film diffraction modulators fabricated in this research were operated at frequencies up to 500 KHz. Pulse response times were on the order of 0.2 μs , and drive voltages for 90% intensity modulation were as low as 8 volts.

Several material problems were encountered in this work. We

technique to grow films with smooth surfaces. We were able to grow films with thicknesses less than 15-20 nm. The substrates therefore had to be carefully polished before any further work could be attempted. The thin films were characterized unusually high dielectric loss tangents on the order of 10^{-1} at 100 KHz, the bulk KTN values for $\tan \delta \approx 0.001$.¹ As a result, the conductivity in these films at 100 KHz was as great as $10^{-1} (\Omega \text{ cm})^{-1}$, an order of magnitude greater than the reported dc conductivity of bulk KTN material.^{6c} We found that thin film dielectric parameters differed significantly from reported values for bulk crystal of the same composition. In particular, the paraelectric-ferroelectric phase transition temperatures were higher for the thin film material than for comparable bulk material. The peak dielectric constants of the thin films measured at the transition temperature were lower than the values reported for bulk KTN.¹

Two device problems became apparent when the thin film modulators were tested. The bandwidth of the modulators was limited not by device capacitance but rather by power dissipation in the device caused by the large ac conductivity of the films. Power dissipation in the device implies an increase in the temperature of the film, a decrease in the electro-optically induced index change, and hence a decrease in the depth of modulation for a given drive voltage. Since the conductivity increases with frequency, temperature increases in the film become significant as the frequency of operation is increased. We also observed that the experimental dc modulation characteristics of our devices differed significantly, in the low voltage region, from the theoretical behavior which would be expected for devices using quadratic

electro-optic material. It was shown that if the material and device problems described above could be overcome, it would be possible to design a KTN diffraction modulator, using our electrode geometry, that would operate with a drive voltage of 2.9 volts over a frequency range of 44 MHz.

6.2 Future Work

The experimental results presented in this thesis, in particular the performance of our two KTN modulators, have demonstrated that KTN thin films can be used for the fabrication of efficient electro-optical devices in applications where a low drive voltage rather than a large bandwidth is desired. However, before practical KTN devices can be fabricated, additional work on several materials problems is necessary. Specifically, the controlled growth of KTN films must be achieved. Film dielectric loss must be reduced and the dielectric properties of these films must be understood.

An attempt must be made to quantitatively characterize the influence of soak periods, temperature lowering, and substrate rotation on the growth rates of the KTN thin films. This would be the first step in trying to reduce film thicknesses and to improve the film surface. The growth of thinner films with smooth surfaces may require the use of a diluted melt, i. e., the addition of a flux, to slow the growth process. From a device standpoint, the importance of thin KTN films cannot be overstated. Besides allowing for single mode operation, thin films reduce the capacitance and conductance of the device, thereby extending both the thermal and circuit bandwidths of the device.

The problem of large dielectric loss in our films must be studied. It would be interesting to see what effect SnO_2 in the melt has on reducing

not only the dc conductivity of the films but also the ac conductivity of the films. Our experimental evidence indicates that using SnO_2 in the melt significantly reduces the ac conductivity of the crystallized films. The effects of impurities in the starting chemical powders used in the melt on the ac and dc conductivities of the films should also be examined.

The issue of the dielectric properties of the KTN films and their marked difference from the properties of bulk KTN material needs explanation. The problem of strain on the film caused by lattice mismatch between film and substrate should be considered as a possible explanation for the difference between the thin film and bulk parameters.

Finally, we emphasize that the major materials contribution of this research is the growth of single crystal KTN thin films. In this thesis we have considered only the possible electro-optic applications of these films. We suggest that there are several non-electrooptic applications which are possible with these films.

KTN is a ferroelectric material. When it is in its paraelectric state, dielectric constant and temperature vary in a well defined manner (Curie- Weiss relation). Using an interdigital electrode on a KTN thin film, a large capacitance can be generated in a small area. Applications in temperature sensing by monitoring changes in capacitance could be possible.

If KTN films which were ferroelectric at room temperature could be grown, it would be possible to use the pyroelectric effect in KTN for temperature or heat sensing applications. Though lattice mismatch problems between film and substrate might prevent the growth of good quality ferroelectric films, the fact that we were able to cycle our paraelectric films through the phase transition and back to room temperature

without any apparent damage indicates that room temperature KTN ferroelectric films could be grown on KTaO_3 substrates.

KTN has always been a versatile material because its dielectric, electrooptic, and optical properties can be changed by varying the Nb content of the KTN composition. The fact that KTN can be grown in thin film form adds to this versatility because now planar and integrated circuit techniques can be used to fabricate more efficient and compact dielectric and optical devices.

References

1. F. S. Chen, J. E. Geusic, S. K. Kurtz, J. G. Skinner, S. H. Wemple, "Light modulation and beam deflection with potassium tantalate niobate crystals", *Journal of Applied Physics*, 37, No. 1, 388 (1966).
2. S. K. Kurtz, "Design of an electrooptic polarization switch for a high capacity, high speed digital light deflection system", *Bell System Technical Journal*, 8, 1209 (1966).
3. J. T. Milek, M. Neuberger, *Handbook of Electronic Materials - Linear Electrooptic Modular Materials*, Vol. 8, IFI/Plenum, New York, p. 223 (1972).
4. L. T. Todd, "Dielectric and optical study of $\text{KTa}_{1-x}\text{Nb}_x\text{O}_3$ mixed crystals", S.M. Thesis, M.I.T., unpublished (1970).
5. S. Triebwasser, "Study of ferroelectric transitions of solid solution single crystals of KNbO_3 - KTaO_3 ", *Physical Review* 114, No. 1, 63 (1959).
6. A. Reisman, E. Banks, "Reactions of group V-B pentoxides; thermal, density, and x-ray studies of the system KNbO_3 - NaNbO_3 and KTaO_3 - KNbO_3 ", *Journal of the American Chemical Society*, 80, 1887 (1958).
7. A. Reisman, F. Holtzberg, M. Berkenblit, M. Berry, "Reactions of the group V-B pentoxides and carbonates; thermal and x-ray phase diagrams of the system K_2O or K_2CO_3 with Ta_2O_5 ", *Journal of the American Chemical Society*, 78, 4514 (1956).
8. P. W. Whipps, "Growth of high quality crystals of KTN", *Journal of Crystal Growth*, 12, 120 (1972).
9. T. G. Davis, "Ferroelectric properties of sodium tantalate - potassium tantalate mixed crystals", S.M. Thesis, M.I.T., unpublished (1965).
10. S. H. Wemple, M. DiDomenico, Jr., "Electrooptic and nonlinear optical properties of crystals" in *Applied Solid State Science*, Vol. 2, New York, p. 264 (1972).
11. J. E. Geusic, S. K. Kurtz, L. G. Van Uitert, S. H. Wemple, "Electrooptic properties of some ABO_3 perovskites in the paraelectric phase", *Applied Physics Letters*, 4, No. 8, 141 (1964).
12. P. H. Smakula, P. C. Claspy, "Electrooptic effects in LiNbO_3 and KTN", *Trans. of the Metallurgical Society of the A.I.M.E.*, 239, 422 (1967).

13. A. J. Fox, P. W. Whipps, "Longitudinal quadratic electrooptic effect in KTN", *Electronic Letters* 7, 134 (1971).
14. S. E. Miller, "Integrated optics: an introduction", *Bell System Technical Journal* 48, 2059 (1969).
15. P. K. Tien, "Light waves in thin films and integrated optics", *Applied Optics* 10, 2395 (1971).
16. W. S. Chang, M. W. Muller, F. J. Rosenbaum, "Integrated optics" in *Laser Applications*, Vol. 2, Academic Press, New York, p. 227 (1974).
17. H. Kogelnik, "An introduction to integrated optics", *IEEE Transactions on Microwave Theory and Techniques*, MTT-23, No. 1, 2 (1975).
18. I. P. Kaminow, "Optical waveguide modulators", *IEEE Transactions on Microwave Theory and Techniques*, MTT-23, No. 1, 57 (1975).
19. W. S. C. Chang, "Integrated optics at 10.6 μm wavelength", *IEEE Transactions on Microwave Theory and Techniques*, MTT-23, No. 1, 31 (1975).
20. V. Evtuhov and A. Yariv, "GaAs and GaAlAs devices for integrated optics", *IEEE Transactions on Microwave Theory and Techniques*, MTT-23, No. 1, 44 (1975).
21. P. K. Tien, R. J. Martin, S. L. Blank, S. H. Wemple, L. J. Varnerin, "Optical waveguides in single crystal garnet films", *Applied Physics Letters* 21, No. 5, 207 (1972).
22. J. M. Hammer, W. Phillips, "Low-loss single mode optical waveguides and efficient high speed modulation of $\text{LiNb}_x\text{Ta}_{1-x}\text{O}_3$ on LiTaO_3 ", *Applied Physics Letters* 24, No. 11, 545 (1974).
23. R. Ulrich and H. Weber, "Solution deposited thin films as passive and active light guides", *Applied Optics* 11, No. 2, 428 (1972).
24. R. Ulrich, H. Weber, E. Chandross, W. Tomlinson, E. Franke, "Embossed optical waveguides", *Applied Physics Letters* 20, No. 6, 213 (1972).
25. D. Hensler, J. Cuthbert, R. J. Martin, P. K. Tien, "Optical propagation in sheet and pattern generated films of Ta_2O_5 ", *Applied Optics* 10, No. 5, 1037 (1971).
26. R. Shubert, J. Harris, "Optical guided wave focussing and diffraction", *Journal of the Optical Society of America*, 61, 154 (1971).

27. D. Russo, C. Kumar, "Sputtered ferroelectric thin-film electro-optic modulator", *Applied Physics Letters* 23, 229 (1973).
28. Y. Lee, S. Wang, "Tantalum oxide light guide on lithium tantalate", *Applied Physics Letters* 25, 164 (1974).
29. J. C. Webster, F. Zernike, "Push-pull thin film modulator", *Applied Physics Letters* 26, 465 (1975).
30. H. F. Taylor, W. Martin, D. Hall, V. Smiley, "Fabrication of single crystal semiconductor optical waveguides by solid state diffusion", *Applied Physics Letters* 21, 95 (1972).
31. I. P. Kaminow, J. R. Carruthers, "Optical waveguiding layers in LiNbO_3 and LiTaO_3 ", *Applied Physics Letters* 22, 326 (1973).
32. R. D. Standley, V. Ramaswamy, "Nb-diffused optical waveguides: planar and embedded strip guides", *Applied Physics Letters* 25, 711 (1974).
33. R. Schmidt, I. P. Kaminow, "Metal diffused optical waveguides in LiNbO_3 ", *Applied Physics Letters* 25, 458 (1974).
34. J. Noda, T. Saku, N. Uchida, "Fabrication of optical waveguiding layer by Cu diffusion", *Applied Physics Letters* 25, 308 (1974).
35. J. M. Hammer, D. J. Channin, M. T. Duffy, "Low-loss epitaxial ZnO optical waveguides", *Applied Physics Letters* 21, 358 (1972).
36. P. K. Tien, R. Martin, R. Wolfe, R. LeCraw, S. L. Blank, "Switching and modulation in magneto-optic waveguide of garnet films", *Applied Physics Letters* 21, 394 (1972).
37. E. Garmire, "Optical waveguides in single layers of $\text{Ga}_{1-x}\text{Al}_x\text{As}$ grown on GaAs substrates", *Applied Physics Letters* 23, 403 (1973).
38. V. Ramaswamy, "Epitaxial electro-optical mixed crystal $(\text{NH}_4)_x\text{K}_{1-x}\text{H}_2\text{PO}_4$ Film Waveguide", *Applied Physics Letters* 21, 183 (1972).
39. D. J. Channin, J. M. Hammer, M. T. Duffy, "Scattering in ZnO -sapphire waveguides", *Applied Optics* 14, No. 4 (1975).
40. R. Ulrich, "Optimum excitation of optical surface waves", *Journal of the Optical Society of America* 61, No. 11, 1467 (1971).
41. H. Kogelnik, T. P. Sosnowski, "Holographic thin film couplers", *Bell System Technical Journal* 49, 1602 (1970).

42. H. Klug, L. Alexander, X-Ray Diffraction Procedures, New York, John Wiley and Sons, Inc. (1959), p. 677.
43. R. Ulrich and R. Torge, "Measurement of thin film parameters with a prism coupler", Applied Optics 12, No. 12, 2901 (1973).
44. M. A. R. P. deBarros, M. Wilson, "High speed electro-optic diffraction modulation for baseband operation", Proceedings of IEE 119, No. 7, 807 (1972).
45. D. J. Channin, "Voltage induced optical waveguide", Applied Physics Letters 19, No. 5, 128 (1972).
46. I. P. Kaminow, J. R. Carruthers, "Thin film lithium niobate electrooptic light modulator", Applied Physics Letters 22, No. 10, 540 (1973).
47. P. K. Tien, S. Riva-Sanseverino, A. A. Ballman, "Light beam scanning and deflection in epitaxial LiNbO_3 electrooptic waveguides", Applied Physics Letters 25, No. 10, 563 (1974).
48. J. Polky, J. Harris, "Interdigital electrooptic thin film modulator", Applied Physics Letters 21, No. 7, 307 (1972).
49. J. M. Hammer, D. J. Channin, M. T. Duffy, "Fast electrooptic waveguide deflector modulator", Applied Physics Letters 23, No. 4, 176 (1973).
50. J. M. Hammer, D. J. Channin, M. T. Duffy, C. C. Neil, "Highspeed electrooptic waveguide grating modulator using epitaxial ZnO ", IEEE Journal of Quantum Electronics QE-11, No. 4, 138 (1975).
51. J. Noda, N. Uchida, T. Saku, "Electrooptic diffraction modulator using outdiffused waveguiding layer in LiNbO_3 ", Applied Physics Letters 25, No. 3, 131 (1974).
52. I. P. Kaminow, V. Ramaswamy, R. V. Schmidt, E. H. Turner, "Lithium niobate ridge waveguide modulator", Applied Physics Letters 24, No. 12, 622 (1974).
53. J. Noda, N. Uchida, S. Saito, "Electro-optical amplitude modulation using three dimensional LiNbO_3 waveguide fabricated by TiO_2 diffusion", Applied Physics Letters 27, No. 1, 19 (1975).
54. J. Noda, N. Uchida, M. Minakata, "Electrooptic intensity modulation in LiTaO_3 ridge waveguide", Applied Physics Letters 26, No. 6, 298 (1975).
55. S. Vehara, K. Takamoto, S. Matsuo, "Optical intensity modulator with three-dimensional waveguide", Applied Physics Letters 26, No. 6, 296 (1975).

56. W. Martin, "A new waveguide switch/modulator for integrated optics", *Applied Physics Letters* 26, No. 10, 562 (1975).
57. M. Born, E. Wolf, *Principles of Optics*, Pergamon Press, New York (1970), Chapter 14.
58. F. S. Chen, "Modulators for optical communications", *Proceedings of the IEEE* 58, No. 10, 1440 (1970).
59. I. P. Kaminow, E. Turner, "Electrooptic light modulators", *Proceedings of the IEEE* 54, 1374 (1966).
60. W. R. Klein, B. D. Cook, W. Mayer, "Light diffraction by ultrasonic gratings", *Acustica* 15, No. 2, 67 (1965).
61. W. R. Klein, B. D. Cook, "Unified approach to ultrasonic light diffraction", *IEEE Transactions on Sonics and Ultrasonics* SU-14, No. 3, 123 (1967).
62. E. A. Geiss, J. D. Kuptsis, E. A. White, "Liquid phase epitaxy growth of magnetic garnet films by isothermal dipping in a horizontal plane with axial rotation", *Journal of Crystal Growth* 16, 36 (1972).
63. H. L. Levinstein, J. W. Nielsen, L. J. Varnerin, "Garnets for bubble devices", *Bell Laboratories Record* 51, No. 7, 218 (1973).
64. S. Miyazawa, S. Fushimi, S. Kondo, "Optical waveguide of LiNbO_3 thin film grown by liquid phase epitaxy", *Applied Physics Letters* 26, No. 1, 8 (1975).
65. A. Ballman, H. Brown, P. K. Tien, R. Martin, "Growth of single crystalline waveguiding thin films of piezoelectric sillenites", *Topical Meeting on Integrated Optics*, January 1974.
66. W. A. Bonner, E. F. Dearborn, L. G. Van Uitert, "Growth of potassium tantalate niobate single crystals for optical applications", *Ceramic Bulletin* 44, No. 1, 9 (1965).
67. W. R. Wilcox, L. D. Fullmer, "Growth of KTaO_3 - KNbO_3 mixed crystals", *Journal of the American Ceramic Society* 49, No. 8, 415 (1966).
68. A. L. Gentile, F. H. Andres, "A constant temperature method for the growth of KTN single crystals", *Materials Research Bulletin* 2, 853 (1967).
69. P. W. Whipps, "Growth of high quality crystals of KTN", *Journal of Crystal Growth* 12, 120 (1972).
70. A. Reisman, S. Triebwasser, F. Holtzberg, "Phase diagram of

the system $\text{KTaO}_3\text{-KNbO}_3$ by the methods of differential thermal and resistance analysis", *Journal of the American Chemical Society* 77, 4228 (1955).

71. S. A. Levy, R. Gashler, "On the origin of lamellae in high resistivity KTN", *Materials Research Bulletin* 3, 417 (1968).
72. R. L. Barnes, "A survey of precision lattice parameter measurements as a tool for the characterization of single crystal materials", *Materials Research Bulletin* 2, 273 (1967).
73. S. H. Wemple, "Polarization effects on magnetic resonances in ferroelectric potassium tantalate", Ph.D. Thesis, M.I.T., unpublished (1963).
74. J. T. Carlo, "Magnetoelastic devices utilizing a spatially varying magnetization", Ph.D. Thesis, M.I.T., unpublished (1973).
75. C. G. Fonstad, A. Linz, R. Rediker, "Vapor phase growth of stannic oxide single crystals", *Journal of the Electrochemical Society* 116, 1269 (1969).
76. R. Gentilman, "Study of chemical vapor deposition of magnetic garnets", Ph.D. Thesis, M.I.T., unpublished (1973).
77. E. Mosekilde, P. Lebwohl, D. Carlson, "Transient heat flow from an epitaxial layer into the substrate", *Proceedings of the IEEE* 59, 1030 (1971).
78. C. Hu, "Electrooptic modulation in grain oriented ZnO films", *IEEE/OSA Conference on Laser Engineering and Applications* (1975).
79. F. K. Reinhart, B. I. Miller, "Efficient $\text{GaAs-Al}_x\text{Ga}_{1-x}\text{As}$ double-heterostructure light modulators", *Applied Physics Letters* 20, No. 1, 36 (1972).
80. A. Y. Cho, F. K. Reinhart, "Growth of three-dimensional waveguides for integrated optics by molecular-beam-epitaxy method", *Applied Physics Letters* 21, No. 8, 355 (1972).
81. V. Ramaswamy, R. D. Standley, "Growth strains and losses in Nb-diffused LiTaO_3 optical film waveguides", *Applied Physics Letters* 26, No. 1, 10 (1975).
82. K. Ogawa, W. S. C. Chang, "Analysis of holographic thin film grating coupler", *Applied Optics* 12, No. 9, 2167 (1973).
83. G. Shirane, R. Newnham, R. Pepinsky, "Dielectric properties and phase transitions of NaNbO_3 and $(\text{Na,K})\text{NbO}_3$ ", *Physical*

Review 96, No. 3, 581 (1954).

44. S. D. Personick, "Receiver design for digital fiber optic communications systems", Bell System Technical Journal 52, No. 6, 843 (1973).
45. V. Belruss, J. Kalnajs, A. Linz, "Top-seeded solution growth of oxide crystals from nonstoichiometric melts", Materials Research Bulletin 6, 899 (1971).

Massachusetts Institute of Technology, Cambridge, Massachusetts
Department of Electrical Engineering and Computer Science and
Center for Materials Science and Engineering
Crystal Physics Laboratory

ENERGY TRANSFER IN SENSITIZED RARE EARTH LASERS*

by

Donald Earl Castleberry

TECHNICAL REPORT NO. 19

September, 1975

* The research covered by this Report was sponsored by the Advanced Research Projects Agency under Contract No. DAHC.15-73-C-0316, and by the Advanced Research Projects Agency and the Office of Naval Research under Contract No. N00014-75-C-1084. The author was supported in part by a National Science Foundation Graduate Fellowship. The views and conclusions contained in this document are those of the authors and should not be interpreted as necessarily representing the official policies, either expressed or implied, of the Advanced Research Projects Agency or the U. S. Government.

ENERGY TRANSFER IN SENSITIZED RARE EARTH LASERS

by

Donald Earl Castleberry

(This report is based on the thesis which was submitted in partial fulfillment of the requirements for the degree of Doctor of Philosophy at the Massachusetts Institute of Technology.)

ABSTRACT

Energy transfer in sensitized rare earth laser materials has been studied. It has been shown that upconversion can seriously reduce the efficiency of energy transfer from the pump levels of the sensitizer ions to the upper laser level in materials such as Er^{3+} or Yb^{3+} sensitized Ho^{3+} laser materials and Yb^{3+} sensitized Tm^{3+} laser materials. A model of energy transfer in the Yb^{3+} - Tm^{3+} system was analyzed which showed the importance of upconversion and how to minimize its effects. The effects of upconversion were experimentally demonstrated in the Er^{3+} - Ho^{3+} system, including the reduction in the efficiency of the $\alpha\beta$ -YLF laser by 50%.

Laser operation of the LiYbF_4 :5% Tm, 0.25% Ho material has been demonstrated. Room temperature LED pumped cw operation of this material appears feasible.

The $\text{Ho } ^5\text{I}_7 \leftrightarrow ^3\text{H}_4$ energy transfer was studied. An approximate distribution function which describes the thermal equilibrium between Ho ions in the $^5\text{I}_7$ level and Tm ions in the $^3\text{H}_4$ level was derived.

Sensitized laser materials can be used in efficient miniature lasers. Using an internal reflection miniature resonator, single mode cw laser operation of $\alpha\beta$ -YLF was achieved in a 0.2 mm^3 volume. This resonator can be easily coupled to thin film optical waveguides.

ACKNOWLEDGEMENTS

The author wishes to express his sincere appreciation to Dr. Arthur Linz for his continuous support and thoughtful encouragement while supervising this research. The author is also most grateful to Dr. Hans P. Jenssen for his valuable suggestions and advice; without the many helpful discussions, this work could not have been done.

The author wishes to thank Professor D. J. Epstein and Professor J. Kong for their active interest in this research.

The author would like to thank all members of the Crystal Physics group for their friendship and assistance throughout this work. Special thanks are due to Dr. David Gabbe for growing the LiYF_4 crystals.

The author is grateful to Ms. Delphine Radcliffe for her competent typing of the manuscript and to Mr. John Mara for his skillful drawing of the illustrations.

TABLE OF CONTENTS

	Page
ABSTRACT	2
ACKNOWLEDGEMENTS	3
TABLE OF CONTENTS	4
LIST OF FIGURES	6
LIST OF TABLES	9
 CHAPTER 1	
INTRODUCTION	10
1.1 Forward	10
1.2 Energy Transfer in Rare Earth Crystals	11
1.3 Sensitized Lasers	20
 CHAPTER 2	
EXPERIMENTAL TECHNIQUES	23
2.1 LiYF ₄ Crystal Growth	23
2.2 Spectroscopic Measurements	23
2.3 Laser Operation of Materials	27
 CHAPTER 3	
ENERGY TRANSFER IN SENSITIZED HOLMIUM LASER MATERIALS	32
3.1 Upconversion	34
3.1.1 Experimental Results on Er ³⁺ Sensitized Materials	44
3.1.2 Experimental Results on Yb ³⁺ Sensitized Materials	49
3.2 Ho ⁵ I ₇ ↔ Tm ³ H ₄ Energy Transfer	54
 CHAPTER 4	
USE OF SENSITIZED MATERIALS FOR MINIATURE LASERS	67
4.1 Sensitized Laser Materials and Pump Sources	68

TABLE OF CONTENTS (continued)

	Page
4.2 Internal Reflection Resonator . . .	72
4.2.1 Modes of Internal Reflection Resonator	74
4.2.2 Output Coupling	77
4.2.3 Diffraction Loss	81
4.2.4 Waveguide Coupling	82
4.2.4.1 Direct Coupling	83
4.2.4.2 Grating Coupler	85
4.2.5 Experimental Results	86
CHAPTER 5 RESULTS AND CONCLUSIONS	91
APPENDIX 1 MODES IN A TWO-DIMENSIONAL DIELECTRIC RESONATOR	96
APPENDIX 2 MEASUREMENT OF THE REFRACTIVE INDICES OF LiYF_4	105
APPENDIX 3 SOLUTION OF RATE EQUATIONS	108
REFERENCES	109

LIST OF FIGURES

Figure No.		Page
1.1	Energy Levels of Rare Earth Ions	13
1.2	Relaxation of Isolated Ions: (a) Radiative Decay; (b) Multiphonon Decay	16
1.3	Energy Transfer Processes	18
2.1	Fluorescence Spectra Measurement Setup	25
2.2	Pulsed Fluorescence Measurement Setup	28
2.3	Variable Temperature Laser Cavity	29
3.1	Energy Transfer in $\alpha\beta$ -YLF	33
3.2	Energy Levels of Yb^{3+} , Tm^{3+} and Ho^{3+} in LiYF_4	35
3.3	Decay and Energy Transfer Processes for the Yb^{3+} - Tm^{3+} System	39
3.4	Energy Level Populations as a Function of Pump Rate	41
3.5	Dependence of Transfer Efficiency on Pump Rate	43
3.6	Energy Levels of Er^{3+} , Tm^{3+} and Ho^{3+} in LiYF_4	45
3.7	$\text{Ho } ^5\text{I}_7$ Fluorescence Intensity vs Pump Power Density	47
3.8	$\text{Ho } ^5\text{I}_6$ Fluorescence Intensity vs Pump Power Density	48
3.9	Experimental Setup for LiYbF_4 :5% Tm, 0.25% Ho Laser	51
3.10	Pump Power Density vs Distance at Threshold for a Tungsten Filament Pump Lamp	53
3.11	Room Temperature $\text{Ho } ^5\text{I}_7$ Absorption Spectrum and $\text{Tm } ^3\text{H}_4$ Fluorescence Spectrum	55
3.12	Crystal Field Split Energy Level of $\text{Tm } ^3\text{H}_4$ and $^3\text{H}_6$ and $\text{Ho } ^5\text{I}_7$ and $^5\text{I}_8$ Multiplets	57

LIST OF FIGURES (continued)

Figure No.		Page
3.13	Occupation Factor of Upper and Lower Laser Levels vs Temperature	61
3.14	Threshold Population in Ho 5I_7 - Tm 3H_4 Levels vs Temperature	63
3.15	Ho 5I_7 - Tm 3H_4 Fluorescence Spectrum vs Temperature	64
3.16	2.06 μm Fluorescence Branching Ratio and Occupation Factor of Upper Laser Level vs Temperature	66
4.1	Room Temperature Absorption Spectrum of LiYbF ₄ and Typical LED Emission Spectrum	69
4.2	Effective Absorption Coefficient vs Distance for LiYbF ₄ when Pumped by a LED at 300°K . .	70
4.3	Effective Absorption Coefficient vs Shift of Peak Diode Emission	71
4.4	Schematic of Internal Reflection Resonator . .	73
4.5	Region of k-space Available for Total Internal Reflection Modes	75
4.6	Internal Reflection Modes for a Laser Material .	76
4.7	Transmission Across Coupling Gap	79
4.8	Fractional Transmission Loss of Resonator vs Mode Angle for 2, 3, 4, and 5 μm Gaps . .	80
4.9	Laser Mode Coupled to Guide by a Grating . .	84
4.10	Experimental Setup for Internal Reflection Laser	87
4.11	Output Spectra of Internal Reflection Resonator: (a) Near Threshold; (b) Twice Threshold . .	89

LIST OF FIGURES (continued)

Figure No.		Page
A-1	Two-dimensional Dielectric Cavity	97
A-2	Region of k-space Available for Total Internal Reflection Modes	103
A2-1	Refractive Indices of LiYF_4	107

LIST OF TABLES

Table No.		Page
1.1	Possible Infrared Sensitized Rare Earth Lasers	22
2.1	LiYF ₄ Crystals	24
A-1	Modes in a Two-dimensional Dielectric Cavity .	101
A2-1	Refractive Index of LiYF ₄	106

CHAPTER 1

INTRODUCTION

1.1 Foreword

The interaction of rare earth ions in insulating crystals can result in energy transfer between the rare earth ions. That is, if an ion is placed in an excited energy level by the absorption of optical radiation, all or part of this excitation energy can be transferred to other rare earth ions. An important application of energy transfer is sensitized optically pumped lasers. Here, pump light is absorbed by one class of ions, called sensitizer ions, and the excitation energy is transferred to the laser ion, called the activator ion. The use of energy transfer has resulted in very efficient optically pumped solid-state lasers. In the remainder of this chapter the energy transfer and relaxation processes which are important to the understanding of sensitized rare earth lasers will be reviewed.

Chapter 2 will discuss experimental techniques used in this research. The growth and properties of LiYF_4 , the host crystal used, are described. The spectroscopic techniques used to measure energy transfer rates are described; these include measurements under normal low intensity pumping conditions as well as high intensity pumping measurements where nonlinear transfer processes such as upconversion are important. The methods for obtaining laser operation with the sensitized rare earth materials are also described.

Some of the important results of this research are discussed in Chapter 3. It is shown that upconversion is an important and poorly understood energy transfer process in sensitized rare earth laser

materials, and that sensitizer and activator ion concentrations must be optimized to reduce its effect. A Yb^{3+} sensitized Ho^{3+} laser material that can be pumped by a LED is also demonstrated. The important energy transfer process between the $\text{Ho } ^5\text{I}_7$ and $\text{Tm } ^3\text{H}_4$ energy levels is also discussed.

Chapter 4 discusses the use of sensitized rare earth laser materials in miniature lasers. With sensitized materials, the sensitizer ions can be chosen to match the pump source; for example, the Yb^{3+} absorption band efficiently matches the emission spectrum of a GaAs:Si LED. A miniature internal reflection resonator is described which is compatible with thin film optical waveguides. Using this type of resonator, single mode cw laser operation in 0.2 mm^3 laser volume is demonstrated.

In the final chapter, the preliminary experimental and theoretical results of Chapters 3 and 4 are summarized and future extensions of this work are suggested.

1.2 Energy Transfer in Rare Earth Crystals

A rare earth ion in a crystal which is in an excited electronic state can relax toward the ground state by several processes; these include (1) radiative decay, (2) multiphonon decay where the excitation energy is converted to lattice phonons, and (3) energy transfer where all or part of the excitation energy is transferred to a nearby ion and any mismatch in energy requires the participation of phonons to conserve energy. Use of the rare earths in lasers requires knowledge of the various relaxation processes and rates. This is especially true in sensitized laser materials, where energy is absorbed by sensitizer ions and transferred to the active ions, since in these materials there are many competing decay and transfer

processes. The concentrations of the various sensitizer ions and active ions must be optimized so that the desired transfer and decay steps occur preferentially over other possible relaxation processes.

The positions of the energy levels of rare earths in crystals are well understood and can usually be determined by "first principles" calculations. However, satisfactory "first principles" calculations of most relaxation processes have not been successful, and a phenomenological approach is generally used. The phenomenological approach is very useful in calculating relaxation rates in specific systems from a small number of experimentally determined parameters. In this section, rare earth energy levels and the relaxation processes which are important to laser materials will be discussed.

The rare earths of the lanthanide series (lanthanum through lutetium) are characterized by successive filling of the 4f shell. These ions are usually found in crystals in the trivalent state. The optical spectra of these ions arise from transitions between levels of the $4f^N$ ground configuration. The degeneracy of the $4f^N$ configuration is split by the Coulomb field of the electrons yielding terms ^{2S+1}L with separations on the order of 10^4 cm^{-1} . The degeneracy of the ^{2S+1}L terms is split by spin orbit coupling into J levels with separations on the order of 10^3 cm^{-1} . Finally the $2J+1$ free ion degeneracy is further reduced by the static crystal field yielding a Stark manifold with separations on the order of 10^2 cm^{-1} . The J levels are referred to by the Russell-Saunders notation $^{2S+1}L_{2J+1}$. Since the crystal field splitting is small, the position of the J manifolds does not vary much from host to host. The energy levels of all the rare earth ions in LaCl_3 have been determined by Dieke¹ and are shown in Fig. 1. The lines shown are the J manifolds,

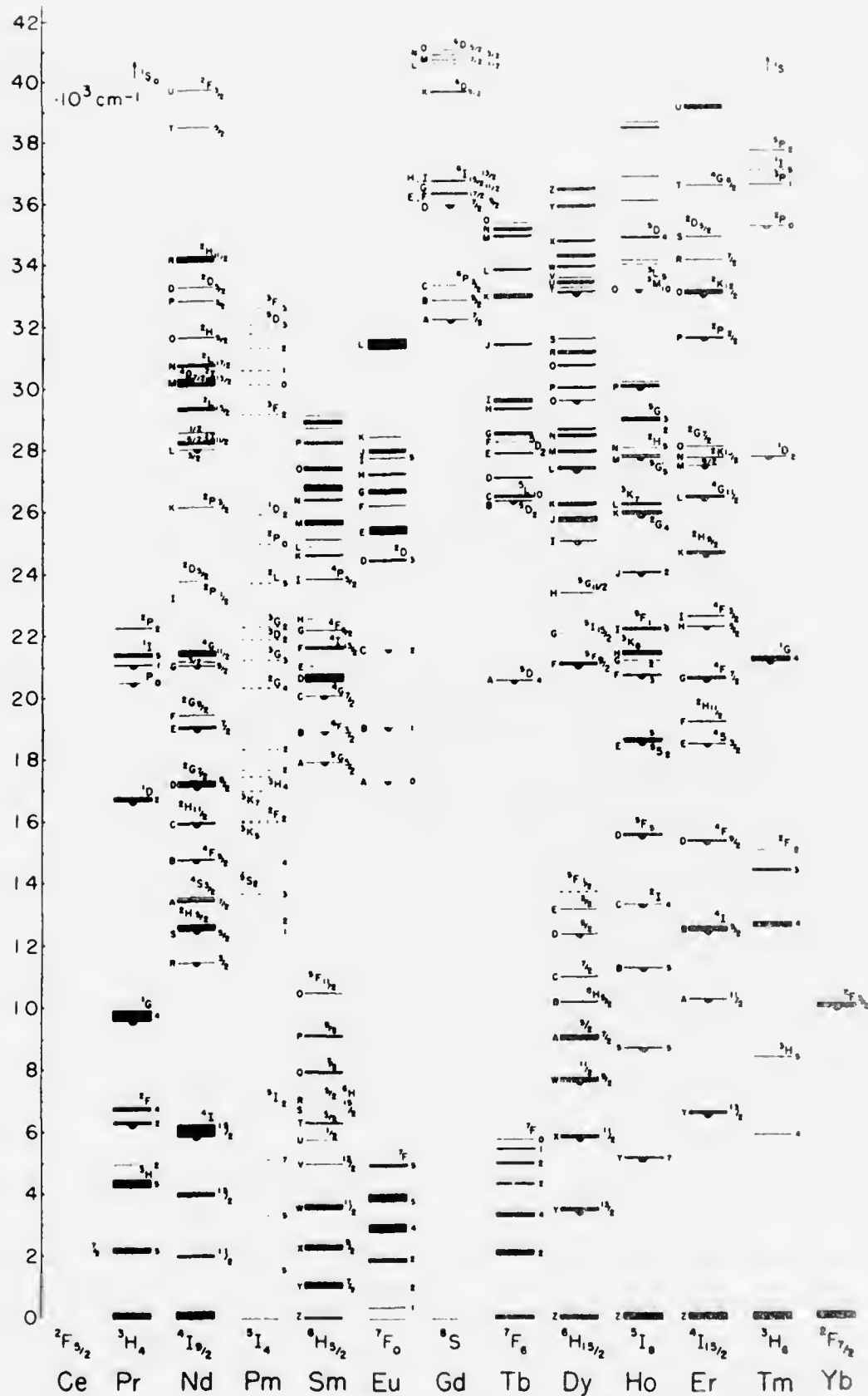


Fig. 1.1 Energy Levels of Rare Earth Ions.

and the width of the lines shows the extent of the crystal field splitting. A semicircle under the line indicates that fluorescence is observed from that level in LaCl_3 . Many of the energy levels of the rare earths in LiYF_4 have been measured experimentally from low temperature absorption and fluorescence spectra.^{2, 3} Good agreement between experimental and calculated energy levels has been obtained by diagonalizing a Hamiltonian that describes the free-ion and crystal-field interaction in a basis of states spanning the $4f^N$ configuration.^{4, 5}

If an ion is placed in an excited energy level by, for example, the absorption of optical radiation, it is important to understand how the ion decays back to the ground state. Excellent and comprehensive reviews of relaxation phenomena in rare earth materials have been presented by Riseberg and Weber⁶ and by Watts⁷. In the remainder of this section, a brief phenomenological description of the relaxation processes which are important to the understanding of sensitized laser materials will be given.

Relaxation of the crystal field split levels of a J manifold is extremely rapid, perhaps faster than 10^{12} sec^{-1} . This is because energy level separations are on the order of phonon energies and one or two phonon processes are very probable. This rapid relaxation gives rise to lifetime broadening of absorption and fluorescence spectra. Because of this rapid thermal equilibrium of the levels in a J manifold, the J manifold can be treated as a whole, when considering the slower radiative and nonradiative decay processes to other J manifolds. However, the transition probabilities from individual levels are not equal and it is sometimes necessary to consider individual transition strengths and the Boltzman population of the individual levels.

A simplified energy level diagram for a rare earth ion which

illustrates the important relaxation processes between J manifolds is shown in Fig. 1.2. Radiative decay is shown in Fig. 1.2a. Since the optical spectra of rare earth ions arise from intra $4f^N$ electron transitions, electric-dipole transitions are parity forbidden for free ions. However, for an ion in a crystal site which lacks inversion symmetry, the odd components of the static crystal field mix configurations of odd parity into the $4f^N$ configuration. Therefore, electric-dipole transitions do occur and their selection rules are determined by symmetry of the crystal field levels. Magnetic-dipole and electric-quadrupole transitions are allowed, but contributions to radiative decay are usually small.

When the energy difference ΔE between J manifolds becomes smaller, the probability for radiative transition between the manifolds decreases and the probability of multiphonon decay increases. This is shown in Fig. 1.2b. For multiphonon relaxation across an energy gap ΔE to the next lowest J manifold, n phonons of energy $\hbar\omega_{\text{eff}}$ are required to conserve energy; that is,

$$n \hbar\omega_{\text{eff}} = \Delta E. \quad (1.1)$$

Since lowest order processes (smallest n) are most probable, the phonon frequency ω_{eff} is usually close to the maximum of the phonon spectrum. The relaxation rate for multiphonon decay can be shown to obey the expression

$$W = C e^{-\alpha \Delta E}$$

where C and α are constants characteristic of a given material.⁸ This simple exponential dependence has been experimentally established and values of C , α , ω_{eff} , and W have been determined for a wide variety of rare earth doped crystals,⁹ including LiYF_4 .²



(a) Radiative decay (b) Multiphonon decay

Fig. 1.2 Relaxation of Isolated Ions: (a) Radiative Decay; (b) Multiphonon Decay.

Only when rare earth ions in solids are well separated can they be treated as isolated ions. As the concentration is increased, energy transfer between ions may occur as the ion spacing becomes sufficiently small. Energy transfer can occur through paramagnetic exchange interactions or electric and magnetic multipolar interactions. Transfer probabilities for these interactions were first derived in a classic paper by Dexter.¹⁰ Regardless of the type of interaction, a phenomenological rate equation model approach is usually valid and useful, as will be discussed later.

The most obvious evidence for energy transfer includes sensitized luminescence, where excitation of one type of ion (sensitizer) results in fluorescence from another type of ion (activator), and fluorescence quenching, where the addition of an ion to a normally fluorescing material results in nonradiative decay. Several energy transfer processes are shown in Fig. 1.3. The simplest process is shown in Fig. 1.3a, where an ion A in excited state E_A decays to state E'_A with the excitation of nearby ion B from its ground state E_B to excited state E'_B . The process is resonant if $E_A - E'_A = E'_B - E_B$. If ions A and B are identical, then resonant energy transfer may occur as shown in Fig. 1.3b; this gives rise to spatial energy migration. Nonresonant energy transfer can also occur as shown in Fig. 1.3c, with the excess energy given to phonons. The transfer probability is analogous to multiphonon decay;¹¹ that is

$$W = C' e^{-\beta \Delta E}.$$

The parameters C' and β have been determined for many crystals,¹¹ including LiYF_4 .² Resonant and nearly resonant transfer rates can be fast, perhaps greater than 10^8 sec^{-1} , for concentrated rare earth

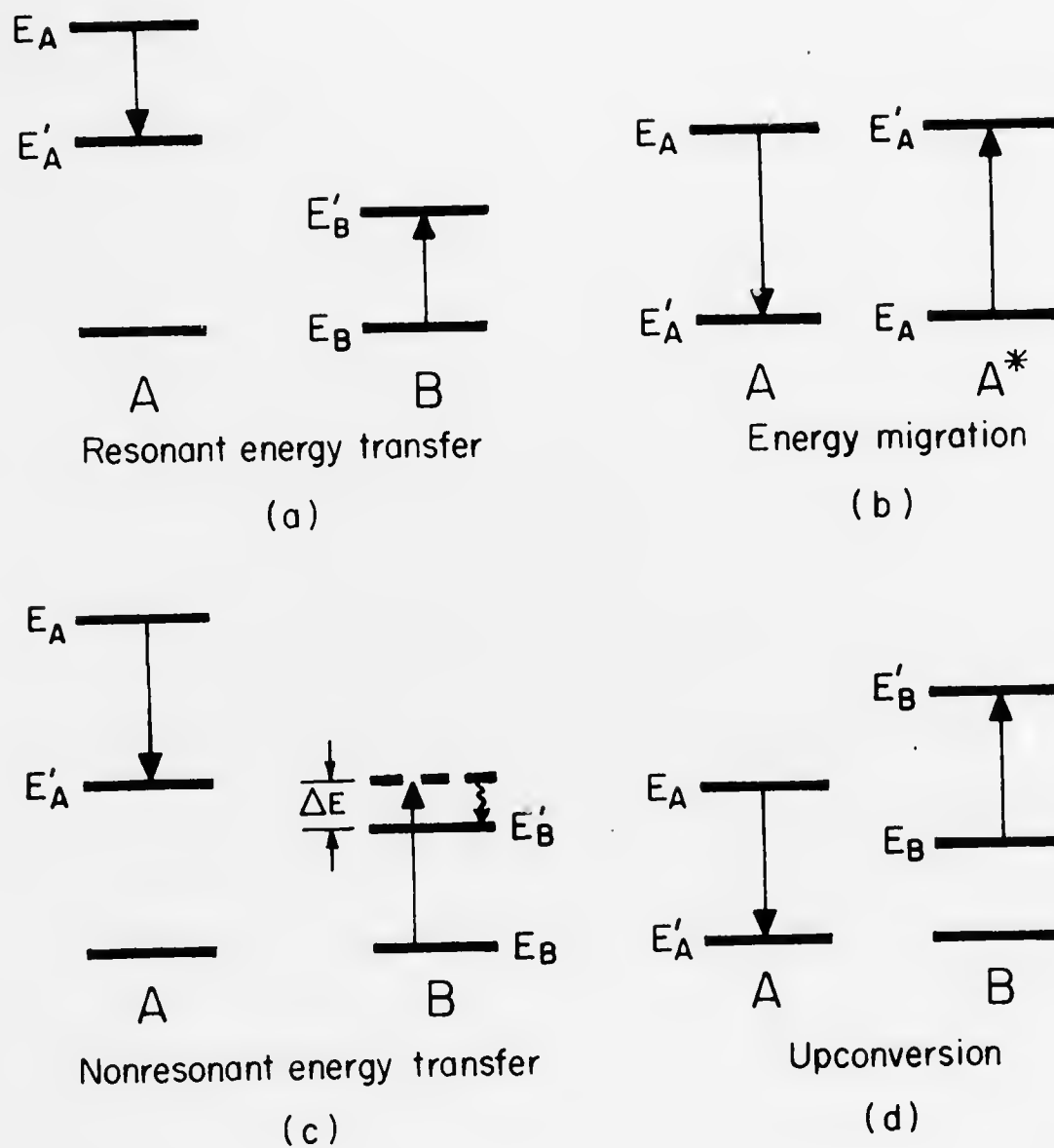


Figure 1.3 Energy Transfer Processes

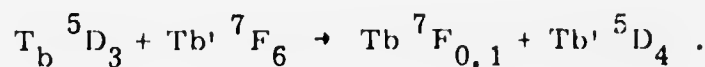
materials. Another type of energy transfer is upconversion, as shown in Fig. 1.3d. Initially two nearby ions are in excited states E_A and E_B , and ion A transfers its energy to ion B, thus resulting in ion B excited to a higher state than either of the two initial states. This is the basis of infrared to visible upconverter phosphors.

In concentrated rare earth materials, such as those investigated in this thesis, energy migration among sensitizer ions occurs in a random walk manner until the excitation is on an ion with a nearby acceptor, which acts as a quenching center or energy sink. Rapid energy diffusion can lead to a spatial equilibrium of excitation within the sensitizer system. The rate limiting step for the excitation relaxation then becomes either the sensitizer-activator transfer rate or the acceptor relaxation rate. In the limit of fast diffusion, the use of a rate equation model is appropriate.¹²

One of the most important applications of energy transfer is the development of rare earth solid state lasers. An example of its use is in the design of the $\text{LiYF}_4:\text{Tb}$ green laser.¹³ The laser transition is from the $^5\text{D}_4$ multiplet to the $^7\text{F}_5$ multiplet. For optical pumping, most light is absorbed by levels above the $\text{Tb } ^5\text{D}_3$. Because of the small energy gaps, these levels decay rapidly to the $^5\text{D}_3$ by multiphonon decay. However, the $^5\text{D}_3$ to $^5\text{D}_4$ energy gap is too large for efficient multiphonon decay; that is, the multiphonon decay rate is much less than the $^5\text{D}_3$ radiative decay rate. This problem can be avoided by increasing the Tb concentration ($> 25\%$) so that the probability of nearest neighbor Tb^{3+} ions is high. The $^5\text{D}_3$ can then decay to the $^5\text{D}_4$ by the resonant energy transfer process



or



Finally, the terminal laser level $^7\text{F}_5$ is rapidly depleted by multiphonon decay, so that four level laser operation is possible.

1.3 Sensitized Lasers

One of the most important applications of energy transfer is sensitized optically pumped lasers. Here, pump light is absorbed by one class of ions, sensitizer ions, and the excitation energy is transferred to the active ions or laser ions. This multiple doping of laser materials can result in increased pump light absorption and pumping efficiency. In addition, sensitizer ions can be chosen such that their absorption spectra match the emission spectra of different pump sources. The most successful sensitized laser is the $2\text{ }\mu\text{m}$ Ho^{3+} laser sensitized with Er^{3+} , Yb^{3+} , and Tm^{3+} . This is also the most efficient optically pumped solid-state laser ever operated.

The $2\text{ }\mu\text{m}$ Ho^{3+} laser transition is from the lowest level in the $^5\text{I}_7$ multiplet to an upper level in the $^5\text{I}_8$ ground multiplet. Since the terminal laser level is approximately 2 kT above the ground state at room temperature, there is a large terminal level population and the laser transition is essentially three level in character at room temperature. At reduced temperatures, such as 77°K , the terminal level population is negligible for most laser applications, so the laser transition is then essentially four level in character.

The multiply sensitized Ho^{3+} laser was first developed by Johnson,

et al. in the $\text{Y}_3\text{Al}_5\text{O}_{12}$ (YAG) host.¹⁴ Since then, Ho^{3+} laser action has been reported in a number of hosts; the most successful one for room temperature pulsed operation is LiYF_4 (YLF).¹⁵ A typical composition is $\text{LiYF}_4:50\%\text{Er}$, $6.7\%\text{Tm}$, $0.34\%\text{Ho}$, which is commonly called $\alpha\beta$ -YLF.

There are more than fifty J manifolds which are active in the optical pumping of $\alpha\beta$ -YLF. Since each of these pump levels can decay by any of the relaxation processes discussed in section 1.2, it is an extremely complex problem to analyze the methods by which energy is transferred from the pump levels to the upper laser level $\text{Ho } ^5\text{I}_7$. Although no complete model of energy transfer has been attempted, many of the important transfer steps have been studied.¹⁶ Additional important transfer processes have been identified in the course of this research.

Several other lasers using Yb, Tm, or Er as sensitizers are listed in Table 1.1. Many of these were investigated in this research.

In order to optimize the performance of a sensitized laser, it is necessary to know in detail what energy transfer steps are involved, their rates, and their dependence on the concentrations of the different ions. Furthermore, the optimum concentration may depend on type of laser operation desired, cw, long pulse, or Q-switched, on the operating temperature of the material, and on the spectral characteristics of the pump source. Thus an adequate model of the laser material and its desired operating characteristics is needed to optimize the laser material.

Table 1.1

Possible Infrared Sensitized Rare Earth Lasers

Laser Transition	Laser Wavelength	Principal Sensitizer Ion	Pump Band
Ho: $^5I_7 - ^5I_8$	2 μm	Er ³⁺	1.5 μm
Ho: $^5I_7 - ^5I_8$	2 μm	Yb ³⁺	0.96 μm
Ho: $^5I_6 - ^5I_7$	3 μm	Yb ³⁺	0.96 μm
Ho: $^5I_6 - ^5I_7$	3 μm	Er ³⁺	1.0 μm
Ho: $^5I_6 - ^5I_8$	1.2 μm	Yb ³⁺	0.96 μm
Ho: $^5S_4 - ^5I_8$	0.54 μm	Yb ³⁺	0.96 μm
Tm: $^3H_4 - ^3H_6$	1.8 μm	Er ³⁺	1.5 μm
Tm: $^3H_4 - ^3H_6$	1.8 μm	Yb ³⁺	0.96 μm
Tm: $^3F_4 - ^3H_5$	2.3 μm	Yb ³⁺	0.96 μm
Tm: $^3F_4 - ^3H_4$	1.5 μm	Yb ³⁺	0.96 μm
Tm: $^3F_4 - ^3H_6$	0.8 μm	Yb ³⁺	0.96 μm
Er: $^4I_{13/2} - ^4I_{15/2}$	1.6 μm	Yb ³⁺	0.96 μm

CHAPTER 2

EXPERIMENTAL TECHNIQUES

2.1 LiYF₄ Crystal Growth

LiYF₄ has the scheelite (CaWO₄) structure and belongs to the tetragonal space group C_{4h}⁶. Rare earth dopants go into the crystal host substitutionally for Y³⁺ and can be substituted up to 100% in the case of the heavier rare earth ions. The Y³⁺ site symmetry is S₄. The LiYF₄ (YLF) crystals studied in this research were grown by a top-seeded solution technique in a high purity argon atmosphere.¹⁷ All feed materials were purified by a variety of chemical separation techniques, zone refining, and hydrofluorination.¹⁶ This purification was especially important for heavily doped materials, because of fast energy migration to quenching centers in crystals with high rare earth concentrations. For example, in the best LiErF₄, which was shown to have less than 5 ppm of other rare earth impurities, the fluorescent lifetime of the Er ⁴I_{13/2} level was about half the lifetime of the Er ⁴I_{13/2} level in crystals doped with less than 1% Er. All LiYF₄ samples used were high purity, high optical quality single crystals. A list of the crystals studied is given in Table 2.1.

2.2 Spectroscopic Measurements

The measurement of fluorescence intensities and lifetimes is the primary method of studying energy transfer in crystals. The experimental setup used to measure fluorescence spectra is shown schematically in Fig. 2.1. Measurements were made on single crystal samples whose sides were cut along the crystallographic axes. Samples were optically thin at the fluorescing wavelengths. For low intensity pumping

Table 2.1
LiYF₄ Crystals

Growth Run Number	Percent Substitution for Y ³⁺ in LiYF ₄			
	Yb ³⁺	Er ³⁺	Tm ³⁺	Ho ³⁺
159	-	50	1.0	0.3
171	-	50	3.5	0.3
193	10	20	6.7	0.5
213	50	49	1.0	0.05
217	-	99.5	0.5	-
219	-	99	1.0	-
224	-	50	5.0	0.25
225	-	100	-	-
226	-	100	-	0.05
230	-	100	-	-
231	-	100	-	0.05
232	-	100	-	0.3
234	-	100	-	-
236	-	100	-	0.05
238	-	100	-	0.3
248	95	-	5.0	0.25

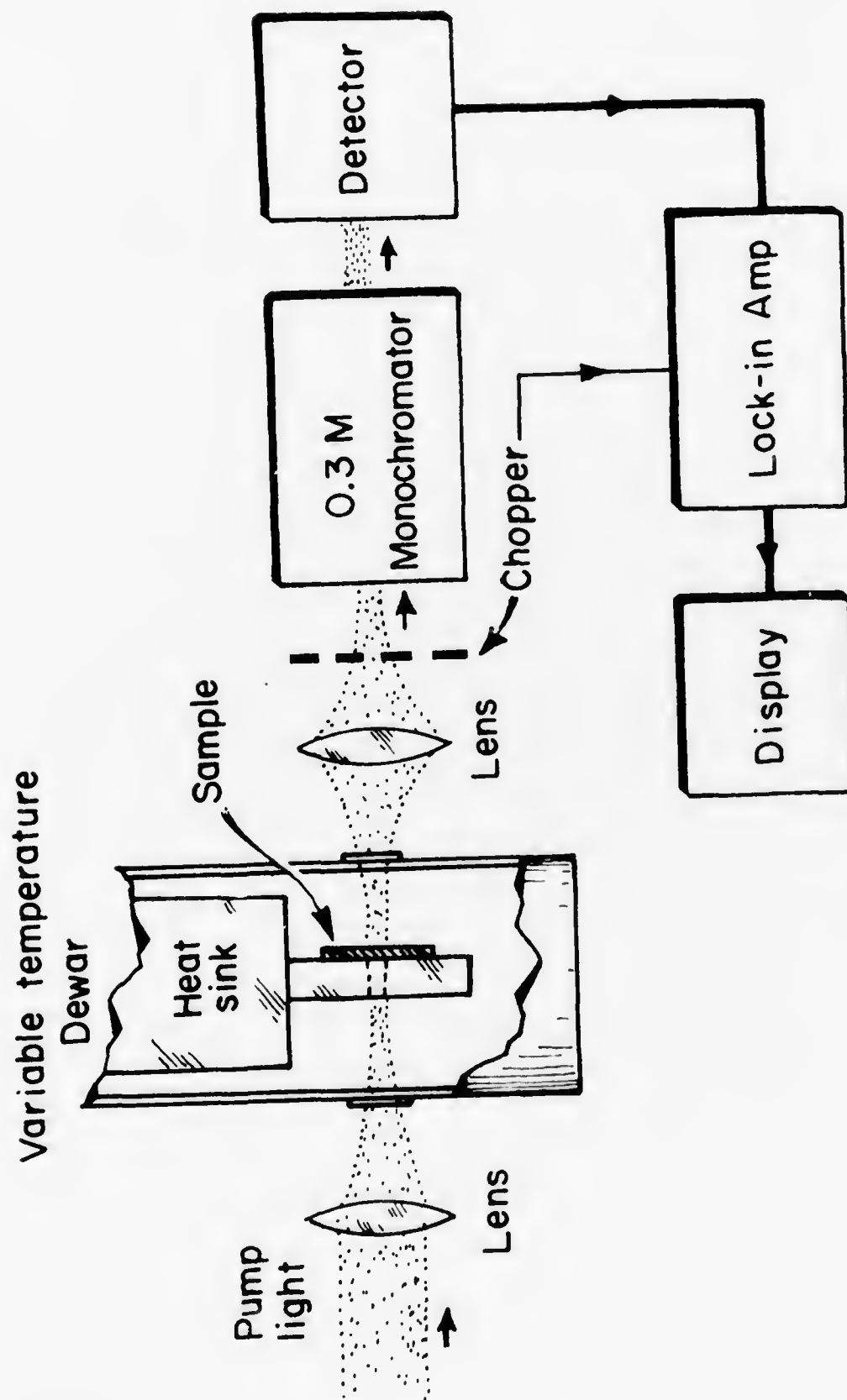


Fig. 2.1 Fluorescence Spectra Measurement Setup.

(less than 10 W/cm^2 absorbed light), a xenon arc lamp or a tungsten iodine lamp was used with a Bausch and Lomb high intensity grating monochromator for wavelength selective pumping. For high intensity pumping (to greater than 10^4 W/cm^2 absorbed), a 10 watt cw argon ion laser was used.

Samples were mounted on the cold finger of a Janis Model DT variable temperature dewar so that spectra could be measured over the range from liquid helium temperatures to room temperature. For laser pumping special care was taken to heat sink the samples. The laser beam was focused onto the sample through a hole in the heat sink which was just large enough to pass the beam, and the sample was bonded to the copper heat sink with indium solder. An estimate of the temperature rise in the sample is given in section 2.3.

Sample fluorescence was collected with a simple lens, chopped, and focused on the input slits of a McPherson Model 218 0.3 m grating monochromator. The light was synchronously detected with a variety of detectors. An RCA C7164R photomultiplier was used for wavelengths up to $0.75 \mu\text{m}$, a dry ice-cooled RCA 7102 photomultiplier in the near infrared region from $0.75 \mu\text{m}$ to $1.2 \mu\text{m}$, and a liquid nitrogen-cooled InAs photodiode detector in the infrared to $3 \mu\text{m}$.

The measurement of excited state lifetimes can be used to determine energy transfer rates. The lifetime (τ_a) of an excited state a is given by

$$1/\tau_a = \sum_b W_{ab}^R + W_a^P + \sum_i W_i^T$$

where W_{ab}^R is radiative decay rate to a final state b. The nonradiative decay includes the multiphonon decay rate W_a^P and energy transfer rates

W_i^T arising from ion-ion interactions. The radiative quantum efficiency η_a is given by

$$\eta_a = \frac{\sum_b W_{ab}^R}{\sum_b W_{ab}^R + W_a^P + \sum_i W_i^T} = \tau \sum_b W_{ab}^R$$

By measuring the lifetime in materials with very low rare earth concentrations such that ion-ion interactions do not occur, one can determine $W_{ab}^R + W_a^P$. This together with a measurement of τ_a allows one to determine η_a and the total energy transfer rates $\sum_i W_i^T$.

Lifetimes were measured by pulsed excitation as shown in Fig. 2.2. The pulsed light source was a xenon flashlamp, repetitively pulsed at rates up to 30 Hz. The pulse width was less than 10 μ s and the energy was about 5 joules per pulse. The light was filtered with a high intensity grating monochromator for selective energy level excitation. Fluorescence was detected using the same detectors as used for continuous fluorescence. The detected signal was amplified with a PAR Model 113 Pre-Amp and averaged with a Scientific Instruments Corporation (CAT-10) Computer-of-Average-Transients. Lifetimes greater than 10 μ s could be measured with this technique.

2.3 Laser Operation of Materials

The experimental setup for laser operation of the Er^{3+} sensitized Ho^{3+} materials is shown in Fig. 2.3. A nearly confocal laser resonator was formed with two mirrors with a radius of curvature $R = 10$ cm separated by a distance $d = 10.7$ cm. The Gaussian beam radius ω_0 of the TEM_{00} mode at the center of the resonator is given by

$$\omega_0^2 = \frac{\lambda}{2\pi} \sqrt{d(2R - d)}$$

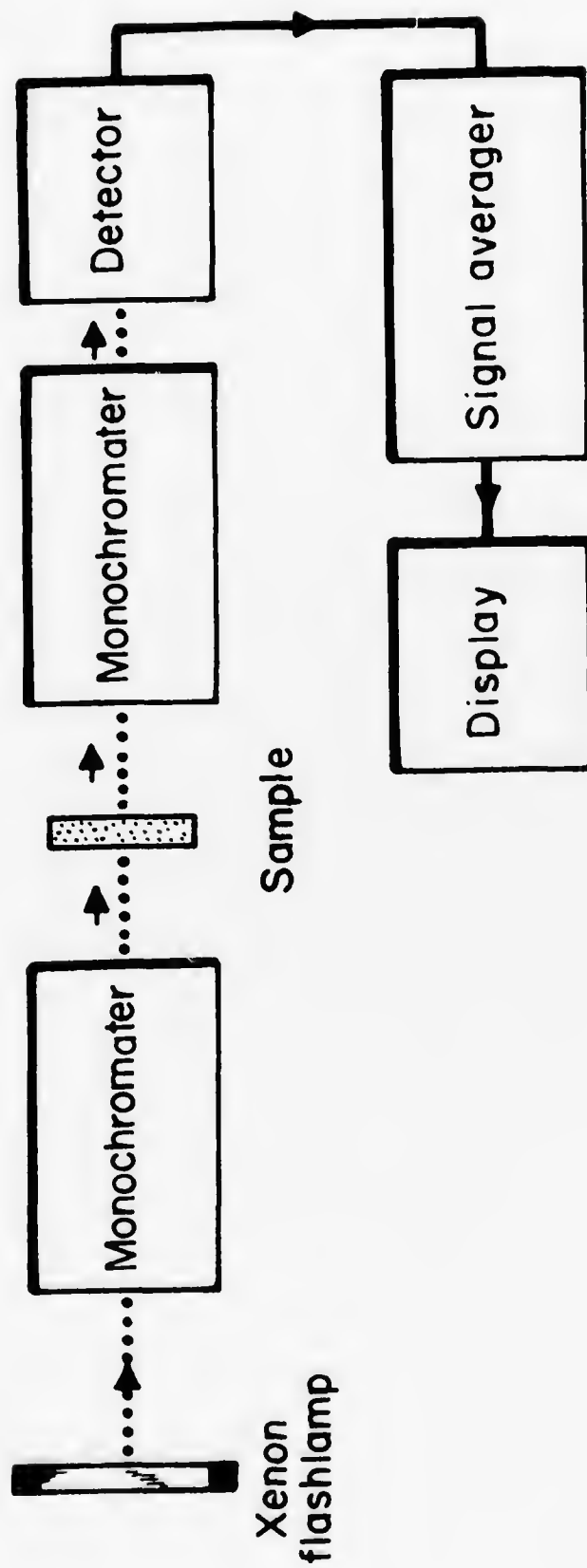


Fig. 2.2 Pulsed Fluorescence Measurement Setup.

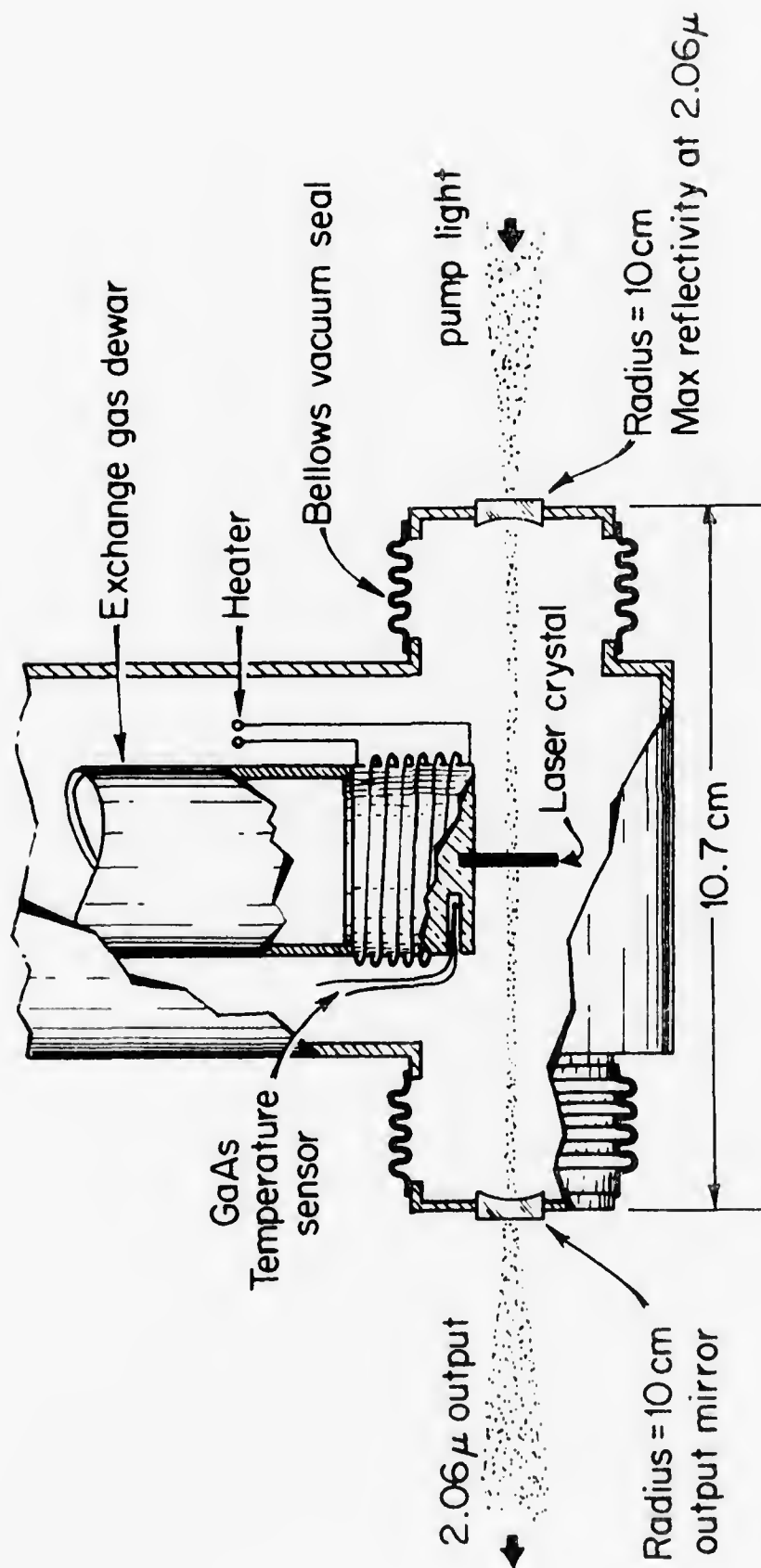


Fig. 2.3 Variable Temperature Laser Cavity.

where λ is the laser wavelength. For $\lambda = 2 \mu\text{m}$, the beam diameter is $2 \omega_0 = 0.36 \text{ mm}$. A laser crystal, which was typically $\frac{1}{2}$ -mm thick, was mounted in the center of the resonator on the cold finger of a variable temperature dewar (4.2°K to 300°K). The crystal was longitudinally pumped with a cw krypton or argon ion laser. The pump beam was focused so that its beam diameter at the crystal was the same as the resonator beam diameter ($2 \omega_0$). This minimized the peak pump intensity necessary to achieve a desired average pump intensity throughout the mode volume, which is important when energy transfer efficiency is a nonlinear function of pump power as shown in section 3.1.

Since Ho:YLF is a quasi three level laser material, its threshold is a strong function of temperature, as shown in section 3.2. Special care was taken to heat sink the samples. The samples were mounted with indium solder to the copper heat sink. Both the pump and sample laser beams passed through a hole of diameter approximately $6 \omega_0$ in the heat sink. The temperature rise of the laser for this "optimum" heat sinking can be estimated as follows. Heating of the crystal is due to that fraction of the pump beam power absorbed which is not emitted as fluorescence. Because of the Gaussian profile of the TEM_{00} beam, the heating of the crystal is nonuniform transverse to the beam, but if we assume for simplicity that heating along the axis is uniform, the radial heat conduction problem has the solution:¹⁸

$$T(0) - T(r) = \frac{q_0 \omega_0^2}{4k} \left[E_1\left(\frac{r^2}{\omega_0^2}\right) + \ln\left(\frac{r^2}{\omega_0^2}\right) + \gamma \right]$$

where T is the temperature at radial position r ; q_0 is the thermal power density on axis; k is the thermal conductivity of the crystal; $E_1(r^2/\omega_0^2)$

is the exponential integral of first order, and γ the Euler constant. If the crystal is in good thermal contact with the heat sink at $r = 3 \text{ mm}$, then the temperature rise in the center of $\frac{1}{2}$ -mm thick crystal is $\Delta T = 0.7^\circ\text{K/mw}$. Heating along the axis is not uniform, but of the form $e^{-\alpha x}$ where α is the pump beam absorption coefficient. For $\alpha = 50 \text{ cm}^{-1}$, this produces a larger peak temperature rise than predicted above, and it is estimated to be $\Delta T = 1^\circ\text{K/mw}$.

For laser operation of the Yb^{3+} sensitized Ho^{3+} laser materials, samples were transversely pumped with a tungsten lamp. Because of the large absorption coefficient of the $0.96 \text{ }\mu\text{m}$ pump light, the gain region of the laser crystal was typically $100 \text{ }\mu\text{m}$ thick. In order to have the resonator mode diameter well within the gain region, the resonator mirrors were applied directly on the ends of the crystal. This is described in greater detail in section 3.1.2.

CHAPTER 3

ENERGY TRANSFER IN SENSITIZED HOLMIUM LASER MATERIALS

In order to understand and predict the performance of sensitized Ho^{3+} laser materials, it is necessary to understand the processes of energy transfer from the pump levels of sensitizer ions to the Ho^{5}I_7 upper laser level. Many of the important energy transfer steps in $\alpha\beta$ -YLF have been studied.¹⁶ In this work the key energy levels (see Fig. 3.1) below $\text{Er}^{4}\text{S}_{3/2}$ were selectively excited so that the transfer rates to the Ho^{5}I_7 level and the quantum efficiency of the excitation of the Ho^{5}I_7 level could be measured. It was found that when the Tm^{3+} concentration is greater than 5%, the quantum efficiency of energy transfer from the $\text{Er}^{4}\text{S}_{3/2}$ level to the Tm^{3}H_4 and Ho^{5}I_7 levels is 3; that is, for each Er^{3+} ion excited to the $^{4}\text{S}_{3/2}$ level, three excited ions are produced in the Ho^{5}I_7 - Tm^{3}H_4 system. This occurs through a series of resonant transfer steps as illustrated in Fig. 3.1. This is significant for pulsed $\alpha\beta$ -YLF lasers pumped by xenon flashlamps, since much of the pump light is absorbed into energy levels directly above the $\text{Er}^{4}\text{S}_{3/2}$ level, which rapidly relax by multiphonon decay to the $\text{Er}^{4}\text{S}_{3/2}$ level. Even higher pumping quantum efficiency may occur for absorption bands well above the $\text{Er}^{4}\text{S}_{3/2}$ level. Despite the high pumping efficiency of $\alpha\beta$ -YLF laser materials, experimental laser performance has not been as efficient as would be predicted from these energy transfer models. Other energy transfer processes must be occurring, which limit the performance of $\alpha\beta$ -YLF.

In the first part of this chapter it will be shown that upconversion is an additional important energy transfer process in sensitized laser materials, especially in Er^{3+} or Yb^{3+} sensitized Ho^{3+} laser materials.

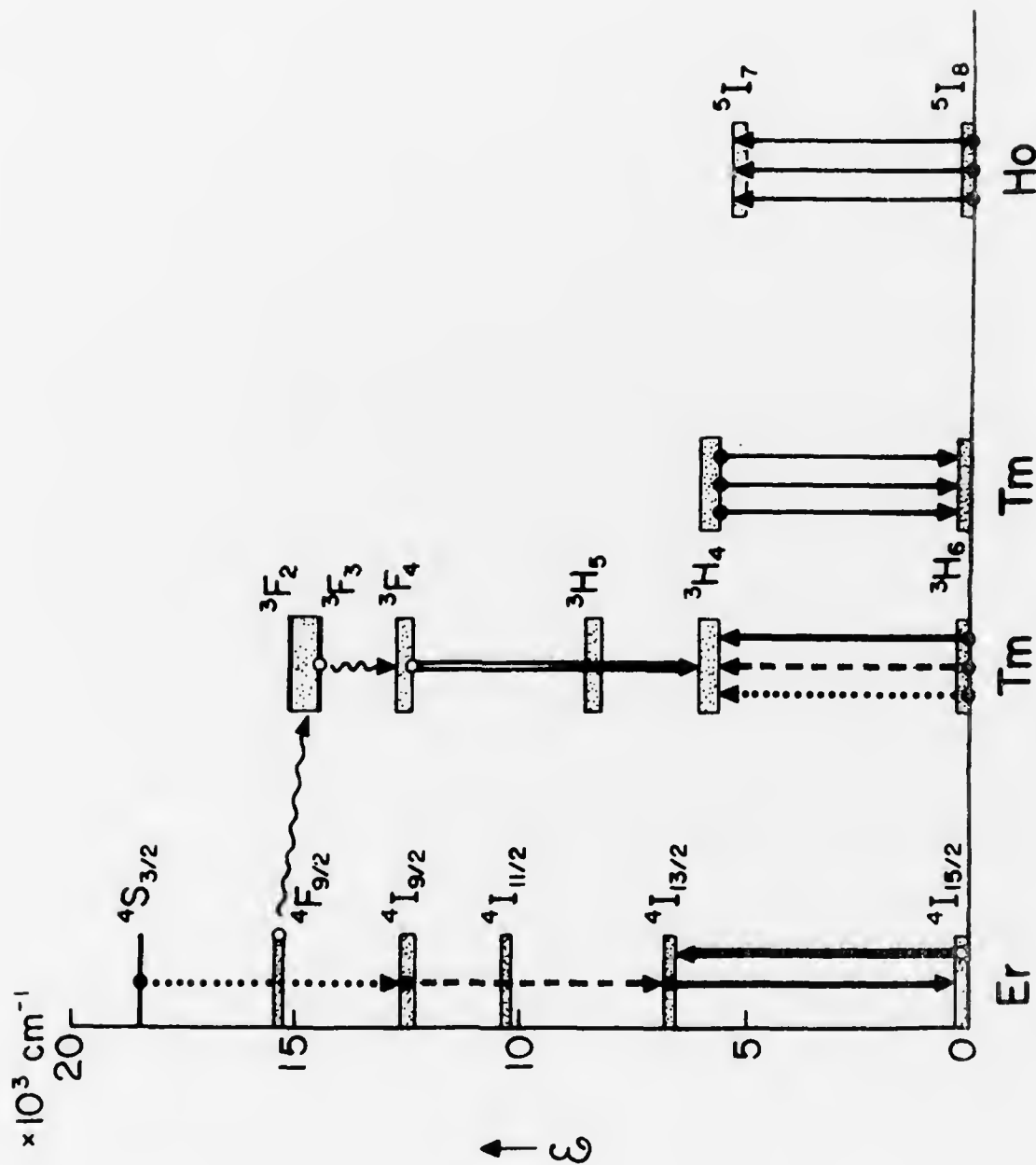


Fig. 3.1 Energy Transfer in $\alpha\beta$ -YLF.

In order to understand the effect of upconversion on laser performance, energy transfer and upconversion in the $\text{Yb}^{3+} - \text{Tm}^{3+}$ system was modelled. This is a much simpler system than the $\text{Er}^{3+} - \text{Ho}^{3+}$ system; however, similar upconversion and energy transfer processes occur in the $\text{Er}^{3+} - \text{Ho}^{3+}$ system and the effects of upconversion on Er^{3+} sensitized Ho^{3+} laser materials and $\alpha\beta$ -YLF laser materials were experimentally demonstrated. The model of the $\text{Yb}^{3+} - \text{Tm}^{3+}$ system was also used to predict the performance of Yb^{3+} sensitized Tm^{3+} laser materials and Yb^{3+} and Tm^{3+} sensitized Ho^{3+} laser materials. A Yb^{3+} and Tm^{3+} sensitized Ho^{3+} laser was experimentally demonstrated. This material is potentially important for LED pumped miniature lasers. In the remainder of this chapter, the $\text{Tm}^{3+} \text{H}_4 \rightarrow \text{Ho}^{3+} \text{I}_7$ energy transfer process, which is important in determining Yb^{3+} and Tm^{3+} or Er^{3+} and Tm^{3+} sensitized Ho^{3+} laser threshold, will be considered.

3.1 Upconversion

Examples of upconversion materials on which many studies have been made are the infrared-to-visible upconversion phosphors, where infrared light, which is absorbed by Yb^{3+} ions, is converted to visible light and emitted by Ho^{3+} , Er^{3+} , or Tm^{3+} ions.^{12, 19} One infrared-to-visible upconversion process for $\text{Yb}^{3+} - \text{Ho}^{3+}$ in LiYF_4 has been studied by Watts.²⁰ The efficiency of the infrared-to-visible upconversion was successfully explained by a rate equations model. Here a Yb^{3+} ion which is excited to the $^2\text{F}_{5/2}$ level (see Fig. 3.2) nonresonantly transfers its energy to the $\text{Ho}^{3+} \text{I}_6$ level. Next, a second excited Yb^{3+} ion resonantly transfers its energy to the previously excited Ho^{3+} ion and raises it to the overlapping $^5\text{S}_2$, $^5\text{F}_4$ levels. The $^5\text{S}_2$, $^5\text{F}_4$ levels then radiatively decay producing green fluorescence. There is another upconversion

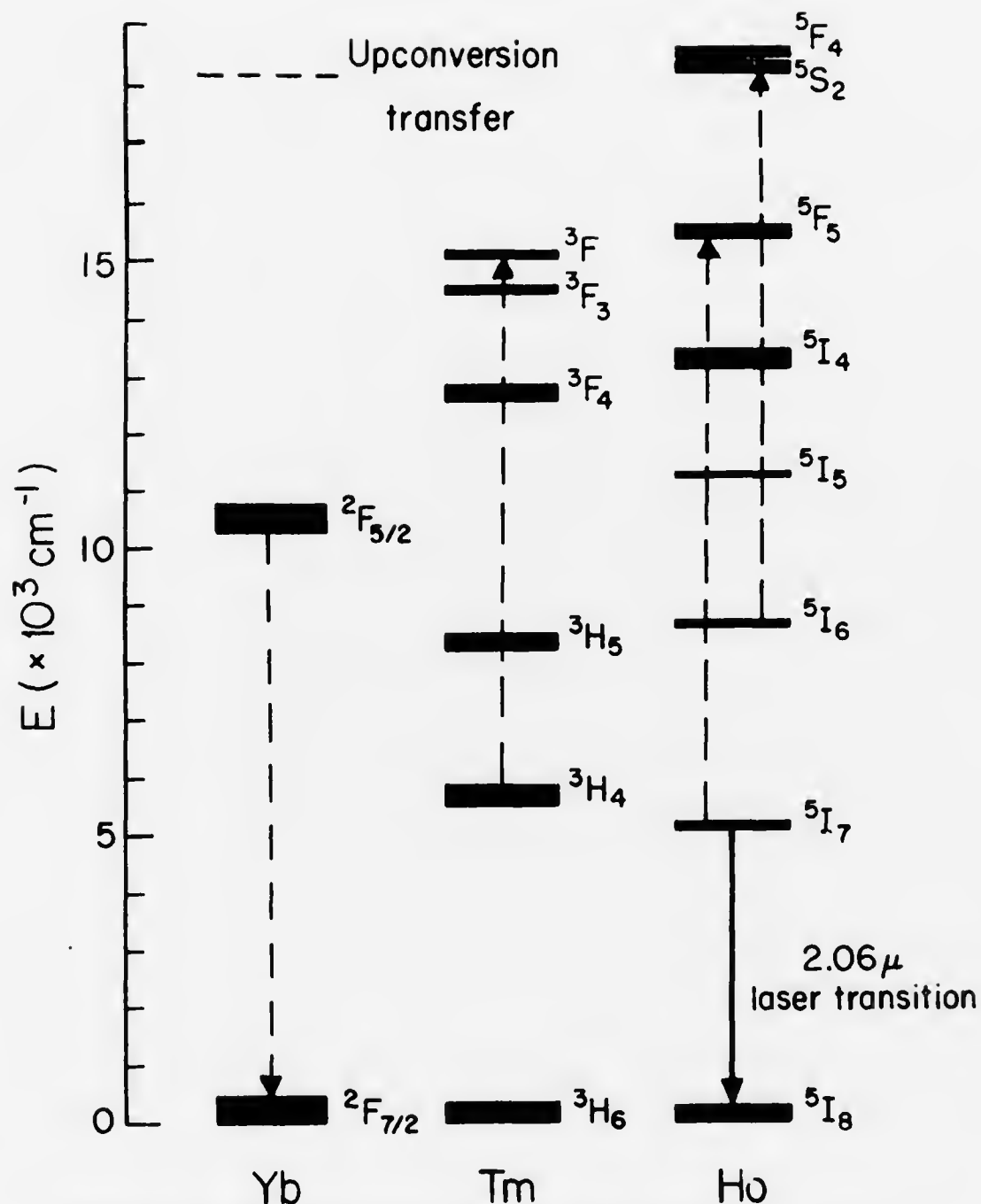


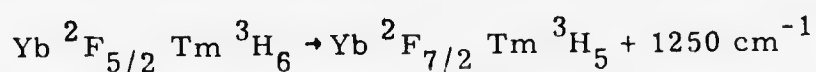
Figure 3.2 Energy Levels of Yb^{3+} , Tm^{3+} and Ho^{3+} in LiYF_4

step possible in the $\text{Yb}^{3+} - \text{Ho}^{3+}$ system which may have an important effect for $\text{Ho } ^5\text{I}_6$ or $^5\text{I}_7$ laser materials. As before, an excited Yb^{3+} ion raises a Ho^{3+} ion to the $^5\text{I}_6$ level. However, the $^5\text{I}_6 - ^5\text{I}_7$ energy gap is small enough so that the multiphonon decay rate is approximately equal to the radiative decay rate. Thus about half of the Ho^{3+} ions in the $^5\text{I}_6$ level decay to the $^5\text{I}_7$ level by multiphonon decay. In this second upconversion step, an excited Yb^{3+} ion can interact with a Ho^{3+} ion in the $^5\text{I}_7$ level, raising it to the $^5\text{F}_5$ level. The Ho^{3+} ions in the $^5\text{F}_5$ level can relax by both radiative decay and multiphonon decay. For radiative decay the most probable transition is to the ground state; therefore the energy required to excite the two Yb^{3+} ions is not transferred to the $\text{Ho } ^5\text{I}_7$ or $^5\text{I}_6$ levels and is lost as $\text{Ho } ^5\text{F}_5$ fluorescence. For multiphonon decay the $\text{Ho } ^5\text{F}_5$ relaxes to the $\text{Ho } ^5\text{I}_6$ level and the energy required to excite the second Yb^{3+} ion is lost as phonons. The effect of upconversion processes on the $\text{Ho } ^5\text{I}_6$ or $^5\text{I}_7$ levels is difficult to observe under low intensity pumping, since the probability of energy migration through the $\text{Yb } ^2\text{F}_{5/2}$ levels to an excited Ho^{3+} ion is less than the probability of normal $\text{Yb } ^2\text{F}_{5/2} \rightarrow \text{Ho } ^5\text{I}_6$ transfer. Therefore at low pump intensities, the Yb^{3+} to $\text{Ho } ^5\text{I}_6$ or $^5\text{I}_7$ transfer quantum efficiency is near unity. However, under high intensity pumping, the probability of upconversion may be high and the transfer quantum efficiency decreases to zero. The result is that laser materials which look efficient in low intensity spectroscopy experiments may not work at all at the high pump rates needed for laser operation. The upconversion rates can be determined from the saturation of the $\text{Ho } ^5\text{I}_7$ or $^5\text{I}_6$ fluorescence. This effect is due to the saturation of the $\text{Ho } ^5\text{I}_7$ or $^5\text{I}_6$ population which occurs when the rate of depletion by the upconversion transfer exceeds the normal

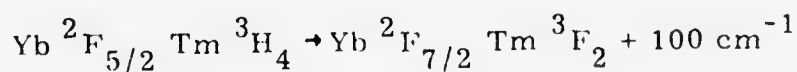
radiative or multiphonon decay rate.

For Yb^{3+} or Er^{3+} sensitized laser materials, fast energy migration among the sensitizer ions occurs when their concentration is high (usually greater than 10%). The excited sensitizer ions then effectively see a spatially averaged environment and rate equation models can be used. This form of analysis has been successfully applied to several infrared-to-visible upconverter systems.^{12, 19, 20, 21}

The remainder of this section will discuss the Tm^{3+} doped LiYbF_4 system which was chosen for first detailed modelling of the effect of upconversion because most of the transfer rates can be easily measured. Two possible Yb^{3+} sensitized Tm^{3+} laser transitions are the $\text{Tm } ^3\text{H}_4 \rightarrow ^3\text{H}_6$ laser and the $\text{Tm } ^3\text{F}_4 \rightarrow ^3\text{H}_4$ laser. The second transition requires upconversion for its operation since the $\text{Tm } ^3\text{F}_4$ level is higher in energy than the $\text{Yb } ^2\text{F}_{3/2}$ pump level. The energy levels of Yb^{3+} and Tm^{3+} are shown in Fig. 3.2. The upconversion process considered in this system involves two energy transfer steps. The first is a non-resonant transfer

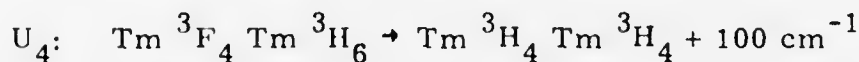
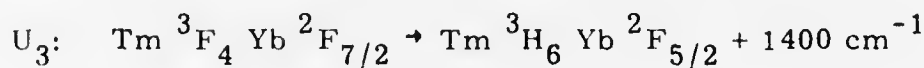
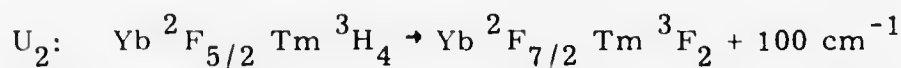
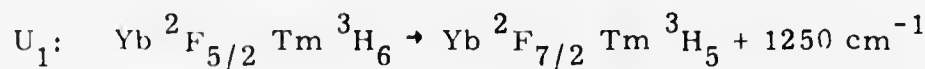


with the excess energy being taken by lattice phonons. The Tm^3H_5 rapidly decays to $^3\text{H}_4$ by multiphonon decay. The second transfer is more nearly resonant



The $^3\text{F}_2$ then decays rapidly to the $^3\text{F}_4$. The first energy transfer step is the desired one for a $\text{Tm } ^3\text{H}_4 \rightarrow ^3\text{H}_6$ laser. The second transfer step, the upconversion step, depletes the upper laser level population, thus reducing the efficiency of the desired transfer process.

To study the populations in various excited levels and the transfer efficiencies, a simple rate equation model was used. The model in Fig. 3.3 shows the transfer processes considered. The populations of the i^{th} level of the activator (Tm^{3+}) and the sensitizer (Yb^{3+}) are denoted by A_i and S_i , respectively. The Tm^3F_2 , $^3\text{F}_3$, and $^3\text{F}_4$ are labeled together as A_3 since the $^3\text{F}_2$ and $^3\text{F}_3$ decay rapidly ($< 10 \mu\text{s}$) to the $^3\text{F}_4$; likewise, the $^3\text{H}_5$ and $^3\text{H}_4$ are labeled A_2 . The transfer rate constants U_i are for the following processes:



With R_s defined as the inverse of the $\text{Yb } ^2\text{F}_{5/2}$ fluorescent lifetime and with R_2 and R_3 defined respectively as the fluorescent decay rates of the $\text{Tm } ^3\text{H}_4$ and $^3\text{F}_4$ levels, the rate equations become:

$$\begin{aligned} \dot{S}_2 &= X(S_1 - S_2) - U_1 A_1 S_2 - U_2 A_2 S_2 + U_3 A_3 S_1 - R_s S_2 \\ \dot{A}_2 &= U_1 A_1 S_2 - U_2 A_2 S_2 + 2U_4 A_1 A_3 - R_2 A_2 \\ \dot{A}_3 &= U_2 A_2 S_2 - U_3 A_3 S_1 - U_4 A_1 A_3 - R_3 A_3 \end{aligned} \quad (3.1)$$

The pump rate $X = \sigma\Phi$, where σ is the $\text{Yb } ^2\text{F}_{5/2}$ absorption cross section, and Φ is the pump photon flux. The A_i and S_i are normalized such that

$$A_1 + A_2 + A_3 = C_{\text{Tm}}, \quad (3.2)$$

where C_{Tm} is the fraction of Yb^{3+} sites occupied by Tm^{3+} . Therefore,

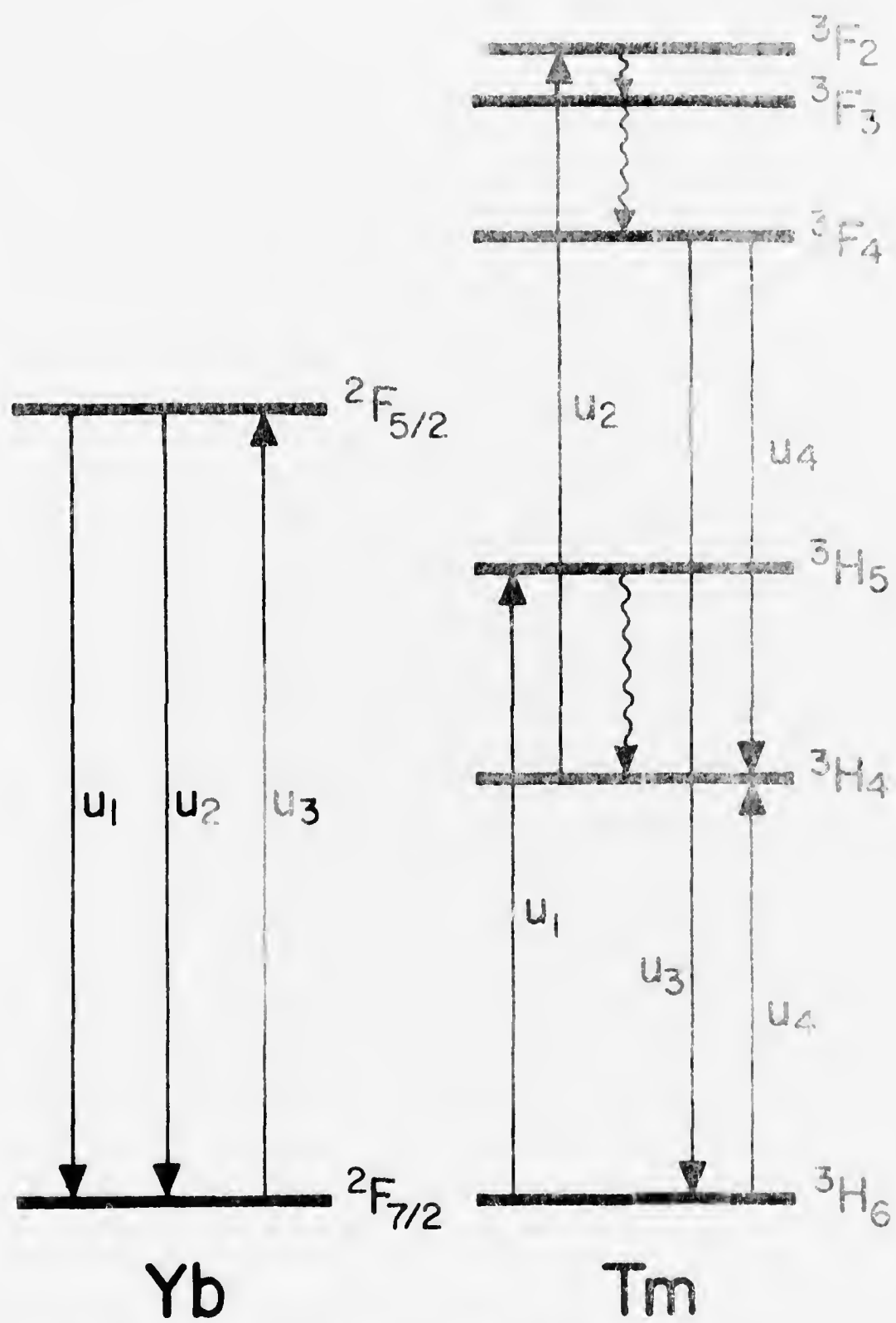


Fig. 3.3 Decay and Energy Transfer Processes for the $\text{Yb}^{3+} - \text{Tm}^{3+}$ System.

$$S_1 + S_2 = 1 - C_{Tm} \quad (3.3)$$

The rate constants were measured by pulsed excitation in the following crystals: LiYbF_4 , $\text{LiYb}_{0.995}\text{Tm}_{0.005}\text{F}_4$, $\text{LiYb}_{0.99}\text{Tm}_{0.01}\text{F}_4$ and $\text{LiY}_{0.98}\text{Tm}_{0.02}\text{F}_4$. The R_i were obtained from fluorescent lifetime measurements. U_1 was obtained from the $\text{Yb } ^2\text{F}_{5/2}$ decay time and the $\text{Tm } ^3\text{H}_4$ build-up time in $\text{LiYb}_{0.995}\text{Tm}_{0.005}\text{F}_4$; likewise, U_3 was measured from the $\text{Tm } ^3\text{F}_4$ decay time. U_4 was obtained from the concentration dependence of the $^3\text{F}_4$ lifetime in the three Tm-doped crystals. U_2 cannot be measured by simple pulsed excitation experiments, so the value used for this rate constant was one measured in YF_3 .¹⁹ This is reasonable since other energy relaxation rates that have been reported in YF_3 ¹⁹ are nearly equal to those measured in LiYF_4 . The rate constants used in the model are:

	Rate (sec^{-1})
R_S	394
R_2	85.5
R_3	770
U_1	2.4×10^5
U_2	1.4×10^8
U_3	1.17×10^4
U_4	10^6

The three nonlinear coupled rate equations were numerically solved (see Appendix 3) for the steady state values of S_2 , A_2 , and A_3 , for a wide range of pump rate X . The results are shown in Fig. 3.4 for Tm

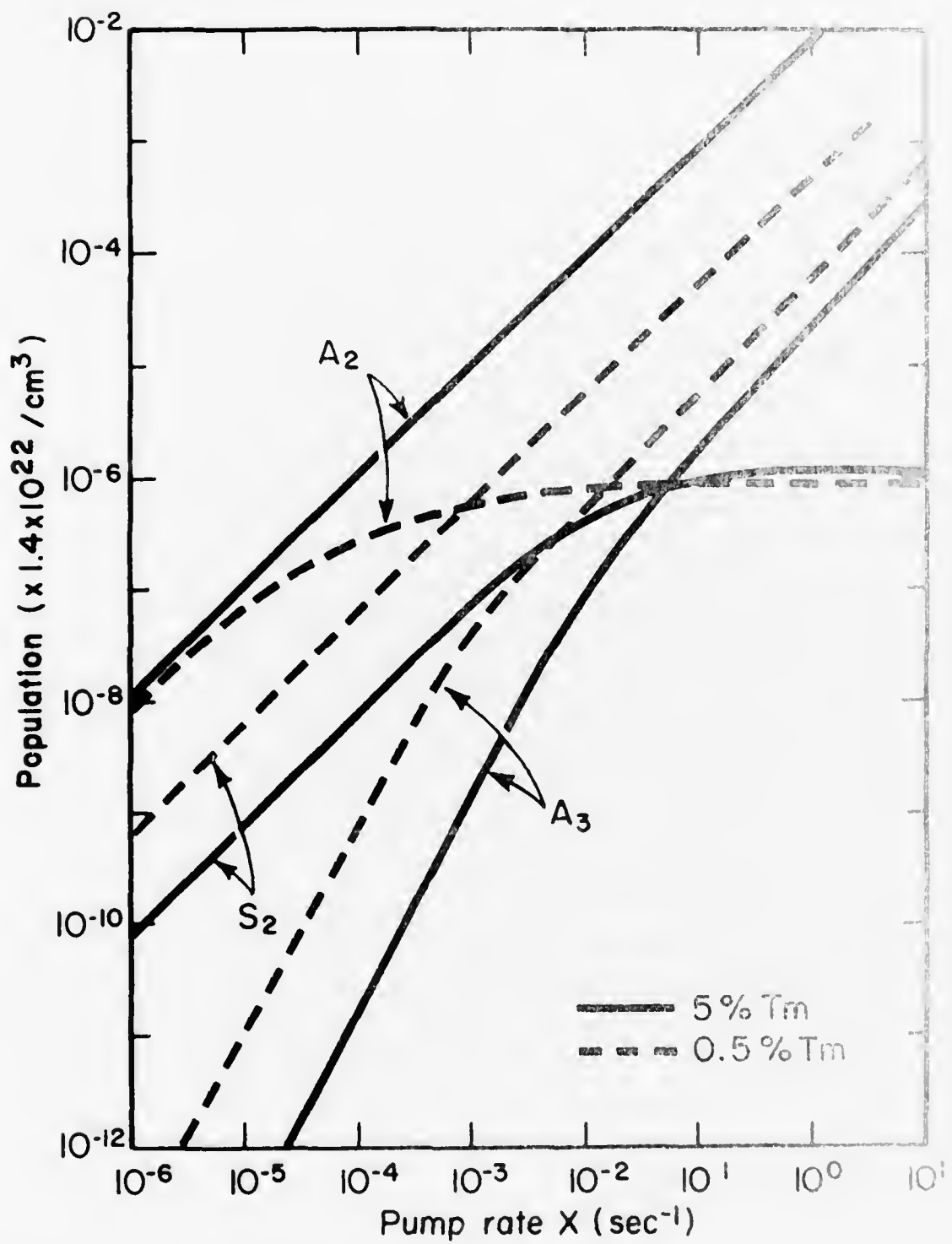


Fig. 3.4 Energy Level Populations as a Function of Pump Rate.

concentrations of 0.5% and 5%. The pump rate is the Yb^{3+} pump rate. At low pump rates ($X \sim 10^{-5} \text{ sec}^{-1}$) S_2 and A_2 increase linearly and A_3 quadratically with pump rate. This is the regime in which most spectroscopy experiments are performed. Laser operation usually requires pump rates greater than $X \approx 0.1 \text{ sec}^{-1}$; here, the populations begin to saturate, showing that laser materials which perform well in low intensity spectroscopic measurements may behave very differently under laser pumping conditions.

cw laser operation of the transition $\text{Tm } ^3\text{F}_4 \rightarrow ^3\text{H}_4$ does not appear possible. This transition requires upconversion to populate the $\text{Tm } ^3\text{F}_4$ level, since it is higher in energy than the $\text{Yb } ^2\text{F}_{5/2}$ pump level. However, the maximum pump rate obtainable with cw incoherent pump sources is on the order of $X = 1$. Figure 3.4 shows that the $\text{Tm } ^3\text{F}_4$ level (A_3) population is about $7 \times 10^{17}/\text{cm}^3$. At the available pump rates, the gain corresponding to this population is not sufficient to overcome unavoidable material and resonator losses.

The $\text{Yb } ^2\text{F}_{5/2}$ to $\text{Tm } ^3\text{H}_4$ transfer efficiency is shown in Fig. 3.5. A room temperature cw Yb-sensitized $\text{Tm } ^3\text{H}_4 \rightarrow ^3\text{H}_6$ laser would require low (0.5%) Tm concentration because it is a quasi three-level laser; however, Fig. 3.5 shows that transfer efficiency would be very small and this laser material would not work. With high Tm concentration ($> 5\%$) the transfer efficiency remains high at high pump rates. The transfer efficiency increases with increasing Tm concentration because the $\text{Yb } ^2\text{F}_{5/2}$ level is more rapidly quenched; therefore the probability of upconversion decreases. However, 5% Tm^{3+} would not be acceptable for a room temperature cw $\text{Tm } ^3\text{H}_4 \rightarrow ^3\text{H}_6$ laser because of the excessively large pump rates needed to overcome the large terminal laser level

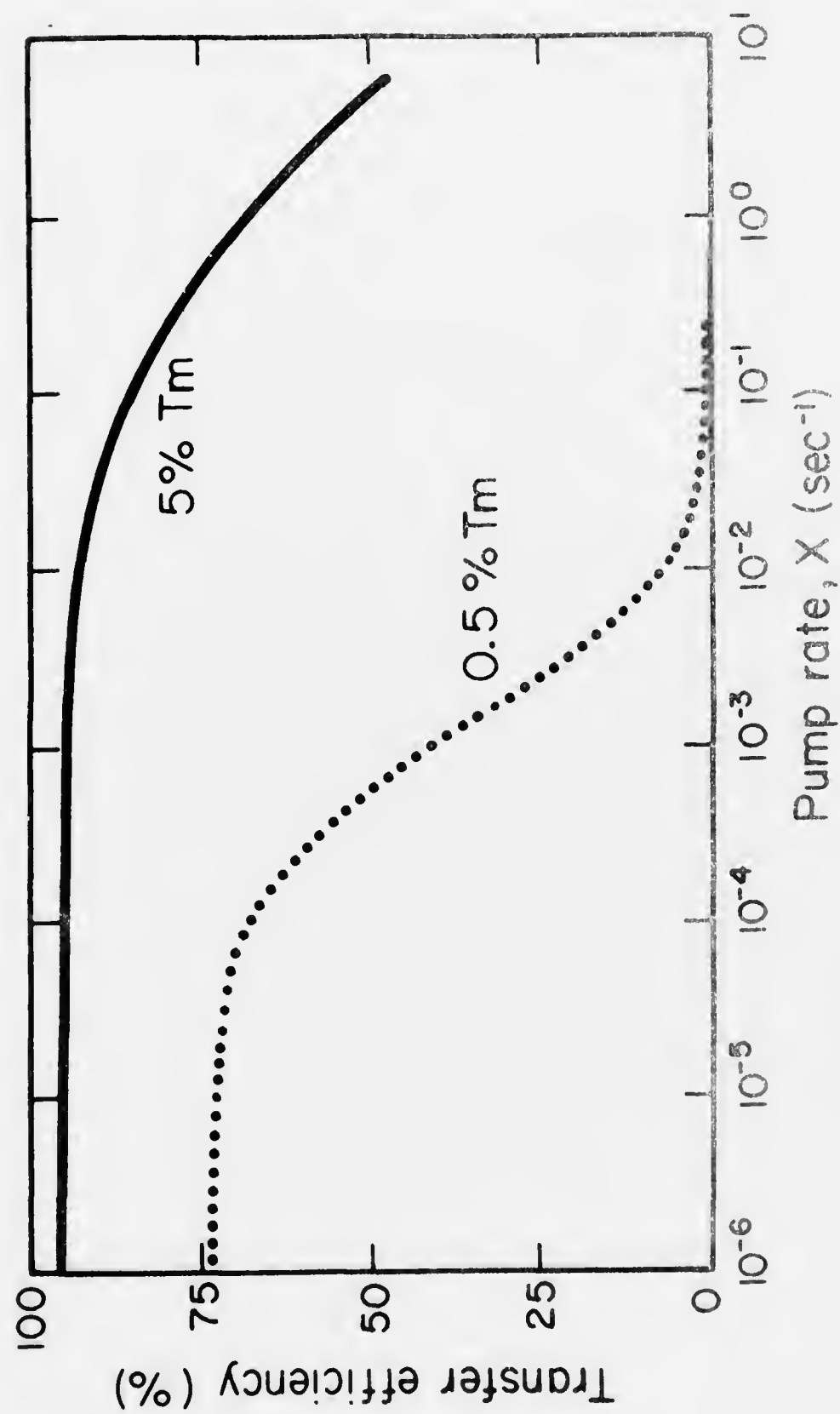


Fig. 3.5 Dependence of Transfer Efficiency on Pump Rate.

population, where the terminal laser level is an upper level in the Tm^{3+}H_6 multiplet. At reduced temperatures the terminal laser level population decreases and cw laser operation of this material appears feasible.

Use of this efficient transfer for a Ho^{3+} laser will be described in section 3.1.2. A similar upconversion process is found in the Er^{3+} - Ho^{3+} system as described in section 3.1.1. Here the reduction in transfer efficiency at high pump rates is experimentally verified.

3.1.1 Experimental Results on Er Sensitized Materials

Room temperature pulsed laser operation is easily achieved in normal $\alpha\beta$ -YLF materials such as $\text{LiY}_{0.5}\text{Er}_{0.45}\text{Tm}_{0.05}\text{F}_4:0.25\% \text{Ho}$ using xenon flashlamps as the pump source. However, for room temperature cw operation using an LED or a tungsten filament as the pump source, it initially appeared not necessary to have Tm^{3+} in the material. Furthermore, since the Tm^{3+}H_4 and Ho^{3+}I_7 multiplets lie close in energy, energy transfer between the Tm^{3+}H_4 and Ho^{3+}I_7 occurs in both directions, and at room temperature about half of the excited ions are Tm^{3+} (see section 3.2). Thus, the elimination of Tm^{3+} from the laser material would eliminate the energy stored in the Tm^{3+}H_4 levels and double the Ho^{3+}I_7 quantum efficiency. Therefore, a crystal of $\text{LiErF}_4:0.3\% \text{Ho}$ was grown for laser testing. Even though spectroscopic measurements show high transfer efficiency from Er^{3+} to the Ho^{3+}I_7 level at low intensity pumping, laser operation could not be achieved with this material, even at 77°K.

To understand this problem, experiments were performed to measure the fluorescence intensity versus pump power at the pump intensities usually needed for laser operation. Optically thin samples of

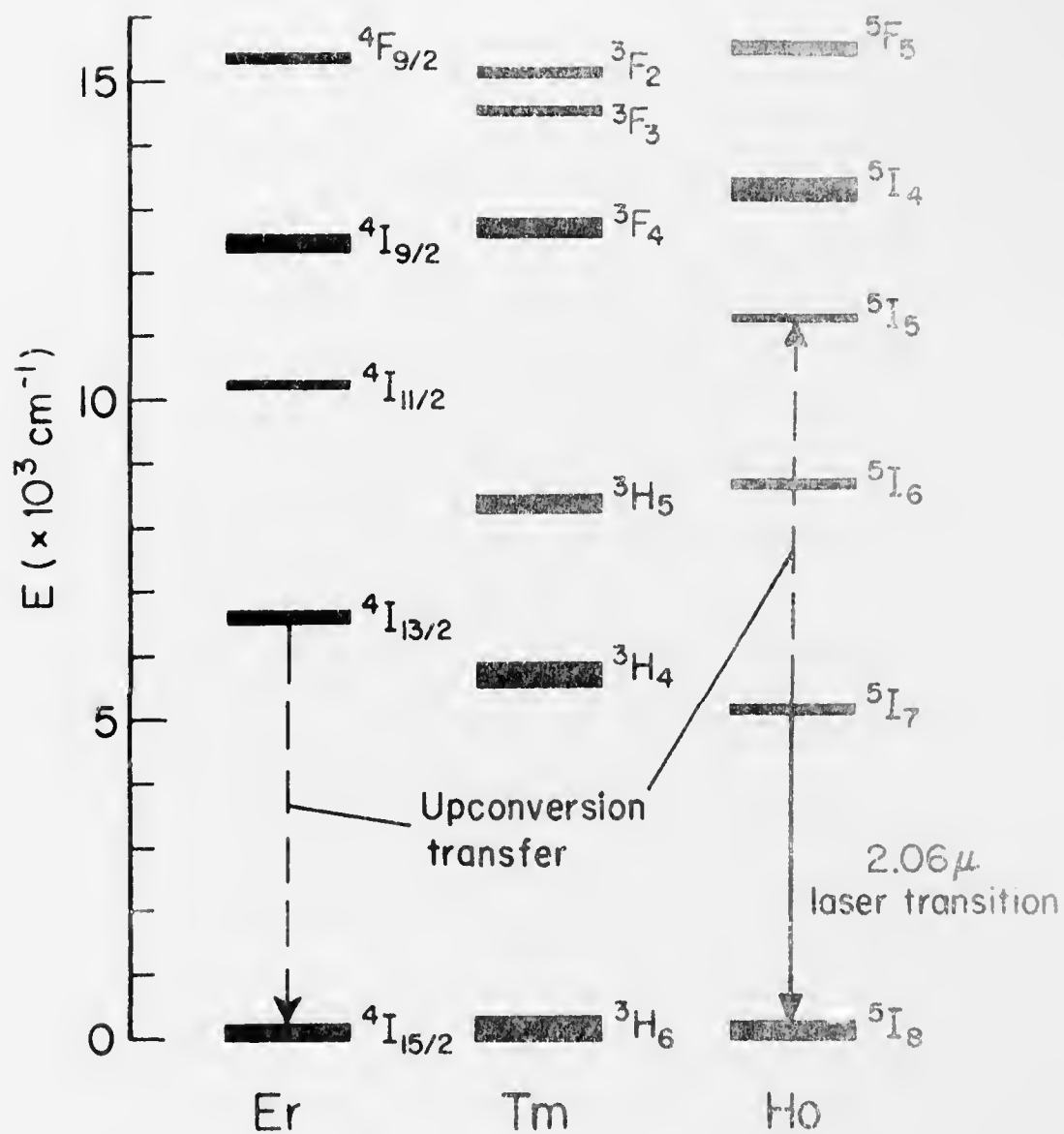
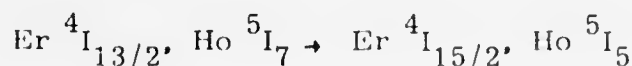


Fig. 3.6 Energy Levels of Er^{3+} , Tm^{3+} and Ho^{3+} in LiYF_4 .

LiErF_4 :0.3% Ho and $\text{LiY}_{0.5}\text{Er}_{0.45}\text{Tm}_{0.05}\text{F}_4$:0.35% Ho at room temperature were pumped at 514.5 nm with a cw argon laser. The $2\text{ }\mu\text{m}$ Ho $^5\text{I}_7$ and the $1.2\text{ }\mu\text{m}$ Ho $^5\text{I}_6$ fluorescent lines were monitored.

The Ho $^5\text{I}_7$ fluorescence intensity versus pump power for the two materials is shown in Fig. 3.7. At low pumping intensities the fluorescence is linearly proportional to pump power and the LiErF_4 :Ho fluorescence efficiency is 1.3 times that of $\alpha\beta$ -YLF. This value is expected since in $\alpha\beta$ -YLF the transfer quantum efficiency from the $\text{Er } ^4\text{S}_{3/2}$ pump level to the $\text{Tm } ^3\text{H}_4$ - Ho $^5\text{I}_7$ system is ~ 3 .¹⁶ Since half of the energy in the $\text{Tm } ^3\text{H}_4$ - Ho $^5\text{I}_7$ system is in the Ho $^5\text{I}_7$ level, the net transfer efficiency is $\sim 3/2$. The transfer quantum efficiency for LiErF_4 :Ho is ~ 2 .¹⁶ Therefore the expected fluorescence ratio is $\sim 4/3$. As the pump power is increased, the LiErF_4 :Ho fluorescence saturates at a level approximately 1/2 that needed for laser threshold. The $\alpha\beta$ -YLF fluorescence continues to increase although it also shows some decrease in transfer efficiency. The Ho $^5\text{I}_6$ fluorescence was also monitored as is shown in Fig. 3.8. At low pump intensities in the Ho $^5\text{I}_6$ fluorescence varies quadratically with pump power. This is characteristic of fluorescence arising from an upconversion process. This would be the



upconversion step. The Ho $^5\text{I}_5$ rapidly decays to the fluorescing level Ho $^5\text{I}_6$ by multiphonon emission. At higher pump powers the fluorescence varies linearly when the Ho $^5\text{I}_7$ population saturates and then saturates when essentially all of the Ho ions are excited.

This situation is very similar to LiYbF_4 :0.25% Tm which was

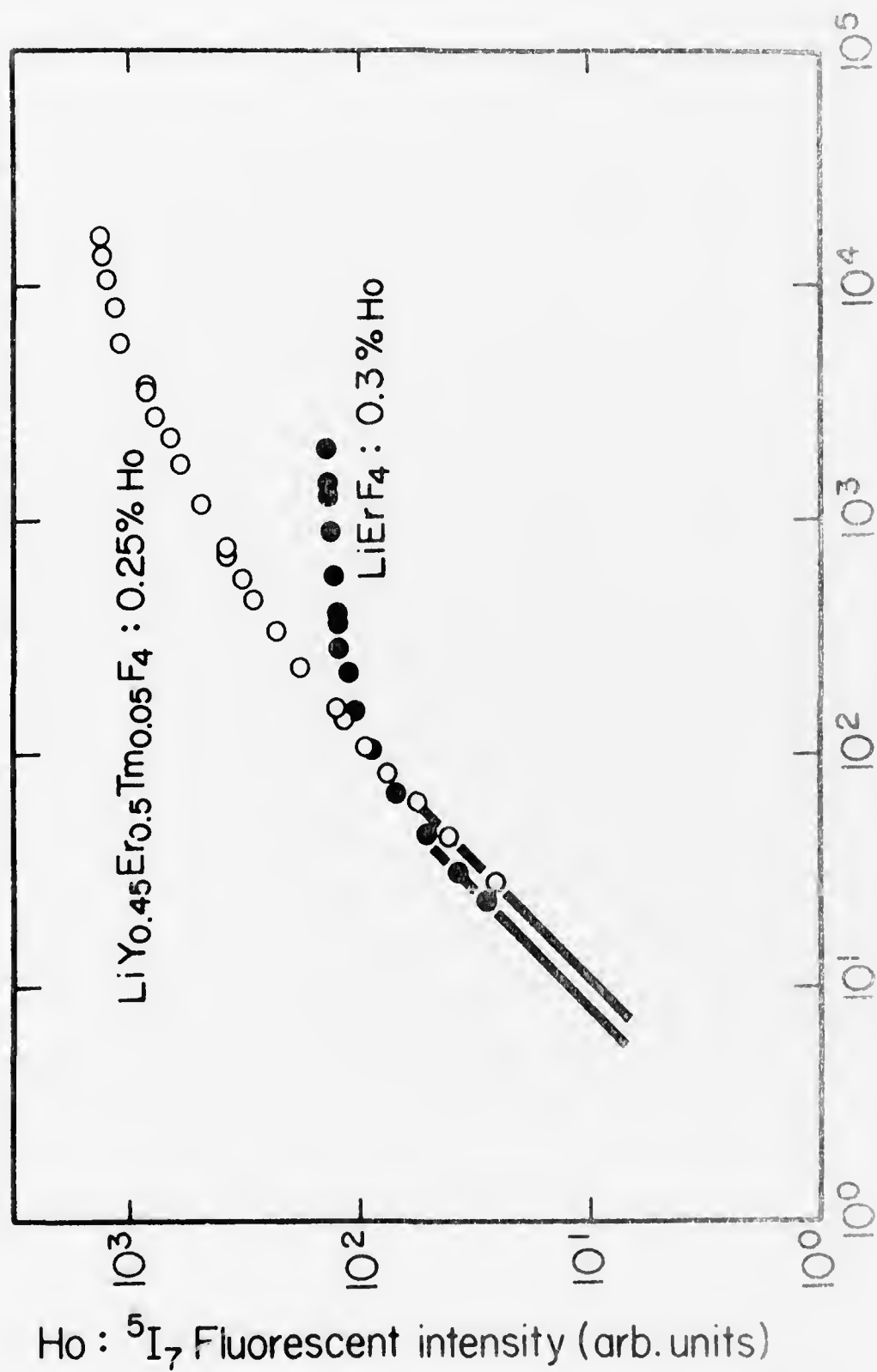


Fig. 3.7 Ho 5I_7 Fluorescence Intensity vs Pump Power Density.

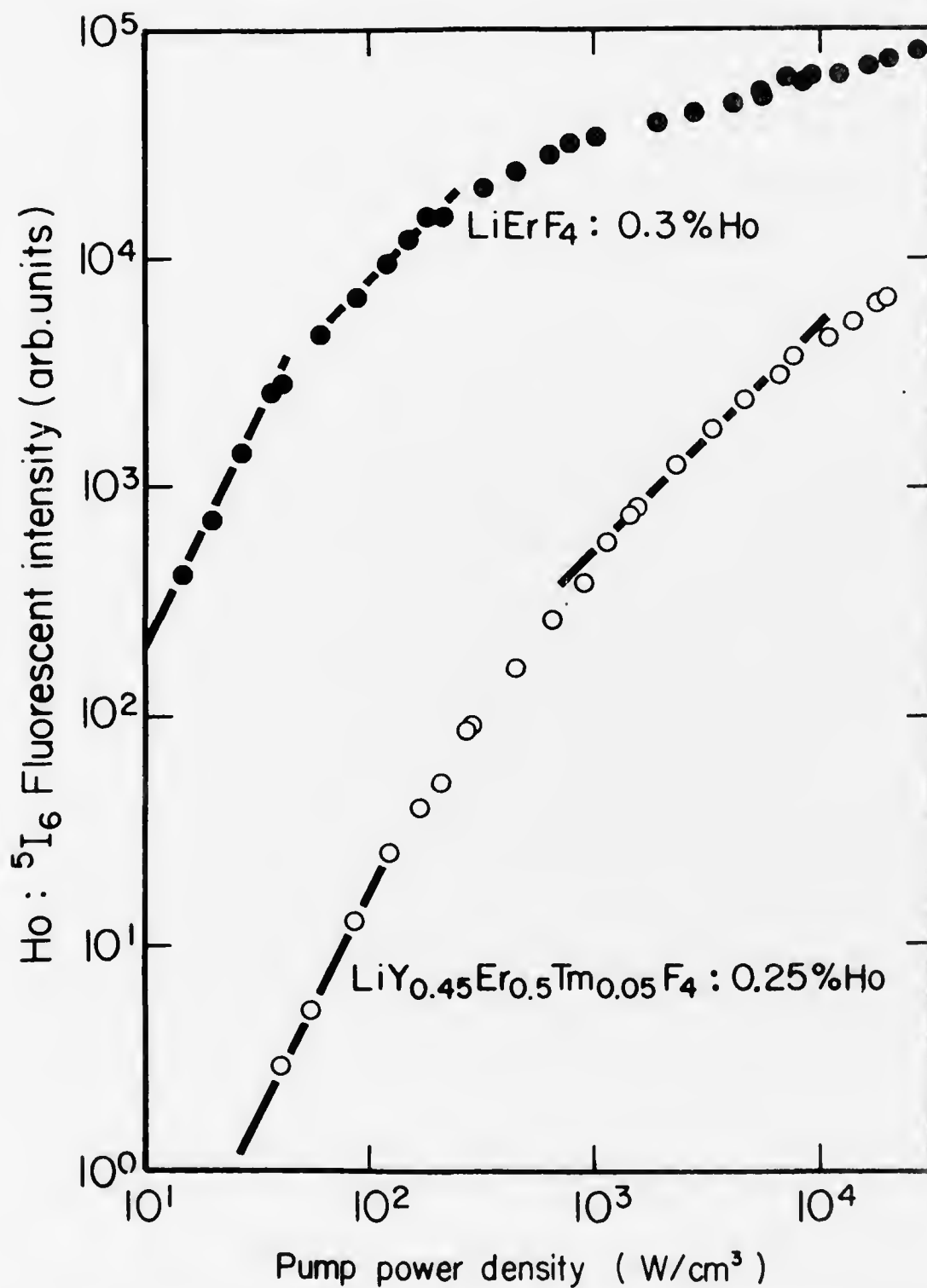


Fig. 3.8 Ho 5I_6 Fluorescence Intensity vs Pump Power Density.

modelled in section 3.1. There it was shown that upconversion can cause fluorescence saturation at a level far below that needed for laser operation. That is, the saturation in the $\text{Ho } ^5\text{I}_7$ fluorescence in $\text{LiErF}_4:0.3\% \text{ Ho}$ shown in Fig. 3.7 is similar to A_2 in Fig. 3.4, and the behavior of the $^5\text{I}_6$ fluorescence shown in Fig. 3.8 is similar to A_3 in Fig. 3.4.

The important role of Tm in Er^{3+} sensitized Ho^{3+} laser materials is now easily seen. In $\text{LiErF}_4:\text{Ho}$, energy transfer from $\text{Er } ^4\text{I}_{13/2}$ to $\text{Ho } ^5\text{I}_7$ is fast (0.8 ms) compared to the $\text{Er } ^4\text{I}_{13/2}$ (15 ms) fluorescent lifetime so that the transfer efficiency is high, but is slow compared to the transfer time in $\alpha\beta\text{-YLF}$ ($< 10 \mu\text{s}$). Tm is needed to rapidly quench the $\text{Er } ^4\text{I}_{13/2}$ level before upconversion can take place.

This upconversion step may also be limiting the performance of $\alpha\beta\text{-YLF}$, as evidenced by the following facts. When the $\text{Er } ^4\text{I}_{13/2}$ level in $\alpha\beta\text{-YLF}$ is pumped with $1.5 \mu\text{m}$ light, fluorescence is observed at $1.2 \mu\text{m}$ from the $\text{Ho } ^5\text{I}_6$ level. Also, when $\alpha\beta\text{-YLF}$ is flashlamp pumped at intensities near that needed for laser threshold, the $\text{Ho } ^5\text{I}_7$ lifetime is $\sim 7 \text{ ms}$ as compared to 13 ms at low intensity pumping. Thus the $\text{Ho } ^5\text{I}_7$ level is $\sim 50\%$ quenched, perhaps by this upconversion step. More accurate measurements of transfer rates and further system modelling are needed to fully understand this problem.

3.1.2 Experimental Results on Yb Sensitized Materials

In section 3.1 it was shown that energy transfer from the $\text{Yb } ^2\text{F}_{5/2}$ level to the $\text{Tm } ^3\text{H}_4$ level is efficient when the Tm concentration is at least 5%. Therefore a $2.06 \mu\text{m}$ Ho^{3+} laser material with composition $\text{LiYbF}_4:5\% \text{ Tm}, 0.25\% \text{ Ho}$ was chosen. A crystal with this composition was grown and successful laser operation was achieved.

In this material pump light is absorbed by Yb^{3+} and followed by rapid and efficient transfer to the $\text{Tm } ^3\text{H}_4$ level. The addition of 0.25% Ho does not alter these transfer steps since LiYbF_4 doped with 0.25% Ho alone shows slow and inefficient transfer from the $\text{Yb } ^2\text{F}_{5/2}$ to the $\text{Ho } ^5\text{I}_7$ level. Thus the $\text{Yb } ^2\text{F}_{5/2}$ to $\text{Ho } ^5\text{I}_7$ transfer must take place by way of the rapid $\text{Yb } ^2\text{F}_{5/2}$ to $\text{Tm } ^3\text{H}_4$ transfer. Finally, rapid transfer from the $\text{Tm } ^3\text{H}_4$ level to the upper laser level $\text{Ho } ^5\text{I}_7$ occurs. It will be shown in section 3.2 that the distribution of excitations in the $\text{Ho } ^5\text{I}_7 - \text{Tm } ^3\text{H}_4$ system is in thermal equilibrium, and with a Tm:Ho concentration ratio of 20:1, half of the excitations in the $\text{Ho } ^5\text{I}_7 - \text{Tm } ^3\text{H}_4$ system are in Tm at room temperature. Thus the addition of 0.25% Ho will not appreciably change the results of Fig. 3.5. That is, for the Yb pump rate needed for laser threshold of $X \approx 0.2 \text{ sec}^{-1}$, the transfer efficiency from Yb to the $\text{Tm } ^3\text{H}_4 - \text{Ho } ^5\text{I}_7$ system is at least 80% at room temperature. Therefore, room temperature cw laser operation of this material is expected when suitable pump sources, such as a high brightness LED, are available.

At reduced temperatures, much lower pump rates are needed for laser threshold, since more of the excited ions in the $\text{Ho } ^5\text{I}_7 - \text{Tm } ^3\text{H}_4$ system are in the upper laser level, as described in section 3.2. At liquid nitrogen temperature, successful laser operation of this material was achieved with a tungsten filament pump source.

The experimental details are shown in Fig. 3.9. The laser crystal was 2.0 mm long with plane parallel ends upon which evaporated silver mirrors were applied. The crystal was then mounted on the cold finger of a liquid nitrogen dewar. A linear tungsten filament was imaged onto the crystal to form an illuminated region 2.0 mm x 0.5 mm on the surface of the crystal.

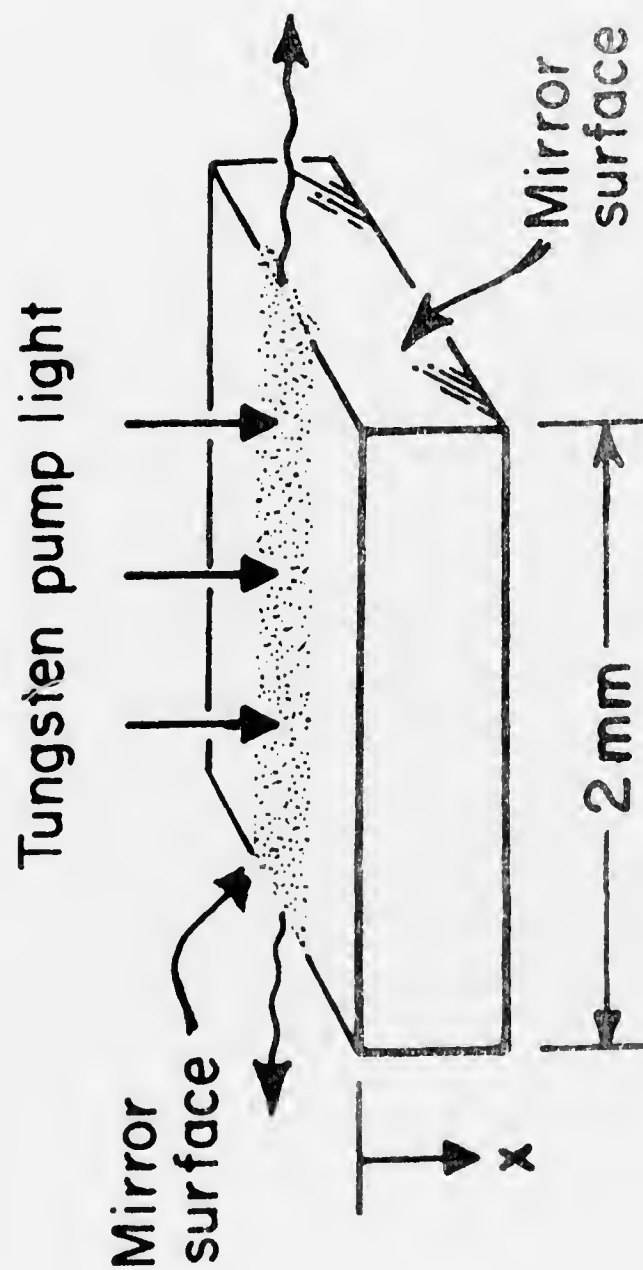


Fig. 3.9 Experimental Setup for LiYbF_4 :5% Tm, 0.25% Ho Laser.

The effective pumping power density w at a distance x into the crystal can be found from the expression

$$w(x) = \int \alpha(\lambda) e^{-\alpha(\lambda)x} \Phi(\lambda) d\lambda \quad (3.4)$$

where $\Phi(\lambda)$ is the spectral irradiance of the pump light at the crystal surface;

$\alpha(\lambda)$ is the absorption coefficient of the Yb $^2F_{5/2}$ absorption band, and the integral is taken over the entire absorption band.

The shape of the function $\Phi(\lambda)$ is just the known spectral irradiance of the tungsten pump lamp. The amplitude of $\Phi(\lambda)$ at a particular wavelength λ_0 was determined by measuring the power transmitted through an interference filter with known transmission characteristics centered at λ_0 . Thus the entire function $\Phi(\lambda)$ is determined. Equation (3.4) was numerically integrated and the effective pump power density versus distance at threshold is shown in Fig. 3.10. The accuracy of the measurement of threshold pump power density is estimated to be $\pm 20\%$. The divergence θ of the output beam was about 1° , which implies that the lasing volume was about $\frac{\lambda}{\theta} \approx 100 \mu\text{m}$ thick. From Fig. 3.6 the average pump power density in the lasing volume at threshold was $30 \pm 6 \text{ w/cm}^3$.

To see if the measured threshold pump power is a reasonable value, we can predict what it should be by making the following assumptions: (1) The temperature of the crystal is 80°K ; (2) the energy transfer quantum efficiency from Yb to Ho is unity; and (3) the reflectivity of the mirrors is 98.5%. The threshold pump power density P_{th} is given by

$$P_{th} = \frac{hc (\mathcal{L}_O + \mathcal{L}_R)}{2 \lambda_p f_u \tau \sigma L} \quad (3.5)$$

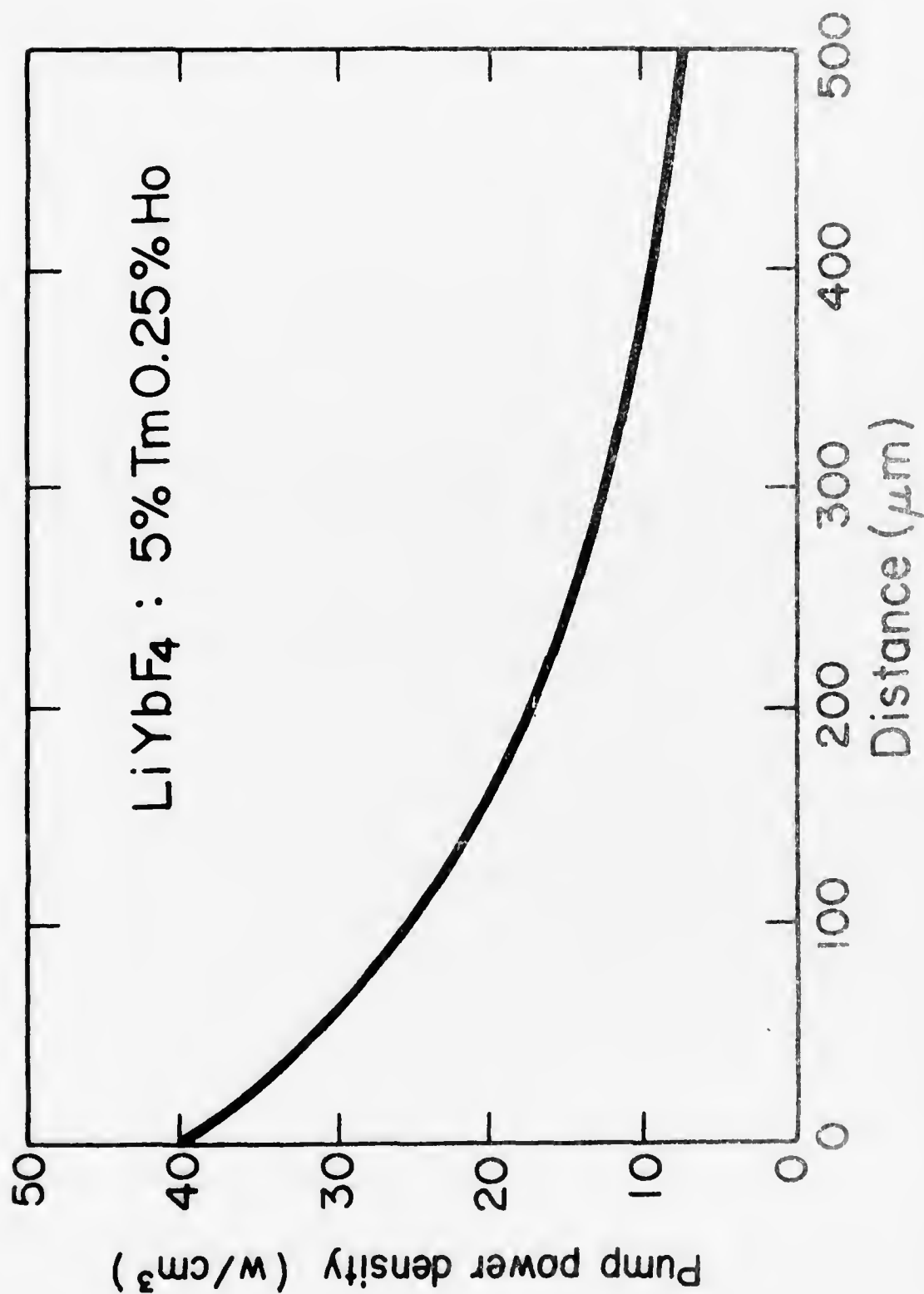


Fig. 3.10 Pump Power Density vs Distance at Threshold for a Tungsten Filament Pump Lamp.

where h is Planck's constant, c is the velocity of light, λ_p is the pump wavelength, f_u is the fraction of excited ions in the upper laser level, τ is the fluorescence lifetime of the upper laser level, σ is the stimulated emission cross section, and L is the length of the crystal. \mathcal{L}_0 is the non-resonant round trip cavity loss; assuming only mirror losses, $\mathcal{L}_0 = 2/4n \frac{1}{R}$, where R is the mirror reflectivity. \mathcal{L}_R is the resonant loss and is given by $\mathcal{L}_R = 2 \sigma N f_1 L$, where N is the concentration of lasing ions in the material and f_1 is the occupation factor of the lower laser level. For the assumptions listed above, the calculated threshold pump power density is 29 w/cm^2 , which is in good agreement with the experimental value.

3.2 Ho $^5I_7 \rightarrow$ Tm 3H_4 Energy Transfer

One of the key energy transfer steps in Ho³⁺ laser materials sensitized with Tm³⁺ and other ions such as Er³⁺, Yb³⁺, Ni²⁺, and Cr³⁺, is the Ho $^5I_7 \rightarrow$ Tm 3H_4 transfer. When the Tm concentration is greater than a few percent, energy transfer between the Ho 5I_7 and the Tm 3H_4 levels is very fast compared to the lifetimes of the multiplets. This is a resonant transfer, as can be seen from the overlap of the Tm 3H_4 fluorescent bands and the Ho 5I_7 absorption bands in Fig. 3.11. Since the transfer is resonant, it occurs in both directions with a rate perhaps 10^4 faster than the fluorescent decay rate, and a thermal equilibrium between Ho ions in the 5I_7 level and Tm ions in the 3H_4 level is reached. In order to predict laser performance of these materials, it is necessary to know: (1) what fraction of the excited ions are in the upper laser level, the lowest level in the Ho 5I_7 multiplet; (2) how this fraction varies with temperature; and (3) how it depends on the Tm and Ho

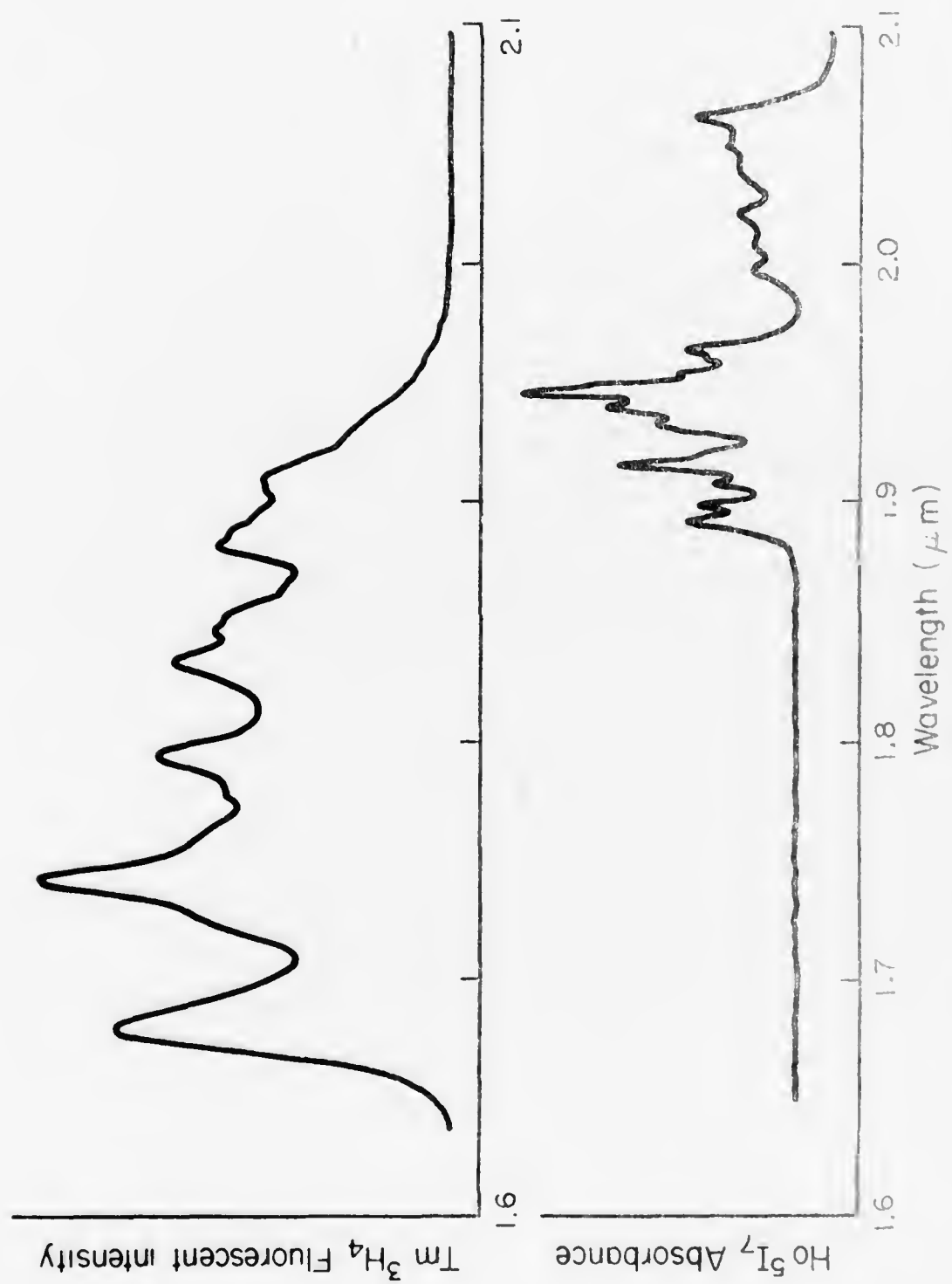


Fig. 3.11 Room temperature $\text{Ho } 5\text{I}_7$ Absorption Spectrum and $\text{Tm } 3\text{H}_4$ Fluorescence Spectrum.

concentrations in the crystal.

In order to answer these questions, it is necessary to examine the energy transfer processes in great detail. Resonant transfer processes will be considered first, although nonresonant processes also play an equally important role. Shown in Fig. 3.12 are the crystal field split energy levels of the Ho 5I_7 and 5I_8 and the Tm 3H_4 and 3H_6 multiplets in $LiYF_4$. Also shown on the energy level diagram are transitions which are resonant to within 1 cm^{-1} . Since transition linewidths are approximately 20 cm^{-1} at room temperature, there are many other resonant transitions possible at room temperature. If the Ho $^5I_7 \leftrightarrow$ Tm 3H_4 transfer was due to only one resonant transition, such as the Tm ($5605\text{ cm}^{-1} \leftrightarrow 422\text{ cm}^{-1}$) \leftrightarrow Ho ($5182\text{ cm}^{-1} \leftrightarrow 0\text{ cm}^{-1}$), the Ho $^{3+}$ to Tm $^{3+}$ transfer rate would be given by

$$W_{\text{Ho} \rightarrow \text{Tm}} = w_0 \cdot p_{422}(\text{Tm}) \cdot p_{5182}(\text{Ho})$$

where w_0 is the temperature-independent resonant transfer rate constant between the two levels, p_{422} is the probability of finding the Tm ion at the 422 cm^{-1} level, and p_{5182} is the probability of finding the Ho ion at the 5182 cm^{-1} level. The values of $p_{422}(\text{Tm})$ and $p_{5182}(\text{Ho})$ are given by the Boltzmann distribution,

$$p_{422}(\text{Tm}) = \frac{\exp(-422/kT)}{\sum_{^3H_6} \exp(-\Delta_i/kT)}$$

$$p_{5182}(\text{Ho}) = \frac{\exp(-(5182-5155)/kT)}{\sum_{^5I_7} \exp(-\Delta_j/kT)}$$

where $\Delta_{i,j}$ is equal, respectively, to the difference between the energies of each level of the 3H_6 and 5I_7 multiplets and the energies of the lowest

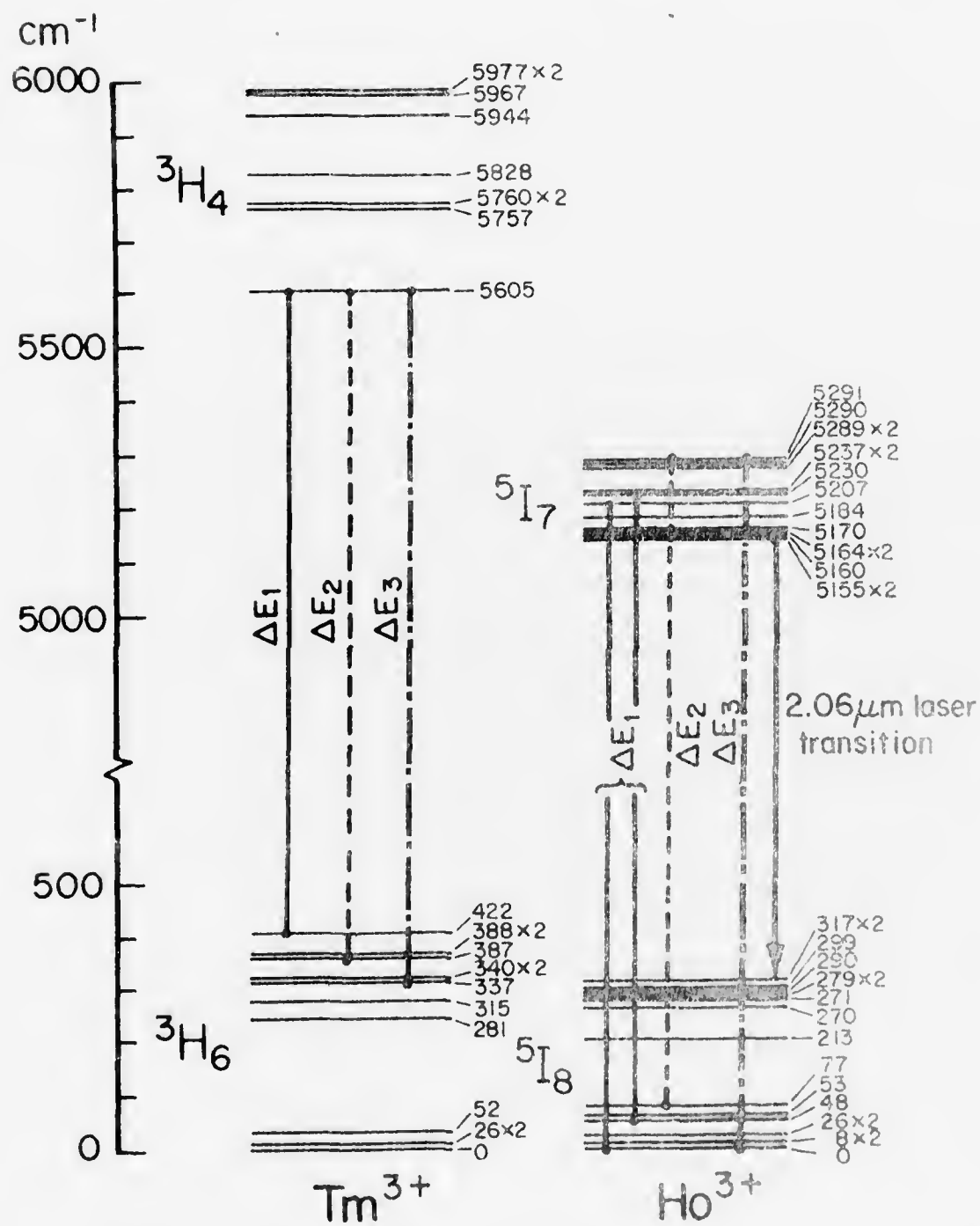


Fig. 3.12 Crystal Field Split Energy Level of $Tm^{3+} 3H_4$ and $3H_6$ and $Ho^{3+} 5I_7$ and $5I_8$ Multiplets.

levels in the 3H_6 (0 cm^{-1}) and 5I_7 (5155 cm^{-1}) multiplets, respectively. Likewise, the Tm^{3+} to Ho^{3+} transfer rate would be given by

$$W_{Tm \rightarrow Ho} = w_o \cdot P_{5605}(Tm) \cdot p_0(Ho)$$

The transfer rate constant w_o is the same for $W_{Ho \rightarrow Tm}$ and $W_{Tm \rightarrow Ho}$ since the transfer is resonant. The $p_i(Tm)$ and $p_j(Ho)$ determine the temperature dependence of the transfer rates.

Actually, there are many resonant transitions between $Ho({}^5I_7)$ and $Tm({}^3H_4)$, so the total resonant transfer rate is given by

$$W_{Tm \rightarrow Ho}^R = \sum_i w_i \cdot p_i(Tm) \cdot p_i(Ho) \quad (3.6)$$

where the sum is over all resonant transitions; likewise for $W_{Ho \rightarrow Tm}^R$.

Nonresonant transfer processes also contribute to the total $Tm \leftrightarrow Ho$ transfer. It has been shown that nonresonant transfer rates involving a small number of phonons can be as fast as resonant transfer rates.³⁵ Therefore, a sum analogous to equation (3.6) of nonresonant transfer processes must be included to find the total transfer rate.

$$W_{Tm \rightarrow Ho}^T = W_{Tm \rightarrow Ho}^R + W_{Tm \rightarrow Ho}^{NR} \quad (3.7)$$

where $W_{Tm \rightarrow Ho}^{NR}$ is a sum analogous to equation (3.6). Once $W_{Tm \rightarrow Ho}$ and $W_{Ho \rightarrow Tm}$ have been determined, the occupation factor of the upper laser level can be determined from the rate equations:

$$\frac{dN_{{}^5I_7}}{dt} = W_{Tm \rightarrow Ho} \cdot N_{{}^3H_4} - W_{Ho \rightarrow Tm} \cdot N_{{}^5I_7}$$

$$\frac{dN_{3H_4}}{dt} = W_{Ho \rightarrow Tm} \cdot N_{5I_7} - W_{Tm \rightarrow Ho} \cdot N_{3H_4}$$

The steady state solution is then

$$\frac{N_{5I_7}}{N_{3H_4}} = \frac{W_{Tm \rightarrow Ho}}{W_{Ho \rightarrow Tm}}$$

Although the above analysis is important for understanding how energy is transferred between the Ho^{3+} and Tm^{3+} ions, the actual determination of transfer rates by this method is not feasible. Since there are a large number of transfer processes in equation (3.7) and the transfer time is much faster than the lifetimes of the multiplets, the use of a thermal distribution to describe the populations of the levels of the combined $Ho^{5I_7} - Tm^{3H_4}$ system is justified. As a first order approximation, which appears to fit the experimental data, a Boltzmann distribution is used. The total number of states per unit volume available to the excitation energy in the $Ho^{5I_7} - Tm^{3H_4}$ system is $15 N_{Ho} + 9 N_{Tm}$, where 15 is the number of states in the Ho^{5I_7} multiplet, 9 is the number of states in the Tm^{3H_4} multiplet, and N_{Ho} and N_{Tm} are the concentrations of Ho and Tm, respectively, in the crystal. Then the partition function for the $Ho^{5I_7} - Tm^{3H_4}$ system is

$$Z = N_{Ho} \cdot \sum_{5I_7} e^{-\frac{E_i - E_0}{kT}} + N_{Tm} \cdot \sum_{3H_4} e^{-\frac{E_i - E_0}{kT}} \quad (3.8)$$

where E_0 is the energy of the lowest level in the $Ho^{5I_7} - Tm^{3H_4}$ system.

which is the lowest level of the Ho 5I_7 multiplet and the upper laser level for the 2.06 μm laser transition. Then the fraction of ions in the Ho 5I_7 - Tm 3H_4 system that are in the upper laser level or the occupation factor for the upper laser level f_u is

$$f_u = \frac{N_{\text{Ho}}}{Z} = \frac{1}{\sum_{^5I_7} e^{-\frac{(E_i - E_o)}{kT}} + \left(\frac{N_{\text{Tm}}}{N_{\text{Ho}}}\right) \sum_{^3H_4} e^{-\frac{(E_i - E_o)}{kT}}} \quad (3.9)$$

Likewise, the fraction of excited ions that are Ho $^{3+}$ is

$$f_{\text{Ho}} = \frac{N_{\text{Ho}} \cdot \sum_{^5I_7} e^{-\frac{(E_i - E_o)}{kT}}}{Z} \quad (3.10)$$

The fraction of Ho ions in the lower laser level (E_L) is given by the Boltzmann distribution describing the 5I_8 multiplet

$$f_L = \frac{e^{-E_L/kT}}{\sum_{^5I_8} e^{-E_i/kT}} \quad (3.11)$$

The two occupation factors f_u and f_L are plotted in Fig. 3.13 as a function of temperature. Neglecting loss, laser threshold requires that the number of ions in the upper laser level equal the number of ions in the lower laser level. That is, the number of excited ions (N_{ex}) needed in the Ho 5I_7 - Tm 3H_4 system for laser threshold is

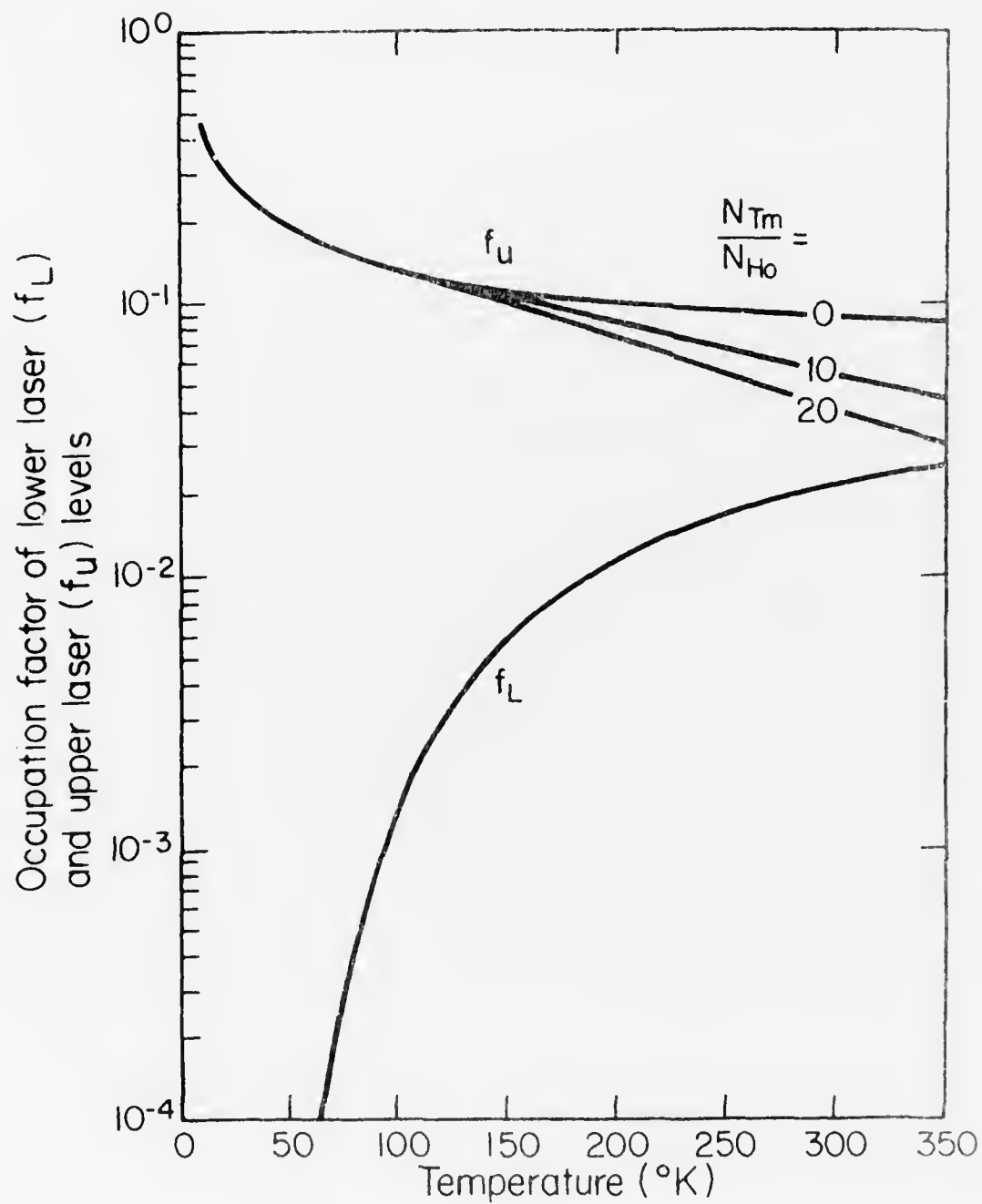


Fig. 3.13 Occupation Factor of Upper and Lower Laser Levels vs Temperature.

$$f_u N_{ex} - f_L (N_{Ho} - f_{Ho} N_{ex}) = 0. \quad (3.12)$$

Therefore, threshold requires

$$\frac{N_{ex}}{N_{Ho}} = \frac{f_L}{f_u + f_L \cdot f_{Ho}} \quad (3.13)$$

The results of this calculation as a function of temperature are shown in Fig. 3.14 for $(N_{Tm}/N_{Ho}) = 20$ and $N_{Tm} = 0$. This shows that at 300°K in a crystal with $N_{Tm}/N_{Ho} = 20$, about half of the excited ions are Tm. Resonator loss \mathcal{L} will require additional excited ions ΔN_{ex} to obtain laser threshold

$$\Delta N_{ex} = \frac{\ln(\mathcal{L})}{\sigma \cdot f_u \cdot L} \quad (3.14)$$

where σ is the emission cross section and L is the length of the gain media (see equation (3.5)).

The approximate distribution function in equation (3.9) is extremely useful in calculating laser thresholds from the threshold equation (equation (3.13)). To see if equation (3.9) adequately describes the Ho 5I_7 - Tm 3H_4 distribution, the fluorescence branching ratio of the 2.06 μ m laser transition line was measured, and laser threshold was measured as a function of temperature.

The fluorescence spectra of the Ho 5I_7 and Tm 3H_4 levels in LiYb_{0.95}Tm_{0.05}F₄:0.25% Ho were measured as a function of temperature; examples for several temperatures are shown in Fig. 3.15. From this, the 2.06 μ m fluorescence branching ratio β as a function of temperature was determined; this ratio is defined as

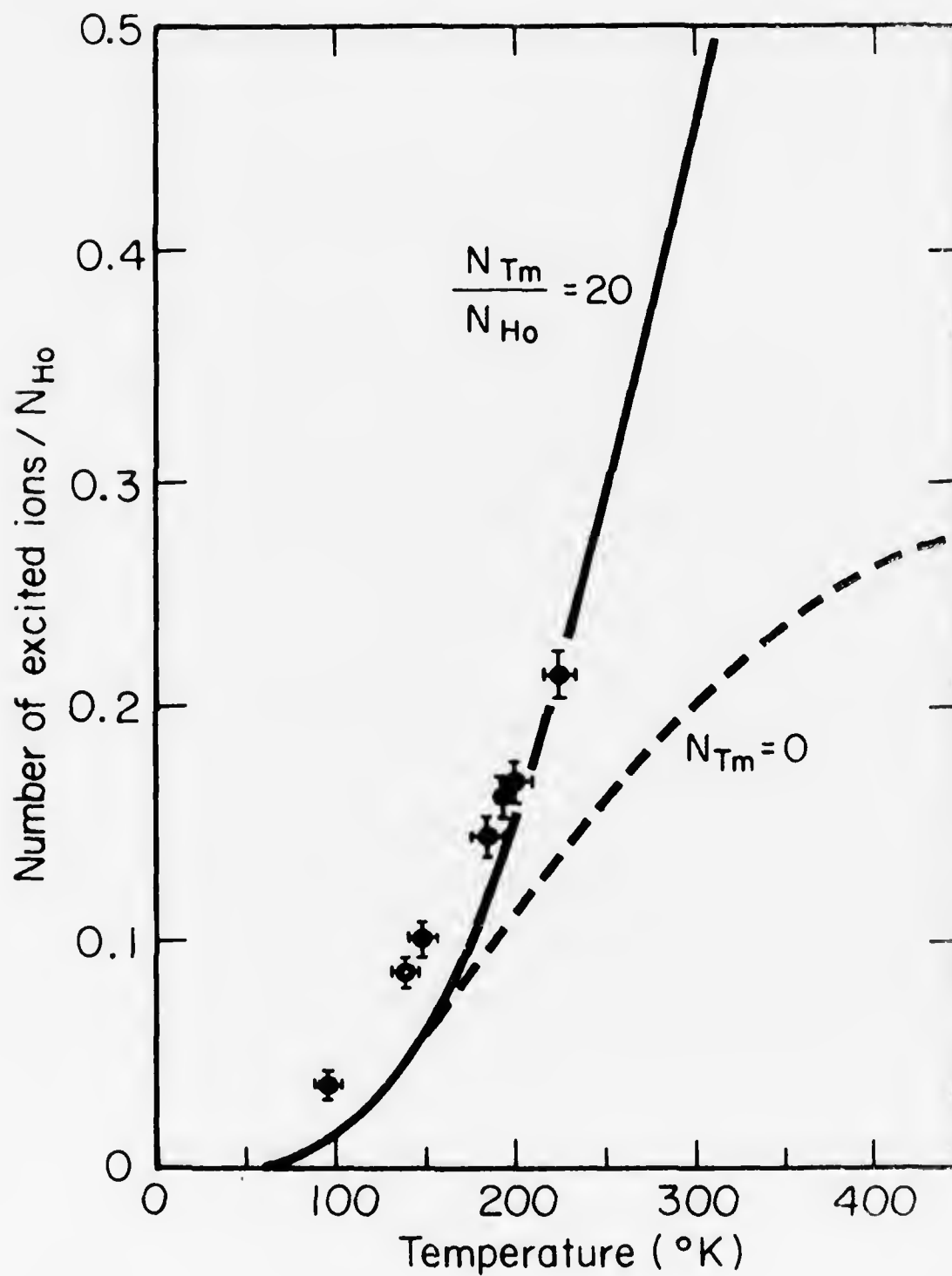


Fig. 3.14 Threshold Population in Ho $^5\text{I}_7$ - Tm $^3\text{H}_4$ Levels vs Temperature.

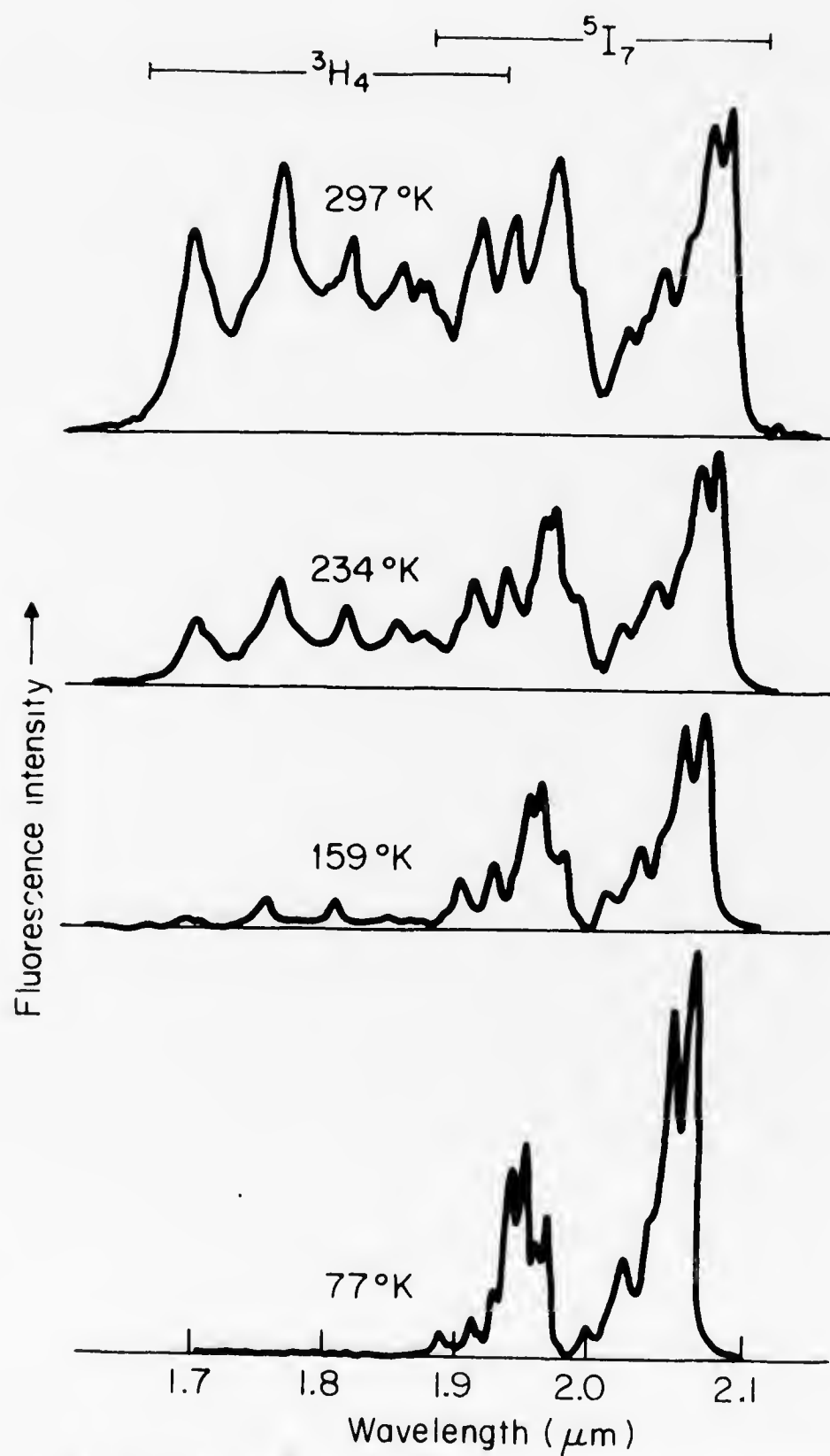


Fig. 3.15 $\text{Ho } ^5\text{I}_7 - \text{Tm } ^3\text{H}_4$ Fluorescence Spectrum vs Temperature.

$$\beta = \frac{\int_{2.06 \mu\text{m}} I(\lambda) d\lambda}{\int_{5I_7 + 3H_4} I(\lambda) d\lambda} \quad (3.15)$$

where $I(\lambda)$ is fluorescence intensity, the integral in the numerator is over the $2.06 \mu\text{m}$ fluorescent line, and the integral in the denominator is over the entire fluorescent spectrum. The branching ratio is plotted in Fig. 3.16 along with the occupation factor of the upper laser level as determined from equation (3.9). It can be seen that $\beta \propto f_u$.

Laser measurements on $\alpha\beta$ -YLF laser material were made in order to verify the temperature dependence of laser threshold as predicted by equation (3.13). In this experiment a $\frac{1}{2}$ -mm thick sample of $\alpha\beta$ -YLF with composition $\text{LiY}_{0.45}\text{Er}_{0.5}\text{Tm}_{0.05}\text{F}_4:0.25\% \text{Ho}$ was pumped with a krypton ion laser (6471 \AA) in a resonator formed by two maximum reflectivity mirrors as described in section 2.3. The resonator loss was estimated to be less than 0.5%. The measured laser threshold for the $\alpha\beta$ -YLF material versus temperature is shown in Fig. 3.14. Since the thermal resistance from active volume of the crystal to the copper block was high in this experiment, the rise in temperature from that measured at the copper block was large and was estimated to be 6°K per milliwatt of absorbed pump power. The temperature shown by the data points are the estimated temperatures in the lasing volume of the crystal. It can be seen that the experimental data agrees reasonably well with the laser threshold predicted by equation (3.13).

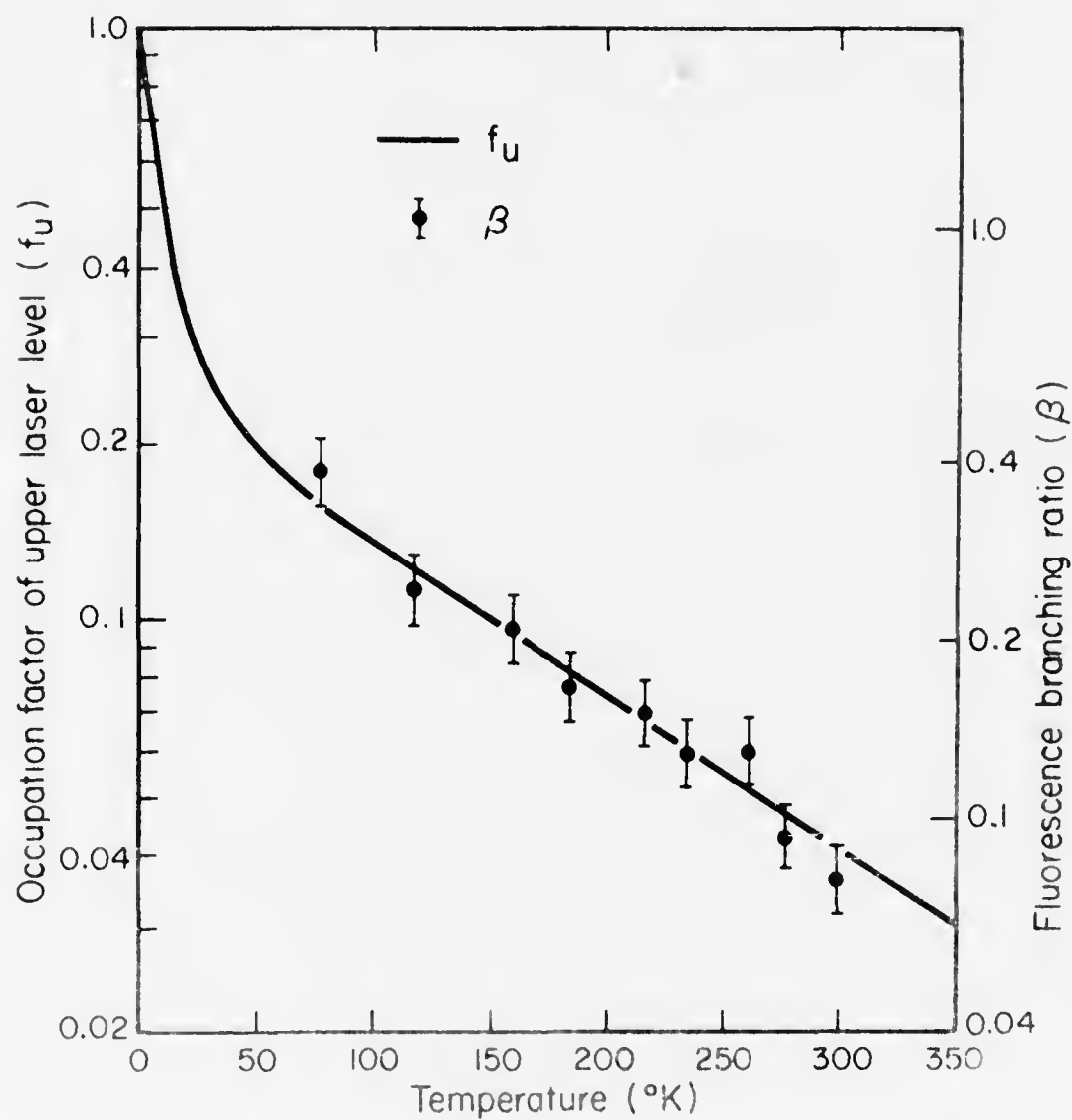


Fig. 3.16 2.06 μm Fluorescence Branching Ratio and Occupation Factor of Upper Laser Level vs Temperature.

CHAPTER 1

USE OF SENSITIZED MATERIALS FOR MINIATURE LASERS

Miniature rare earth lasers are potentially important as laser sources for fiber optic communications and integrated optical circuits.^{22, 23} In order to make an efficient miniature rare earth laser, it is necessary to have a large absorption coefficient at the pumping wavelengths. Typically, the largest peak absorption coefficient for a useful intra $4f^N$ pumping transition in "100% doped" rare earth crystals is about $\alpha = 100 \text{ cm}^{-1}$. Therefore a miniature laser might have a typical dimension of $1/\alpha = 100 \mu\text{m}$ in the pumping direction. "100% doped" rare earth materials do not always work. For example, with $1.06 \mu\text{m}$ Nd^{3+} laser materials, as the Nd^{3+} concentration is increased and the Nd^{3+} - Nd^{3+} ion separation decreases, ion pair energy transfer occurs, which depopulates or quenches the upper laser level. For most laser hosts such as $\text{Y}_3\text{Al}_5\text{O}_{12}$ (YAG) and LiYF_4 , this occurs at a Nd^{3+} doping of about 2%. Only in special hosts, where the rare earth sites are well separated and therefore have low site density, does 100% doping work as in $\text{NdP}_5\text{O}_{14}$.²⁴ For example, cw operation of a waveguide laser consisting of a crystalline fiber of $\text{Nd}_{0.5}\text{La}_{0.5}\text{P}_5\text{O}_{14}$, $12 \times 12 \mu\text{m}$ in cross section and 0.68 mm in length, has been reported using a laser as the pump source.²⁵ Nd^{3+} materials have the disadvantage that pump absorption bands are usually narrow and pumping with incoherent sources is relatively inefficient. However, sensitized materials have the advantage that "100% doping" of the sensitizer ions is allowed in most crystal hosts and sensitizer ions can be picked to match the pump source. This will be discussed in the first part of this chapter. In the second

part of this chapter a novel miniature laser resonator which is compatible with thin film waveguides is discussed.

4.1 Sensitized Laser Materials and Pump Sources

When designing a sensitized laser material, it is usually necessary to take into consideration the spectral characteristics of the pump source. Examples of possible sensitizers for the $2.06 \mu\text{m}$ Ho^{3+} laser are Er^{3+} , Yb^{3+} , Ni^{2+} , and Cr^{3+} . Er^{3+} has a very strong absorption band at $1.5 \mu\text{m}$, which is near the peak output of a 3200°K tungsten filament; it also has many absorption bands in the visible and near ultraviolet which are efficiently pumped with a xenon flashlamp. Yb^{3+} has a broad absorption band centered at $0.96 \mu\text{m}$, which matches the emission of a Si-doped GaAs LED. Ni^{2+} and Cr^{3+} have very broad absorption bands in the visible and near infrared and are, therefore, potentially efficient sensitizers for pumping with a tungsten filament or an LED.

Optically pumping Yb^{3+} sensitized laser materials with light-emitting diodes is potentially very efficient since the diode's emission can be matched to the broad Yb^{3+} absorption band shown in Fig. 4.1. Also shown in Fig. 4.1 is the emission spectra of a Si-doped GaAs LED. Peak emission is at 967 nm and the full width at half maximum is 600 nm . To find the effective absorption coefficient for LED pumping of LiYbF_4 , equation 3.4 can be solved where $\Phi(\lambda)$ is the LED spectral irradiance. The effective absorption coefficient $\alpha_{\text{eff}}(x)$ is defined such that the pump power density $W(x)$ at a distance x into the crystal is given by the expression $W(x) = \alpha_{\text{eff}}(x) \cdot I$, where I is the pump intensity at the surface of the crystal. The results are shown in Fig. 4.2. Since the peak diode emission shifts with temperature and Si concentrations, it is important to know how the effective absorption coefficient varies. This

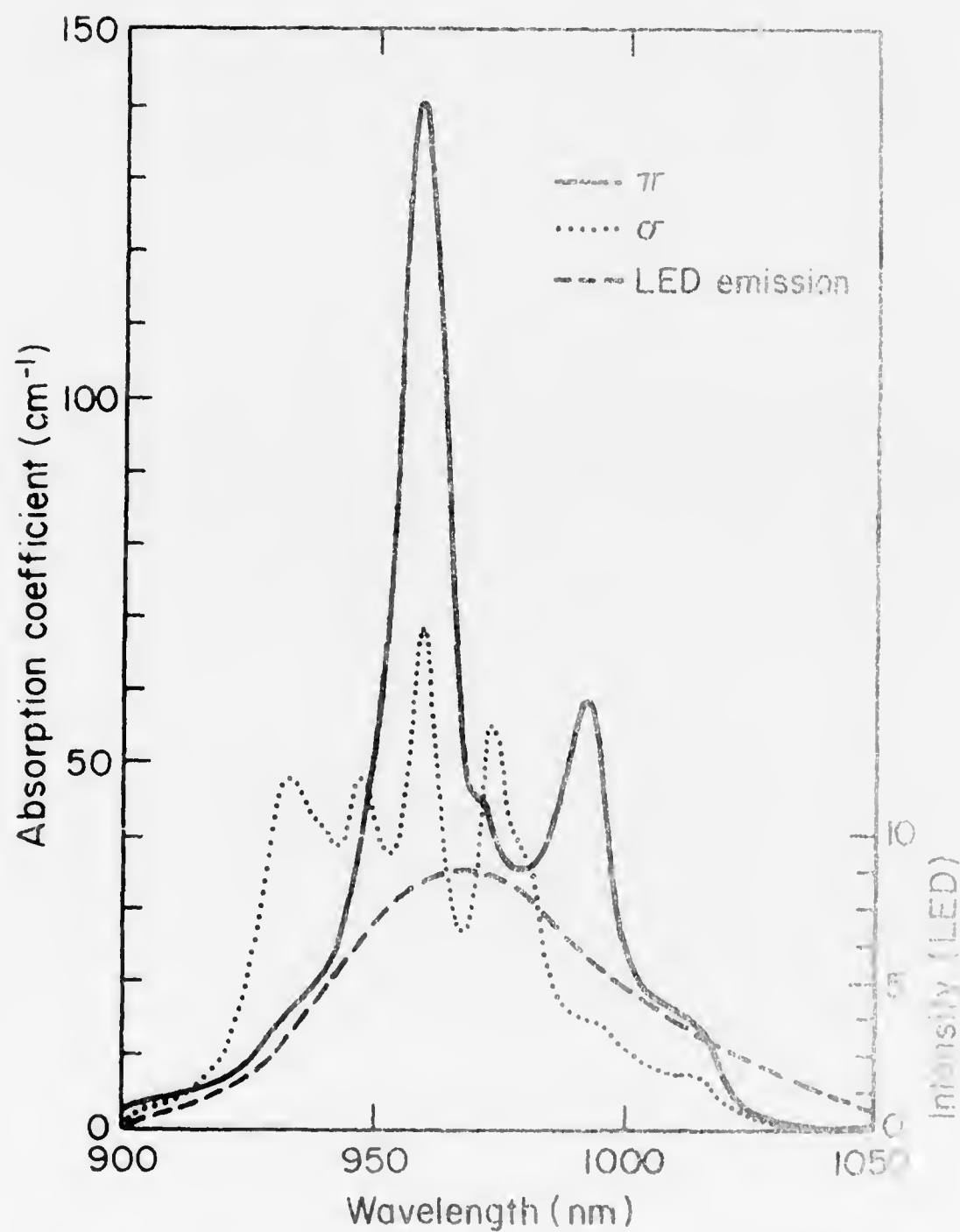


Fig. 4.1 Room Temperature Absorption Spectrum of LiYbF_4 and Typical LED Emission Spectrum.

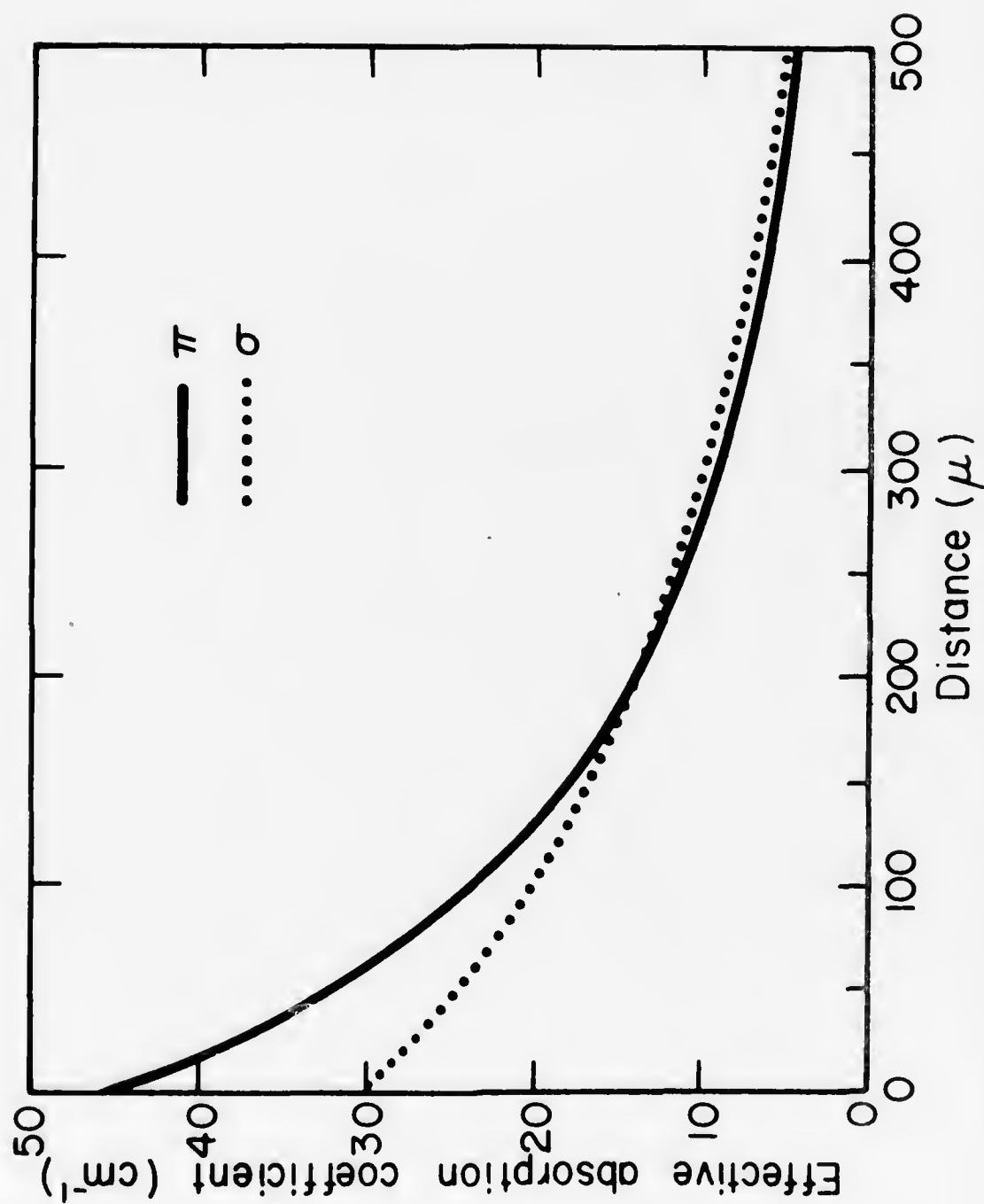


Fig. 4.2 Effective Absorption Coefficient vs Distance for LiYbF₄ when Pumped by a LED at 3000K.

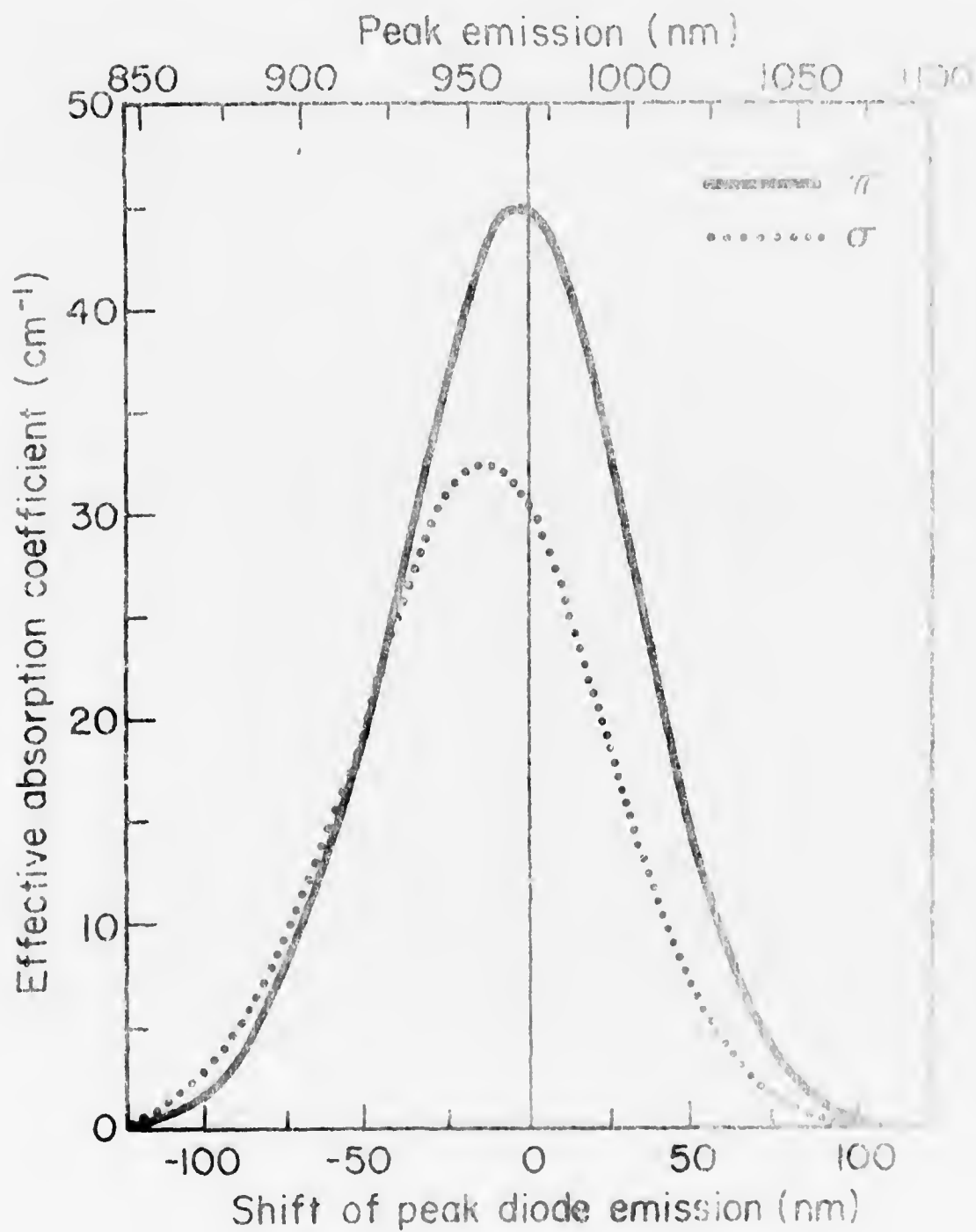


Fig. 4.3 Effective Absorption Coefficient vs Shift of Peak Diode Emission.

is shown in Fig. 4.3.

In the experiment described in section 3.1.2, a threshold pump power density of 35 w/cm^3 was required. Reference to Fig. 4.2 and the use of the average of the σ and π absorption coefficients shows that this threshold pump power would require 1 w/cm^2 flux from an LED. This is not a severe requirement. Since at liquid nitrogen temperatures the laser threshold is determined mainly by resonator losses, a much lower threshold would be expected with higher quality mirrors.

At room temperature, laser threshold is determined mainly by resonant loss of the large terminal level population. For room temperature LED pumped laser operation of LiYbF_4 :5% Tm, 0.25% Ho, the threshold pump power can be calculated from equation 3.5. Neglecting resonator losses, 280 w/cm^3 is needed for threshold. This will require 8.0 w/cm^2 flux from an LED.

4.2 Internal Reflection Resonator

A necessary element of a laser is the resonant cavity. As a laser source for integrated optics, the resonator should allow single mode operation and easy coupling to thin film waveguides. One resonator configuration is the one-dimensional Fabry-Perot type, where a miniature rod or fiber has mirrors coated on the two ends. A laser of this type would have to be coupled to a thin film waveguide by a prism or grating coupler. For miniature lasers, another type of resonator may be more attractive. Here light is confined to the cavity by total internal reflection in two dimensions. The evanescent field associated with total internal reflection can be used to couple to an output structure, as shown schematically in Fig. 4.4.

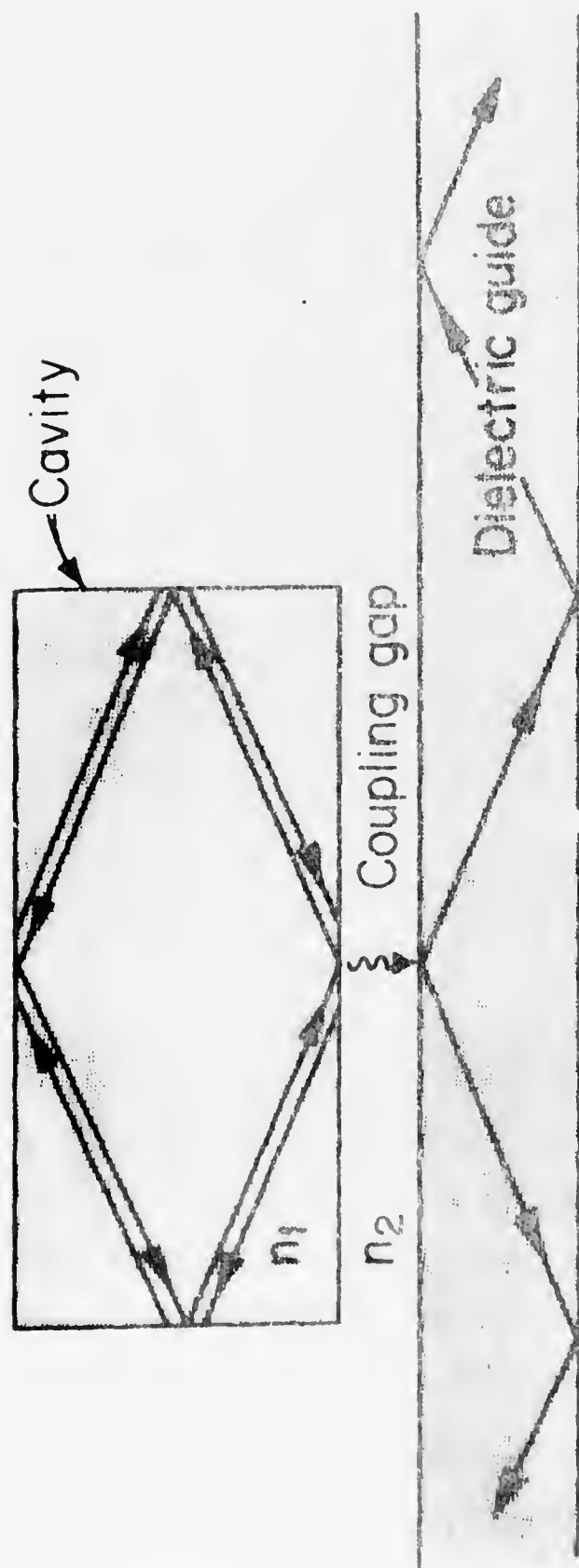


Fig. 4.4 Schematic of Internal Reflection Resonator.

4.2.1 Modes of Internal Reflection Resonator

In the absence of the waveguide shown in Fig. 4.4 the resonator is closed on four sides by total internal reflecting dielectric boundaries and open on the other two sides. It is shown in Appendix 1 that, in a rectangular crystal, the condition for total internal reflection modes to exist is $n_1 > \sqrt{2} n_2$, where n_1 is the refractive index of the crystal and n_2 is the index of the surrounding medium. This is equivalent to requiring that the critical angle for total internal reflection θ_c is less than 45° . This can be seen by considering a ray reflecting off the faces of the resonator. A ray reflected off a face at an angle θ will reflect off an orthogonal face at an angle $90^\circ - \theta$. For the ray to be totally reflected inside the resonator the conditions $\theta > \theta_c$ and $90^\circ - \theta > \theta_c$ must be met. From this it follows that $\theta_c < 45^\circ$. Figure 4.5 shows the region of k-space available for internal reflection modes in a rectangular crystal of LiYF_4 (n_1) in vacuum (n_2). The index of refraction of LiYF_4 is given in Appendix 2. The angle $\delta\theta$ (see Appendix 1) is given by

$$\delta\theta = 90^\circ - 2 \sin^{-1} (n_2/n_1) \quad (4.1)$$

which for $n_1 = n_e$ is 3.4° . It will be shown in section 4.2.3 that diffraction losses can limit the propagation vector to the x-z plane, so that a two-dimensional analysis of the resonator modes is adequate.

When the laser wavelength and the fluorescent linewidth of the resonator material are taken into account, the allowed modes are further reduced to the small region of k-space shown in Fig. 4.6. Here $k_0 = 2\pi n_1/\lambda$ where λ is the laser wavelength and Δk is the fluorescent linewidth. The allowed modes form a two-dimensional grid of points in k-space with spacing approximately π/a in k_x and π/b in k_z (see

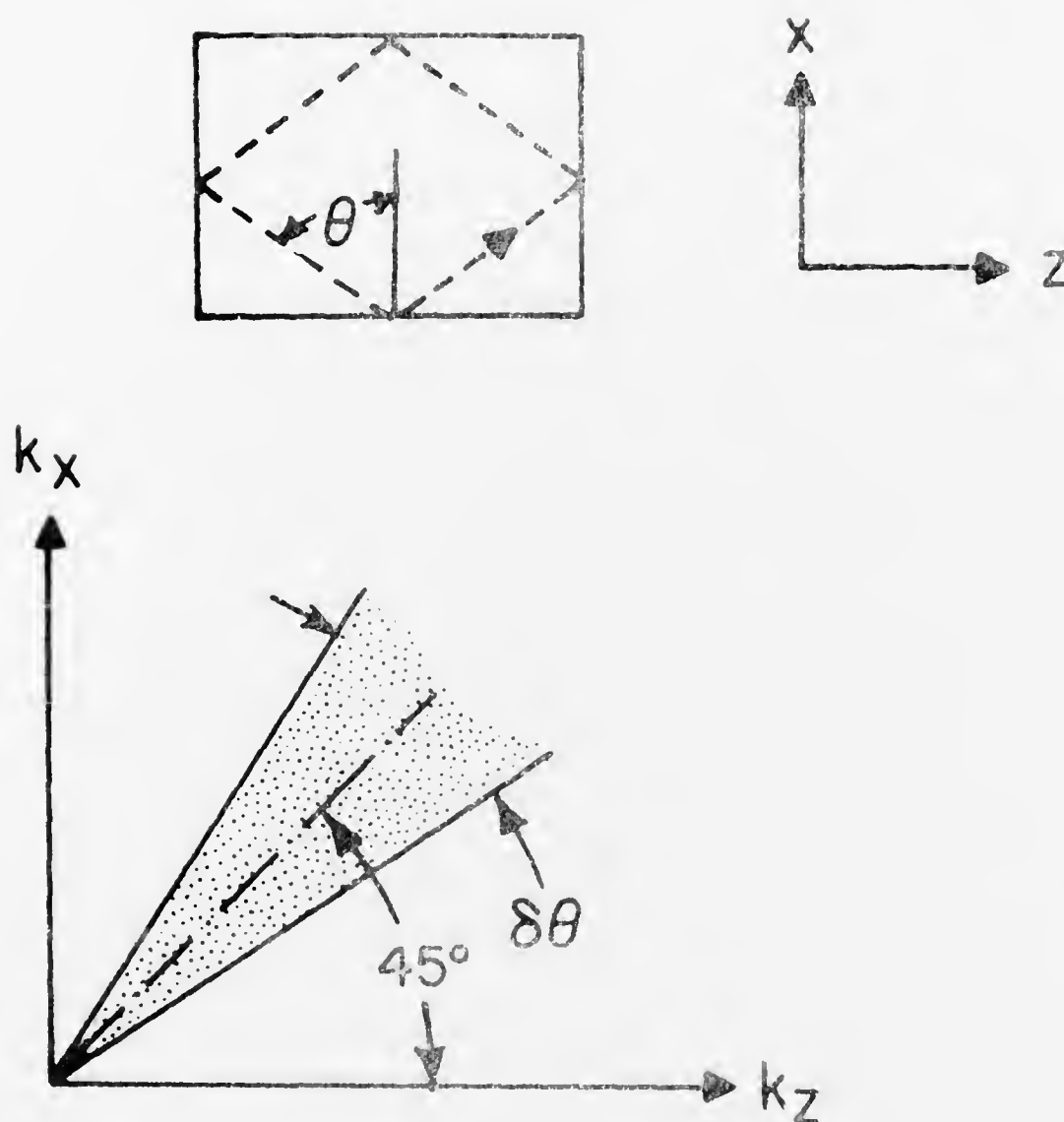


Fig. 4.5 Region of k -space Available for Total Internal Reflection Modes.

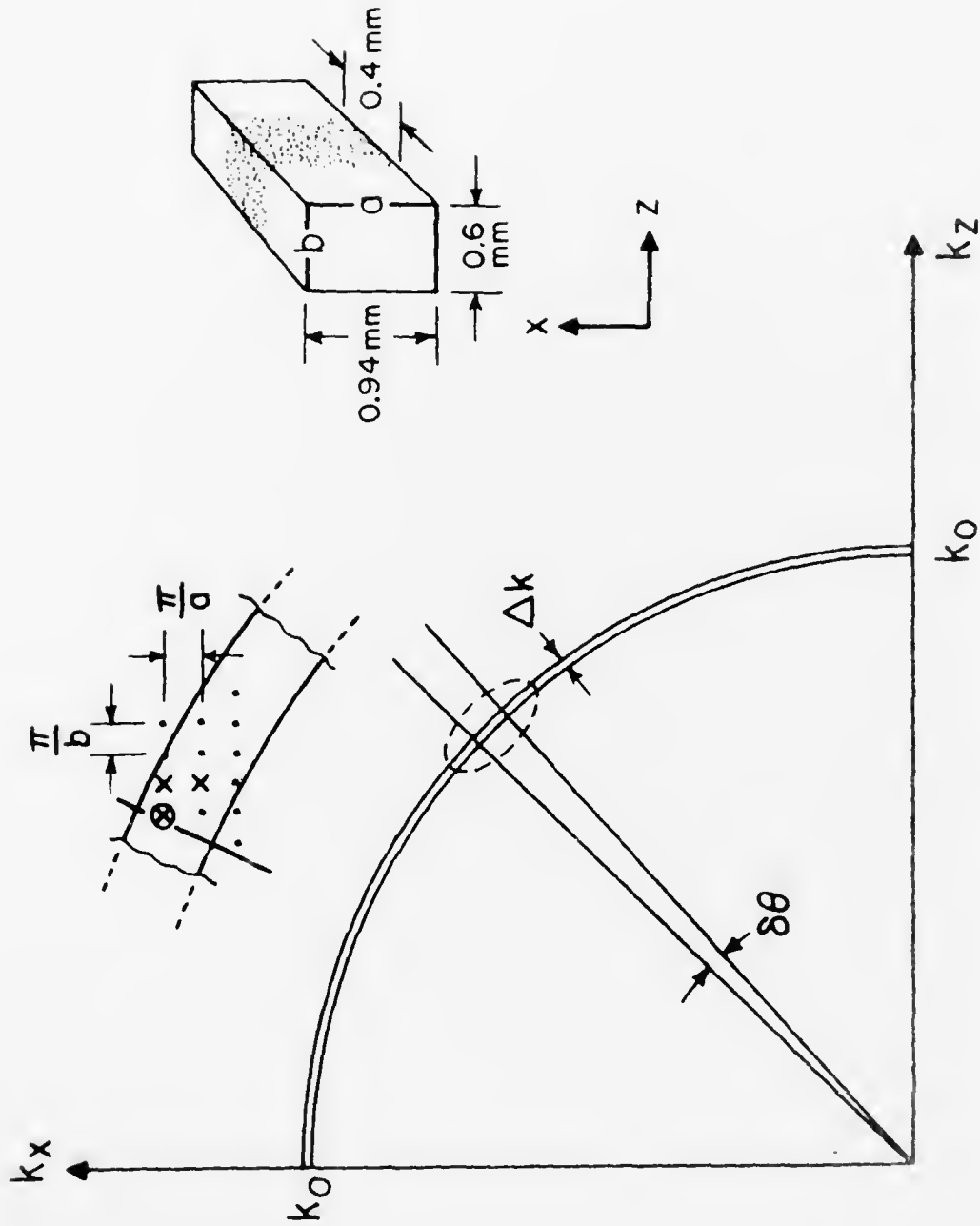


Fig. 4.6 Internal Reflection Modes for a Laser Material.

Appendix 1). For the $2.06 \mu\text{m}$ Ho:LiYF₄ laser material, there are approximately 40 modes within this region for a resonator with $a = b = 0.5 \text{ mm}$.

The number of allowed modes can be decreased by adjusting the critical angle so that it is closer to 45° . This can be done by changing n_1 or n_2 , or by coating one or more of the faces with a dielectric layer to change the critical angle at only one boundary. Also, the number of modes could be decreased by making a and b smaller. However, in the next section it will be shown that single mode laser operation is possible without resorting to these techniques.

4.2.2 Output Coupling

Light is coupled out of the resonator through the evanescent field associated with total internal reflection. When another optical element (n_3), such as a prism or waveguide, is placed at a distance g from the base of the resonator, the evanescent field can extend into it and excite a propagating wave. Each mode in Fig. 4.6 has an angle θ with respect to the x -axis which determines the coupling strength. The decay length l of the evanescent field is given by

$$l = \frac{1}{k_o \sqrt{n_1^2 \sin^2 \theta - n_2^2}} \quad (4.2)$$

Thus, when $\theta \approx \theta_c$, l can be greater than g and the mode is strongly coupled to the substrate. When $\theta > \theta_c$, l can be much less than g and the mode is very weakly coupled to the substrate. Proper choice of the gap g insures that laser operation can occur in only the lowest loss, or equivalently the most weakly coupled, modes.

To calculate this coupling or transmission across the gap, we can

model the fields inside the resonator as two plane waves with mode angle $\pm \theta$ reflecting off the base of the resonator. To calculate the power transmission coefficient, consider the geometry shown in Fig. 4.7. Assuming the problem is independent of y , that is $\partial/\partial y = 0$, there are two independent solutions to Maxwell's equations. The solution for TE fields is:

$$T = 1 - \frac{(k_1 k_3 + \beta^2)^2 \cdot (e^{-\beta g} - e^{\beta g}) + \beta^2 (k_3 - k_1)^2 (e^{-\beta d} + e^{\beta d})}{(k_1 k_3 - \beta^2)^2 \cdot (e^{-\beta g} - e^{\beta g}) + \beta^2 (k_3 + k_1)^2 (e^{-\beta d} + e^{\beta d})} \quad (4.3)$$

where

$$\begin{aligned} k_1^2 &= n_1^2 k_o^2 - (n_1 k_o \sin \theta)^2 \\ k_3^2 &= n_3^2 k_o^2 - (n_1 k_o \sin \theta)^2 \\ \beta^2 &= -n_2^2 k_o^2 + (n_1 k_o \sin \theta)^2 \end{aligned}$$

When the transmission at the other three boundaries of the resonator is included, which is zero for internal reflection modes, results like those of Fig. 4.8 are obtained. Figure 4.8 shows the calculated transmission loss versus mode angle for a $\lambda = 2 \mu\text{m}$ TE cavity mode in LiF_4 coupled across 2, 3, 4, and 5 μm gaps into a LiYF_4 prism, where \vec{E} is parallel to the c axis of the crystal ($n_1 = n_e$) in both the resonator and the prism. This is for the particular case of a square resonator ($a = b$). The transmission loss plotted is the fractional energy lost during the time $\tau \approx 2\sqrt{2}a/c$, the transit time for a ray to circulate around the resonator. The loss per pass rather than cavity Q is used in keeping with the conventional method of describing resonator loss for lasers. For mode angles less than 43.3° (the critical angle for $n_1 = n_e$)

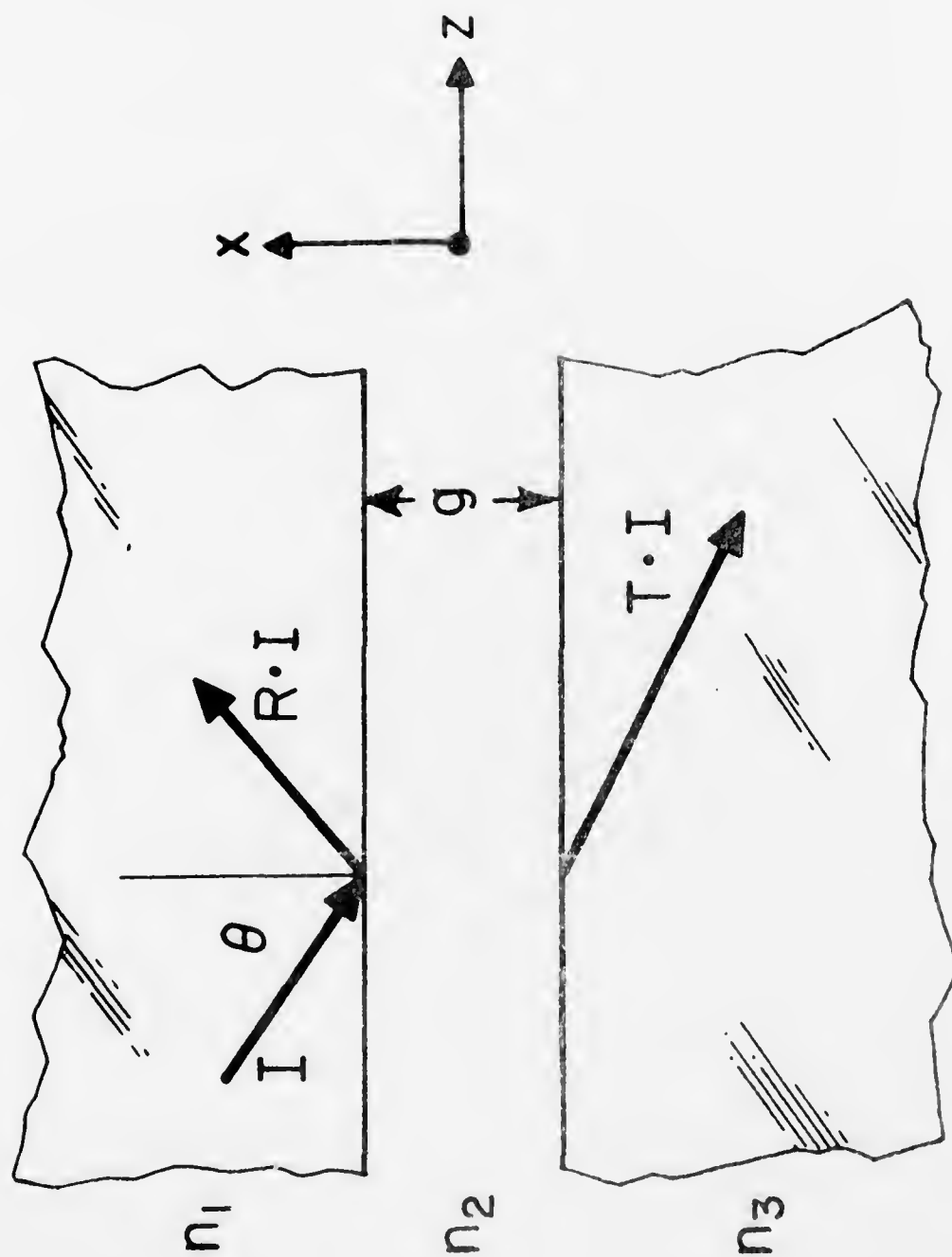


Fig. 4.7 Transmission Across Coupling Gap.

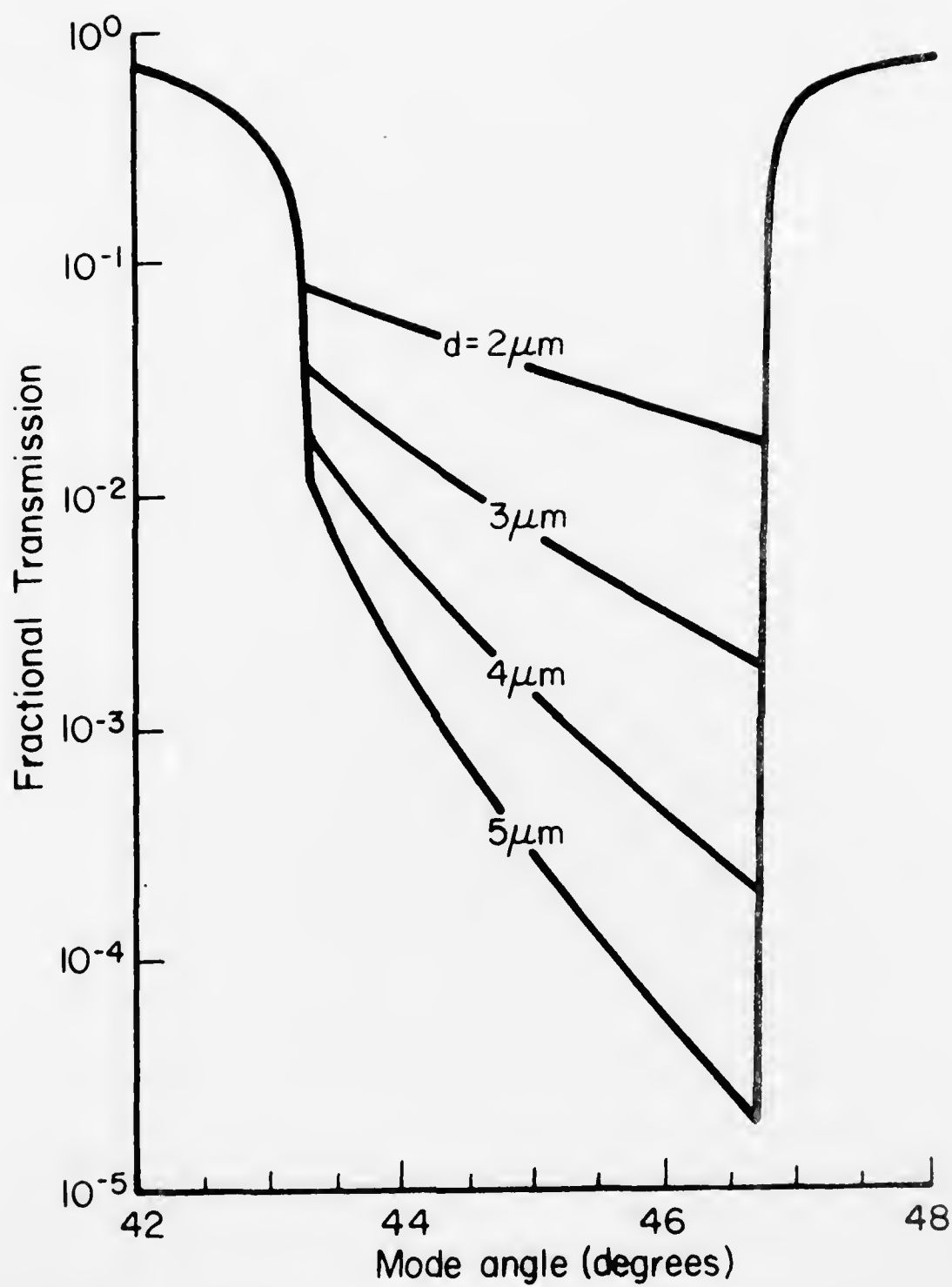


Fig. 4.8 Fractional Transmission Loss of Resonator vs Mode Angle for 2, 3, 4, and 5 μm Gaps.

there is transmission through both "a" faces; thus the loss is high. When the mode angle increases above 43.3° (the critical angle), we enter a region of internal reflection, and transmission of energy out of the cavity occurs via the evanescent field across the gap. With increasing angle toward 46.7° ($90^\circ - \theta_c$), the evanescent field decays more rapidly and there is progressively less transmission across the gap. Above 46.7° , the evanescent field still exists at the coupling face, where the condition for internal reflection is still maintained. However, we no longer satisfy this condition on the orthogonal b faces, and consequently the transmission loss of the cavity rapidly increases as energy is radiated from the two b faces. Similar results are obtained for TM modes.

For a miniature laser of the size we are considering ($a = b \approx 0.5$ mm), efficient laser operation will probably require a resonator loss of less than 1%. Furthermore, once the lowest loss mode ($\theta = 90^\circ - \theta_c$) reaches laser threshold, the gain of the laser material is clamped. Because of the appreciable change in loss of adjacent modes in Fig. 4.6, only the lowest loss mode will oscillate and single mode operation is possible.

4.2.3 Diffraction Loss

If the resonator were infinitely long in the y direction, the field would be independent of y, as assumed before, and the only loss would be output coupling, if material losses such as absorption and scattering are neglected. However, since the resonator is open in the y direction with a finite length t, there is an additional loss--diffraction loss.

To estimate the size of the diffraction loss, we will assume a resonator with square cross section ($a = b$) and with modes near 45° . As far as diffraction losses are concerned, this resonator is equivalent

to a resonator formed by two infinite strip mirrors of width t separated by a distance $d = \sqrt{2}a$. This problem has been solved.^{26, 27} In the low loss region which we are interested in, the power loss per transit \mathcal{L} is given by:

$$\mathcal{L} = 0.13 m^2 N^{-3/2} \quad (4.4)$$

where m is the transverse mode number and N is the "Fresnel number"

$$N = \frac{t^2}{4d\lambda} \quad (4.5)$$

Note that the lowest order ($m = 1$) even symmetric mode has a diffraction loss that is one-fourth that of the next higher mode ($m = 2$). For example, consider a resonator with $a = b = t = 0.5$ mm and $\lambda = 2$ microns; then $\mathcal{L} \approx 4 \times 10^{-4}$. Comparing this loss to the transmission loss in Fig. 4.8, it can be seen that diffraction losses can be neglected for coupling gaps less than 4 microns.

4.2.4 Waveguide Coupling

To couple light from the internal reflection laser to a thin film optical waveguide, it is necessary to match the z -component of the resonator mode phase constant k_z with the phase constant β_m of the waveguide mode. When k_z can be made equal to β_m , direct coupling occurs and the problem is analogous to the prism coupler.²⁸ When k_z is not equal to β_m , the phase matched condition can still be obtained by use of a grating coupler. In the grating coupler the spatial periodicity of the grating provides an additional k -vector, which is used to make up the difference in phase. In the case of a LiYF_4 resonator ($n_1 = 1.46$), it was found that the laser mode had $\theta = 46.7^\circ$; therefore $k_z/k_0 = n_1 \sin \theta \approx 1.1$. However, practical thin film waveguides have $\beta/k_0 > 1.5$. Thus direct coupling cannot occur, but it will be shown how a

grating can be used to achieve waveguide coupling.

4.2.4.1 Direct Coupling

The conditions necessary to achieve direct coupling can be found in the analyses of the prism coupler. The lowest loss mode of the internal reflection resonator has a mode angle $\theta = 90^\circ - \theta_c$; so, $k_z/k_o = n_1 \sin 90^\circ - \sin^{-1}(1/n_1)$. Therefore, for $\beta/k_o > 1.5$ it is necessary for $n_1 > 1.8$. Direct phase matching can occur with high index ($n_1 > 1.8$) laser materials. Since k_z is set by the resonator index, the waveguide must be constructed such that $\beta_n = k_z$. This can be done by controlling the waveguide and substrate indices and the waveguide thickness.

4.2.4.2 Grating Coupler

Use of a grating coupler to excite guided waves in optical thin films was first demonstrated by Dakss, et al.²⁹ Several detailed theoretical analyses soon followed.^{30, 31} The problem of coupling an internal reflection resonator to an optical waveguide by use of an etched grating coupler differs from those previously analyzed in that, instead of a propagating laser beam striking the grating, we have an evanescent field extending from the resonator to the grating. It is the size of the gap g that determines the resonator loss, while it is the efficiency of the grating coupler which determines whether the power loss is coupled to the waveguide or lost into the substrate or other unwanted modes. The basic etched grating coupler is shown in Fig. 4.9. However, before such a coupler can be built, it is necessary to know the expected efficiency as a function of the groove shape, spacing, depth and the length of grating.

It was shown in the last section that direct coupling could not be used when $n_g k_o > k_z > n_s k_o$. In this case light is transmitted into the substrate (coupled to a substrate mode). To couple the light into a wave-

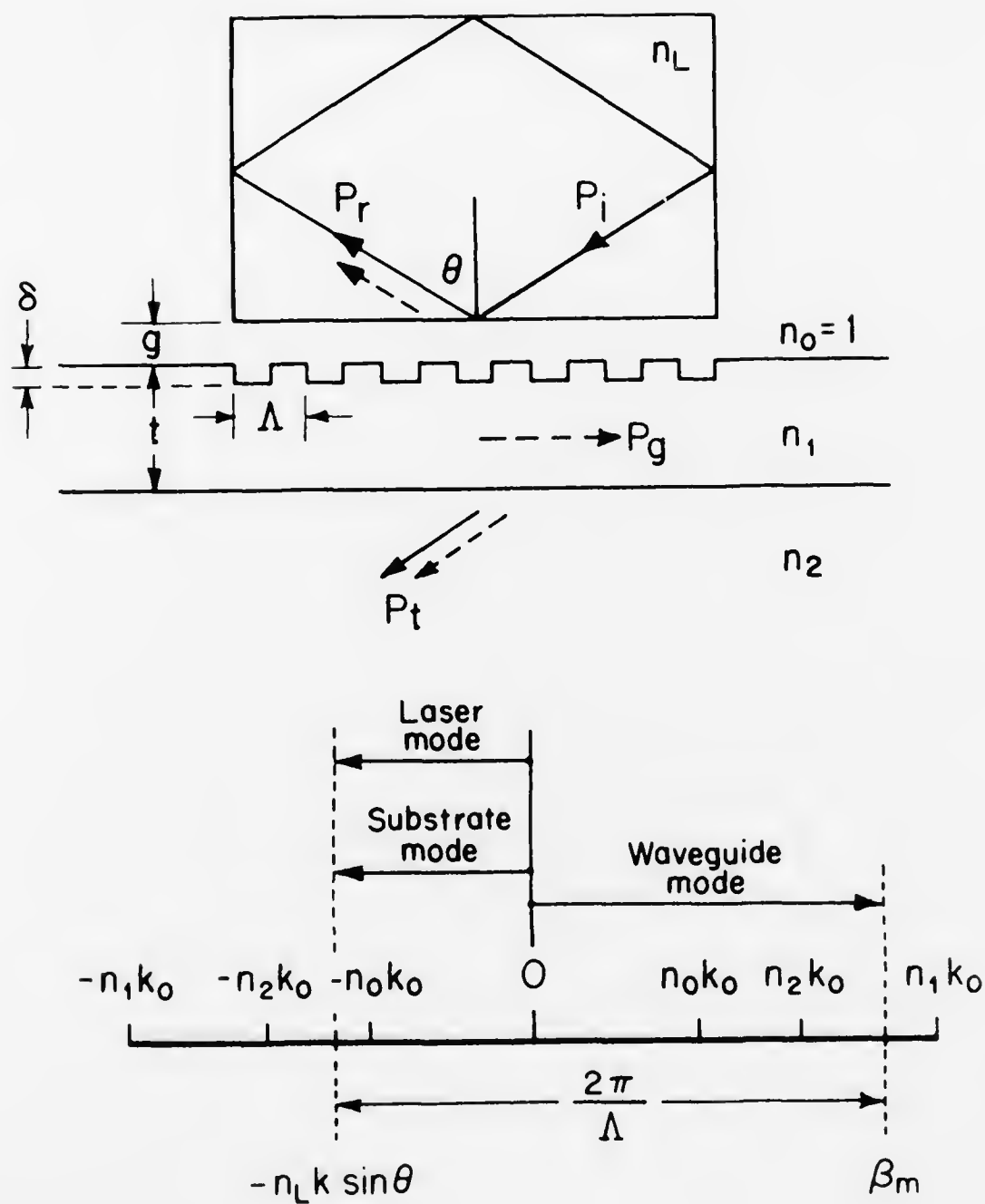


Fig. 4.9 Laser Mode Coupled to Guide by a Grating.

guide, it is first necessary to choose a proper grating periodicity for diffraction into the waveguide mode. The propagation constants must satisfy the phase-matching condition.

$$k_z = \beta_m + \left(\frac{2\pi}{\Lambda}\right)N \quad (4.6)$$

where Λ is the grating period and N is an integer representing the diffraction order. The lower part of Fig. 4.9 shows the desired choice for coupling of a laser mode (substrate mode) to a waveguide mode propagating in the opposite direction ($N = -1$). Any other choice of N and thus Λ will result in light being coupled to other unwanted modes. Since excitation of a substrate mode is unavoidable, the grating length and shape must be designed to maximize the ratio of guide to substrate power.

The magnitude of the electric field at the grating surface will be from equation 4.2 approximately

$$E_o = E_L e^{-g/l} \quad (4.7)$$

where E_L is electric field inside the resonator. The various orders of diffracted modes extract their energy from two sources, the E_o and the m^{th} guided wave mode. Thus, the guided wave must be a "leaky" mode, where the leakage is the diffraction loss of the guided wave interacting with the grating. When $E_o = 0$, the guided mode amplitude will decline as $\exp -\alpha_m z$, where α_m is the sum of the coupling coefficients between the waveguide mode and all diffracted orders. Thus it is obvious that the grating length should equal the resonator length a . For first order backward excitation ($N = -1$), $\alpha_m = \alpha_{ms}$, where α_{ms} is the coupling

coefficient between the waveguide mode and the substrate mode. The coupling between the waveguide mode and the resonator mode will be neglected because of the large coupling gap g . Expressions for α_{ms} can be found in the literature.^{9,10}

The power in the waveguide mode builds as

$$P_g(z) = \frac{E_o^2 n_1 k \cos \theta}{\omega \mu_o} \frac{(1 - e^{-\alpha_m z})^2}{\alpha_m} \quad (4.8)$$

Thus the coupling efficiency is

$$\eta = 2 \frac{[1 - \exp(-\alpha_{ms} a)]^2}{\alpha_{ms} a} \quad (4.9)$$

The maximum efficiency $\eta_{\max} = 81\%$ is independent of the groove depth as long as the grating and laser size satisfy the relation $\eta_{ms} a = 1.25$.

If the phase matching condition is not exactly satisfied the maximum coupling efficiency is reduced by a factor $(\sin \Delta\beta / \Delta\beta)^2$. Therefore, the accuracy which the phase matching condition must satisfy is

$$|\Delta\beta| < \frac{\pi}{a} \quad (4.10)$$

Using typical numbers ($\Lambda = 0.5 \mu\text{m}$, $a = 250 \mu\text{m}$, $\lambda_o = 2 \mu\text{m}$), we find that Λ has to be fabricated to within a tolerance of 0.1%, provided that k_z and β_m are known exactly. This should be easily obtainable.

4.2.5 Experimental Results on the Internal Reflection Resonator

Using the internal reflection resonator, single mode cw laser action at $2.06 \mu\text{m}$ was obtained in a single crystal of $\text{LiY}_{0.462}\text{Er}_{0.035}\text{Ho}_{0.003}\text{F}_4$. The experimental details are shown in Fig. 4.10. The laser crystal with its four long sides polished and with dimensions

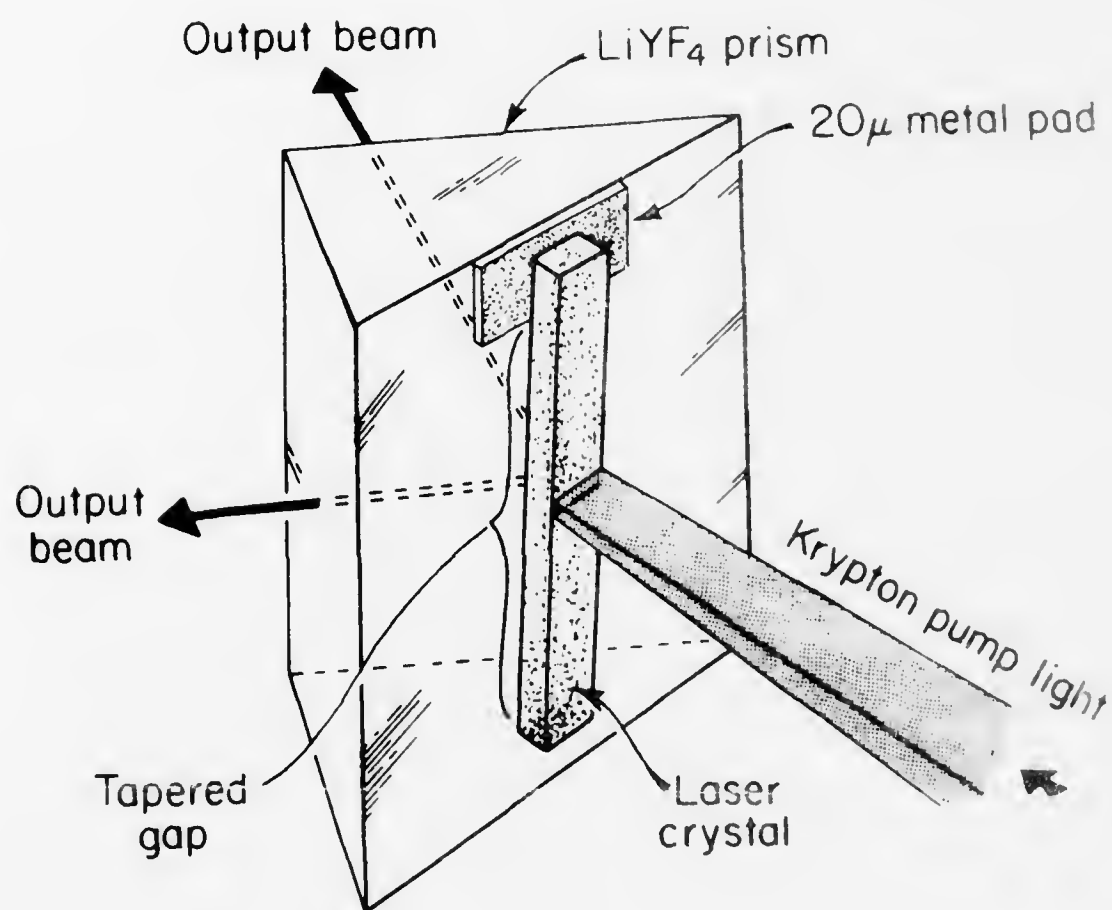


Fig. 4.10 Experimental Setup for Internal Reflection Laser.

0.94 mm x 0.60 mm and 5 mm long was mounted over an undoped LiYF_4 prism. The c-axis of the crystal was parallel to the long sides. A tapered gap was formed by resting one end of the crystal on top of a 20-micron thick evaporated indium pad while the other end rested on the prism. A 0.5 mm wide region of the crystal was pumped with the output of a cw krypton ion laser (6471 Å). By varying the position of the pumped region along the length of the crystal, the output could be observed as a function of coupling strength. The laser crystal and prism were mounted in vacuum in a liquid nitrogen dewar.

Output spectra of the laser are shown in Fig. 4.11. Threshold was reached with approximately 20 mW pump power. Near threshold laser action took place in only one mode, as is evident from the single line in the spectrum. The linewidth is the resolution limit of the spectrometer. With pump power about twice threshold, two other modes appear. The unequal spacing of the modes can be explained by considering the modes of a two-dimensional resonator as shown in Fig. 4.6. The wavelength spacing of the resonator modes is

$$\Delta\lambda \approx \frac{-\lambda_o^2}{2\sqrt{2}n_1} \left(\frac{p}{a} + \frac{q}{b} \right) \quad (4.11)$$

where p and q are integers. With the laser line in Fig. 4.11a equal to λ_o ($p = 0, q = 0$), the laser lines in Fig. 4.11b correspond to Δ ($p = 0, q = 1$) = $-1.1 \times 10^{-3} \mu\text{m}$ and $\Delta\lambda$ ($p = -1, q = 1$) = $0.62 \times 10^{-3} \mu\text{m}$. The experimental values are in precise agreement with these predictions. The relative positions of these modes in k -space are shown in the inset in Fig. 4.6.

Output powers of 5 mW were measured with 150 mW pump power

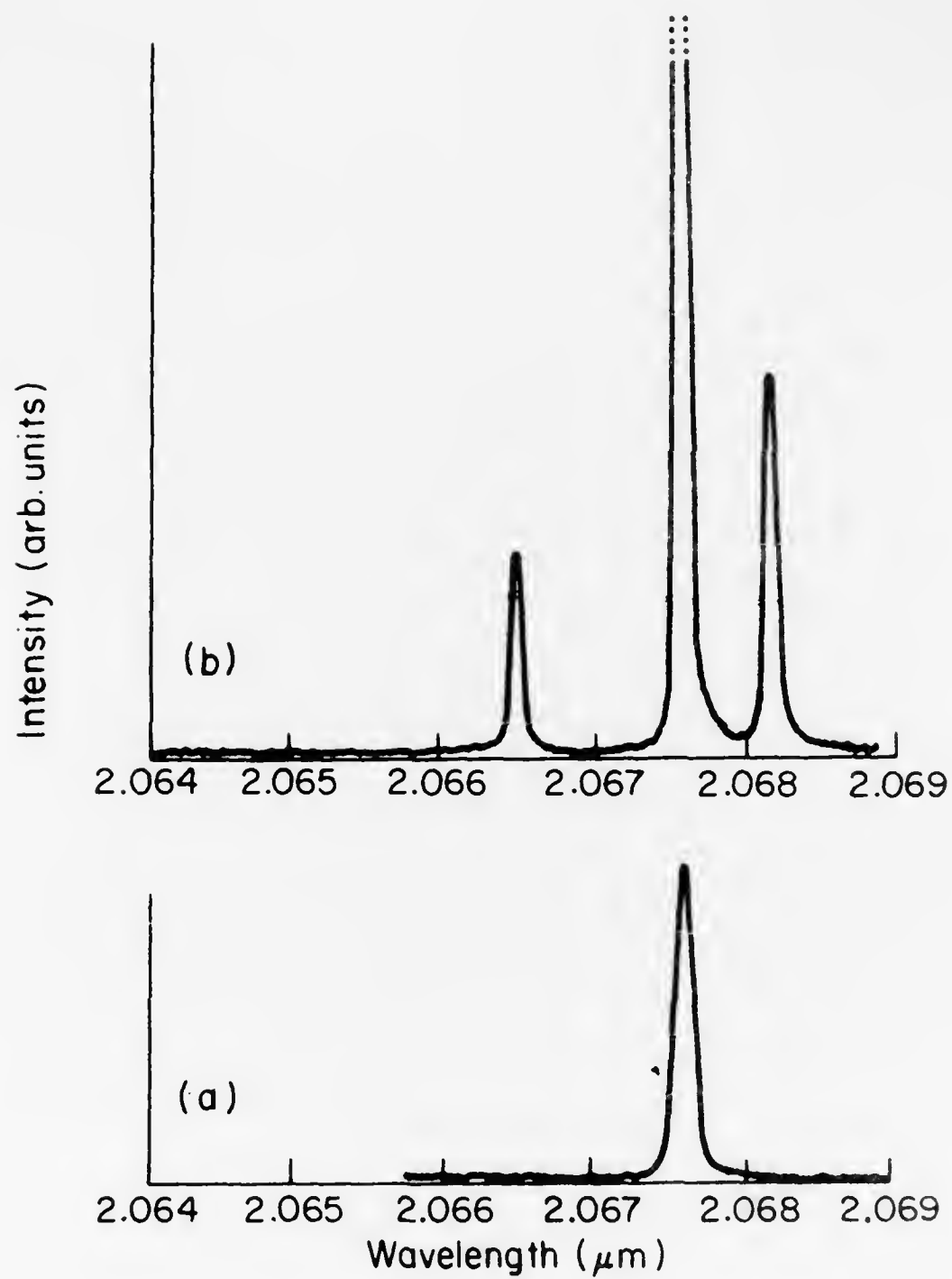


Fig. 4.11 Output Spectra of Internal Reflection Resonator:
(a) Near Threshold; (b) Twice Threshold.

and a gap size of 5 microns. The threshold did not increase monotonically with decreasing gap size, indicating that losses associated with edge chipping and other crystal defects partially determined the threshold.

Lower thresholds are to be expected with more careful sample preparation. Heating of the laser crystal is also a severe problem here since the crystal is only cooled at the two ends where it touches the prism.

CHAPTER 5

RESULTS AND CONCLUSIONS

It has been shown that upconversion is a very important energy transfer process in sensitized rare earth laser materials such as Er^{3+} or Yb^{3+} sensitized Ho^{3+} laser materials and Yb^{3+} sensitized Tm^{3+} laser materials. The importance of upconversion on the laser performance of these materials has not previously been recognized. Upconversion in these materials can decrease the efficiency of energy transfer from the pump levels of the sensitizer ions to the upper laser level, Ho^5_{17} , Ho^5_{16} , or $\text{Tm}^3_{H_4}$. Since the upconversion process is a nonlinear function of pump rate, its effects on this transfer efficiency may not be seen at the low pumping rates with which most spectroscopic measurements of these materials are performed. Only at the high pump rates needed for laser operation does upconversion reduce this energy transfer efficiency, often so severely that laser operation is not possible.

Since the effects of upconversion are often difficult to observe, perhaps the simplest method of studying these effects is with a mathematical model of the energy transfer processes which occur in these materials. When sensitizer ion concentrations are sufficiently high ($> 10\%$), a rate equation model can be used to accurately describe energy transfer within these materials. Once a sufficiently detailed model has been constructed, the energy transfer processes important to laser operation can be determined. The effect of upconversion as a function of pump intensity and the energy transfer efficiency as a function of pump intensity can be determined. With a model, the concentrations of the sensitizer and activator ions can be easily varied to enhance desired energy transfer processes and suppress undesirable processes such as

upconversion, so that the optimum concentrations of the ions can be found.

A model of energy transfer in the $\text{Yb}^{3+}\text{-Tm}^{3+}$ system was analyzed which showed the importance of upconversion and how to minimize its effects. Upconversion in this system is so severe that a Yb^{3+} sensitized $\text{Tm}^{3+}\text{H}_4 \rightarrow {}^3\text{H}_6$ laser material such as $\text{LiYbF}_4\text{:0.25\% Tm}$ cannot work, since the energy transfer efficiency is very low at high pump rates. However, with $\text{LiYbF}_4\text{:5\% Tm}$, the transfer efficiency remains high, so that laser operation of this material appears possible, probably at reduced temperatures. Since the $\text{Tm}^{3+}\text{H}_4 \rightarrow {}^3\text{H}_6$ laser is a quasi three-level laser, the room temperature threshold pump power with 5% Tm would be exceedingly high. However, at reduced temperatures (77°K), the terminal laser level population is much lower, and, therefore, the threshold pump power is greatly decreased.

An adequate model of the $\text{Yb}^{3+}\text{-Tm}^{3+}$ system requires the measurement of ten energy transfer and decay rates; however, in the $\text{Er}^{3+}\text{-Ho}^{3+}$ system there is a much larger number of possible energy transfer steps. Thus, rather than using a rate equation model, the effects of upconversion were experimentally demonstrated in the $\text{Er}^{3+}\text{-Ho}^{3+}$ system. In $\text{LiErF}_4\text{:0.3\% Ho}$, upconversion causes the Ho^{5}I_7 fluorescence intensity versus pump rate to saturate at a level below that needed for laser operation. In $\text{LiErF}_4\text{:5\% Tm, 0.25\% Ho}$ ($\alpha\beta\text{-YLF}$), the 5% Tm sufficiently reduces the probability of upconversion so that laser operation is easily achieved. However, upconversion is still occurring and may be reducing the efficiency of the $\alpha\beta\text{-YLF}$ laser by 50%. Although $\alpha\beta\text{-YLF}$ is the most extensively studied sensitized laser material, an adequate model of its energy transfer processes is still not available.

Results of the Yb^{3+} - Tm^{3+} system model led to the demonstration of the LiYbF_4 :5% Tm, 0.25% Ho laser material. The addition of 0.25% Ho does not significantly change the energy transfer model, since, in this material, the energy transfer from Yb^{3+} to the $\text{Ho } ^5\text{I}_7$ level is through the $\text{Tm } ^3\text{H}_4$ level. From the success of this laser, it appears that its energy transfer processes are adequately understood. With 5% Tm, upconversion does not reduce the Yb^{3+} to $\text{Ho } ^5\text{I}_7$ transfer efficiency, which is greater than 80% at threshold pump rates. At liquid nitrogen temperatures, this material has a low threshold and could be easily pumped with an LED which emits less than 1.0 w/cm^2 . Since this is a quasi three-level laser material, the room temperature threshold is greater, and diodes which emit more than 8.0 w/cm^2 will be needed. This is not a severe requirement for an LED. This material compares favorably with other LED pumpable laser materials, such as Nd-YAG and $\text{NdP}_5\text{O}_{14}$, which will require LED's that emit more than 12 w/cm^2 , assuming the LED emission spectrum has a full width at half-maximum of 60 nm.³⁶

Since Tm^{3+} is necessary in Yb^{3+} or Er^{3+} sensitized Ho^{3+} laser materials to reduce upconversion, another important energy transfer step is the $\text{Ho } ^5\text{I}_7 \leftrightarrow \text{Tm } ^3\text{H}_4$ transfer. The $\text{Ho } ^5\text{I}_7$ and $\text{Tm } ^3\text{H}_4$ levels lie close in energy, so the transfer occurs in both directions with a rate perhaps 10^4 faster than the fluorescent decay rate, and a thermal equilibrium between Ho ions in the $^5\text{I}_7$ level and Tm ions in the $^3\text{H}_4$ level is reached. An approximate distribution function which describes the populations of the levels as a function of temperature was found to fit the experimental data. This distribution function is extremely useful in predicting the Ho^{3+} $2.06 \mu\text{m}$ laser threshold as a function of temperature.

Since high concentrations of sensitizer are allowed in these laser materials, the absorption length of pump light is small, typically less than $200\text{ }\mu\text{m}$. Therefore, these materials can be used in efficient miniature lasers. However, the short absorption length produces high pump power densities and, for a miniature cw laser, heat sinking the material is a severe problem, which should be investigated more fully in the future.

One problem with constructing a miniature laser is how to make a resonator. One possible solution is the use of a miniature Fabry-Perot type resonator as was used in laser testing of materials in this research. Another possible solution is an internal reflection resonator. Using an internal reflection miniature resonator, single mode cw laser operation of $\alpha\beta$ -YLF was achieved in a 0.2 mm^3 volume. The internal reflection resonator laser can easily be coupled to thin film optical waveguides for use as a laser source for integrated optical circuits. Future efforts should be directed toward waveguide coupling as well as LED pumping.

There are many other promising sensitized lasers that have not yet been fully investigated; for example, for operation at 77°K , there is the $1.9\text{ }\mu\text{m}$ $\text{Tm } ^3\text{H}_4 \rightarrow ^3\text{H}_6$ laser sensitized with Yb^{3+} or Er^{3+} , as discussed above. For room temperature operation, there is the $3\text{ }\mu\text{m}$ $\text{Ho } ^5\text{I}_6 \rightarrow ^5\text{I}_7$ laser sensitized with Yb^{3+} . This laser material would require a large Ho^{3+} concentration ($> 5\%$) to reduce upconversion. It also might be necessary to add another sensitizer ion, possibly Tb^{3+} or Eu^{3+} , to quench the lower laser level $\text{Ho } ^5\text{I}_7$. Although LiYF_4 was the host crystal used in this research, future investigation should include other host crystals. Once a detailed model of energy transfer in one host is established, the extension to other hosts should only require the growth

of a small number of crystals to determine the rate constants, rather than the very long process of experimentally optimizing the material performance. Future efforts in developing sensitized rare earth lasers should include extensive modelling of the energy transfer processes. Only then can optimum laser performance of these materials be expected.

APPENDIX 1

MODES IN A TWO-DIMENSIONAL DIELECTRIC RESONATOR

Our objective is to find the normal modes that exist in the two-dimensional dielectric cavity shown in Fig. A-1. The cavity has a rectangular cross section with a length a in the x -dimension, b in the z -dimension. The cavity index, n_1 , is less than n_2 , the index of the surrounding medium. An "exact" solution to this electromagnetic problem can only be carried out numerically; however, a reasonably accurate closed form solution is attainable if we introduce some simplifications based on the physics of the problem. It is evident that for a cavity with dimensions large compared to a wavelength most of the energy will be confined to region 1 when the conditions for total internal reflection are satisfied. The energy stored outside the cavity is small because in this region the fields are evanescent. Within the cavity we expect the fields to be essentially harmonic. If we, in fact, take the solutions to be harmonic, we can match the fields on the four surfaces of the cavity to exponentially decaying fields outside. While this solution will match the boundary conditions on the faces, it will fail at the corners. Despite this failure the solutions should exhibit little error as long as most of the energy is confined to the cavity.

Proceeding along these lines we shall construct solutions which behave in the following way: in region 1 the field varies sinusoidally in x and z ; in regions 2 and 4 the variation is sinusoidal in z and exponential in x ; in 3 and 5 we have sinusoidal variation along x and exponential dependence on z . These assumed fields fail as an exact solution because they are incompatible in the "corner" regions indicated by the shaded

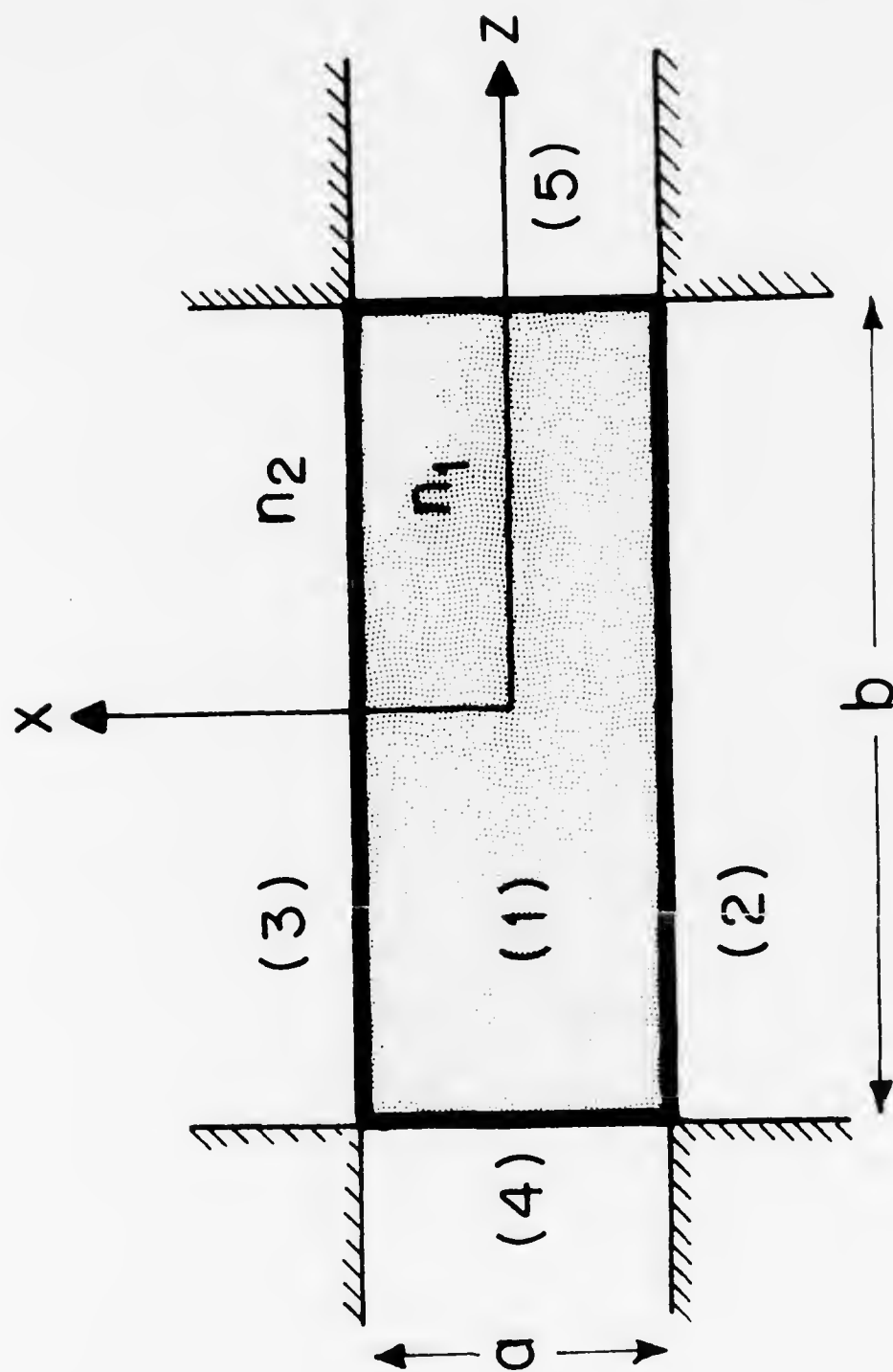


Fig. A-1 Two-dimensional Dielectric Cavity.

boundaries in Fig. A-1.

Our representation shall be in terms of modes TE and TM to z .

For modes TM to z , $E_z = f(x) g(z)$. There are four cases to consider:

(1) $f(x)$ and $g(z)$ are even; (2) $f(x)$ is even and $g(z)$ is odd; (3) $f(x)$ is odd and $g(z)$ is even; and (4) $f(x)$ and $g(z)$ are odd.

For case (1), we choose in region 1

$$E_z = A \cos(k_x x) \cos(k_z z) \quad |x| < \frac{a}{2}; \quad |z| < \frac{b}{2} \quad (\text{A-1})$$

and in regions 2, 3, 4 and 5

$$E_z = B e^{-u|x|} \cos(k_z z) \quad |x| > \frac{a}{2}; \quad |z| < \frac{b}{2} \quad (\text{A-2})$$

and

$$E_z = C e^{-v|z|} \cos(k_x x) \quad |x| < \frac{a}{2}; \quad |z| > \frac{b}{2} \quad (\text{A-3})$$

Upon substitution in Maxwell's equations we obtain for each region

$$k_x^2 + k_z^2 = k_1^2 = \omega^2 \epsilon_1 \mu_0 \quad (\text{A-4})$$

$$k_z^2 - u^2 = k_2^2 = \omega^2 \epsilon_2 \mu_0 \quad (\text{A-5})$$

$$k_x^2 - v^2 = k_2^2 = \omega^2 \epsilon_2 \mu_0 \quad (\text{A-6})$$

The field components transverse to z can be found from

$$\vec{E}_t = \frac{1}{k^2 - k_z^2} \left[\frac{\partial}{\partial z} (\nabla_t E_z) + i\omega\mu \vec{\nabla}_t \times H_z \right] \quad (\text{A-7})$$

$$\vec{H}_t = \frac{1}{k^2 - k_z^2} \left[\frac{\partial}{\partial z} (\nabla_t H_z) - i\omega\epsilon \vec{\nabla}_t \times E_z \right] \quad (\text{A-8})$$

from which we obtain

$$H_y = A \left(\frac{i\omega\epsilon_1}{k_x} \right) \sin(k_x x) \cos(k_z z) \quad |x| < \frac{a}{2}; \quad |z| < \frac{b}{2} \quad (\text{A-9})$$

$$H_y = B \left(\frac{-i\omega\epsilon_0}{u} \right) e^{-u|x|} \cos(k_z z) \quad |x| > \frac{a}{2}; \quad |z| < \frac{b}{2} \quad (\text{A-10})$$

Continuity of E_z and H_y at $x = \pm \frac{a}{2}$ requires that

$$A \cos\left(\frac{k_x a}{2}\right) = B e^{-\frac{ua}{2}} \quad (\text{A-11})$$

$$A \frac{\epsilon_1}{k_x} \sin\left(\frac{k_x a}{2}\right) = -B \left(\frac{\epsilon_2}{u}\right) e^{-\frac{ua}{2}} \quad (\text{A-12})$$

The ratio of the first equation to the second gives

$$-\left(\frac{k_x a}{2}\right) \cot\left(\frac{k_x a}{2}\right) = \frac{\epsilon_1}{\epsilon_2} \left(\frac{ua}{2}\right) \quad (\text{A-13})$$

Likewise, matching E_x and H_y at $z = \pm \frac{b}{2}$ yields

$$-\left(\frac{k_z b}{2}\right) \cot\left(\frac{k_z b}{2}\right) = \frac{\epsilon_1}{\epsilon_2} \left(\frac{vb}{2}\right) \quad (\text{A-14})$$

Equations A-13 and A-14 determine the k_x 's and k_z 's and resonant frequencies of the even TM modes. These equations can be transformed to a more useful form by using equations A-4 through A-6 to express u and v in terms of k_x , k_z , ϵ_1 , and ϵ_2 . We obtain

$$-\left(\frac{\epsilon_2}{\epsilon_1}\right) k_x^2 \cot^2\left(\frac{k_x a}{2}\right) + \left(\frac{\epsilon_1}{\epsilon_2}\right) k_z^2 = k_x^2 + k_z^2 \quad (\text{A-15})$$

$$-\left(\frac{\epsilon_2}{\epsilon_1}\right)k_z^2 \cot^2\left(\frac{k_x b}{2}\right) + \left(\frac{\epsilon_1}{\epsilon_2}\right)k_x^2 = k_x^2 + k_z^2 \quad (\text{A-16})$$

Similarly, the characteristic equations for TM modes of symmetry types (2), (3) and (4) can be found. There is complete duality between the TM and TE modes of the resonator; so the characteristic equations must be dual. The results are presented in Table A-I. Although the characteristic equations cannot be solved exactly, simple graphical solutions do exist. Consider the even TM modes. From equations A-15, A-16

$$\left(\frac{\epsilon_1}{\epsilon_2}\right)k_z^2 \geq k_x^2 + k_z^2 \quad (\text{A-17})$$

$$\left(\frac{\epsilon_1}{\epsilon_2}\right)k_x^2 \geq k_x^2 + k_z^2 \quad (\text{A-18})$$

because in equations A-15 and A-16 the first term on the left in both equations is a negative quantity. Thus we obtain

$$\left[\left(\frac{\epsilon_1}{\epsilon_2}\right) - 1\right]k_z^2 = \left[\left(\frac{n_1}{n_2}\right)^2 - 1\right]k_z^2 \geq k_x^2 \quad (\text{A-19})$$

$$\left[\left(\frac{\epsilon_1}{\epsilon_2}\right) - 1\right]k_x^2 = \left[\left(\frac{n_1}{n_2}\right)^2 - 1\right]k_x^2 \geq k_z^2 \quad (\text{A-20})$$

Therefore there are no solutions (i. e., no resonant modes) for $\frac{n_1}{n_2} < \sqrt{2}$. Only for $\frac{n_1}{n_2} > \sqrt{2}$ do resonant modes exist and the range of k_x and k_z is limited by equations A-19 and A-20 to the region of k -space shown in Fig. A-2, where

Table A-I

Modes in Two-Dimensional Dielectric CavityI. TM Modes $E_z = f(x)g(z)$

$$f(x) \text{ even: } -\left(\frac{\epsilon_2}{\epsilon_1}\right)k_x^2 \cot^2\left(\frac{k_x a}{2}\right) + \left(\frac{\epsilon_1}{\epsilon_2}\right)k_z^2 = k_x^2 + k_z^2$$

$$f(x) \text{ odd: } -\left(\frac{\epsilon_2}{\epsilon_1}\right)k_x^2 \tan^2\left(\frac{k_x a}{2}\right) + \left(\frac{\epsilon_1}{\epsilon_2}\right)k_z^2 = k_x^2 + k_z^2$$

$$g(z) \text{ even: } -\left(\frac{\epsilon_2}{\epsilon_1}\right)k_z^2 \cot^2\left(\frac{k_z b}{2}\right) + \left(\frac{\epsilon_1}{\epsilon_2}\right)k_x^2 = k_x^2 + k_z^2$$

$$g(z) \text{ odd: } -\left(\frac{\epsilon_2}{\epsilon_1}\right)k_z^2 \tan^2\left(\frac{k_z b}{2}\right) + \left(\frac{\epsilon_1}{\epsilon_2}\right)k_x^2 = k_x^2 + k_z^2$$

II. TE Modes $H_z = f(x)g(z)$

$$f(x) \text{ even: } -\left(\frac{\epsilon_1}{\epsilon_2}\right)k_x^2 \cot^2\left(\frac{k_x a}{2}\right) + \left(\frac{\epsilon_1}{\epsilon_2}\right)k_z^2 = k_x^2 + k_z^2$$

$$f(x) \text{ odd: } -\left(\frac{\epsilon_1}{\epsilon_2}\right)k_x^2 \tan^2\left(\frac{k_x a}{2}\right) + \left(\frac{\epsilon_1}{\epsilon_2}\right)k_z^2 = k_x^2 + k_z^2$$

$$g(z) \text{ even: } -\left(\frac{\epsilon_1}{\epsilon_2}\right)k_z^2 \cot^2\left(\frac{k_z b}{2}\right) + \left(\frac{\epsilon_1}{\epsilon_2}\right)k_x^2 = k_x^2 + k_z^2$$

$$g(z) \text{ odd: } -\left(\frac{\epsilon_1}{\epsilon_2}\right)k_z^2 \tan^2\left(\frac{k_z b}{2}\right) + \left(\frac{\epsilon_1}{\epsilon_2}\right)k_x^2 = k_x^2 + k_z^2$$

$$\delta\theta = 90^\circ - 2 \sin^{-1} \left(\frac{n_2}{n_1} \right) \quad (\text{A-21})$$

Since $\cot^2 \left(\frac{k_x a}{2} \right)$ goes from $+\infty$ to 0 to $+\infty$ for $\frac{2\pi p}{a} \leq \frac{2\pi(p+1)}{a}$ where p is any positive integer, there are at most two solutions of equation A-15 in the interval $\frac{2\pi p}{a} \leq k_x \leq \frac{2\pi(p+1)}{a}$ for k_z fixed. Furthermore, only one of these solutions satisfies equation A-13, since u is positive. The same considerations are true for equation A-6. Therefore, there is only one resonant mode in the interval

$$\frac{2\pi p}{a} < k_x < \frac{2\pi(p+1)}{a} \quad \text{and} \quad \frac{2\pi q}{b} < k_z < \frac{2\pi(q+1)}{b}$$

where p and q are any positive integers and k_x and k_z also satisfy equations A-19 and A-20. So the mode density is $\frac{ab}{4\pi^2}$ in the allowed region for each symmetry type. For the four types of TM mode symmetry, the mode density is ab/π^2 ; likewise for TE modes. Finally, the number of resonant modes (TM or TE) in a frequency interval $\Delta\omega$ is

$$\Delta N = \left\{ \frac{\pi}{2} - 2 \sin^{-1} \left(\frac{n_2}{n_1} \right) \right\} \frac{ab}{\pi^2} \frac{n_1^2 \omega}{c^2} \Delta\omega \quad (\text{A-22})$$

The modes of each symmetry type are spaced in intervals $2\pi/a$ in k_x and $2\pi/b$ in k_z . While this mode spacing is not exact, it is an excellent approximation when the cavity dimensions are very large compared to the wavelength λ . When n_1/n_2 is slightly greater than $\sqrt{2}$, examination of the characteristic equations in Table A-1 shows that modes of different symmetry type are spaced in intervals π/a in k_x and π/b in k_z . This is the domain which applies to the experimental situation ($n_1/n_2 = 1.46$) as shown in Fig. 4.6. Therefore,

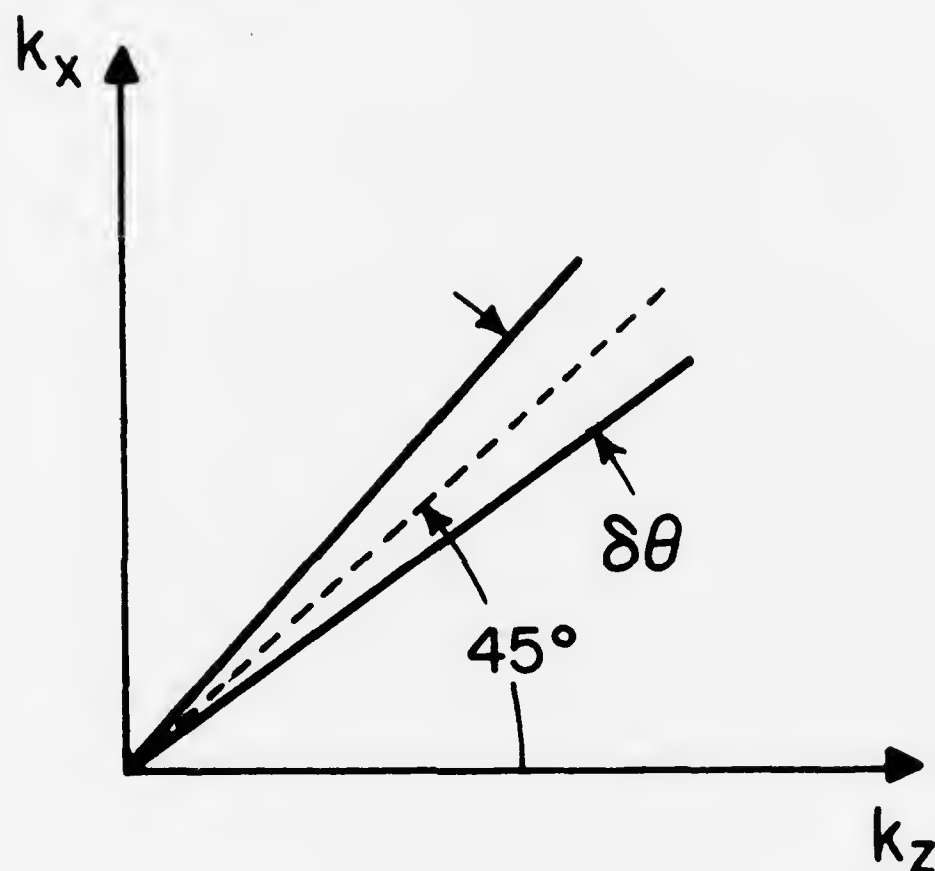


Fig. A-2 Region of k -space Available for Total Internal Reflection Modes.

$$k_1^2 = n_1^2 k_o^2 \approx \left(\frac{p\pi}{a}\right)^2 + \left(\frac{q\pi}{b}\right)^2 \quad (\text{A-23})$$

where $k_o = 2\pi/\lambda_o$, λ_o is the free space wavelength, and p and q are positive integers. An expression for the incremental mode spacing at large wavenumbers can be obtained if we take the derivative of equation A-23:

$$n_1^2 k_o \Delta k_o = \left[\left(\frac{p\pi}{a}\right) \left(\frac{\pi}{a}\right) \Delta p + \left(\frac{q\pi}{b}\right) \left(\frac{\pi}{b}\right) \Delta q \right] \quad (\text{A-24})$$

for n_2 and n_1 chosen so that the sector of allowed modes in k -space is small, we have

$$\left(\frac{p\pi}{a}\right) \approx \left(\frac{q\pi}{b}\right) \approx \frac{n_1 k_o}{\sqrt{2}} \quad (\text{A-25})$$

Upon substituting this result into equation A-24 we obtain, after some simplification,

$$\Delta\lambda = -\frac{\lambda_o^2}{2\sqrt{2} n_1} \left(\frac{\Delta p}{a} + \frac{\Delta q}{b} \right) \quad (\text{A-26})$$

where Δp and Δq are positive and negative integers and may include zero.

APPENDIX 2

MEASUREMENT OF THE REFRACTIVE INDICES OF LiYF_4

The little published data on the refractive indices of LiYF_4 have differed considerably.^{32, 33} To clarify this situation we have measured the indices by the method of minimum deviation on an instrument similar to one described by Bond.³⁴

From a single crystal of LiYF_4 , a 60° prism, 1.5 cm on a side and 1.0 cm high, was fabricated. The c-axis was parallel to the faces of the prism. The measurements were made for wavelengths between 0.225 μm and 2.6 μm , which is the range of the detection system. A tungsten lamp for the visible and infrared and a deuterium lamp for the ultraviolet were chopped and used as sources. Light was synchronously detected with a PbS detector in the infrared and a photomultiplier tube in the visible and ultraviolet.

The results are tabulated in Table A2-1 and presented graphically in Fig. A2-1. The errors are estimated to be less than $\Delta n = \pm 0.0002$, $\Delta\lambda = \pm 0.001 \mu\text{m}$. The data are in agreement with the n_D values given by Thoma.³²

Table A2-1

Refractive Index of YLF

Index Tolerance \pm 0.0002

Wavelength μ	n_e	n_o
2.600	1.4602	1.4381
2.400	1.4617	1.4397
2.200	1.4632	1.4411
2.000	1.4645	1.4424
1.800	1.4658	1.4437
1.600	1.4670	1.4449
1.400	1.4681	1.4460
1.200	1.4693	1.4471
1.000	1.4708	1.4485
0.900	1.4716	1.4492
0.800	1.4726	1.4502
0.700	1.4741	1.4516
0.600	1.4762	1.4535
0.500	1.4796	1.4567
0.450	1.4822	1.4590
0.400	1.4858	1.4624
0.350	1.4913	1.4674
0.300	1.5001	1.4754
0.250	1.5156	1.4895
0.225	1.5287	1.5014

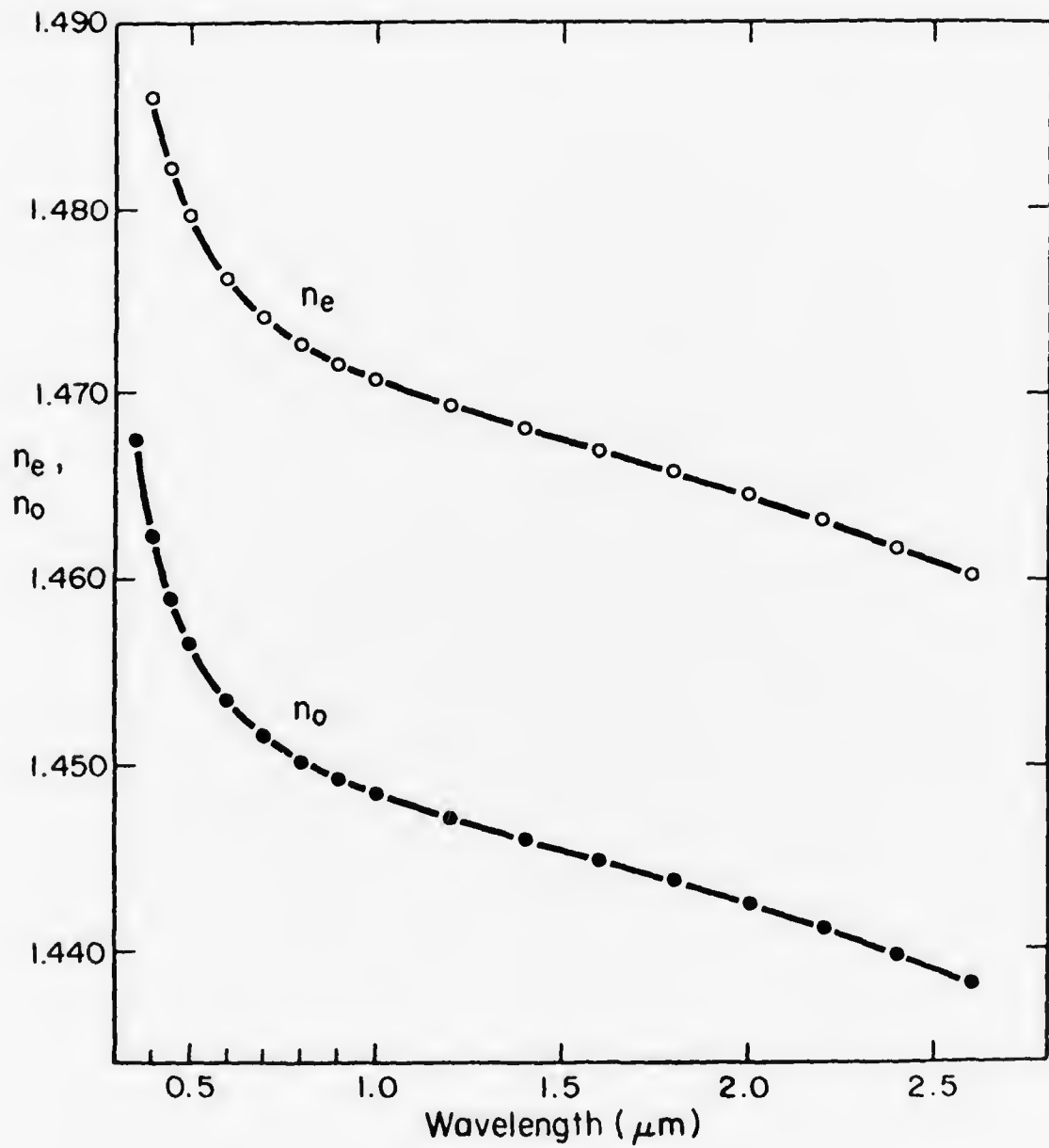


Fig. A2.1 Refractive Index of LiYF_4 .

APPENDIX 3

SOLUTION OF RATE EQUATIONS

The steady state solution of a system of nonlinear coupled rate equations

$$\frac{dX_1}{dt} = F_1(\underline{X})$$

$$\begin{array}{c} \cdot \\ \cdot \\ \cdot \end{array} \quad \begin{array}{c} \cdot \\ \cdot \\ \cdot \end{array}$$

$$\frac{dX_n}{dt} = F_n(\underline{X})$$

was obtained by finding the solution vector \underline{X} of a set of n simultaneous, nonlinear equations:

$$F_1(\underline{X}) = 0$$

$$\begin{array}{c} \cdot \\ \cdot \\ \cdot \end{array}$$

$$F_n(\underline{X}) = 0$$

The solution \underline{X} was numerically found using the subprogram ZEROIN, a double precision FORTRAN IV routine available at the M.I.T. Information Processing Center. ZEROIN computes \underline{X} for a system of equations with $2 \leq n \leq 20$ by an iterative method starting from a user-supplied estimate of the solution vector. Output codes indicate if convergence was obtained.

REFERENCES

1. G. H. Dieke, Spectra and Energy Levels of Rare Earth Ions in Crystals (Wiley Interscience, New York, 1968).
2. H. P. Jenssen, Phonon Assisted Laser Transitions and Energy Transfer in Rare Earth Laser Crystals, Technical Report No. 16, M.I.T. Crystal Physics Laboratory, Cambridge, September, 1971.
3. M. R. Brown, K. G. Roots, and W. A. Shand, "Energy levels of Er^{3+} in LiYF_4 ", J. Phys. C 2, 593 (1969).
4. H. P. Jenssen, A. Linz, R. P. Leavitt, C. A. Morrison, and D. E. Wortman, "Analysis of the Optical Spectrum of Tm^{3+} in LiYF_4 ", Phys. Rev. B 11, 92 (1975).
5. N. Karayianis, D. E. Wortman, and H. P. Jenssen, "Analysis of the Optical Spectrum for Ho^{3+} in LiYF_4 ", to be published.
6. L. A. Riseberg and M. J. Weber, "Relaxation Phenomena in Rare Earth Luminescence" in Progress in Optics (in press).
7. R. K. Watts in Optical Properties of Ions in Solids, edited by B. DiBartolo (Plenum Press, New York, 1975).
8. W. D. Partlow and H. W. Moos, "Multiphonon Relaxation in $\text{LaCl}_3:\text{Nd}^{3+}$ ", Phys. Rev. 157, 252 (1967).
9. L. A. Riseberg and H. W. Moos, "Multiphonon Orbit-Lattice Relaxation of Excited States of Rare-Earth Ions in Crystals", Phys. Rev. 174, 429 (1968).
10. D. L. Dexter, "A Theory of Sensitized Luminescence in Solids", J. Chem. Phys. 21, 836 (1953).
11. T. Miyakawa and D. L. Dexter, "Phonon Sidebands, Multiphonon Relaxation of Excited States, and Phonon-Assisted Energy Transfer between Ions in Solids", Phys. Rev. B1, 2961 (1970).
12. F. Auzel, "Materials and Devices Using Double-Pumped Phosphors with Energy Transfer", Proc. IEEE 61, 758 (1973).
13. H. P. Jenssen, D. Castleberry, D. Gabbe, and A. Linz, "Stimulated Emission at 5445 Å in $\text{Tb}^{3+}:\text{YLF}$ ", IEEE J. Quantum Electron. QE-9, 665 (1973).
14. L. F. Johnson, J. E. Geusic, and L. G. Van Uitert, "Efficient High-Power Coherent Emission from Ho^{3+} Ions in Yttrium Aluminum Garnet, Assisted by Energy Transfer", Appl. Phys. Lett. 8, 200 (1966).

15. E. P. Chicklis, et al., "High Efficiency Room Temperature 2.06 μ m Laser Using Sensitized $\text{Ho}^{3+}:\text{YLF}$ ", *Appl. Phys. Lett.* 19, 119 (1971).
16. E. P. Chicklis, R. C. Folweiler, C. S. Naiman, D. R. Gabbe, A. Linz, and H. P. Jenssen, "Development of Multiply Sensitized $\text{Ho}:\text{YLF}$ as a Laser Material", Tech. Report ECOM-73-0066-F, October 1974.
17. D. Gabbe and A. L. Harmer, "Scheelite Structure Fluorides: the Growth of Pure and Rare Earth Doped LiYF_4 ", *J. Cryst. Growth* 3, 544 (1968).
18. A. Stein, "Thermooptically Perturbed Resonators", *IEEE J. Quantum Electron.* QE-10, 427 (1974).
19. F. W. Ostermayer, Jr., J. P. van der Ziel, H. M. Marcos, L. G. Van Uitert, and J. E. Geusic, "Frequency Upconversion in $\text{YF}_3:\text{Yb}^{3+}, \text{Tm}^{3+}$ ", *Phys. Rev. B* 3, 2698 (1971).
20. R. K. Watts, "Infrared to Visible Conversion in $\text{LiYF}_4:\text{Yb}, \text{Ho}$ ", *J. Chem. Phys.* 53, 3552 (1970).
21. R. A. Hewes and J. F. Sarver, "Infrared Excitation Processes for the Visible Luminescence of $\text{Er}^{3+}, \text{Ho}^{3+}$ and Tm^{3+} in Yb^{3+} -Sensitized Rare-Earth Trifluorides", *Phys. Rev.* 182, 427 (1969).
22. S. E. Miller, "A Survey of Integrated Optics", *IEEE J. Quantum Electron.*, QE-8, 199 (1972).
23. P. K. Tien, "Light Waves in Thin Films and Integrated Optics", *Appl. Opt.* 10, 2395 (1971).
24. B. C. Tofield, H. P. Weber, T. C. Damen, and P. F. Liao, "Optical Properties of Neodymium Pentaphosphate - A High Nd-Concentration Laser Material", *J. Solid State Chem.* 12, 207 (1975).
25. H. P. Weber, P. F. Liao, B. C. Tofield, and P. M. Bridenbaugh, "cw Fiber Laser of NdLa Pentaphosphate", *Appl. Phys. Lett.* 26, 692 (1975).
26. A. G. Fox and Tingye Li, "Resonant Modes in a Maser Interferometer", *B.S.T.U.* 40, 453 (1961).
27. L. A. Vainshtein, "Open Resonators for Lasers", *Soviet Physics J.E.T.P.* 17, 709 (1963).
28. P. K. Tien and R. Ulrich, "Theory of Prism-Film Coupler and Thin-Film Light Guides", *J. Opt. Soc. Am.* 60, 1325 (1970).
29. M. L. Dakss, L. Kuhn, P. F. Heidrich, and B. A. Scott,

- "Grating Coupler for Efficient Excitation of Optical Guided Waves in Thin Films", Appl. Phys. Lett. 16, 523 (1970).
30. J. H. Harris, R. K. Winn, and D. G. Dalgoutte, "Theory and Design of Periodic Couplers", Appl. Opt. 11, 2234 (1972).
31. K. Ogawa, W. S. C. Chang, B. L. Sopori, F. J. Rosenbaum, "A Theoretical Analysis of Etched Grating Couplers for Integrated Optics", IEEE J. Quantum Electron. QE-9, 29 (1973).
32. R. E. Toma, et al. "Phase Equilibria in the System LiF-YF_3 ", J. Phys. Chem. 65, 1096 (1961).
33. W. A. Shand, "Single Crystal Growth and Some Properties of LiYF_4 ", J. Crystal Growth 5, 143 (1969).
34. W. L. Bond, "Measurement of the Refractive Indices of Several Crystals", J. Appl. Phys. 36, 1674 (1965).
35. G. M. Zverev, G. Ya. Kolodnyi, and A. M. Onishchenko, "Resonant and Nonresonant Processes of Excitation Energy Transfer from Tm^{3+} of Ho^{3+} Ions to the Er^{3+} Ions in $(\text{Y, Er})_3\text{Al}_5\text{O}_{12}$ Crystals", Soviet Physics JETP 30, 435 (1970).
36. S. Singh, D. C. Miller, J. R. Potopowicz, and L. K. Shick, "Emission cross section and fluorescence quenching of Nd^{3+} lanthanum pentaphosphate", J. Appl. Phys. 46, 1191 (1975).

UNCLASSIFIED

Document not included

SECURITY CLASSIFICATION OF THIS PAGE (When Data Entered)

REPORT DOCUMENTATION PAGE		READ INSTRUCTIONS BEFORE COMPLETING FORM
1. REPORT NUMBER	2. GOVT ACCESSION NO.	3. RECIPIENT'S CATALOG NUMBER
4. TITLE (and Subtitle) Optoelectronic Materials and Components: Miniaturized Laser Sources and Thin Film Modulators		5. TYPE OF REPORT & PERIOD COVERED Final Technical June 1, 1975 - Sept. 30, 1975
7. AUTHOR(s) D.J. Epstein, C.G. Fonstad, H.P. Jenssen and A. Linz		6. PERFORMING ORG. REPORT NUMBER
9. PERFORMING ORGANIZATION NAME AND ADDRESS Center for Materials Science & Engineering Massachusetts Institute of Technology Cambridge, Massachusetts 02139		8. CONTRACT OR GRANT NUMBER(s) N00014-75-C-1084
11. CONTROLLING OFFICE NAME AND ADDRESS Procuring Contracting Officer Office of Naval Research Department of the Navy, Arlington, VA 22217		10. PROGRAM ELEMENT, PROJECT, TASK AREA & WORK UNIT NUMBERS 5D10
14. MONITORING AGENCY NAME & ADDRESS (if different from Controlling Office) ONR Resident Representative Massachusetts Institute of Technology Room E19-629 Cambridge, Massachusetts 02139		12. REPORT DATE September 30, 1976
		13. NUMBER OF PAGES 308
		15. SECURITY CLASS. (of this report) Unclassified
		15a. DECLASSIFICATION/DOWNGRADING SCHEDULE
16. DISTRIBUTION STATEMENT (of this Report) Unlimited		
17. DISTRIBUTION STATEMENT (of the abstract entered in Block 20, if different from Report) Unlimited		
18. SUPPLEMENTARY NOTES		
19. KEY WORDS (Continue on reverse side if necessary and identify by block number) Optoelectronics, integrated optics, lasers, miniaturized lasers, light emitting diodes, rare earth lasers, optically pumped lasers, thin film modulators, fluorides, yttrium lithium fluoride, gallium arsenide, gallium arsenide-antimonide, potassium tantalate, potassium tantalate niobate, energy transfer, electrooptic materials, liquid phase epitaxy.		
20. ABSTRACT (Continue on reverse side if necessary and identify by block number) Objectives of the program were: (1) development of rare earth doped materials suitable for optically pumped minilasers; (2) development of LED pumps for these materials; (3) growth and evaluation of electrooptical thin films for miniaturized optical modulators. Several laser materials based on LiYF_4 (YLF) and its isomorphs were investigated and cw operation at $2.06\mu\text{m}$ was obtained at 77°K , in a minilaser based on $\alpha\text{8YLF:Ho}$, operating in a 0.1mm^3 internal reflection mode dielectric cavity. (Over)		

DD FORM 1 JAN 73 1473

EDITION OF 1 NOV 65 IS OBSOLETE
S/N 0102-014-6601

SECURITY CLASSIFICATION OF THIS PAGE (When Data Entered)

Abstract continued:

Minilaser operation was also obtained in a crystal of $\text{LiYbF}_4:\text{Tm},\text{Ho}$. This material was selected for study because it can be pumped by an LED.

An important part of the research was a study of energy transfer in laser hosts doped with both sensitizer and activator rare earth ions. Nonlinear transfer associated with upconversion processes was found to be extremely important in determining the threshold for lasing.

Among the material systems investigated as likely candidates for pump diodes were: $\text{GaAs}:\text{Si}$, $\text{Ga}(\text{As},\text{Sb}):\text{Si}$ and the quaternary Al-Ga-As-Sb . Diodes from the first two systems were fabricated in a one step LPE process, made possible because Si, in these compounds, behaves as an amphoteric dopant. Diodes in the system $\text{Ga}(\text{As},\text{Sb}):\text{Si}$ showed an emission spectrum 25% narrower than comparable diodes of $\text{GaAs}:\text{Si}$. Studies of the quaternary system were only exploratory.

Thin films of KTN capable of guiding light were grown, by LPE, on potassium tantalate substrates. The films were of reasonably good optical quality; attenuation was about 8db/cm at $0.6\mu\text{m}$. Electrooptic properties of thin films were evaluated by fabricating several diffraction modulators; one of these gave full modulation at 8 volts drive.

END OF CONTRACT REPORT

Period: July 1, 1975 -- September 30, 1976

Title: Research in Material Sciences

Project Title: Superconducting Transition Metal Alloys

Contract Number: N00014-75-C-1084

ARPA Order Number: 2994

Program Code Number: 5D10

Name of Contractor: Massachusetts Institute of Technology
Cambridge, Massachusetts 02139

Principal Investigator: N.J. Grant (617) 253-5638

Project Scientists or Engineers: R.M. Rose (617) 253-3230

M.L.A. MacVicar (617) 253-6261

J.L. Bostock (617) 253-7607

Effective Date of Contract: June 1, 1975

Contract Expiration Date: September 30, 1976

Amount of Contract: \$325,000

Amount of Project: \$120,000

Sponsored By

Advanced Research Projects Agency

ARPA Order No. 2994

The views and conclusions contained in this document are those of the authors and should not be interpreted as necessarily representing the official policies, either expressed or implied, of the Advanced Research Projects Agency or the U.S. Government.

SUMMARY

This project had two primary objectives: to unravel the complex problem of microscopic superconductivity in high T_c Al5 materials by tunneling experiments, and to develop materials for practical superconducting microwave cavities. In this report we list publications since June 1, 1975, which have resulted from our efforts and which serve as a record of our accomplishment. Part I, then, consists of a list of articles already published, of articles in press and accepted for publication, and of articles now in preparation for submission. Part II consists of a recently completed thesis by Kofi Agyeman, who investigated the suitability and feasibility of Mo-Re alloy as a superconducting microwave cavity material.

Concerning our first objective, we are still continuing to investigate Nb_3Sn and Nb_3Ge and Nb_3Al . The work on Nb_3Sn and Nb_3Ge will come to completion in the next few months. Our activity in the area of the second objective, microwave cavity materials, terminates with the expiration of this contract.

PART I: Publications

Published

"Does Strong Coupling Theory Describe Superconducting Nb?", J. Bostock, V. Diadiuk, W.N. Cheung, K.H. Lo, R.M. Rose, and M.L.A. MacVicar, Phys. Rev. Lett. 36, 603 (1976).

"A New Perspective on Anisotropy and Multiple Energy Gaps in Superconductors," K.R. Milkove, J. Bostock and M.L.A. MacVicar, Sol. State Comm. 19, 1095 (1976).

To Be Published

"Determination of the Superconducting Strong-Coupling Microscopic Parameters of Nb by Electron Tunneling," J. Bostock, V. Diadiuk, W.N. Cheung, K.H. Lo, R.M. Rose, and M.L.A. MacVicar, J. Ferroelectrics.

"Superconductivity in Niobium: Implications for Strong-Coupling Superconducting Theory," J. Bostock, K.H. Lo, W.N. Cheung, V. Diadiuk, and M.L.A. MacVicar, Second Conference on d- and f-band Superconductivity; Rochester, New York, 1976, AIP Proceedings Volume.

"An Evaluation of the Validity of Superconducting Evidence for Anisotropy and Multiple Gaps," Invited Paper, J. Bostock and M.L.A. MacVicar, International Conference on Anisotropy Effects in Superconductors; Vienna, Austria, 1976, Plenum Press.

"Tunneling Junction Phenomena: An Answer to Unanswered Questions," M.L.A. MacVicar, J. Bostock and K.R. Milkove, International Conference on Anisotropy Effects in Superconductors; Vienna, Austria; 1976, Plenum Press.

"Superconducting $\text{Mo}_{0.75}\text{Re}_{0.25}$ Cavities at X-band," Kofi Agyeman, I.M. Puffer, J.A. Yasaitis, and R.M. Rose, 1976 Applied Superconductivity Conference; Stanford University; 1976, IEEE Proceedings.

In Preparation

"The Electron-Coupled Phonon Spectrum of Niobium," J. Bostock, K.H. Lo, W.N. Cheung, V. Diadiuk, K.R. Milkove, and M.L.A. MacVicar

"Proximity Effect Tunneling into Nb_3Al ," J. Bostock, V. Diadiuk, J.A. Gregory, and M.L.A. MacVicar.

"Electron Tunneling as a Tool for Observing Anisotropy of Superconductors and Artifacts of Junction Preparation," J. Bostock, K.R. Milkove, and M.L.A. MacVicar.

"Solutions to the Eliashberg Gap Equation Near T_c for Single Crystal Niobium," T. Gerling, V. Diadiuk, and J. Bostock.

"Review of Superconducting Tunneling: What is Known and What is Not," J. Bostock and M.L.A. MacVicar

PART II

**MICROWAVE SURFACE RESISTANCE
OF SUPERCONDUCTING ALLOYS**

Kofi Agyeman

**Ph.D.
Department of Physics, MIT
August 1976**

Table of Contents

	Page
Abstract.....	ii
Acknowledgements.....	iii
List of Figures.....	vii
List of Tables.....	ix
CHAPTER I: INTRODUCTION.....	1
1.A Review of RF Superconductivity Research.....	1
1.B Objective of Thesis and Text Organization...	4
CHAPTER II: THEORY OF RF SUPERCONDUCTIVITY.....	6
2.A Introduction.....	6
2.B The Surface Resistance of Superconductors...	6
2.B.i The Temperature-Dependent Surface Resistance	6
2.B.ii The Residual Surface Resistance.....	16
2.C The RF Critical Magnetic Field.....	18
CHAPTER III SUPERCONDUCTING MATERIALS FOR RF STUDIES....	21
3.A Introduction.....	21
3.B Desirable Material Properties for High RF Performance.....	21
3.C Review of RF Work on Elemental Superconductors.....	25
3.D Review of RF Work on Alloys and Intermetallic Compounds.....	26

	Page
CHAPTER IV: THE METALLURGY AND SUPERCONDUCTIVITY	
OF THE Mo-Re SYSTEM.....	32
4.A Introduction.....	32
4.B Metallurgy of the Mo-Re system.....	32
4.C Superconductivity in $\text{Mo}_{0.75}\text{Re}_{0.25}$	36
CHAPTER V: EXPERIMENTAL PROCEDURES AND TECHNIQUES.....	39
5.A Measurement Theory and Techniques.....	39
5.A.i Definitions.....	39
5.A.ii Measurement Theory	40
5.A.iii Microwave Circuits and Measurement Procedures.....	48
5.B Design and Constuction of Microwave Cavities.	56
5.B.i Microwave Resonant Cavity.....	56
5.B.ii Starting Material.....	57
5.B.iii Cavity Design and Machining.....	60
5.C Preparation of Cavity Surface for Testing....	64
5.C.i Cleaning for Preliminary Testing.....	64
5.C.ii Electropolishing Set-up and Procedures.....	65
5.C.iii Heat Treatment Procedures.....	70
5.C.iv Cavity Handling and Assembling Procedures....	74
5.C.v Cryogenic Equipment.....	75
CHAPTER VI: RESULTS, DISCUSSIONS AND CONCLUSIONS.....	78
6.A Summary of Measurements.....	78

	Page
6.B Discussions on Experimental Observations....	85
6.B.i Estimated Errors.....	85
6.B.ii Types of $Q_0(T)$ Curves.....	85
6.B.iii Effects of Surface Treatment and Processing.	89
6.B.iv Trends in Peak Surface Magnetic Fields.....	92
6.B.v Surface Resistance Curves.....	92
6.B.vi The Superconducting Energy Gap.....	93
6.C Surface Mechanisms to Explain the Observed Trends.....	94
6.D Further Discussions.....	100
6.E Summary and Conclusions.....	103
6.F Suggestions for Future Work.....	104
APPENDIX A: DERIVATION OF EXPRESSIONS FOR CAVITY GEOMETRIC FACTORS.....	126
APPENDIX B: CALCULATION OF THEORETICAL Q_0 FOR A COMPOSITE CAVITY.....	131
APPENDIX C: PEAK MAGNETIC FLUX DENSITIES ON THE CAVITY WALLS.....	136
APPENDIX D: CALCULATION OF $2\Delta(0)/k_B T_C$ for $Mo_{0.75}Re_{0.25}$ from BCS.....	139
REFERENCES:	141
BIOGRAPHICAL NOTE:	147

List of Figures

	Page
Figure 1. Density of Electron States for a BCS Superconductor.....	13
Figure 2a. Phase Diagram of the Mo-Re System.....	34
Figure 2b. T_c vs. Composition for the Mo-Re System.....	35
Figure 3. Waveforms Observed on the Oscilloscope for Two values of the Coupling Coefficient, β	43
Figure 4. Illustration of the Oscilloscope Trace During Magnetic Breakdown.....	47
Figure 5. Schematic of the Microwave Circuit for Low Power Measurements.....	50
Figure 6. Photographs of Typical Oscilloscope Traces During RF Measurements.....	51
Figure 7. Schematic of the Microwave Circuit for High Power Measurements.....	54
Figure 8. Cross-sectional view showing Cavity Design and Assembly.....	61
Figure 9. Schematic for the Electropolishing Equipment	66
Figure 10. SEM Pictures of the as-machined Cavity Surface and the Electropolished Surface.....	67
Figure 11. Schematic of the RF Furnace Used in Heat-Treating the Mo-Re Cavities.....	71
Figure 12. SEM Pictures of Ti-contaminated Alloy Surface After Heat Treatment.....	72

	Page
Figure 13. Cryogenic Equipment During RF Measurements...	76
Figure 14. $Q_0(T)$ Curves for Cavity Mo-Re(I).....	107
Figure 15. $Q_0(T)$ and $R(T)$ Curves for Cavity Mo-Re(II)...	108
Figure 16. $Q_0(T)$ Curves for Cavity Mo-Re(II).....	110
Figure 17. Theoretical $Q_0(T)$ Curves for Pb, In and Composite Pb/In Cavity.....	111
Figure 18. $Q_0(T)$ Curves for Cavity Mo-Re(III) before and after Electropolishing.....	112
Figure 19. Examples of $Q_0(T)$ and $R(T)$ Curves for Cavity Mo-Re(III).....	113
Figure 20. High Power Test of Cavity Mo-Re(III): Q_0 vs. Peak Surface Magnetic Field.....	115
Figure 21. Examples of $Q_0(T)$ and $R(T)$ Curves for Cavity Mo-Re(III).....	116
Figure 22. Examples of $Q_0(T)$ and $R(T)$ Curves for Cavity Mo-Re(III); also showing Q_0 vs Peak Surface Magnetic Field.....	118
Figure 23. Examples of $Q_0(T)$ and $R(T)$ Curves for Cavity Mo-Re(III).....	121
Figure 24. High Power Test of Cavity Mo-Re(III): Q_0 vs. Peak Surface Magnetic Field.....	123
Figure 25. Examples of $Q_0(T)$ and $R(T)$ Curves for Cavity Mo-Re(III).....	124

List of Tables

Table I:	Chemical and Spectrographiic Analysis of the Electron beam-melted Mo-Re Alloy...	Page 58
Table II:	The Important Dimensions and Resonant Frequencies of the Three Mo-Re Cavities...	62
Table III:	Summary of RF Measurements on Mo-Re(I)....	79
Table IV:	Summary of RF measurements on Mo-Re(II)...	82
Table V:	Summary of RF Measurements on Mo-Re(III)..	83

CHAPTER I:

I. INTRODUCTION

A. Review of RF Superconductivity Research

From the early 1960's, there has been considerable interest in the use of superconductors for rf devices. At the present time a variety of these high-frequency components are being used (or being designed) as high-Q filters and tank circuits, resonators for oscillators and particle accelerators, energy storage devices, transmission lines, delay lines, antennas, mixers, frequency converters, amplifiers, and detectors. Hartwig⁽¹⁾ has given a review of the literature of these devices. The common feature of all rf applications of superconductivity is a large reduction in surface resistance when the metal passes into the superconducting state. At microwave frequencies, one can achieve surface resistances as much as six orders of magnitude lower than the best values for devices made with copper.

In addition to the spectacular reduction in surface resistance, superconducting resonant cavities can have very high magnetic and electric field densities while maintaining high rf parameters. Values of Q greater than 10^{10} have been maintained in resonators containing rf magnetic fields greater than 1000G and rf electric fields of order 70MV/m ⁽²⁾. These experimental facts suggest the great potential of superconducting resonators for applications as linear accelerators and

particle accelerators. Even though such applications using normal state resonators are now in existence, high fields can only be produced for a few microseconds at a time because of the large amount of heat generated. It is anticipated that the accelerating fields in superconducting particle accelerator could either be continuous wave (cw) or have very large duty ratios.

For reasons to be discussed in Chapter III, niobium and lead have been intensively studied for rf applications. Elaborate techniques for fabricating and processing resonant structures of niobium have been developed by two main research groups. At Stanford University, Turneaure and his co-workers^(2, 3) have developed surface preparation procedures involving chemical polishing and ultra-high vacuum anneal. More recently, Karlsruhe⁽⁴⁾ and Siemens⁽⁵⁾ have pioneered other methods involving electropolishing of the resonator surfaces and subsequent anodizing. Both of these techniques have resulted in the lowest values of the residual surface resistance ($R_0 \approx 2 \times 10^{-9} \Omega$)^(2, 6, 7) and the highest rf critical magnetic field measured in any material to date:

$$H_{\text{crf}} = 1080\text{G for a TM-mode cavity}^{(2)}$$

$$\text{and } H_{\text{crf}} = 1180\text{G for a TE-mode cavity.}^{(8)}$$

High quality lead surfaces have also been prepared which achieve $R_0 \approx 3 \times 10^{-8} \Omega$ ⁽⁹⁾ and $H_{\text{crf}} \approx 750\text{G}$. The advantage of

using lead is that relatively high-quality cavities can be fabricated using inexpensive laboratory techniques.⁽⁹⁾

For really high-field applications, lead is not very useful since it has been established that for the modes used in particle accelerators (TM modes), Q_0 (unloaded Q) is considerably lower than desired when larger electric fields are present at the surface. For niobium, results such as those quoted above can only be obtained after elaborate and costly procedures. Furthermore, it is not possible to maintain the good values for long periods of time. These problems were solved to some extent by applying the anodic oxide protective layers mentioned previously. In order to act as an effective protective layer, this oxide must be a very low-loss dielectric, like Nb_2O_5 . However, it has been found⁽¹⁰⁾ that other lower niobium oxides like NbO and NbO_2 can be formed between the Nb metal surface and Nb_2O_5 . This has been found to result in a slow deterioration of initially excellent rf parameters of anodized niobium cavities. Another problem associated with anodized niobium cavities is electron loading⁽¹¹⁾ which is observed in TM-mode cavities (useful for particle accelerator applications) and is due to electron emission resulting from the presence of large electric fields normal to the surface. This initial emission of electrons at the surface often leads to multiple emission of secondary electrons, in synchronism with the high frequency of the

rf fields (multipactoring).

In view of the difficult surface problems associated with niobium, there is need to investigate other superconductors as possible rf materials. As will be discussed in Chapter III, for really high rf performance (high Q_0 and high breakdown fields), only superconductors with high T_c and high critical fields are considered. Since niobium and lead are already the two elemental superconductors with the highest T_c ($T_c = 9.25\text{K}$ for Nb and $T_c = 7.2\text{K}$ for Pb) and critical magnetic fields ($H_{c1}(0) = 1850\text{G}$ for pure Nb and $H_c(0) = 803\text{G}$ for Pb), attention must turn to alloys and intermetallic compounds. A serious challenger to niobium must combine good superconducting properties with superior metallurgical and surface properties. The criteria for superconducting and material properties are fully discussed later. Recently, some attempts have been made to determine the rf properties of selected alloys and intermetallic compounds; (12, 13, 14, 15, 16) a study of one such alloy, $\text{Mo}_{0.75}\text{Re}_{0.25}$, is the subject of this thesis.

B. Objective of Thesis and Text Organization

The superconducting and metallurgical properties of $\text{Mo}_{0.75}\text{Re}_{0.25}$ suggest that this alloy could be a competitor to niobium in practical rf applications. These favorable properties include (1) A high T_c ($= 10.2\text{K}$); (2) nearly

ideal magnetization curves; (3) moderately high H_{c1} ($\approx 500G$) and a high H_c ($\approx 1600G$); (4) it is a solid solution alloy; and (5) its superconducting parameters are not adversely affected by interstitials. Further discussion of these points is found in Chapter IV. This work follows a feasibility study of this alloy carried out in this laboratory.⁽¹⁶⁾ It is aimed at the development of surface preparation procedures and careful measurements of the important rf parameters for this alloy.

A discussion of the theory of rf superconductivity is given in Chapter II as a basis for the particular measurements carried out in this work. The materials requirements for high performance rf structures is the subject of Chapter III, together with a review of the results of rf studies on various metals. In Chapter IV, emphasis is placed on the $Mo_{0.75}Re_{0.25}$ alloy as an attractive rf material. Discussions of its metallurgical as well as its superconducting properties are given. In Chapter V, the experimental procedures used to investigate the rf properties of this alloy are described. In the last Chapter (Chapter VI), the experimental results are presented, together with their implications and the conclusions which can be drawn from them.

CHAPTER II:

II. THEORY OF RF SUPERCONDUCTIVITY

A. Introduction

In this chapter the features of the theory of rf superconductivity which are relevant to this work are reviewed. The theory of surface resistance at microwave frequencies is discussed first, beginning with general definitions which hold for all metals. After pointing out the main differences between normal and superconducting metals, the various theories of the surface resistance of superconductors are discussed. These include the two-fluid model approximations of London and others, and the more exact BCS description. A discussion of the residual surface resistance is also presented. The chapter ends with a review of various theories concerning the rf critical magnetic field.

B. The Surface Resistance of Superconductors

i.) The Temperature-Dependent Surface Resistance.

The response of a metal surface to an applied electromagnetic field can be characterized by a complex surface impedance Z , defined as:

$$Z = R_s + iX = E_t/H_t \quad (2.1)$$

where E_t and H_t are the tangential electric and magnetic fields at the surface of the metal. The magnitude of the

surface resistance R_s , determines the level of power dissipation, P_d , into the metal. The relationship between the surface resistance and the power dissipation is:

$$P_d = \frac{1}{2} R_s \int_{\text{surface}} H_t^2 dA \quad (\text{MKS}) \quad (2.2)$$

The surface reactance, X , is related to the phase shift of a wave when it is reflected from the surface. It can be expressed in terms of an effective penetration depth, δ_{eff} , of the fields in the following way:

$$X = \frac{1}{2} \mu \omega \delta_{\text{eff}} \quad (2.3)$$

At room temperature, the response of a normal metal to rf fields obeys Ohm's Law and Maxwell's Equations, which means that the induced current is proportional to the local electric field via a constant σ , the dc conductivity of the metal. A surface impedance can be described, in this case, in terms of a classical skin depth, δ_c

$$\delta_c = \left(\frac{2}{\mu \omega \sigma} \right)^{1/2} \quad (2.4)$$

The surface impedance, then, is given by

$$Z_c = \left(\frac{1}{2} \mu \omega \right) \delta_c [1 + i] \quad (2.5)$$

At low temperature, the classical treatment proves inadequate. Although Maxwell's equations are still valid, Ohm's law cannot account for the new relation between the rf currents and

fields in metals. To see why this is so it can be seen that in equation (2.5), when the normal metal is cooled, its electronic mean free path increases, thereby causing an increase in σ , which in turn leads to a decrease in δ_c and hence a decrease in the surface impedance. There is, however, a lower limit to Z_c , which occurs when the mean free path, ℓ becomes comparable to δ_c , the classical skin depth. When $\ell \geq \delta_c$ the relation between the current and the fields becomes non-local, as described by Chambers;⁽¹⁷⁾ thus Ohm's Law does not hold because the current at a point depends upon the electric field in a region of size on the order of the electronic mean free path surrounding the point. The result is that the surface impedance is observed to be temperature-independent.

This is the well-known anomalous skin depth regime. The detailed theory for the anomalous skin effect has been worked out by Reuter and Sondheimer,⁽¹⁸⁾ Dingle,⁽¹⁹⁾ Mattis and Bardeen,⁽²⁰⁾ and others. Maxwell⁽²¹⁾ gives a good review of this literature. The existence of this effect explains why, for normal metals, one cannot obtain an arbitrarily large decrease in the surface impedance by progressively cooling the metal since the surface impedance is then not much affected by temperature changes.

The particular features of superconductors that allow

them to have surface resistances several orders of magnitude lower than the lowest attainable surface resistance for a normal conducting metal are now discussed. First, the two-fluid model will be described since it gives a helpful, phenomenological insight into the behavior. After this introduction, the more rigorous theoretical descriptions will be given in a form that will bring out the most important and relevant points.

With applied dc, a superconductor is known to have zero resistance; but at finite frequencies, there is a non-zero surface resistance. In the two-fluid model of a superconductor one assumes that the electron gas consists of normal electrons and superconducting electrons. The total current density at a point, then, has two components: a normal component which obeys Ohm's Law and a complementary supercurrent component which is resistanceless. The amount of supercurrent component varies continuously from zero at the transition temperature to unity at zero temperature. London⁽²²⁾ has given some relations that describe how the superconducting electrons move under applied electric fields as well as how they respond to static magnetic fields. At microwave frequencies, the effect of the electric field on the superconducting electrons is not important because of the lossless nature of their motion. A magnetic field, however, causes these electrons to move in such a way that

the magnetic field is excluded from the interior of the conductor. The magnetic field level decays exponentially into the metal within a penetration depth λ . This distance is much less than δ_c at microwave frequencies. From equation (2.3) it is clear that the surface reactance of a superconductor is determined by λ , the penetration depth, since $\delta_{\text{eff}} = \lambda$ in this case.

On the other hand, the normal electrons in this model are assumed to be able to respond to an electric field just as if the metal were normal. If there is a magnetic field H_t , within the penetration depth region, the oscillating magnetic flux density is of the order given by $\sim \lambda H_t$. This in turn induces an electric field parallel to the surface which is proportional to $\omega \lambda H_t$, ω being the angular frequency of the field. The normal electrons will move under the influence of this electric field and power will be dissipated as a result. It is reasonable to further assume that the dissipated power will be proportional to the density of normal electrons, f_n , which has the following temperature dependence in the two-fluid model:

$$f_n = (T/T_c)^4 = t^4 \quad (2.6)$$

The dissipated power in this scheme should also vary as the square of the induced electric field. Thus, one expects

that the surface resistance in the two-fluid model will have the following frequency and temperature dependencies:

$$\begin{aligned} R_s &\propto f_n (\omega \lambda H_t)^2 \\ &= \omega^2 \lambda^2 H_t^2 t^4 \end{aligned} \quad (2.7)$$

The above, rather simple view of the physical situation, has been more rigorously expanded by several workers (23, 24) in order to arrive at theoretical descriptions consistent with observed behavior. For example, non-locality between current and fields has been worked into the model. Before the advent of the BCS theory, to be described next, these attempts succeeded in improving upon both the frequency and temperature dependencies of R_s . To summarize, most of the theoretical and experimental work resulted in the following qualitative description of the surface resistance:

$$r(\omega, t) = A(\omega) f(t) + r_0 \quad (2.8)$$

where $r(\omega, t)$ is a ratio of the surface resistance in the superconducting and normal states; $A(\omega)$ is a function of the frequency; $f(t)$ is a function of the reduced temperature whose form is very model-dependent; and r_0 is a residual surface resistance ratio. It will be seen in what follows that the more exact descriptions follow the form of equation (2.8) except that the details of $A(\omega)$ and especially $f(t)$, are quite different and reflect the correctness of the BCS

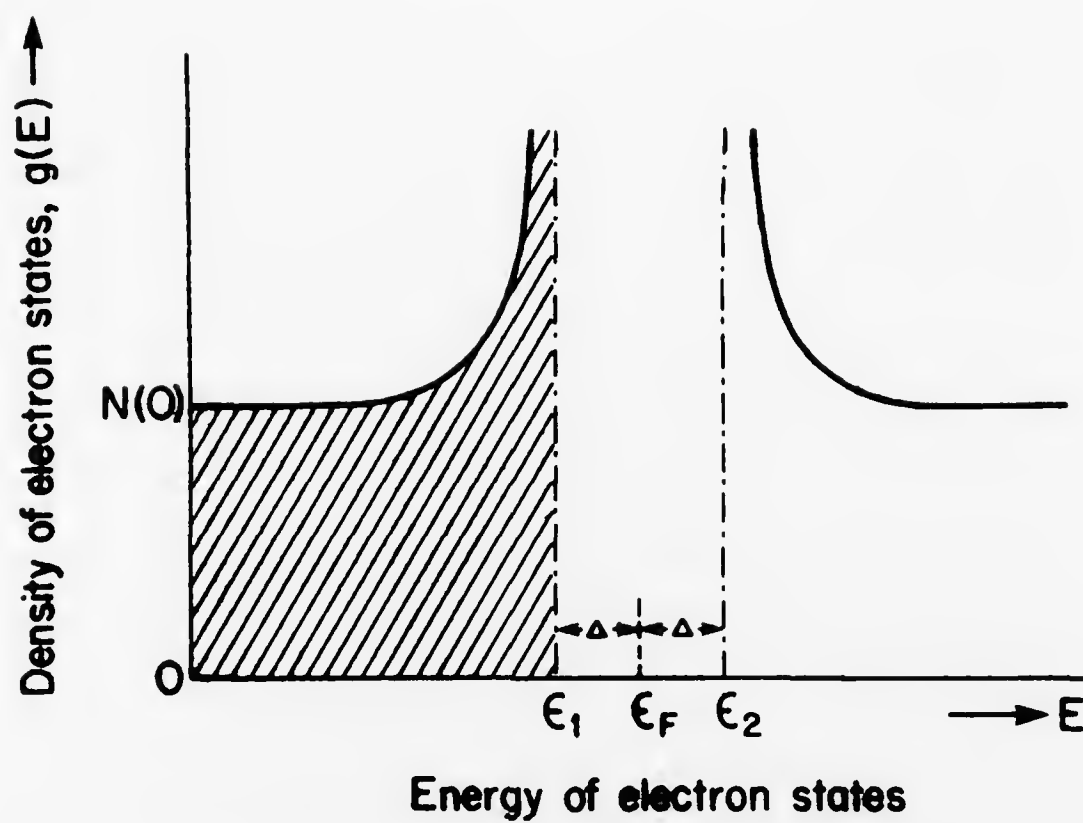
description.

The BCS theory of superconductivity⁽²⁵⁾ has been very successful in describing many properties of superconductors. Mattis and Bardeen⁽²⁰⁾ and independently Abrikosov, Gor'kov, and Khalatnikov⁽²⁶⁾ have worked out a theory of the surface impedance based on the BCS pairing interaction. Before discussing the results of these more exact theories, the simple argument is first used to get the essential temperature dependence of the surface resistance within the BCS theory.

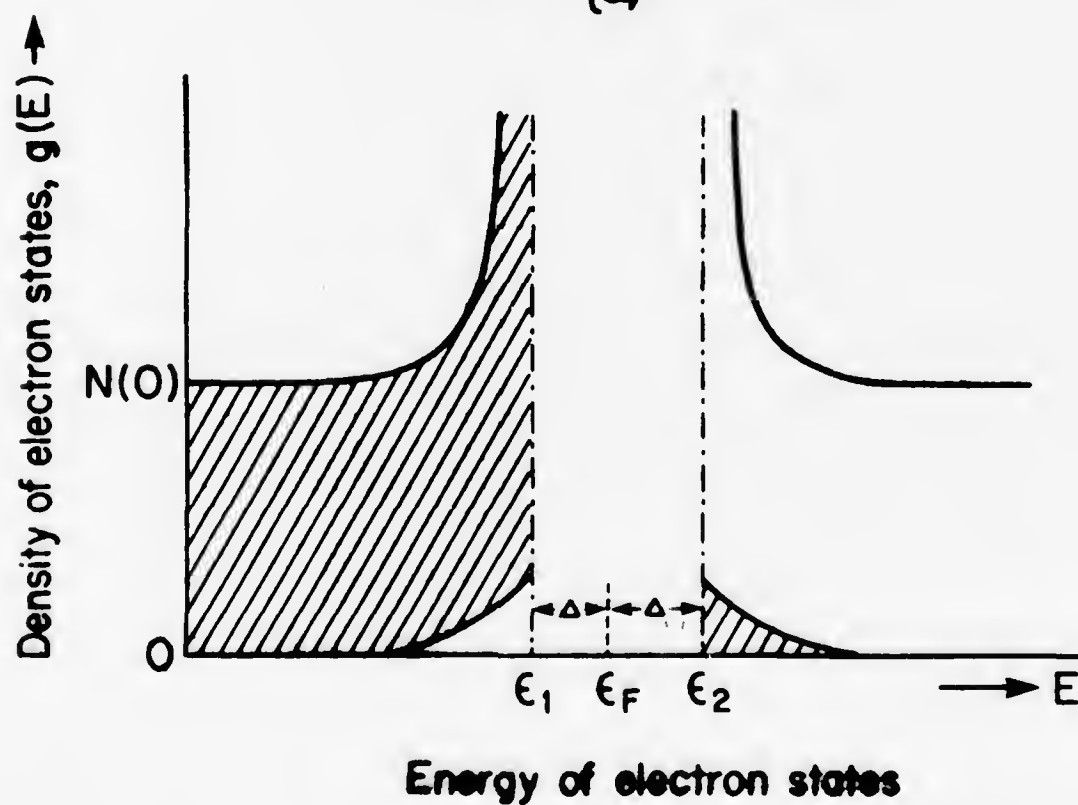
Of crucial importance in the BCS theory is the existence of an energy gap, 2Δ , in the superconducting density of states. Figure 1 shows the main features of the BCS density of states. At absolute zero, Figure 1a shows the Fermi level ϵ_F in the middle of the energy gap 2Δ , and inverse square root singularities in the density of states at the gap edges ϵ_1 and ϵ_2 . Ground state electron pairs, that is, electrons in the condensed state participating in the BCS pair interaction, must acquire energy of at least 2Δ in magnitude before the pair is broken. This requires (at $T = 0$) the absorption of a photon (or phonon) with a minimum of frequency given by $2\Delta/h \approx 100\text{GHz}$. Once a pair is broken, the electrons can be excited across the gap and behave like normal state electrons, and therefore produce

13a.

Figure 1. Density of Electron States for a BCS Superconductor;
(a) For $T = 0K$ and (b) For $T \neq 0K$



(a)



(b)

a surface resistance. Thus at $T = 0$ and at ordinary microwave frequencies (between 1 and 12GHz), one expects the BCS surface resistance to be zero.

The situation is different for a finite temperature less than the transition temperature. In Figure 1b it is clear that electrons can be thermally excited across the energy gap 2Δ . As the temperature increases, there will be an increasing electron excitation since the energy gap decreases with the rise in temperature. The number of the electrons excited across the gap is proportional to the Fermi-Dirac (F-D) distribution function. When the temperature is low enough (i.e. $T \ll 0.5 T_c$) one can approximate the F-D distribution by the function $\exp(-\Delta/k_B T)$. Because the transition across the gap is thermally assisted it requires photons of lower frequency ($\leq 10\text{GHz}$) to excite electrons to higher states. After such an excitation, an electron tends to relax back to lower energy states, causing power dissipation and hence producing a finite, measurable surface resistance. For low temperatures ($T < 0.5 T_c$), the superconducting surface resistance is approximately proportional to the number of thermally excited electrons crossing the energy gap, which, as seen from above is, in turn, proportional to $\exp(-\Delta/k_B T)$ which results in:

$$R_{\text{BCS}} \propto \exp(-\Delta/k_B T) \quad (2.9)$$

As mentioned before, Mattis and Bardeen (M-B)⁽²⁰⁾ and Abrikosov et al. (AGK)⁽²⁶⁾ have developed the exact theory of the surface impedance of superconductors. Their expressions, worked out for the surface impedance in various frequency and temperature ranges, are extremely complicated. The following discussion is limited to the important parameters needed for computation of the surface resistance and to the expected temperature- and frequency-dependence of the expressions. At a fixed frequency, the surface resistance is a function of the following parameters: the electronic mean free path in the normal state; the Fermi velocity V_F (which gives the coherence length, ξ); the London penetration depth λ_L ; the transition temperature T_C , and the energy gap at absolute zero, $2\Delta(0)$. For example, in the Pippard limit ($\xi_0 \gg \lambda_L$), Abrikosov et al.⁽²⁶⁾ obtained for the temperature range $\hbar\omega \ll k_B T \ll \Delta$, the following expression for the superconducting surface resistance $R_S(T)$:

$$\frac{R_S(T)}{R_n} = \frac{8}{3\pi} \left(\frac{\hbar\omega}{\pi\Delta} \right)^{1/3} \sinh \left(\frac{\hbar\omega}{2k_B T} \right) K_0 \left(\frac{\hbar\omega}{2k_B T} \right) \exp \left(\frac{-\Delta}{k_B T} \right) \quad (2.10)$$

where K_0 is the modified Bessel function of zero order and R_n is the normal state surface resistance. Equation (2.10) is approximate; in fact, the exact results require extensive numerical calculations. Turneaure⁽²⁷⁾ and Halbritter⁽²⁸⁾ have developed computer programs which calculate such surface impedances. A brief introduction to the theory

is given in Appendix B. To summarize, both the M-B and the AGK theories predict a superconducting surface resistance which, for $T < 0.5T_C$ decreases exponentially with decreasing temperature and is roughly quadratic in frequency. Experiments have shown, however, that at low temperatures, there is also a residual surface resistance (see next section) which is usually taken to be temperature-independent. This means that the total surface resistance of a superconductor can be written in a form very similar to equation (2.8):

$$R = AR_S(T) + R_0 \quad (2.11)$$

where $R_S(T)$ is the M-B (or AGK) surface resistance; R_0 is the residual term and A is a scaling constant which is very nearly unity. A rather rough approximation for $R_S(T)$ resulting from the M-B treatment of the problem (ref. 20) is

$$R_S(T) \propto \frac{\omega^2}{T} \exp\{-\Delta(T)/k_B T\} \quad (2.12)$$

Equation (2.12) is useful because it gives the major frequency and temperature dependencies. More detailed calculations,⁽²⁹⁾ which take into account mean free path effects, give a slightly different frequency dependence.

ii.) The Residual Surface Resistance

The residual surface resistance term R_0 , may be a combination of several possible loss mechanisms. Except in a few cases it has proved to be difficult trying to separate out a specific loss mechanism for study. Perhaps

the best understood source is that due to trapped magnetic flux in the superconductor. Magnetic flux can be trapped in the superconductor if it passes into the superconducting state in the presence of an ambient magnetic field. There will be regions of degraded superconductivity at those areas on the surface where the magnetic flux leaves the surface. Compared with the rest of the surface these regions are "lossy". The most detailed study of this phenomenon was done by Pierce⁽⁹⁾ on lead-plated cavities. He found that the residual resistance arising from this source is proportional to the applied magnetic field and hence to the trapped magnetic flux. Other workers⁽⁸⁾ have found a quadratic dependence on applied magnetic field using massive niobium cavities. Power loss due to the trapped flux mechanism may be two-fold, namely, Ohmic losses⁽³⁰⁾ and absorption due to oscillation of the pinned fluxoids responding to Lorentz forces in the manner described by Rabinowitz.⁽³¹⁾ In the presence of a large ac field, $H_p \cos \omega t$, Rabinowitz has further derived a critical power loss which is associated with local heat generation at the fluxoid. The subject of critical magnetic fields is discussed more fully in the next section.

It has also been found experimentally that dielectric losses may contribute to R_0 . Dielectric losses are proportional to the square of the electric field, E^2 , at the surface

Thus, they should be more prominent in cases where the electric fields are normal to the surface, e.g. for a TM_{010} -mode cavity. Experiments^(3, 32) in which such effects have been proved have also shown that such cavities are much more prone to have increased residual resistance as the result of poor vacuum than for cavities without large electric field on their surfaces.

A rather exotic loss mechanism that has been much discussed in the literature is that arising from phonon generation. This was proposed by Halbritter⁽³³⁾ and Passow,⁽³⁴⁾ and further developed by Kartheuser and Rodriguez.⁽³⁵⁾ According to these workers, there are several possible coupling mechanisms for phonon generation. Among the more important of these is the coupling of the electric field (parallel to the surface) to the ions in the superconductor, and the coupling of the normal electric field to the electric dipole at the surface. Of these two, the first may be enhanced by surface roughness. Several types of frequency dependence have been predicted for phonon generation, varying from ω^0 through ω^2 .

C. The RF Critical Magnetic Field

Another important measurable quantity to be considered is the critical magnetic field at the surface. It has been observed that during rf measurement on a superconducting

cavity, there exists a well-defined rf magnetic field level at which a drastic drop in Q_0 (the unloaded Q) occurs. At the present time, neither the theoretical nor the experimental situation concerning this breakdown field, H_{crf} , is completely understood.

For type I materials one expects that when the peak magnetic field inside the cavity is equal to H_C , the thermodynamic dc critical magnetic field, (i.e. $H_{crf} = H_C$) there will be a large increase in the surface resistance since the material then passes into the normal state. Thus at a particular temperature, the breakdown field (H_{crf}) should be limited by $H_C(T)$ for type I materials. This has been confirmed by Turneaure⁽²⁷⁾ for tin at 2.85 GHz and Bruynseraede et al.,⁽¹⁴⁾ for lead and indium, also at 2.85 GHz. It must be mentioned, however, that even for this simpler case (i.e. for type I) the breakdown can occur before $H_C(T)$ is reached because the surface condition is important. Also, the measurements referred to above were all done on cavities with no rf electric fields at the surface. Lower breakdown fields than $H_C(T)$ are to be expected when electric fields are present at the surface (as in TM modes) because of the electron loading problems associated with multipactoring⁽¹¹⁾ (see section 1.A, page 3, for definition) and field emission⁽³⁶⁾.

Breakdown in type II materials is even less well

understood. Since at the lower critical field (H_{C1}) the vortices generated by the rf field can enter the material, it was originally assumed that H_{Crf} would be bounded by H_{C1} . And, in fact, in the majority of experimental work, the reported breakdown fields have been considerably lower than H_{C1} . Halbritter⁽³⁷⁾ argues, however, that rf breakdown is unrelated to H_{C1} , but rather, is limited by the thermodynamic critical field H_C , just as for type I materials. Experimental work of Schnitzke et al.⁽³⁸⁾ on Nb and by Giordano et al.,⁽¹²⁾ on Nb-Ti seem to substantiate Halbritter's theoretical arguments in that breakdown fields were measured which were greater than H_{C1} . An important part of any rf measurement of type II material therefore is to measure H_{erf} and compare it with the various measured critical magnetic fields (H_{C1} , H_C and H_{C2}). In fact, knowledge of the attainable levels of H_{Crf} for type II materials provides one of the main reasons for experimenting with materials other than Nb.

CHAPTER III

III. SUPERCONDUCTING MATERIALS FOR RF STUDIES

A. Introduction

Certain superconducting as well as metallurgical properties are conducive to high rf performance. In this chapter, a discussion of these properties in relation to previous work done on the elemental superconductors (e.g. Nb and Pb) and also on alloy and intermetallic superconductors (e.g. Nb - Ti, Pb - Bi, In - Pb, and Nb₃Sn) is given

B. Desirable Material Properties For High RF Performance

The accumulated evidence resulting from intensive study of niobium and other materials suggests that, in order to give high performance, i.e. high Q and high breakdown fields, a material must have the following properties:

(a.) High T_c 's

It should be a superconductor with relatively high transition temperature, T_c . This is because critical magnetic fields scale with T_c . Of course, high T_c 's also imply lower refrigeration costs, an important consideration in large scale applications of rf superconductivity.

(b.) High Critical Fields

Concomitantly with high T_c 's, superconductors with high critical fields are desirable. If the super-

conductor is type I, $H_C(T)$, the thermodynamic critical field must be relatively high since, as discussed in Chapter II, $H_C(T)$ is the limiting value to the breakdown magnetic field in this case. When dealing with Type II materials, high $H_C(T)$ is still to be desired since recent theoretical arguments by Halbritter⁽³⁷⁾ suggest that $H_C(T)$, and not H_{C1} , may be the ultimate limit to the breakdown field. At the same time, the present experimental situation dictates that type II materials with relatively high H_{C1} should be used since H_{C1} has been the practical limit attainable in most cases.

(c.) Well-characterized Magnetization Curves

A great deal can be learned about the surface condition of a type II material from its magnetization curves. Thus, if the magnetization curve is reversible or nearly so, it implies there is little or no trapped magnetic flux, implying that trapped flux will play a minor role in the loss mechanisms of the residual surface resistance. Magnetization studies also give a measure of the surface barrier as well as the amount of surface inhomogeneities. Also, from such magnetization measurements and a knowledge of the mean free path one can determine

the Ginzburg-Landau parameter, κ . Since κ is defined as the ratio of the two characteristic lengths, $\lambda(T)$ and $\xi(T)$ (i.e. $\kappa = \lambda(T)/\xi(T)$), materials with relatively low κ must be preferred. Physically, the lower κ is, the larger the coherence length $\xi(T)$, and therefore, the more difficult it is to nucleate normal regions at the surface. Thus, if κ is low, higher breakdown fields may be possible since the mechanism of normal region nucleation will certainly induce breakdown.

(d.) Surface Homogeneity

Metallurgically, the surface must be homogeneous. This is particularly important in the case of alloys since precipitation of other alloy-phases of inferior superconducting properties, or even being a normal metallic phase, is a possibility. Therefore, if it is an alloy, it must be single phase with favorable superconducting properties. For an intermetallic compound one must insure that the correct stoichiometry is used throughout the material since the presence of off-stoichiometric species can degrade superconductivity in the areas where such species occur.

(e.) Chemically Stable Surface

The surface must be stable against surface reactions

with the atmosphere. If, however, oxides are formed, they should either be superconducting or be very low loss dielectrics. In fact, one successful surface treatment for niobium has been the anodization of thick niobium oxides on previously electropolished surfaces.⁽⁸⁾ Such oxides form a protective, low-loss dielectric layer.

(f.) High Purity Bulk Material

The effect of interstitials on rf properties has been found to be considerable in certain cases. For example, 400ppm of interstitial oxygen reduces H_{c1} in niobium by a factor of two.⁽³⁹⁾ Also, relatively small amounts of impurities can substantially reduce H_{c1} in niobium. It is important, therefore, that the starting material be very pure.

(g.) Workability

Another crucial requirement is that the material be workable. The difficulty in machining and shaping some alloys and intermetallic compounds has stood in the way of intensive study of these materials. (Micro-wave resonator structures, especially the TM modes have complicated geometries). For example, the brittle nature of most A-15 superconductors, the instability of the crystal lattice and the ill-defined

surface layer, have all, until recently⁽¹⁵⁾ conspired to prevent experimenters from considering A-15 materials as resonator materials. Ideally, material for rf work must be easy to machine or form into the required shapes.

C. Review Of RF Work On Elemental Superconductors

To date most of the experimental efforts have been concentrated on niobium and lead. These elemental superconductors have the highest transition temperatures ($T_c = 9.25K$ for Nb and $T_c = 7.2K$ for Pb) and the highest critical magnetic fields $H_c(0) = 1980G$ for Nb and $H_c(0) = 803G$ for Pb) of all materials which can be obtained commercially in the required purity. Moreover, they are easily fabricated into complex shapes. Clean and relatively unstrained surfaces can be obtained for them. However, rather expensive and stringent methods are necessary in the case of niobium. Even so, the behavior is quite unpredictable if the surface is exposed to atmosphere during preparation.

For niobium cavities, fabrication and processing techniques have been developed at Stanford University⁽³⁾ as part of a program to build a superconducting linear accelerator, and also at Karlsruhe⁽⁴⁾ and Siemens.⁽⁵⁾ The Stanford procedure involves starting with very pure, electron beam melted material which is then subjected to various

chemical polishing and uhv annealing steps. The Siemens process involves applying a layer of amorphous Nb_2O_5 as the final step after electropolishing; no high temperature anneals are done. Both these efforts have resulted in the lowest values of the residual surface resistance ($R_o \approx 2 \times 10^{-9} \Omega$) (2, 6, 7) and the highest rf critical magnetic fields measured to date in any material ($H_{\text{crf}} = 1080\text{G}$ for a TM-mode cavity⁽²⁾ and $H_{\text{crf}} = 1180\text{G}$ for a TE-mode cavity⁽⁸⁾).

For lead, relatively less stringent fabrication techniques have given good results. For example, the common laboratory technique of electroplating lead on OFHC grade copper has resulted in residual surface resistance, $R_o \approx 3 \times 10^{-8} \Omega$ and $H_{\text{crf}} \approx 750\text{G}$.⁽⁹⁾

D. Review of RF Work On Alloys And Intermetallic Compounds

Due to the problems associated with alloys and intermetallic compounds, not much work has been done on these materials. Recently, rather encouraging results have appeared in the literature for some alloys and one A-15 superconductor. In this section, brief summaries of these results are given.

(a.) Nb-Ti

Two different research groups have worked on this alloy system. Soumpasis and Luder⁽⁴⁰⁾ investigated

the properties of $\text{Nb}_{0.52}\text{Ti}_{0.48}$ rectangular cavity resonating in the TE_{011} mode at 9.125 GHz. They measured a Q_0 of 2×10^4 at 4.2K in the absence of a magnetic field. At 10kG, Q_0 dropped to 1×10^4 .

Recently, Giordano et al.⁽¹²⁾ have carried out a more careful study of the rf properties of the Nb-Ti alloy system. They studied the surface resistance of a $\text{Nb}_{0.4}\text{Ti}_{0.6}$ cavity as a function of frequency in the range from 2 to 8 GHz and as a function of temperature below 4.2K. These authors found good agreement between the temperature-dependent part of the surface resistance and the calculated surface resistance based on the BCS theory. The magnitude and frequency dependence of the temperature-independent residual surface resistance observed suggested that the behavior of types I and II superconductors is the same. The highest Q_0 measured was $Q_0 = 2.9 \times 10^9$ at 1.5K in a TE_{011} -mode cavity at 3.9 GHz. A coaxial Nb cavity with a Nb-Ti rod as a centerpiece was used to study rf breakdown and its relationship to ac loss, magnetization and penetration depth. They further suggest that the low thermal conductivity of type II superconductors may limit peak fields, and that the use of films (in the case of $\text{Nb}_{0.40}\text{Ti}_{0.60}$ they estimated films

to be 0.01 to 0.1mm thick) deposited on pure niobium or copper may be advantageous. Their highest magnetic breakdown field was 120G (on the rod sample), suggesting that H_{c1} , at least in this case, is not a limit on the breakdown field since H_{c1} for this alloy was estimated to be 75G.

(b.) Pb-Bi

The Karlsruhe group has studied the rf properties of Pb-Bi in some detail. Flécher⁽¹³⁾ has published results on rf absorption measurements at 2,6GHz of $Pb_{0.96}Bi_{0.04}$ prepared in an ultra-high vacuum apparatus. He reports a Q_0 of 3×10^9 at 2K, corresponding to a residual surface resistance of $2 \times 10^{-7} \Omega$.

Buckel et al.⁽⁴¹⁾ studied a more concentrated Pb-Bi alloy, $Pb_{0.55}Bi_{0.45}$, which was condensed on cold substrates and subsequently annealed. Films of this composition, >1 micron thick, were evaporated onto a lead TE_{011} mode cavity. A difference in the temperature-dependent surface resistance for films condensed at 8K and after annealing at 300K was observed, with the freshly condensed films having a higher surface resistance than the annealed films for a particular temperature. The difference resulted from a change

in the electronic mean free path. Hasse and Lachman⁽⁴²⁾ have studied the Pb-Bi system in order to identify the effect of Bi impurities on the rf properties of lead. No correlation of residual rf absorption with mean free path was seen

(c.) In-Pb

Bruynseraede et al.⁽¹⁴⁾ measured the surface resistance of $\text{In}_{0.92}\text{Pb}_{0.08}$ between 1.5K and 4.2K using TE_{011} -mode cavities resonant at 2.85 GHz. Their cavity was a composite one-with the In-Pb alloy as one endplate of a cylindrical electroplated lead cavity. They extracted the surface resistance of the In-Pb portion of the cavity from the total measured surface resistance in the manner shown in Appendices A and B. The temperature-dependence of the In-Pb surface resistance was found to be in good agreement with the calculated surface resistance based on BCS theory. The largest breakdown field measured for this alloy (~90G) is a factor of three smaller than its H_{C1} ($H_{C1} = 270\text{G}$).

(d.) Nb_3Sn

Because of their high T_c and critical fields, the A-15 intermetallic compounds like Nb_3Sn and Nb_3Ge deserve study for possible rf applications in spite of the material problems mentioned in the previous

section. Hillenbrand et al.⁽¹⁵⁾ at Siemens and Kneisel et al.⁽⁴³⁾ at Karlsruhe, have both reported results on Nb₃Sn films deposited on niobium cavities. Both of these groups produced the Nb₃Sn layer by heating niobium cavity structures in a saturated tin vapor. The first group obtained a layer several microns thick after heating the niobium at about 1000°C for 20 hours. Their best rf parameter values are: $Q_0 \approx 1.0 \times 10^9$, corresponding to a residual surface resistance of $\sim 0.78 \mu\Omega$, and a breakdown field of about 470G. The values resulted from Nb₃Sn surfaces prepared by alternately anodizing and dissolving the oxide. The dissolution of the oxide is accompanied by removal of material from the surface, thus resulting in polishing the surface. This process is called oxypolishing.

The Karlsruhe group has done more detailed studies on their surface-reacted Nb₃Sn rf structures. In particular, they have done x-ray diffraction work on the films as well as measurement of the 30kHz penetration depth from which they obtained a T_c of $\sim 18.25K$. They also determined the surface resistance and the surface electric fields for a TM₀₁₀-mode cavity. Their residual surface resistance was

below $1\mu\Omega$; a peak electric field of 8MV/m was obtained.

(e.) Mo-Re

Preliminary investigation of the rf properties of this alloy in our laboratory suggested that a more detailed study of it might be fruitful in rf applications.⁽⁴⁴⁾ Yasaitis and Rose⁽¹⁶⁾ studied a composite cavity composed of a niobium cup and a $\text{Mo}_{0.75}\text{Re}_{0.25}$ end-plate. The analysis of their data was similar to that of Bruynseraede et al.⁽¹⁴⁾ for In-Pb discussed before and the subject of Appendix B. The residual surface resistance estimated for the Mo-Re portion of the cavity was $2.8\mu\Omega$. Also, they estimated that the breakdown field on the alloy had a lower bound of 102G.

CHAPTER IV:IV. THE METALLURGY AND SUPERCONDUCTIVITY OF THE Mo-Re SYSTEMA. Introduction

In this chapter a discussion of the metallurgy and superconductivity of the Mo-Re system is given with special emphasis on the composition used in this work. The attractive features that make an intensive study on the particular composition chosen worthwhile are highlighted.

B. Metallurgy of the Mo-Re System

In 1955 Geach and Hughes⁽⁴⁵⁾ discovered the so-called "Rhenium ductilizing effect". They found that alloys of W-25^a/_ORe and Mo-35^a/_ORe showed a large improvement over pure tungsten and molybdenum in fabricability and low-temperature ductibility in the as-cast condition. A similar effect was found in Cr-35^a/_ORe by Klopp et al.⁽⁴⁶⁾ Thus the effect is common to all three Group VIA elements. In addition to Re, other known ductilizing solutes include Ru, Fe, and Co; in addition, M_n , Tc, Os, and Ir have been suggested by Klopp⁽⁴⁷⁾ as possible candidates as ductilizers. He has also reviewed the suggested mechanisms that cause this effect. At present, all known or anticipated ductilizers are from Group VIIA and VIIIA of the Periodic Table. In what follows, discussion is focused on the Mo-Re system.

The addition of rhenium to molybdenum results in a

b.c.c. solid solution (β -phase) up to about 35^a/_O (50% by weight)Re. This b.c.c. structure has no anomalies in crystal structure or electrical conductivity. Hardness increases with rhenium addition and lattice straining occurs until the σ -phase begins to form. This σ -phase has a tetragonal structure isomorphic with the σ -phase found in Fe-Cr alloys and corresponds to, approximately, Mo₂Re₃. Another intermediate phase is found in the region of 76^a/_ORe. This, the χ -phase, has the b.c.c. structure and is isomorphic with α -Mn. It has the approximate formula MoRe₃. Since the superconducting properties of the σ -phase are not as attractive as those of the b.c.c. solid solution, and the χ -phase is normal, the composition chosen for study in this work is far from the region of the high Re part of the phase diagram. The Mo-25^a/_ORe alloy is a good choice for study since precipitation of σ - and χ -phases is not a hazard.

Although in the as-cast condition the 35^a/_O alloy is about three times as hard as pure molybdenum, it can undergo high deformation even at room temperature and has a low rate of work hardening, as has been convincingly shown by Jaffee et al.⁽⁴⁸⁾ The Mo-25^a/_ORe alloy behaves in much the same way but to a lesser extent. One of the published phase diagrams of the Mo-Re system⁽⁴⁹⁾ is reproduced in Figure 2a.

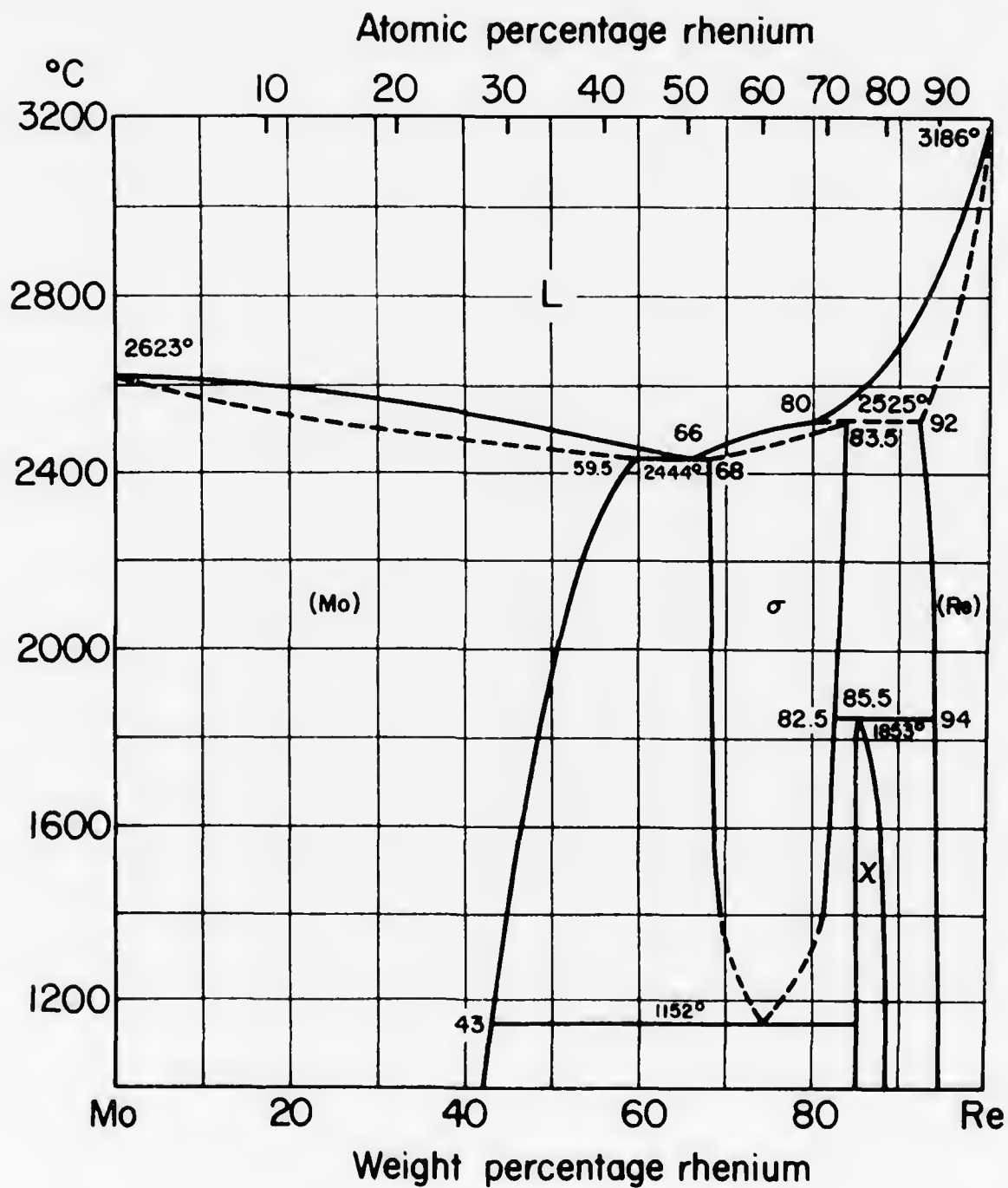


Figure 2a. Phase Diagram of the Mo-Re System. ⁽⁴⁹⁾

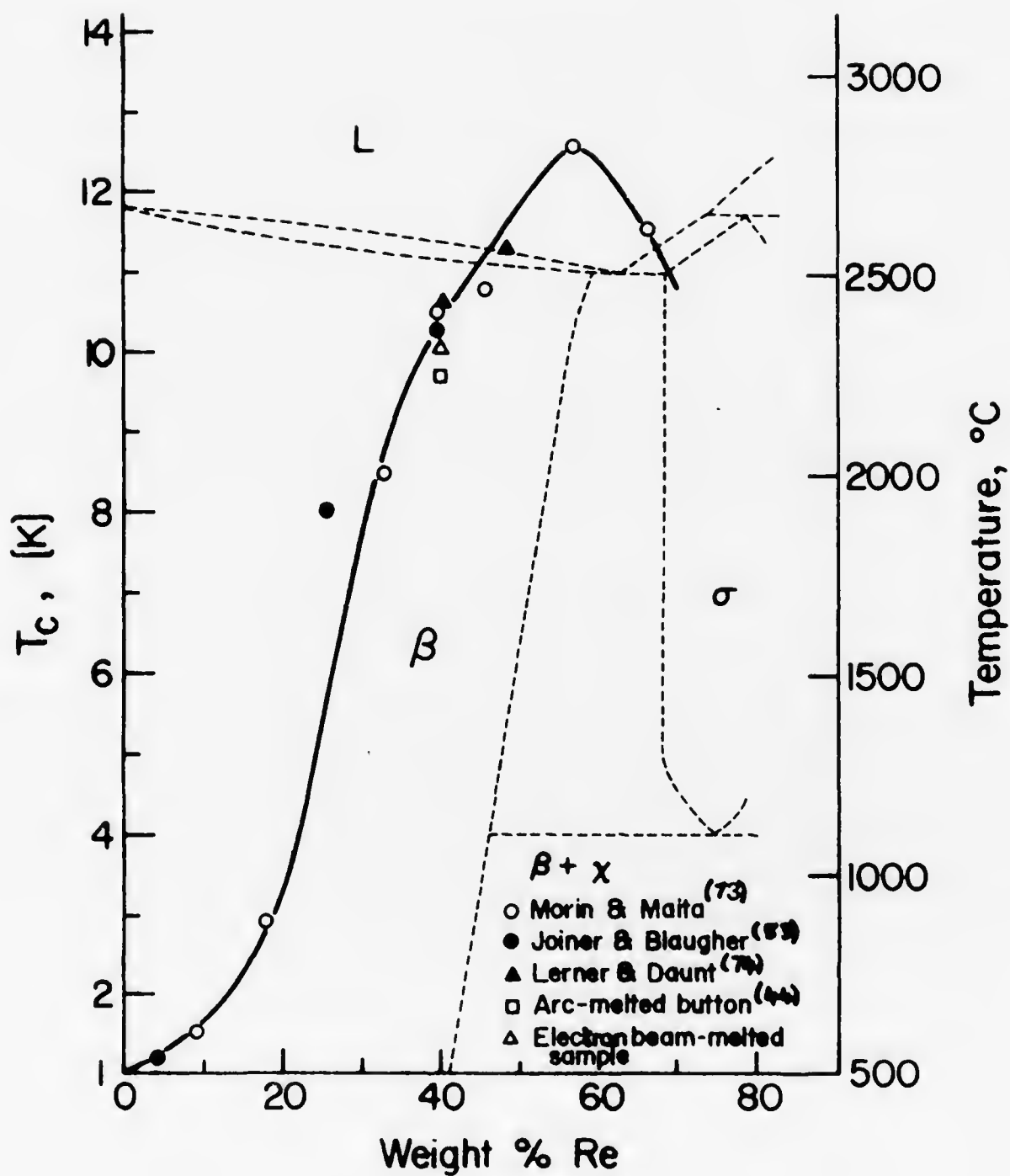


Figure 2b. T_c vs. Composition for the Mo-Re System.

As has already been discussed, the tolerance of a superconducting material for oxygen and other interstitial elements is a very important consideration in rf work. Several years ago, it was found in this laboratory⁽⁵⁰⁾ that in the Mo-Re system, the solubility for interstitial elements has a minimum at $25a/o\text{Re}$. When this is coupled with the fact that Mo-Re alloys have unusual tolerance for oxygen,⁽⁴⁸⁾ the one interstitial element most likely to degrade rf properties, one concludes that the $\text{Mo-}25a/o\text{Re}$ composition is a most logical metallurgical choice for rf study.

Yet another attractive feature of $\text{Mo-}25a/o\text{Re}$ is the fact that it can be polished electrolytically (with solutions used for molybdenum) to a highly bright and mirror-like surface, smooth enough for rf applications. Some caution is however, needed during high temperature annealing since molybdenum evaporates preferentially from the surface⁽⁵¹⁾ if the temperature is above 2000°C .

C. Superconductivity In $\text{Mo}_{0.75}\text{Re}_{0.25}$

Superconductivity in Mo-Re alloys has been studied by several investigators. The approximate variation of T_c with composition is depicted in Figure 2b, where it is seen to peak at compositions which can include the two-phase ($\beta+\sigma$) region. Both the solid solution b.c.c.- and σ -phases are

superconducting, with the T_c of the σ -phases varying from 5.90K to 8.4K.⁽⁵²⁾ As mentioned before, $\text{Mo}_{0.75}\text{Re}_{0.25}$ was chosen in order to avoid nucleating σ -phases, with their lower T_c 's. Also, this particular composition remains single phase up to its melting point; whereas, for example, $\text{Mo}_{0.66}\text{Re}_{0.34}$, even though it has higher T_c and critical fields, is unsuitable because it contains both β - and σ -phases below about 1250°C.

$\text{Mo}_{0.75}\text{Re}_{0.25}$ has a T_c of about 10.2K, which is higher than the T_c for either niobium or lead. In the well-annealed state, its thermodynamic critical magnetic field, $H_c(0)$, lies between 1500G and 1600G.⁽⁵³⁾ H_{c1} is about 500G, while H_{c2} is about 7kG. From section 3.B. it can be seen that these values are expected to yield good rf parameters. In view of the fact, however, that breakdown fields tend to be much lower than H_{c1} , the H_{c1} of about 500G for the alloy must be viewed as not overly encouraging.

A feature of $\text{Mo}_{0.75}\text{Re}_{0.25}$ which is expected to promote good rf performance is the fact that in the annealed state it shows an essentially reversible magnetization behavior, with less than 2% trapped flux.⁽⁵³⁾ This is very important because the Ginzburg-Landau parameter, κ , for the alloy is large ($\kappa \approx 3.7$) compared with κ for pure niobium ($\kappa \approx .805$),⁽⁵⁴⁾ and this amount of trapped flux is believed to

be the smallest for materials with large values of κ . The almost complete absence of trapped flux in the annealed state should improve the level of rf magnetic field which an rf cavity made with $\text{Mo}_{0.75}\text{Re}_{0.25}$ is capable of maintaining without breakdown.

Superconductivity in many materials degrades in the presence of interstitials. Thus, as mentioned before, critical fields of niobium are reduced by interstitial oxygen. It has also been found that implanting Kr^+ ions in niobium films depresses its T_c from the bulk value at a rate of 0.19K/at .% of dissolved Kr.⁽⁵⁵⁾ Other noble gases have similar effects on niobium. On the other hand, the T_c of both molybdenum and rhenium are enhanced when implanted with noble gases.⁽⁵⁶⁾ In fact, xenon ion beam sputtered molybdenum and rhenium films have T_c 's as high as 7.2K and 5.9K, respectively, compared with 0.9K and 1.69K for the pure materials. Other noble gases have similar, less dramatic effects on Mo and Re. Thus the exposed surface of the electropolished Mo-Re cavity pieces may be well-protected from the atmosphere if assembled in noble gas. Such behavior would also make glow-discharge cleaning of cavity surfaces in an argon atmosphere a good surface treatment step.

CHAPTER V:V. EXPERIMENTAL PROCEDURES AND TECHNIQUESA. Measurement Theory And Techniquesi.) Definitions

A convenient way to determine the surface resistance of a metal is by measuring the unloaded quality factor, Q_0 , of a microwave resonator of the material. The unloaded Q of a resonator is defined by

$$Q_0 = \frac{\omega_0 U}{P_d} \quad (5.1)$$

where ω_0 is the resonant frequency, U is the energy stored in the electromagnetic fields inside the resonator, and P_d is the total power dissipated in the walls of the resonator averaged over a cycle. Q_0 is related to the surface resistance, R_s in the following way:

$$Q_0 = \Gamma / R_s \quad (5.2)$$

where Γ is a factor depending only on the mode and geometry of the cavity. Expressions for Γ are derived in Appendix A.

Because of the necessity of coupling in energy from outside the resonator via a suitable transmission line, in practice one first determines the loaded Q , Q_L . It is important to note that Q_L is smaller than Q_0 since the coupling mechanism is a source of energy loss. Thus a certain amount of power, P_c will be radiated out of the

transmission line, with the level of P_c being directly proportional to the total stored energy in the resonator, U . A coupling Q , Q_c can thus be defined by

$$Q_c = \frac{\omega_o U}{P_c} \quad (5.3)$$

The loaded Q , Q_L , can then be written as

$$1/Q_L = 1/Q_o + 1/Q_c \quad (5.4)$$

for the case where we have only one coupling port. Rearranging equation (5.4), we get

$$Q_o = Q_L(1 + Q_o/Q_c) \quad (5.5)$$

One then defines the coupling coefficient, β as

$$\beta = \frac{Q_o}{Q_c} \quad (5.6)$$

β is directly measurable by the measurement technique to be described. Expressions for β , depending on the level of coupling and the various power levels are given below.

ii.) Measurement Theory

Of the various types of Q -measurement for resonators, the decrement method is particularly suited to high- Q resonators because this method does not need the high degree of frequency stability which is required in other types of measurement. For example, when using the voltage standing wave Ratio(VSWR)⁽⁵⁷⁾ method to determine

Q , the frequency must be constant, at least during the time needed to measure a single standing-wave ratio. In the decrement method the resonator is driven by a pulsed signal (e.g. a square-wave). During the period when the pulse is off, the natural fields in the resonator decay exponentially with time and the time constant of the decay determines the Q . The output signal from the cavity can be observed by means of a square-law detector and an oscilloscope (to be described later).

The formulas for the unloaded $Q(Q_0)$, the coupling coefficient, β , as well as the theoretical maximum magnetic and electric field levels of a superconducting cavity have been derived by several workers.^(27, 58, 59) In what follows, only the most important relations necessary for correct interpretation of observations made during rf tests of a microwave cavity are given. It is assumed that: (1) only one mode of the cavity and only the dominant mode of the transmission line are used; (2) the transmission line is lossless and has a VSWR of 1.0; and (3) the transmission line is terminated with a perfectly matched load at the generator. We also assume that the cavity has only one coupling port. The microwave equipment used will be described in the next section. It is sufficient to point out here that a single transmission line is used to provide incident power on the resonator surface. The reflected wave from the resonator is

detected by means of a directional coupler, a crystal detector and an oscilloscope. The oscillator must be stable enough to stay within the resonator bandwidth ω_0/Q_L , and is turned on and off by a microwave switch. Referring to Figure 3, the incident power P_i is turned on with the switch at $t=t_0$ and off at $t=t_1$. The behavior of the power at the detector for two values of the coupling coefficient, β , defined in equation (5.6) are also shown in Figure 3. At $t=t_0$, provided $Q_L \gg 1$, P_i is almost totally reflected from the coupling network at the resonator. Thus, it can be assumed that $P(0) \approx P_i$ if the microwave switch is sufficiently fast (i.e., the square wave has very small rise-time). As the resonator fills with energy and the reflected power from the resonator builds up, it begins to cancel the reflected power from the coupling network. This causes a drop in the total power level. If $(t_1 - t_0) \gg Q_L/\omega$, P will approach a constant value, P_r . At t_1 , after P_i is turned off, P consists only of the radiated wave P_e as shown. Q_L is then determined from the decay time after t_1 , τ . Care must be taken to insure that the time interval $(t_1 - t_0)$ is long enough so that a steady state is reached and P_r is constant.

The value of the coupling coefficient, β can be determined from the three power levels, P_i , P_r , and P_e after making sure the oscillator is tuned to ω_0 , the resonant frequency of the resonator and that a steady state condition has been

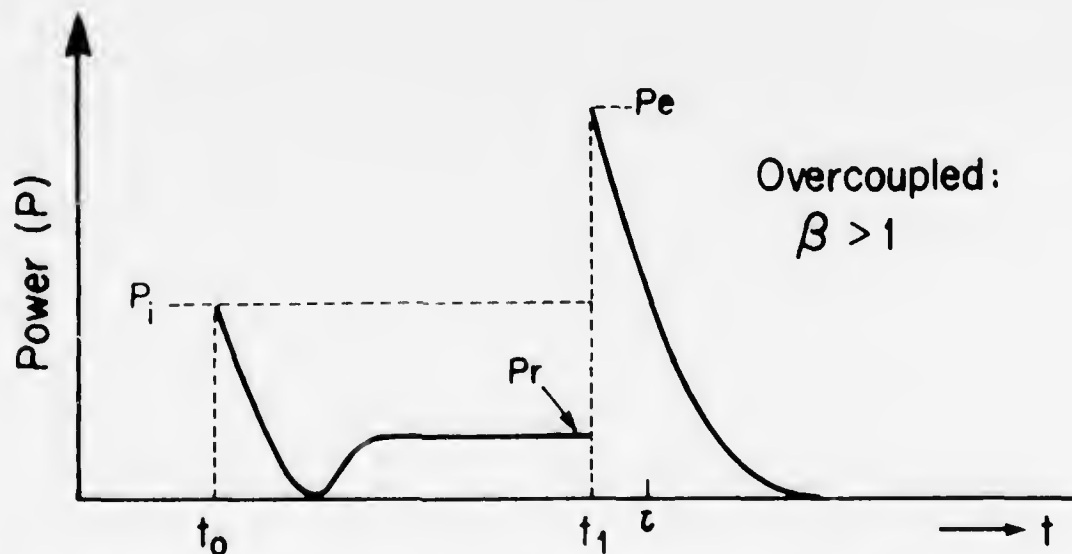
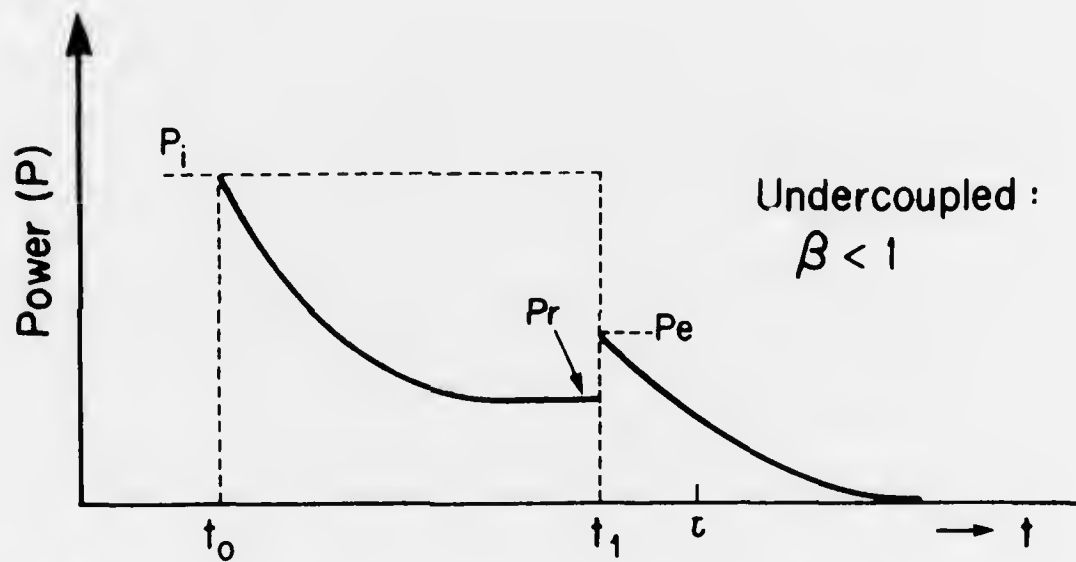
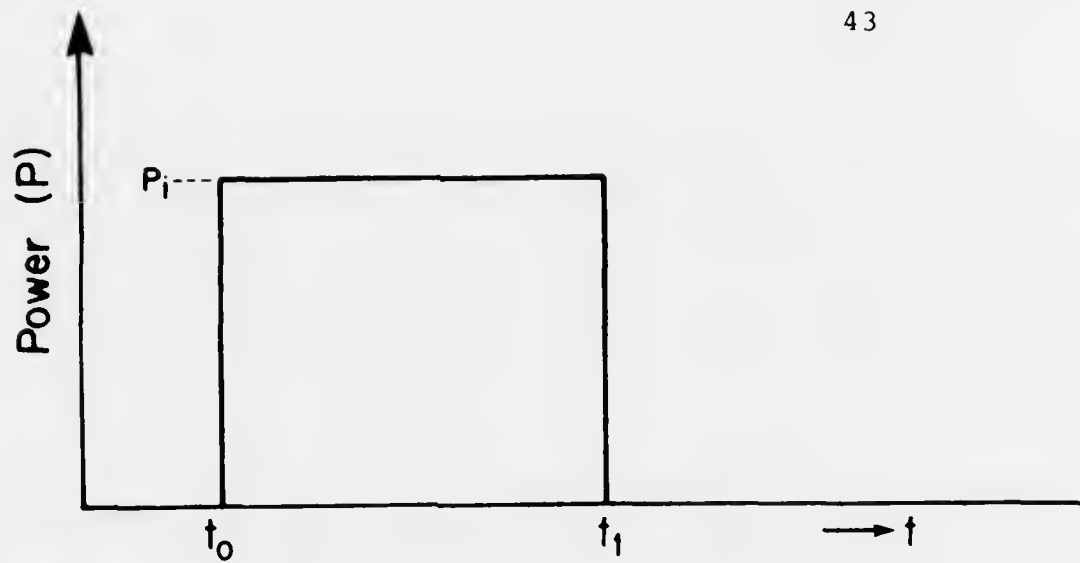


Figure 3. Waveforms Observed on the Oscilloscope for Two values of the Coupling Coefficient, β .

reached. Expressions for β have been given by Weaver⁽⁵⁸⁾ and Loew⁽⁵⁹⁾ from the square-law detected pulse shapes. For the undercoupled case ($\beta < 1$), β is given by any of the equivalent relations:

$$\beta = \frac{1 - \sqrt{P_r/P_i}}{1 + \sqrt{P_r/P_i}} \quad (5.7a); \quad \beta = \frac{\sqrt{P_e/P_i}}{2 - \sqrt{P_e/P_i}} \quad (5.7b); \quad \beta = \frac{1}{1 + 2\sqrt{P_r/P_e}} \quad (5.7c)$$

For the overcoupled ($\beta > 1$) case; β is given by

$$\beta = \frac{1 + \sqrt{P_r/P_i}}{1 - \sqrt{P_r/P_i}} \quad (5.8a); \quad \beta = \frac{\sqrt{P_e/P_i}}{2 - \sqrt{P_e/P_i}} \quad (5.8b); \quad \beta = \frac{1}{1 - 2\sqrt{P_r/P_e}} \quad (5.8c)$$

According to theory, all these expressions must be consistent with each other. They must also agree with the definition of β given in equation (5.6), which can also be expressed in terms of P_i , P_e , and P_r . The power dissipated in the resonator walls in the steady state is given by

$$P_d = P_i - P_r \\ = \frac{\omega_0 U}{Q_0} \quad (5.9)$$

At t_1 , after P_i is turned off, P consists only of the radiated wave P_e , which is given by

$$P_e = \frac{\omega_0 U}{Q_c} \quad (5.10)$$

From equations (5.6), (5.9) and (5.10),

$$\beta = \frac{Q_o}{Q_c} = \frac{P_e}{P_d} \quad \text{or} \quad (5.11)$$

$$\beta = \frac{P_e}{P_i - P_r}$$

The requirement that the measured values of P_i , P_r , and P_e must lead to a single value of β provides a convenient way to check the correctness of the experimental set-up. For example, if there are discrepancies in the β -values, it might be that the crystal detector being used is not square-law, or that there are losses or mismatches in the transmission line. Also, the directional coupler for the oscilloscope arm might not have good directivity, or the frequency might be off-resonance. In general, more errors are introduced in the measurement when β is large so that it is a good practice to arrange to use small β -values. A rather convenient β -value to use is $\beta = 1/3$. This gives the most accurate measurement for β since, then, the coupling is such that $P_e = P_r$.

As mentioned before, Q_L can be determined by measuring the time constant, τ , for the decay of P_e . The relationship between Q_L and τ is derived in the following way: In the lumped equivalent circuit for the microwave network, the current, $i_e(t)$ associated with the radiated electromagnetic wave has the following form:

$$i_e(t) \propto e^{-\omega_0 t / 2Q_L} \quad (5.12)$$

which gives

$$P_e(t) \propto e^{-\omega_0 t / Q_L} \quad (5.13)$$

The ratio of $P_e(t)$ at two different times, t_1 and t_2 is:

$$\frac{P_e(t_1)}{P_e(t_2)} = \exp\left[\frac{\omega_0(t_2 - t_1)}{Q_L}\right] \quad (5.14)$$

If $(t_2 - t_1) = \tau$, the time constant, then from equation (5.14), $P_e(t_1)/P_e(t_2) = 2$, by definition. Thus,

$$Q_L = \frac{\omega_0 \tau}{\ln 2} \quad (5.15)$$

Combining equations (5.5), (5.6), and (5.15) gives the following expression for Q_0 ,

$$Q_0 = (1 + \beta) \left(\frac{\omega_0 \tau}{\ln 2} \right) \quad (5.16)$$

Expressions for the peak magnetic flux densities on the cavity walls are derived in Appendix C for the particular geometries and frequency used. These are given by

$$B_{\max} = C_m \sqrt{Q_0 P_d} \text{ (Gauss)} \quad (5.17)$$

where P_d is the power dissipated in the cavity in watts and C_m is a factor determined by geometry and frequency. In order to measure the breakdown field, the incident power is

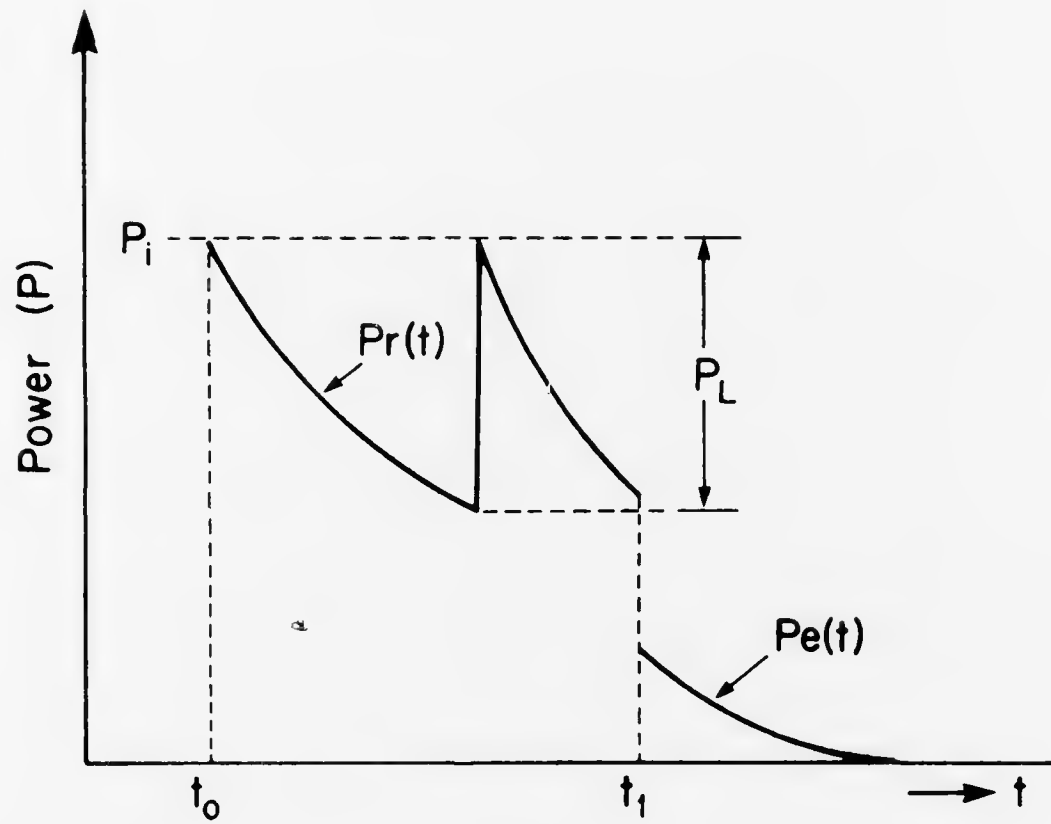


Figure 4. Illustration of the Oscilloscope Trace During Magnetic Breakdown.

increased in the manner to be described in the next section until a discontinuity occurs in the reflected power, as depicted in Figure 4. The difference between the incident power level and the reflected power level just before breakdown, P_L , is then used in equation (5.17), together with the measured Q_0 just before breakdown, to determine B_{\max} for the cavity.

iii. Microwave Circuits and Measurement Procedures

Even though the decrement method for measuring Q_0 does not need the high degree of stability required in other measurement techniques, there are still some frequency stability requirements to be met. For example, it is expected that the short-term frequency stability of the microwave signal generator be within about 5% of the cavity bandwidth, $\Delta\omega = \omega_0/Q_L$. Furthermore, this stability must be maintained to within the time constant (τ) for the natural cavity decay. Several stabilization techniques have been discussed in the literature. Among these are the automatic frequency control (AFC) method of Pound⁽⁵⁷⁾ and the phase-locked stabilization technique described by Turneaure.⁽²⁷⁾ An extremely simple but effective way to stabilize microwave oscillators is by the method of passive stabilization. In this method, the oscillator is stabilized by the reaction from a high-Q circuit, which in the case being considered,

is the superconducting cavity. The superconducting cavity is directly coupled to the microwave oscillator and by tuning the latter to the resonant frequency of the cavity and adjusting the electrical length between the cavity and the oscillator it is possible to lock the two frequencies onto each other.

Low incident-power measurements were carried out with the microwave circuit* shown schematically in Figure 5. The Gunn oscillator ⁽⁶⁰⁾ could be mechanically tuned over a range of $\pm 600\text{MHz}$ about the center frequency of 11.2GHz . Fine-tuning was done by adjusting the varactor tuning diode to provide an electronic tuning range of about 6MHz . The switching speed of the PIN diode switch, defined as the time interval between 10% and 90% of the output rf power level, was less than 20nsec , and the nominal isolation characteristic between the ON and OFF states was 65db . This switching speed of less than 20nsec was more than sufficient for the decay times ($>30\mu\text{sec}$) measured with the oscilloscope.

*The microwave circuits described here, with some modifications, were developed by Dr. John A. Yasaitis, now at Lincoln Laboratory, M.I.T. The author is grateful to him, not only for the chance to use the equipment, but also for his continuing interest in this work.

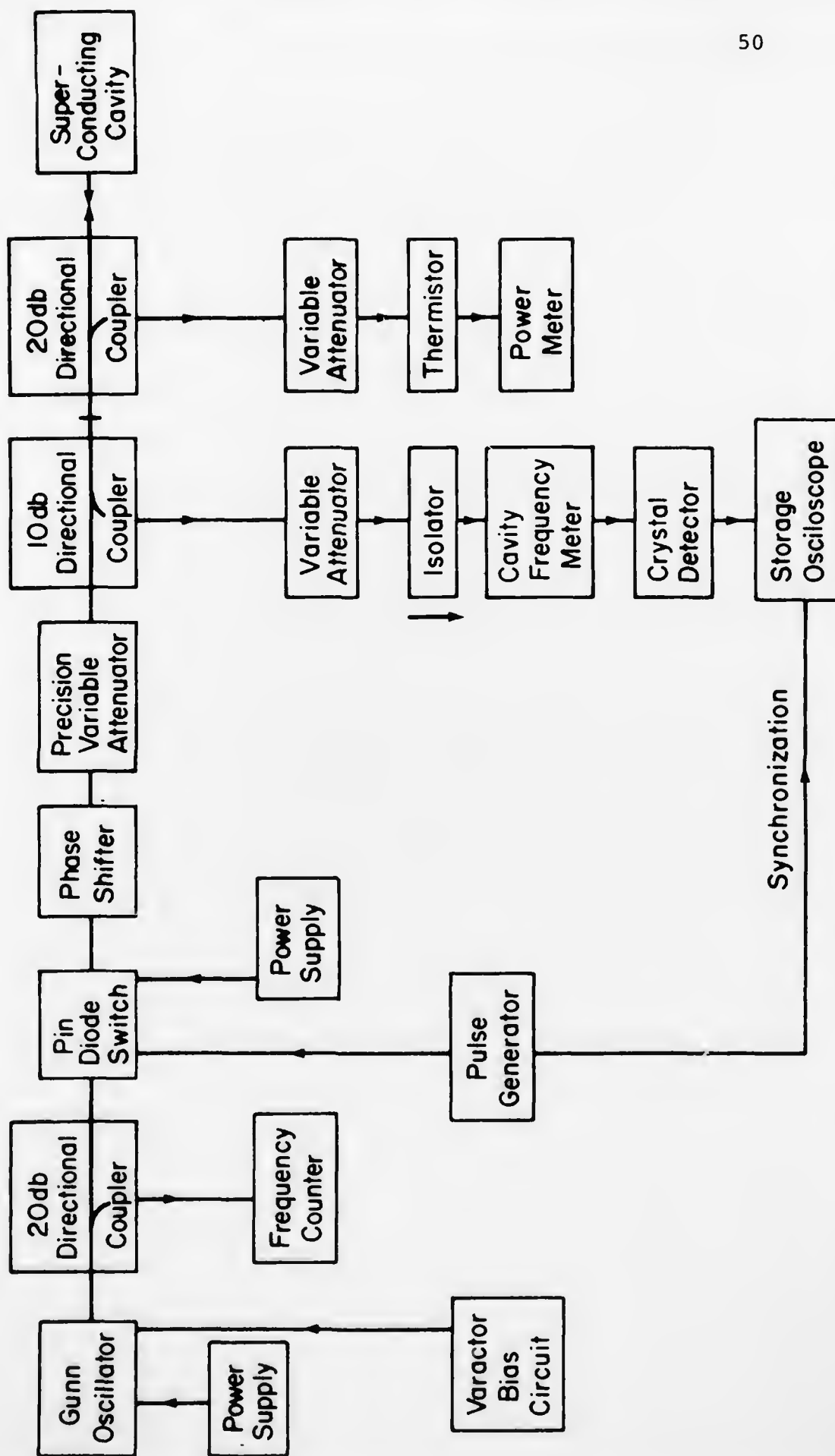
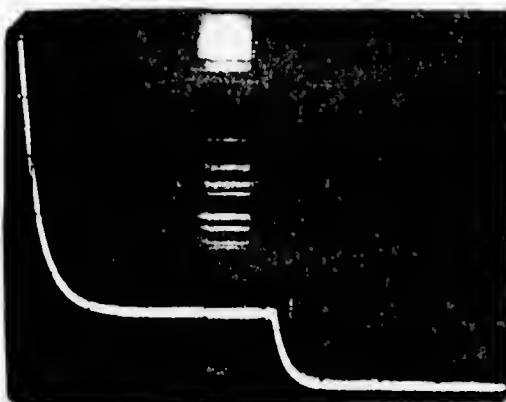


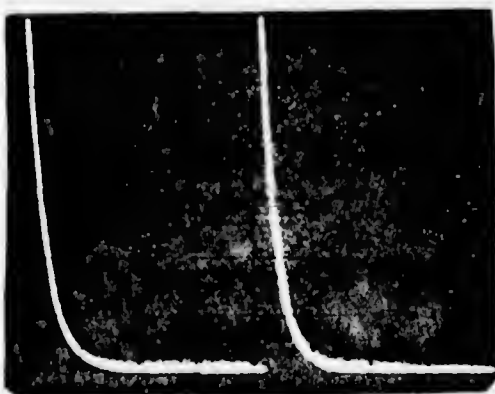
Figure 5. Schematic of the Microwave Circuit for the Low Power Measurements.



(a) $\beta = 1/3$

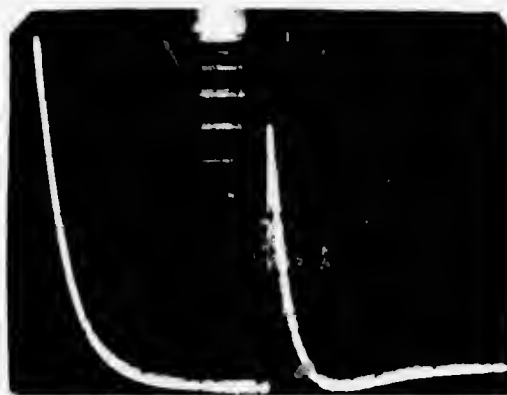


(b) $1/3 < \beta < 1$

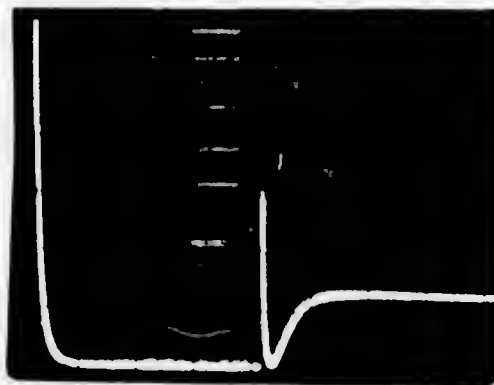


(c) $\beta = 1$

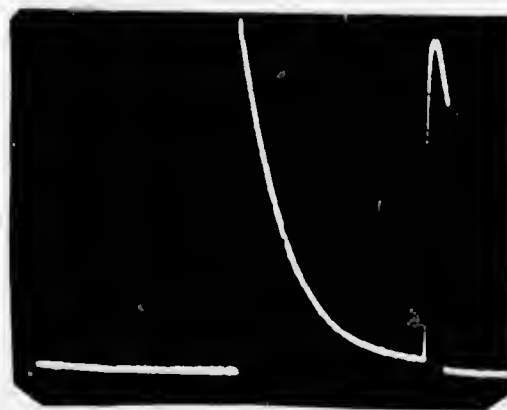
Figure 6. Photographs of typical oscilloscope traces during rf measurement.



(d) $\beta > 1$



(e) $\beta > 1$



(f) Magnetic Breakdown.

The incident power level could be varied from the maximum oscillator output (75mw) to about 1mw by means of the precision variable attenuator. The Thermistor/Power meter⁽⁶¹⁾ combination allowed the incident power level to be determined. The reflected power could be observed on the oscilloscope and during data taking, the traces on the oscilloscope were triggered by a signal taken from the square wave pulse generator,⁽⁶²⁾ which controlled the diode switch. In this way, the switching action was synchronized to the ON-OFF states of the oscilloscope traces. Very accurate frequency measurements were achieved using the automatic frequency counter,⁽⁶³⁾ and double-checked with the cavity frequency meter. The transmission line VSWR was roughly 1.30 from the directional couplers to the cavity. The mismatch was mainly due to the mylar vacuum window at the top end of the evacuated waveguide terminated by the cavity.

In order to lock the oscillator onto the resonant frequency of the cavity, the reflected wave was first obtained on the oscilloscope. The oscillator was then tuned by using the mechanical and varactor tuning attachments and slowly adjusting the phase shifter until a discontinuous drop was observed in the reflected power. The varactor tuning bias and the phase shifter were then further adjusted

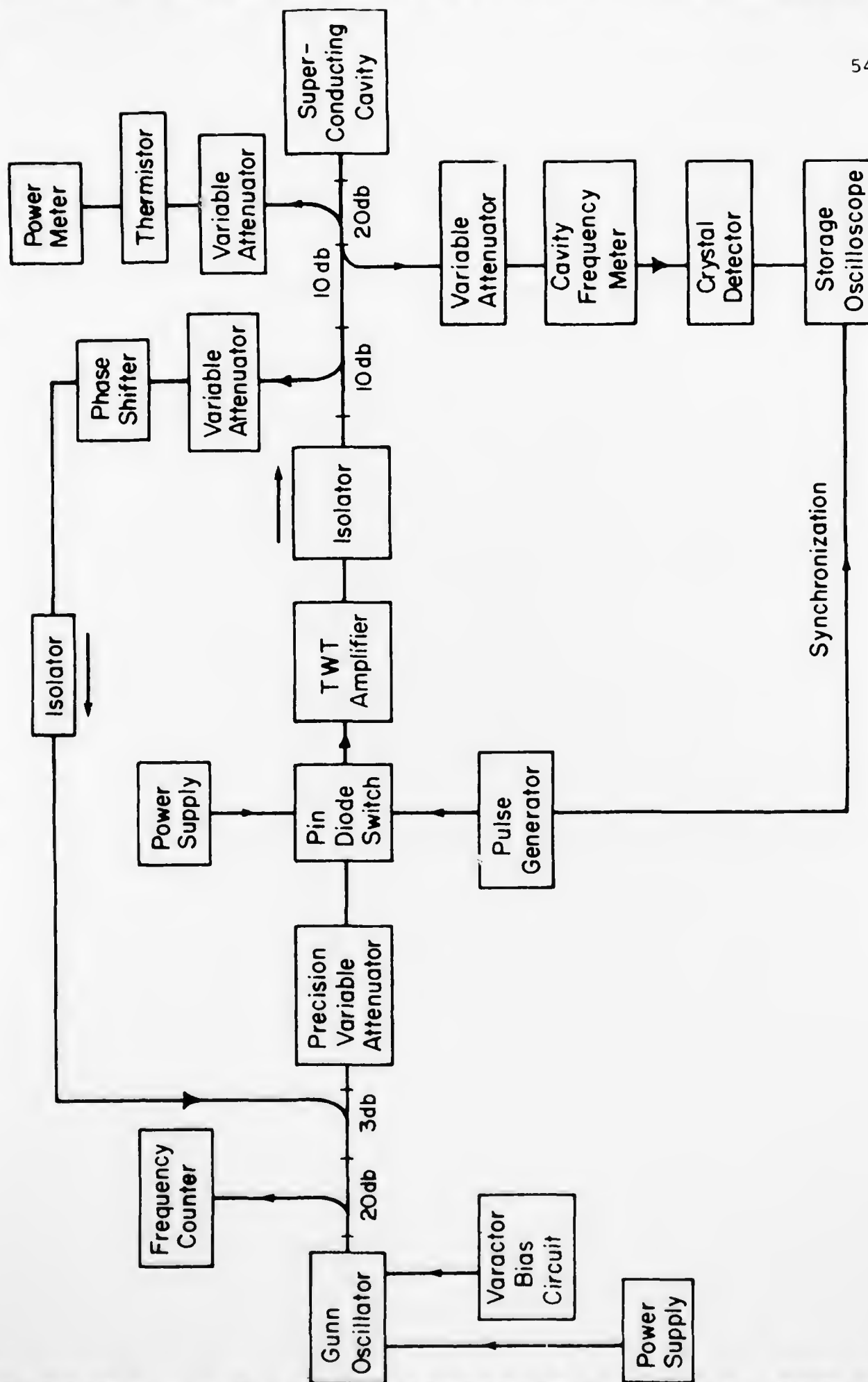


Figure 7. Schematic of the Microwave Circuit for High Power Measurements.

to the resonant frequency which corresponded to a minimum in the reflected wave. Values of the reflected power, P_r , the incident power, P_i , the radiated power, P_e and the time constant, τ , could then be determined after adjusting the coupling mechanism on the cavity for a convenient value of the coupling coefficient, β . During each measurement it was important to be certain that the oscillator was at the cavity resonance. This was done by adjusting the phase shifter and the varactor tuning bias for a minimum in the reflected power, or a maximum in the radiated power, both at $t=t_1$ in Figure 3. Oscilloscope photographs of typical traces for various values of the coupling constant are shown in Figure 6.

The microwave equipment used for high power measurements is shown schematically in Figure 7. Unlike the low power circuit, the reflected power from the cavity is made to return to the Gunn Oscillator by a path different from that taken by the incident power. The output power from the oscillator was amplified by the TWT amplifier⁽⁶⁴⁾ in order to provide high incident power on the superconducting cavity. The two isolators were used to insure that the incident and reflected waves were unidirectional. Ten per cent of the power reflected from the cavity is thus coupled to the oscillator in order to provide the

stabilization of the oscillator described before. The phase shifter in this "feedback arm" of the circuit is again used to adjust the electrical length between the cavity and the oscillator to an integral number of half-wavelengths. After mechanical tuning, the phase shifter and the varactor tuning bias can be used to lock the cavity and oscillator to each other as in the low power case. All the other components of the circuit have the same functions described before. By means of the precision attenuator it was possible to vary the incident power at the cavity from about 8 watts down to about 1mw. Figure 6(f) shows a photograph of a typical oscilloscope trace during breakdown.

B. Design and Construction of Microwave Cavities

i.) Microwave Resonant Cavity

The cylindrical TE_{011} mode cavity is particularly suited to material studies for the following reasons: First, electric fields are zero on the surface of such a cavity and therefore there is no possibility of power dissipation arising from electron emission and dielectric loss at the cavity surface. Second, the magnetic field is zero at the corner of the TE_{011} mode cavity; thus, the cavity can be constructed with joints at the corner where losses related to the joints are minimized. This is fortunate because it is obviously easier to have sealing joints at the corners of such a geome-

try. Third, the TE_{011} mode cavity has such a simple geometry that the stringent machining tolerances required for a cavity can be realized. Unfortunately, for the cylindrical cavity the TM_{111} mode is degenerate with the TE_{011} mode. Thus it is necessary to eliminate coupling to the undesirable TM_{111} since the Q of this mode is lower than that of the TE_{011} mode and its excitation results in a lowered cavity Q by transfer of energy to the low- Q mode. Separation of modes is usually accomplished by changing the geometry at the corners of the cavity. This is enough to perturb only the frequency of the TM_{111} mode since the electromagnetic fields at the corners are large for this mode but zero for the TE_{011} mode. The excitation of the TM_{111} mode can be further avoided by minimizing any asymmetry in geometry such as departure from right circular cylindrical geometry. Further consideration of these points and how they affected the design of our cavities can be found in Section V.B.iii.

ii.) Starting Material

Both the molybdenum and rhenium used to prepare the alloy had a nominal purity of 99.99% and were purchased from Rhenium Alloys Corp. of Elyria, Ohio.⁽⁶⁵⁾ The two elements were blended together (from 6lb. of Re powder and 9lb. of Mo powder), pressed, and sintered into bars by the supplier. Melting this into an ingot was done by Stellite

TABLE 1 (67b) -

Material: Mo-Re

Sample Designation:	#1	#2
Chemical Analysis (wt.%):		
Mo	62.65; 62.95	61.30; 61.35
Re	37.25; 36.95	38.60; 38.55
C	.004	.004
N	<.0001	<.0001
O	.002	.002
Semi-Quantitative Spectrographic Analysis:		
Fe	30 ppm	30 ppm
Sn	25 ppm	25 ppm
Zn	20 ppm	20 ppm
Others, Total	<10 ppm	<10 ppm

Table I: Chemical and Spectrographic Analysis of the Electron Beam-melted Mo-Re Alloy.

Division of Cabot Corp.⁽⁶⁶⁾ The pressed and sintered powders were double electron beam-melted into an ingot approximately 2.5 inches in diameter and 6.5 inches long.

The as-received material was then chemically analyzed at two testing laboratories.⁽⁶⁷⁾ In general, there was good agreement between the two and one set of results is shown in Table I. The T_c of the alloy was measured by means of an ac susceptibility apparatus. The measured T_c for material from interior of ingot was 10.1K and exhibited an extremely sharp transition (transition range $<.2K$). Material from the end of the ingot showed a larger transition range ($\approx .5K$) suggesting segregation, possibly due to more rapid cooling at the termination of the melt.

An attempt was also made to determine the crystal structure of the alloy by means of x-ray powder techniques. The alloy was powdered by filing off material from a piece held in a lathe. The powder produced was fine enough to pass a 325-mesh screen. Powder patterns were then obtained before and after a treatment consisting of a 65-hour anneal at $1000^\circ C$ and water quenching. As expected the alloy had the b.c.c. structure. The as-cast and the as-annealed samples had lattice parameters of 3.1397 \AA and 3.1213 \AA , respectively. Several low-angle peaks were present in the powder patterns of the as-cast material.

These peaks completely disappeared on annealing.

iii.) Cavity Design and Machining

A schematic of the cavity design is shown in Figure 8. The diameter (D) and length (L) of the cavities were chosen to give resonant frequencies close to the center frequency of 11.2GHz for the Gunn oscillator. The position and size of the coupling iris was found to be as important as other workers^(9, 68) have reported. For the first two cavities (labelled Mo-Re(I) and Mo-Re(II) in Table II), the iris was .149 inch in diameter and .108 inch long and it was placed at the magnetic field maximum of the waveguide mode and at two-thirds the magnetic field maximum at the cavity end-plate. Microwave tests indicated that this diameter for the iris was too big, resulting in large losses at the coupling and hence low coupling Q's. Hence, for Mo-Re(III) (see Table II), the iris diameter was initially machined to be .110 inch and subsequently enlarged to .120 inch. The iris in this case was placed at the position of maximum magnetic field at the cavity end-plate. The main disadvantage of the latter arrangement was that enhanced magnetic field near the iris could induce premature magnetic field breakdown. Coupling Q's in excess of 1.4×10^9 were measured using the smaller coupling iris.

It was possible to vary the coupling coefficient

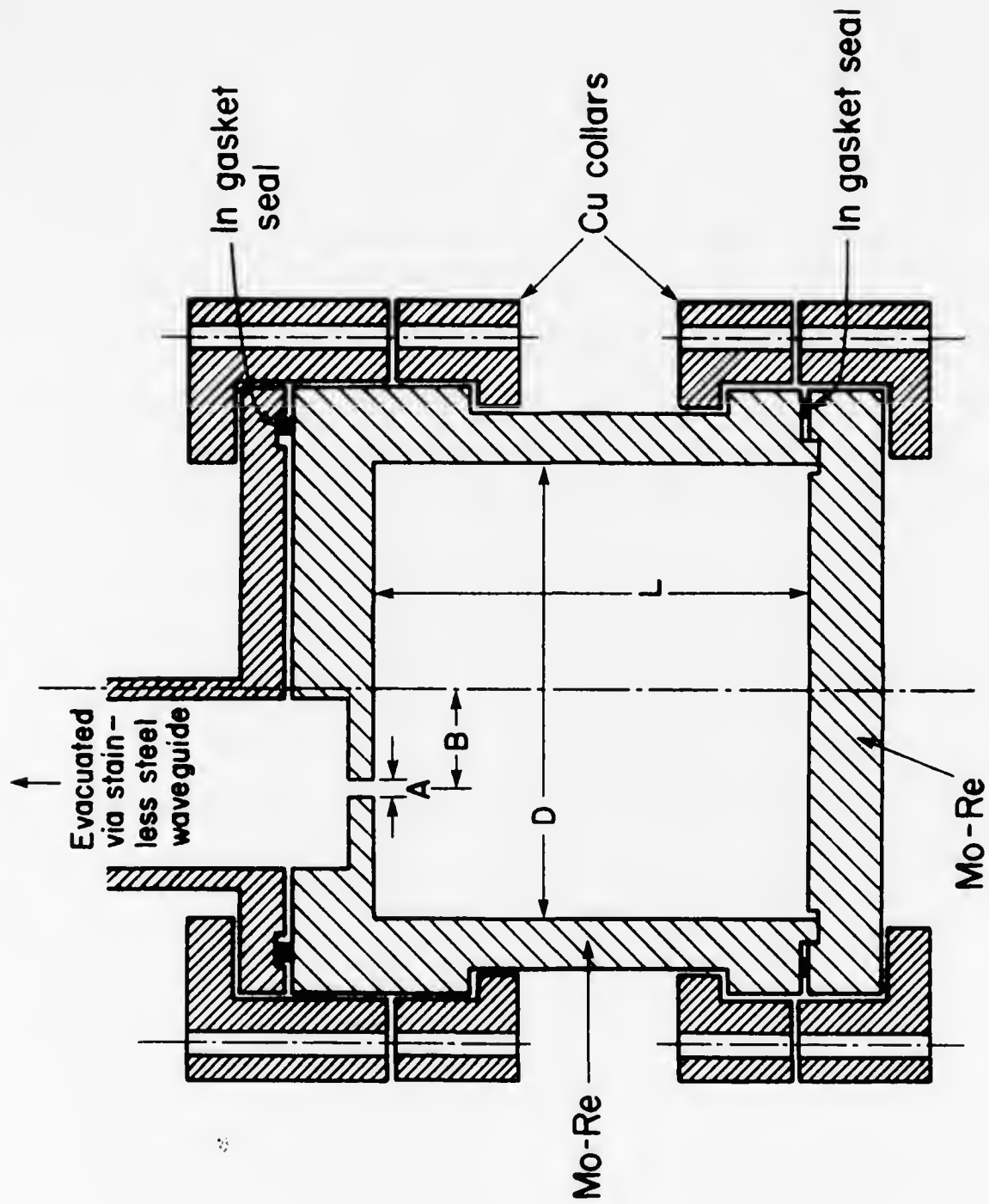


Figure 8. Cross-sectional view showing Cavity Design and Assembly.

TABLE II

SAMPLE DESIGNATION	D (Inches)	L (Inches)	D/L	A (Inches)	B (Inches)	F ₀ (GHz)	Γ (Ω)
Mo-Re (I)	1.552	.924	1.680	.149	.175	11.256	731
Mo-Re (II)	1.552	.923	1.681	.149	.175	11.257	731
Mo-Re (III)	1.38	1.37	1.007	.120	.331	11.281	780

Table II: The Important Dimensions and Resonant Frequencies of the Three Mo-Re Cavities.

by means of a coupling mechanism consisting of a .100 inch diameter Mo-Re rod-and-miniature Cu-bellows system that allowed the end of the rod to move across the diameter of the iris. The fraction of the iris covered by the probe determined the value of the coupling coefficient -- with maximum coupling, at a particular temperature, occurring when the probe is completely out of the iris cross-section. The rod-bellows system could be actuated from outside the dewar. In this way, the coupling coefficient could be varied by a factor of 30.

Another important design consideration is the ratio of the cavity diameter to its length, i.e. D/L . As shown in Table II, two values of this ratio were used in this work, and their implications for the measured breakdown fields are found in the next chapter and also in Appendix C. The crucial dimensions of the three Mo-Re cavities machined are shown in Table II.

The cavities were machined by the Metals Division of Thermo Electron Corp.⁽⁶⁹⁾ in Woburn, Massachusetts. The important dimensions shown in Table II were kept within tolerances of $\pm .001$ inch. All the machining was done using carbide tools with the exception of the rectangular recess at the end of the cavity (shown in Figure 8) which was done by means of electrical discharge machining (EDM) with a

copper-tungsten alloy electrode. Polishing the interior of the cavity was done with Al_2O_3 and SiC polishing paper and an oil lubricant, the final polishing being done with 600 grit paper. No further polishing was required prior to the electropolishing of the cavity pieces to be described in the next section.

C. Preparation Of Cavity Surfaces For Testing

Usually a preliminary series of rf tests were performed on a cavity in its as-machined state after thorough cleaning (described below). The two main surface preparation techniques used were electropolishing and ultra-high vacuum anneal. The procedures followed in each of these steps are described below.

i. Cleaning For Preliminary Testing

The as-received cavity was degreased in a hot vapor of trichloroethylene in order to eliminate the oil used in the mechanical polish and the dielectric fluid from the EDM. In the most successful preliminary cavity test, i.e. for Mo-Re(III), the cavity was subsequently cleaned with a cleanser (trademarked PEX⁽⁷⁰⁾). Next, the cavity pieces were cleaned ultrasonically in trichloroethylene, acetone and methanol (in order). Finally the cavity was rinsed several times in reagent methanol and in distilled water. Before assembling, the cavity pieces were normally

stored in methanol.

ii.) Electropolishing Set-up and Procedures

A schematic of the circuit used for electropolishing the Mo-Re cavity pieces is shown in Figure 9. The electrolyte was prepared by mixing five parts of methanol and one part of concentrated sulfuric acid.^(51, 44) Specifically, 1500 ml of methanol was put in a 2-liter nalgene conical flask in an ice bath and 300 ml of conc. H_2SO_4 was slowly poured in -- care being necessary because of the heat evolved during the mixing. The electrolyte was then allowed to cool down in dry ice until its temperature was about $-5^{\circ}C$. This was done because the cell temperature rose an average of $3^{\circ}C$ during each polishing step.

A stainless steel cathode was used for the electropolishing. A cylindrical cathode, $3/8$ inch or $5/8$ inch in diameter (depending on the cup diameter) and about 1-1/2 inches long, was used for the Mo-Re cup and symmetrically held in position, leaving about 1 cm clearance between the end of the cathode and the bottom of the cup. The cathode used for the Mo-Re end-plate was a circular disk, .05 inch thick and 2-1/2 inches in diameter. The distance between the cathode and the surface of the end-plate was about $3/8$ inches. A vertical arrangement for all the electrodes was found to give the best polishing condition.

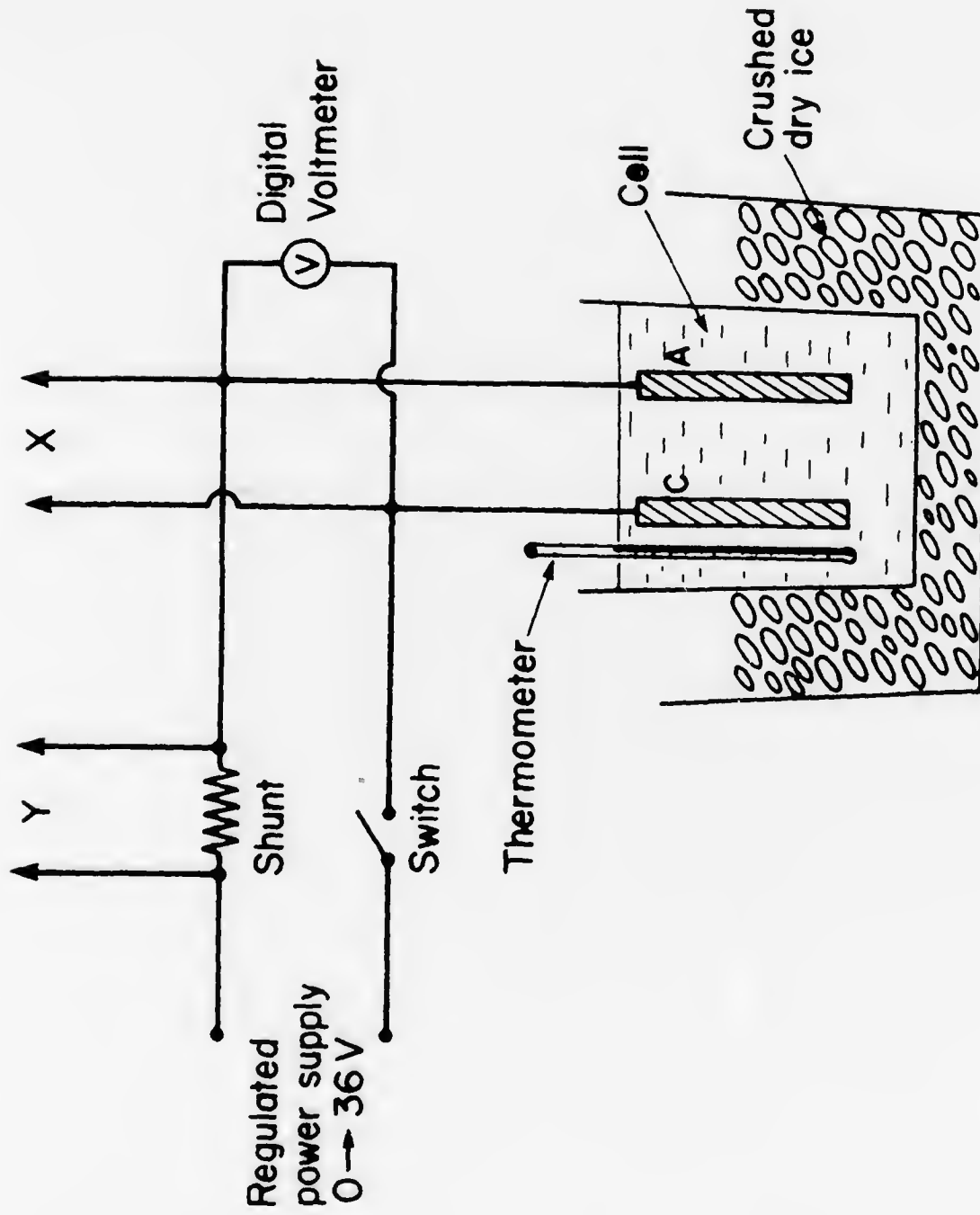
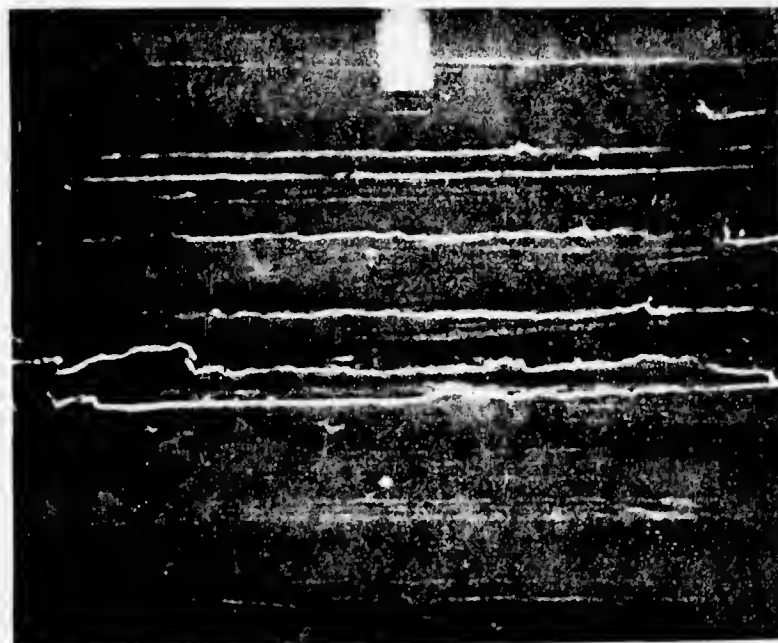


Figure 9. Schematic for the Electropolishing Equipment.

(a)



(b)

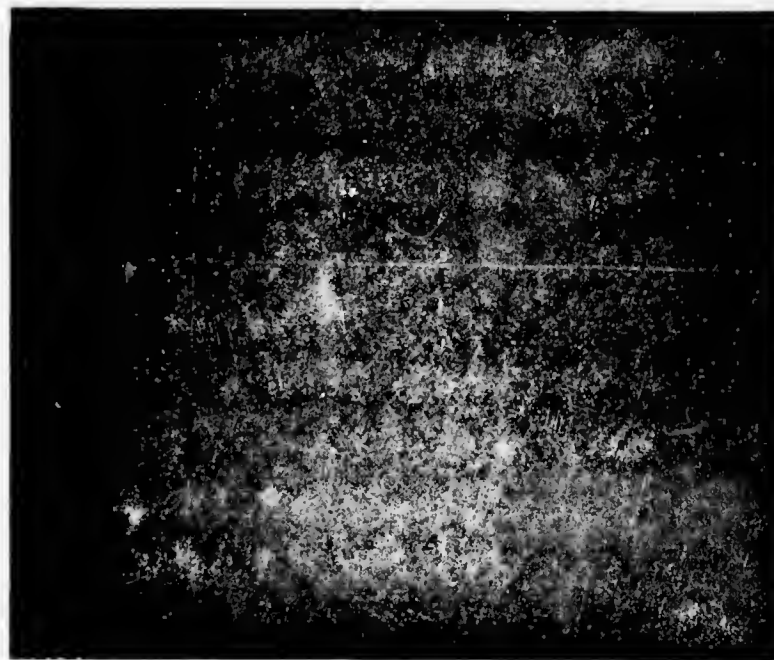


Figure 10a. Scanning Electron Micrograph of the as-machined
Cavity Surface; Magnification: X1100

Figure 10b. Scanning Electron Micrograph of the Electropolished
Cavity Surface; Magnification: X1000

Figure 10c. Scanning Electron Micrograph of the Electropolished Alloy Surface after exposure to Air for about three weeks: Magnification: X500

Note the spots occurring at the surface, probably due to the nucleation of oxides.

Figure 10d. Scanning Electron Micrograph of freshly Electropolished Alloy Surface: Magnification: X500
Note the absence of the spots seen in fig. 10c.

With the electropolishing apparatus depicted in Figure 9 , the cavity pieces were polished in the following manner: when the switch was closed the voltage was increased continuously from zero until a plateau ⁽⁷¹⁾ was observed in the I-V plot on the X-Y recorder; this is the optimum polishing voltage. The switch was then opened. In subsequent polishing intervals, closing the switch insured polishing because the voltage has been set at the plateau. Each polishing interval lasted about 50 seconds. During the polishing, a thick blue layer of reaction products was formed around the anode. This was removed between polishing steps by shaking the workpiece vigorously in methanol. A typical current density at optimum polishing was $.31 \text{ amp/cm}^2$. A single polishing interval was found to remove approximately 4 microns of metal from the surface. After about ten polishings, the surface of the alloy was remarkably smooth and mirror-like. Figure 10 shows scanning electron micrographs of the surface before and after electropolishing.

After the last polishing, the cavity pieces were thoroughly rinsed in methanol and distilled water. This was a very important step in the whole surface preparation procedure as any traces of electrolyte remaining on the surface might result in a low rf performance. Typically, the samples were vigorously shaken in methanol, then in distilled water. This was followed by a methanol rinse,

then distilled water, often alternating between the two rinses several times. After three or four additional methanol rinses, the cavity pieces were stored, completely submerged in methanol and protected from dust by a teflon plate cover.

iii.) Heat Treatment Procedures

The schematic of the rf induction furnace used to heat-treat the Mo-Re cavity pieces is shown in Figure 11. On some occasions a furnace using a copper concentrator and a 1200 liter per sec. diffusion pump aided by Ti sublimation pumping was used. This latter furnace has been described elsewhere.⁽⁴⁴⁾ With the furnace shown in Figure 11, it was routinely possible to heat-treat the samples in the low 10^{-8} Torr range at temperatures ranging from 1500°C to 1850°C. After baking out the system the furnace could be operated in the top 10^{-9} Torr range at temperatures close to 1850°C. Baseline pressures of 4×10^{-10} Torr were attainable after bake-out. The temperature during the anneal was determined by means of a two-color pyrometer with a built-in mechanism for emissivity and glass absorption corrections. It was found that alloy surfaces unprotected from Ti vapor became contaminated with Ti. This took the form of Ti-rich precipitates on the surfaces as shown in Figure 12. The possible influence of such Ti contamination on the rf performance of the Mo-Re cavities

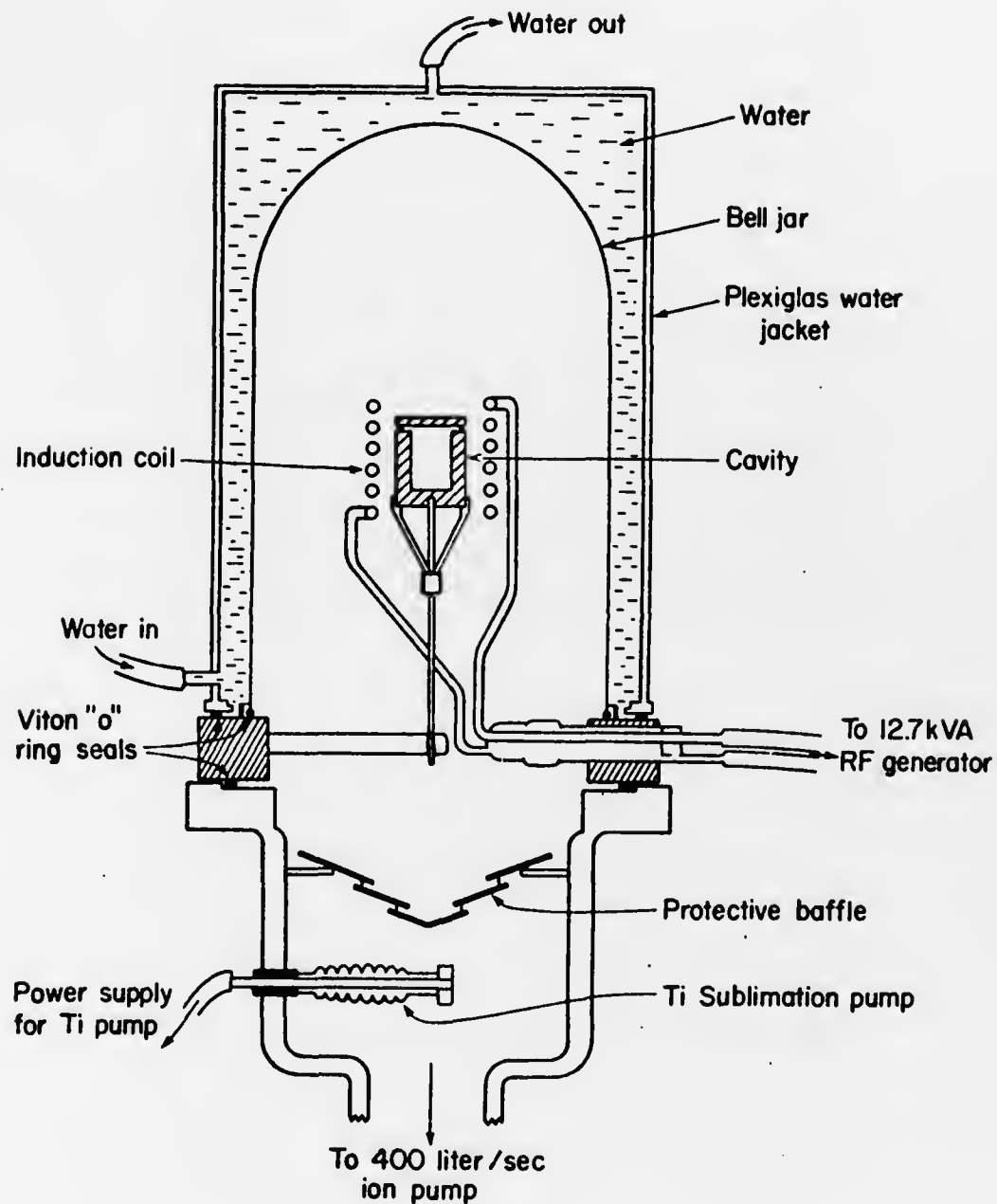
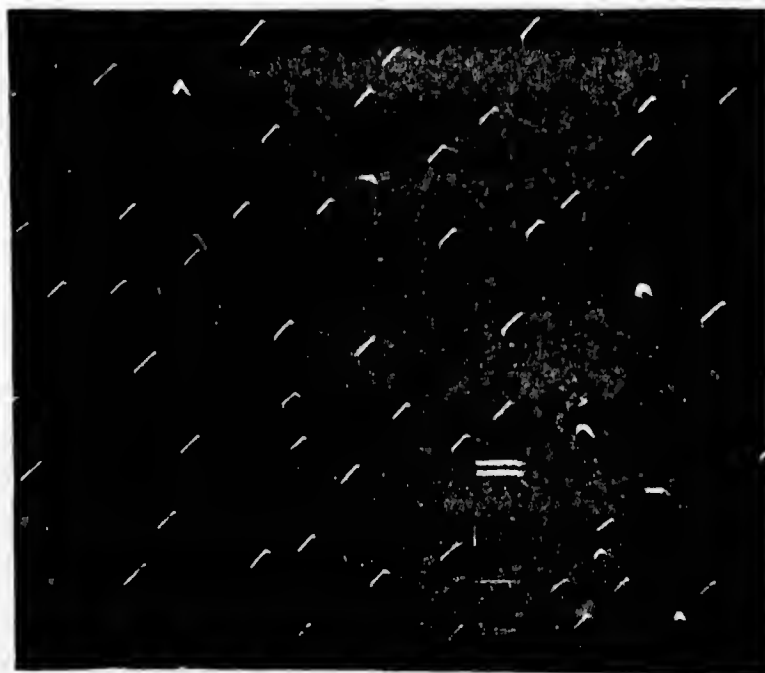
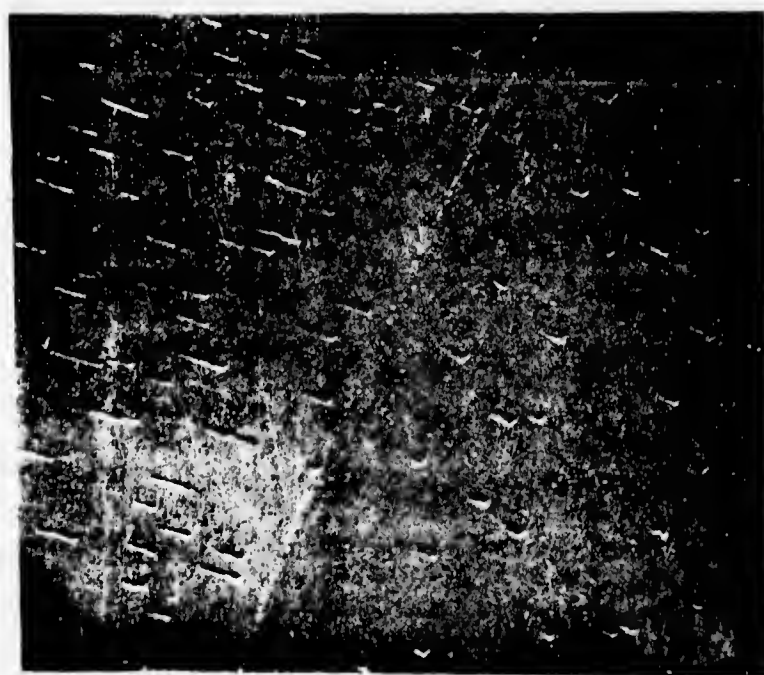


Figure 11. Schematic of the RF Furnace used in Heat-Treating the Mo-Re Cavities.



(a)



(b)

Figure 12a. Scanning Electron Micrograph of Ti-contaminated $\text{Mo}_{0.75}\text{Re}_{0.25}$ Surface after Heat Treatment; Surface unprotected from Ti vapor of the Ti Sublimation pump during the Heat Treatment. Magnification: X875

Figure 12b. SEM of Alloy Surface Treated as in Figure 12a. Magnification: X500

is discussed in the next chapter.

With the above rf equipment, the following procedures were employed in heat-treating the Mo-Re cavity pieces. After microwave tests had been performed on the electropolished cavities as described in the last section, the cavity pieces were again electropolished a few times and set up in the furnace as shown in Figure 11. After the pressure had reached the middle 10^{-9} Torr range, the rf generator was turned on. Typically it took about ten minutes to reach operating temperature. This temperature was maintained for periods of time ranging from four to eight hours. After the anneal the heat source was turned off and the work pieces allowed to furnace-cool. The handling and assembly of a cavity after the anneal were done in a way to maximize protection from the atmosphere. After the heat treatment the surfaces had lost some of the lustre that resulted from electropolishing; also, there was a large increase in grain-size at the surface due to recrystallization.

Another heat-treatment technique that was tried during the course of this work was hydrogen anneal. This was done in a quartz-tube furnace at 1000°C in flowing hydrogen which was burned at the efflux end of the tube. This was done to reduce any oxides of molybdenum or

rhodium that may have formed on the surface of the alloy.⁽⁷²⁾ Results of rf tests after this surface treatment are given in the next chapter.

iv.) Cavity Handling and Assembling Procedures

In order to protect the as-prepared cavity surface from dust and other foreign matter, the assembling of the cavity was done in a glove-box constructed especially for this purpose. Attached to this glove-box was a dust collector (Torit number 54 cloth filter type). This could remove dust particles down to 1 micron in size (with a collection efficiency of 99.7% or better) from the work area. Before introducing the cavity pieces, the box and all the equipment used for the assembly, including the indium gaskets, copper screws and collars as well as the parts for the variable coupling mechanism were thoroughly cleaned. [cleaning of the indium gaskets and coupling parts was done ultrasonically in trichloroethylene, acetone and methanol]. Either pure dry N_2 or Ar gas was recirculated through the dust collector/glove-box system for at least thirty minutes -- prior to insertion of the cavities in the box.

The cavity was assembled, as shown in Figure 8, after attaching the coupling mechanism. Care was necessary to ensure that the In gasket seal was compressed uniformly around the circumference. The Cu collars had been machined

in such a way that when they met, the In gasket squashed down to a predetermined thickness that was enough to vacuum-seal the cavity. There was only a slight difference in the assembling procedures for the heat-treated samples and the electropolished and/or as-machined samples. In the former case the cavity was assembled without delay after removal from the furnace, while for electropolished samples it was necessary to dry the cavity pieces in the glove-box after removal from the final methanol rinse before assembly. The assembled cavity, vacuum sealed to a 45° waveguide twist, was then attached (by means of an indium gasket seal) to the end of the waveguide leading to the test equipment. The coupling iris was always kept pointing down in order to prevent dust particles from falling into the cavity.

v.) Cryogenic Equipment

The essential features of the cryogenic equipment are shown schematically in Figure 13. The as-assembled cavity is shown in place. The joints indicated by I_1 and I_2 were vacuum-sealed by compressing .013 inch thick In gaskets down to .007 inch. The 10 mils thick stainless steel waveguide was prevented from collapsing during evacuation by means of the brass rods soft-soldered on its wide walls as shown in Figure 13. Because of its low thermal conductivity relative to copper, the stainless steel waveguide prevented

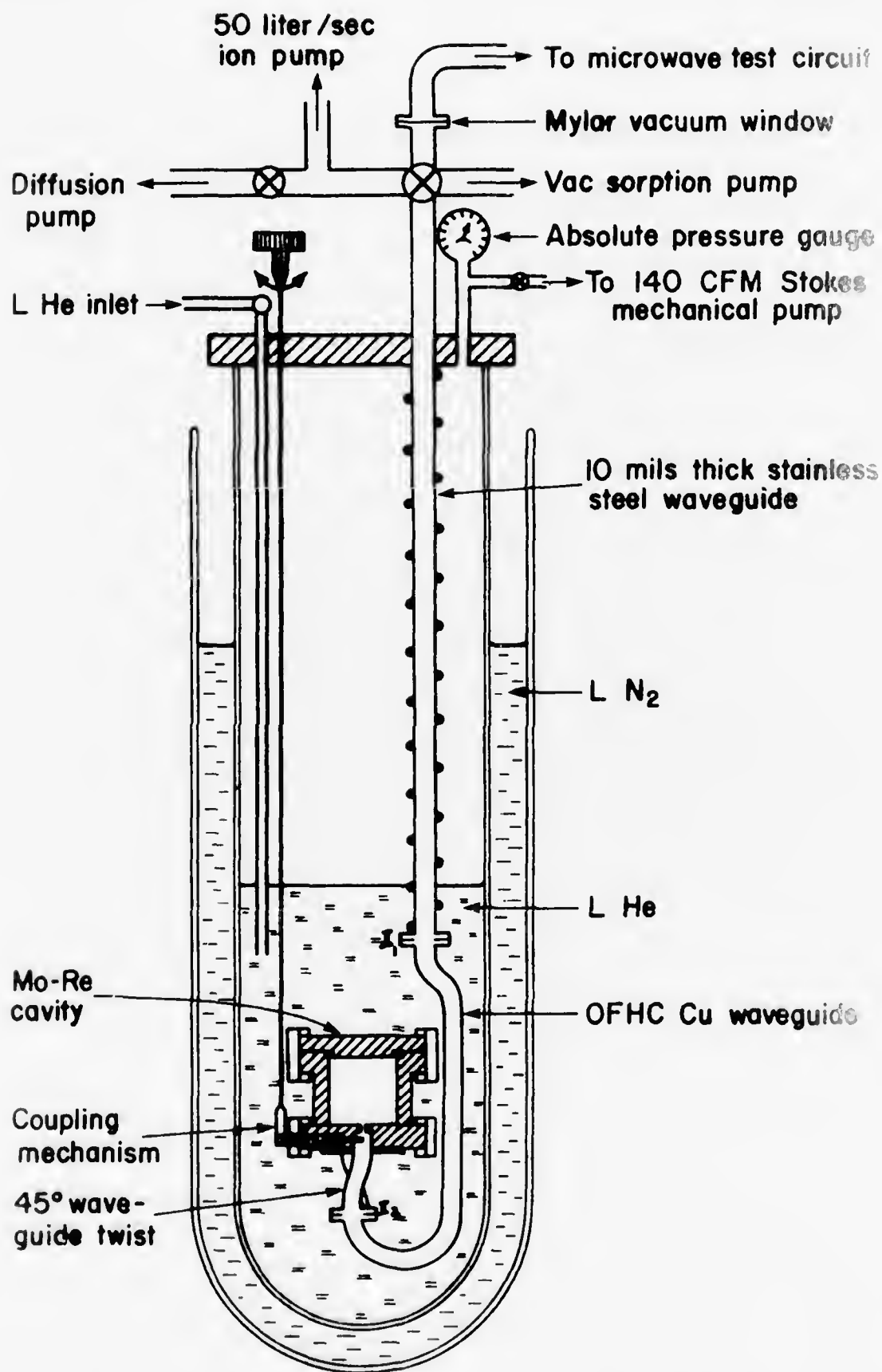


Figure 13. Cryogenic Equipment During RF Measurements.

excessive heat conduction from outside to the cavity. The 10 mils thick mylar vacuum window was sealed to the waveguide by means of a viton gasket. Rough-pumping on the cavity/waveguide system was done by either the diffusion pump or the liquid nitrogen sorption pump. Pressures as low as 5×10^{-8} Torr could be obtained in the cavity during testing by means of the 50 liter per sec ion pump. The temperature of the helium bath was monitored and controlled by standard vapor pressure techniques. The entire dewar system was surrounded by a double magnetic shield so that the cavity could be cooled in an ambient magnetic field less than 10^{-4} G. The magnetic shield consisted of two concentric cylinders of .031 inch thick μ -metal.

CHAPTER VI:VI. RESULTS, DISCUSSIONS AND CONCLUSIONSA. Summary of Measurements

Summaries of measurements made on the three Mo-Re cavities investigated are given in Tables III, IV, and V. The Q_0 values at $T = 1.4K$ and the corresponding residual surface resistance values and breakdown magnetic fields (when measured) are given in these tables. The Q_0 values for the test runs not entered in the tables were either too small to be measurable with the decrement technique or were about 1×10^5 . Magnetic breakdown fields were determined when Q_0 values of 3×10^8 or larger were obtained. Superconducting energy gap values, $\Delta(0)$, were determined whenever it was possible to obtain the BCS part of the surface resistance, as will be explained later. Trends observed in the shapes of the surface resistance curves and measured Q_0 values, as well as the dependence of Q_0 on the peak magnetic field at the surface of the cavities are discussed following these tables. "E-P" stands for "Electropolished" in the tables.

TABLE III: SUMMARY OF RF MEASUREMENT ON MO-RE (I)

Test No. And Date	Cavity Status And Treatment	Qo at Temp.	Residual Surface Re- sistance, R_o (Ω)	Breakdown Field (Gauss) at 1.4K	Remarks
4 8/12/74	As-received Cavity: Ultrasonically cleaned in trichlor, acetone and methanol	8.6×10^5 (1.4K)	8.5×10^{-4}	-	First three test runs and run #5 gave similar results
6 10/8/74	E-P cavity; removed 32 μ m. Rinsed in dist. H ₂ O, NH ₄ OH and methanol	1.2×10^7 (1.4K)	6.1×10^{-5}	-	Gunn oscillator off-resonance
7 10/29/74	E-P cavity; removed 12 μ m. Rinsed in dist. H ₂ O, NH ₄ OH and methanol	1.0×10^7 (2.6K)	-	-	Bad vacuum in cavity due to He leak.
8 11/13/74	E-P cavity; removed 16 μ m rinsed in dist. H ₂ O and methanol	4.5×10^7 (1.4K)	1.7×10^{-5}	-	Gunn oscillator off-resonance.
9 11/23/74	After #8 cavity cleaned and annealed at 1800°C for 8 hrs. in RF Furnace with diffusion pump	1.0×10^9 (1.4K)	7.3×10^{-7}	-	Cavity furnace-cooled tested 10 hrs. after removal from furnace surface contaminated with diffusion pump oil.
10 11/25/74	Retest of #9, as set-up.	3.1×10^8 (1.4K)	2.3×10^{-6}	-	Between #9 and #10 vacuum maintained in cavity.
11 12/5/74	Oil on surface in test #9 removed in hot trichlor vapor; cavity rinsed in methanol.	1.7×10^8 (2.2K)	-	-	Cavity disassembled on 12/3/74 and de- greased on 12/4/74. Leak developed at 2.2K.

TABLE III (continued)

Test No. And Date	Cavity Status And Treatment	Q _o at Temp.	Residual Surface Re- sistance, R _o (Ω)	Breakdown Field (Gauss) at 1.4K	Remarks
12 12/7/74	Re-rinsed cavity after #11	4.3 x 10 ⁸ (1.4K)	1.7 x 10 ⁻⁶	-	Leak in #11 due to bad In seal.
13 12/19/74	E-P cavity; removed 12μm. Rinsed in dist. H ₂ O and methanol.	2.8 x 10 ⁷ (1.4K)	2.6 x 10 ⁻⁵	-	Some pitting on surface after E-P.
14 1/4/75	E-P cavity; then an- nealed at 1550°C for 8 hrs. in rf furnace with ion pump.	8 x 10 ⁸ (1.4K)	9.1 x 10 ⁻⁷	-	Evidence of bad In- joint seen in Q _o (T) curve.
15 1/11/75	High power test of #14 set-up.	4.2 x 10 ⁸ (1.4K)	1.7 x 10 ⁻⁶	80	Q _o decreased with field.
16 1/29/75	E-P cavity; removed 32μm. High power test.	1.0 x 10 ⁸ (1.4K)	7.3 x 10 ⁻⁶	-	Oscilloscope traces at breakdown highly unstable.
17 7/4/75	E-P remachined cavity; removed 32μm; then an- nealed in H ₂ furnace at 1000°C for 4 hrs.	1.6 x 10 ⁷ (1.4K)	4.6 x 10 ⁻⁵	-	Between #16 and #17, interior of cavity remachined.
18 7/16/75	Cavity annealed in H ₂ furnace at 1000°C for 4 hrs.	1.4 x 10 ⁶ (1.4K)	5.2 x 10 ⁻⁴	-	-
19 10/3/75	E-P cavity (12μm re- moved); surface treated by glow dis- charge cleaning in Ar.	5.2 x 10 ⁷ (1.4K)	1.4 x 10 ⁻⁵	-	-

TABLE III (continued)

Test No. And Date	Cavity Status And Treatment	Q_0 at Temp.	Residual Surface Re- sistance, R_0 (Ω)	Breakdown Field (Gauss) at 1.4K	Remarks
20 10/13/75	Repeated cavity treat- ment of test #19	6.0×10^5 (1.4k)	1.2×10^{-3}	-	-
21 1/10/76	Size of coupling iris reduced. Cavity E-P (44 μ m) and rinsed in dist. H_2O , NH_4OH and methanol.	3.0×10^7	2.4×10^{-5}	-	Diameter of iris reduced by electron beam-welding a Mo-Re plug and drilling smaller hole.

TABLE IV: SUMMARY OF RF MEASUREMENTS ON Mo-Re (II)

Test No. And Date	Cavity Status And Treatment	Q_0 at 1.4K	Surface Re- sistance, $R_0(\Omega)$	$\frac{\Delta(0)}{k_B T_C}$	Breakdown Field (Gauss) at 1.4K	Remarks
1 2/15/75	As-received cavity "degreased" in hot trichlor vapor, then cleaned ultrasonically in trichlor, acetone, and methanol.	1.0×10^6	7.3×10^{-6}	-	-	See Fig. 10 for SEM picture.
2 3/6/75	E-P cavity; removed 60 μ m. Rinsed in dist. H ₂ O and methanol.	6.4×10^7	1.1×10^{-5}	-	-	Shape of $Q_0(T)$ curve hints of composite cavity (curve B of Fig. 15a.)
3 3/13/75	Cavity from #2 an- nealed at 1650°C for 3-3/4 hrs. in RF furnace (ion pump).	5.8×10^7	1.3×10^{-5}	-	-	Shape of $Q_0(T)$ curve similar to above.
6 2/19/76	Cavity mechanically polished with 600 paper. E-P cavity (removed 16 μ m). As- sembled in Ar atmo- sphere. Low and high power tests.	5.2×10^8	1.4×10^{-6}	1.80	73	Between #3 and #6, V.Low Q_0 values (<105) Obtained obtained after E-P or annealing.
7 2/23/76	Retest of #6; cavity under vacuum between two tests.	4.8×10^8	1.52×10^{-6}	1.78	-	
8 3/1/76	E-P cavity (12 μ m); rinsed in dist. H ₂ O and methanol.	1.62×10^8	4.5×10^{-6}	-	-	Bad In joint (see curve B of Fig. 16).

TABLE V: SUMMARY OF RF MEASUREMENTS ON Mo-Re(III)

Test No. And Date	Cavity Status And Treatment	Q_0 at 1.4K	Residual Surface Re- sistance, $R_0(\Omega)$	$\frac{\Delta(0)}{k_B T_C}$	Breakdown Field (Gauss) at 1.4K	Remarks
1 4/10/76	"Degreased" as- received cavity in hot trichlor vapor. Cavity washed and rinsed with dist. H ₂ O and methanol.	1.84×10^8	4.2×10^{-6}	-	-	New In seal design (see Fig. 8). Assembled in Ar.
2 4/12/76	Retest of #1, as is.	1.70×10^8	4.6×10^{-6}	-	-	High power tests n not possible due to instabilities in line shapes at high power.
3 4/14/76	E-P cavity (removed 40 μ m). Rinsed in dist. H ₂ O and methanol.	1.19×10^9	6.6×10^{-7}	1.82	-	Assembled in Ar.
4 4/16/76	Retest of #3 as set- up. Low and high power tests.	1.37×10^9	5.7×10^{-7}	1.78	176	Q_0 increased slightly with field before breakdown.
5 4/20/76	Retest #3, as set- up.	1.33×10^9	5.9×10^{-7}	1.78	-	-
6 4/23/76	Exposed cavity from #3 set-up to air for 36 hrs. Low and high power tests.	9.6×10^8	8.1×10^{-7}	1.69	124	Note drop in $\Delta(0)/k_B T_C$. Q_0 decreased slightly with field.
7 4/29/79	E-P cavity (removed 20 μ m). Rinsed in dist. H ₂ O and methanol. High and low power tests.	1.37×10^9	5.7×10^{-7}	1.78	136	Q_0 dropped sharply at 67G field level.

TABLE V (continued)

Test No. And Date	Cavity Status And Treatment	Q_0 at 1.4K	Residual Surface Re- sistance, R_0 (Ω)	$\frac{\Delta(0)}{k_B T_c}$	Breakdown Field (Gauss) at 1.4K	Remarks
8 5/4/76	Retest of #7 set-up at low power.	6.75×10^8	1.16×10^{-6}	1.77	-	-
9 5/12/76	E-P cavity (removed 16 μ m). Rinsed in dist. H ₂ O and methanol	3.3×10^7	2.4×10^{-5}	-	-	-
10 5/13/76	Cavity surface mechan- ically polished with 600 grit SiC paper. Then E-P (removed 16 μ m) Rinsed in dist. H ₂ O and methanol.	2.38×10^8	3.28×10^{-6}	-	-	-
11 5/26/76	E-P cavity (removed 36 μ m). Rinsed in dist. H ₂ O and methanol.	9.5×10^7	8.2×10^{-6}	-	-	-

B. Discussions on Experimental Observations

i.) Estimated Errors

The important cavity dimensions of Table II were known to an accuracy better than .1%. Thus, the resulting uncertainty in Γ , the geometric factor, was also less than .1% since these dimensions were used to calculate Γ . (equation A-17) The errors involved in the measurement of the resonant frequency were considered to be negligible compared with other errors of measurement.

In calculating Q_0 (and hence the surface resistance), the major sources of error were in the estimation of the time constant, τ , and in the value of the coupling constant (β). For a proper experimental arrangement (see Section 5.A.ii) and for $\beta \leq 1$, the error introduced in Q_0 resulting from the uncertainty in determining β was $\leq 2\%$. An additional error of about 5% was introduced from estimating the value of the time constant (τ) from the oscilloscope traces. The errors in temperature reading ($<1\%$) were small compared with these latter errors. Thus, the total error in the determination of Q_0 (and the surface resistance) was about 7%.

ii.) Types of $Q_0(T)$ Curves

Three different types of $Q_0(T)$ curves were

observed. Some of these resulted from improper experimental set-up and could therefore not be used to characterize the rf and superconducting properties of the alloy.

(a) Measurements affected by In vacuum seal

The first type of $Q_0(T)$ curve showed the effect of the indium joint used in sealing the cavity endplate to the cup. This took the form of a sharp increase in Q_0 at 3.4K, the T_C of indium, and is thus due to the indium seal becoming superconducting. This behavior was observed only in the first two cavities (Mo-Re(I) and Mo-Re(II)). The reason for this is that in these two cavities, the geometry of the indium joint was such that during the compression of the indium gasket the indium could "spill" over the step at the end of the cup and therefore become part of the cavity interior. Examples of test runs in which the indium joint affected the results can be seen in Fig. 14 (curve A), Fig. 15a (curve A) and Fig. 16 (curves A and B). This troublesome effect of indium vacuum seals has been reported by other workers⁽⁷⁵⁾ and has been known to reduce Q -values. Another effect one might expect from such a joint is for the indium, with its relatively low H_C , to limit the maximum

magnetic fields attainable in the cavities. This is supported by the lower breakdown fields observed in the first two cavities.

(b) $Q_0(T)$ for a composite cavity

The second type of $Q_0(T)$ curve observed is represented by curve (B) of Fig. 15a and curve (A) of Fig. 18. This is the shape of the $Q_0(T)$ curve one expects when there are two different types of superconducting materials (i.e., with a large difference in their T_C 's) composing the cavity. The calculation of the theoretical $Q_0(T)$ for such a composite cavity is sketched in Appendix B and illustrated in Fig. 17 (for a composite lead/indium cavity). Experimental $Q_0(T)$ curves for such a cavity have been reported by Bruynseraede et al.⁽¹⁴⁾ and their results agree with curve (C) of Fig. 17 for the lead/indium cavity. Thus, the second type of $Q_0(T)$ curves obtained in this work, which have the same general shape of curve (C) of Fig. 17 was assumed to have resulted from some form of composite cavity configuration. In fact, the type of $Q_0(T)$ plot discussed above in (a) is for a composite Mo-Re/In cavity. To see how plausible this claim is, curves (A) of Fig. 14

and (B) of Fig. 16 can be compared with the theoretical $Q_0(T)$ for the lead/indium cavity (curve C of Fig. 17). The composite $Q_0(T)$ curves shown in Fig. 15a (curve B) and in Fig. 18 (curve A) probably resulted from the presence of areas of weakened superconductivity at the surface or from Ti contamination of the surface during the uhv anneal of the cavity pieces (see Fig. 12). It is also of interest to note that a composite-like $Q_0(T)$ curve was obtained for test runs on the as-received cavity (curve A of Fig. 18). In such a state one expects lowered T_c in the machine-damaged layer at the surface and hence the possibility of composite cavity behavior.*

(c) $Q_0(T)$ for complete $\text{Mo}_{0.75}\text{Re}_{0.25}$ Cavity

The third type of $Q_0(T)$ curve is represented by curve B of Fig. 14, curve B of Fig. 18, and by Figs. 19a, 21a, 22a, 23a, and 25a. This is the type of curve expected for a material whose surface resistance is the sum of a BCS part and the residual surface resistance (see equation (2.11)). These curves were thought to characterize the $\text{Mo}_{0.75}\text{Re}_{0.25}$ alloy surface better than the types discussed above and were therefore

* The lack of knowledge about some of the material parameters for the Mo-Re alloy prevented the calculation of composite Mo-Re/Ti or Mo-Re/In $Q_0(T)$ curves.

the kind used to extract the superconducting energy gap value for the alloy.

iii.) Effects Of Surface Treatment And Processing

Under certain conditions, the rf parameters at low temperature (Q_0 at 1.4K and R_0) did not degrade as long as a high vacuum was maintained in the cavity: for test runs on electropolished surfaces, if the incident power levels were not excessive (i.e. < 0.5 watt), continuous pumping on the cavity resulted in Q_0 (at 1.4K) values which differed from each other by factors within or close to the estimated errors. Thus, in one particular test run, Q_0 at 1.4K changed from 1.19×10^9 (after initial set-up), to 1.37×10^9 after one day. After four days, the measured Q_0 at 1.4K was 1.33×10^9 . (See runs 3, 4, and 5 of Table V). Another example of this observation is found in runs 6 and 7 of Table IV. In this case, Q_0 at 1.4K changed from 5.2×10^8 to 4.8×10^8 after four days. Even though the residual Q_0 did not change in any drastic way in these cases, it was however observed that residual loss mechanisms set in at progressively higher temperature as the cavity was allowed to sit in vacuum. This can be seen by comparing curve (A) of Fig. 15a and curve (A) of Fig. 16 (runs 6 and 7 of Table IV) where the onset of saturation in the $Q_0(T)$ curve became less abrupt with time. A slow formation of several monolayers of oxide on the surface is blamed for this, as will be discussed below.

The cavity surface was relatively stable to exposure to air. This can be seen by comparing $Q_0(T)$ curves in Fig. 21a and Fig. 22a (test runs 5 and 6 of Table V). After run 5, the cavity was exposed to air for 36 hours. Then it was evacuated again and retested. Q_0 at 1.4K changed from 1.33×10^9 to 9.6×10^8 , a drop of about 28%. Unprotected niobium cavity surfaces exposed to air for only eight hours have shown orders of magnitude drops in Q_0 .⁽⁷⁶⁾ The exposure of the cavity surface to air resulted in a relatively large drop in the superconducting energy gap. Evidence of this can be seen by comparing test runs 4, 5, and 6 of Table V in which $\Delta(0)/k_B T_C$ changed from 1.78 to 1.69 after 36 hours exposure to air (runs 5 and 6) whereas $\Delta(0)/k_B T_C$ remained unchanged (=1.78) when vacuum was maintained in cavity (runs 4 and 5). The reason for this is thought to be a more rapid formation of oxides at the surface during the exposure. The mechanisms involved in this oxide formation are discussed later.

It was observed that rf parameters degraded progressively as more material was removed from the surface by electro-polishing. After removing about 3 mils (76 μ m) from the surface the Q_0 values measured were quite low ($<5 \times 10^7$). In order to return to high Q_0 values it was necessary to polish the surface mechanically with 600 grit SiC paper in order to reach fresh material. When about 3mils (76 μ m) of material were removed

from the cavity surface during the initial electropolishing of the cavity (run #2 of Table IV) the measured Q_o was low (6.4×10^7). After mechanically polishing the surface and removing only $16\mu\text{m}$ from the surface (run #6 of Table IV) Q_o increased to 5.2×10^8 . The explanation of this behavior must be found in either the diffusion of reaction products into the alloy during electropolishing or the formation of a thin layer of oxide at the surface. Preferential polishing of one of the component metals cannot be ruled out. Further consideration of mechanisms responsible for this behavior can be found in section 6.C.

The results of rf measurements on diffusion oil-contaminated cavity surface are given in test runs 9 and 10 of Table III. A film of diffusion pump oil (Dow Corning 705 oil) was inadvertently left on the surface of the cavity after the uhv anneal in the rf furnace using the 1200 liter per sec diffusion pump. Even with the oil at the surface the initial Q_o (at 1.4K), measured about 12 hours after removal from the high vacuum set-up, was high (1.0×10^9). This indicated that the oil film probably acted as a protective layer during this time interval, preventing any direct reaction between the residual oxygen and the alloy surface. After two and a half days, Q_o (at 1.4K) had degraded by a factor of three to about 3×10^8 . It is

possible that a slow diffusion process set in during which the oil was broken down into its components and the smaller ions (like O^{2-}) diffused into the alloy. The exact mechanism by which this process takes place is unknown to the author.

iv.) Trends in Peak Surface Magnetic Fields

High power tests were performed on the cavities only when Q_0 at 1.4K exceeded about 3×10^8 . Examples of Q_0 versus peak surface magnetic fields are shown in Figs. 20, 22c and 24. The data shown in Figs. 20 and 22c were taken before and after the 36 hour exposure of the cavity surface to air. Before the exposure, Q_0 actually increased slightly with increasing field, then remained constant before breakdown (Fig. 20). The reverse behavior was observed after the exposure (Fig. 22c). When power in excess of 3 watts was accidentally made to fall on the cavity surface, the plot of Q_0 vs. peak surface magnetic field showed some interesting features (Fig. 24). The Q_0 was fairly constant up to 67G, where a sharp drop in Q_0 occurred. Q_0 continued to decrease until it reached a minimum at a field level of about 96G. Beyond this point, Q_0 increased slightly until breakdown finally occurred at 136G as shown in Fig. 24. No consistent explanation can be offered for these differences in behavior at high power.

v. Surface Resistance Curves

Examples of the temperature-dependent surface resistance curves are shown in Fig. 15b, 19b, 21b, 22b, 23b, and 25b. These plots, derived from the $Q_0(T)$ curves, exhibit the features expected for a material whose surface resistance

consists of a BCS part and a residual part.^(77,78) The BCS surface resistance values at a given temperature were found by subtracting R_0 from the total measured surface resistance value, $R(T)$. A plot of the resulting surface resistance, $(R(T)-R_0)$ was found to be a linear function of reciprocal temperature as shown in Figs. 15b, 19b, 21b, 22b, 23b, and 25b. Fig 21b is interesting in that there was a systematic departure of $R(T)-R_0$ from linearity at low temperature, indicated by the dashed line in the Figure. Further significance of the linearity of the $(R(T)-R_0)$ plot, namely, the determination of the superconducting energy gap, is described below.

vi.) The Superconducting Energy Gap

As mentioned above, the BCS part of the surface resistance can be obtained by subtracting the measured residual surface resistance from the total measured resistance at a particular temperature,

$$R_{\text{BCS}}(T) = R(T) - R_0 \quad (6.1)$$

This was done for all the logarithmic plots of surface resistance of the Mo-Re alloy versus reciprocal temperature as shown in Fig. 15b, 19b, 21b, 22b, 23b, and 25b. In order to obtain the energy gap value, the expression $\exp(-\Delta(T)/k_B T)$ was fitted to the measured $(R(T) - R_0)$, after neglecting the

temperature dependence of the energy gap in the range of temperature of interest. Justification for the latter step can be found in Mühlischlegel's Table, ⁽⁷⁹⁾ where it is seen that between 4.2K and 1.4K the change in $\Delta(T)$ resulting from the temperature variation is only 1.5%, (for $T_C=10.1K$) which is well within the precision with which Δ can be determined by the surface resistance method. Thus, the expression actually fitted to the measured $R(T) - R_0$ was $\exp(-\Delta(0)/k_B T)$. The energy gap values obtained are shown in the figures for the surface resistance plots and in Tables IV and V. The average value of the energy gap parameter at absolute zero obtained in this way was

$$\Delta(0) = (1.78 \pm 0.04) k_B T_C \quad (6.2)$$

It was observed that $\Delta(0)$ decreased slightly with time for successive measurements of the same experimental set-up. An example of this behavior is seen in test runs 6 and 7 of Table IV in which $\Delta(0)$ was observed to change from $1.80 k_B T_C$ to $1.78 k_B T_C$ after four days. Also for test runs 3, 4, and 5 of Table V, $\Delta(0)$ dropped from $1.82 k_B T_C$ to $1.78 k_B T_C$, five days after initial set-up. The trend was seen in test runs 7 and 8 of Table V, for which, after five days, $\Delta(0)$ decreased from $1.78 k_B T_C$ to $1.77 k_B T_C$. Exposure of the cavity surface to air for 36 hours resulted in a rather substantial drop in $\Delta(0)$ as shown in test runs 5 and 6 and Figures 21b and 22b where it is seen that the exposure

caused $\Delta(0)$ to be changed from $1.78k_B T_C$ to $1.69k_B T_C$. The most plausible explanation for this decrease in the energy gap with time is the formation of surface oxide layers. A few monolayers can form even in a good vacuum but growth can be fairly rapid in air, thus accounting for the more drastic drop in $\Delta(0)$ when the cavity was exposed to air. The oxidation mechanisms and how they affect rf parameters and $\Delta(0)$ are more fully discussed in section 6.C.

A calculation of the energy gap at absolute zero for $\text{Mo}_{0.75}\text{Re}_{0.25}$, using the expression from BCS theory, is given in Appendix D. The value of $\Delta(0)$ obtained is $1.74k_B T_C$ which is in good agreement with the value of $1.78k_B T_C$ obtained from the surface resistance curves. From the value of the ratio of T_C to Debye temperature ($T_C/\theta_D = .026$ for $\text{Mo}_{0.75}\text{Re}_{0.25}$ ⁽⁷³⁾) the alloy could be a relatively strong coupling superconductor (compared with $T_C/\theta_D = .07$ ⁽⁸⁰⁾ and $T_C/\theta_D = .037$ ⁽⁸⁰⁾ for lead and niobium respectively; for weak-coupling materials, $T_C/\theta_D \leq .003$ ⁽⁸⁰⁾). However, the reduced gap values obtained in this work suggest that the alloy is quite BCS-like.

C. Surface Mechanisms To Explain The Observed Trends

The most attractive explanation for the observed trends in the rf and superconducting parameters is that after surface treatments involving either heat-treatment or electropolishing, surface oxides form and that these oxides affect the superconductivity at the surface of the alloy. It is expected that on the clean metal surface resulting from the electropolishing, the sticking probability for oxygen adsorption will be very

nearly unity. At room temperature and at a gas pressure of 10^{-6} Torr a monolayer of adsorbed gas forms on the metal surface in approximately one second.⁽⁸¹⁾ After this initial, fast formation of the first few monolayers, the sticking coefficient falls to a low value and it takes considerably longer to form the next monolayers. For the Mo-Re alloy surface, one can estimate that during the assembly of the cavity, an oxygen coverage of several monolayers (<10 monolayers) forms on the surface. After reducing the pressure on the cavity surface to $<10^{-6}$ Torr, the build-up of oxygen at the surface continues but at a slower rate. If a sticking coefficient (α) of 10% ($\alpha=.1$) is assumed, at the typical pressure in the cavity during testing (7×10^{-8} Torr) monolayer time is about 30 mins. This accumulation of oxygen at the alloy surface can explain the lowering trend in the value of the superconducting energy gap parameter, $\Delta(0)$, with time, for cavities kept under vacuum. A full discussion of this possibility is given later in this section.

For electropolished alloy surfaces exposed to the atmosphere for several hours, the formation of very thin oxide films can be expected. According to the low temperature oxidation theory of Fehlner and Mott,^(82, 83) the growth of such oxide films can occur by the diffusion of metal ions and electrons through the initial oxides and their reaction with the oxygen at the oxide-gas interface. The metal ions can move through the oxide either by the outward movement of interstitials or the inward movement of cation vacancies depending on the type of oxide formed. The work of Jaffee

and Sims⁽⁸⁴⁾ on arc-cast alloys of Mo-Re alloys of varying oxygen content has indicated that a complex oxide, possibly of the form MoReO_4 , can occur. It is reasonable to expect such an oxide since the two stable oxides known to form on both molybdenum and rhenium are the two isomorphic rutile oxides MoO_2 and ReO_2 and therefore a mutual solid solution of the two is expected.⁽⁸⁵⁾

Evidence for the formation of surface oxides on the electropolished alloy surface was obtained after two different surface studies. The more direct evidence resulted from SEM work (see Figures 10c and 10d, pages 67, 68). SEM pictures of alloy surfaces exposed to atmosphere for periods of time in excess of three weeks revealed spots on the surface that could be the nucleation centers for oxides (Fig. 10c) (SEM pictures of freshly prepared alloy surfaces showed no such surface structure.) Such oxide precipitates have been found on heated Mo-Re foils by Witcomb.⁽⁸⁶⁾ It is quite possible that the electropolished alloy surface has a reactivity approaching the heated alloy surface and hence the possibility of oxide precipitate formation on both surfaces. Witcomb studied his surfaces by hot-stage transmission electron microscopy and thus obtained better structural resolution of the oxides compared with the SEM work. An indirect evidence for the presence of oxides at the alloy surface resulted from Electron Probe Microanalysis work on $\text{Mo}_{0.75}\text{Re}_{0.25}$ buttons. One such button was electropolished and

analyzed for the molybdenum and rhenium content at the surface. Then it was allowed to sit in atmosphere for about three weeks and reanalyzed. Drastic reductions were seen in the Mo and Re at the surface. In conjunction with the SEM work on similarly prepared alloy surfaces, it is reasonable to conclude that the balance in composition at the surface is oxygen. When the button was electropolished again and reanalyzed without delay, the Mo and Re contents were close to the values obtained after the first electropolishing.

The presence of oxides on the surface of heat-treated Mo-Re surfaces is much easier to explain since Witcomb's work,⁽⁸⁶⁾ quoted above, showed direct evidence of oxide formation for surfaces heated to lower temperatures (1200K versus about 1800K used in this work). Witcomb⁽⁸⁶⁾ also observed the occurrence of preferential evaporation of the molybdenum from the surface, a process that can lead to the formation of σ -phases at the Mo-depleted regions and consequent depression of superconductivity.

The formation of adsorbed monolayers of oxygen on the cavity surface under high vacuum and the growth of thin oxide layers ($<100\text{\AA}$) on surfaces exposed to atmosphere can account for the trends in rf and superconducting parameters discussed in the previous section: When the cavity surface was kept under high vacuum ($\approx 7 \times 10^{-8}$ Torr), the Q_0 value

remained fairly constant. A slight lowering trend was however observed in the values of the energy gap value, $\Delta(0)$. When the surface was exposed to air for several hours (~36 hours), relatively substantial drops in both Q_0 (from 1.3×10^9 to 9.7×10^8 at 1.4K) and $\Delta(0)$ (from $1.78k_B T_C$ to $1.69k_B T_C$, a drop of 5%) occurred. It is suggested that as long as the cavity surface is under high vacuum the formation of true oxides at the surface is very slow. The presence of the few monolayers at the surface of the Mo-Re alloy is not expected to change the superconducting properties in any drastic way, as has already been discussed in Chapter IV. Thus, rf parameters like Q_0 should remain unchanged, as observed. An oxide of the alloy is expected to form at the surface when exposed to the atmosphere for several hours. If the oxide is normal conducting (like ReO_2), a weakening of the superconductivity in the Mo-Re alloy is expected. This is caused by the proximity effect between the alloy and the oxide layer. The measured 5% drop in the energy gap of the alloy after exposure to air for 36 hours supports the proximity effect argument, since an induced superconducting energy gap of the oxide layer implies a corresponding lowering of the energy gap of the alloy. However, the 5% drop in $\Delta(0)$ was not large enough for quantitative arguments to be made about the thickness of the oxide layer even though an upper limit

of about 150\AA would be consistent with the observed change in $\Delta(0)$.

The observation that rf parameters of the Mo-Re alloy deteriorate with continued electropolishing can be explained by assuming a build-up of diffused reaction products in the surface layer ($<500\text{\AA}$). During the polishing action, a breakdown of the electrolyte into free radicals (including SO_4^{2-} , OH^- , singly ionized hydrogen, H^+ and doubly ionized oxygen O^{2-}) is expected to occur. Driven by the electro-chemical potential at the anode, a complicated reaction between the metal and these radicals takes place as evidenced by the thick blue anodic layer (see Section 5.C.ii). It is also possible that the smaller ions present at the surface, of the alloy, notably H^+ and O^{2-} , can be driven into the metal surface by a process involving recombination and grain boundary diffusion.* Even though interstitials do not degrade superconductivity in $\text{Mo}_{0.75}\text{Re}_{0.25}$, the cumulative effect of reaction products at the grain boundaries, especially hydrogen, might be the creation of new sources of loss at the surface and hence lowered Q_0 (or increased residual surface resistance) as has been observed.

D. Further Discussions

For alloys the highest value of Q_0 to be found in the literature is $\sim 3 \times 10^9$, measured at 3.9GHz and at 1.5K⁽¹²⁾

*The author is grateful to Professor R.M.Latanision for drawing his attention to the possibility of this mechanism.

for a $\text{Nb}_{0.4}\text{Ti}_{0.6}$ cavity. A Q_0 of 3×10^9 has also been measured in a $\text{Pb}_{0.96}\text{Bi}_{0.04}$ cavity resonant at 2.60GHz and at 2K.⁽¹³⁾ The latter Q_0 corresponded to a residual surface resistance of $2 \times 10^{-7} \Omega$. For intermetallic compounds the latest results have been reported on Nb_3Sn by Pfister.⁽⁸⁷⁾: $Q_0 = 6 \times 10^9$ at 1.5K for oxy-polished $\text{Nb}_3\text{Sn-TE}_{011}$ cavities at 9.5GHz. The fabrication of the Nb_3Sn cavities was described in section 3.D. Against these values of Q_0 and R_0 should be compared the Q_0 of 1.37×10^9 at 1.4K and R_0 of $5.7 \times 10^{-7} \Omega$, the best Q_0 and R_0 values obtained by this author for $\text{Mo}_{0.75}\text{Re}_{0.25}$ cavities.

The highest breakdown field measured in the $\text{Mo}_{0.75}\text{Re}_{0.25}$ cavities was 176G. This is the highest value of breakdown field (H_{crf}) ever measured for an alloy. For the $\text{Nb}_{0.4}\text{Ti}_{0.6}$ cavity of reference 12, the highest breakdown field measured in the cavity was only 35G. A maximum field of 120G was measured on this alloy surface in a coaxial cavity configuration in which the alloy formed the center conductor of a cylindrical niobium cavity. It is interesting to note that this maximum field value of 120G is greater than H_{c1} ($\approx 75\text{G}$) for the alloy, a result which supports Halbritter's⁽³⁷⁾ theoretical arguments that H_{c1} is not the limit to the breakdown field for type II superconductors.

In the case of the Mo-Re alloy, the highest breakdown field of 176G is less than half the value of H_{c1} ($\approx 500\text{G}$)

for the alloy. The H_{crf} value of $\text{Nb}_{0.4}\text{Ti}_{0.6}$ mentioned above and the highest value of H_{crf} for the Mo-Re alloy of this work are much lower than the latest reported H_{crf} value for Nb_3Sn : For this compound a H_{crf} value of about 1000G⁽⁸⁷⁾ has been measured; this value is, again in support of Halbritter,⁽³⁷⁾ much higher than H_{cl} (~170G) for Nb_3Sn . It is possible that breakdown takes place prematurely for the Mo-Re alloy because of the grain boundary segregation mechanism mentioned in the last section. The accumulation of hydrogen and other reaction products at the grain boundaries will result in regions with poorer thermal conductivity, a situation which can cause thermal runaway and hence early breakdown in the cavities.

The 28% drop in residual Q_0 after exposure to air for 36 hours is quite encouraging, especially when compared with the behavior of similarly treated niobium surfaces. Thus, Allen et al⁽⁷⁶⁾ found that after only eight hours exposure of a niobium cavity surface to air, the Q_0 dropped by more than two orders of magnitude (from $>5 \times 10^{11}$ to 1.5×10^9). This supports the claim made earlier (Chapter IV), that this particular composition of the Mo-Re alloy system has quite stable superconducting properties even when the surface condition is altered due to the presence of adsorbed gases and interstitials.

E. Summary and Conclusions

RF measurements on three superconducting Mo-Re alloy cavities undertaken in this research has yielded Q_0 values ($\approx 1.4 \times 10^9$) which are among the highest reported to date for alloys and intermetallic compounds. In addition, the highest breakdown field (176G) measured is the best value for an alloy at the present time even though it is much lower than the highest reported breakdown field for an intermetallic compound. Also the breakdown fields were found to be much lower than H_{c1} for the alloy. It is argued that much higher breakdown fields are possible once grain boundary segregation and formation of surface oxides are eliminated or minimized. Thus, the peak fields obtained in this work cannot be used to disprove Halbritter's theoretical prediction that breakdown fields higher than H_{c1} are possible.

From the temperature-dependent surface resistance, the superconducting energy gap for $\text{Mo}_{0.75}\text{Re}_{0.25}$ was determined for the first time and compared with the calculated value from BCS theory. The agreement between the theory and experiment was quite good.

In addition to the rf and superconducting parameters mentioned above, certain trends were observed which were functions of time and cavity surface processing. In

order to explain these trends, mechanisms involving the formation of surface oxides and diffusion leading to grain boundary segregation have been suggested.

Surface preparation procedures, capable of producing smooth and bright alloy surfaces for the rf measurements were developed. The two main methods used were electropolishing and uhv anneal. It was found that prolonged electropolishing resulted in lowered rf parameters indicating the cumulative effect of surface reaction products which were not removed by the rinsing procedures employed in this work.

F. Suggestions for Future Work

In view of the excellent superconducting properties of the Mo-Re alloy studied, further research is necessary. In particular,

(a.) Surface preparation procedures can be studied further. For example, new electrolytes can be tried for the electropolishing of the surface that might result in even more stable surfaces. Recently, an electrolyte composed of 1 gm NaOH, 35gm $K_3Fe(CN)_6$ and 150ml H_2O has been found to polish molybdenum and its alloys quite well⁽⁸⁸⁾ and could be tried with the Mo-Re alloy.

(b.) Sputtered Mo-Re films (especially those having the approximate composition of $\text{Mo}_{0.7}\text{Re}_{0.3}$) have T_C 's up to ~15K.⁽⁸⁹⁾ This represents an increase in T_C of 2-3K over the corresponding bulk values and is attributed to the formation of a metastable A-15 phase in the sputtered films. Upper critical fields of over 100kG have also been measured in some of these high T_C Mo-Re films.⁽⁹⁰⁾ Because of the high T_C and critical fields of the Mo-Re films, good rf parameters are expected from resonant cavities fabricated with these films. Investigations using sputtered films offer a way of varying the composition of the alloy and determining the effect of such variation on the rf properties. Another incentive to working with Mo-Re films instead of massive structures is the high cost of rhenium (~\$1000 per lb.).

(c.) In the course of the present investigation, it became clear that a surface study of the alloy is interesting in its own right. For example, the reaction of Ti vapor and the heated alloy surface which produced crystallographically oriented precipitates (see Fig. 12) can be further studied. The regular geometric precipitates at the

alloy surface were completely unexpected; studying them will reveal the nature of the diffusion and solubility of Ti in the Mo-Re alloy. The exact composition of these precipitates can be further studied by more accurate methods involving Electron Probe Microanalysis. By means of Hot Stage TEM, it will also be possible to study not only the nucleation stages during the formation of these precipitates but also the crystal planes on which they occur.

Note: Since reference to the following figures is in no particular order in Chapter VI, they have been grouped together at the end of the Chapter for convenience.

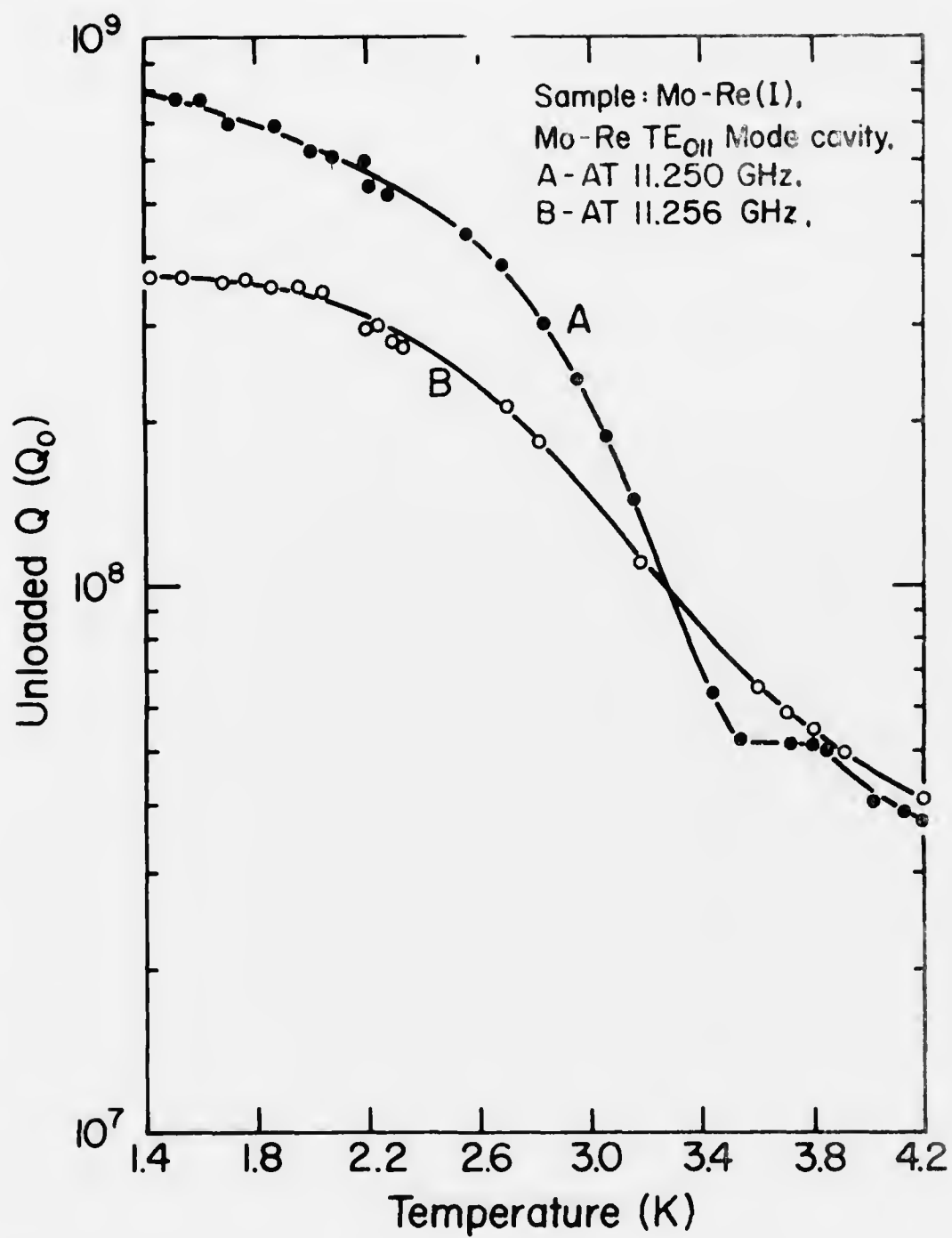


Figure 14. $Q_0(T)$ Curves for Cavity Mo-Re(I).

Figure 15a.

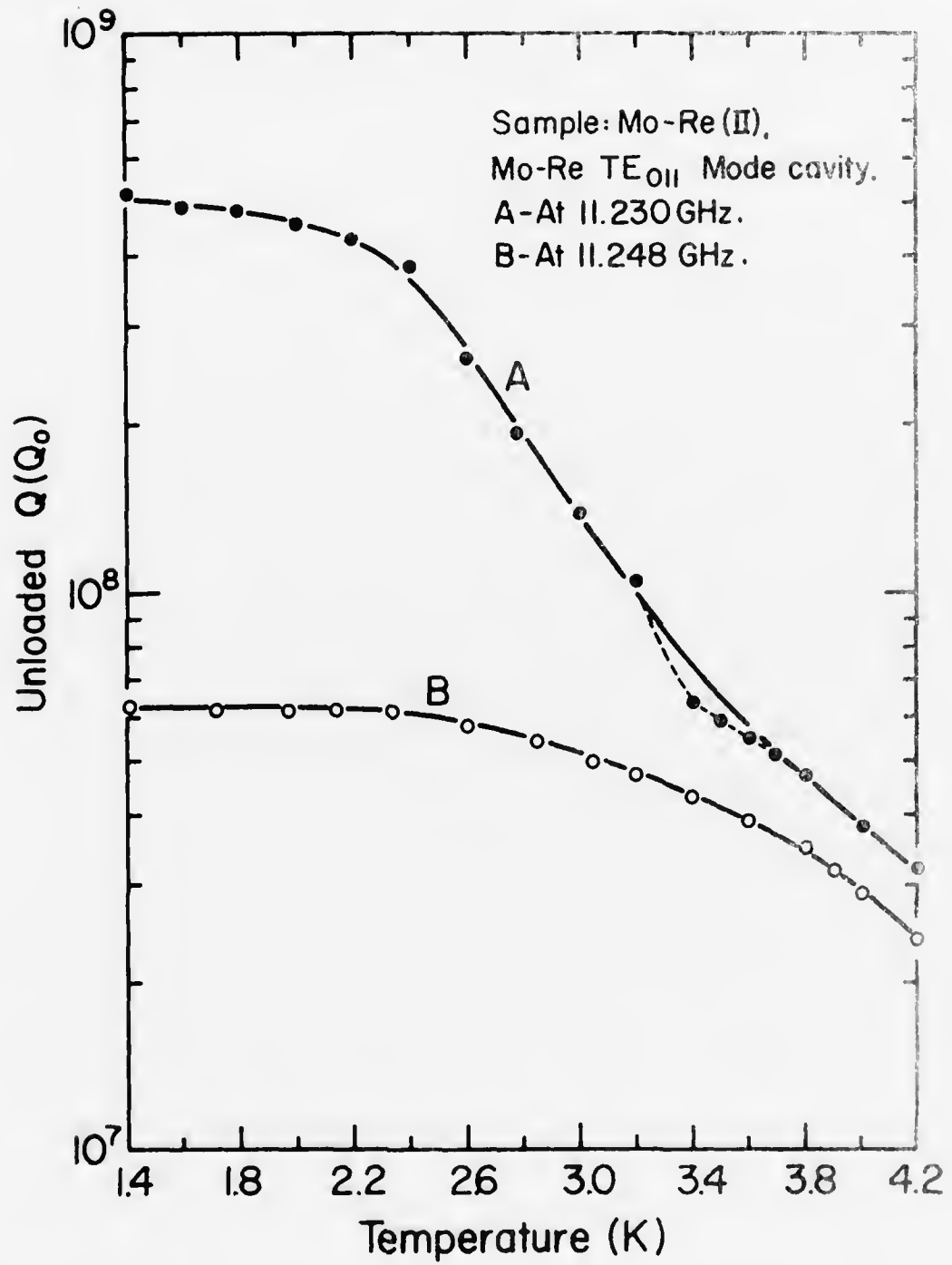
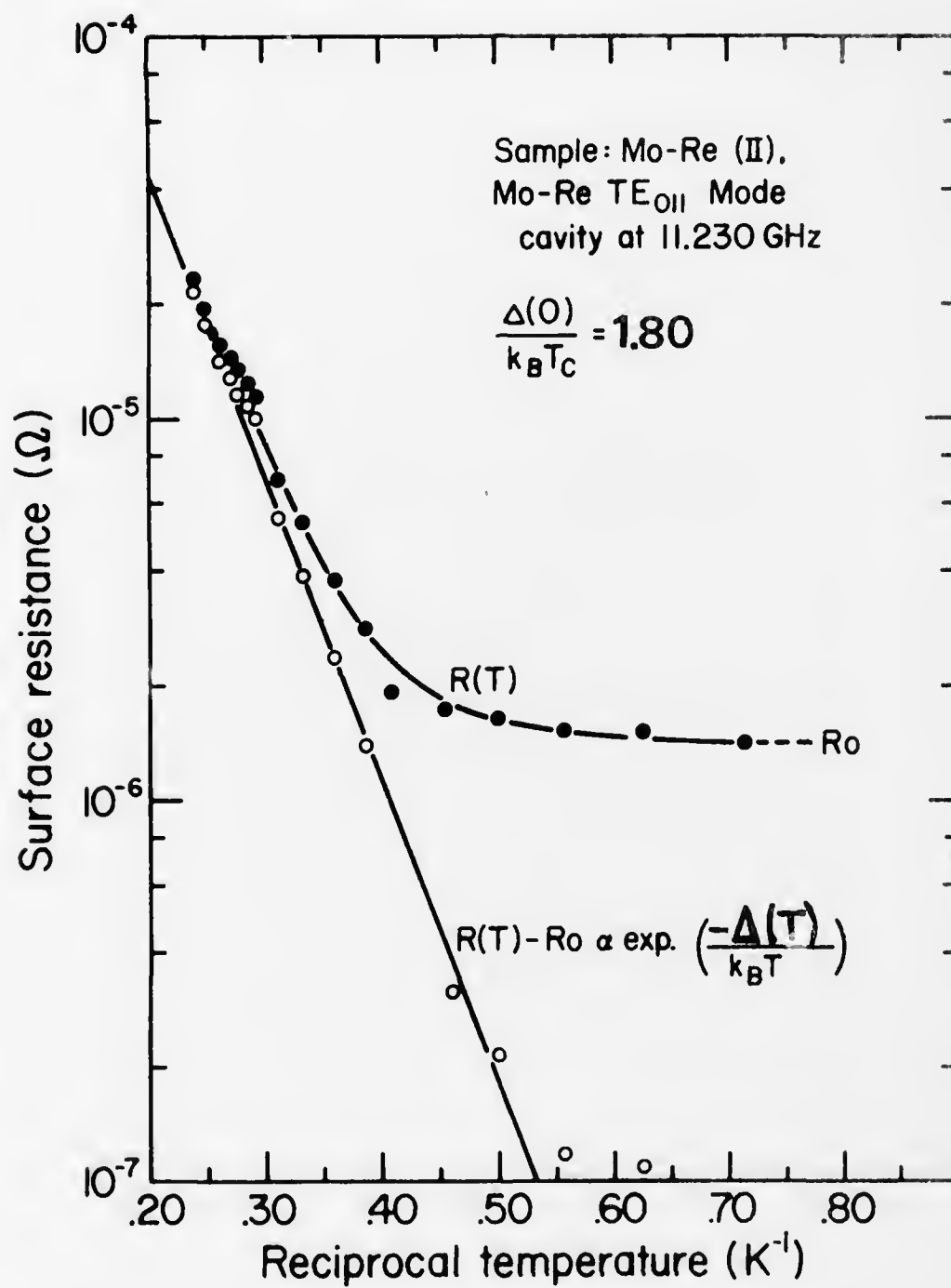
Figure 15. $Q_0(T)$ and $R(T)$ Curves for Cavity Mo-Re(II).

Figure 15b.



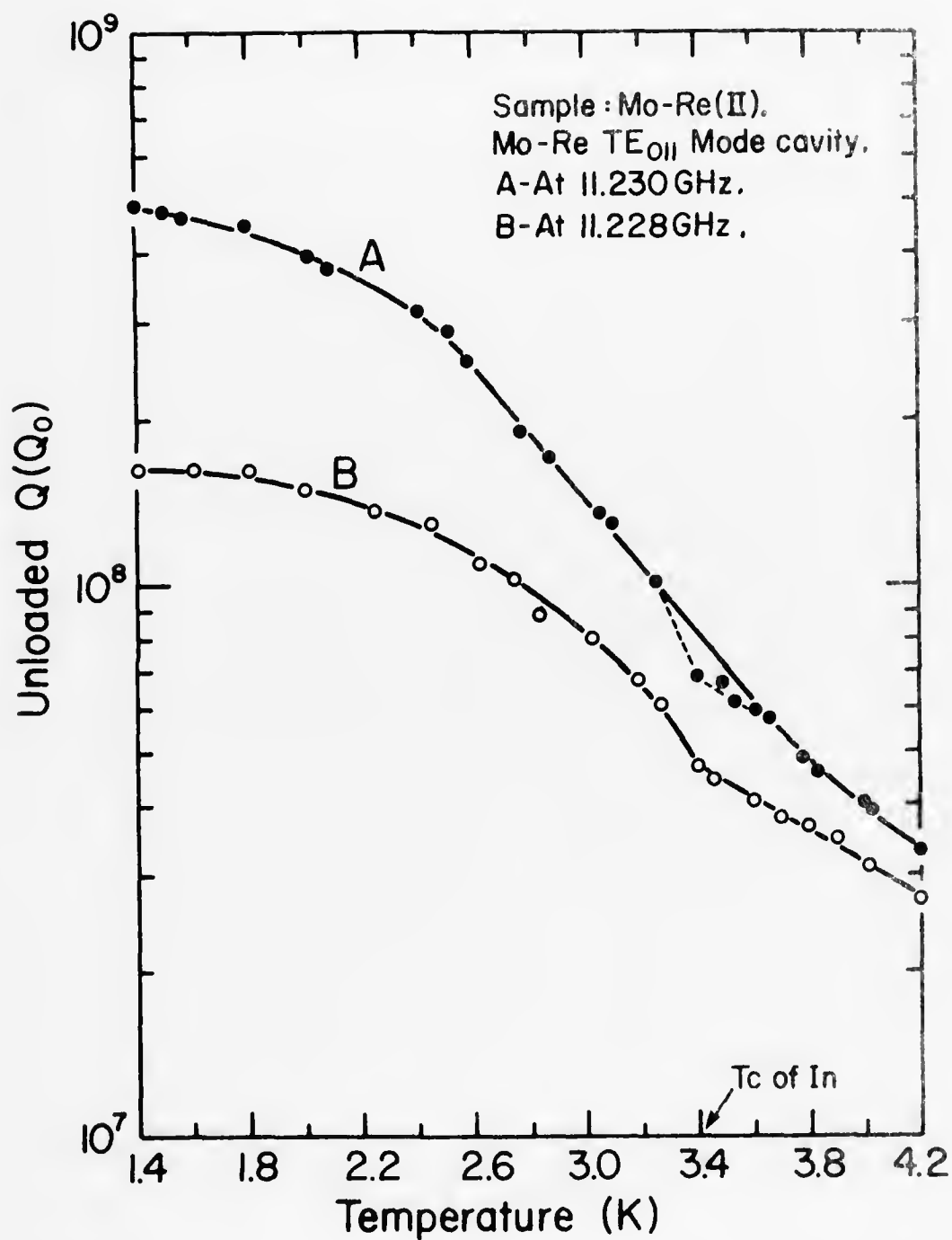


Figure 16. $Q_0(T)$ Curves for Cavity Mo-Re(II).

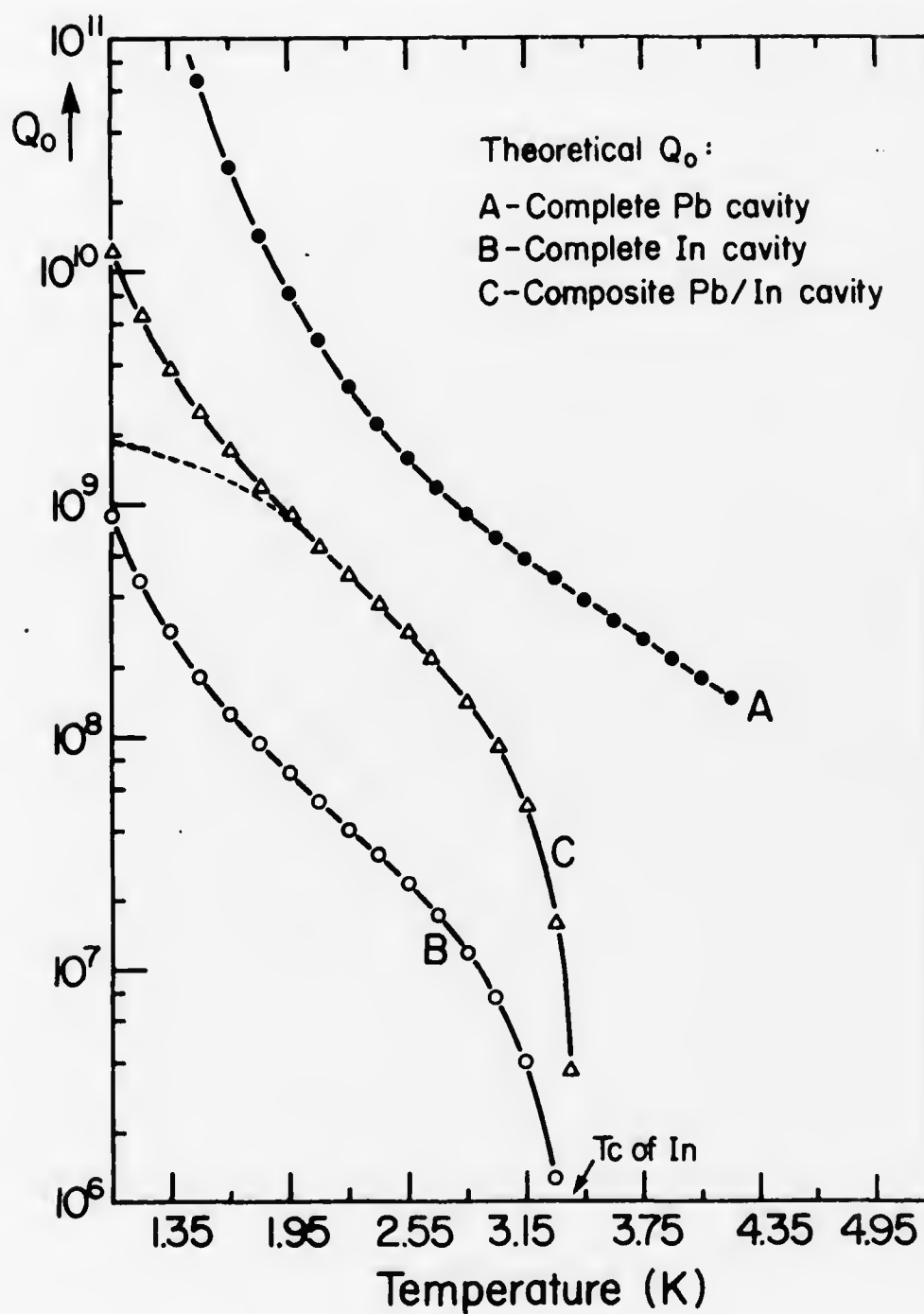


Figure 17. Theoretical $Q_0(T)$ Curves for Pb, In and Composite Pb/In Cavity.

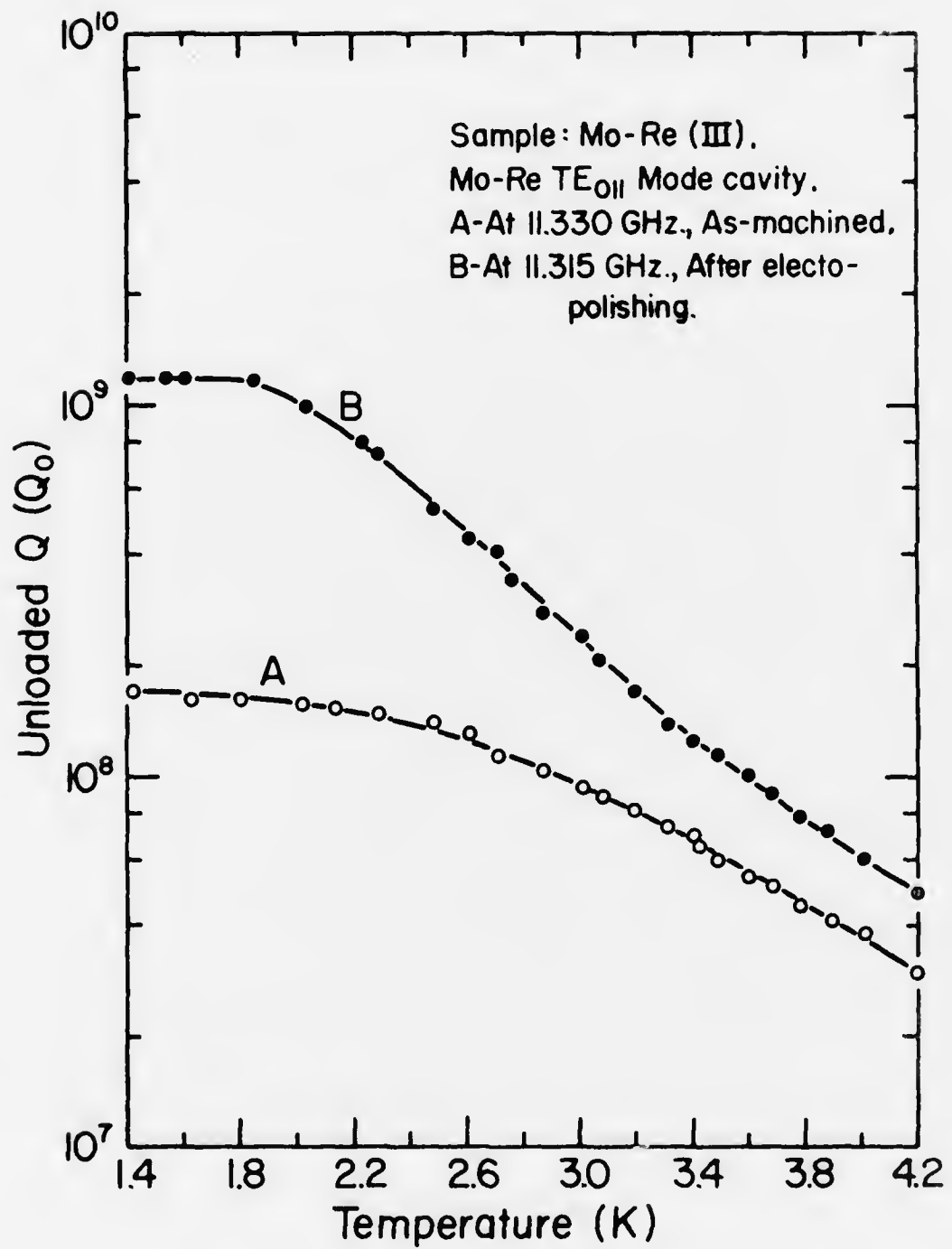


Figure 18. $Q_0(T)$ Curves for Cavity Mo-Re(III) before and after Electropolishing.

Figure 19a.

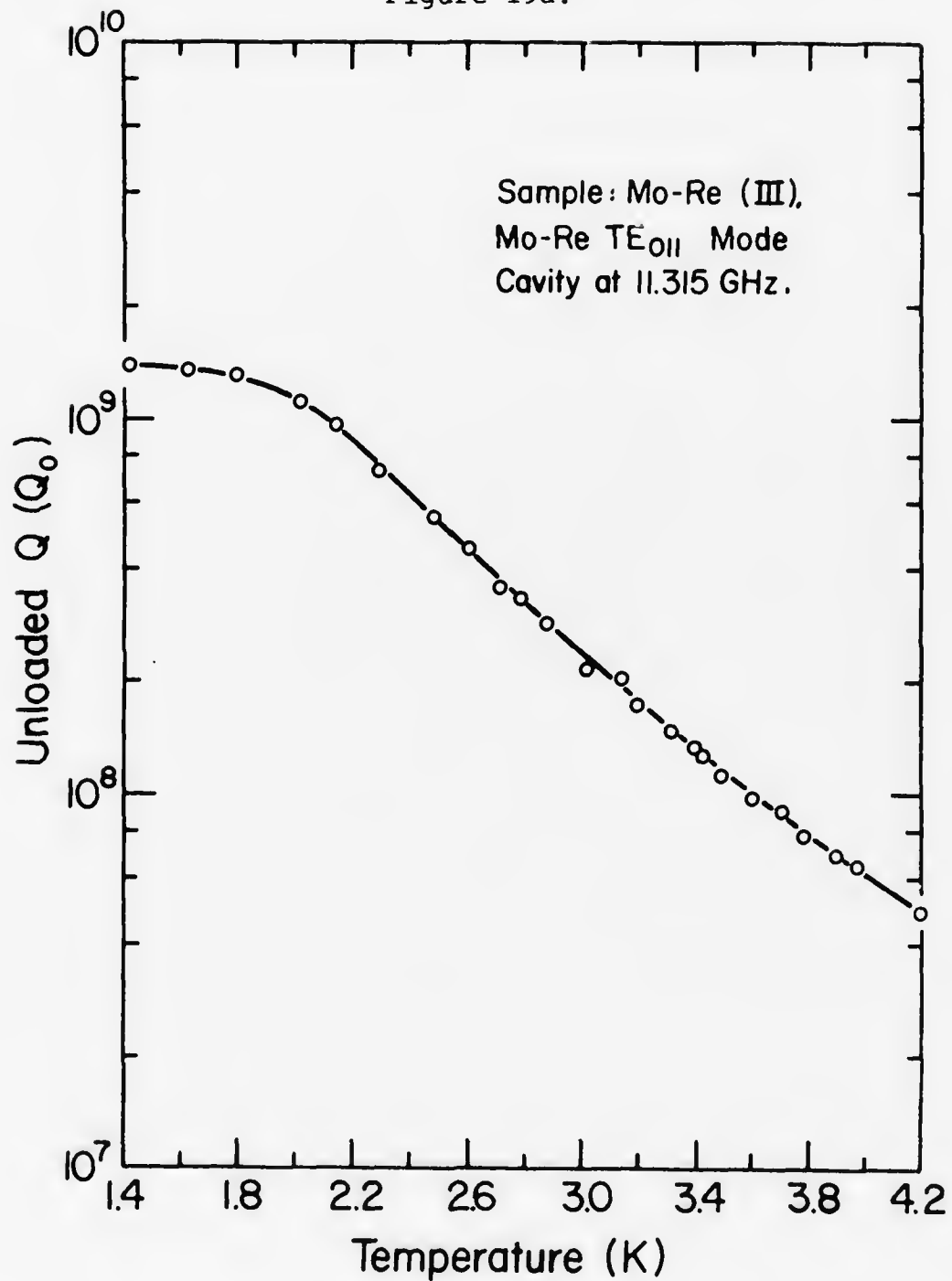
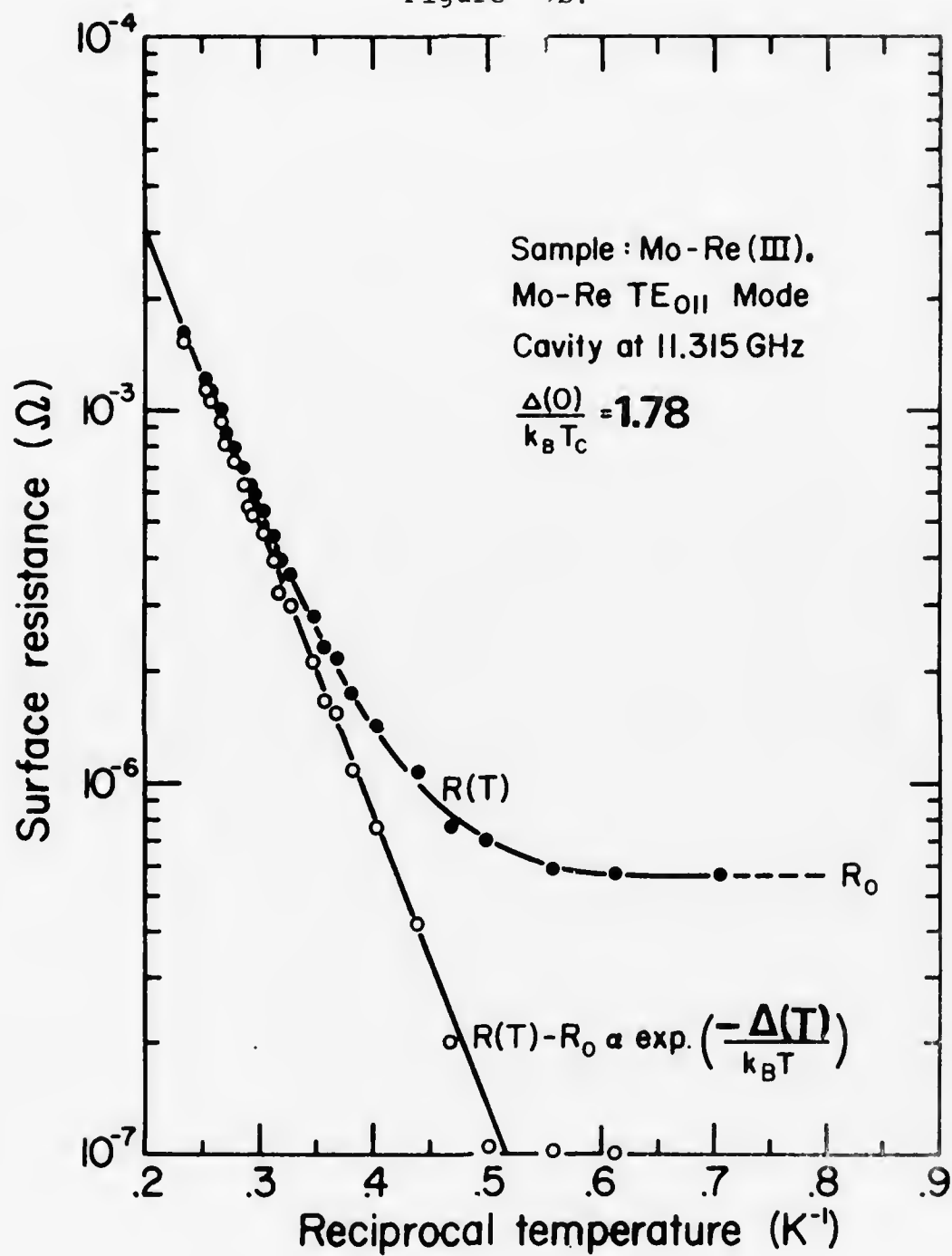


Figure 19. Examples of $Q_0(T)$ and $R(T)$ Curves for Cavity Mo-Re(III).

Figure 9b.



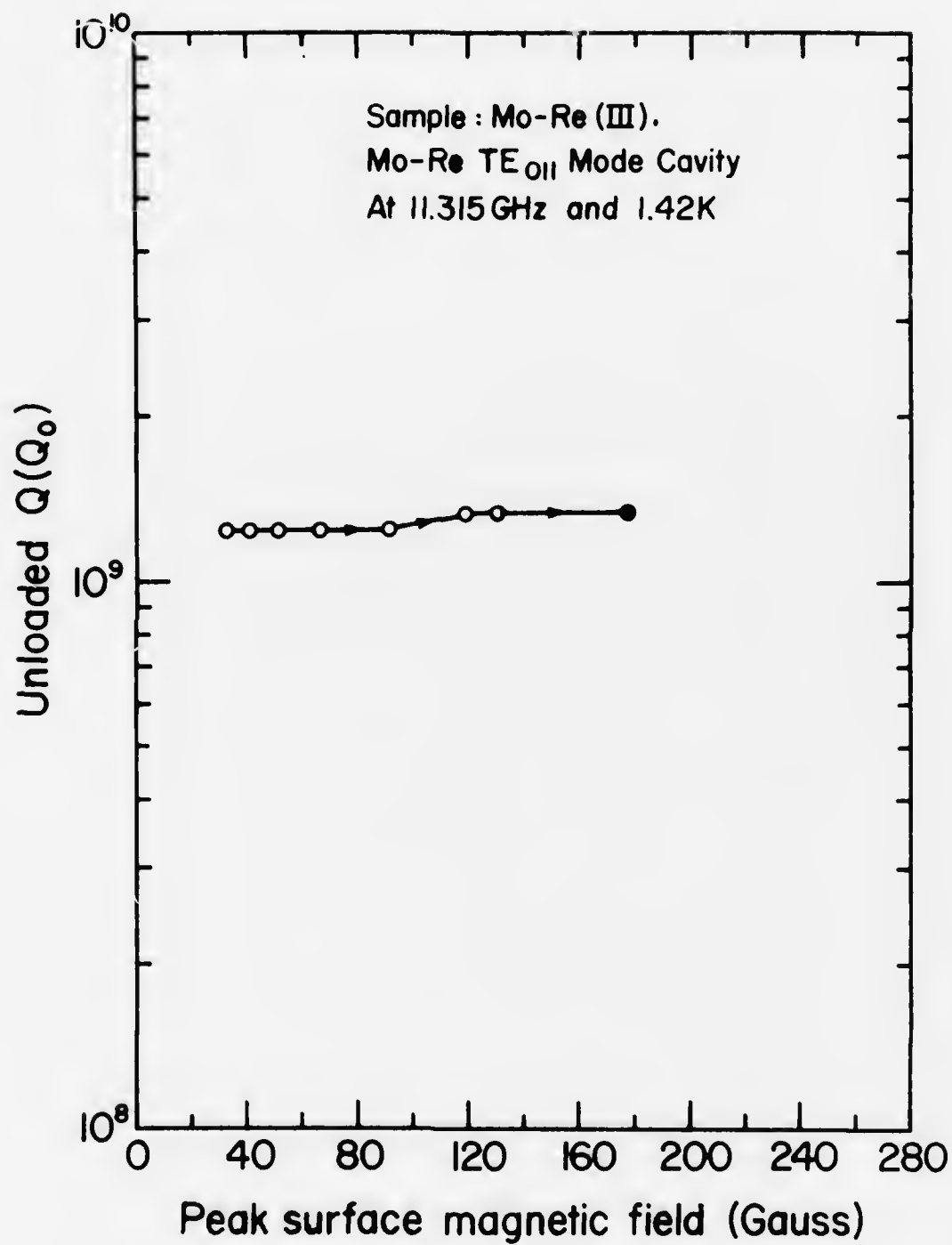


Figure 20. High Power Test of Cavity Mo-Re(III): Q_0 vs. Peak Surface Magnetic Field.

Figure 21a.

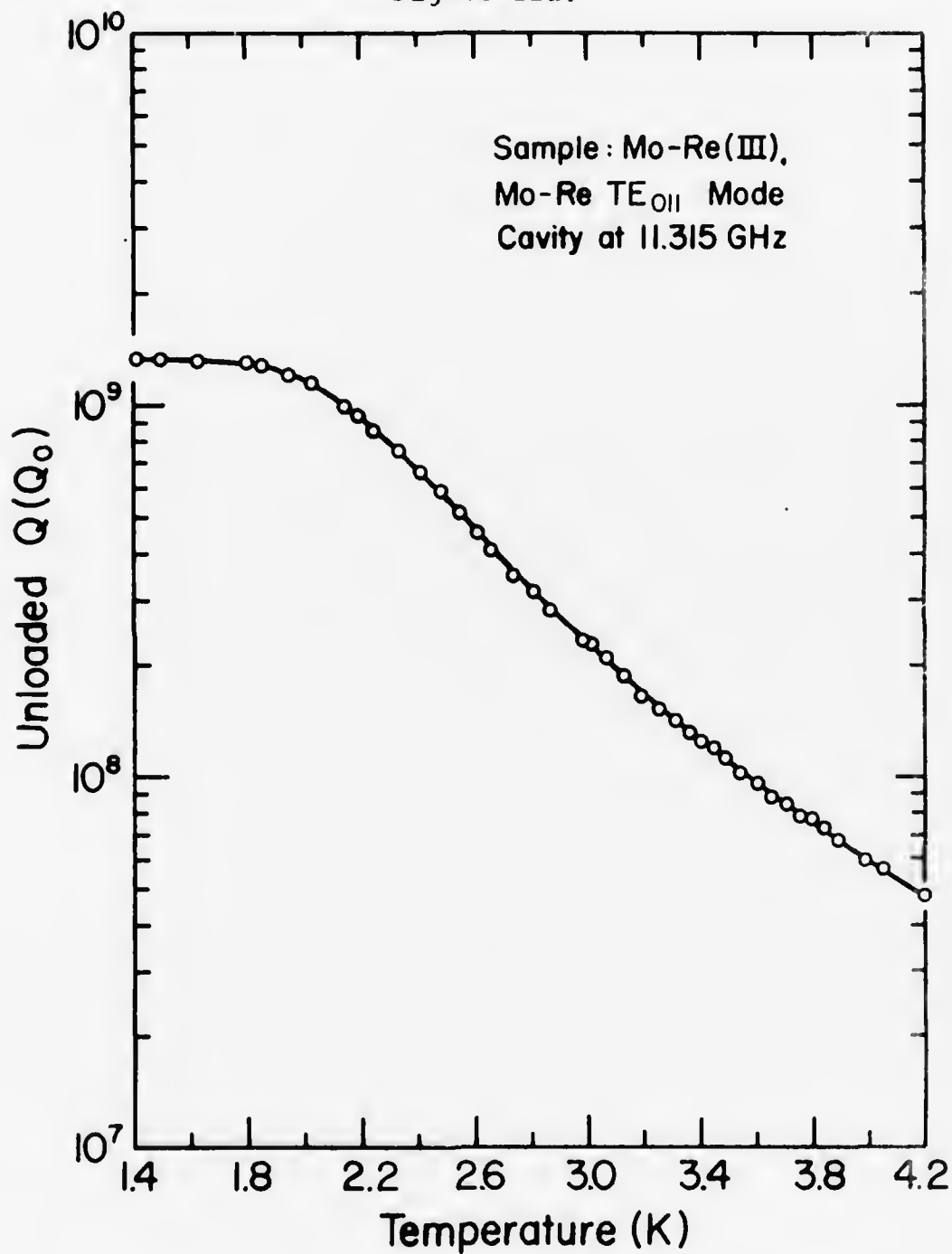


Figure 21. Examples of $Q_0(T)$ and $R(T)$ Curves for Cavity Mo-Re(III).

Figure 21b.

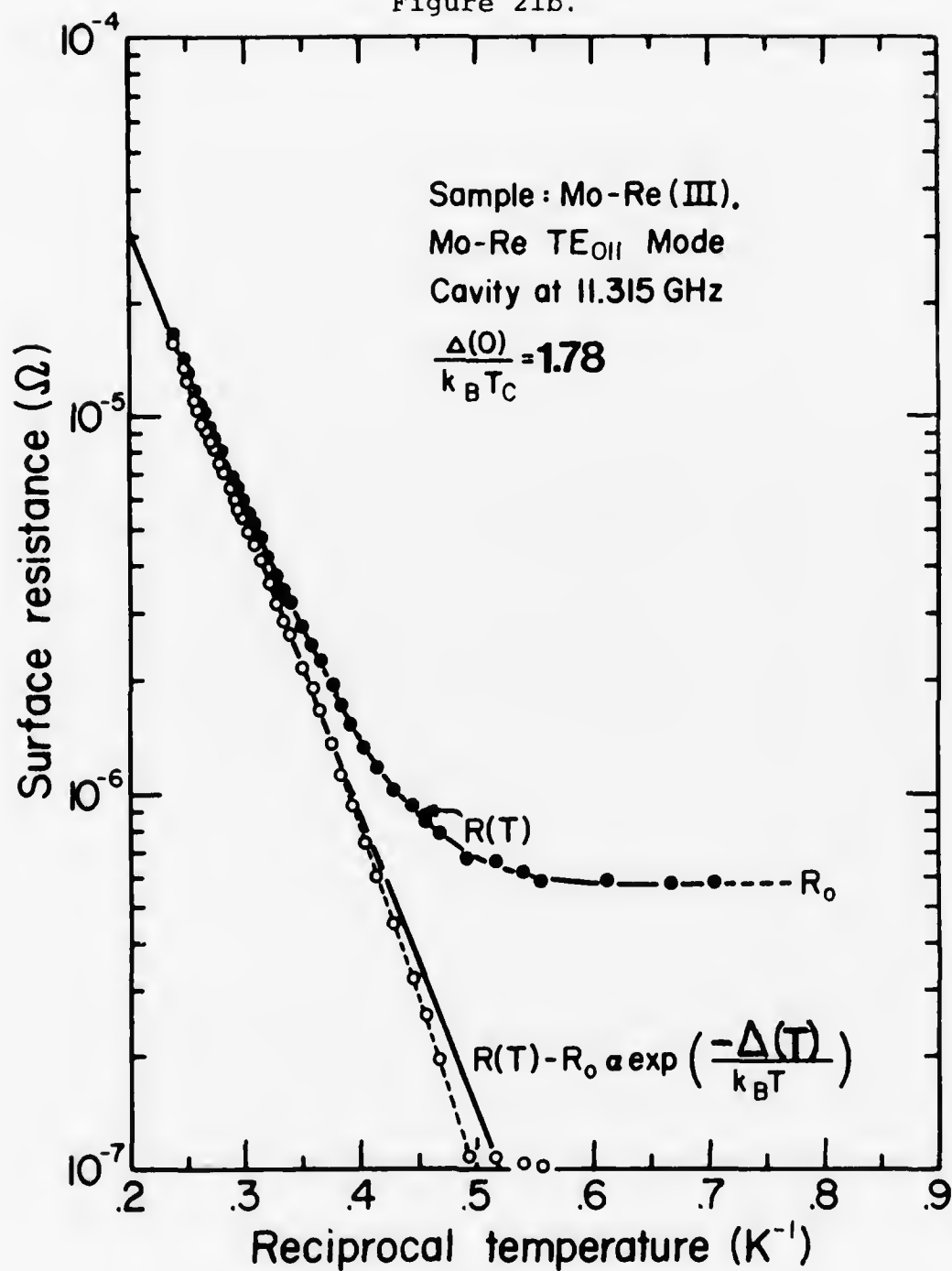


Figure 22a.

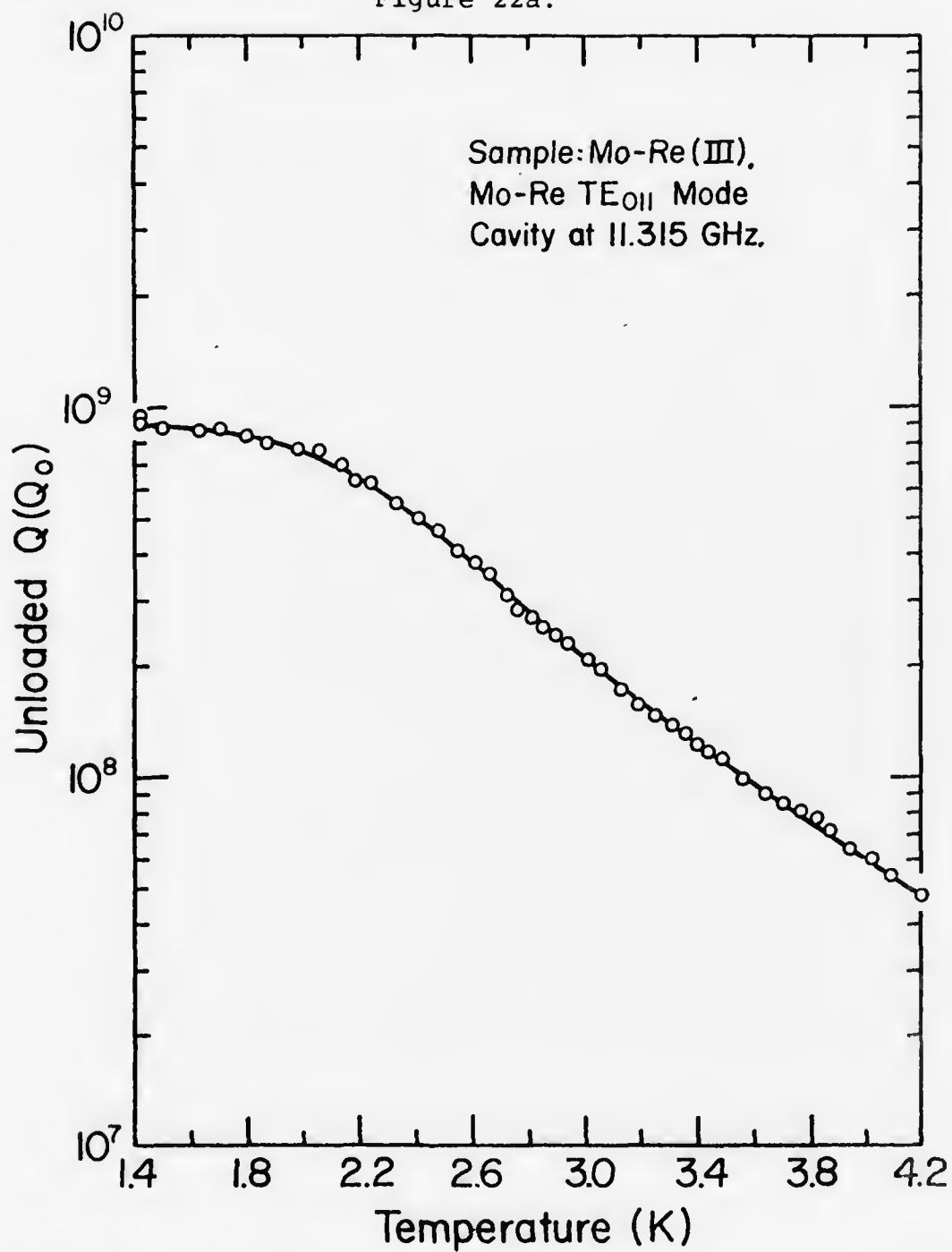


Figure 22. Examples of $Q_0(T)$ and $R(T)$ Curves for Cavity Mo-Re(III); also showing Q_0 vs. Peak Surface Magnetic Field Plot.

Figure 22b.

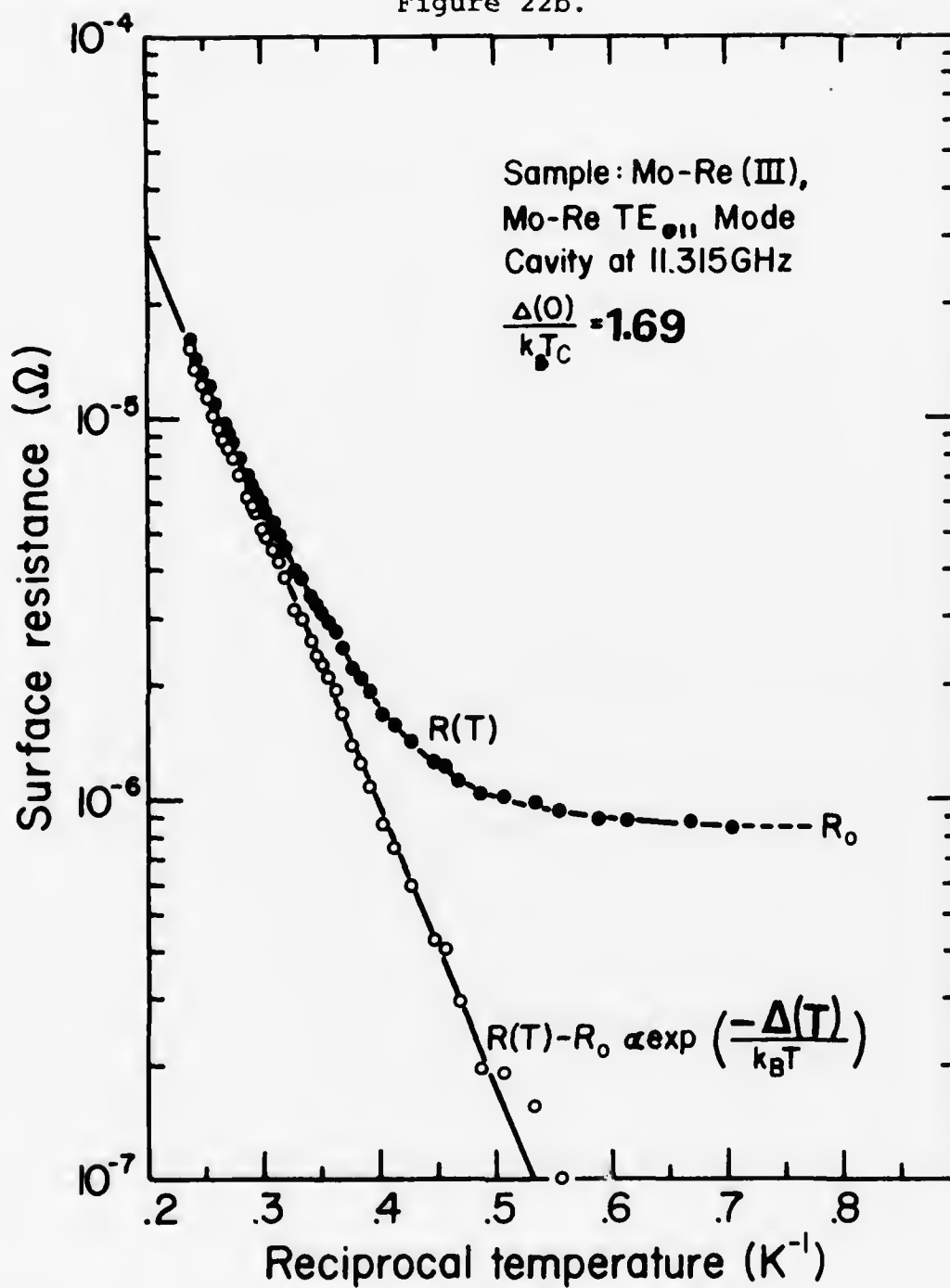
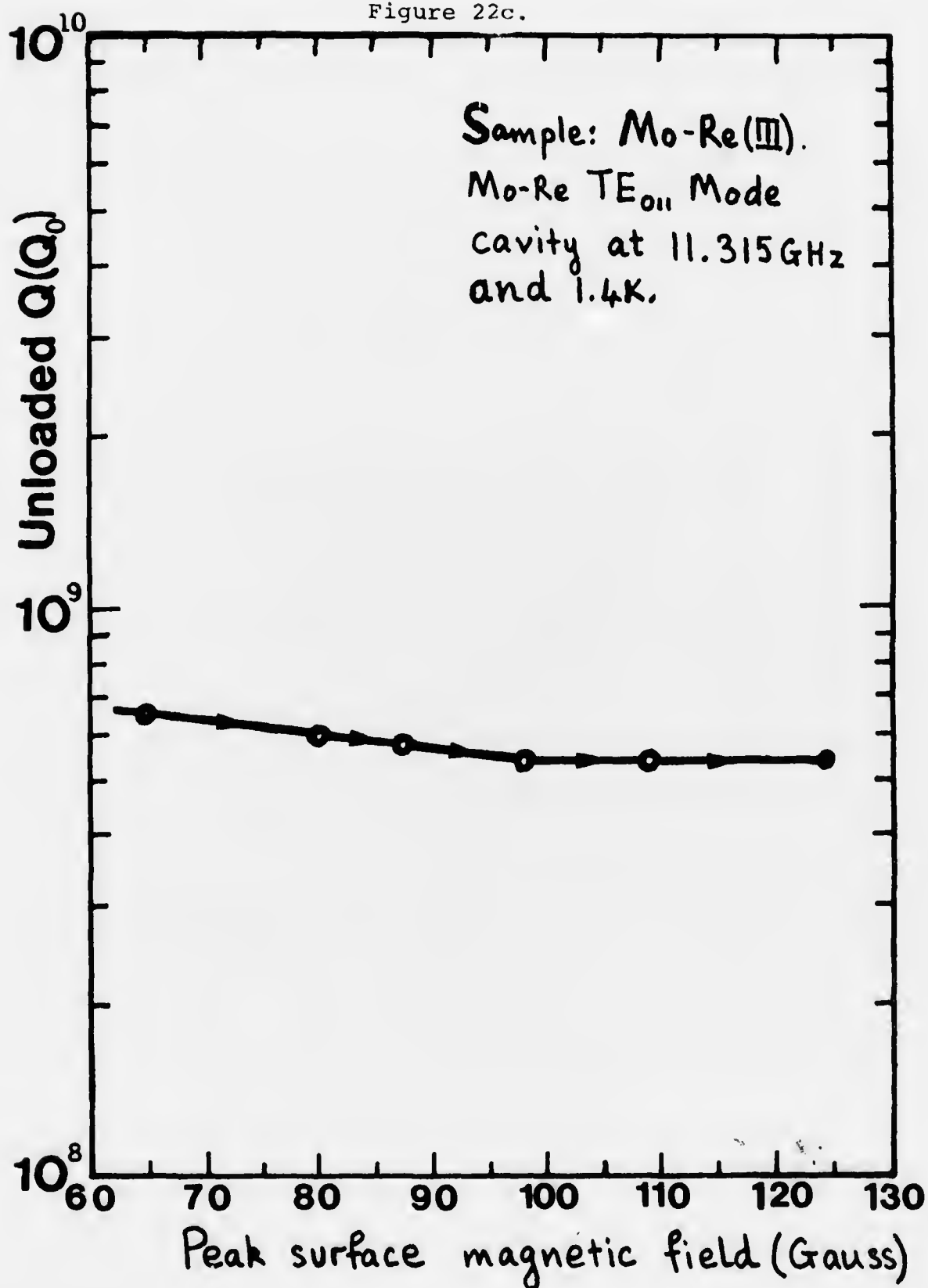


Figure 22c.



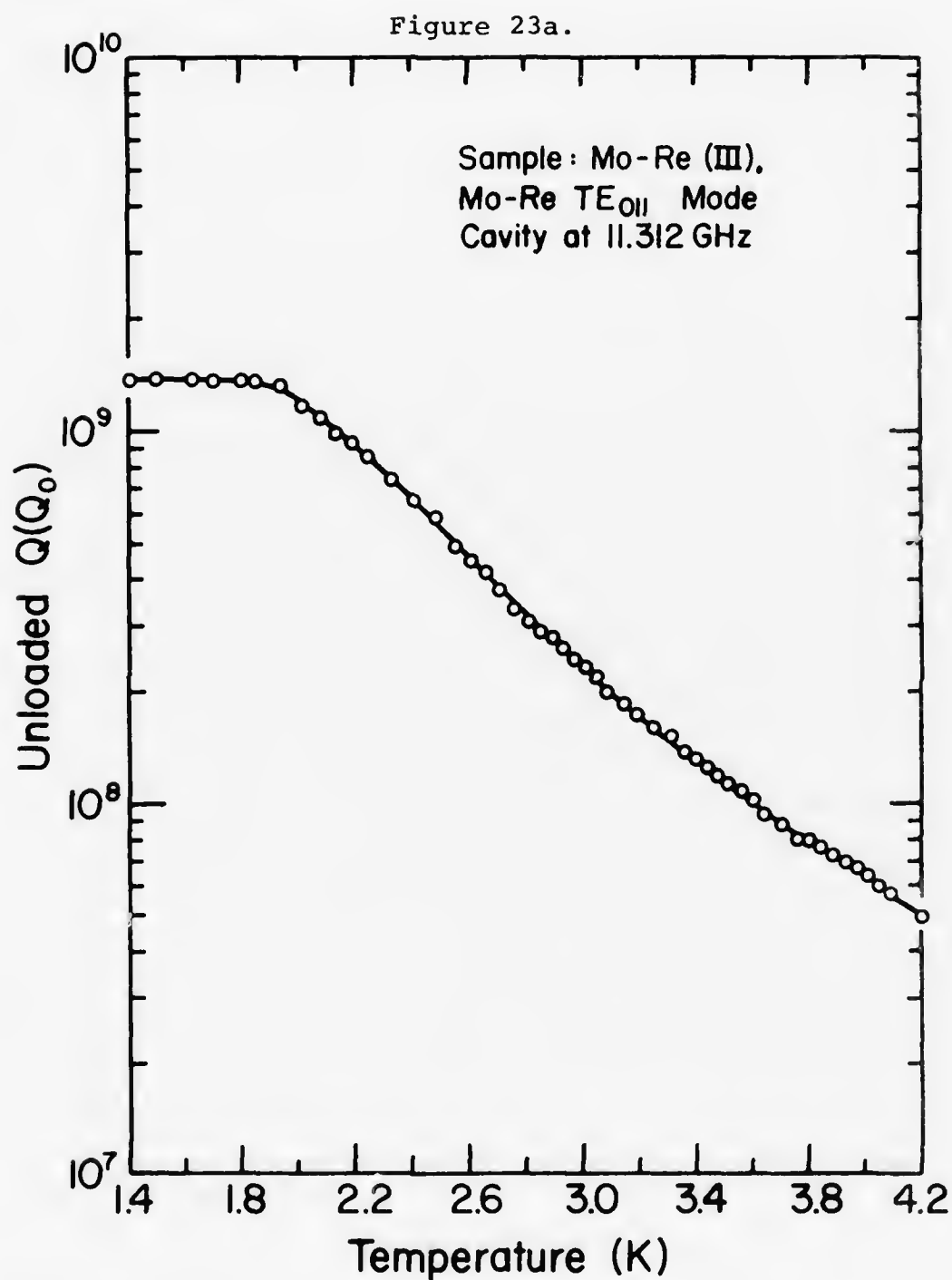
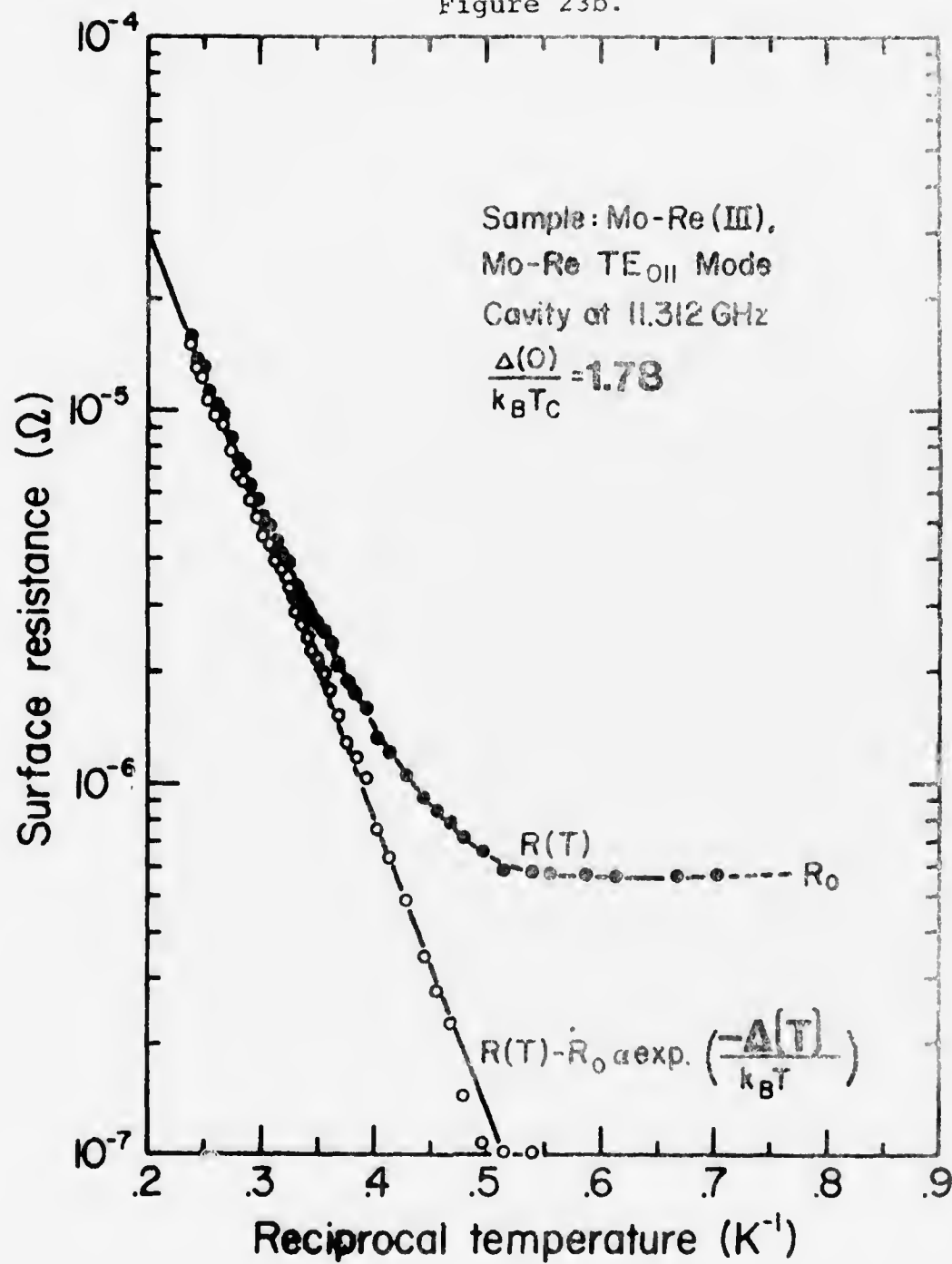


Figure 23. Examples of $Q_0(T)$ and $R(T)$ Curves for Cavity Mo-Re (III).

Figure 23b.



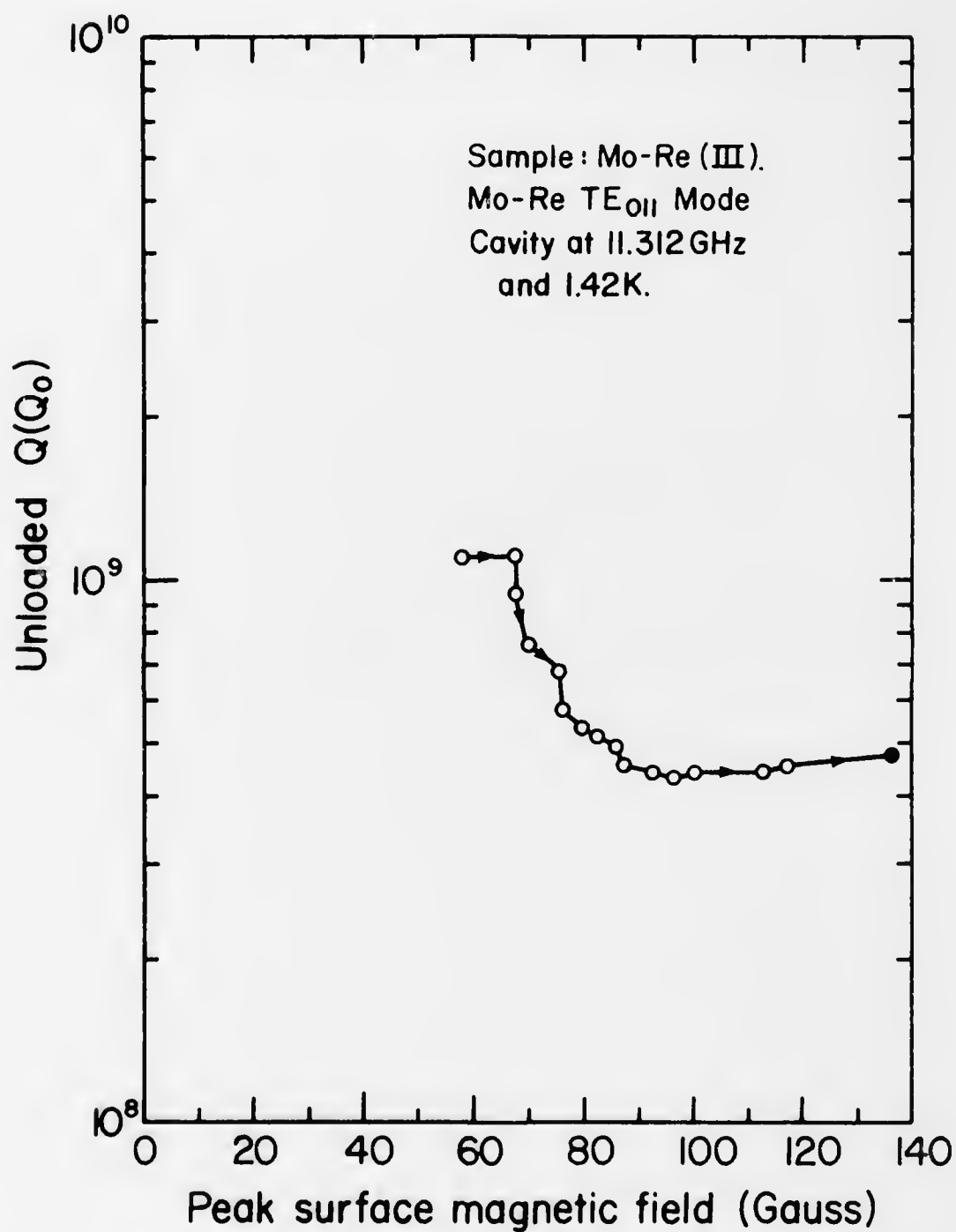


Figure 24. High Power Test of Cavity Mo-Re(III): Q_0 vs. Peak Surface Magnetic Field.

Figure 25a.

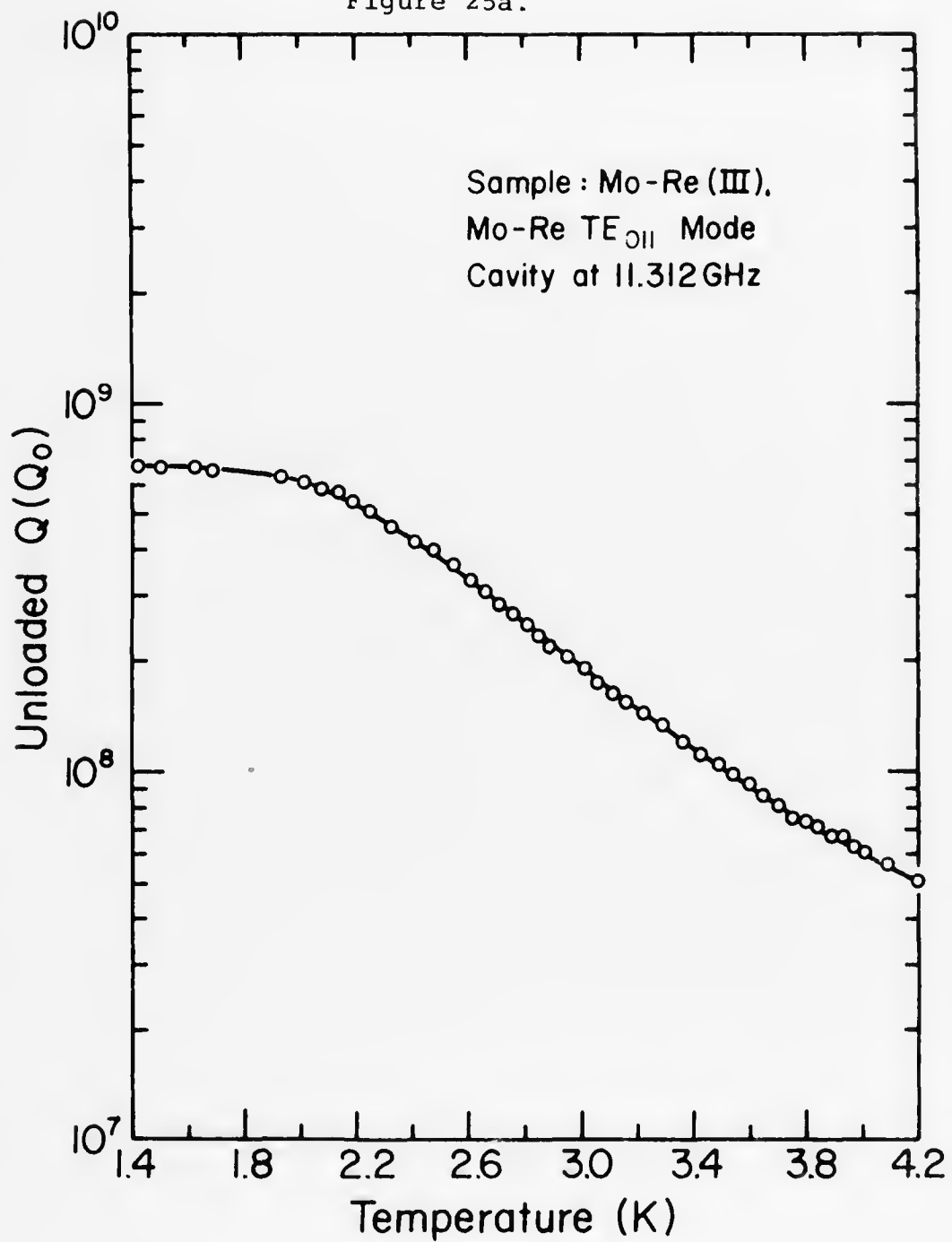
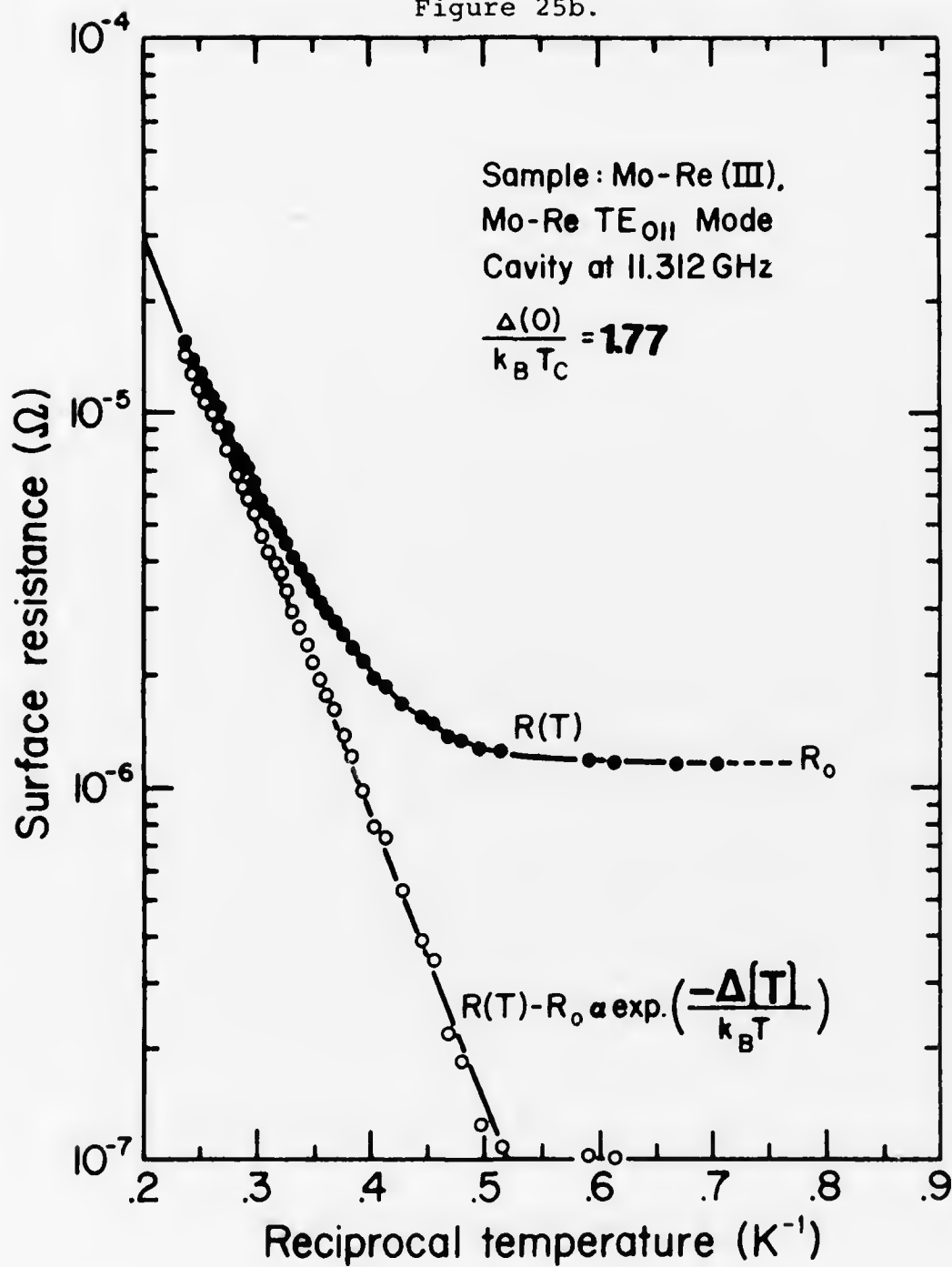


Figure 25. Examples of $Q_0(T)$ and $R(T)$ Curves for Cavity Mo-Re(III).

Figure 25b.



APPENDIX A

DERIVATION OF EXPRESSIONS FOR CAVITY GEOMETRIC FACTORS

In this Appendix, standard methods are used to derive expressions from which the geometric factor, Γ , for the TE_{011} -mode cavity can be calculated. Also, partial geometric factors, which are used in Appendix B for the calculation of Q_0 for a composite cavity, are given.

Consider a cylindrical TE_{011} cavity whose length is L and whose radius is a (MKS units). In the natural cylindrical coordinates (ρ, θ, z) , the various fields for the general case of TE_{lmn} mode are given by (91)

$$E_\rho = -\sqrt{\frac{\mu}{\epsilon}} \frac{J_l(k_1 \rho)}{k_1 \rho} \sin l\theta \sin k_3 z \quad (A-1)$$

$$E_\theta = -\sqrt{\frac{\mu}{\epsilon}} J'_l(k_1 \rho) \cos l\theta \sin k_3 z \quad (A-2)$$

$$E_z = 0 \quad (A-3)$$

$$H_\rho = \frac{k_3}{k} J'_l(k_1 \rho) \cos l\theta \cos k_3 z \quad (A-4)$$

$$H_\theta = -l \frac{k_3}{k} \frac{J_l(k_1 \rho)}{k_1 \rho} \sin l\theta \cos k_3 z \quad (A-5)$$

$$H_z = \frac{k_1}{k} J_l(k_1 \rho) \cos l\theta \sin k_3 z \quad (A-6)$$

Where $k_1 = \frac{r_{lm}}{a}$, $k_3 = \frac{n\pi}{L}$,

$$k^2 = k_1^2 + k_3^2, \quad \lambda = \frac{2\pi}{k},$$

and $r_{lm} = m^{\text{th}}$ zero of $J'_l(x)$.

For the TE_{011} mode,

$$l = 0, \quad m = n = 1.$$

Hence, the expressions for E_θ , H_ρ , and H_z above become:

$$E_\theta = -\sqrt{\frac{\mu}{\epsilon}} J'_0\left(\frac{r_{01}}{a}\rho\right) \sin\left(\frac{\pi z}{L}\right) \quad (\text{A-7})$$

$$H_\rho = \frac{k_3}{k} J'_0\left(\frac{r_{01}}{a}\rho\right) \cos\left(\frac{\pi z}{L}\right) \quad (\text{A-8})$$

$$H_z = \frac{k_1}{k} J_0\left(\frac{r_{01}}{a}\rho\right) \sin\left(\frac{\pi z}{L}\right) \quad (\text{A-9})$$

The total stored energy in the cavity, U , is first calculated.

This can be found from the energy in the electric fields at the instant when they have their maximum value. The stored energy is given by:

$$U = \frac{\epsilon}{2} \int_0^{2\pi} \int_0^a \int_0^L |E_\theta|^2 dz \rho d\rho d\theta$$

Thus, using (A-7):

$$\begin{aligned} U &= \frac{\epsilon}{2} \int_0^{2\pi} \int_0^a \int_0^L \frac{\mu}{\epsilon} \left[J'_0\left(\frac{r_{01}}{a}\rho\right) \right]^2 \sin^2\left(\frac{\pi z}{L}\right) dz \rho d\rho d\theta \\ &= \frac{L\mu}{2\pi} \int_0^{2\pi} \int_0^a \left[J'_0\left(\frac{r_{01}}{a}\rho\right) \right]^2 \left\{ \frac{\pi z}{2L} - \frac{1}{4} \sin\left(\frac{2\pi z}{L}\right) \right\} \Big|_0^L \rho d\rho d\theta \\ &= \frac{\pi\mu L}{2} \int_0^a \left[J'_0\left(\frac{r_{01}}{a}\rho\right) \right]^2 \rho d\rho \end{aligned}$$

And finally,

$$U = \frac{\pi\mu L}{4} a^2 J_0^2(r_{01}) \quad (\text{A-10})$$

To calculate the power dissipated in the walls of the cavity per cycle the expressions for the magnetic field

at the cavity walls are used. From equations (A-8) and (A-9), the magnetic field on the end-plates (i.e. at $z = 0, L$) is given by

$$H_\rho = \frac{k_3}{k} J'_0\left(\frac{r_{01}}{a} \rho\right) \quad (\text{A-11})$$

while the magnetic field on the cylindrical wall (i.e. at $\rho = a$) is given by

$$H_z = \frac{k_1}{k} J_0(r_{01}) \sin\left(\frac{\pi z}{L}\right) \quad (\text{A-12})$$

Using the boundary conditions which relate the surface current density and the magnetic field at the surface the expression for the power dissipated in the cavity walls, W_L is:

$$\begin{aligned} W_L &= \frac{R_s}{2} \left\{ 2 \int_0^{2\pi} \int_0^a H_\rho^2(z=0) \rho d\rho d\theta + a \int_0^{2\pi} \int_0^L H_z^2(\rho=a) dz d\theta \right\} \\ &= R_s \int_0^{2\pi} \int_0^a \left(\frac{k_3}{k}\right)^2 \left[J'_0\left(\frac{r_{01}}{a} \rho\right)\right]^2 \rho d\rho d\theta \\ &\quad + a \frac{R_s}{2} \int_0^{2\pi} \int_0^L \left(\frac{k_1}{k}\right)^2 J_0^2(r_{01}) \sin^2\left(\frac{\pi z}{L}\right) dz d\theta \end{aligned}$$

where R_s is the surface resistance and equations (A-11) and (A-12) have been used. Doing the integrations involved,

$$W_L = \pi R_s \frac{J_0^2(r_{01})}{k^2} \left[k_3^2 a^2 + \frac{L a}{2} k_1^2 \right] \quad (\text{A-13})$$

Expressions for U and W_L in equations (A-10) and (A-13), respectively, can now be used to obtain an expression for Q_0 . By definition

$$Q_0 = \frac{\omega U}{W_L} \quad (\text{A-14})$$

Hence

$$\begin{aligned} Q_0 &= \frac{\omega \pi \mu k^2 L a^2 J_0^2(r_{01})}{4 \pi R_s J_0^2(r_{01}) [k_3^2 a^2 + \frac{L a}{2} k_1^2]} \\ &= \frac{\omega \mu L a^2 k^2}{4 \pi R_s [k_3^2 a^2 + \frac{L a}{2} k_1^2]} \end{aligned} \quad (\text{A-15})$$

As discussed in the text (equation (5.2)), Q_0 can also be expressed as

$$Q_0 = \Gamma / R_s, \quad (\text{A-16})$$

where Γ is a geometric factor depending only on the mode and geometry of the cavity. From (A-15) and (A-16) then

$$\Gamma = \frac{\omega \mu L a k^2}{2 [2 k_3^2 a + L k_1^2]} \quad (\text{A-17})$$

so that Γ can easily be calculated for a particular cavity if the resonant frequency and the dimensions are known.

The above analysis assumes that R_s is uniform over the interior surface of the cavity. If, on the other hand, the end-plates are made of different materials from the

cylindrical portion it is usually assumed that R_s is the sum of the surface resistances of the various areas, weighted by some partial geometric factors.⁽¹⁴⁾ Say R_1 , R_2 , and R_3 are the surface resistance of the cylindrical wall and the two end-plates, respectively, then from the calculation of W_L ,

$$\begin{aligned}
 Q_o &= \frac{w \mu L a k^2}{4 R_s [a k_3^2 + \frac{L}{2} k_1^2]} \\
 &= \frac{w \mu L a k^2}{4 \left[\frac{L}{2} k_1^2 R_1 + \frac{a}{2} k_3^2 R_2 + \frac{a}{2} k_3^2 R_3 \right]} \quad (A-18)
 \end{aligned}$$

Thus

$$R_s = \left(\frac{1}{2 a k_3^2 + L k_1^2} \right) \{ L k_1^2 R_1 + a k_3^2 (R_2 + R_3) \} \quad (A-19)$$

(A-19) is used in Appendix B to calculate the Q_o of a composite cavity of two different materials.

APPENDIX BCALCULATION OF THEORETICAL Q_0 FOR A COMPOSITE CAVITY

The calculation of the theoretical Q_0 for various cavity configurations is outlined in this Appendix. As discussed in the text, areas of "weakened" superconductivity can exist over the surface of the resonator. Detailed calculation of the surface resistance (or Q_0) in such a case, taking into account the weak spots, is extremely difficult. However, the case of a composite cavity is a rough approximation to this situation. A composite cavity is defined as one whose major portion is constructed of a material with high T_c , like niobium or lead while a smaller, but geometrically identifiable area is of a material with relatively low T_c , like indium. Specifically, a TE_{011} mode cavity is considered whose cylindrical portion and one end-plate are of lead ($T_c = 7.2K$) while the other end-plate is of indium ($T_c = 3.4K$).

The calculations involve using Halbritter's Computer Program⁽²⁸⁾ for computing the surface impedance of the superconductors involved and, using equation (A-19) of Appendix A, to calculate the total surface resistance of the whole cavity. Q_0 is then easily obtained from the surface resistance and the geometrical factor Γ , which is derived in Appendix A.

The surface impedance Z is given by

$$Z = R + iX. \quad (B-1)$$

where R is the surface resistance while X is the surface reactance. Another way of writing (B-1) is in terms of the penetration of the magnetic field $H(z, t)$ into the wall:

$$\begin{aligned} Z &= i\omega\mu_0 \int_0^\infty \frac{H(z, t)}{H(0, t)} dz \\ &= i\omega\mu_0 \frac{A(0, t)}{B(0, t)} \end{aligned} \quad (B-2)$$

The fields $H(z, t)$ and $A(z, t)$ satisfy the following equations and boundary conditions:

$$(a) \quad - \frac{\partial^2 A(z, t)}{\partial z^2} = \mu_0 j(z, t) \quad (B-3)$$

which is the equation resulting from Maxwell's equations but with the $\frac{\partial^2}{\partial t^2}$ term neglected (for frequencies lower than 10^{13}Hz).

(b) the material equation:

$$j(z, t) = - \int_{-\infty}^0 dt' \int Q(z-z', t+t') A(z', t') dz' \quad (B-4)$$

(c) the boundary conditions for the fields:

$$\left. \begin{aligned} \frac{\partial A(z, t)}{\partial z} \Big|_{z=0} &= B(0, t) \\ A(\infty, t) &= 0 \end{aligned} \right\} \quad (B-5)$$

(d) the boundary conditions for the charge carriers at the surface:

Specular ($p = 1$) and diffuse ($p = 0$) reflection. (B-6)

When the integral kernel $Q(z, t)$ is Fourier - transformed to $Q(k, \omega)$, the surface impedance is then given by Reuter and Sondheimer⁽¹⁸⁾ as:

$$Z_s = \frac{i\mu_0\omega}{\pi} \int_{-\infty}^{\infty} \frac{dk}{k^2 + \mu_0 Q(k, \omega)} \quad (\text{B-7})$$

for specular reflection and

$$Z_D = i\mu_0\omega \frac{\pi}{\int_0^{\infty} dk \ln \left\{ 1 + \mu_0 Q(k, \omega)/k^2 \right\}} \quad (\text{B-8})$$

for diffuse reflection. The transformed kernel $Q(k, \omega)$ is a very complicated function and the major part of the computer program is devoted to its calculation in the manner discussed by Halbritter.⁽²⁸⁾ (see reference 28 for the full details of the calculation of $Q(k, \omega)$).

From equation (A-19) of Appendix A, the total surface resistance for a composite cavity can be written as:

$$R_s = \left(\frac{1}{2ak_3^2 + Lk_1^2} \right) \left\{ Lk_1^2 R_1 + ak_3^2 (R_2 + R_3) \right\} \quad (\text{B-9})$$

where R_1 , R_2 , and R_3 are the surface resistances of the cylindrical portion and the two end-plates, respectively, L is the cavity length and a is the radius of the cavity. The values of R_1 , R_2 , and R_3 depend only on material parameters,

namely: the critical temperature T_C , the gap value at absolute zero $\Delta(0)$, the London penetration depth at absolute zero $\lambda_L(0)$, the mean free path ℓ and the Fermi velocity v_F . In the case where one end-face is of the same material as the cylindrical wall,

$$R_1 = R_3 \quad (\text{B-10})$$

Hence (B-9) becomes

$$R_s = \left(\frac{1}{2ak_3^2 + Lk_1^2} \right) \{ (Lk_1^2 + ak_3^2)R_1 + ak_3^2 R_2 \} \quad (\text{B-11})$$

For a cavity (Mo-Re(III)) with $2a/L = 1$ (or $\Gamma = 780\Omega$) equation (B-11) becomes

$$R_s = 0.92807R_1 + 0.07193R_2 \quad (\text{B-12})$$

when $2a/L = 1.68$ (i.e. Mo-Re(I) and Mo-Re(II)), $\Gamma = 731\Omega$ and equation (B-11) becomes

$$R_s = 0.77836R_1 + 0.22164R_2 \quad (\text{B-13})$$

Once the total surface resistance has been calculated, Q_0 can be obtained using

$$Q_0 = \Gamma/R_s \quad (\text{B-14})$$

In the text, calculated Q_0 values for composite cavities are compared with Q_0 values for single-element cavities. Also, the expected shapes of the Q_0 vs. temperature curves are compared with experimental curves obtained

in this work. The case in which areas of weakened superconductivity exist on the cavity surface is also discussed using these calculated Q_0 curves as a basis.

APPENDIX CPEAK MAGNETIC FLUX DENSITIES ON THE CAVITY WALLS

The calculation of the peak magnetic fields at the cavity walls is given in this Appendix. The derivation is limited to the TE_{011} mode (used in this work). For each of the two geometries used, the expressions for the maximum fields on the end-walls and on the cylindrical walls are derived.

As in Appendix A, a TE_{011} cavity whose length is L and whose radius is a (in MKS units) is considered. Excluding the $\exp(-i\omega t)$ time-dependence, the fields in the cavity relevant to the calculation may be written as: (58)

$$H_z = H_0 J_0\left(\frac{r_{01}}{a}\rho\right) \sin\left(\frac{\pi z}{L}\right) \quad (C-1)$$

$$H_\rho = -H_0 \sqrt{\left(\frac{2\pi a}{\lambda r_{01}}\right)^2 - 1} J_1\left(\frac{r_{01}}{a}\rho\right) \cos\left(\frac{\pi z}{L}\right) \quad (C-2)$$

$$E_\theta = i \sqrt{\frac{\mu_0}{\epsilon_0}} \left(\frac{2\pi a}{\lambda r_{01}}\right) J_1\left(\frac{r_{01}}{a}\rho\right) \sin\left(\frac{\pi z}{L}\right) \quad (C-3)$$

where λ is the free space wavelength and $r_{01} = 3.832$.

The energy stored in the cavity is given by

$$\begin{aligned} U &= \frac{\epsilon_0}{2} \int_0^L \int_0^{2\pi} \int_0^a \rho |E_\theta|^2 d\rho d\theta dz \\ &= \mu_0 \left[\frac{\pi^3 a^4 L J_0^2(r_{01})}{(r_{01} \lambda)^2} \right] H_0^2 \end{aligned} \quad (C-4)$$

The above integration is the same as those given in Appendix A. Now, since from equation (5.1) in the text, $Q_0 = \frac{\omega_0 U}{P_d}$, and by definition, $B_0 = \mu_0 H_0$, substituting for U in (C-4) gives:

$$B_o = \frac{(r_{o1}) \sqrt{Q_o P_d}}{(\pi a)^2 \sqrt{2 \epsilon_o L} |J_o(r_{o1})| f_o^{3/2}}, \quad (C-5)$$

where f_o is the resonant frequency and P_d is in watts.

Substituting for H_o in (C-1) and (C-2) gives:

$$B_z = \frac{(r_{o1}) J_o\left(\frac{r_{o1}}{a} \rho\right) \sqrt{Q_o P_d} \sin\left(\frac{\pi z}{L}\right)}{(\pi a)^2 \sqrt{2 \epsilon_o L} |J_o(r_{o1})| f_o^{3/2}} \quad (C-6)$$

$$B_\rho = \frac{-\sqrt{\left(\frac{2\pi a}{\lambda r_{o1}}\right)^2 - 1} J_1\left(\frac{r_{o1}}{a} \rho\right) \sqrt{Q_o P_d} \cos\left(\frac{\pi z}{L}\right)}{(\pi a)^2 \sqrt{2 \epsilon_o L} |J_o(r_{o1})| f_o^{3/2}} \quad (C-7)$$

The maximum flux density on the end wall occurs at a radius

$\rho = .48a$, while for the cylindrical wall, it occurs at

$z = L/2$. Thus, from (C-6) and (C-7),

$$B_{z_{\max}} = J_o(3.832) B_o, \quad (C-8)$$

$$B_{\rho_{\max}} = \sqrt{\left(\frac{2\pi a}{\lambda r_{o1}}\right)^2 - 1} J_1[(3.832)(.48)] B_o. \quad (C-9)$$

Case I (Mo-Re(I) and Mo-Re(II))

For the TE_{011} mode cavity with $f_o = 11.25\text{GHz}$,

$a = 0.0197\text{m}$ and $L = .0235\text{m}$,

$$B_o = 3.252 \times 10^{-2} \sqrt{Q_o P_d (\text{W})} \text{ G.} \quad (C-10)$$

Hence, from (C-8) and (C-9),

$$\begin{aligned} B_{z_{\max}} &= .403 B_o \\ &= 1.31 \times 10^{-2} \sqrt{Q_o P_d (\text{W})} \text{ G,} \end{aligned} \quad (C-11)$$

$$\begin{aligned}
 B_{\rho_{\max}} &= .395 B_O \\
 &= 1.28 \times 10^{-2} \sqrt{Q_O P_d (W)} \text{ G.}
 \end{aligned}
 \tag{C-12}$$

Case II (Mo-Re(III))

For this case $f_O = 11.28 \text{ GHz}$, $a = .01753\text{m}$, and $L = .0348\text{m}$, and

$$B_O = 3.340 \times 10^{-2} \sqrt{Q_O P_d (W)} \text{ G} \tag{C-13}$$

$$\begin{aligned}
 B_{z_{\max}} &= .403 B_O \\
 &= 1.34 \times 10^{-2} \sqrt{Q_O P_d (W)} \text{ G}
 \end{aligned}
 \tag{C-14}$$

$$\begin{aligned}
 B_{\rho_{\max}} &= .240 B_O \\
 &= .803 \times 10^{-2} \sqrt{Q_O P_d (W)} \text{ G}
 \end{aligned}
 \tag{C-15}$$

APPENDIX DCalculation of $(2\Delta(0)/k_B T_c)$ for $\text{Mo}_{0.75}\text{Re}_{0.25}$ from BCS

The energy gap at absolute zero, $\Delta(0)$, of a superconductor is given within the BCS theory by the following expression: ⁽²⁵⁾

$$\frac{2\Delta(0)}{k_B T_c} = 2 H_c(0) \left[\frac{v}{4\pi N(0) k_B^2 T_c^2} \right]^{1/2} \quad (\text{D-i})$$

where v is the molar volume in cm^3/mole and $N(0)$, the density of states of one spin per unit energy at the Fermi surface, is expressed in states $\text{erg}^{-1} \text{mole}^{-1}$.

For the $\text{Mo}_{0.75}\text{Re}_{0.25}$ alloy:

(a.) The molar volume is given by

$$v = \frac{[(95.94)(.75) + (186.2)(.25)]}{12.855} \text{ cm}^3/\text{mole}$$

$$= 9.2185 \text{ cm}^3/\text{mole}$$

(Atomic numbers for Mo and Re are 95.94 and 186.2 respectively; density of the alloy is 12.855 gm/cm^3).

$$(b) H_c(0) = 1600 \text{ G}$$

$$(c) N(0) = \frac{.85 N_A}{1.60219 \times 10^{-12}} \text{ states erg}^{-1} \text{ mole}^{-1}$$

($H_c(0)$ and $N(0)$ values for the alloy were calculated from the specific heat data of Morin and Maita (see reference 73)); N_A is Avogadro's Number.

$$(d) \quad T_c = 10.1\text{K}$$

Using these values in (D-1) gives

$$\frac{2\Delta(0)}{k_B T_c} = 2(1600) \left[\frac{(9.2185)(1.60219)}{4\pi(6.022)(0.85)(1.38)^2(10.1)^2 10^3} \right]^{1/2}$$

$$\frac{2\Delta(0)}{k_B T_c} = 3.48 \quad (D-2)$$

REFERENCES

1. Hartwig, W. H., Proc. IEEE, Vol.61, #1, 58 (1973).
2. Turneaure, J. P., and Viet, N. T.,
Appl. Phys. Lett. 16, 333 (1970).
3. Turneaure, J. P., and Weissman, I.,
J: Appl. Phys. 39, 4417 (1968).
4. Kneisel, P., Stoltz, O., and Halbritter, J.,
IEEE Trans. Nucl. Sci. NS-18, 158 (1971).
5. (a.) Martens, H., Diepers, H., and Sun, R.K.,
Phys. Lett. 34A, 439 (1971).
(b.) Diepers, H., Schmidt, O., Martens, H., and Sun, F. S.,
Phys. Lett. 37A, 139 (1971).
6. Kneisel, P., Stoltz, O., and Halbritter, J.,
Proc. 1972 Appl. Superconductivity Conf.
Annapolis, Maryland.
IEEE Pub. No.72CHO682-5-TABSC, p.657.
7. Kneisel, P., Stoltz, O., and Halbritter, J.,
Proc. 13th Int. Conf. Low Temp. Physics,
Boulder, Colorado, 1972.
8. Diepers, H., and Martens, H.,
Phys. Lett. 38A, 337 (1972).
9. Pierce, J. M., J. Appl. Phys., 44, 1342 (1973).
10. Gray, K. E., Appl. Phys. Lett. 27, #8, 402 (1975).
11. Halbritter, J., Particle Accelerators, 3, 163 (1972).
12. Giordano, S., Hahn, H., Halama, H. J., Luhman, T. S.,
and Bauer, W.,
IEEE Trans. on Magnetics, Vol. MAG-11, #2, (1975)
p.437.
13. Flécher, P., Nucl. Instr. & Methods, 75, 29, (1969).
14. Bruynseraede, Y., Gorle, D., Leroy, D., and Marignot, P.,
Physica, 54, 137 (1971).

15. Hillenbrand, B., Martens, H., Pfister, H., Schnitzke, K.,
and Ziegler, G.,
IEEE Trans. on Magnetics, VOL. MAG-11, #2, (1975), p.420.
16. Yasaitis, J. A., and Rose, R.M.,
IEEE Trans. on Magnetics, Vol. MAG-11, #2, (1975), p.434.
17. Chambers, R. G., Proc. Roy.Soc. A215, 481 (1952).
18. Renter, G. E. H., and Sondheimer, E. H.,
Proc. Roy. Soc. A195, 336 (1946).
19. Dingle, R. B., Physica 19, 311 (1953).
20. Mattis, D. C., and Bardeen, J.,
Phys. Rev. III, 412 (1958).
21. Maxwell, E. in Progress in Cryogenics, Vol. 4
Academic Press (1964), K. Mendelssohn, Editor.
22. London, H., Proc. Roy. Soc. A176, 522 (1940).
23. Maxwell, E., Marcus, P. M., and Slater, J. C.,
Phys. Rev. 76, 1332 (1949).
24. Shoenberg, D., Superconductivity, (Cambridge University
Press, London, 1960).
25. Bardeen, J., Cooper, L. N., and Schrieffer, J. R.,
Phys. Rev. 108, 1175 (1957).
26. Abrikosov, A. A., Gor'kov, L. P., and Khalatnikov, I. M.,
Soviet Physics, JETP, 35(8), No. 1, 182 (1959).
Soviet Physics, JETP, 37(10), No. 1, 132 (1960).
27. Turneaure, J. P., High Energy Physics Laboratory
Report No. 507 (Stanford University) (1967).
28. Halbritter, J., Externer Bericht 3/70-6,
Kernforschungszentrum, Karlsruhe, W. Germany.
29. Halbritter, J., Z. Physik, 238, 466 (1970).
30. Victor, J. M., and Hartwig, W. H.,
J. Appl. Phys. 39, 2539 (1968).
31. Rabinowitz, M., J. Appl. Phys. 42, 88 (1971).

32. Weissman, I., and Turneaure, J. P.,
Appl. Phys. Lett. 13, 390 (1968).
33. Halbritter, J., J. Appl. Phys. 42, 82 (1971).
34. Passow, C., Phys. Rev. Lett. 28, 427 (1972).
35. Karthenser, E. P., and Rodriguez, S.,
Appl. Phys. Lett. 24, 338 (1974).
36. Moretti, A., Dawson, J. W., Peerson, J. J., Lill, R. M.
and Rebuehr, M. T., IEEE Trans. Nucl. Sci. NS-18, 186 (1971)
37. Halbritter, J., Proc. 1972 Appl. Superconductivity Conf.,
Annapolis, Maryland, Edited by Long, J. M., and Gauster,
W. F., (New York, IEEE) p. 662.
38. Schnitzke, K., Martens, H., Hillenbrand, B., and Diepers, H.
Phys. Lett. 45A, 241 (1973).
39. Tedmon, C. S., Rose, R. M., and Wulff, J.,
J. Appl. Phys. 36, 164 (1965).
40. Soumpasis, D., and Luders, K.,
J. Appl. Phys. 41, 2475 (1970).
41. Buckel, W., Hasse, J., and Reichert, V.,
Phys. Lett. 37A #5, 457 (1971).
42. Hasse, J., and Lachmann, J.,
Z. Physik, 258, 136 (1973) (In German).
43. Kneisel, P., Stoltz, O., and Halbritter, J.,
Interner Bericht 75-105-LIN, June 1975,
Kernforschungszentrum, Karlsruhe, W. Germany.
44. Yasaitis, J. A., Ph.D. Thesis, M.I.T. (Dept. of Metallurgy
and Materials Science, 1974) Unpublished.
45. Geach, G. A., and Hughes, J. E., Plansee Proc.
2nd Seminar, Reutte/Tyrol, 1955, p.245.
46. Klopp, W. D., Holden, F. C., and Jaffee, R. I.
Battelle Mem. Inst. (Contract NONR-1512 (00)), July 1960.
47. Klopp, W. D., J. Less-Common Metals, 42, 261 (1975).
48. Jaffee, R. I., Sims, C. T., and Harwood, J. J.,
Plansee Proc., 3rd Seminar, Reutte/Tyrol, 1958, p.380.

49. Metals Handbook, 8th Edition p. 320, American Soc. for
Met., Metals Park, Ohio (1973).
50. Brophy, J., Rose, R. M., and Wulff, J.,
J. Less-Common Metals, 5, 90 (1963).
51. Dinkinson, J. M., and Richardson, L. S.,
Trans. Am. Soc. Metals, 51, 1055 (1959).
52. Roberts, B. W., in Intermetallic Compounds,
Westbrook, J. H., (Ed.). Wiley-Interscience, N.Y. (1967).
53. Joiner, W. C. H., and Blaugher, R. D.,
Rev. Modern Physics, 36, 67 (1964).
54. French, R. A., Cryogenics, 8, 301 (1968).
55. Heim, G., and Kay E., J. Appl. Phys. 46, 4006 (1975).
56. Schmidt, P. H., J. Vac. Sci. Technol. 10, 611 (1973).
57. Ginzton, E. L., Microwave Measurements, p. 400,
McGraw-Hill Book Co. (1957).
58. Weaver, J. N., SLAC-TN-68-21, July (1968).
59. Loew, G. A., SLAC-TN-68-25, November (1968).
60. Purchased from: Electronic Tube Div. of Sperry-Rand Corp.,
Gainesville, Florida. Model No. SSX-12011.
61. Purchased from: PRD Electronics, Inc., Westbury, N.Y.
Meter: Type 686-A. Thermistor Mount: 628A-A.
62. General Radio, Tupe 1340 Pulse Generator.
63. Purchased From: EIP Corp., Santa Clara, California;
Model No. 350C.
64. Purchased From: Electron Dynamics Div. of Hughes Air-
craft Co., 1177H Series.
65. Address: Rhenium Alloys Corp., P. O. Box 245, Elyria,
Ohio, 44035.
66. Address: Stellite Division, Cabot Corp., 1020 West Park
Ave., Kokomo, Indiana, 46901.
67. (a) Central Analytical Facility, M.I.T.
(b) Lehigh Testing Laboratories, Inc.,
P. O. Box 1241, Wilmington, Del. 19899.

68. Hahn, H., Halama, H. J., and Foster, E. H.,
J. Appl. Phys. 39, 2606 (1968).
69. Address: 9 Crane Court, Woburn, Mass.
The Author wishes to thank Mr. Paul Bergendahl for
his help and cooperation during the machining work.
70. Manufactured by: Pecks Products Co., 610 E. Clarence,
St. Louis, Mo. 63147.
71. Tegart, W. J. McG., The Electrolytic and Chemical Polishing of Metals, Pergamon Press. London (1959) p.2.
72. (a) Druce, J. G. F., Rhenium, Cambridge University Press,
(1948).

(b) Killerffer, D. H., and Linz, A., Molybdenum Compounds,
Interscience Publishers, N.Y. (1952) p.
73. Morin, F. J., and Maita, J. P., Phys. Rev. 129, 1115 (1963).
74. Lerner, E., and Daunt, J., Phys. Rev. 142, 251 (1966).
75. Weaver, J. N., High Energy Physics Laboratory,
Stanford University, Publication HEPL-PC-1, (1968).
76. Allen, M. A., Farkas, Z. D., Hogg, H. A., Hoyt, E. W. and
Wilson, P. B., IEEE Trans. Nucl. Sci., NS-18, 168 (1971).
77. Giordano, S., Hahn, H., Halama, H. J., Varmazis, C., and
Rinderer, L., J. Appl. Phys. 44, 4185 (1973).
78. Halbritter, J., J. Appl. Phys. 42, 82 (1971).
79. Mühlischlegel, B., Z Physik, 155, 313 (1959).
80. Gladstone, G., Jensen, M. A., and Schrieffer, J. R., in
Superconductivity, Parks, R.D., (Ed.), Vol. 2,
Marcel Dekker, Inc., N.Y. p.781.
81. Lawless, K. R., Rep. Prog. Phys. 37, 231 (1974).
82. Fehlner, F. P., and Mott, N. F., J. Oxidation Metals,
2, 59 (1970).
83. Fehlner, F. P., and Mott, N. F., Oxidation of Metals
and Alloys, (Metals Park: ASM) (1971), p.37.
84. Jaffee, R. I., and Sims, C. T., Battelle Mem. Inst. Tech.
Rept. April, 1958.

85. Goldschmidt, H. J., Interstitial Alloys, Betterworths, London, 1967, p. 369.
86. Witcomb, M. J., J. Less-Common Metals, 41, 45 (1975).
87. Pfister, H., Cryogenics, 16, 17 (1976).
88. Coons, W. C., and Isoty, L. R., Metal Progress, 109, 36 (1976).
89. Gavalier, J. R., Janocko, M.A., and Jones, C. K., Appl. Phys. Lett. 21, 179 (1972).
90. Gavalier, J. R., Janocko, M. A., Hulm, J. K., and Jones, C.K., Proc. 1972 Appl. Superconductivity Conf., Anapolis, Maryland, Edited by Long, H. M., and Gauster, W. F., (New York, IEEE) p. 419.
91. Wilson, I., Schramm, D., and Kinzer, J., Bell Syst. Tech. Journal, 25, 408 (1946).

BIOGRAPHICAL NOTE

The author was born at Barekese, near the City of Kumasi, in the Republic of Ghana. After attending elementary and middle schools in his hometown, he studied at Prempeh College (actually, a secondary school) in Kumasi. He received the Ordinary level and Advanced level Certificates at Prempeh in 1964 and 1966 respectively. From 1966 to 1970, he was a student at the University of Ghana from where he graduated with a B.Sc.(Honours) degree in Physics and Mathematics. Since September 1970, he has been a graduate student at M.I.T., receiving the S.M. degree in Physics in June of 1973.

He is a member of the American Association for the Advancement of Science and the Society of Sigma Xi.

REPORT DOCUMENTATION PAGE		READ INSTRUCTIONS BEFORE COMPLETING FORM
1. REPORT NUMBER #1	2. GOVT ACCESSION NO.	3. RECIPIENT'S CATALOG NUMBER
4. TITLE (and Subtitle) RESEARCH IN MATERIALS SCIENCE: Superconducting Transition Metal Alloys.		5. TYPE OF REPORT & PERIOD COVERED 1 June, 1975 -- 30 Sept. 1976
7. AUTHOR(s) J.L. Bostock M.L.A. MacVicar R.M. Rose		6. PERFORMING ORG. REPORT NUMBER
9. PERFORMING ORGANIZATION NAME AND ADDRESS Center for Materials Science and Engineering, Massachusetts Institute of Technology Cambridge, Massachusetts 02139		8. CONTRACT OR GRANT NUMBER(s) N00014-75-C-1084
11. CONTROLLING OFFICE NAME AND ADDRESS Procuring Contracting Officer Office of Naval Research Department of the Navy, Arlington, VA 22217		10. PROGRAM ELEMENT, PROJECT, TASK AREA & WORK UNIT NUMBERS 5D10
14. MONITORING AGENCY NAME & ADDRESS (if different from Controlling Office) ONR Resident Representative Massachusetts Institute of Technology Room E19-629 Cambridge, Massachusetts 02139		12. REPORT DATE 30 September, 1976
		13. NUMBER OF PAGES 1
		15. SECURITY CLASS. (of this report) Unclassified
		15a. DECLASSIFICATION/DOWNGRADING SCHEDULE
16. DISTRIBUTION STATEMENT (of this Report) Unlimited		
17. DISTRIBUTION STATEMENT (of the abstract entered in Block 20, if different from Report) Unlimited		
18. SUPPLEMENTARY NOTES Part II: Microwave Surface Resistance of Superconducting Alloys, a thesis submitted in partial fulfillment of the requirements for Degree of Doctor of Philosophy by Kofi Agyeman.		
19. KEY WORDS (Continue on reverse side if necessary and identify by block number) Mo-Re alloys, X-Band cavities, superconducting rf properties, surface resistance, breakdown fields, superconducting energy gap, alloy oxidation, surface preparations, microwave cavity.		
20. ABSTRACT (Continue on reverse side if necessary and identify by block number) Part I is a listing of major papers resulting from research carried out under this contract. Part II is a description of the microwave cavity research using a Mo _{0.75} Re _{0.25} X-band removable backplate cavity. Various surface preparations and the resulting cavity behavior as a function of time and exposure to different atmospheres are discussed. From measure- ments of the surface resistance as a function of temperature, Q-values, residual surface resistance, and energy gap parameters were determined. For		

Unclassified

SECURITY CLASSIFICATION OF THIS PAGE(When Data Entered)

BLOCK 20

a material with a gap of $(1.78 \pm .04)k_B T$, the optimum values of Q_0 and R_0 were 1.4×10^9 and $.57 \mu\Omega$. Breakdown magnetic fields were also determined; the highest observed was 176 G. Directions for improving cavity performance are suggested.

SECURITY CLASSIFICATION OF THIS PAGE(When Data Entered)

FINAL TECHNICAL REPORT

Period: July 1, 1976 - September 30, 1976

Title: Research in Materials Sciences

Project Title: Chemical Synthesis Using High Temperature
Lithium Vapor Species

Contract Number: N00014-75-C-1084

ARPA Order Number: 2994

Program Code Number: 5D10

Name of Contractor: Massachusetts Institute of Technology
Cambridge, Mass. 02139

Principal Investigator: N.J. Grant (617) 253-5638

Project Scientists or Engineers: Prof. R. J. Lagow (617) 253-5617

Effective Date of Contract: June 1, 1975

Contract Expiration Date: September 30, 1976

Amount of Contract: \$325,000

Amount of Project: \$ 65,000

Sponsored by
Advanced Research Projects Agency

ARPA Order No. 2469

The views and conclusions contained in this document are those of the authors and should not be interpreted as necessarily representing the official policies, either expressed or implied of the Advanced Research Projects Agency or the U.S. Government.

PHD's GRANTED

Lawrence A. Shimp - PHD, Massachusetts Institute of Technology, 1976.

ACADEMIC POSITIONS

Dr. John A. Morrison - Assistant Professor of Chemistry,
University of Illinois at Chicago
Circle, 1976.

Dr. Larry G. Snedden - Assistant Professor of Chemistry,
University of Pennsylvania, 1975.

Publications

1. C. Chung and R. J. Lagow, "The Reaction of Lithium Atoms at 1000°C With Chlorocarbons; A New Route to Polyolithium Compounds", Chem. Comm., 1079 (1972).
2. L. A. Shimp and R. J. Lagow, "The Reaction of Carbon Vapor With Lithium Atoms: A Direct Synthesis of Polyolithium Compounds", J. Amer. Chem. Soc., 95, 1343 (1973).
3. L. G. Sneddon and R. J. Lagow, "Vapor Synthesis of Polyolithium Compounds: The Effect of Halogens in Activating the Carbon-Hydrogen Bond", Chem. Comm., 302 (1975).
4. J. A. Morrison, C. Chung, R. J. Lagow, "The Reaction of Lithium Vapor with Alkenes: A New Synthesis for Polyolithium Compounds", J. Amer. Chem. Soc., 97, 5015 (1975).
5. L. A. Shimp and R. J. Lagow, "The Reaction of Lithium Vapor With Organometallic Compounds", Chem. Comm. (in press).
6. J. A. Morrison and R. J. Lagow, "A New Synthesis for Tetralithiomethane", submitted to J. Amer. Chem. Soc.
7. L. A. Shimp, C. Chung, J. A. Morrison and R. J. Lagow, "The Reaction of Lithium Vapor with Benzene", J. Inorg. and Nuc. Chem. (in press).
8. L. G. Sneddon and R. J. Lagow, "The Reaction of Lithium Vapor with Polymer Surfaces", (in preparation).

Summary of Research Progress in the Synthesis Characterization
and Reactions of Polylithium Compounds
8-16-75

Over the past three months, this project has reached a degree of maturity such that the phase of our research program involving the synthesis of polymers and diamond-like materials has been initiated. The initial studies in several areas have been very promising. However, the major problem remains the purification and separation of the novel polylithium compounds.

The polymer synthesis program is developing in three different areas. These are the synthesis of polymers in a high pressure - high temperature apparatus, the synthesis of three dimensional polymers in solution, and the synthesis of polymers by means of gas phase reaction. The first high pressure - high temperature studies were conducted a month ago in a tetrahedral anvil system. A large amount of effort has been devoted over the past year to the construction of a large high temperature - high pressure press which is capable of obtaining 40 Kilo-bar pressures at 400°C with significant reaction container sizes on the order of 2 inches in diameter. Calibration runs were made in November on this new apparatus. Because the starting materials for these polymer syntheses had been produced in our program several months ago and because the potential value of these experiments is so great, a graduate student was flown to a tetrahedral anvil facility in Houston to conduct preliminary studies on the program and in a related area. Even though the container size for such a high pressure device is only one-eighth inch in diameter, eight experiments were conducted. The results are now being evaluated. With the completion of the larger scale high pressure apparatus extensive experimentation will be undertaken in this area during the next fiscal year, with this being one of the most important efforts anticipated.

Very promising and exciting results have been obtained in the development of synthetic reactions in solution between monomer polylithium compounds and difunctional alkanes. The reaction of dilithiomethane, H_2CLi_2 , with methylene chloride, H_2CCl_2 , and with 1,2 dichloroethane have yielded higher alkanes and a polymer which is very much like polyethylene. This result is a giant step toward the synthesis of three dimensional

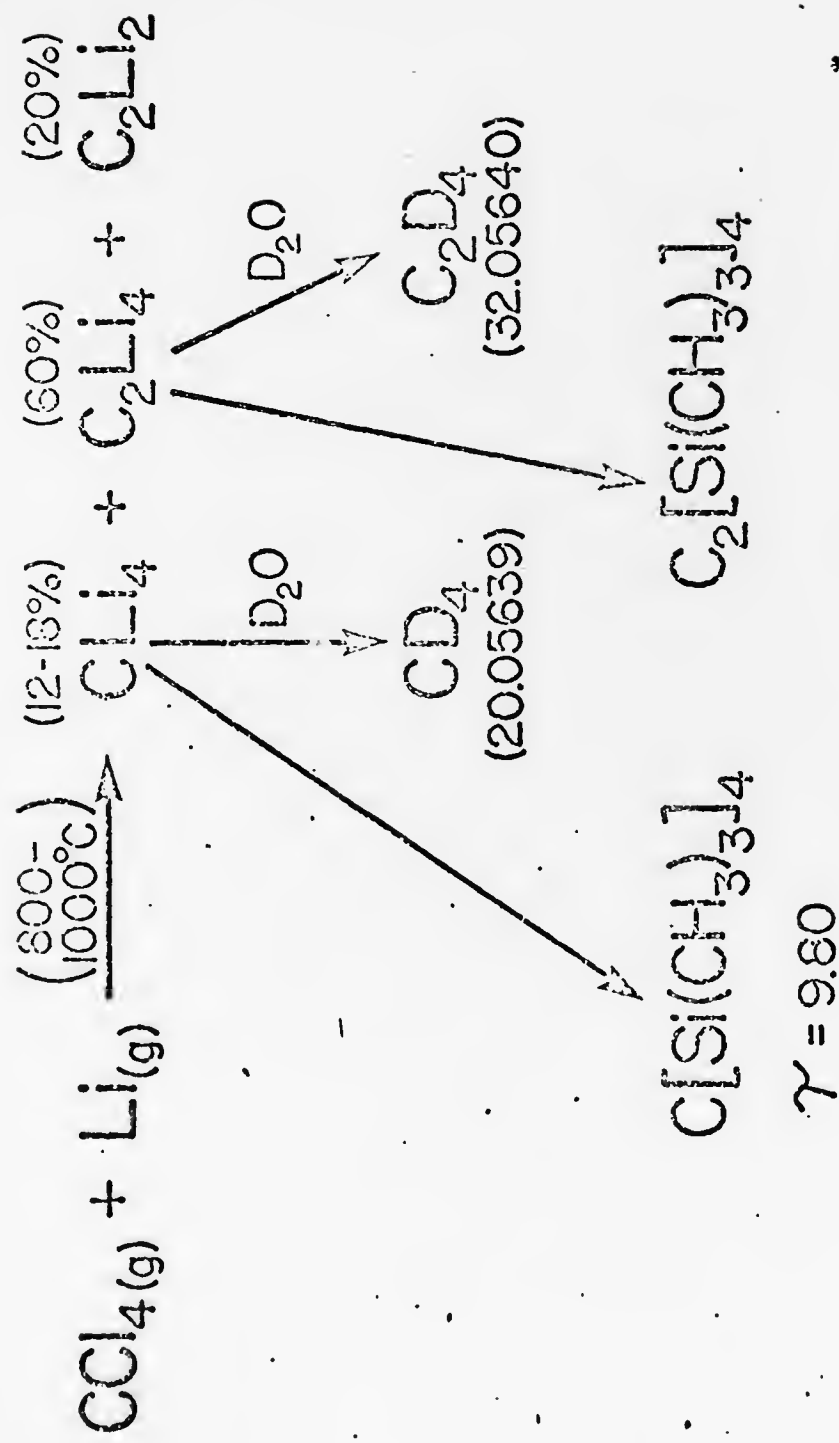
polymers from other polylithium compounds and indicates the feasibility of such processes. Efforts to maximize and establish the molecular weights are underway.

The discovery that polylithium compounds such as C_3Li_4 may be vaporized without extensive decomposition has led to an experimental program designed to study the reaction of such vapor species with difunctional monomeric materials. The degree of polymerization of such reaction products is under study.

Earlier in our program, a study of the reaction of carbon tetrachloride, CCl_4 and the reaction of hexachloroethane C_2Cl_6 was conducted with lithium vapor at a $1000^\circ C$.¹ The products of the initial reaction were tetralithiomethane CLi_4 and tetralithioethulene Li_2C-CLi_2 . (See Figure 1.) These compounds were characterized and it has been found that they react with various organic and inorganic substrates in the manner characteristic of other lithium compounds such as the conventionally prepared monolithium compounds. This experimental result provides evidence of the suitability of such polylithium compounds for reactions as monomers in the proposed diamond-like polymer systems. Subsequently, the reaction of hexachloroethane (see Figure 2) with lithium produced hexolithioethane in approximately 80 per cent yield. Again this material has been shown to be a potentially reactive monomer.

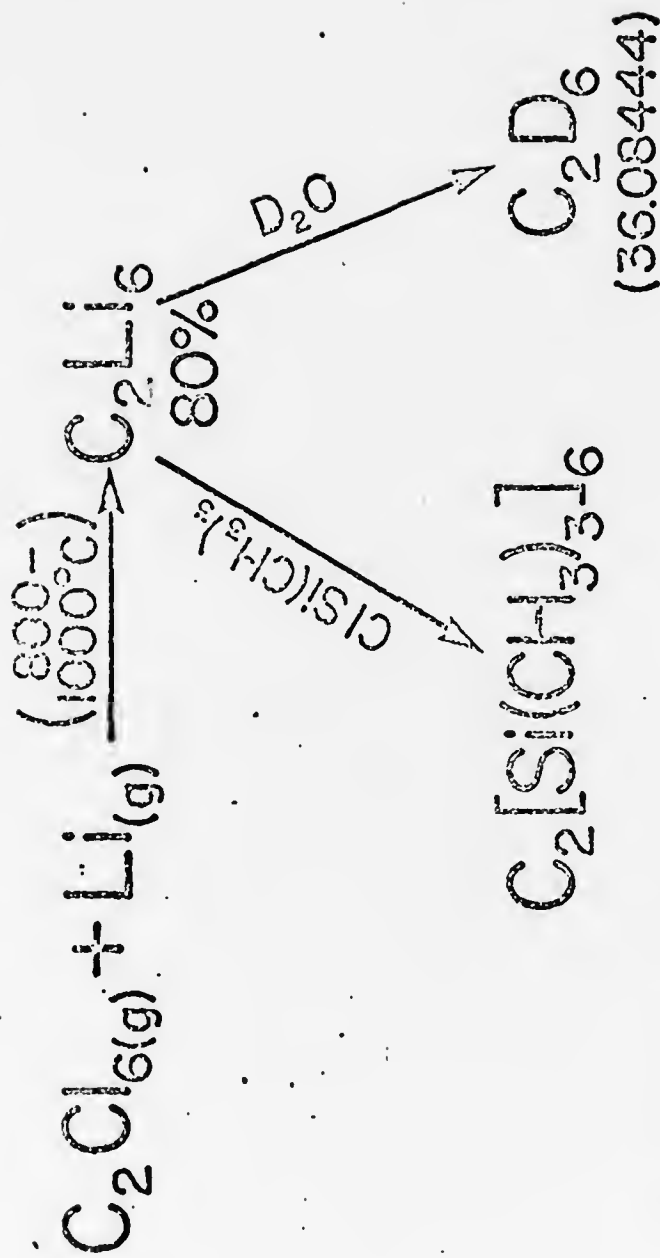
A study of the reaction of carbon vapor generated from a carbon arc apparatus at $2500^\circ C$ (see Figure 3) was undertaken to establish an alternative method for synthesizing polylithium compounds.² (See Figure 4.) The principal product was C_3Li_4 which appears to have the allene structure and might be an attractive monomer. Varying amounts of tetralithiomethane and tetralithioethylene were also produced in this study.

A third publication has resulted from the reaction of lithium vapor with benzene.³ While for most of our systems the reactants are admitted to the reactor at room temperature and reacted with the high temperature lithium vapor, initial studies giving a small yield of hexalithiobenzene prompted us to do a more extensive study based on the reaction of lithium vapor plus benzene at various temperatures. A new type of reactor was designed for this purpose. At room temperature one gets a distribution of lithiated benzene ranging from over the range of $C_6Li_{6-n}H_n$ where $n = 1$ to 6. At room temperature the species of highest yield is dilithiobenzene. As one raises the temperature progressively to $800^\circ C$ a



C. Chung and R.J. Lagow, Chem. Comm. 1078 (1972)

Fig. 1



C. Chung and R.J. Lagow,
Chem. Comm. 1078, (1972)

Fig. 2

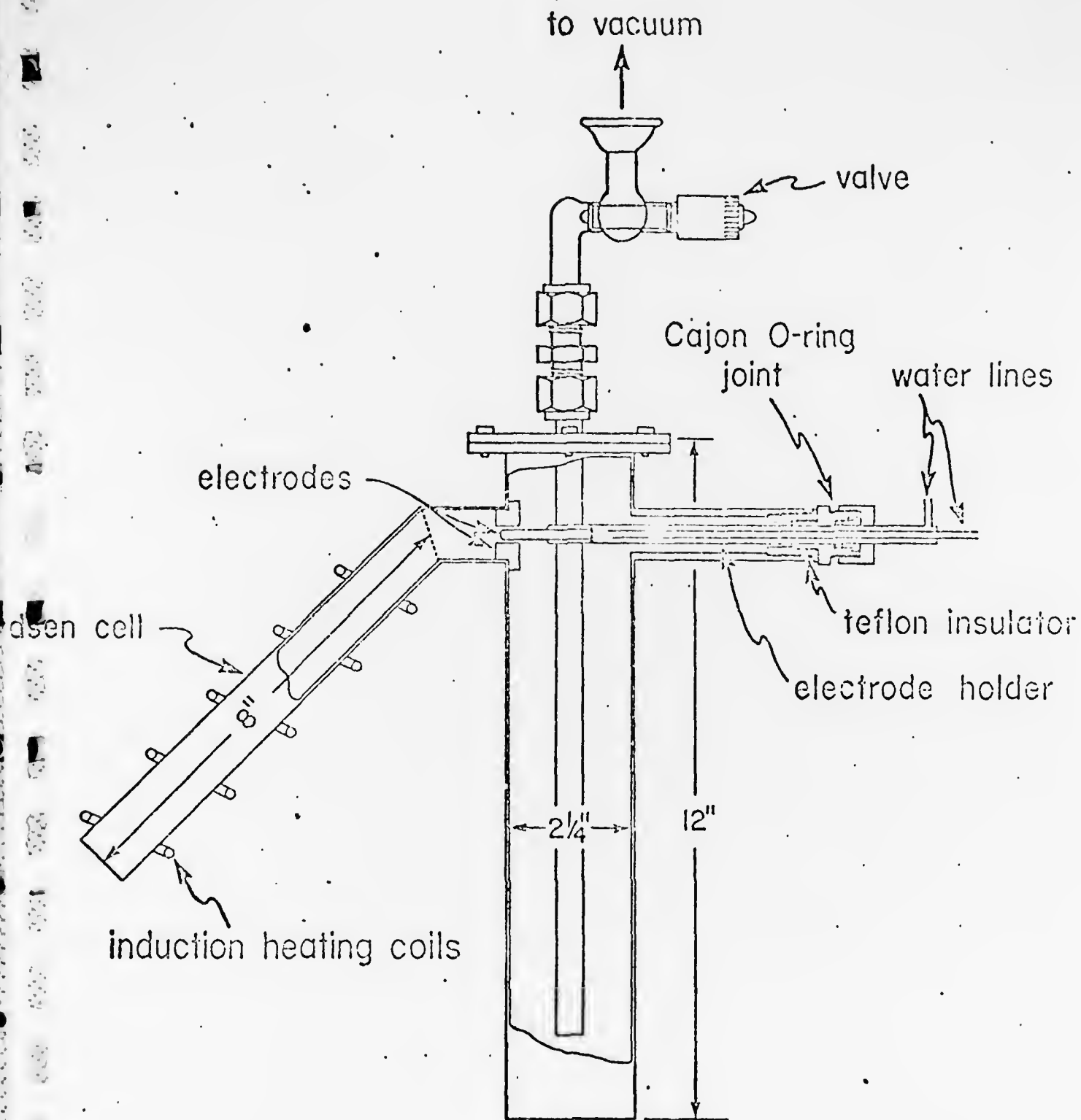
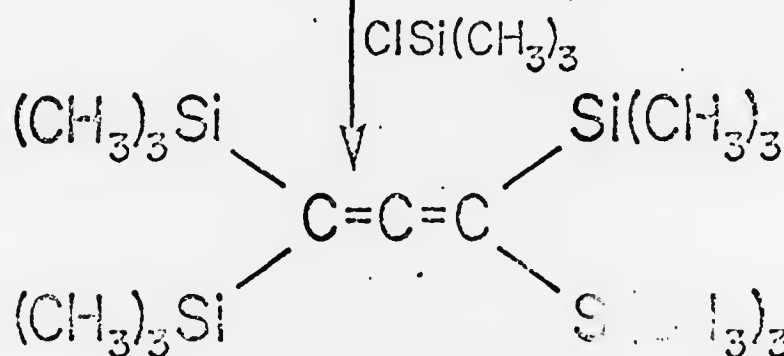
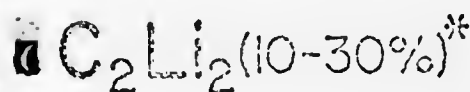
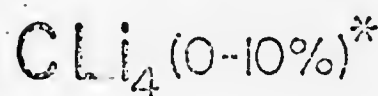
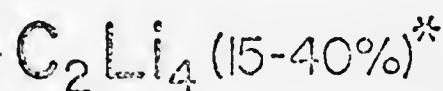
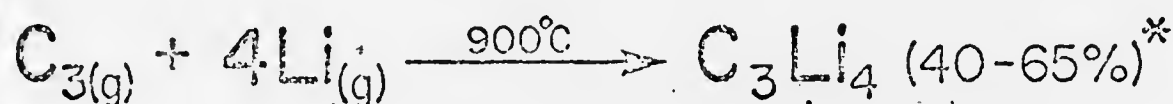
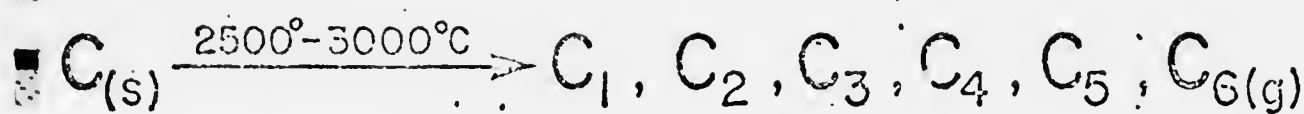


Fig. 3



$$\gamma = 9.89$$

* Based on Carbon Vaporized

L. A. Shimp and R. J. Lagow, J. Am. Chem. Soc. 95,
1343 (1973)

Fig. 4

shift toward the higher benzene polylithium compounds is noted. The temperature of the benzene is raised to 900°C and a striking new result is attained. One begins to obtain polylithiated cyclohexanes from the benzene starting material. This results from a tendency for the lithium to add to the double bonds as well as replace the protons on the ring. Studies were made up to temperatures of 1200°C producing such striking compounds as perlithiocyclohexane and $\text{C}_6\text{Li}_6\text{H}_6$. It has been found subsequently that the reaction of hexachlorobenzene with lithium provides a much cleaner route to hexalithiobenzene.⁴

The reaction of methane gas with lithium has also been extensively investigated.⁵ We predicted and found that lithium at 1000° will not react with methane gas at room temperature. The activation energy for this reaction appears to be in the 30 kcal mole range. Lithium at 1000°C usually has about 3 kcal mole of translational or kinetic energy and only a very small percentage of lithium in the first excited electronic state. Therefore, the activation energy for the lithium-methane reaction is not likely to be available under these reaction conditions. The reaction between methane and lithium would be a very important one for the production of tetralithiomethane which we consider to be one of the important materials in subsequent polymer synthesis. We have used several approaches to provide the activation energy for this reaction. We have found that if we either electronically excite the lithium or vibrationally excite the methane the reaction proceeds in a satisfactory manner. We have conducted an experiment in which the methane was heated to 900°C and obtained satisfactory results. Increased temperatures populate higher vibrational states in the methane and thus allow a very significant decrease in the activation energy of the reaction. We also used a radio frequency source to excite the lithium vapor electronically and produced a successful reaction. Still another piece of work has been done using a methane plasma source which vibrationally excites the methane and allows the reaction to proceed. The most important result in this area is discussed in the "newest results" section and involve the study of the reaction of laser induced electronically excited lithium.

In the study of tetralithiomethane, a fourth synthesis is being completed which involves initial synthesis of dilithiomethane and subsequent pyrolysis to give a substantial yield of tetralithiomethane.⁶ Using this method we have obtained substantial quantities of tetralithiomethane.

Extensive work has been done on solvent systems for tetralithiomethane so that one may do the polymer synthesis in solution. Several successful solvent systems are being developed and the concentrations of the polylithium compounds in solution are being determined by NMR studies and the preparation of derivatives.

An extensive study has been recently completed on the reactions of olefins with lithium vapor.⁷ (See Figure 5.) A large number of new polylithium compounds such as tetralithio cyclohexadiene, 2,3 dilithio 2 butene, 2,3 tetralithio 2 butene, 1,2 dilithio isobutane, 1,4 dilithio 2 butene, and 1,2 trilithio isobutane have been prepared in this study. We have seen instances of both substitution for hydrogen on sites requiring a low activation energy for reaction and addition to double bonds. This study has established another general route to polylithium compounds.

Studies of reactions of inorganic species with lithium have also been undertaken. The reaction of silicon tetrachloride, SiCl_4 , with lithium has been recently studied and the polylithium compound SiLi_4 was obtained in good yield.⁸ Hydrolysis and deuterolysis of the compound produced silanes and perdeutero silanes. A subsequent study of the reaction of tetralithiosilane with methyl chloride resulted in a 15 per cent yield of tetramethyl silane indicating that the SiLi_4 is also a potential monomer. The reaction of BCl_3 and PCl_3 are currently under study. A fair yield of trimethylborane $\text{B}(\text{CH}_3)_3$ was obtained from the reaction of BLi_3 with methyl chloride. Additionally the synthesis of polylithiated carboranes has been attempted and a workup is now in progress. Isolation of a higher purity SiLi_4 is being undertaken. It should be pointed out that if the diamond syntheses from tetralithiomethane are successful, a synthesis of a silicon analog for a diamond will be attempted using the SiLi_4 . Such a diamond-like silicon structure would have many unusual electrical and physical properties. This type of structure has been the object of numerous unsuccessful synthetic studies utilizing the phase diagram of silicon. This potentially valuable species has previously eluded all other synthetic approaches.

Major Products of the Reaction of Lithium with Alkenes

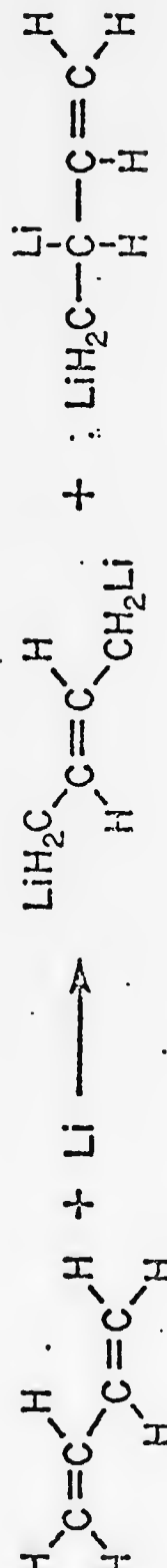
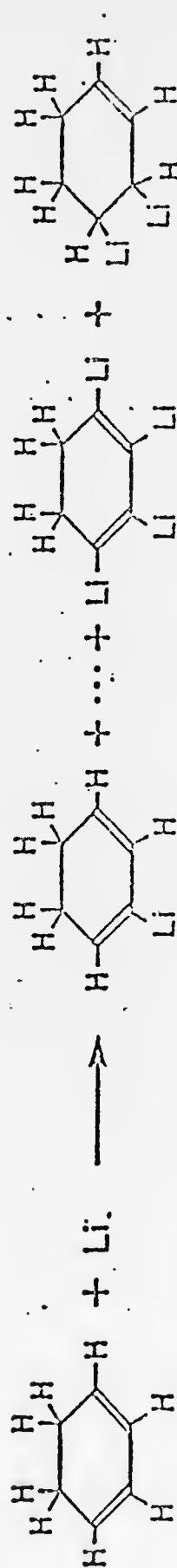
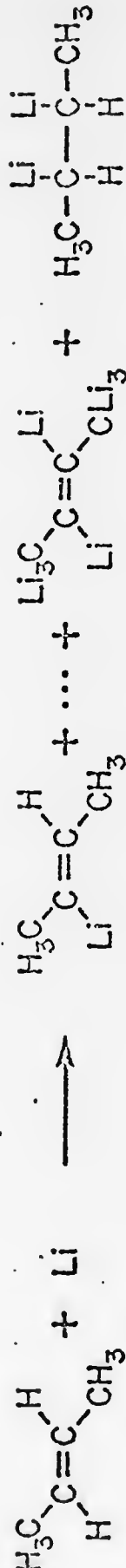
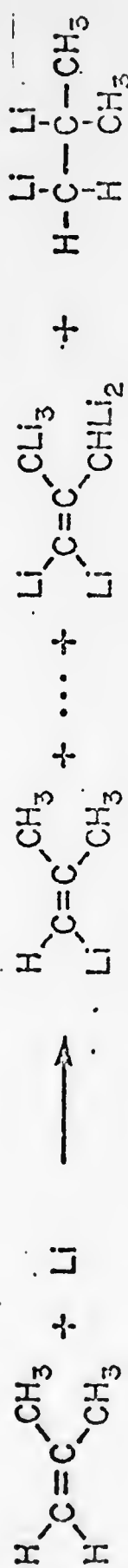


Fig. 5

Most Recent Results

One of the most exciting recent results in this area is the synthesis of the first polylithium ethers. $C_3Li_7OC_3Li_7$ has been prepared recently and is being characterized. This development opens many possibilities in the polymer area such as using structures with ether linkages as monomers and the possibility of obtaining other oxygen containing polylithium compounds.

Another completed study⁹ has indicated that perlithiocarbons may be obtained by the reaction of lithium vapor with partially chlorinated hydrocarbons. Perlithio propane C_3Li_6 has been obtained from several monochloro isomers. Similar reactions have produced other novel polylithium compounds. These results suggest that the replacement of a halogen by lithium is so exothermic, that the activation energy required for the lithium to abstract hydrogen is available. The result is similar to that obtained with a vibrationally excited alkane and suggests vibrational excitation.

Recently structural studies have been initiated on several polylithium compounds. We have been interested in the lithium and carbon 13 NMR spectra and the laser-Raman spectra of polylithium compounds both in solution and in the solid state. Very encouraging results have been obtained. Such studies will also lead to accurate methods for determination of concentration of reactive polylithium intermediates in solution and for identification of polylithium compounds.

A major breakthrough¹⁰ of great significance in synthetic chemistry and of prime interest in physical chemistry has come about through a collaboration with Professor J. S. Steinfield of our department. Lithium vapor generated at 1000°C has been selectively excited to the first excited electronic state (1.56 eV above ground state) with a tunable dye laser in 80 per cent yield. This electronically excited lithium has been found to react very efficiently with methane in contrast to no reaction at all when lithium is in the ground state. This reaction opens a whole new field of synthetic chemistry: the reaction of electronically excited lithium vapor. This chemistry will surely differ greatly from the chemistry of lithium vapor in the ground state. This event is also very significant because it is believed to be the first study of any synthetic reaction of a selectively electronically excited metal vapor and because it may provide input into synthetic routes to $ClLi_4$ and C_2Li_6 .

Crystal structures of two of the new polylithium compounds have been completed in collaboration with Prof. Galen Stucky of the University of Illinois.

References

1. C. Chung and R.J. Lagow, "The Reaction of Lithium Atoms at 1000° C with Chlorocarbons; A New Route to Polylithium Compounds", Chem. Comm. 1079 (1972).
2. L.A. Shimp and R.J. Lagow, "The Reaction of Carbon Vapor with Lithium Atoms; A Direct Synthesis of Polylithium Compounds", J. Amer. Chem. Soc. 95, 1343 (1973).
3. L.G. Sneddon and R.J. Lagow, "Vapor Synthesis of Polylithium Compounds: The Effect of Halogens in Activating the Carbon-Hydrogen Bond", J. C. S. Chem. Comm. 302 (1975).
4. J.A. Morrison, C. Chung and R.J. Lagow, "The Reaction of Lithium Vapor with Alkenes: A New Synthesis for Polylithium Compounds", J. Amer. Chem. Soc. 97, 5015 (1975).
5. L.A. Shimp, C. Chung, J.A. Morrison and R.J. Lagow, "The Reaction of Lithium Vapor with Benzene", J. Am. Chem. Soc. (in press).
6. L.A. Shimp and R.J. Lagow, "The Reaction of High Temperature Lithium Vapor with Methane", submitted to J. Am. Chem. Soc.
7. J.A. Morrison and R.J. Lagow, "A New Synthesis for Tetralithiomethane", submitted to J. Am. Chem. Soc.
8. J.A. Morrison and R.J. Lagow, "The Synthesis of SiLi_4 and GeLi_4 ", submitted to J. Chem. Soc.
9. R.J. Lagow, L.A. Shimp, F. Lucer and J.S. Steinfield, "The Reaction of Laser-Induced Electronically-Excited Lithium with Methane", (manuscript in preparation).
10. R.J. Lagow, G.D. Stucky, K.M. Abraham and J.A. Morrison, "The Structure of Dilithiomethane", (manuscript in preparation).

[Reprinted from the Journal of the American Chemical Society, 97, 5015 (1975).]
Copyright 1975 by the American Chemical Society and reprinted by permission of the copyright owner.

Reaction of Lithium Vapor with Alkenes. A New Synthesis for Polylithium Compounds.

Sir:

It has recently been reported that at elevated temperatures lithium vapor reacts with chlorocarbons¹ and with carbon vapor² to produce novel polylithium organic compounds. The reaction of excess lithium vapor with several alkenes has been studied and it has been found that both substitution of lithium for hydrogen and addition of lithium to the double bonds occur to produce polyolithiated alkanes and alkenes.

A large excess of lithium (>15 g) was vaporized at 700–800° in an evacuated stainless steel reactor (Figure 1) with an inconel Knudsen cell (A) which was heated resistively. Simultaneously, the alkene was slowly vaporized into the circular tube (B) above the Knudsen cell. During the 30-min reaction period, products were collected as solids on the liquid nitrogen cooled cold finger (C). The pressure in the reactor during the reaction was approximately 10^{-3} Torr. After the reaction the contents of the reactor were warmed to room temperature and removed under argon.

The very reactive solids obtained from the reaction looked metallic but were very brittle. Frequently, portions of the solid were colored, the hue varying from red to black. The products were carefully hydrolyzed by both H_2O and D_2O in a standard vacuum line to yield alkenes and alkanes

which were identified by comparing 1H NMR data, mass spectral fragmentation patterns and, if necessary, GLC retention times to authentic samples. The relative amount of lithiation was determined by low resolution mass spectroscopy (70 eV) of the deuterated alkenes recovered from the

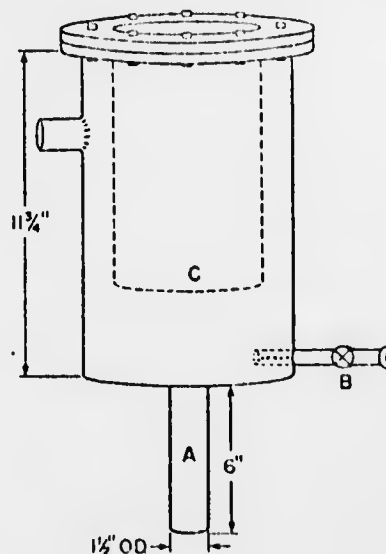
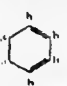
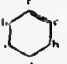


Figure 1. Inverted Dewar type reactor.

Table I. Hydrocarbon Chemical Shifts, $\tau \pm 0.02$ ppm

Compounds	From lithiated alkenes ^a				Reference compounds			
	HA	HB	HC	HD,E	HA	HB	HC	HD,E
Isobutene Products								
$(\text{HA})_3\text{C}=\text{CH}_2^b$	8.34	5.42			8.38	5.44		
$(\text{HA})_3\text{CCH}^b$	9.14	...			9.13	...		
2-Butene Products								
$\text{HA}_2\text{CCH}^b\text{C}=\text{C}(\text{H})\text{CH}_3$	8.56 ^c	4.90			8.47 ^d	4.73 ^d		
Cyclohexadiene Products								
	7.90	4.16			7.86	4.17		
cyclohexadiene								
	8.37	8.07	4.42		8.39	8.04 ^d	4.41 ^d	
cyclohexene								
cyclohexane	8.58				8.56 ^d			
Butadiene Products								
$\text{HA}_2\text{CH}^b\text{CH}^b\text{C}=\text{CHDHE}$	9.03	7.95	...	~5.09 ^f	9.02	8.02	4.22	~5.10 ^f
$\text{HA}_2\text{C}(\text{H}^b)\text{C}=\text{C}(\text{H})\text{CH}_3$	8.47 ^c	4.70			8.47 ^d	4.73 ^d		

^a If the polyolithio products were hydrolyzed with D_2O , the resonances were further split by H-D coupling. ^b Very weak signal, the expected decet is further split by second-order effects. ^c Mixture of cis and trans isomers. ^d From reference 3. ^e Not observed. ^f The difference in the chemical shifts of these protons is very small.

reaction of the solids with D_2O . High resolution mass spectroscopy was used to determine accurately the composition of each low resolution peak. It was assumed that the parent ion peak intensities were proportional to the amount of the polyolithioalkene originally present. The degree of lithiation was usually confirmed by reaction of the solids with chlorotrimethylsilane to yield the poly(trimethylsilyl) derivatives.

Isobutene, 1.5 g, was treated with lithium as described above; the solid was hydrolyzed with H_2O , and the resulting very volatile liquids were separated into two fractions using GLC. These fractions were regenerated isobutene in 26% yield based upon the amount of isobutene consumed, and isobutane in 4% yield. When the product was hydrolyzed with D_2O , the high resolution mass spectra (CEC21-110B mass spectrometer) of the isobutene fraction contained parent ion peaks for $\text{C}_4\text{H}_7\text{D}$ (57.06897), $\text{C}_4\text{H}_6\text{D}_2$ (58.07459), $\text{C}_4\text{H}_5\text{D}_3$ (59.08079), and $\text{C}_4\text{H}_4\text{D}_4$ (60.08779) in the ratio of 10:4:3:1. This indicates the substitution of from one to four hydrogen atoms by lithium in isobutene. The low resolution mass spectra of the isobutene fraction also contained less intense parent ions due to the substitution of as many as seven of the original eight hydrogen atoms in the isobutene molecule. The mass spectrum of the products obtained from the reaction of Me_3SiCl with the solid indicated the presence of at least four trimethylsilyl groups on isobutene. The mass spectra of the deuterated isobutane fraction contained peaks at m/e 60-63 which indicates the presence of up to five deuterium atoms in the isobutane molecule. Figure 2 schematically presents the products from the reaction of the alkenes with lithium vapor. The two types of reactions represented are the stepwise replacement of hydrogen atoms by lithium and the saturation of the double bond to produce alkanes. Table I is a comparison of the ^1H NMR data of the hydrocarbons recovered from the hydrolysis reactions with data compiled from the literature or collected from standard samples. The ^1H NMR spectrum of the deuterated isobutene was integrated and the ratio of methyl protons to vinyl protons was found to be 6:1 indicating that substitution at the vinyl position is preferential.

The reaction of 1.5 g of *trans*-2-butene with lithium, followed by deuterolysis, gave a 10% yield of deuterated 2-butenes. The mass spectra of these products contained parent ions for $\text{C}_4\text{H}_7\text{D}$ (57.06831) and $\text{C}_4\text{H}_6\text{D}_2$ (58.07519) in a 3:2 ratio. A much less intense peak (~4%) for C_4H_8 (64.11280) indicates that all the hydrogen atoms were sub-

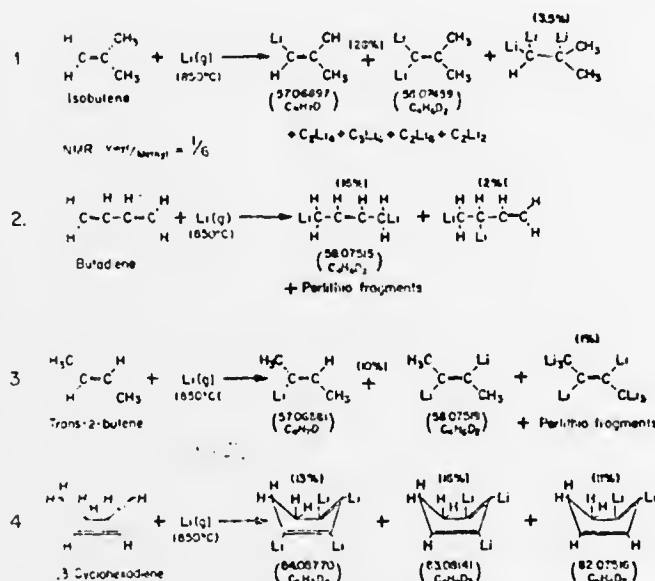


Figure 2. Major products of the reaction of lithium with alkenes.

stituted with lithium in a small percentage of the starting 2-butene. In the deuterated hydrolysis products a parent peak for $\text{C}_4\text{H}_8\text{H}_2^+$ (66.12700) was found which indicates that in ~0.1% of the products lithium has added across the double bond. The ^1H NMR integral spectrum for the D_2O hydrolysis products (Table I) revealed a 12:1 ratio for the 1,4 to the 2,3 protons indicating preferential reaction at the unsaturated sites.

The reaction of 1.5 g of 1,3-cyclohexadiene with lithium gave polyolithium compounds which yielded on hydrolysis 1,3-cyclohexadiene, cyclohexene, and cyclohexane in the ratio of 3:4:3. The total yield of the cyclic C_6 species was 54%. After hydrolysis with D_2O the mass spectra of the cyclohexadiene products contained parent ions for $\text{C}_6\text{H}_4\text{D}_4^+$ (84.08771), $\text{C}_6\text{H}_5\text{D}_3^+$ (83.08141), and $\text{C}_6\text{H}_6\text{D}_2^+$ (82.07516) in the relative intensities of 1.0:1.2:1.3. The lithiation was confirmed by derivation with Me_3SiCl ; mass spectral peaks were observed for $\text{C}_6\text{H}_7\text{SiMe}_3^+$ (m/e 152), $\text{C}_6\text{H}_6(\text{SiMe}_3)^+$ (m/e 224), $\text{C}_6\text{H}_5(\text{SiMe}_3)^+$ (m/e 296), and $\text{C}_6\text{H}_4(\text{SiMe}_3)^+$ (m/e 368). Addition of lithium to one of the double bonds was indicated by mass spectral parent ions due to $\text{C}_6\text{H}_4\text{D}_6^+$ (m/e 88.1192) and to both double bonds

by a molecular ion due to $C_6H_4D_6^+$ (m/e 90 131 30) in the deuterated hydrolysis product

In the preceding examples a large fraction of the products was derived from the replacement of hydrogen by lithium to yield polythioalkenes. The reaction of 1,3-butadiene, however, yields compounds resulting from the addition of two lithium atoms to the double bonds of that compound. Thus, reaction of the lithiated products with H_2O did not regenerate butadiene, but instead gave a 10% yield of butenes. 1H NMR spectra and GLC retention times indicated that the ratio of 1,4 addition to 1,2 addition was 8:1. Derivation with Me_4SiCl yielded a liquid possessing a small peak in the mass spectrum at m/e 200 having the appropriate isotopic distribution for a species with two silicon atoms (calcd mol wt for $Si_2C_4H_{12}$ is 200), and peaks with larger ion intensities at $P - n-CH_3^+$. One explanation for the dilithio product is the facile reaction of lithium with the di-radical 2-butene produced from butadiene as the first step in the free radical polymerization of that compound.

In general both the mass spectra fragmentation patterns and the integrated 1H NMR spectra indicated that substitution of the vinyl protons is preferred to substitution of the methyl protons. With the exception of butadiene it seems likely that the first reaction of alkenes with lithium is the

substitution of a vinylic hydrogen with subsequent replacement of both vinyl and alkyl hydrogens. This last step is in competition with reactions in which lithium is added across the double bond. Under the reaction conditions (800°, gaseous alkali metal) fragmentation of the alkenes leads to C_4Li_4 , C_2Li_6 , C_2Li_4 , and C_2Li_2 whose combined yields vary from 25 to 50%.

Acknowledgment. We are grateful for support for this work from the Advanced Research Projects Agency. The authors thank Dr. Charles Hignite and Professor Klaus Bie-man for high resolution mass spectra.

References and Notes

- (1) C. Chung and R. J. Lagow, *J. Chem. Soc., Chem. Commun.*, 1078 (1972).
- (2) L. A. Shimp and R. J. Lagow, *J. Am. Chem. Soc.*, **95**, 1343 (1973).
- (3) J. W. Emsley, J. Feeney and L. H. Sutcliffe, "High Resolution Nuclear Magnetic Resonance", Pergamon Press, London, 1966.
- (4) Alfred P. Sloan Fellow.

J. A. Morrison, C. Chung, R. J. Lagow*⁴

Department of Chemistry, Massachusetts Institute of Technology, Cambridge, Massachusetts 02139

Received February 3, 1975

Vapour Synthesis of Polylithium Compounds: the Effect of Halogens in
Activating the Carbon-Hydrogen Bond

By L. G. SHERDON and R. J. LAGOW

(Department of Chemistry, Massachusetts Institute of Technology, Cambridge, Massachusetts 02139)

Reprinted from

Journal of The Chemical Society
Chemical Communications

1975

The Chemical Society, Burlington House, London W1V 0BN

Vapour Synthesis of Polylithium Compounds: the Effect of Halogens in Activating the Carbon-Hydrogen Bond

By L. G. SNEDDON and R. J. LAGOW

(Department of Chemistry, Massachusetts Institute of Technology, Cambridge, Massachusetts 02139)

Summary Reaction of lithium vapour with partially halogenated propanes at 800–1000 °C followed by hydrolysis with D₂O in tetrahydrofuran indicates that saturated and unsaturated perolithiated C₂ and C₃ compounds and probably CLi₄ are formed.

RECENT studies have demonstrated that the reaction of excess of lithium vapour at 800–1000 °C with perhalogenated organic compounds led to the first perolithiated alkanes: tetralithiomethane and hexalithioethane. We now report that perolithio products may also be obtained by reaction of lithium vapour with only partially halogenated hydrocarbons. Alkanes in their ground vibrational states do not react with lithium vapour.¹ Probably the very exothermic reaction of lithium at the halogenated sites produces vibrationally excited carbon-hydrogen bonds which react with lithium vapour.

The reaction of lithium vapour with various partially halogenated propanes was carried out as described previously.² In a typical reaction, ca. 5 g of lithium was vaporized during 30–35 min and allowed to react with 0.50 g of 1-bromopropane. The reaction vessel was then opened under argon and the brittle grey solid was removed. This solid was then hydrolysed in tetrahydrofuran solution at –10 °C with D₂O in a vacuum line.

The volatile products of the hydrolysis were then separated by vacuum line fractionation. The material passing a –128 °C trap and stopping in a –196 °C trap (the C₂–C₃ hydrocarbons) was then analysed by g.l.c. using a 10 m × ¼ in Durapak phenyl isocyanate on Porasil C column. The individual compounds were identified by comparison of their retention times with those of known compounds. The mass and i.r. spectra of the C₂–C₃ fraction indicated that the products appear to be totally deuteriated with only a small

TABLE

	$\text{CH}_3\text{CICH}_2\text{CH}_2\text{Cl}$	$\text{CH}_3\text{CICH}_2\text{CICH}_2\text{Cl}$	$\text{CH}_3\text{CH}_2\text{CH}_2\text{Br}$	$\text{CH}_3\text{CHBrCH}_2\text{CH}_3$
CD_3CD_2	3.8%	4.5	10.3	6.0
CD_3-CD_2	0.2	0.6	2.6	0.9
$\text{CD}_3\text{CD}_2\text{CD}_2$	12.7	23.6	7.9	1.4
$\text{CD}_3\text{CD}_2\text{CD}_2$	9.2	9.1	10.8	16.0
$\text{CD}_3\text{C}=\text{CD}_2$	0.6	1.3	4.4	0.9
$\text{CD}_3\text{C}\equiv\text{CD}_2$	11.9	0	0	2.8

amount of partially deuterated species. The total yield of the C_2 - C_3 fraction varied greatly, ranging from 45 to 11% in different runs with 1-bromopropane. The other products which were not identified were probably CD_4 (not trapped at -195°C) and higher molecular weight material resulting from polymerization of the perlithe propanes. Yields of the C_2 - C_3 fraction in other reactions were: from 2-bromopropane, 26 and 29%; 1,2,3-trichloropropane, 39 and 23%; and 1,3-dichloropropane, 38.6%.

Yields of the individual products in the C_2 - C_3 fractions (based on the halogenated propanes consumed) are given in the Table. These data reveal that both fragmentations to give C_2Li , C_2Li_2 , and presumably CLi , and eliminations to give C_3Li and C_3Li_2 are competing against the reaction to give perlithepropene C_3Li_4 . It is significant that the highest yields of C_3Li_4 were obtained from those propanes containing only one halogen atom, while when more than one halogen atom was present, the major product was perlithepropene. This result suggested that it might be possible to synthesize larger perlithehydrocarbons by using only a few selectively placed halogens to activate the molecule.

As a test of this hypothesis we also studied the reaction of

¹ C. Chung and R. J. Lagow, *J.C.S. Chem. Comm.*, 1972, 1078.

² L. A. Shimp and R. J. Lagow, to be published.

lithium vapour with several partially halogenated butanes. The reactions, hydrolysis with D_2O , and separation of the products were carried out as described above, but in contrast to the result with the partially halogenated propanes, no perlithebutanes were obtained. For the reaction of 2-chlorobutane with lithium vapour, 16.2% $\text{C}_4\text{H}_9\text{D}$ and no perdeuterated butane were obtained, the remaining observed products being C_3D_4 and C_3D_5 . Similar results were obtained from the reaction with 2-chloroisobutane and 1-chlorohexane. In each case only the monosubstituted derivative and fragmentation products were obtained. The reaction of 1,4-dichlorobutane with lithium vapour gave only fragmentation products and no disubstituted derivatives. This result is consistent with the higher yield of C_3Li obtained from 1-bromopropane. The reaction of lithium with 1,5-dichloropentane or 1,6-dichlorohexane might be expected to produce complete lithium substitution on the alkane.

We thank the Advanced Research Projects Agency for support, and the Alfred P. Sloan Foundation for a fellowship (R.J.L.).

(Received, 21st February 1975; Com. 217.)

Reaction of Carbon Vapor with Lithium Atoms. A Direct Synthesis of Polylithium Compounds

Sir:

The reaction of lithium atoms with chlorocarbons has been shown to produce tetralithiomethane and hexalithioethane from analogous chlorocarbon starting materials.¹ It is well known that carbon vapor, usually produced with a carbon arc or by vaporizing carbon with a laser, consists of the carbon species C^+ through C_6^+ with C_2 in highest concentration. Carbon vapor is known to be reactive.² A study of the reaction of atomic lithium with carbon vapor species was therefore deemed worthwhile since it was very unlikely that these reactive species would combine to give only lithium carbide C_2Li_2 .

A stainless steel reactor was used (Figure 1) in which carbon vapor was generated by an arc between movable graphite electrodes positioned at the orifice of the lithium Knudsen cell. The reaction vessel was evacuated to 10^{-6} Torr, and the Knudsen cell, containing 11 g of lithium, was heated to 800–850° by induction or resistance heating. The lower walls of the reactor were cooled to -196° , and the arc was initiated with an 18-V, 250-A ac source. After 45 min the reaction was terminated. The extremely air- and moisture-sensitive products were handled with care under argon.

The products were hydrolyzed at 0° , passed through a trap at -30° to remove H_2O , and collected at -196° . The yield (gas measurement) of gaseous products averaged 11 mmol/45 min. The hydrolysis products were characterized using a high-resolution double-focusing C.E.C.-21-110B mass spectrometer at 70 eV. Parent ions were observed for CH_4^+ (16.03133), $C_2H_2^+$ (26.01671), $C_2H_4^+$ (28.03081), and $C_3H_4^+$ (40.03177). The principal product, C_3H_4 , ranged from 40 to 65% of the volatile products. Percentage yields of other hydrocarbons were CH_4 , 0–10%, and C_2H_2 , 10–30%. The yield of C_2H_4 averaged 15%, but occasionally accounted for 45% of the volatile products. Spectroscopic quantities of several higher molecular weight products were also observed.

The principal product, C_3Li_4 ,⁴ which is known to be

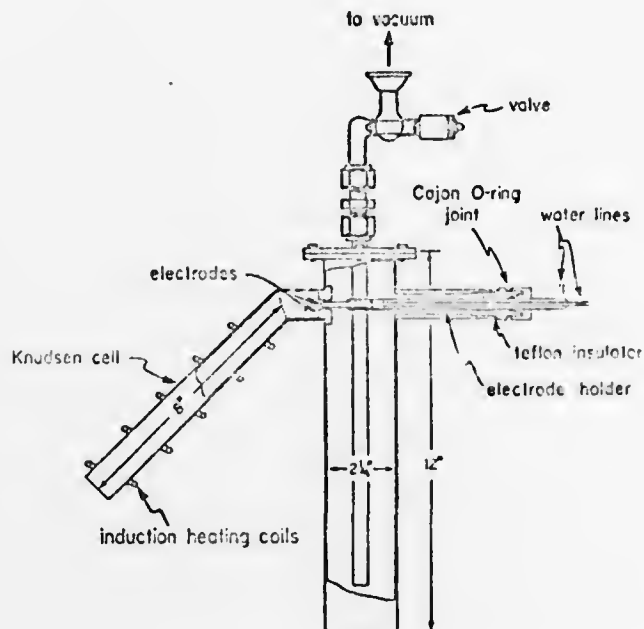


Figure 1.

soluble in THF, was then derivatized by adding $ClSi(Me)_3$ to a -78° THF solution of the reaction product and warmed with stirring over a 24-hr period. A white compound, $C_3(SiMe_3)_4$, was recovered and was characterized by its mass and nmr spectra. A parent ion was observed at 328 and a $(P - CH_3)^+$ peak occurred at 313 with the appropriate silicon isotopic distributions. The H^1 nmr spectrum of the compound in CCl_4 gave a singlet at τ 9.89 which is in agreement with the spectrum previously reported (τ 9.90) for $C_3(SiMe_3)_4$.⁴

Acknowledgment. We are grateful to the Advanced Research Project Agency and the National Science Foundation for support of this work. The authors thank Dr. Charles Hignite and Professor Klaus Biemann for the work in high-resolution mass spectroscopy.

(4) R. West and P. C. Jones, *J. Amer. Chem. Soc.*, **91**, 6155 (1969); R. West, P. A. Carney, and I. C. Mueco, *ibid.*, **87**, 3788 (1965).

L. A. Shimp, R. J. Lagow*

Department of Chemistry, Massachusetts Institute of Technology
Cambridge, Massachusetts 02139

Received December 9, 1972

(1) C. Chung and R. J. Lagow, *J. Chem. Soc., Chem. Commun.*, 1078 (1972).

(2) J. Drowart, R. P. Burns, G. DeMeola, and M. G. Inghram, *J. Chem. Phys.*, **41**, 1131 (1964).

(3) P. S. Skelland R. R. Engel, *J. Amer. Chem. Soc.*, **87**, 1135 (1965).

Reaction of Lithium Atoms at 800 °C with Chlorocarbons; A New Route to
Polylithium Compounds

By C. CHUNG† and R. J. LAGOW*

(Department of Chemistry, Massachusetts Institute of Technology, Cambridge, Massachusetts 02139)

Reprinted from

Journal of the Chemical Society
Chemical Communications

1972

The Chemical Society, Burlington House, London W1V 0BN

Reaction of Lithium Atoms at 800 °C with Chlorocarbons; A New Route to Polyolithium Compounds

By C. CHUNG† and R. J. LAGOW*

(Department of Chemistry, Massachusetts Institute of Technology, Cambridge, Massachusetts 02139)

Summary Reaction of excess of atomic lithium at 800–1000 °C with carbon tetrachloride and hexachloroethane produces tetralithiomethane and hexalithioethane, the first examples of perthiated alkanes; the new compound tetralithioethylene is also produced in the first reaction.

The preparation of polyolithium compounds from chlorocarbons in solution has been precluded by formation of reactive intermediates, such as dichlorocarbene, which react with the solvent. We have used a large excess of lithium vapour under high vacuum conditions to prevent reaction of intermediates with species other than atomic lithium.

Lithium was vaporised in a stainless steel reactor with a stainless steel Knudsen cell heated resistively, and the chlorocarbon vapour, at room temperature, was admitted through a tube above the Knudsen cell orifice. Products were collected on liquid nitrogen-cooled coldfinger.

A large excess (9–11 g) of high-purity lithium metal was vaporized during 30–45 min and allowed to react with *ca.* 1.5 g of CCl_4 . The product was a brittle grey-white solid which was extremely sensitive to air and moisture and, in contrast to lithium, exploded violently on contact with water. It was removed under argon and hydrolysed at 0 °C with D_2O in a vacuum line. The products were collected, expanded into a gas-phase molecular weight apparatus for a mass balance measurement and then recondensed.

The total yield of products varied from 95 to 99% (based on CCl_4). The products were then separated, collected, and characterized with a high-resolution double-focussing C.E.C.-21-110B mass spectrometer and again on a Hitachi RMU-6 mass spectrometer, both at 70 eV. Strong parent ions were observed for CD_4^+ (20.05639), C_2D_4^+ (32.05640), and C_4D_4^+ (28.02819). The yield of CD_4 ranged from 10 to 18% based on CCl_4 [average *ca.* 14% (1 mmol)]. The average

† O. Z. Wizard Memorial Postdoctoral Fellow.

yield of C_4D_4 was 61% (ca. 3.4 mmol) and the average yield of C_5D_4 was 20% (ca. 1.1 mmol). A derivative of the reactive solid was formed with neat chlorotrimethylsilane, and a small amount of solid was recovered for spectroscopic work. Its n.m.r. spectrum showed a singlet at τ 5.80 ($CHCl_3$ internal standard), in agreement with the spectra reported for $C(SiMe_3)_4$.¹ The mass spectrum showed a parent peak at 504 and a $P-CH_3$ peak [$C(SiMe_3)_4$] with the appropriate isotope distribution for silicon. $C_2(SiMe_3)_4$ was also produced and was characterized by a parent peak at 316 with a silicon isotope pattern and a singlet in its n.m.r. spectrum.

Under similar experimental conditions, ca. 1.5 g of hexachloroethane was allowed to react with excess of lithium vapour. The very reactive solid was then hydrolysed with D_2O and handled similarly to the CCl_4 product. In several experiments the hydrolysis product was entirely C_2D_6 , and the mass spectra contained the parent ion $C_2D_6^+$ (36.08444), and ions for $C_2D_5^+$ (34.07010), CD_3^+ (18.02204), and CD_2^+ (16.02842). The yields averaged 80% based on C_2Cl_6 (ca. 5.1 mmol of C_2D_6). In other experiments where it appears that the lithium vapour concentration was less, 10–20% of $C_2D_4^+$ and $C_2D_2^+$ were observed and the total yield of deuterated products was still ca. 60%. The solid was also

treated with neat $ClSiMe_3$ and a small amount of solid product was recovered. It showed a strong mass spectral peak at m/e 231 [$C(SiMe_3)_4^+$] with the appropriate silicon isotopic pattern and a singlet in the $SiMe$ region in its n.m.r. spectrum. It is not surprising that no parent ion was observed for $C_4(SiMe_3)_4$ owing to the high degree of steric interference of the trimethylsilyl groups.

If the lithium concentration is reduced by a factor of two during the reaction with CCl_4 or C_2Cl_6 , the products are more complex and a number of high molecular weight products are observed after deuteration. Most are unsaturated species such as C_4D_2 and some contain as many as six carbon atoms. Presumably these result from recombination of reactive species such as dilithiocarbene instead of further reaction with lithium.

The reaction of lithium vapour with chlorocarbons at high temperatures appears to provide a general route to the little known polylithiocarbons. Present work is directed toward finding satisfactory solvents for these interesting species.

This work was supported by the Advanced Research Projects Agency. The authors thank Dr. Charles Hignite and Professor Klaus Biemann for high resolution mass spectra.

(Received, 4th July 1972; Com. 1163.)

¹ R. L. Meeley and M. I. Scott, *J. Organometallic Chem.*, 1965, 4, 98.

document not included

REPORT DOCUMENTATION PAGE		READ INSTRUCTIONS BEFORE COMPLETING FORM
1. REPORT NUMBER #2	2. GOVT ACCESSION NO.	3. RECIPIENT'S CATALOG NUMBER
4. TITLE (and Subtitle) Research in Materials (Chemical Synthesis Using High Temperature Lithium Vapor Species)		5. TYPE OF REPORT & PERIOD COVERED Final Technical 1 July 1975 - 30 Sept. 1976
7. AUTHOR(s) R. J. Tagow		6. PERFORMING ORG. REPORT NUMBER
9. PERFORMING ORGANIZATION NAME AND ADDRESS Massachusetts Institute of Technology Center for Materials Science & Engineering Cambridge, Mass. 02139		8. CONTRACT OR GRANT NUMBER(s) N00014-75-C-1084
11. CONTROLLING OFFICE NAME AND ADDRESS Procuring Contracting Officer Office of Naval Research Dept. of Navy, Arlington, Va. 22217		10. PROGRAM ELEMENT, PROJECT, TASK AREA & WORK UNIT NUMBERS 5D10
14. MONITORING AGENCY NAME & ADDRESS (if different from Controlling Office) ONR Resident Representative Massachusetts Institute of Technology Room E49-629 Cambridge, Mass. 02139		12. REPORT DATE 30 Sept 1976
		13. NUMBER OF PAGES 8
16. DISTRIBUTION STATEMENT (of this Report) Unlimited		15. SECURITY CLASS. (of this report) Unclassified
17. DISTRIBUTION STATEMENT (of the abstract entered in Block 20, if different from Report) Unlimited		15a. DECLASSIFICATION/DOWNGRADING SCHEDULE
18. SUPPLEMENTARY NOTES		
19. KEY WORDS (Continue on reverse side if necessary and identify by block number) lithium, polylithium compounds, high temperature chemistry, organolithium compounds, polymeric intermediates, reactive intermediates		
20. ABSTRACT (Continue on reverse side if necessary and identify by block number) Recent work in our laboratory has resulted in the discovery of several routes to polylithiocarbon, perlithiocarbon, and inorganic polylithium species. Previously for these classes of compounds, there were very few known examples, and there were no general synthetic routes in the litera- ture. The new synthetic methods are all in the early stages of development and all involve the reaction of high temperature lithium vapor in the range of 800-1000°C with various organic, inorganic and polymeric species.		

During the past year we have succeeded in the synthesis of the first polylithioalkanes, tetralithiomethane, $C(Li)_4$, and hexalithioethane, C_2Li_6 . We have also prepared hexalithiobenzene, C_6Li_6 , and presently have characterized over thirty such polylithium compounds. An intensive study of these species is now underway and efforts are underway to prepare other polylithiated species. It now appears that polythiocarbons will be very useful reagents in organic synthesis as well as important monomers and crosslinking agents in polymer synthesis. The synthesis of several types of three dimensional polymers and high temperature materials is under way and is based in routes involving these new polylithium species. The preparation of new series of diamond-like polymeric materials has been proposed and should result in a class of high performance materials. Very significant progress has been made over the last year in the polymer area, although a significant amount of time and effort was spent on the construction of high temperature-high pressure apparatus for such syntheses. Polylithium compounds may also be useful as catalysts.